

Integrated Adsorber Concepts for Use in Direct Air Capture and Power-to-Gas Applications

Zur Erlangung des akademischen Grades eines

Dr.-Ing.

von der Fakultät Bio- und Chemieingenieurwesen
der Technischen Universität Dortmund
genehmigte Dissertation

vorgelegt von

M.Sc. Carsten Drechsler

aus

Castrop-Rauxel

Tag der mündlichen Prüfung: 25.11.2021

1. Gutachter: Prof. Dr. David W. Agar
2. Gutachter: Prof. Dr.-Ing. Marcus Grünewald

Dortmund 2021

© Carsten Drechsler 2021

This work is subject to copyright. All rights are reserved. For reproduction, storage or transmission, whether of the whole work or of part of this publication, in any form or by any means, prior written permission of the author must be obtained.

*"Our knowledge can be only finite,
while our ignorance must necessarily be infinite."*

Karl Raimund Popper (1902–1994)¹

Acknowledgments

This contribution has been realized during my stay as a graduate research assistant at the Chair of Chemical Reaction Engineering (CVT), TU Dortmund University, from March 2017 to May 2021. I would like to use this opportunity to thank the various people who supported me during this time.

I would especially like to thank Prof. David W. Agar for the opportunity of realizing this work in the friendly and supporting environment at the CVT Chair. I really appreciate our conversations and his endless support and guidance, not only with respect to the research work, but also from a general academic and especially personal point of view.

I also would like to express my special thanks to Prof. Marcus Grünewald, Prof. Norbert Kockmann and PD Dr.-Ing. Christoph Held who acted as referees and chairman of the examination board, respectively. I really value their interest in my research work.

Realization of this work was significantly eased by the supportive environment within the Faculty of Biochemical and Chemical Engineering. Of the various chairs of which the scientific and technical staff was always available with support on a theoretical and experimental level, I would like to mention in particular the Chairs of Fluid Mechanics and of Biomaterials and Polymer Sciences. In this context, I would also like to thank the electrical-, glass- and mechanical workshops of TU Dortmund University. Realization of the experimental setups would hardly have been possible without their great work.

My special thanks go to the great team of the CVT chair. I would like to make a special mention of the administrative and technical staff, who supported the research work by enabling a pleasant and productive working atmosphere. Also, I thankfully emphasize the very enriching collaborations with the students, who have realized their research internships and theses within the framework of this project or have participated in it as student assistants. With regard to the scientific colleagues, probably a large part of the following pages would not suffice to express my gratitude duly. I have been most privileged to be part of such a great scientific team and even more important to call you my friends. None of you have ever hesitated to share knowledge or offer support, and the various activities we have realized alongside our research work have been very enriching not only during my time at the CVT Chair, but also beyond.

Last, but not least, I can not express in words the gratitude I have for my friends and family. In particular, I would like to name my parents Monika and Uli, my grandmother Martha, my twin brother Tobias and his wife Miriam, and finally my wife Jana. You have been the center of my life over the past decades and made it something special. Without the everlasting kindness of all of you, the realization of this contribution would not have been possible.

Zusammenfassung

Die Anwendung technologischer Konzepte zur direkten Abtrennung des Treibhausgases Kohlenstoffdioxid (CO₂) aus atmosphärischer Luft (*Direct Air Capture, DAC*) wird als einer der vielversprechendsten Ansätze zur Abschwächung des anthropogenen Treibhauseffekts betrachtet. Deren großtechnischer Einsatz wird jedoch durch verschiedene intrinsische Limitierungen erschwert, welche sich insbesondere aus dem stark verdünnten Zustand von CO₂ in der Atmosphäre ergeben und in einen unzulässig hohen CO₂-spezifischen Energiebedarf des Abtrennungsprozesses resultieren können.

Durch Detailmodellierung und Simulationsstudien wird gezeigt, dass die in dieser Arbeit entwickelten Wärmeintegrationsstrategien und deren technische Realisierungen innerhalb neuartiger *Band-* (*MBtA*) und *Wanderbettadsorberkonzepte* (*MBdA*) eine signifikante Reduktion des CO₂-spezifischen Wärmebedarfs von thermischen Sorbentregenerationskonzepten ermöglichen. Die Problematik von Wasserkoadsorption auf *DAC*-Sorbentien, welche im Rahmen ausführlicher experimenteller Studien innerhalb dieser Arbeit bestätigt wird, kann jedoch zu einem zusätzlichen, signifikanten CO₂-spezifischen Wärmebedarf innerhalb des Regenerationszyklus des Sorbents führen. Insbesondere eine Rückgewinnung der im desorbierten Wasserdampf gespeicherten Latentwärme durch *mechanische Brüdenkompression* (*MVR*) wird innerhalb dieser Arbeit als ein vielversprechender ingenieurtechnischer Ansatz zur Reduzierung der H₂O-Koadsorption bedingten Energiestrafe identifiziert.

Die entwickelten Konzepte werden innerhalb eines *Power-to-Gas* (*PtG*) Prozesses als wärmeeffiziente CO₂-Quelle integriert. In diesem Zusammenhang zeigen durchgeführte Detailsimulationen und Pinchanalysen, dass durch eine gezielte Ausnutzung der Synergien innerhalb der Prozessstruktur ein hoch-ressourceneffizienter *DAC-PtG* Prozess realisiert werden kann. Dieser ermöglicht eine autotherme Produktion von Methan ausschließlich auf der Basis von erneuerbaren Energien und den Edukten Kohlenstoffdioxid und Wasser, welche aus atmosphärischer Luft gewonnen werden.

Abstract

The application of technological concepts for removal of the greenhouse gas carbon dioxide (CO₂) from the atmosphere (*direct air capture, DAC*) is considered to be one of the most promising approaches to mitigate the anthropogenic greenhouse effect. But its large-scale application is hampered by several intrinsic limitations. These result in particular from the highly diluted state of CO₂ in the atmosphere and can lead to an impedingly high CO₂-specific energy demand of the capture process.

In-depth modeling and simulation show that the heat integration strategies developed in this work and their technical realization within novel *belt (MBtA)* and *moving bed adsorber (MBdA)* concepts allow for a significant reduction of the CO₂-specific heat demand of thermal sorbent regeneration concepts. However, the problem of water co-adsorption on *DAC* sorbents, which is confirmed by experimental studies within the framework of this contribution, can lead to an additional, significant CO₂-specific heat demand within the sorbent regeneration cycle. Recovery of the latent heat stored in the desorbed water vapor by *mechanical vapor compression (MVR)* is identified as a promising engineering approach to reduce the energy penalty attributed to H₂O co-adsorption.

The concepts developed are integrated as heat-efficient CO₂ sources within a *power-to-gas (PtG)* process. Detailed modeling and pinch analysis reveal that a highly resource-efficient *DAC-PtG* process can be realized by targeted utilization of the synergies within the process structure. Autothermal production of methane solely based on renewable energy supply and on the educts carbon dioxide and water, captured from ambient air, seems feasible.

Publications

Parts of this thesis have been published in the contributions outlined below, which were realized during the preparation of this work. Paraphrases and results of the original contributions have been used within this thesis, with modifications being applied whenever considered reasonable. The author significantly contributed to all contributions named, e.g., with regard to idea generation, design of the work, modeling/simulation, conduction of experimental work, data evaluation and preparation of manuscripts.

Peer-reviewed journal articles

1. Drechsler, C.; Agar, D. W. Characteristics of DAC operation within integrated PtG concepts. *Int. J. Greenhouse Gas Control* **2021**, *105*, 103230.
2. Drechsler, C.; Agar, D. W. Intensified integrated direct air capture - power-to-gas process based on H₂O and CO₂ from ambient air. *Appl. Energy* **2020**, *273*, 115076.
3. Drechsler, C.; Agar, D. W. Comparison of Highly Heat-Integrated Adsorber Concepts for Use in Direct Air Capture Processes. *Chem. Ing. Tech.* **2020**, *92*, 282–287.
4. Drechsler, C.; Agar, D. W. Investigation of water co-adsorption on the energy balance of solid sorbent based direct air capture processes. *Energy* **2020**, *192*, 116587.
5. Drechsler, C.; Agar, D. W. Simulation and optimization of a novel moving belt adsorber concept for the direct air capture of carbon dioxide. *Comp. Chem. Eng.* **2019**, *126*, 520–534.

Conference talks

1. Drechsler, C.; Agar, D. W. Development of an intensified integrated DAC-PtG process for sustainable production of CH₄ from CO₂ and H₂O. Presented at Wissenschaft trifft Wirtschaft: Forschung für eine klimaneutrale und wettbewerbsfähige Grundstoffindustrie, online, Germany, December 4, 2020.
2. Drechsler, C.; Agar, D. W. Hoch-Energieintegrierte Adsorberkonzepte für eine Anwendung in Direct Air Capture Verfahren. Presented at Jahrestreffen der ProcessNet-Fachgruppen Adsorption und Hochdruckverfahrenstechnik, Freiberg, Germany, February 18-20, 2019.

3. Asmanoglo, C.; Agar, D. W. Entwicklung wärmeintegrierter Adsorber/Desorber-Konzepte für eine Anwendung in Direct Air Capture (DAC) Technologien. Presented at Doktorandenseminar der 1. Statuskonferenz zur BMBF Fördermaßnahme CO₂Plus, Berlin, Germany, April 17-18, 2018.

Conference poster presentations

1. Drechsler, C.; Agar, D. W. Analyse der Wasser-Co-Adsorption auf die Energiebilanz von Direct Air Capture Verfahren mit festen Sorbentien. Presented at Abschlusskonferenz zur BMBF Fördermaßnahme CO₂Plus, Berlin, Germany, September 24-25, 2019.
2. Drechsler, C.; Agar, D. W. Highly heat-integrated temperature-vacuum-swing adsorption process for the direct air capture of carbon dioxide. Presented at Gordon Research Conference on Carbon Capture, Utilization and Storage, Les Diablerets, Switzerland, May 05-10, 2019.
3. Drechsler, C.; Agar, D. W. Highly heat-integrated temperature-vacuum-swing adsorption process for the direct air capture of carbon dioxide. Presented at Gordon Research Seminar on Carbon Capture, Utilization and Storage, Les Diablerets, Switzerland, May 04-05, 2019.
4. Asmanoglo, C.; Agar, D. W. Entwicklung wärmeintegrierter Adsorber/Desorber-Konzepte für eine Anwendung in Direct Air Capture (DAC) Technologien. Presented at 1. Statuskonferenz zur BMBF Fördermaßnahme CO₂Plus, Berlin, Germany, April 17-18, 2018.

Contents

List of tables	xv
List of figures	xvii
Notation	xix
Abbreviations	xix
Chemical species	xxi
Variables and parameters	xxiii
Indices	xxvii
Dimensionless numbers	xxxiii
1 Introduction	1
1.1 Motivation	3
1.1.1 Global warming and greenhouse gases	3
1.1.2 International responses to global warming	4
1.1.3 Scientific contributions to efforts against global warming	4
1.2 Negative emission technologies	7
1.3 Scope of the research conducted	10
2 Basic considerations of DAC	13
2.1 State of the art	15
2.2 Intrinsic constraints of DAC	16
2.2.1 Thermodynamic minimum energy demand	17
2.2.2 Pressurizing the air	18
2.2.3 Thermal energy demand	21
2.2.4 Ab- and adsorption concepts in DAC applications	21
2.3 Approaches to heat integrated DAC concepts	22
2.3.1 The minimum degree of heat integration within the DAC unit	22
2.3.2 Approaches to increase the efficiency of thermal integration	24
2.4 Summary and conclusion	30
3 Characterization of the sorbent	31
3.1 State of the art	33
3.1.1 Sorbents for DAC	33
3.1.2 Adsorption mechanism of CO ₂ and H ₂ O on SAS	34

3.1.3	Lewatit VP OC 1065	35
3.2	Adsorption properties of the sorbent	36
3.2.1	Materials and methods	36
3.2.2	Adsorption properties under dry conditions	40
3.2.3	Adsorption properties under humid conditions	44
3.3	Additional properties of the sorbent	48
3.3.1	Mechanical, thermophysical and chemical properties	48
3.3.2	Thermal stability	49
3.4	Summary and conclusion	50
4	Approaches to intensified heat integrated DAC units	51
4.1	State of the art	53
4.2	Conceptual design	54
4.2.1	General considerations	54
4.2.2	Moving belt adsorber: conceptual design	55
4.2.3	Moving bed adsorber: conceptual design	56
4.3	Feasibility study and constraints	57
4.3.1	Sorbent movement and gas sealing	58
4.3.2	Heat and mass transfer	59
4.3.3	Large-scale realization	62
4.4	In-depth simulation	62
4.4.1	Simulation results TCSA – MBtA	63
4.4.2	Simulation results TVCSA – MBdA	68
4.5	Experimental investigation of transport phenomena	70
4.6	Cost estimation and net negative emission	71
4.7	Summary and conclusion	74
5	Handling water co-adsorption	75
5.1	State of the art	77
5.2	Quantifying the influence of water co-adsorption	77
5.2.1	Energy penalty of water co-adsorption	78
5.2.2	Water desorption on unit operation level	79
5.3	Counteracting the influence of water co-adsorption	81
5.3.1	General considerations	81
5.3.2	Post-desorption recovery	83
5.3.3	Concept to counteract the influence of water co-adsorption	90
5.4	Summary and conclusion	91
6	Intensified mass and energy integrated DAC - PtG process	93
6.1	State of the art	95
6.2	Methanation of CO ₂	96
6.3	Process design and key process units	97
6.3.1	Basic considerations	97
6.3.2	Detailed investigation of electrolysis operation	102
6.3.3	Detailed investigation of reactor operation	105

6.4	Process performance	107
6.4.1	Potential for autothermal operation	107
6.4.2	Process water balance	108
6.4.3	Influence of DAC operation point on process performance	110
6.4.4	Energy flow analysis	114
6.4.5	Economics and ecological impact	117
6.5	Summary and conclusion	118
7	Conclusions and implications for future research	119
7.1	Conclusions	121
7.2	Implications for future research	123
A	Appendix: Characterization of the sorbent	125
A.1	State of the art: liquid sorbents	125
A.2	Applicability of BTC and TGA: ranges of validity	125
A.3	BTC experiments	126
A.3.1	Material and experimental design	126
A.3.2	Sorbent loading	132
A.3.3	Pressure levels	136
A.3.4	Temperature levels	137
A.3.5	Relative humidity levels	137
A.3.6	Kinetic parameters	137
A.3.7	Error estimation	144
A.4	TGA experiments	149
A.4.1	Material and methods	149
A.4.2	Sorbent mass	150
A.4.3	Sorbent loading	150
A.4.4	Pressure levels	151
A.4.5	Temperature levels	151
A.4.6	Kinetic parameters	152
A.4.7	Error estimation	155
A.5	Isotherm data fitting	156
A.6	Additional properties of the sorbent	158
A.6.1	Density and void fraction	158
A.6.2	Flowability of the sorbent	160
B	Appendix: Approaches to intensified heat integrated DAC units	161
B.1	Energy demand and economics of DAC	161
B.2	Feasibility study	161
B.2.1	Sorbent movement and gas sealing	161
B.2.2	Heat and mass transfer	161
B.2.3	Large scale realization	166
B.3	MBtA	167
B.3.1	MBtA: thermophysical and adsorption properties	167
B.3.2	MBtA: model	170

B.3.3	MBtA: numeric	174
B.3.4	MBtA: parameter set	174
B.4	MBdA	175
B.4.1	MBdA: thermophysical and adsorption properties	175
B.4.2	MBdA: model	175
B.4.3	MBdA: numeric	179
B.4.4	MBdA: parameter set	179
B.5	Experimental investigation of transport phenomena	179
B.5.1	Experimental setting	180
B.5.2	Adsorber design	180
B.5.3	Experimental procedure and data evaluation	181
B.6	Cost estimation	183
B.6.1	Equipment-related costs	183
B.6.2	Sorbent-related costs	187
B.6.3	Energy-related costs and carbon footprint	187
B.6.4	Additional component-related costs	188
B.6.5	Zone length-specific contributions to CO ₂ -specific capture costs	188
C	Appendix: Handling water co-adsorption	189
C.1	Thermophysical properties	189
C.2	Equilibrium adsorber model	189
C.3	Integrated DAC–MVR operation	191
C.3.1	DAC unit operation	191
C.3.2	Heat transfer between DAC and MVR	191
C.3.3	Mechanical vapor recompression MVR	191
C.3.4	Characteristic energy flows	193
D	Appendix: Intensified heat and mass integrated DAC - PtG process	195
D.1	Thermophysical properties	195
D.1.1	Species in the liquid and gas/vapor phase	195
D.1.2	Zeolite 3A and water adsorption on zeolite 3A	195
D.1.3	Lewatit and adsorption of species on Lewatit	196
D.2	Models of the main equipment	196
D.2.1	Model: condenser	196
D.2.2	Model: direct air capture unit	197
D.2.3	Model: electrolysis	202
D.2.4	Model: evaporator	204
D.2.5	Model: heater and cooler	205
D.2.6	Model: mixing of streams	205
D.2.7	Model: multi-stage vapor recompression unit	205
D.2.8	Model: pump	205
D.2.9	Model: reactor	206
D.2.10	Model: throttling valve	207
D.2.11	Model: water adsorber	207
D.3	Process operation	210

D.3.1	Condensers	210
D.3.2	Heating of streams before the Sabatier reactors	210
D.3.3	Water adsorber regeneration cycle	210
D.3.4	Water recycle	211
D.3.5	Additional water supply	214
D.3.6	Strip gas supply to the DAC unit	214
D.3.7	Numeric for recycles	215
D.4	Operation parameters used in the parameter studies	216
D.4.1	Operation parameters: reference configuration	216
D.4.2	Operation parameters: reactor operation	216
D.4.3	Operation parameters: potential for autothermal operation	217
D.4.4	Operation parameters: process water balance	217
D.4.5	Operation parameters: DAC unit operation point	217
D.4.6	Operation parameters: energy flow analysis	217
	References	219
	Student support	247
	Additional support	251
	Curriculum vitae	253

List of tables

1.1	Comparison of different approaches to NETs	9
2.1	Basic comparison of the direct and indirect heat integration concept	29
3.1	Toth isotherm parameter sets	41
3.2	Isotherm data fit of H ₂ O adsorption on Lewatit	46
3.3	CO ₂ adsorption on Lewatit under humid conditions	47
3.4	Mechanical, thermophysical and chemical properties of Lewatit	49
4.1	Comparison of MBtA and MBdA concept	57
4.2	MBtA: influence of thermal conductivity on MBtA performance	67
6.1	Synergies within the DAC–PtG process	99
A.1	BTC: equipment and material	130
A.2	BTC: characteristics of adsorber	132
A.3	BTC: CO ₂ loading in dry atmosphere	134
A.4	BTC: CO ₂ loading in humid atmosphere	135
A.5	BTC: H ₂ O loading	136
A.6	BTC: kinetic constant obtained from 1-parameter fit	142
A.7	BTC: Arrhenius parameters obtained from 1-parameter fit	142
A.8	BTC: effective diffusion coefficient estimated from kinetic constant	143
A.9	BTC: effective diffusion coefficient estimated based on theory	143
A.10	BTC: error estimation for CO ₂ adsorption from dry gas phase	145
A.11	BTC: error estimation for H ₂ O adsorption	147
A.12	BTC: error estimation for CO ₂ adsorption from humid gas phase	148
A.13	TGA: equipment and material	149
A.14	TGA: sorbent loading	151
A.15	TGA: kinetic constant obtained from 2-parameter fit	154
A.16	TGA: exponent of the driving force term obtained from 2-parameter fit	154
A.17	TGA: kinetic constant obtained from 1-parameter fit	155
A.18	TGA: Arrhenius parameters obtained from 1-parameter fit	156
A.19	TGA: error estimation	157
B.1	DAC technologies: state of the art	162
B.2	MBtA: thermal conductivities used in evaluation of transfer resistances	166
B.3	MBtA: thermophysical properties used in the MBtA concept	168

B.4	MBtA: spatial boundary condition of temperature profile	172
B.5	MBtA: spatial boundary condition of concentration profile	173
B.6	MBtA: parameter set	174
B.7	MBdA: thermophysical properties of the thermal oil	175
B.8	MBdA: parameter set	180
B.9	Transport phenomena: equipment and material	181
B.10	Transport phenomena: operation and design parameters	182
B.11	Costs: estimates for additional costs	185
B.12	Costs: contributions to zone length-specific equipment costs	187

List of figures

1.1	Evolution of atmospheric CO ₂ content and of CO ₂ emissions	5
1.2	Mitigation pathways compatible with the 1.5 °C target	6
1.3	CO ₂ mitigation strategies	7
1.4	Graphical abstract of thesis content	11
2.1	Thermodynamic minimum energy demand for CO ₂ separation	18
2.2	Pressurization energy and pressure losses in air capture applications	19
2.3	Influence of air velocity on DAC design	20
2.4	Minimum efficiency of thermal integration in DAC unit	24
2.5	Basic temperature profiles for heat integration between DAC units	25
2.6	Thermal integration of multiple DAC units	26
2.7	Concepts for integration of sorbent sensible heat	27
3.1	Chemical structure of Lewatit VP OC 1065	35
3.2	BTC: basic measurement principle	37
3.3	BTC: simplified flow diagram of the experimental setup	38
3.4	TGA: basic measuring principle and experimental setting	39
3.5	Isotherm data of CO ₂ adsorption on Lewatit	40
3.6	Isosteric heat of adsorption	43
3.7	Kinetic fit to BTC and TGA data	44
3.8	H ₂ O adsorption on Lewatit	47
3.9	CO ₂ adsorption on Lewatit under humid conditions	48
4.1	Evaluation of TVCSA operation	55
4.2	Moving belt adsorber concept	56
4.3	Moving bed adsorber concept	57
4.4	Energy demand of sorbent movement	58
4.5	Influence of the solid transfer medium on conductive heat losses	60
4.6	Improvement of heat transfer	61
4.7	Large-scale realization	63
4.8	MBtA: model	63
4.9	MBtA: characteristic profiles	64
4.10	MBtA: operation and design parameters	66
4.11	MBdA: simulation results	69
4.12	Experimental investigation of mass transport limitations	70
4.13	MBtA: economy and ecology	72

4.14	MBdA: economy and ecology	73
5.1	Influence of H ₂ O co-desorption on DAC energy demand	78
5.2	Working capacities based on equilibrium adsorber models	79
5.3	Species' partial pressure in the DAC product gas	80
5.4	Measures to counteract the influence of water co-adsorption	81
5.5	Membrane- and sorbent-based strategies to limit H ₂ O co-adsorption influence	84
5.6	Principle of multi-stage mechanical vapor recompression	85
5.7	MVR: water recovery and not recovered water	86
5.8	MVR: contributions to MVR–DAC energy balance and energy ratios . . .	87
5.9	MVR: compression energy requirement	88
5.10	MVR: energy ratios, compression ratios and outlet temperatures	89
6.1	Analysis of reaction equilibrium of the methanation reaction	97
6.2	Process: water and heat management system	98
6.3	Process: flow sheet of the intensified integrated DAC–PtG process	100
6.4	Electrolysis: rel. electric energy demand and electrochem. compression . . .	102
6.5	Electrolysis: overall energy demand and relative energy demand	103
6.6	Electrolysis: water efficiency and product gas mole fraction	104
6.7	Reactor: temperature, catalyst mass and CO ₂ conversion	106
6.8	Process: composite curves for operation at different cell voltages	108
6.9	Process: major water sinks, sources and recycles	109
6.10	DAC unit: influence of slip ratio on catalyst mass and conversion	110
6.11	DAC unit: influence of slip ratio on reactor temperature and product gas .	111
6.12	DAC unit: DAC product gas composition and level of MVR water recovery	112
6.13	DAC unit: reaction section educt gas water content and catalyst mass . . .	113
6.14	DAC unit: hydrogen losses and attributed energy penalties	114
6.15	Process: composite curves	115
6.16	Process: characteristic energy flows	116
7.1	Graphical abstract of main findings	121
A.1	BTC: detailed flow sheet	128
A.2	BTC: humidifier	129
A.3	BTC: closeup of adsorber	131
A.4	BTC: breakthrough curves for CO ₂ and H ₂ O	133
A.5	BTC: visualization of parameters obtained from the kinetic fit	142
A.6	TGA: visualization of parameters obtained from 2-parameter kinetic fit . .	153
A.7	TGA: visualization of parameters obtained from 1-parameter kinetic fit . .	155
A.8	Isotherm data of CO ₂ adsorption on Lewatit	159
A.9	Parity plot for H ₂ O loadings (BET and GAB isotherm model)	160
B.1	Mechanical tension in wire and wire mass fraction	165
B.2	Adsorber design for experimental analysis of mass transport phenomena . .	182

Notation

Abbreviations

<i>AE</i>	<i>Alkaline electrolysis</i>
<i>APS</i>	<i>American Physical Society</i>
<i>AR</i>	<i>Afforestation/reforestation</i>
<i>BC</i>	<i>Biochar</i>
<i>BECCS</i>	<i>Bioenergy with carbon capture and storage</i>
<i>BET</i>	<i>Brunauer, Emmett, Teller</i>
<i>BTC</i>	<i>Breakthrough curve</i>
<i>CCS</i>	<i>Carbon capture and storage</i>
<i>CCSU</i>	<i>Carbon capture and storage/utilization</i>
<i>CCU</i>	<i>Carbon capture and utilization</i>
<i>CPU</i>	<i>Central processing unit</i>
<i>CSS</i>	<i>Cyclic steady state</i>
<i>DAC</i>	<i>Direct air capture</i>
<i>EDS</i>	<i>Energy-dispersive X-ray spectroscopy</i>
<i>EW</i>	<i>Enhanced weathering</i>
<i>FVS</i>	<i>Finite volume scheme</i>
<i>GAB</i>	<i>Guggenheim, Anderson, de Boer</i>
<i>GHG</i>	<i>Greenhouse gases</i>
<i>GMST</i>	<i>Global mean surface temperature</i>
<i>IPCC</i>	<i>Intergovernmental Panel on Climate Change</i>
<i>IR</i>	<i>Infrared spectroscopy</i>
<i>ISBL</i>	<i>Inside battery limits</i>
<i>LCA</i>	<i>Life cycle assessment</i>
<i>LHHW</i>	<i>Langmuir-Hinshelwood-Hougen-Watson</i>

<i>LU</i>	<i>Land use</i>
<i>MBdA</i>	<i>Moving bed adsorber</i>
<i>MBtA</i>	<i>Moving belt adsorber</i>
<i>MOF</i>	<i>Metal-organic framework</i>
<i>MOL</i>	<i>Method of lines</i>
<i>MSA</i>	<i>Moisture-swing-adsorption</i>
<i>MVR</i>	<i>Mechanical vapor recompression</i>
<i>n-BET</i>	<i>BET model with limited number of adsorption layers</i>
<i>NET</i>	<i>Negative emission technology</i>
<i>OF</i>	<i>Ocean fertilization</i>
<i>PDAE</i>	<i>Partial differential algebraic equation</i>
<i>PEM</i>	<i>Polymer electrolyte membrane</i>
<i>PtG</i>	<i>Power-to-gas</i>
<i>PtL</i>	<i>Power-to-liquid</i>
<i>PtX</i>	<i>Power-to-X</i>
<i>RF</i>	<i>Radiative forcing</i>
<i>SAS</i>	<i>Supported amine sorbents</i>
<i>SCS</i>	<i>Soil carbon sequestration</i>
<i>SNG</i>	<i>Substitute natural gas</i>
<i>SOEC</i>	<i>Solid oxide electrolysis</i>
<i>SST</i>	<i>Sea surface temperature</i>
<i>TCSA</i>	<i>Temperature-composition-swing-adsorption</i>
<i>TGA</i>	<i>Thermogravimetric analysis</i>
<i>TPCSA</i>	<i>Temperature-pressure-composition-swing-adsorption</i>
<i>TSA</i>	<i>Temperature-swing-adsorption</i>
<i>TVCSA</i>	<i>Temperature-vacuum-composition-swing-adsorption</i>
<i>TVSA</i>	<i>Temperature-vacuum-swing-adsorption</i>
<i>UN</i>	<i>United Nations</i>
<i>UNCED</i>	<i>United Nations Conference on Environment and Development</i>
<i>UWS</i>	<i>Upwind scheme</i>
<i>V2A</i>	<i>V2A steel, steel 1.4301</i>

Chemical species

ABS	Acrylonitrile butadiene styrene
Air	Air
Ami	Amine
Al ₂ O ₃	Aluminum oxide
B	Base
C	Carbon (element)
CH ₄	Methane
CO	Carbon monoxide
CO ₂	Carbon dioxide
Ca	Calcium
CaCO ₃	Calcium carbonate
CaO	Calcium oxide
Ca(OH) ₂	Calcium hydroxide
Cu	Copper
EG	Expanded natural graphite
H	Hydrogen (element)
H ₂	Hydrogen (molecule)
H ₂ O	Water
Ine	Inert
KOH	Potassium hydroxide
N	Nitrogen (element)
N ₂	Nitrogen (molecule)
N ₂ O	Nitrous oxide
Na	Sodium
NaOH	Sodium hydroxide
O	Oxygen (element)
O ₂	Oxygen (molecule)
PEI	Polyethyleneimine
PS	Polystyrene
PTFE	Polytetrafluorethylen
R	Rest

Variables and parameters

a	$\text{m}^2 \text{kg}^{-1}$ $\text{m}^2 \text{m}^{-2}$	Specific area
a_{BET}	$\text{m}^2 \text{kg}^{-1}$	<i>BET</i> surface area
b_{Tot}	Pa^{-1}	Adsorption affinity (<i>Toth</i> model)
c	mol m^{-3}	Molar concentration
c_{BET}	—	Adsorption affinity (<i>BET</i> and <i>GAB</i> model)
c_p	$\text{J kg}^{-1} \text{K}^{-1}$ $\text{J K}^{-1} \text{mol}^{-1}$	Heat capacity at constant pressure
c_{wet}	Varies	Constant in isotherm fit under humid conditions
c	Varies	Specific costs
$CEPCI$	—	<i>Chemical Engineering Plant Cost Index</i>
CI	—	<i>Carr index</i>
C	\$	Costs
D_{dif}	$\text{m}^2 \text{s}^{-1}$	Diffusion coefficient
$D_{\text{dif,eff}}^*$	$\text{m}^2 \text{s}^{-1}$	Pseudo, lumped diffusion coefficient
D_{dis}	$\text{m}^2 \text{s}^{-1}$	Dispersion coefficient
D	m	Diameter
e	J mol^{-1}	Specific energy
E_A	J mol^{-1}	Activation energy
\dot{E}	J s^{-1}	Energy flow
f	Varies	General function
$f_{D_{\text{dif}}}$	—	Correction factor in calculation of binary diffusion coefficients
f_{frc}	—	Friction coefficient
f_{wei}	Varies	Weighting function
g	J mol^{-1}	Specific <i>Gibbs</i> free energy
h	J kg^{-1} J mol^{-1}	Specific enthalpy
h_{df}	$\text{J K}^{-1} \text{m}^{-2} \text{s}^{-1}$	Driving force constant
H	J	Enthalpy
H	m	Distance, height, width
i	—	Counting index, index of specie, unit, property or iteration
I	—	Number of species, streams, units or iterations

Notation

k_{df}	m s^{-1} $\text{kg}^{n_{ord}-1} \text{mol}^{1-n_{ord}} \text{s}^{-1}$	Driving force constant
k_{Bol}	J K^{-1}	<i>Boltzmann</i> constant
k_{Far}	A s mol^{-1}	<i>Faraday</i> constant
k_{Hen}	$\text{mol Pa}^{-1} \text{kg}^{-1}$	<i>Henry</i> constant
K_{eq}	–	Equilibrium constant
K_{GAB}	–	Multilayer correction factor (<i>GAB</i> model)
L	m	Length, width
m	kg	Mass
M	mol kg^{-1}	Molar mass
\dot{m}	kg s^{-1}	Mass flow
\dot{M}	$\text{kg m}^{-2} \text{s}^{-1}$	Specific mass flow
n	mol	Number of moles
n_{BET}	–	Number of layers (<i>BET</i> model)
n_{ord}	–	Reaction order
\dot{n}	mol s^{-1}	Mole flow
\dot{N}	$\text{mol m}^{-2} \text{s}^{-1}$	Specific mole flow
p	Pa	Pressure
q	J mol^{-1}	Specific heat
\mathbf{q}	mol kg^{-1}	Sorbent loading
$\mathbf{q}_{max,Tot}$	mol kg^{-1}	Maximum sorbent loading (<i>Toth</i> model)
Q	J	Heat
\dot{q}	$\text{J mol}^{-1} \text{s}^{-1}$ $\text{J m}^{-2} \text{s}^{-1}$	Specific heat flow
\dot{Q}	J s^{-1}	Heat flow
r_{rea}	mol s^{-1}	Rate of reaction
r_{th}	$\text{K}^1 \text{m}^2 \text{s}^1 \text{J}^{-1}$	Specific thermal resistance
R^2	–	Coefficient of determination
R_{id}	$\text{J K}^{-1} \text{mol}^{-1}$	Ideal gas constant
s	$\text{J K}^{-1} \text{mol}^{-1}$	Specific entropy
S	–	Selectivity
t	s	Time
t_{Tot}	–	Heterogeneity parameter (<i>Toth</i> model)
T	K $^{\circ}\text{C}$	Temperature

$T_{0,\text{Tot}}$	K	Reference temperature (<i>Toth</i> model)
u	m s^{-1}	Velocity
U	V	Voltage
v	$\text{m}^3 \text{kg}^{-1}$	Specific volume
V	m^3	Volume
\dot{V}	$\text{m}^3 \text{s}^{-1}$	Volume flow
x	m	Length coordinate (along the x-axis), parallel to bed movement, vertical direction
X	—	Conversion
y	—	Mole fraction (gas phase)
y	m	Length coordinate (along the y-axis), parallel to gas movement in adsorption zone, horizontal direction
z	m	Length coordinate (along the z-axis), orthogonal to gas movement in adsorption zone, horizontal direction
$\alpha_{0,\text{Tot}}$	—	<i>Toth</i> isotherm parameter
α_{rep}	°	Angle of repose
α_{unf}	—	Uniformity coefficient
δ_{err}	Varies	Error
$\Delta h_{0,\text{Tot}}$	J mol^{-1}	Adsorption enthalpy at zero loading (<i>Toth</i> model)
ϵ	—	Porosity
ϵ_{pai}	J	Minimum of pair-potential energy
η	—	Efficiency
λ	$\text{J K}^{-1} \text{m}^{-2} \text{s}^{-1}$	Thermal conductivity
μ	Pa s	Dynamic viscosity
ν	—	Stoichiometric coefficient
ρ	kg m^{-3}	Density

Notation

σ	N m^{-2}	Tension
σ_{col}	m	Collision diameter
τ	—	Tortuosity
ϕ	—	Ratio, fraction
ϕ_{Cot}	—	Contingency cost factor
$\phi_{\text{D\&E}}$	—	Design and engineering cost factor
ϕ_{ISBL}	—	Inside battery limits cost factor
ϕ_{OSBL}	—	Outside battery limits cost factor
ϕ_{rh}	—	Relative humidity
$\phi_{t_{\text{opr}}, t_{\text{yea}}}$	h a^{-1}	Operation time per year (8000 h a^{-1})
Φ	Varies	General variable, parameter, thermophysical quantity
Φ_{dec}	Varies	Decision variable
ψ	—	Void fraction
χ_{Tot}	—	<i>Toth</i> isotherm parameter
ω	—	Acentric factor
$\Omega_{D_{\text{dif}}}$	—	Collision integral for diffusion
Ω_{μ}	—	Collision integral for viscosity

Indices

0	Reference state
adi	Additional
ads	Adsorption
age	Aging
asp	Aspired
Ads	Adsorption unit, adsorption zone
Air	Air
Amb	Ambient, ambient conditions ($T = 298.15 \text{ K}$, $p = 10^5 \text{ Pa}$)
Ami	Amine
B	Bed
Belt	Belt
BB	Bed to Bed
BET	Brunauer, Emmett, Teller
BF	Bed to Fluid or vice versa
BG	Bed to Gas or vice versa
BT	Bed to transfer medium or vice versa
BW	Bed to wall or vice versa
cap	Captured
cha	Characteristic
coc	Co-current
col	Collision
com	Compression, compressibility
con	Condensation
coo	Cooling
cos	Construction
cri	Critical
cuc	Counter-current
Car	Carrier
Cat	Catalyst
Cha	Channel
Com	Compressor unit
Con	Condenser unit
Coo	Cooling zone, cooler
Cot	Contingency
dea	Dead time
dec	Decision
dep	Depreciation
dem	Demand

des	Desorption
df	Driving force
dir	Direct
dri	Drift
dry	Dry
DAC	<i>Direct air capture</i> unit
Des	Desorption zone
D&E	Design and engineering
eff	Effective
elc	Electrolysis
ele	Electric
emi	Emission
end	End
eql	Equilibrium
exc	Exchange
exp	Experiment
ext	External
Elc	Electrolysis unit
Elv	Elevator unit
Eqp	Equipment
Evp	Evaporator
fie	Fine
fin	Final
Fin	Fin
Fun	Functional unit
G	Gas phase
Gla	Glass
GAmb	Gas to ambient phase or vice versa
GEx	Gas to external phase or vice versa
GP	Gas to particle phase or vice versa
GT _L	Gas to transfer medium phase or vice versa, interface between gas and transfer medium phase
hea	Heating
Hea	Heating zone, heat exchanger unit
Hex	External heating zone
Hou	Housing
Hum	Humidifier
HyCO	CO hydrogenation
ide	Ideal

in	In
ind	Indirect
int	Integration
inv	Invest
Ine	Inert
IR	Infrared gas analyzer
ISBL	Inside battery limits
Ite	Iteration
kin	Kinetic
Knu	Knudsen
ldf	Linear driving force
lif	Lift
loa	Loaded, i.e., with adsorbed species
los	Loss
lv	Liquid phase to vapor phase or vice versa, evaporation
L	Liquid phase
Lew	<i>Lewatit VP OC 1065</i>
max	Maximum
mea	Measured
men	Mean
min	Minimum
mix	Mixture
mol	Molecular
mon	Mono
mul	Multi
Mat	Material
Mes	Mesh
Met	Methanation
MFC	Mass flow controller
Mix	Mixing chamber (unit)
MVR	Mechanical vapor recompression
noi	Measurement noise
ope	Open
opr	Operation
ord	Order
out	Out
OSBL	Outside battery limits
pin	Pinch

Notation

prs	Contact pressure
purge	Purge
P	Particle, particle phase
PEx	Particle to external phase or vice versa
PT _L	Particle to transfer medium phase or vice versa, interface between particle and transfer medium phase
Por	Pore
Prc	Process
Pro	Product
Prs	Contact pressure (unit)
Pum	Pump (unit)
rea	Reaction
rec	Recovery
ref	Reference
rel	Relative
rep	Repose (angle)
res	Residence time
rWGS	<i>Reverse water gas shift</i>
Rea	Reactor unit
sam	Sample
sat	Saturation
sca	Scaled
sen	Sensible
sep	Separation
sim	Simulation
sin	Sink
sli	Slip
spe	Specific
sta	Start
sup	Superficial
Sab	<i>Sabatier</i> reaction
Sca	Scale
Soa	Sorbate
Sol	Solid
Sor	Sorbent
Spe	Specie
Str	Stream
Sup	Support
tap	Tapped
the	Thermal
thn	Thermoneutral

T	Transfer medium (general)
T _L	Transfer medium liquid
TGA	<i>TGA</i> unit
The	Thermocouple
Tot	<i>Toth</i> isotherm model
unf	Uniformity
U	Unit
Voi	Void
wei	Weighting
wet	Wet
wor	Work
W	Wall
Wir	Wire
yea	Year
Z3A	<i>Zeolite 3A</i>
Σ	Sum, total

Dimensionless numbers

Bi	$\frac{k_{\text{dif}} \cdot L_{\text{cha}}}{D_{\text{dif}}}$	<i>Biot</i> number
Nu	$\frac{h_{\text{dif}} \cdot L_{\text{cha}}}{\lambda}$	<i>Nusselt</i> number
Pr	$\frac{\mu \cdot c_p}{\lambda}$	<i>Prandtl</i> number
Re	$\frac{\rho \cdot u \cdot L_{\text{cha}}}{\mu}$	<i>Reynolds</i> number
Sc	$\frac{\mu}{\rho \cdot D_{\text{dif}}}$	<i>Schmidt</i> number
Sh	$\frac{k_{\text{dif}} \cdot L_{\text{cha}}}{D_{\text{dif}}}$	<i>Sherwood</i> number

1 Introduction

Abstract

Carbon dioxide (CO₂) can be identified as one of the main *greenhouse gases* (*GHGs*) that cause global warming. Several strategies for reduction of its emissions and consecutive storage (*Carbon Capture and Storage, CCS*) or utilization (*Carbon Capture and Utilization, CCU*) have been developed in the last decades. However, the current evolution of the carbon dioxide content in the atmosphere indicates that the chance of meeting the targets formulated in the *Parisian Agreement on Climate Change* by solely reducing CO₂ emissions may already has been passed. In this respect, besides other *negative emission technologies* (*NETs*), *direct air capture* (*DAC*) processes that remove CO₂ from ambient air are identified as promising, additional measures in the attempt of preventing the serious long-term consequences caused by global warming.

This chapter is structured as follows:

Section 1.1 Motivation

motivates the research objectives by giving a brief overview of the problem of global warming and *greenhouse gas* emissions the world is currently facing. With special focus on CO₂, scientific contributions to limit global warming are outlined. An analysis of possible CO₂ mitigation pathways is carried out.

Section 1.2 Negative emission technologies

takes into account the results outlined in Section 1.1, which indicate that large-scale application of *NETs* will be of high importance at the end of this century. Thus, various approaches to *NETs* are compared. Results of this analysis underline high importance of increased research in intensified energy integrated *DAC* technologies.

Section 1.3 Scope of the research conducted

summarizes the results presented in Sections 1.1 - 1.2. Based on the key findings extracted, the research objectives of this contribution are formulated.

1.1 Motivation

The first major conclusion formulated in the *Intergovernmental Panel on Climate Change (IPCC)* fifth assessment report²

*”Human influence on the climate system is clear, and recent anthropogenic emissions of greenhouse gases are the highest in history”*²

indicates the current discrepancy between the awareness of the anthropogenic influence on the climate system and the countermeasures taken. Hereafter, the scientific data available with respect to global warming (Section 1.1.1) and the responses of the international community to this phenomenon (Section 1.1.2) are outlined. Motivated by this information, possible research scenarios to be realized with respect to *GHG* mitigation (Section 1.1.3) are investigated.

1.1.1 Global warming and greenhouse gases

The world’s *global mean surface temperature (GMST)* increase over the last 50 years has almost doubled compared to the previous century and the last decade was most likely the warmest period of the last century.² In good agreement with other publications^{3,4}, data provided by Morice et al.⁵ indicate a drastic increase in the mean temperature rise per decade from 0.062 °C (1880-2012) to 0.155 °C (1979-2012). The tendencies presented do not only show a significant acceleration of *GMST* increase, but also indicate that the magnitude of the increase is alarming. A similar conclusion can be drawn from the evolution of the world’s *sea surface temperature (SST)*. Temperature increases of up to 0.124 °C per decade have been observed with comparable accelerating tendencies being noticed.⁶⁻⁹

Strong correlations are recognizable between the evolution of key *GHG* concentrations in the atmosphere and global temperature increase. The nitrous oxide (N₂O) concentration of 332 ppb¹⁰ only exceeded its pre-industrial level (270 ppb in 1750¹¹) by 23 % in 2019, whereas significant higher increases for carbon dioxide (49 %, 278 ppm in 1750,¹² 413 ppm in 2020¹⁰) and methane (159 %, 722 ppb in 1750,¹³⁻¹⁵ 1867 ppb in 2019¹⁰) have been noticed. Moreover, there is general agreement that human activity-based primary emissions from fossil fuels¹⁶ and secondary emissions from land use are the main driving forces of these drastic increases¹⁵.

In this respect, especially CO₂ emissions have a considerable influence on the climate system. Its *Radiative Forcing (RF)*, i.e., its influence on the net change in the earth’s system energy balance over a defined period of time, of 1.7 W m⁻² between 1750 and 2011 accounts for more than half of the anthropogenic *GHG* induced *RF*.^{15,17} In other words, *GHGs* in the atmosphere decrease the net heat flow from earth to space. This is well known as *GHGs* reflect a fraction of the earth’s long-wave (infrared) heat radiation and, thus, decrease outgoing thermal radiation to space. As a consequence, the presence of naturally present *GHGs*, e.g., water vapor, is of high importance. Without them reflecting the thermal radiation of the earth, the global mean temperature would decrease to -18 °C.¹⁸ However, bearing in mind that the overall radiative flux from the sun is in the order of magnitude of 340 W m⁻²,¹⁹ the significant influence of *GHG* emissions on the

earth's energy system becomes apparent. Presence of anthropogenic *GHGs* unbalances the earth's energy system and in response to this perturbation the system follows a trajectory to a new equilibrium state at an elevated temperature level.

1.1.2 International responses to global warming

Noticing the increasing amount of environmental problems, the world might be confronted with in the 21st century, the first *United Nations (UN)* meeting on behalf of a sustainable development of the world was already held in Rio de Janeiro, Brazil, in June 1992. The major result of this *United Nations Conference on Environment and Development (UNCED)*²⁰ was the agreement on *Agenda 21*²¹, which might be interpreted as a guideline to achieve a more sustainable development of the world in the centuries to come.

To ensure the realization of the objectives stated in this agenda, the first *United Nations Climate Change Conference*²² took place in Berlin, Germany, in 1995. The *Berlin Mandat*²³ agreed on at this conference built the basis for negotiations on the reduction of *GHG* emissions. These resulted in the *Kyoto Protocol*²⁴ formulated at the third *UN Climate Change Conference*²⁵ two years later. With this agreement legally binding targets for industrialized countries with respect to emission ceilings had been defined for the first time.

However, since the 21st *United Nations Climate Change Conference*²⁶ at the latest, it has become apparent that the previous efforts of the international community might not suffice to avoid serious long-term consequences of global warming. The urgent appeal to realize all measures which help

"Holding the increase in the global average temperature to well below 2°C above pre-industrial levels and pursuing efforts to limit the temperature increase to 1.5°C above pre-industrial levels, recognizing that this would significantly reduce the risks and impacts of climate change"

formulated in article 2(a) of the *Paris Agreement*,²⁷ shows the severity of the climate problem the world is currently facing.

1.1.3 Scientific contributions to efforts against global warming

Already before the first *UNCED* meeting, it became apparent that a more profound, scientific basis with respect to the complex phenomena of global warming was required. Thus, even if explicitly designed without the authority to issue policy guidelines, founding of the *IPCC*²⁸ in 1988 significantly increased the ability of the *UN* to realize political decisions based on a profound scientific basis. Especially the scientific facts, presented in the *IPCC*'s fifth assessment report², drew significant public and scientific attention. The data summarized clearly indicate that the measures, agreed on by the international community, to counteract the phenomena of global warming were significantly failing. Continuing business as usual would lead to a world that by 2100 would already completely differ from the present state. This interpretation was confirmed by the current *IPCC*'s special reports on ocean and cryosphere²⁹, as well as on climate change and land³⁰, which indicate severe irreversible long-term consequences of the earth's temperature increase.

However, the evolution of the atmospheric CO₂ content depicted in Figure 1.1(a) shows a drastic increase in the past decade. Thus, at present state a CO₂ content higher than 400 ppm is observed, which is more than 30% above its value exhibited in 1850. Even more alarming, by analyzing the slope of the graph, one notices that its second derivative takes a positive value. This means that the CO₂ content in the atmosphere does not only rise, but that the rate at which the increase takes place increases. In the light of these observations, it does not surprise that the overall anthropogenic CO₂ emissions took the highest value ever in 2019 (Figure 1.1(b)). This clearly contradicts the aims formulated at the *United Nations Climate Change Conferences* (Section 1.1.2).

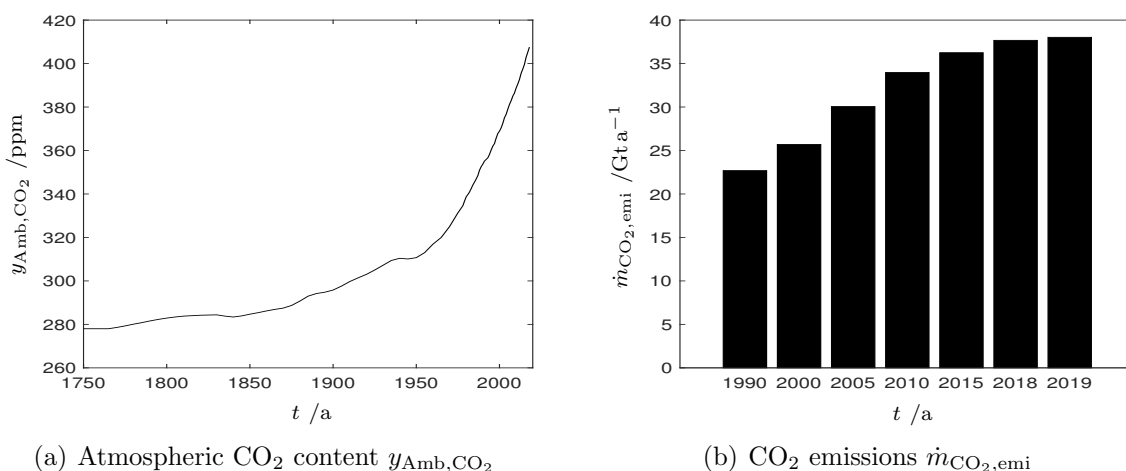


Figure 1.1: Evolution of (a) atmospheric CO₂ content $y_{\text{Amb,CO}_2}$ ^{10,31} and (b) global anthropogenic CO₂ emissions $\dot{m}_{\text{CO}_2,\text{emi}}$ ³² in dependence of time t . Significant increase in CO₂ mole fraction since the industrial revolution in 1850 is visible. Moreover, anthropogenic CO₂ emissions are still rising.

Being aware of the trends described, various scenarios of emission reduction have been analyzed in *IPCC's* fifth assessment report. Severe reliance on *bioenergy with carbon dioxide capture and storage (BECCS)* and on other *negative emission technologies (NETs)*, which aim for direct removal of carbon dioxide from ambient air, is underlined.² To be more specific, 104 out of the 116 scenarios with a high probability of staying below the 2°C target take into account *BECCS*.³³ Even more alarming, to meet the 1.5°C target, large-scale implementation of *NETs* seems unavoidable.³⁴

A similar picture is drawn by the present *IPCC* special report³⁵ that focuses on possible mitigation strategies compatible with the 1.5°C target. Four illustrative model pathways that incorporate no or limited overshoot (scenarios 1–3), as well as higher overshoot (scenario 4), of the atmospheric CO₂ content have been extracted from 90 scenarios proposed in the literature. As shown in Figure 1.2 all model pathways incorporate use of *NETs*. However, scale and time of realization vary between the scenarios. Scenario one is based on the assumptions of a significant reduction in the world energy demand and rapid decarbonization of its energy supply, whereas pathway two accounts for slower and less efficient technological innovations within a society focusing on sustainability. Scenarios three and four take more pessimistic perspectives. Here, the evolution of the world society

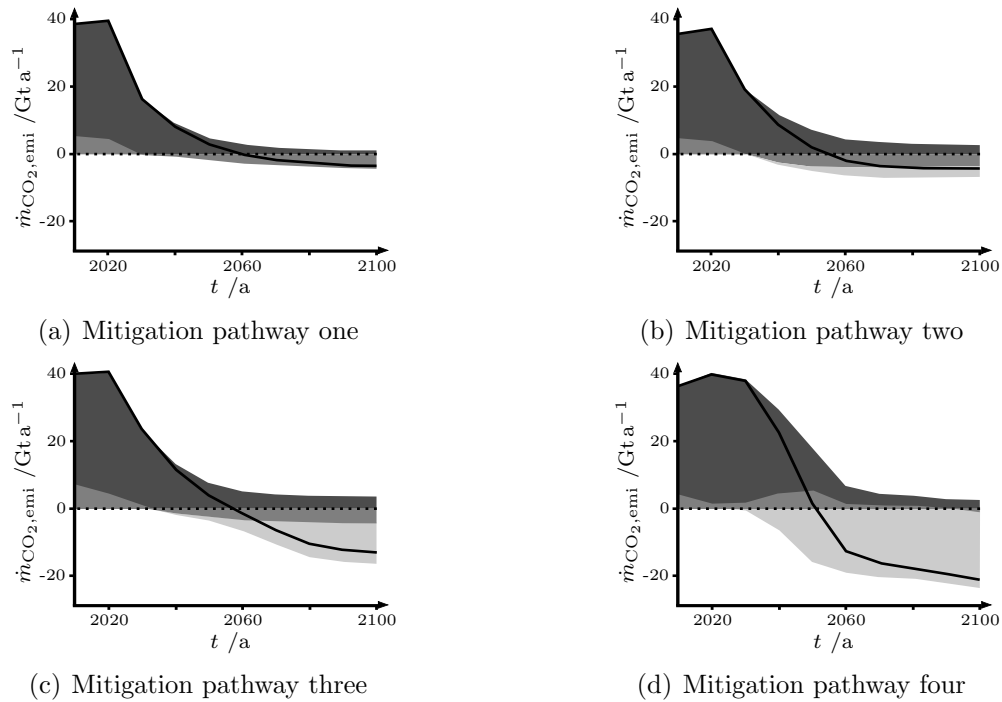


Figure 1.2: Illustrative mitigation pathways compatible with the 1.5 °C target, which incorporate no or limited (a)-(c) and high (d) overshoot of atmospheric CO₂ content. The carbon sources and sinks: fossil fuel and industry (dark), *afforestation/reforestation* (*AR*) and *land use* (*LU*) (intermediate), and *bioenergy with carbon capture and storage* (*BECCS*) (bright) are shown. Net CO₂ emissions are indicated by a solid line (-). Figures are based on *IPCC special report*³⁵.

and technological developments proceed analogously to historical patterns or a greenhouse gas-intensive lifestyle that includes high energy and resource demands is assumed.

Comparing the different mitigation pathways visualized by Figure 1.2, four main conclusions can be drawn:

1. To reach the 1.5 °C target, even in the best case scenarios, net negative carbon emissions, e.g., realized by *afforestation/reforestation* (*AR*), *land use* (*LU*) or *bioenergy with carbon capture and storage* (*BECCS*), become unavoidable
2. The scale of *NETs* realization required will depend on the speed of emission reduction. A slower transition to a sustainable energy supply in the first half of the century will result in the need of increased use of *NETs* at the end of this century
3. Only in the best case scenarios *AR* and *LU* suffice as measures to counteract global CO₂ emissions. In all others scenarios analyzed, implementation of large-scale *CCS* including *BECCS*, which can be regarded as a reference for *NETs* other than *AR* or *LU*, is taken into account
4. Compared to the current CO₂ emissions in the order of magnitude of 40 Gt per year, the accumulated amount of up to 1200 Gt capacity of *NETs* other than *AR* and *LU* till the end of the century seems comparatively high

which stipulate a fast and large-scale development of *NETs*.

1.2 Negative emission technologies

A significant reduction of global net CO₂ emissions is required to reach the targets formulated in the *Parisian Agreement* (Section 1.1.3). This can be realized by various measures as indicated by Figure 1.3. However, significant changes in society lifestyle or far-reaching technological innovations in the world energy supply and management³⁶ might not be realizable in a short period of time. Moreover, a major part of the consumer products used in industrialized countries is carbon-based. Consequently, it remains questionable if a fast decarbonization can be reached in this sector.

Moreover, common point source *carbon capture and storage/utilization (CCSU)* only allows for reducing emissions of concentrated sources, which account for less than half of the global CO₂ emissions.^{37,38} Mobile, small-scale sources, e.g., planes, are in general not affected by this measure. But these significantly contribute to the overall anthropogenic CO₂ emissions so that counteracting these sources is likewise important. In this respect, use of *NETs*, which act as sinks in the global CO₂ balance, is identified as a possible solution.³⁹

Besides the balancing of CO₂ sources hard to decarbonize, the characteristics of *NET* use in principle allow to extend the global carbon budget. This varies with reference to 01.01.2018 between 420 Gt – 840 Gt to keep the global warming below 1.5 °C and between 1170 Gt – 2030 Gt to meet the 2 °C target.³⁵ Thus, the possibility of implementing *NETs* might be interpreted as an excuse to delay decarbonization of the global energy and consumer goods sector. To be more specific, emissions in the early half of the century might be compensated by use of *NETs* at the end of the century. However, as both the scale and time frame of their implementation come with significant uncertainties and, moreover, the ecologic consequences of overshoot scenarios are unpredictable,³⁹ this interpretation of *NETs* seems prohibitive. Rather, this technological approach should be understood as an additional tool that is not to be used as a replacement for common *CCSU* but to support the efforts of net CO₂ emission reduction for scenarios in which point source *CCSU* is hardly applicable.³⁹

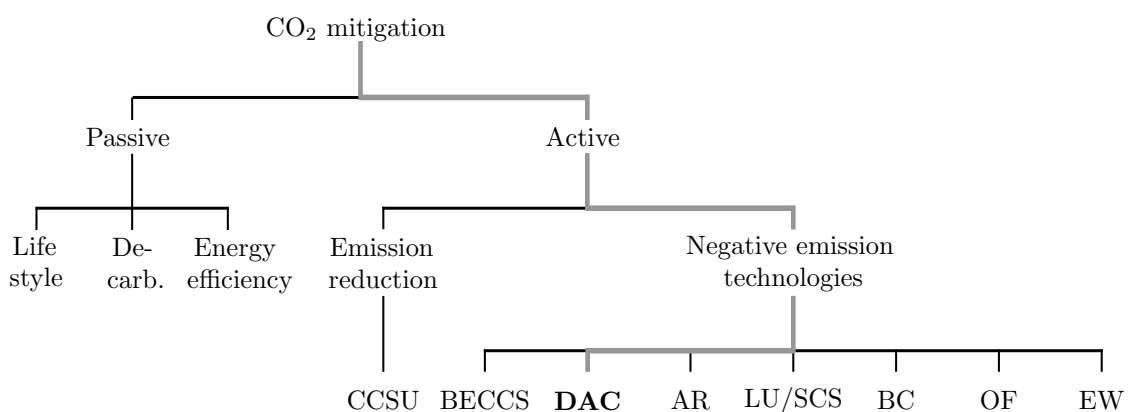


Figure 1.3: Placement of direct air capture amongst other CO₂ mitigation strategies (gray line). As possible active removal strategies of carbon dioxide *carbon capture and storage/utilization* (from point sources) (*CCSU*), *bioenergy with carbon capture and storage* (*BECCS*), *direct air capture* (*DAC*), *afforestation/reforestation* (*AR*), *land use* (*LU*), *soil carbon sequestration* (*SCS*), *biochar* (*BC*), *ocean fertilization* (*OF*) and *enhanced weathering* (*EW*) are shown.

Significant research in the area of *NETs* has been conducted in the past decade. Only a brief overview is given in this contribution, whereas for a deeper insight the reader is referred to more detailed reviews.^{39–43} All *NETs* presented have in common that they are subject to significant drawbacks that at their current state impede their large-scale application.^{43,44} Regarding *BECCS*, which focuses on energy generation from biomass while capturing CO₂, the scale of agricultural ground required may lead to competition with the food industry.⁴⁰ Moreover, high water demand can become a burden to global fresh water supply.⁴⁰ The same holds true for the approach of *afforestation/reforestation (AR)* in which additionally the impact of forestry on the climate system is not completely understood, such that accompanying biophysical effects might lead to an overall negative effect with respect to global warming.^{40,45} However, as no technological innovation is required, *AR* is already realized at large scale.^{46–49}

The concepts of *land use (LU)* and *soil carbon sequestration (SCS)* can readily be applied, as they mainly focus on a sustainable use of land available.^{35,40} However, only a comparatively small contribution of these approaches is estimated³⁹ and especially regarding their potential reversibility, e.g., by intensive farming, these approaches seem less reliable.⁴⁰ Nevertheless, these measures might suffice to slow down the fast increase in atmospheric CO₂ content, e.g., by increase of the current soil carbon content that is 1500 Gt up to 1 m depth and 2400 Gt up to 2 m depth,⁴⁰ by 0.4 % per year, which is the aim of the *4 per mille initiative*⁵⁰ founded after the *Parisian Conference on Climate Change*²⁶. In this respect, present studies even indicate that higher sequestration potentials of up to 1 % per year of the carbon sequestered in soil might be realizable.⁵¹ With focus on an even higher increase of capacity and resistance to decomposition, the pyrolysis of biomass to biochar with high carbon content is taken into account in the *biochar (BC)* concept. While allowing for additional sequestration capacities in the order of 0.5 Gt⁵² to 0.7 Gt⁴⁴ carbon per year, adding biochar to the soil could additionally have a fertilizing effect⁴⁰. However, the question of its long-term stability and possible effects on the earth's radiation balance, e.g., by soil darkening, need to be investigated in more detail.⁴⁰

Ocean fertilization (OF) exploits the potential of biological growth based carbon sinks in oceans. Bearing in mind that phytoplankton growth rate is often limited by nutrients, adding nitrogen, phosphorus or iron can significantly enhance biomass formation.^{40,53,54} Especially use of micro-nutrients is favored to avoid fertilization with large quantities of macro-nutrients, the amount of which required would be up to 20 % of the carbon captured.⁴⁰ However, lack of verification data with respect to the possible scale of this mitigation strategy and concerns regarding ecological consequences, implementation time or unintended effects on the global carbon balance impede its large-scale application.^{55,56}

Aiming for a long-term sequestration, removal of CO₂ from the atmosphere by means of geophysical processes (*enhanced weathering, EW*) is proposed.⁵⁷ But as the kinetics of the mineralization process under ambient conditions work at a geological time scale, acceleration of these, e.g., by increasing the surface to volume ratio of the mineral by grinding, is needed.^{57,58} Consequently, the excessive requirement for land and mineral rocks to be used,⁵⁹ as well as the energy demand of the transportation and grinding process,⁶⁰ are significant burdens of this technology.^{40,43}

Table 1.1: Comparison of different approaches to *NETs* with respect to their potential of being used as large-scale measures at the end of this century. As cost estimations significantly vary within the literature, mean values are shown. The reader is referred to more detailed reviews^{39–41,43} for a deeper insight. Abbreviations used are Ap: Applied, Co: Commercial, De: Demonstration, Pos: Possible, Re: Research, Unc: Uncertain, Vuln: Vulnerable.^{39–41,43,61}

		<i>BECCS</i>	<i>DAC</i>	<i>AR</i>	<i>LU/SCS</i>	<i>BC</i>	<i>OF</i>	<i>EW</i>
Technological maturity		De	De/Co	Ap	Ap	De	Re	Re
CO ₂ capture potential	/Gt a ⁻¹	12.1	>12.1	12.1	11	11	2.5	3.6
Energy demand	/GJ t ⁻¹	-0.8 – -11	12.3	–	–	–	–	12.5
Costs	/\$ t ⁻¹	36	490	24	50	105	460	300
Land requirement		High	Low	High	High	High	–	High
Effect on ecosystems		Yes	No	Yes	No	No	Yes	No
Revers climate effects		Pos	No	Pos	No	Pos	Pos	No
Long-term CO ₂ storage		Yes	Yes	Vuln	Vuln	Vuln	Unc	Yes

In contrast to the aforementioned approaches, the scope of *direct air capture (DAC)* is the implementation of a technological process that directly removes CO₂ from ambient air and provides a stream of this gas in concentrated state for sequestration or further use. Compared to other *NETs* (Table 1.1), air capture is a very promising concept that allows for high capture capacities, without being a burden to the earth’s fresh water supply or being accompanied by significant requirements of arable land. Moreover, this approach is based on technologically mature gas separation technologies ready to be applied on a large scale. But current energy demands and capture costs prohibit an efficient large-scale realization,^{41,43} even if there are attempts to decrease these drawbacks (Section 2.1).

Bearing in mind that *DAC* makes no statement about how the stream of concentrated CO₂ is processed, the implementation of storage or utilization capacities needs to go along with the realization of large-scale *DAC*. Storing CO₂ in suitable geological formations, e.g., in saline aquifers (*Sleipner* project⁶²), oil reservoirs (*Weyburn-Midale* project⁶³) or unminable coal seams (*RECOPOL* project⁶⁴) might buy time if it is not released in the future or even reacts with natural minerals to form carbonates.^{37,65} However, even if the combination of *DAC* with carbon storage (*CarbFix* project⁶⁶) might be a promising approach on a short time scale, the question of how long CO₂ can be stored safely still needs to be answered. Long-term monitoring is mandatory and the main problem of how to deal with the large quantities of CO₂ at hand might become a burden for future generations.⁶⁷

Consequently, (bio-)chemical conversion of CO₂ seems more favorable. One might than speculate about using the concentrated stream of CO₂ in direct or indirect mineralization processes.⁶⁸ However, both processes come along with considerable drawbacks, e.g., high demand of energy or of additives, which impede their large-scale application,⁶⁸ and neglect the potential of CO₂ to be considered as a resource^{69,70} rather than waste. Bearing in mind that the current industrial structure is carbon-based, using the CO₂ captured as feedstock

opens up the possibility of producing basic chemicals^{71,72} or liquid fuels on a carbon neutral basis.⁷³⁻⁷⁵ Moreover, taking into account the production of methane,^{69,76} based on CO₂ from ambient air and on hydrogen (H₂) from renewable energy sources, as natural gas substitute (*SNG*), this approach would not only allow to use current technologies on a carbon neutral basis in the transition period of the global energy system to a renewable basis. Rather, it additionally enables realization of sustainable negative carbon emissions, e.g., by means of methane pyrolysis^{77,78} to form solid carbon.

Summarizing, all *NETs* considered are subject to specific limitations that restrict their large-scale application at present state. Since they allow for realization of a different approach compared to point source *CCSU*, they are neither to be set in competition with *CCSU*, nor among each other. Rather, all approaches should be regarded as complementary tools, as following a single approach will most likely not allow for the amount of net CO₂ emission reduction required. Within this portfolio of possible technological concepts, *DAC* is among the most promising options, being accompanied by a comparatively small set of drawbacks.⁴¹ However, without a profound concept of processing the stream of concentrated CO₂ produced, as well as significant reductions in the capture costs and energy requirements, applying *DAC* at large-scale hardly seems ecologically beneficial in a long-term perspective nor energetically and economically feasible. This motivates an integrated analysis of *DAC* with a CO₂ processing concept, e.g., for the production of *SNG*.

1.3 Scope of the research conducted

Sections 1.1 and 1.2 indicate that against the background of the anthropogenic CO₂ emission-based phenomenon of global warming, reducing or limiting its progression is one of the most severe problems the world is facing in the 21st century. To be more specific:

Section 1.1 Motivation

investigates the background of global warming. The importance of reducing the currently still rising annual, global CO₂ emissions to limit an increase of the ambient CO₂ content is underlined. Possible CO₂ mitigation pathways summarized indicate a high likelihood that the implementation of large-scale *NETs* becomes unavoidable at the end of this century.

Section 1.2 Negative emission technologies

is motivated by the findings presented in Section 1.1 and analyses various strategies for the realization of *NETs*. Especially large-scale use of *DAC* is found to be promising. However, the survey provided indicates that prohibitively high energy requirements impede an efficient large-scale implementation of air capture technologies at current state.

These results motivate the content of this contribution summarized in Figure 1.4. It aims to develop concepts that help to reduce the burdens associated with *DAC*. To this end, novel intensified integrated *DAC* concepts are proposed and customized to the specific constraints arising in CO₂ capture from air (Chapter 2). The potential of realizing an autothermal process design by integrating the approaches to *DAC* developed in a *power-to-gas (PtG)* concept for production of methane via the highly exothermic *Sabatier* re-

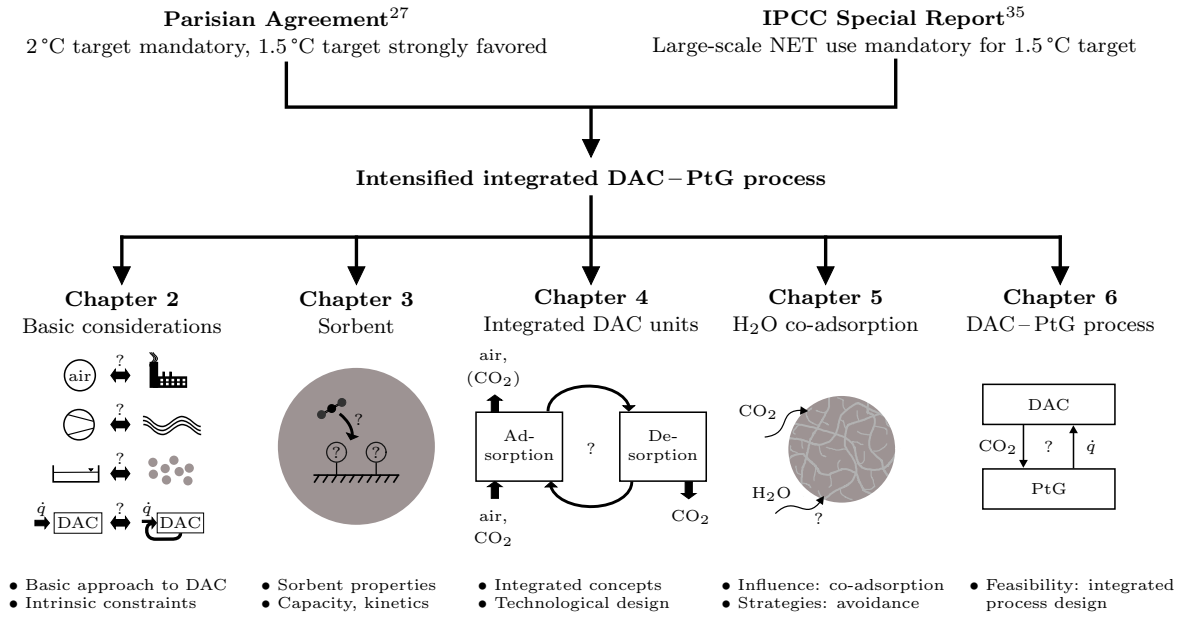


Figure 1.4: Graphical abstract of the thesis content.

action becomes a central aspect of the research conducted. Against this background, applicability of the commercially available sorbent *Lewatit VP OC 1065* as *DAC* sorbent is experimentally investigated with respect to the constraints identified (Chapter 3).

A more detailed analysis of technological strategies for realization of the heat integration approaches formulated is performed in Chapter 4. In particular, the potential of *temperature-composition-swing-adsorption (TCSA)*, as well as of hybrid *temperature-vacuum-composition-swing-adsorption (TVCSA)* concepts, is analyzed under ideal conditions, i.e., dry conditions. The simulation results obtained motivate the realization of a more detailed experimental investigation of transport phenomena, the results of which are summarized in this chapter.

The extension of the idealized analysis by taking into account water co-adsorption phenomena is conducted in Chapter 5. Results obtained indicate that the impact of co-adsorption can significantly be reduced by analyzing the problem via a process-based approach. Besides different strategies to reduce the influence of water co-adsorption, e.g., sorbent modification or use of kinetic effects, especially implementations of *mechanical vapor recompression (MVR)* concepts are analyzed in detail. Aspiring an even higher degree of resource efficiency, a detailed investigation of an integrated *DAC – PtG* process with special focus on synergies that arise from a coupling of the different subprocesses on a mass and energy level is carried out in Chapter 6.

Concluding, Chapter 7 summarizes the results presented. Future research implications resulting from the findings of this work, with respect to the overlaying scope, i.e., the realization of a

resource efficient, autothermal production of CH₄ based on CO₂ captured from air by means of an intensified integrated DAC – PtG process,

are formulated.

2 Basic considerations of DAC

Scientific contributions

Parts of this chapter have been published in the following scientific contributions:

Peer-reviewed journal articles

- Drechsler, C.; Agar, D. W. Comparison of Highly Heat-Integrated Adsorber Concepts for Use in Direct Air Capture Processes. *Chem. Ing. Tech.* **2020**, *92*, 282–287.
- Drechsler, C.; Agar, D. W. Simulation and optimization of a novel moving belt adsorber concept for the direct air capture of carbon dioxide. *Comp. Chem. Eng.* **2019**, *126*, 520–534.

Conference talks

- Drechsler, C.; Agar, D. W. Hoch-Energieintegrierte Adsorberkonzepte für eine Anwendung in Direct Air Capture Verfahren. Presented at Jahrestreffen der ProcessNet-Fachgruppen Adsorption und Hochdruckverfahrenstechnik, Freiberg, Germany, February 18-20, 2019.
- Asmanoglo, C.; Agar, D. W. Entwicklung wärmeintegrierter Adsorber/Desorber-Konzepte für eine Anwendung in Direct Air Capture (DAC) Technologien. Presented at Doktorandenseminar der 1. Statuskonferenz zur BMBF Fördermaßnahme CO₂Plus, Berlin, Germany, April 17-18, 2018.

Conference poster presentations

- Drechsler, C.; Agar, D. W. Highly heat-integrated temperature-vacuum-swing adsorption process for the direct air capture of carbon dioxide. Presented at Gordon Research Conference on Carbon Capture, Utilization and Storage, Les Diablerets, Switzerland, May 05-10, 2019.
- Drechsler, C.; Agar, D. W. Highly heat-integrated temperature-vacuum-swing adsorption process for the direct air capture of carbon dioxide. Presented at Gordon Research Seminar on Carbon Capture, Utilization and Storage, Les Diablerets, Switzerland, May 04-05, 2019.
- Asmanoglo, C.; Agar, D. W. Entwicklung wärmeintegrierter Adsorber/Desorber-Konzepte für eine Anwendung in Direct Air Capture (DAC) Technologien. Presented at 1. Statuskonferenz zur BMBF Fördermaßnahme CO₂Plus, Berlin, Germany, April 17-18, 2018.

Abstract

DAC technologies are regarded as one of the most promising approaches to *NETs*. Analysis of the thermodynamic minimum energy demand for CO₂ capture from air indicates that it does not need to significantly exceed the one present in point source capture. However, specific limitations of *DAC* applications can lead to significantly larger differences in the energy requirements between these two approaches in a technical setting. Especially the question of sorptive–sorber contacting becomes crucial, as, reasoned in the low CO₂ content in the atmosphere, a change of the thermophysical state of air seems to be attributed with impedingly high CO₂-specific energy demands. Moreover, an analysis of the thermal energy demand of *DAC* units, operated in the commonly used *TSA* mode, reveals high potential for decreasing the CO₂-specific heat demand of air capture units by efficient recovery of the sorber sensible heat. In this respect, a detailed investigation of the maximum efficiency of heat recovery indicates that integration concepts, which make use of a transformation of the adsorption process cyclic operation mode from time to space domain, can offer superior heat integration characteristics.

This chapter is structured as follows:

Section 2.1 State of the art

takes into account the results presented in Chapter 1 that indicate *DAC* to be one of the most promising approaches to *NETs*. The current state of knowledge with respect to the implementation of this technology is summarized.

Section 2.2 Intrinsic constraints of DAC

is motivated by the analysis given in Section 2.1 and dedicated to the investigation of the main constraints that large-scale *DAC* units are subject to. Especially considerations with regard to the energy level are taken into account.

Section 2.3 Approaches to heat integrated DAC concepts

deepens the analysis given in Section 2.2 with respect to the CO₂-specific energy demand of *DAC* concepts. Focus is placed on recovery strategies for the sorber sensible heat.

Section 2.4 Summary and conclusion

summarizes the results of this chapter and motivates the main research objectives to be investigated in Chapters 3 and 4.

2.1 State of the art

On a first view, the approach of implementing large-scale air capture facilities might intuitively seem quite ambitious. However, the general concept of separating carbon dioxide from air has successfully been applied for a long period of time, e.g., in submarines or space shuttles,^{17,36,79} with a first patent⁸⁰ dealing with CO₂ removal from air being dated to 1966. Moreover, the basic separation technologies to remove CO₂ from gas streams, e.g., large-scale amine-based flue gas scrubbing in power plants, are currently available at a high level of technological maturity⁸¹ and also the small-scale removal of CO₂ from air, e.g., being required in air liquefying processes,⁸² has been studied for decades.⁸³ Thus, the general question to be answered in the context of CO₂ mitigation strategies is not if air capture is feasible, but if this technology can be implemented with reasonable effort on a large scale. Consequently, since its first mentioning by Lackner et al.⁸⁴ in 1999, significant progress has been achieved in the area of *DAC*,^{17,38,41,67,85} leading to the realization of large-scale demonstration plants in the last decade.

As the scope of *DAC* is comparable to that of point source capture, transfer of technologies designed for this purpose intuitively seems advantageous. However, under the specific constraints of *DAC* (Section 2.2) not all technologies available are beneficial. The ratio of carbon dioxide to other species in air is currently about 1 : 2500 (Figure 1.1(a)). Thus, use of technologies that are based on thermophysical modification of the state of air, i.e., on temperature change or compression, are most likely not affordable.^{36,84} Consequently, cryogenic or membrane processes are in general not considered for *DAC* applications, leaving ab- and adsorption-based separation processes to be investigated in more detail.

Focusing on absorption processes, only use of sorbents that chemically bind CO₂ seems reasonable to ensure high CO₂ adsorption capacities at its low partial pressure in ambient air.^{67,85} Consequently, solutions containing inorganic compounds, e.g., NaOH or KOH, are favored as sorbents compared to organic solutions that physically bind CO₂.^{41,85} For regeneration of these sorbents, either electro dialysis or high-temperature calcination loops are investigated.^{67,85} Being energy- as well as investment-intensive, approaches including electro dialysis^{86,87} are currently not commercially applied.⁸⁵

Compared to the limited amount of publications dealing with electro dialysis-based sorbent regeneration, various research groups^{17,37,88-91} focus on the development of calcination concepts within *DAC* approaches. However, reasoned in the high operation temperatures required for the calcination process (> 700 °C)^{41,85}, these concepts become very energy-intensive. Moreover, use of liquid sorbents can be accompanied by sorbent losses via evaporation and by possible contamination of the liquid phase, e.g., by dust. The latter could be avoided by prior cleaning of the air. However, additional pressure losses arising from use of gas filters might not be affordable from an energy point of view (Section 2.2.2). Nevertheless, despite these hurdles, *Carbon Engineering*⁹² launched a pilot plant based on a KOH loop in 2015, which allows for a CO₂ capacity of 0.6 t day⁻¹.⁹³

Acknowledging that there are approaches to reduce the energy demand of liquid sorbent-based air capture systems,^{94,95} it is at present state considerably high and results in significant project costs.⁹⁶ Consequently, the application of solid sorbents,⁹⁶⁻¹⁰⁴ which among others offer the advantage of a lower heat capacity compared to aqueous systems,

is intensively discussed. Besides solid inorganic-bases materials, organic – inorganic hybrid sorbents, e.g., amine-based ion exchange resins, are subject to a more detailed investigation (Section 3.1).⁶⁷ In general, regeneration of the sorbent by temperature (*TSA*)⁹⁸ or temperature-vacuum-swing (*TVSA*)^{100,103,104} in the low temperature region⁸⁵ is thought of, but also alternative sorbent regeneration strategies, e.g., *moisture-swing-adsorption* (*MSA*), are investigated to reduce the CO₂-specific energy demands.^{99,101,102}

Various companies realized adsorption-based *DAC* units on different scales. Among those, the Swiss company *Climeworks*¹⁰⁵ already offers fully automated *DAC* technologies on a commercial scale. Combining a *TVSA* concept with amine-based sorbents, their basic module offers a capture capacity of 135 kg day⁻¹, while working at regeneration temperatures in the order of 100 °C. This technology is used among other research programs⁸⁵ in the European *CarbFix* project⁶⁶, in which the CO₂ captured is introduced into basaltic rock formations to allow for CO₂ storage via mineral weathering. Moreover, it is used on a commercial basis in the Norwegian *Heroya* project that aims for production of synthetic mineral oil via a *power-to-liquid* (*PtL*) technology, developed by *Sunfire*.¹⁰⁶

Also the U.S. company *Global Thermostat*¹⁰⁷ uses amine-based solid sorbents for its capture technology. Desorption of CO₂ with a purity of 98 % is realized using steam at low temperatures 85 – 100 °C. Allowing for scalability via numbering-up, its basis modules can provide capacities of 2.7 – 11 t day⁻¹ at container size and 137 t day⁻¹ at full-scale design.^{107,108} A first pilot plant erected at *SRI International* (Menlo Park, Canada) in 2010 already offered a capacity of 500 t year⁻¹, which was increased to 1000 t year⁻¹ in 2013. Moreover, a commercially operated *DAC* plant with a planed ultimate nominal CO₂ capacity of 4000 t year⁻¹ was realized in Huntsville, Alabama, in 2018.¹⁰⁹

Besides the concepts of these major companies, several other approaches to *DAC* on an experimental, pilot or commercial scale have been documented (Table B.1). Comparing the publications and process descriptions outlined in more detail, it becomes apparent that two major concerns from an engineering point of view arise in large-scale realization:

1. An efficient way of contacting the sorbent with ambient air, i.e., avoiding high pressure losses within the *DAC* unit^{110,111} (Section 2.2.2)
2. The high CO₂-specific energy demand, arising, besides others, from sorbent temperature change in temperature-swing and from co-adsorption of water (Section 2.2.3)

Especially with regard to point two, a high optimization potential is found (Section 2.3).

2.2 Intrinsic constraints of DAC

Even if the CO₂ content in ambient air (~ 400 ppm) is significantly lower than the one present in flue gas capture processes ($\sim 10 - 15$ %),^{81,112} from a thermodynamic point of view, energy requirement of *DAC* need not to be significantly higher compared to flue gas capture (Section 2.2.1). However, the thermodynamic minimum energy requirement may not reflect the whole characteristics of the capture process. This is, additional energy demands, e.g., for air – sorbent contacting (Section 2.2.2) or for sorbent sensible heat requirements (Section 2.2.3), are not accounted for. Identifying adsorption processes to

be most promising (Section 2.2.4), a more detailed analysis of these technologies reveals that intensified heat integrated *DAC* concepts can help decreasing the gap between real and minimum energy requirements (Section 2.3).

It seems reasonable to define a reference energy level that allows for an interpretation of energy and heat flows with respect to the process design intended. Bearing in mind that the overall scope of this contribution lies in the realization of an autothermal *DAC* – *PtG* approach, with the major heat source being the highly exothermal *Sabatier* reaction



the heat release of this reaction is interpreted as the process natural energy scale. Energy sinks and sources are discussed with reference to this reaction. For the sake of clarity, in general, discussions are given on an energy scale. If exergy levels are used for interpretation purpose, these are explicitly denoted.

2.2.1 Thermodynamic minimum energy demand

Reasoned in the very dilute state of CO_2 in ambient air, *DAC* applications can not capture the same amount of CO_2 at comparable energy demands as capture technologies that use concentrated sources. However, application of *NETs* will most likely become unavoidable in the near future, not to substitute common *CCSU*, but to supplement it (Section 1.1.3). Comparing the two technologies, one has to consider that there exists an essential difference in their scopes. Common *CCSU* aims for emission reduction, i.e., minimizing a carbon source, whereas *DAC* focuses on negative emissions, i.e., on realizing a carbon sink. Ignoring approaches as *BECCS* that in fact include air capture by plant growth, this implies that even if common *CCSU* is applied with 100 % efficiency, it still does not allow for negative emissions.

Even with the arguments given at hand, prohibitively high energy demands of *DAC* would most likely impede its large-scale implementation. In this respect, investigation of the minimum thermodynamic energy demand

$$\Delta g_{\text{sep,CO}_2} = R_{\text{id}} \cdot T_{\text{G}} \cdot \ln \left(\frac{p_{\text{G}}}{p_{\text{G,CO}_2,\text{mix}}} \right) = R_{\text{id}} \cdot T_{\text{G}} \cdot \ln \left(\frac{1}{y_{\text{G,CO}_2,\text{mix}}} \right) \quad (2.1)$$

to extract one mole of CO_2 from an ideal gas mixture of infinite size, allows for a first comparison between air and point source capture technologies.¹¹² Figure 2.1(a) compares the minimum work required to extract CO_2 from a gas mixture in dependence of the CO_2 share present. Even if the CO_2 concentration varies over three orders of magnitude, this does not hold true for the minimum, CO_2 -specific separation work $\Delta g_{\text{sep,CO}_2}$ that only changes by a factor of 3.4. This means that based on thermodynamic considerations removing CO_2 from air ($y_{\text{G,CO}_2,\text{mix}} \approx 400 \text{ ppm}$) does not need to be prohibitively more energy demanding than its removal from flue gas ($10 \% \lesssim y_{\text{G,CO}_2,\text{mix}} \lesssim 15 \%$)^{81,112}. Moreover, based on the results presented, one may conclude that even at lower carbon dioxide concentrations present in the atmosphere, e.g., at $y_{\text{G,CO}_2,\text{mix}} \approx 100 \text{ ppm}$, air capture seems still feasible from an energy point of view.

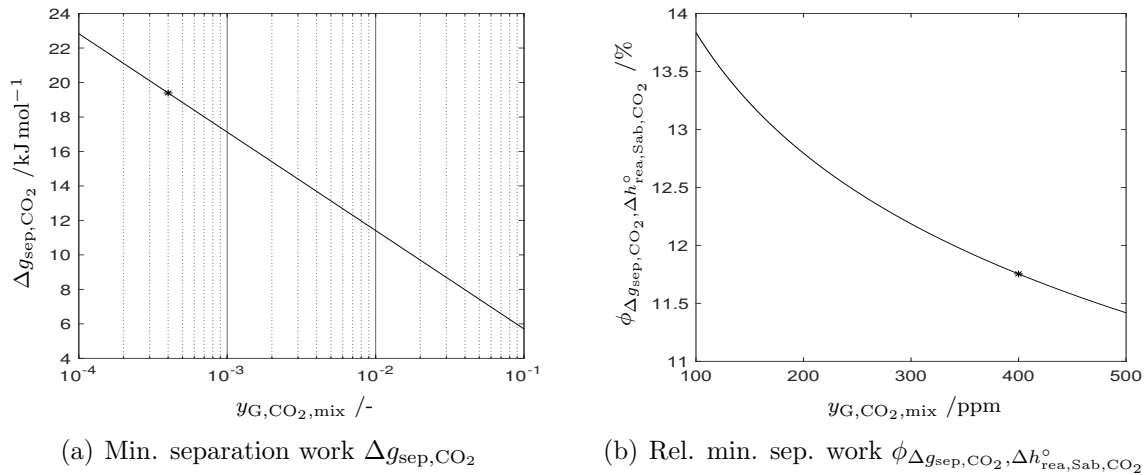


Figure 2.1: (a) Thermodynamic minimum energy demand $\Delta g_{\text{sep,CO}_2}$ and (b) relative thermodynamic minimum energy requirement $\phi_{\Delta g_{\text{sep,CO}_2, \Delta h_{\text{rea,Sab,CO}_2}^\circ}}$ with reference to *Sabatier* reaction heat release for separation of CO₂ from a gas mixture of infinite size with a CO₂ content $y_{\text{G,CO}_2,\text{mix}}$ and temperature of $T_{\text{G}} = 298.15 \text{ K}$. The CO₂ stream separated is at the same pressure as the gas mixture. Ambient CO₂ content ($y_{\text{Amb,G,CO}_2}$) is marked by a star (*).

The relative minimum energy demand with reference to *Sabatier* reaction heat release

$$\phi_{\Delta g_{\text{sep,CO}_2, \Delta h_{\text{rea,Sab,CO}_2}^\circ}} = \frac{\Delta g_{\text{sep,CO}_2}}{\Delta h_{\text{rea,Sab,CO}_2}^\circ} \quad (2.2)$$

allows for a first estimate with regard to the feasibility of an autothermal process design. As indicated by Figure 2.1(b), even in the case of extracting CO₂ from a reservoir with 100 ppm CO₂ share, $\phi_{\Delta g_{\text{sep,CO}_2, \Delta h_{\text{rea,Sab,CO}_2}^\circ}}$ takes values well below 14%. This means that even with a very low efficiency of energy use, the heat release by *Sabatier* reaction can suffice to match the thermodynamic minimum energy requirement. However, a variety of non-idealities and losses need to be considered in the sorbent-based air capture process investigated, which lead to considerable higher energy demands compared to the limiting case analysis given (Sections 2.2.2- 2.2.3, 2.3).

2.2.2 Pressurizing the air

Considering the design of air capture technologies, one may intuitively think of applying membrane-, absorption- or adsorption-based technologies. These are commonly used for separation of small amounts of components that are present in minor quantities in gas mixtures and can not easily be separated, e.g., by condensation. In membrane applications, a maximum driving force of about 40 Pa can be reached in a best case scenario if non-pressurized air is used. One may intuitively think of pressurizing the air, to increase the driving force of mass transfer. If the ambient CO₂ content was in the percentage range, this might be reasonable. However, in air capture applications, the mole fraction of CO₂ currently takes levels of about 400 ppm. This means that every energy input to a volume of air from which CO₂ is to be separated scales at least with a factor of 2500,

if being referred to the amount of CO_2 captured. High CO_2 -specific energy requirements of compression have to be expected, which can result in considerable overall energy demands. To give a reference, at *NET*- CO_2 capacities of 20 Gt a^{-1} that might be required at the end of this century (Section 1.1.3), a CO_2 -specific compression work of 10 kJ mol^{-1} equals a total energy demand in the order of magnitude of 0.8% of the world energy demand in 2018 ($14.3 \cdot 10^3 \text{ Mtoe}^{113}$). As shown by Figure 2.2(a), which visualizes the specific compression energy of air per mole CO_2 present $e_{\text{com,G,sp}_{n\text{CO}_2}}$ in dependence of the pressure change induced $\Delta p_{\text{com,G}}$, energy demands significantly above this level might be required. It becomes apparent that even a very small change in the overall pressure of the gas mixture results in considerable specific energy demands. Consequently, it seems hardly possible to use membrane technologies as main separation step in *DAC*.

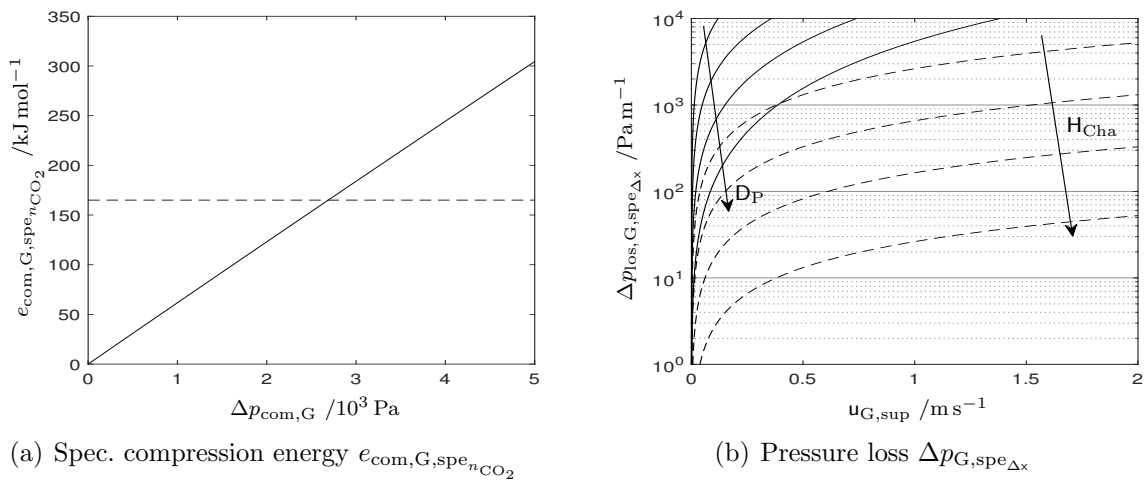


Figure 2.2: (a) Ideal, CO_2 -specific compression energy $e_{\text{com,G,sp}_{n\text{CO}_2}}$ of dry air (-) in dependence of pressure change $\Delta p_{\text{com,G}}$. The initial pressure of the gas phase to be compressed equals 10^5 Pa . Moreover, the heat release of *Sabatier* reaction per mole of CO_2 converted $-\Delta h_{\text{rea,Sab,CO}_2}^\circ$ is shown as a reference (-). Pressurization energy requirement is calculated based on the assumption of ideal, adiabatic compression (Appendix C.3.3.1). (b) Specific pressure loss per adsorber length $\Delta p_{\text{los,G,sp}_{\Delta x}}$ in dependence of the superficial gas velocity $u_{\text{G,sup}}$ for a fixed bed adsorber (-) and monolith adsorber design (--), with sorbent particle diameter D_P and channel width H_{Cha} , respectively, of 0.5, 1, 2 and 5 mm. Void fractions of $\psi_B = 0.38$ (Section 3.3.1) and $\psi_{\text{Cha}} = 0.8$ are assumed for the fixed bed and monolith structure, respectively, which are in the typical ranges for these types of adsorbers ($0.26 \leq \psi_B \leq 0.48$, $0.72 \leq \psi_{\text{Cha}} \leq 0.87$).^{114,115} The pressure loss of the fixed bed is calculated by *Ergun* equation¹¹⁶, whereas for the calculation of pressure losses within the monolith a *Hagen-Poiseuille*-type equation^{116,117} is used. For pressure loss calculations properties of dry air¹¹⁶ at 25°C and 10^5 Pa are used.

A similar difficulty arises in sorbent-based *DAC* concepts. These become subject to the constraint of low pressure losses during air–sorbent contacting, if reasonable energy demands are aspired. As shown by Figure 2.2(b) pressure losses arising in conventional fixed bed adsorbers seem to impede their application in *DAC* concepts. Even use of honeycomb monolithic structures, which are known for their low pressure loss characteristics,^{99,115,117} only allows for small superficial gas velocities that limit the maximum productivity of the *DAC* unit by the convective transport of CO_2 to the sorbent (Figure 2.3(a)).

Bearing in mind that in large-scale realizations of *DAC* processes the question of an efficient sorptive – sorbent contacting becomes crucial, use of kinetic energy present in ambient air, i.e., of natural convection (wind), might be beneficial¹⁷ to avoid air compression. In a best case scenario, this implies realization of *DAC* units at locations that offer steady wind conditions in a reasonable order of magnitude. However, the optimal wind velocity will depend on the contactor design, e.g., Socolow et al.¹⁷ assume air velocities of 2 m s^{-1} , whereas Goldberg et al.¹¹⁸ propose to place air capture units at the Kerguelen plateau region in the Indian Ocean where steady west-northwest wind velocities range $8.1 - 14 \text{ m s}^{-1}$.

Investigating the influence of wind velocity on contactor design, three main considerations may be named which set constraints to possible air velocities with respect to air capture units. These are the amount of CO_2 convectively conveyed to, and through the air capture unit, the maximum allowed pressure loss within the unit and its safe operation. Figure 2.3(a) gives a first impression of the air velocity influence on the maximal productivity of a *DAC* unit by depicting the variation of the CO_2 flow per square meter of unit facing the wind in dependence of the air velocity. Even at the maximum air velocity investigated only $51 \text{ kg h}^{-1} \text{ m}^{-2}$ of CO_2 are flowing through the contactor at CO_2 mole fractions currently present in air. Moreover, to maintain a minimum driving force for the adsorption process, the contactor will most likely not capture CO_2 with an efficiency of 100%. This results in an even lower productivity.

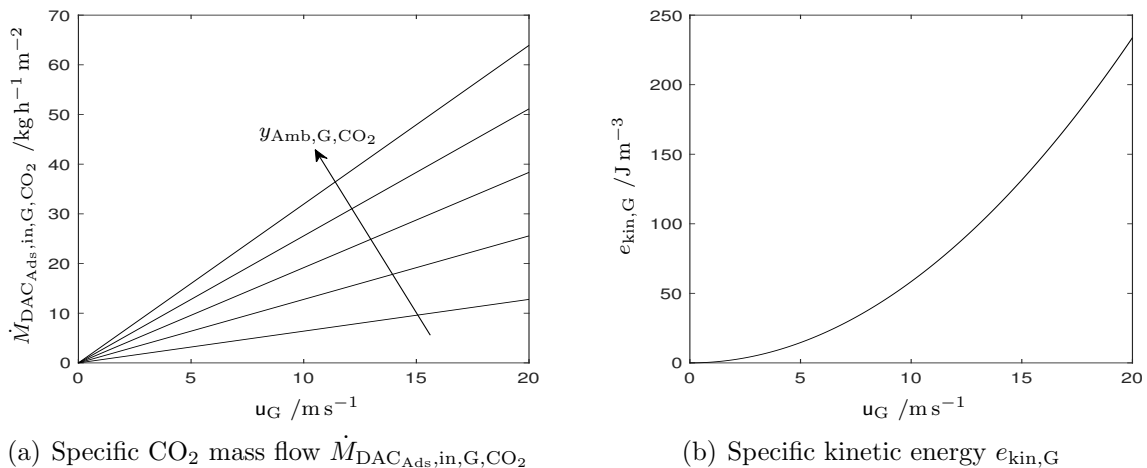


Figure 2.3: (a) Specific CO_2 mass flow per square meter of contactor facing the air flow $\dot{M}_{\text{DAC}_{\text{Ads},\text{in},\text{G},\text{CO}_2}}$ for CO_2 mole fractions in ambient air $y_{\text{Amb},\text{G},\text{CO}_2}$ ranging 100–500 ppm distributed in equal intervals of 100 ppm and (b) specific kinetic energy¹¹⁹ of air $e_{\text{kin},\text{G}}$ in dependence of air velocity u_{G} . Calculations are performed for dry air¹¹⁶ at 25°C and 10^5 Pa .

If compression of air is to be avoided, the kinetic energy of ambient air $e_{\text{kin},\text{G}}$ will determine the maximum allowed pressure loss in the contactor. In this respect, the results summarized in Figure 2.3(b) indicate that even if kinetic energy scales in a quadratic manner with gas velocity,¹¹⁹ pressure losses within the *DAC* unit are allowed to reach 250 Pa in the best case scenario. For technical applications, this maximum pressure loss is very small and the kinetic energy, as well as the maximum productivity, will increase with gas velocity. Thus, one may intuitively aim to investigate higher gas phase velocities. However, with rising air velocities, the forces acting on the *DAC* units will increase. Air

velocities above 20.8 m s^{-1} are already classified as storm.¹²⁰ In this respect, a comparison to well-researched wind turbines that typically operate at wind velocities ranging $6\text{--}16 \text{ m s}^{-1}$ and begin to shut down above 20 m s^{-1} ,¹²¹ may help to estimate a reasonable basis for the design of *DAC* units. On the other hand, if *DAC* units are not to be placed offshore, one has to expect significantly lower air velocities that, e.g., in Germany can be described by *Weibull* distributions with mean velocities in a height of 10 m ranging $2\text{--}6 \text{ m s}^{-1}$.¹²¹

In conclusion, this preliminary analysis indicates that regardless of whether the kinetic energy of the ambient air or additional compression energy is used for air–sorber contacting, realization of low pressure losses will become a crucial design constraint in *DAC* applications. A more detailed investigation of these preliminary findings with respect to a specific adsorber design will be given in Chapter 4.

2.2.3 Thermal energy demand

One may consider to change the air temperature, e.g., aiming for a cryogenic operation to separate CO_2 , as commonly done in feed stream preparation of air separation plants.^{79,81} However, even if cryogenic capture processes of CO_2 from flue gases can be operated at a capture efficiency of 99% at 10^5 Pa , the gas phase has to be cooled down to $-135 \text{ }^\circ\text{C}$.⁸¹ Taking into account the properties of air at ambient conditions,¹¹⁶ a change of air temperature by 1 K would require a CO_2 -specific energy demand of 73 kJ mol^{-1} , which lets the application of cryogenic processes in the context of *DAC* seem unfeasible.

Focusing on *TSA* operation, an other important characteristic of air capture processes with respect to their thermal energy demand is revealed. For exemplifying purpose, the energy demand for cyclic operation between temperature levels that differ by 75 K is investigated based on common sorbent properties, e.g., heat capacity $c_{p,P} = 1.5 \text{ kJ kg}^{-1} \text{ K}^{-1}$ (Section 3.3). A CO_2 -specific energy demand of the sorbent temperature change in the order of magnitude of 113 kJ mol^{-1} is required at a working capacity of 1 mol kg^{-1} , whereas at working capacities of 0.25 mol kg^{-1} the specific energy demand increases to 450 kJ mol^{-1} . A comparison with *Sabatier* reaction heat release (165 kJ mol^{-1}) reveals high influence of this heat demand on the processes overall energy balance. The need for efficient heat integration strategies of the sorbent sensible heat, to minimize the CO_2 -specific energy requirement that currently impedes its efficient large-scale application, is underlined.

Summarizing, high energy requirements of changing air temperature impede use of separation processes based on this principle, e.g., cryogenic concepts. If the application of sorbent-based separation processes is aspired, which use a thermal driving force in the regeneration process, efficient recovery of the sorbent sensible heat becomes crucial to minimize the process energy demand.

2.2.4 Ab- and adsorption concepts in DAC applications

The analysis given in Sections 2.2.2–2.2.3 confirms the tendency observed in the literature review (Section 2.1) that ab- and adsorption processes should predominantly be considered as technological approaches to *DAC*. In this respect, especially research in solid sorbent-based *DAC* technologies has significantly increased in the last decade.^{67,96,122,123} This is reasoned in various advantages attributed to use of solid sorbents. Referring to

the target of this work, besides other sorbent-specific properties (Chapter 3), especially the lower heat capacity of solid compared to liquid sorbents can become a significant advantage in commonly applied, thermally driven regeneration concepts.^{124,125}

In contrast to common *CCSU*, CO₂ is captured from the ambient, such that contamination of the capture unit educt gas by volatile hazardous compounds of the sorbent is to be avoided. Even if this can be ensured, considering for exemplifying purpose an aqueous sorbent system, the saturation pressure of water under ambient conditions, given by *Antoine* equation¹²⁶, is in the order of magnitude of 3.2 kPa. Assuming a change in relative humidity of air by 10% when being contacted with a liquid sorbent, the ratio between the volatile H₂O loss to the ambient and maximum amount of CO₂ capturable is eight. In conclusion, high sorbent losses have to be expected when using liquid sorbents,^{43,67,125} which in the case of aqueous systems might become a strain to fresh water resources.

Moreover, in a non-ideal setting, ambient air will contain contaminants, e.g., dust, which might accumulate in the liquid sorbet, whereas in the case of solid sorbents only minor effort to remove deposits has to be expected. One may argue that use of air filters would be an easy solution to solve this issue. But this would contradict the requirement of low pressure losses in the *DAC* unit determined in the analysis given in Section 2.2.2.

Concluding, the application of solid sorbent-based air capture processes seems most promising compared to other gas separation technologies. Hence, the analysis to follow will focus on this technological approach.

2.3 Approaches to heat integrated DAC concepts

The basic analysis given in Section 2.2 reveals that for an energy efficient application of air capture units their design and operation needs to ensure low pressure losses during air–sorbent contacting and should aim for minimum energy demands in the sorbent regeneration step. Whereas the first aspect named results in specific design constraints for the *DAC* concept (Chapter 4), a more detailed analysis of the *DAC* process energy balance is required to interpret the consequences of the second implication. In this respect, Section 2.3.1 gives a first estimate for the minimum degree of heat integration required within the *DAC* unit to allow for an overall autothermal *DAC–PtG* process. Based on these results, Section 2.3.2 investigates strategies for efficient thermal integration.

2.3.1 The minimum degree of heat integration within the DAC unit

With focus on the heat demand of commonly applied *TSA* concepts, one may define the condition to enable operation of a temperature-swing cycle as

$$Q_{\text{ext}} \geq Q_{\text{ads,CO}_2} + Q_{\text{sen,Sor}} + Q_{\text{sin,adi}} , \quad (2.3)$$

with Q_{ext} being the external heat source available, $Q_{\text{ads,CO}_2}$ defining the heat demand of CO₂ desorption and $Q_{\text{sen,Sor}}$ resembling the contribution of the sorbent temperature change. For a first case analysis only the contributions named are considered, i.e., $Q_{\text{sin,adi}}$ that represents the additional heat sinks or sources becomes zero as they either contribute

little to the overall heat balance, e.g., the sensible heat of the CO₂ adsorbed, or require a more complex investigation to be performed in the subsequent chapters, e.g., water co-adsorption (Chapter 5). This allows to rewrite (2.3) such that a criterion to estimate the feasibility of autothermal operation is received, which reads

$$-\Delta h_{\text{rea,Sab,CO}_2}^{\circ} = \frac{Q_{\text{ext}}}{m_{\text{P}} \cdot \Delta q_{\text{wor,CO}_2}} \geq -\Delta h_{\text{ads,CO}_2} + (1 - \eta_{\text{int,the}}) \cdot \frac{c_{p,\text{P}} \cdot \Delta T_{\text{ads,des}}}{\Delta q_{\text{wor,CO}_2}}. \quad (2.4)$$

The parameter m_{P} defines the mass of sorbent used and Q_{ext} is reformulated assuming the heat release of *Sabatier* reaction to be the only heat source available. Accepting that (2.4) is a strongly simplified version of the overall heat balance, it nevertheless allows for a first insight into the energy balance of the integrated *DAC* unit, which is sufficient at this stage of the investigation. Note that for a given sorptive–sorbent system the heat of adsorption $\Delta h_{\text{ads,CO}_2}$ is defined by the thermodynamics of the gas–solid system, as is the heat capacity of the sorbent. Moreover, the maximum sorbent working capacity $\Delta q_{\text{wor,CO}_2}$ is limited by the equilibrium loading under ambient conditions, whereas a minimum temperature difference between the adsorption and desorption cycle $\Delta T_{\text{ads,des}}$ is required to split the bond between adsorbate and sorbent. Thus, for a given gas–solid system the major degree of freedom that can be varied to satisfy (2.4) is the efficiency of sorbent sensible heat recovery $\eta_{\text{int,the}}$.

Figure 2.4 evaluates the influence of $\Delta q_{\text{wor,CO}_2}$ and $\Delta T_{\text{ads,des}}$ on the minimum efficiency of thermal integration $\eta_{\text{int,the,min}}$ required to satisfy (2.4), for a reference sorbent with $c_{p,\text{P}} = 1.5 \text{ kJ kg}^{-1} \text{ K}^{-1}$ and $\Delta h_{\text{ads,CO}_2} = -84 \text{ kJ mol}^{-1}$ (Chapter 3). If one was able to design a sorbent that requires only small amplitudes of temperature cycling to allow for high working capacity, no heat integration, i.e., $\eta_{\text{int,the,min}} = 0$, would be required to satisfy (2.4). However, reasoned in low partial pressure of CO₂ in the ambient, comparatively low maximum sorbent loadings are to be expected in *DAC* applications (Section 3.1),⁶⁷ while simultaneously the formation of chemical bonds between the adsorbate and sorbent seems to be unavoidable,^{41,85} to ensure reasonable working capacities and to minimize co-adsorption phenomena. Unfortunately, the aspects named clearly contradict the aim of simultaneously realizing high working capacities and low sorbent regeneration temperatures. Moreover, in general one would not operate at working capacities in the vicinity of the maximum loading, to ensure high driving forces of the adsorption process. Consequently, low values of $\Delta q_{\text{wor,CO}_2}$ of less than 1 mol kg^{-1} might be realizable. However, with respect to the data shown in Figure 2.4, it seems that even in the worst case scenario excessively high values of $\eta_{\text{int,the,min}}$ are not required to satisfy (2.4). Consequently, an investigation of possible heat integration strategies within *DAC* units to allow for autothermal operation of the overall process structure seems to be a promising approach.

On the other hand, the results indicate that if a suitable sorbent with high working capacity was available, already comparatively low values of thermal integration might suffice to ensure autothermal operation. This on a first view puts the aim of reaching high values of $\eta_{\text{int,the,min}}$ into question. Nevertheless, the energy spent for CO₂ separation can reach significantly high values, e.g., realization of capture facilities in point sources can already result in an increase of the energy requirement by 25–30%.⁸¹ For exemplifying purpose, focus is placed on a scenario with $\Delta T_{\text{ads,des}} = 75 \text{ K}$ and $\Delta q_{\text{wor,CO}_2} = 0.7 \text{ mol kg}^{-1}$. This

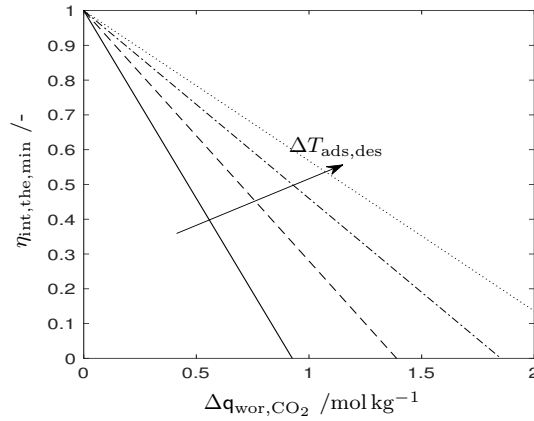


Figure 2.4: Minimum degree of thermal integration $\eta_{\text{int,the,min}}$ to satisfy (2.4) as a function of the CO_2 working capacity $\Delta q_{\text{wor,CO}_2}$ for temperature differences between the ad- and desorption cycle $\Delta T_{\text{ads,des}}$ of 50 (-), 75 (--), 100 (-·) and 125 K (··). Calculations are based on the thermophysical properties of a reference system with $c_{p,P} = 1.5 \text{ kJ kg}^{-1} \text{ K}^{-1}$ and $\Delta h_{\text{ads,CO}_2} = -84 \text{ kJ mol}^{-1}$.

requires the minimum degree of thermal integration to be 50%. If working at $\eta_{\text{int,the,min}}$ is aspired, 50% of the energy stored in the sensible heat of the sorbent is not recovered. This is, the CO_2 -specific energy penalty attributed to the cyclic operation of the sorbent is 80 kJ mol^{-1} , which would result in a loss of heat in the order of magnitude of 1.2 TW, assuming that $20 \text{ Gt a}^{-1} \text{ CO}_2$ are to be captured according to the worst case scenarios summarized by the *IPCC* (Section 1.1.3). A comparison with the currently installed global power generation capacities, which are about 7.8 TW, with power generation by coal ($\sim 2.1 \text{ TW}$) and gas ($\sim 1.9 \text{ TW}$) accounting for more than half of the total capacities,¹¹³ reveals that the loss of thermal energy in the *DAC* unit can be in a significantly high order of magnitude. Even if the comparison given might overestimate the amount of CO_2 captured by *DAC* in the future, it nevertheless motivates realization of high degrees of thermal integration to minimize the thermal losses to the environment. This way, one might free more valuable heat sources at elevated temperature levels, e.g., heat release by *Sabatier* reaction, to be used in additional process steps or for electric power generation.

2.3.2 Approaches to increase the efficiency of thermal integration

The results summarized in Section 2.3.1 indicate that realization of a high degree of thermal integration in the *DAC* unit might be beneficial to reduce the CO_2 -specific energy demand of air capture applications. Common thermal integration strategies are investigated (Section 2.3.2.1) and innovative concepts that make use of adsorber operation in spatial cyclic steady state are proposed (Section 2.3.2.2).

2.3.2.1 Evaluation of common approaches

To reach high levels of thermal integration, one may consider integration of two or more *DAC* units such that the heat released during the cooling stage of one unit is used as heat source for temperature increase from adsorption to desorption level in an other unit. Figure 2.5(a) visualizes this concept for a simple integration of two *DAC* units

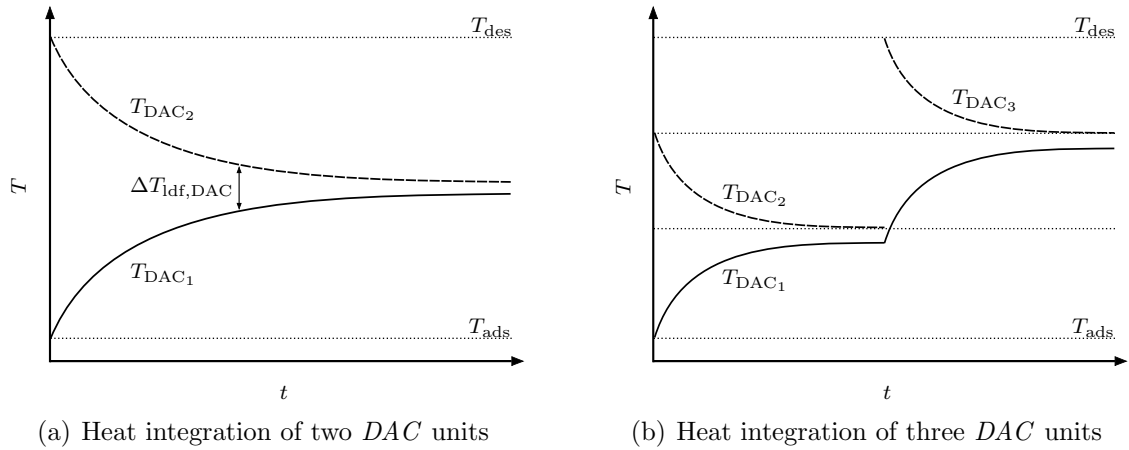


Figure 2.5: Visualization of the temperature profiles for (a) two and (b) three *DAC* units in an integrated approach. The evolution of the *DAC* unit temperatures T_{DAC_i} in dependence of time t for the integration half cycle of one unit, i.e., heating up of *DAC*₁ unit from adsorption temperature T_{ads} to the maximum temperature realizable by a simple co-current heat integration scheme is shown. Moreover, the desorption temperature level T_{des} and the linear driving force of the heat transfer $\Delta T_{\text{lf,DAC}}$ are depicted.

under the constraint of an uniform spatial temperature change within the units. In a best case scenario, i.e., in the case that the minimum temperature difference required for sufficient heat transfer $\Delta T_{\text{lf,DAC}}$ converges to zero, a maximum degree of sensible heat recovery of 50 % is reached. Given that the results summarized in Section 2.3.1 motivate the realization of high degrees of heat recovery, the integration of multiple *DAC* units as visualized in Figure 2.5(b) is conceivable. Applying this integration scheme, the maximum degree of thermal integration can be determined by

$$\eta_{\text{int,the,max,mul}} = 1 - \phi_{\Delta T_{\text{lf,DAC}},\Delta T_{\text{ads,des}}} - \frac{1 - \phi_{\Delta T_{\text{lf,DAC}},\Delta T_{\text{ads,des}}}}{I_{\text{int,DAC}}}, \quad (2.5)$$

with $I_{\text{int,DAC}}$ giving the number of *DAC* units integrated and $\phi_{\Delta T_{\text{lf,DAC}},\Delta T_{\text{ads,des}}}$ being defined as

$$\phi_{\Delta T_{\text{lf,DAC}},\Delta T_{\text{ads,des}}} = \frac{\Delta T_{\text{lf,DAC}}}{\Delta T_{\text{ads,des}}}. \quad (2.6)$$

Focusing on (2.5), asymptotic dependency of $\eta_{\text{int,the,max,mul}}$ on $I_{\text{int,DAC}}$ becomes apparent, which indicates that a significant number of *DAC* units need to be thermally integrated to attain a high degree of heat integration. This observation is underlined by Figure 2.6 that visualizes the evolution of the efficiency of thermal integration in dependence of the number of units being integrated for various values of $\phi_{\Delta T_{\text{lf,DAC}},\Delta T_{\text{ads,des}}}$.

One notices that $\phi_{\Delta T_{\text{lf,DAC}},\Delta T_{\text{ads,des}}}$ determines the maximum level of heat integration that can be reached in the limiting cases of $I_{\text{int,DAC}}$ approaching infinity. However, even in the best case scenario with $\phi_{\Delta T_{\text{lf,DAC}},\Delta T_{\text{ads,des}}} = 0$, a significant number of thermal couplings is required to attain high degrees of $\eta_{\text{int,the,max,mul}}$. Acknowledging that this modular approach can provide high levels of thermal integration, it might entail a considerably

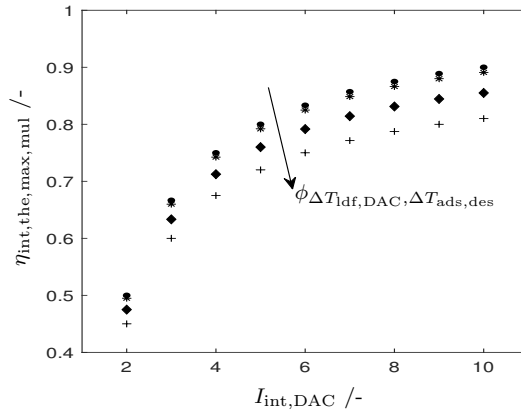


Figure 2.6: Maximum efficiency of thermal integration $\eta_{int,the,max,mul}$ reached via the coupling of multiple *DAC* units in dependence of the number of *DAC* units integrated $I_{int,DAC}$. Ratios between the linear driving force required for heat transfer and the temperature difference between the adsorption and desorption cycle $\phi_{\Delta T_{ldf,DAC}, \Delta T_{ads,des}}$ of 0 (●), 0.01 (*), 0.05 (◆) and 0.10 (+) are investigated.

logistical expense, reasoned in the coupling of multiple, periodically operated *DAC* units. To be more specific, to reach a level of thermal integration of 80 %, in the best case scenario five units need to be integrated simultaneously, whereas for heat integration levels of 90 % a thermal coupling of ten units is required. Consequently, following this approach only seems to be reasonable if a medium level of thermal integration is aspired.

To avoid the challenge of simultaneously coupling multiple *DAC* units, one may consider to use the approach of hot-gas desorption¹²⁷. This is, the strip gas first passes one adsorber in the cooling stage and is afterwards sent to an other unit that is currently in the heating cycle. Heat is transferred from the hot to the cold unit. Temperature and concentration fronts in the units arise that allow for an intensive heat integration. For exemplifying purpose, this concept is applied to a *DAC* approach operating in *TSA* mode with a working capacity of $\Delta q_{wor,CO_2} = 1 \text{ mol kg}^{-1}$. Drawing a basic energy balance allows to estimate the maximum mean CO_2 concentration leaving the adsorber in dependence of the sorbent and stripping gas heat capacity. The stripping gas heat capacity is estimated to take a value of $29 \text{ J K}^{-1} \text{ mol}^{-1}$, which is in the order of magnitude of the heat capacity of hydrogen,¹²⁸ whereas the sorbent heat capacity is estimated to be $1.5 \text{ kJ kg}^{-1} \text{ K}^{-1}$. It can be shown that even in the best case scenario of a negligible small thermal slip between the stripping gas and solid phase, the thermal energy stored in the sensible heat of 52 mol stripping gas is required to heat 1 kg of sorbent. This results in a maximum mean CO_2 mole content at the adsorber outlet of less than 2 %.

In conclusion, the concept of single stage hot-gas desorption, with typical concentration factors ranging 10–20,¹²⁹ does not allow for the high change in the CO_2 share required, e.g., to directly use the product gas in *PtG* applications (~ 500), if hydrogen is used as stripping gas. Moreover, additional drawbacks as the necessity of subsequent gas separation steps or increased energy penalties resulting from H_2O co-desorption can arise. Besides, also a simple coupling of multiple *DAC* units, e.g., by a liquid heat transfer fluid,¹³⁰ does not seem promising (Figure 2.6) with regard to the maximum level of $\eta_{int,the,max,mul}$ attainable and to the drawbacks resulting from the synchronized operation

of multiple *DAC* units. Consequently, alternative heat recovery concepts are required to maximize the efficiency of sorbent sensible heat recovery.

2.3.2.2 Transformation from time to space domain

Bearing the analysis given in Section 2.3.2.1 in mind, it seems reasonable to focus on heat integration within a single *DAC* unit. In this respect, one may consider that from an engineering point of view, the primary question is not *if* enough heat on a sufficiently high temperature level is available for heating of the solid sorbent from adsorption to desorption temperature by means of internal heat exchange, but *when* this heat is available. Transformation of the heat integration problem from time to space domain would allow to thermally couple any point of the sorbent temperature trajectory in the cooling cycle as heat source with a point at lower temperature in the heating cycle. Figure 2.7 visualizes the basic concept behind this heat integration approach. Realization of a direct and indirect heat transfer between the sorbent particles is considered. For the sake of clarity, heat effects arising from the ad- and desorption process are not discussed at this stage.

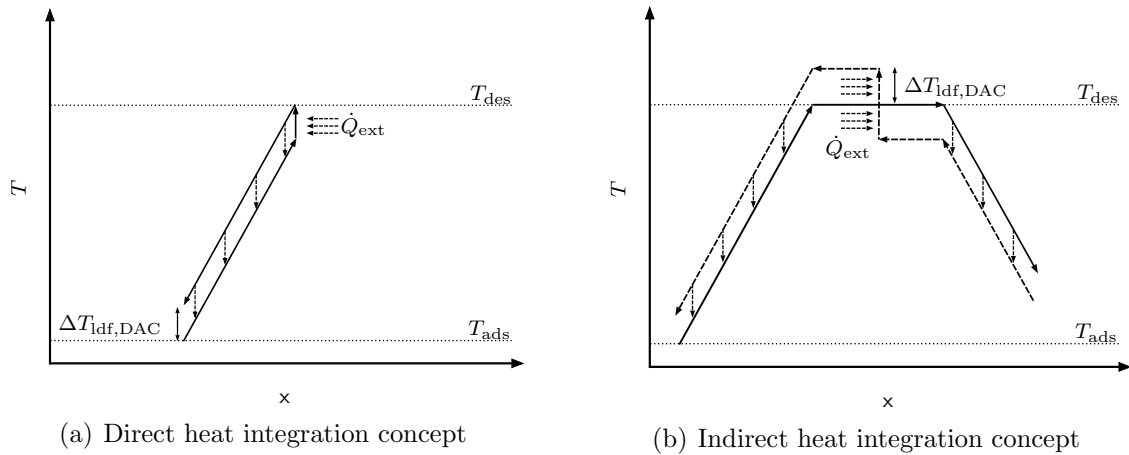


Figure 2.7: Sketch of integration concepts for sorbent sensible heat. (a) Direct and (b) indirect integration strategies are shown, in which a thermal coupling of sorbent particles in the heating and cooling cycle is realized by transformation of the adsorption process cyclic steady state from time to space domain. The evolution of the sorbent temperature profile (-) along the spatial coordinate x is shown. Moreover, the additional liquid heat transfer medium's trajectory of temperature in the indirect concept is depicted by a bold dashed line (- -). Heat flows are visualized by thin dashed arrows (- -). The temperature levels of adsorption (T_{ads}) and desorption (T_{des}), the minimum temperature difference required for efficient heat transfer $\Delta T_{\text{df,DAC}}$ and the external heat provided \dot{Q}_{ext} are shown.

In the direct heat integration concept shown in Figure 2.7(a), heat recovery is enabled by a forced hysteresis in the sorbent temperature profile. To be more specific, if the sorbent particles are moving, counter-current sorbent–sorbent heat exchange can be realized by additional external heating (\dot{Q}_{ext}) that creates a driving force ($\Delta T_{\text{df,DAC}}$) for heat transfer. The trajectory of the sorbent temperature in the spatial coordinate can be summarized as follows: after being contacted with ambient air at temperature T_{ads} , the sorbent temperature is increased by direct heat transfer, e.g., via a solid heat transfer

medium, by counter-current heat exchange with sorbent particles in the cooling stage. A minimum temperature difference of $\Delta T_{\text{ldf,DAC}}$ is required to allow for a sufficiently high heat flow between the streams, limiting the maximum temperature reachable by heat integration. Additional heat input (\dot{Q}_{ext}), e.g., from *Sabatier* reaction, is required to generate a minimum temperature difference of the heat transfer process. In the scenario depicted, this heat input is used to increase the sorbent temperature by $\Delta T_{\text{ldf,DAC}}$ to reach desorption temperature level T_{des} . After the desorption of CO_2 , sorbent sensible heat is recovered via counter-current heat exchange with sorbent particles in the heating stage. Focusing on the characteristic temperature levels exhibited by the sorbent, which reflect the amount of external heat required ($\Delta T_{\text{ldf,DAC}}$) and the overall change in the sorbents sensible heat ($\Delta T_{\text{ads,des}}$), one notices that the efficiency of thermal integration allowed for by the direct heat integration concepts is given by

$$\eta_{\text{int,the,max,dir}} = 1 - \phi_{\Delta T_{\text{ldf,DAC}},\Delta T_{\text{ads,des}}} \quad (2.7)$$

Equation (2.7) specifies the thermal efficiency of the multi-unit heat integration (2.5) in the limiting case of an infinite number of units coupled. Bearing in mind that the ideal counter-current heat exchange resembles an infinite number of heat transfer stages, this does not come by surprise. Nevertheless, the analysis given clearly indicates the direct heat transfer concept to be superior with regard to its ability of reaching high degrees of thermal integration. For a more detailed analysis with respect to the technical realization of this concept, the reader is referred to Chapter 4.

Besides direct heat transfer between the sorbent particles, use of an additional heat transfer medium in counter-current operation to the solid sorbent flow is conceivable to realize high degrees of heat recovery. Figure 2.7(b) visualizes the basic temperature profiles during the heat exchange process. Solid sorbent particles are heated up from adsorption (T_{ads}) to desorption temperature (T_{des}) by means of recuperative heat exchange with the transfer medium. Moreover, in the cooling cycle the sensible heat of the sorbent is recovered via heat transfer from sorbent to transfer medium. Evaluating the evolution of the sorbent and transfer medium temperature profile, one notices that a thermal loss in the order of $2\Delta T_{\text{ldf,DAC}}$ has to be expected. This is also reflected by the heat input to the external transfer medium that increases this medium's temperature by $2\Delta T_{\text{ldf,DAC}}$ to generate the minimum temperature difference required for sufficient heat transfer. Based on these observations, the maximum thermal efficiency, achievable by the indirect heat integration concept, can be estimated by

$$\eta_{\text{int,the,max,ind}} = 1 - 2 \cdot \phi_{\Delta T_{\text{ldf,DAC}},\Delta T_{\text{ads,des}}} \quad (2.8)$$

Use of an additional transfer medium results in a more significant dependency of the minimum thermal loss on $\Delta T_{\text{ldf,DAC}}$, attributed to presence of additional thermal resistances to be overcome during heat transfer between sorbent particles and heat transfer medium. Bearing in mind that the heat flux per transfer area is not only a function of the temperature difference between the streams, but also of the thermal resistance present, one may wonder if $\phi_{\Delta T_{\text{ldf,DAC}},\Delta T_{\text{ads,des}}}$ can be assumed to stay constant throughout the analysis.

Table 2.1: Basic comparison of the direct and indirect heat integration approach with respect to the results of the preliminary analysis given in Section 2.3.2.2.

	Direct heat integration	Indirect heat integration
Coupling of half cycles	Direct	Indirect
Counter-current heat transfer	Sorbent – sorbent	Sorbent – transfer medium
Heat losses	$\propto \Delta T_{\text{ldf,DAC}}$	$\propto 2 \cdot \Delta T_{\text{ldf,DAC}}$
External heat supply	To sorbent	To transfer medium
Operation parameter	Sorbent	Sorbent and transfer medium

Indeed, this is not the case, as the thermophysical properties of the heat transfer media and characteristics of the transfer process can vary between the concepts (Chapter 4).

Acknowledging that this observation indicates that the range of validity of the preliminary analysis given is limited, it nevertheless allows for a first comparison of the characteristics of the concepts, sufficient for the scope of the basic introduction aimed for in this chapter. Table 2.1 summarizes the main differences between the two concepts. Essentially, the key difference of the approaches presented lies in the coupling of the heating and cooling cycle, i.e., a direct thermal coupling of the sorbents or an indirect coupling via an additional transfer medium. Besides a different dependency of the heat loss characteristics on the linear driving force of heat transfer ($\Delta T_{\text{ldf,DAC}}$), this results in the necessity of implementing a direct counter-current movement of solid sorbents in the direct heat integration concept, whereas only a counter-current heat exchange between the sorbent and additional transfer medium needs to be realized in the indirect concept. Even if this difference might not become crucial from a heat integration point of view, it implies significant differences in the design constraints for a technical realization. This is, in contrast to the indirect concept, application of the direct heat integration concept requires the heating and cooling zone length to be of the same length, and movement of the solid phase in the heating and cooling zone can not simultaneously be realized by gravitational forces. Moreover, in the direct concept external heat transfer is bound to the heat exchange with the sorbent, whereas the indirect concept allows for sorbent-independent external heating of the transfer medium. Besides these typical differences, presence of an additional moving transfer medium in the indirect approach can allow for additional degrees of freedom, such that the flexibility of the design and especially of the operation parameters is significantly higher in the indirect concept.

In summary, based on the preliminary analysis given, both concepts can offer a high efficiency of thermal integration that might significantly reduce the impedingly high CO₂-specific energy demand of *DAC* technologies. Based on the temperature profiles and design constraints discussed in this section, a more detailed analysis of a technological realization of the approaches presented is given in Chapter 4.

2.4 Summary and conclusion

The results presented in Chapter 1 indicate large-scale application of *NETs* to become most likely unavoidable in the near future. *DAC* technologies are among the most promising options for realization of *NETs*. But efficient large-scale use of *DAC* is bound to specific limitations that arise from the dilute state of CO_2 in the atmosphere.

Section 2.1 State of the art

summarizes the state of knowledge with respect to currently realized *DAC* technologies. The findings outlined reveal that the concept of extracting CO_2 from air has already been analyzed and applied for several decades. But with CO_2 being the target component in large-scale *DAC* processes, use of the majority of commonly applied technologies is not promising. Solely ad- and absorption-based capture concepts are currently investigated.

Section 2.2 Intrinsic constraints of DAC

confirms the tendencies observed in Section 2.1 by analyzing the intrinsic constraints of *DAC* technologies. Thermodynamic minimum energy demand for CO_2 separation from the ambient is found to only exceed the one of flue gas capture by a factor of less than four (Section 2.2.1). Reasoned in the low ambient CO_2 content, separation technologies that are based on a change of the thermophysical properties of air are not applicable from an energy point of view. This limits the portfolio of separation technologies to ab- and adsorption processes (Sections 2.2.2-2.2.3). Use of solid sorbents seems most promising (Section 2.2.4). With regard to air–sorbent contacting, need of low pressure losses is underlined. Simulation results indicate that gas phase compression by 1% is already accompanied by impedingly high energy demands of about 37% of the *Sabatier* reaction heat release (Section 2.2.2). Analysis of thermal energy demand reveals considerable contributions of the sorbent sensible heat in *TSA* operation (Section 2.2.3).

Section 2.3 Approaches to heat integrated DAC concepts

investigates the minimum efficiency of thermal integration of the sorbent sensible heat that allows for autothermal operation of an integrated *DAC* – *PtG* process (Section 2.3.1). Even if the analysis given indicates that heat recoveries of less than 50% suffice to enable autothermality of the overall process, heat losses attributed to low recoveries of sorbent sensible heat can considerably increase the CO_2 -specific heat demand of the *DAC* process. Different strategies for recovery of the sorbent sensible heat are investigated (Section 2.3.2). Concepts for direct and indirect thermal integration in one *DAC* unit, based on a transformation of the cyclic steady state operation profile of the *DAC* process from time to space domain, are found to provide superior potential for heat integration.

In summary, intensified integrated *DAC* concepts can allow for a significant reduction of the CO_2 -specific heat demand, but their design needs to be adjusted to the specific requirements that result from air being the CO_2 reservoir. Among those, especially realization of low pressure losses within the *DAC* unit is identified as a key design constraint to be analyzed in more detail in Chapter 4. However, before investigating this aspect, a solid sorbent needs to be selected and examined with respect to its ability of technically realizing the heat integration concepts proposed (Chapter 3).

3 Characterization of the sorbent

Scientific contributions

Parts of this chapter have been published in the following scientific contributions:

Peer-reviewed journal article

- Drechsler, C.; Agar, D. W. Investigation of water co-adsorption on the energy balance of solid sorbent based direct air capture processes. *Energy* **2020**, *192*, 116587.

Conference poster presentation

- Drechsler, C.; Agar, D. W. Analyse der Wasser-Co-Adsorption auf die Energiebilanz von Direct Air Capture Verfahren mit festen Sorbentien. Presented at Abschlusskonferenz zur BMBF Fördermaßnahme CO₂Plus, Berlin, Germany, September 24-25, 2019.

Abstract

Among various sorbents proposed for use in *DAC* applications, *supported amine sorbents* (*SAS*) are most promising. Besides superior capture capacity resulting from the formation of strong chemical bonds between the amine moiety and CO_2 , their solid state avoids hurdles that arise within the realization of liquid sorbent-based air capture processes, e.g., sorbent entrainment. Within the class of *SAS*, application of *Lewatit VP OC 1065*, a commercially available, polymeric ion-exchange resin with primary amine moiety, is experimentally investigated with respect to its applicability as *DAC* sorbent. Adsorption isotherm data are found to be well describable by *Toth* model. Adsorption capacities of about 0.9 mol kg^{-1} at ambient CO_2 pressures are revealed.

High levels of water co-adsorption in the order of magnitude of 9 mol kg^{-1} are found under ambient conditions. Experimental results indicate that H_2O adsorption can in good accordance be described as a function of relative humidity by application of *BET*-type isotherm models. Promoting effects of H_2O co-adsorption on CO_2 capacity are confirmed. Decline in enhancing potential of moisture on CO_2 adsorption with raising CO_2 partial pressure is noticed. A severe energy penalty in the sorbent regeneration process is expected based on the order of magnitude of water adsorption found. This motivates research focused on measures that allow limiting the drawbacks resulting from H_2O co-adsorption-based phenomena in process design.

With regard to a possible large-scale application, process relevant thermophysical properties of the sorbent are investigated. High thermal stability and low heat capacity found are favorable for *TSA* applications. Good flowability and mechanical stability seem beneficial for realization of innovative *moving bed adsorber* concepts.

This chapter is structured as follows:

Section 3.1 State of the art

gives a brief overview of the current state of research with respect to *DAC* sorbents. Particular attention is paid to the class of *supported amine sorbents* and, within this, to *Lewatit VP OC 1065*.

Section 3.2 Adsorption properties of the sorbent

is dedicated to the analysis of adsorption properties of the sorbent. In addition to CO_2 adsorption, H_2O co-adsorption and its influence on CO_2 adsorption is investigated.

Section 3.3 Additional properties of the sorbent

summarizes the findings of additional experiments that investigate properties of the sorbent relevant for large-scale use.

Section 3.4 Summary and conclusion

recapitulates the findings of this chapter. Applicability of the sorbent in innovative adsorber concepts (Chapter 4) is confirmed and research of measures to counteract excess H_2O co-desorption (Chapter 5) is motivated.

3.1 State of the art

Section 3.1.1 gives a brief overview of the research performed with regard to *DAC* sorbents. *Supported amine sorbents (SAS)* are revealed to be most promising. Focusing on this class of sorbents, Section 3.1.2 summarizes the current state of knowledge with regard to the interactions between *SAS*, CO_2 and H_2O . Use of the commercially available ion exchange resin *Lewatit VP OC 1065* as reference sorbent is motivated (Section 3.1.3).

3.1.1 Sorbents for DAC

Due to the increasing interest in large-scale *DAC* applications, considerable efforts have been undertaken in recent decades to research suitable sorbents.^{38,67,131} In this respect, ideal sorbent properties might be summarized as follows: high capacity, selectivity and fast kinetics of CO_2 uptake, easy regeneration, low specific heat capacity and high stability.¹³²

Focusing on a simple, not energy intensive regeneration of the sorbent, one would like to use sorbents that bind CO_2 by physical interactions rather than chemical bonds. However, reasoned in the low partial pressure of CO_2 in ambient air, physisorbent materials as *zeolites*, *activated carbon* or *metal-organic frameworks (MOFs)*, developed for point source capture,^{133–135} in general offer very low CO_2 capacity and selectivity under air capture conditions.⁶⁷ Consequently, current research focuses on chemisorbent materials that have shown superior capture characteristics in *DAC* applications.¹¹⁰

From the class of chemisorbents, liquid or solid materials might be used. As discussed in Section 2.2.4 current research focuses on solid sorbents. These offer besides other beneficial characteristics a reduced energy demand in thermal regeneration processes^{136,137} attributed to lower specific heat capacities¹²⁵, higher working capacities¹²⁵, higher CO_2 uptake rates supported by high surface to volume ratios of the porous material,⁹⁹ high chemical stability⁶⁷ and the avoidance of strong corrosive solutions⁹⁹ as well as of liquid entrainment in the air flow^{99,125,137}. Thus, this work focuses on the application of solid sorbents and only a brief summary of the current state of liquid *DAC* sorbents is given in Appendix A.1.

A significant variety of solid sorbents has been developed and tested, which can mainly be assigned to the classes of solid alkali carbonates and organic–inorganic hybrid sorbents.⁶⁷ Within the first class named, one may differentiate between bulk alkali carbonates and supported alkali carbonates. The group bulk alkali carbonates essentially covers pure solid inorganic bases. These sorbents are mainly investigated by Steinfeld and coworkers that research Ca-^{90,138} and Na-based¹³⁹ capture concepts. Among those one may name solar reactor approaches^{90,140} proposed to provide heat at high temperatures required for sorbent regeneration. Besides, various studies aim for a realization of supported alkali carbonates, e.g., by immobilization of alkaline solutions^{67,141} or of alkali metal sorbents^{67,142–144} in porous supports. Offering adsorption capacities in the order of magnitude of 1 mol kg^{-1} at ambient CO_2 concentrations, these sorbents seem to be a promising alternative for air capture applications.^{67,142} However, comparatively high regeneration temperatures ranging $100\text{--}350\text{ }^\circ\text{C}$ are required.^{67,142,144,145} This seems to be

a severe drawback with respect to a possible use of low-temperature waste heat in the regeneration process.

Currently most researched *DAC* sorbents belong to the class of organic–inorganic hybrid materials. The amine–CO₂ interactions, on which sorbents of this class are based, are well known for their superior CO₂ capture characteristics, e.g., from amine scrubbers used in flue gas capture. Different approaches to solid-based *supported amine sorbents (SAS)*¹³⁷ are investigated that might be assigned to the categories⁶⁷:

1. Amines impregnated on porous supports^{146–148}
2. Amines covalently bound to porous supports^{122,149,150}
3. Solid sorbents, realized by polymerization of amine-based monomers^{96,151,152}
4. Combinations of classes one and two^{153–155}

High maximum CO₂ capacities of more than 2 mol kg^{−1} can be reached with these sorbents under ambient conditions.⁶⁷ The strong amine–CO₂ bond formed allows for a highly selective capture process.⁶⁷ Moreover, a comparatively low heat of CO₂ adsorption (40–90 kJ mol^{−1}),^{137,156,157} as well as mild desorption temperatures (100–150 °C)^{137,158} seem beneficial with respect to an energy efficient sorbent regeneration. However, especially the strong interactions of this class of sorbents with water vapor opens up the potential for intensive research and optimization.⁶⁷ Recognizing the superior potential of *SAS* for *DAC* applications,⁶⁷ in this contribution a *SAS* will be used as reference sorbent.

3.1.2 Adsorption mechanism of CO₂ and H₂O on SAS

The amine efficiency $\eta_{\text{Ami,CO}_2}$ is of great importance in the context of *SAS*. It is defined as the molar ratio between CO₂ chemically bound to an amine moiety and the amount of all amine moieties in the sorbent. Primary, secondary and tertiary amine moieties can be present. This opens up a variety of possible reaction mechanisms that can take influence on the maximum amine efficiency and, thus, on the upper limit of CO₂ loading.

In reactions of CO₂ with primary and secondary amines formation of a zwitterion



is observed that is deprotonated by a base (B)



forming the carbamate species. Under dry air capture conditions the base (B) needs to be another amine moiety. This results in a maximum amine efficiency of 0.5.^{67,157,159–161}

Tertiary amine moieties only react with CO₂ in the presence of protic species. To be more specific with respect to *DAC* applications, under humid conditions formation of bicarbonate



and carbonate



become possible reaction paths for primary, secondary and tertiary amines.^{67,157,160} Thus, primary and secondary amines allow for CO_2 to bind in three different ways. Under humid conditions first formation of carbamates is observed that are subsequently converted to carbonates and bicarbonates.¹⁶⁰ Moreover, analysis of (3.I) - (3.IV) with respect to the amine efficiency reveals that under humid conditions this indicator can take a value of 1. In other words, *SAS* can benefit from moisture content in ambient air. In the limiting case this can lead to a doubling of the amine efficiency.^{67,157,160} More detailed insight into the influence of moisture on *SAS* is given in Section 3.2.3.

Also the kinetics and heats of adsorption become of great importance for the design of *DAC* units. Heats of reaction of *SAS* and CO_2 decrease from primary to tertiary amines.¹⁵⁷ Reaction kinetics show a similar trend, with primary amines offering the highest CO_2 uptake rates.¹⁵⁷ Consequently, trade-off considerations between the regeneration energy required and kinetics provided will arise in the selection of the type of amine moiety.

3.1.3 Lewatit VP OC 1065

The commercially available ion exchange resin *Lewatit VP OC 1065*,¹⁶² hereafter *Lewatit*, from *Lanxess* is selected as reference sorbent. Being a divinylbenzene cross-linked polymer, it can be classified as a *SAS* of category two with primary amine moiety (Figure 3.1). Various studies^{137,157,163–168} on this sorbent are published. As expected based on its classification, good adsorption properties, especially at CO_2 levels relevant for point source capture, are confirmed. These motivate research into applicability of *Lewatit* as *DAC* sorbent.

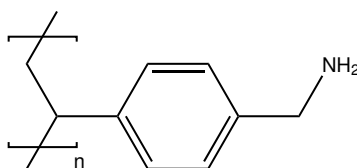


Figure 3.1: Amine repeat unit of *Lewatit*, a class two *SAS* with primary amine moiety.¹⁶³

A detailed literature review reveals that information relevant for *DAC* application, e.g., capacities at low CO_2 pressure levels or analysis of humidity influence on the capture process, is sparsely published.^{137,157,163} In general, large deviations between the data available on this sorbent are observed. The experimental results presented in this contribution help closing these gaps. Insights into the adsorption isotherms of CO_2 over a broad temperature (30–100 °C) and CO_2 partial pressure range (10 Pa–20 kPa) are provided and the influence of humidity on CO_2 adsorption is analyzed in detail.

3.2 Adsorption properties of the sorbent

After providing a brief insight into the experimental methods used (Section 3.2.1), adsorption properties of the sorbent under dry (Section 3.2.2) and humid conditions (Section 3.2.3) are discussed.

3.2.1 Materials and methods

Adsorption properties of sorbents are commonly explored by means of breakthrough curve (*BTC*, Section 3.2.1.1) experiments or thermogravimetric analysis (*TGA*, Section 3.2.1.2).⁶⁷ An investigation of the strengths and of the weaknesses of these methods (Appendix A.2) indicates use of *BTC* to be beneficial if CO₂ partial pressures are in Pa-range, whereas application of *TGA* seems favorable if CO₂ partial pressures take values in kPa-range.

3.2.1.1 Breakthrough curve experiments (*BTC*)

In this section the basic concept of *BTC* experiments and its experimental realization within the framework of this contribution is summarized.

Theory of *BTC* Breakthrough curve experiments allow for indirect determination of the sorbent loading $q_{i_{\text{Spe}}}$ by use of time-resolved information of the mole flow of a specie before ($\dot{n}_{\text{Ads}_{\text{in}},\text{G},i_{\text{Spe}}}$) and after ($\dot{n}_{\text{Ads}_{\text{out}},\text{G},i_{\text{Spe}}}$) an adsorber unit that contains a defined mass of unloaded sorbent (m_{Sor}). Figure 3.2 visualizes the basic measurement principle for an illustrative *BTC* experiment in which the residence time distribution and change in the overall gas flow by adsorption is of negligible influence. In an ideal setting, infinitely small initial breakthrough at the adsorber outlet is expected as response to an ideal step signal at the adsorber inlet from zero to the isotherm reference concentration of the sorptive. This is reasoned in the nearly complete removal of this specie by adsorption on the regenerated sorbent. However, over time the sorbent becomes saturated, i.e., it approaches its equilibrium loading with the gas phase flowing through the adsorber. Thus, the difference between the concentration of the sorptive measured at the inlet and outlet of the adsorber converges to zero and the *BTC* experiment can be stopped.

The sorbent loading can be determined by evaluation of the law of mass conservation

$$q_{i_{\text{Spe}}} = \frac{1}{m_{\text{Sor}}} \cdot \int_{t_{\text{sta}}}^{t_{\text{fin}}} \dot{n}_{\text{Ads}_{\text{in}},\text{G},i_{\text{Spe}}} - \dot{n}_{\text{Ads}_{\text{out}},\text{G},i_{\text{Spe}}} dt . \quad (3.1)$$

If a defined mole flow of an inert carrier gas ($\dot{n}_{\text{Ads},\text{G},\text{Ine}}$) is used, in situ determination of the sorptive mole fraction allows for indirect determination of the sorbent loading. Moreover, the shape of the breakthrough curve will depend on the adsorption isotherms, adsorption kinetics and operation conditions.¹²⁷ Thus, kinetic information can be extracted from *BTC* by fitting the temporal evolution of the specie's mole flow to thermophysical models. The reader is referred to Appendix A.3.2 and A.3.6 for more detailed information on

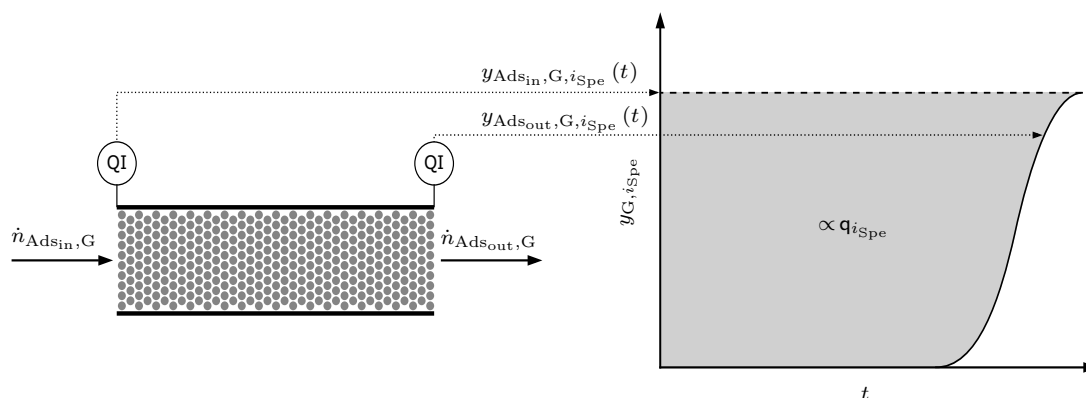


Figure 3.2: Basic measurement principle of a *BTC* experiment. The sorbent loading is determined by analysis of the streams at the adsorber inlet ($\dot{n}_{\text{Ads}_{\text{in},\text{G}}}$) and outlet ($\dot{n}_{\text{Ads}_{\text{out},\text{G}}}$). These contain mole fractions $y_{\text{Ads}_{\text{in},\text{G},i_{\text{Spe}}}}$ and $y_{\text{Ads}_{\text{out},\text{G},i_{\text{Spe}}}}$, respectively, of the specie to be adsorbed. For the simplified case of a negligible influence of the residence time distribution and of the change in the overall gas stream, the sorbent loading $q_{i_{\text{Spe}}}$ becomes proportional to the gray shaded area.

the evaluation of breakthrough curves and on the analysis of adsorption kinetics, which besides others take into account non-constant gas flow and residence time corrections.

Experimental setting Figure 3.3 shows the simplified flow diagram of the experimental setup realized in laboratory-scale. Here, a brief description is provided, whereas for more detailed insight the reader is referred to Appendix A.3.1. Automated plant control is realized via *Labview* user interface.¹⁶⁹ This allows recording of high resolution measurements (sample interval of less than 2 s) of temperature and pressure throughout the plant and inside the adsorber bed, as well as precise control of gas phase volume flows via thermal mass flow controllers from *Bronkhorst (EL-Flow)*.¹⁷⁰ Sorbent bed temperature control is realized by thermo oil flowing through the adsorber heating jacket (Figure A.3), to ensure isothermal conditions (Appendix A.3.4) during the recording of breakthrough curves. For CO_2 adsorption these are measured via two infrared devices, *URAS26 EL3020* from *ABB*,¹⁷¹ which allow for in situ determination of the CO_2 content at the adsorber outlet in the range 0–500 ppm (IR-1) and 0–40 % (IR-2). Moreover, capacitive polymer humidity sensors (*TFS 0100 E*) from *GHM Messtechnik GmbH*¹⁷² installed before and after the adsorber are used to record H_2O breakthrough curves. Humidification of the gas phase is realized by dispersing the gas flow in a tempered vessel of liquid water.

Experimental procedure A typical fill of the adsorber consists of 5 g air dried *Lewatit*¹⁶² (Table 3.4) and 75 g glass beads (0.5 mm)¹⁷³ (Table A.1). *TGA* experiments (Section 3.2.1.2) are performed with a sample of the sorbent each time the fill is changed to determine the mass of unloaded sorbent used. Mass losses attributed to desorption of species bound in the order of magnitude of 15 % are typically found. Breakthrough curves are recorded after sorbent regeneration under nitrogen flow of ca. 1.5 Nl min^{-1} at 100°C . Desorption is assumed to be complete if the humidity level falls below the resolution limit and IR-1 detects carbon dioxide contents of less than 1 ppm, which is typically achieved after 2–2.5 h desorption time. After cooling to adsorption temperature, the gas flow is

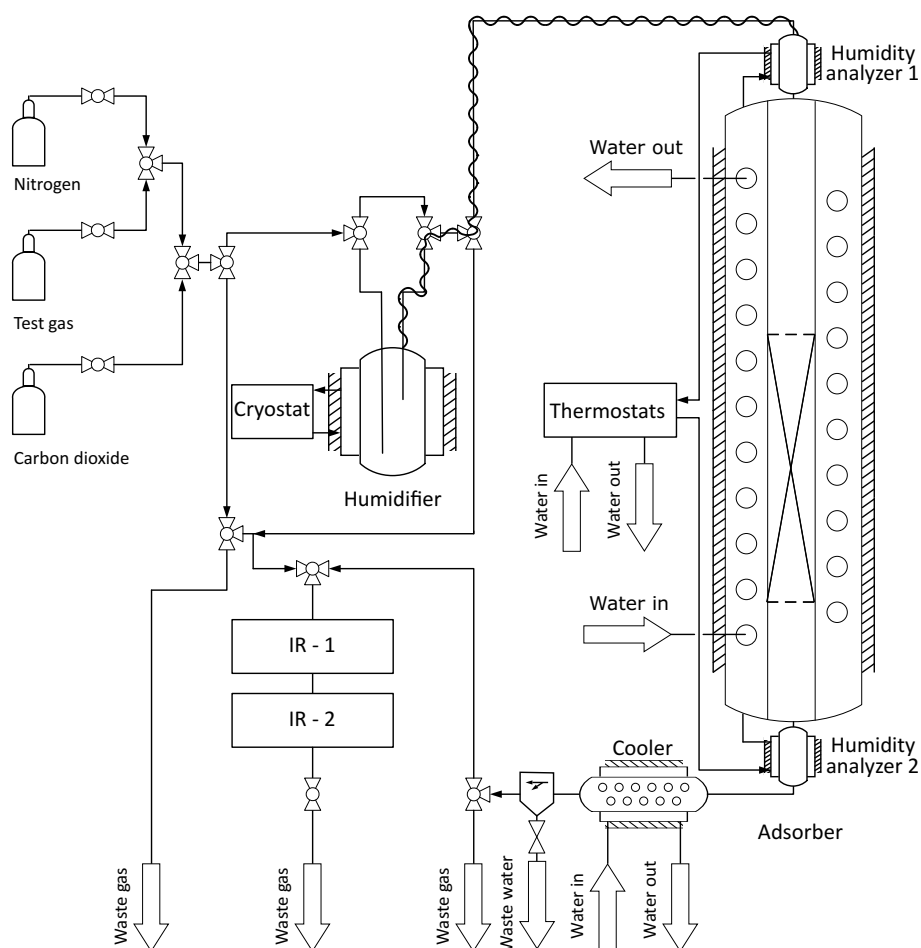


Figure 3.3: Simplified flow diagram of the experimental setup build for the realization of *BTC* experiments on a laboratory-scale. A more detailed flow sheet is provided in Figure A.1. Materials and equipment used are summarized in Table A.1.

switched to the gas with defined CO_2 content to start the adsorption experiment. Measurements are stopped if the change in CO_2 content detected at the adsorber outlet is observed to become small compared to influences of fluctuations observed (Appendix A.3.2). This can take more than 10 h in dependence of the experimental conditions set.

If water breakthrough experiments or co-adsorption measurements are to be performed, instead or before switching to CO_2 gas mixtures, the nitrogen flow is passed through the humidifier to saturate the sorbent with water. The saturation state is indicated by a plateau formation of the humidity data measured (Appendix A.3.2.3), typically reached after 1–1.5 h. In co-adsorption measurements, the sorbent is first presaturated with water. Afterwards the gas flowing through the humidifier is switched to the gas mixture of interest and the CO_2 adsorption measurement starts.

3.2.1.2 Thermogravimetric analysis (TGA)

In this section the measuring principle of *TGA* experiments and the experimental setting used is briefly outlined. For more detailed insight the reader is referred to Appendix A.4.

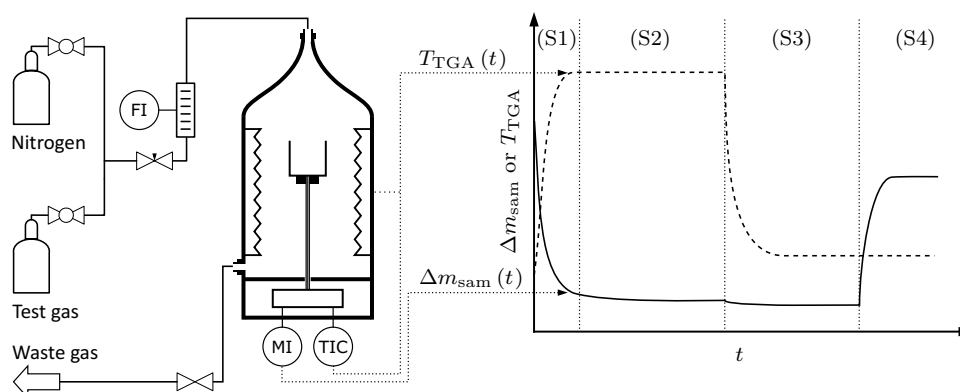


Figure 3.4: Basic measuring principle and experimental setting of *TGA* experiments. The change of the sample mass Δm_{sam} (-) and of the temperature T_{TGA} (- -) in dependence of time t is recorded. The different segments: (S1) heating of the sample, (S2) desorption at constant temperature, (S3) cooling to adsorption temperature and (S4) adsorption are shown. Materials and equipment used are summarized in Table A.13.

Theory of TGA *TGA* experiments aim for determination of the sorbent loading by direct measurement of changes in sample mass. Figure 3.4 visualizes the basic measuring principle. The sorbent is exposed to a defined gas atmosphere in a temperature controlled high precision scale. In segment 1 temperature is increased to desorption level under inert gas (N_2) flow. This results in desorption of species bound to the sorbent, which proceeds in segment 2 at constant temperature. Decreasing the temperature to adsorption level (segment 3), the sorbent is prepared for the adsorption experiment that is induced by switch of the gas phase atmosphere (segment 4). The weight of the pure sorbent is recalculated from the sample mass initially filled in the crucible and its weight change between the start of the experiment and end of the desorption phase. The mass of the components adsorbed is given by the weight change of the sample during segment 4.

Experimental setting The flow sheet of the experimental setting is presented in Figure 3.4. *TGA* device *TG 409 C/3/E* from *Netzsch*¹⁷⁴ is used. Flow of gas is manually adjusted by a three-way valve and by a float-type flow meter with needle valve¹⁷⁵ from *ABB*. For more detailed information the reader is referred to Appendix A.4.1.

Experimental procedure A sample mass of ca. 40 mg air dried *Lewatit* is filled in the solid Al_2O_3 sample carrier. Desorption under N_2 flow of ca. 93 Nml min^{-1} is realized by raising the temperature to 100°C . Selecting the length of segment 1 and 2 to be at least 8 h, steady state conditions at the end of segment 2 are ensured. Similarly, the minimum duration of segment 3 is selected to be 8 h. Thus, typically after 16 h the gas phase is switched to the test gas of similar volume flow and the weight change of the sample is recorded for up to 6.5 h to guarantee steady state conditions (Appendix A.4.3) at the end of segment 4. Also a shorter test program with a duration of 7 h 40 min (segment 1 and 2: 5 h 30 min) is implemented to investigate the mass of the regenerated sorbent, without the need of overnight experiments.

3.2.2 Adsorption properties under dry conditions

In this section the isotherm data (Section 3.2.2.1), heats (Section 3.2.2.2) and kinetics (Section 3.2.2.3) of CO₂ adsorption on *Lewatit* under dry conditions are evaluated.

3.2.2.1 Isotherm data

Figure 3.5 visualizes the isotherm data experimentally determined. A comparatively smooth evolution of the CO₂ loading with temperature and pressure is observed that might be interpreted as a first indicator for the validity of the data set. Monotonic increase of $q_{\text{eq},\text{CO}_2}$ with increasing p_{CO_2} or decreasing T_{ads} is expected. Only *TGA* experiments in the low-temperature region at high CO₂ pressures show slight deviations from this trend. With regard to the literature data presented, a comparatively good agreement between the equilibrium loadings determined in this work and the values observed by other research groups is noticed. In general, the equilibrium loadings published by Brillman and coworkers^{137,157,167} exceed the values found in this work and by Sonnleitner et al.¹⁶⁶. In this respect, larger deviations are especially noticed at high temperature levels.

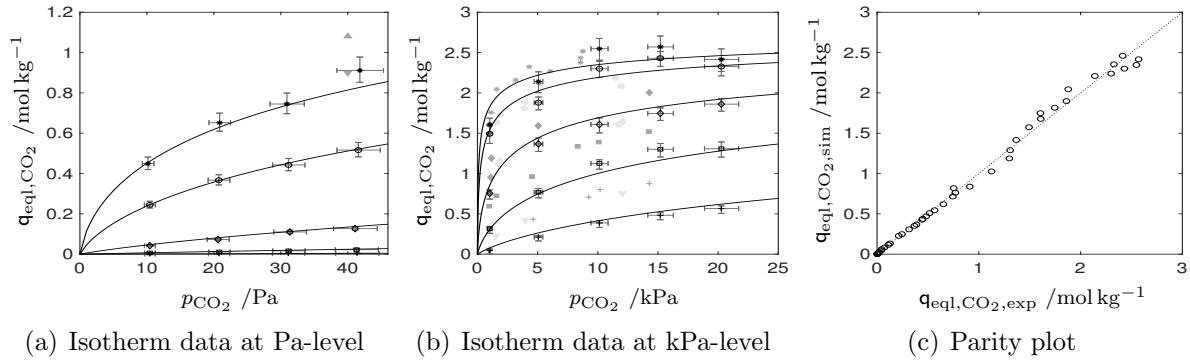


Figure 3.5: CO₂ equilibrium loading $q_{\text{eq},\text{CO}_2}$ on *Lewatit* for the temperatures 30 °C (*), 40 °C (o), 60 °C (◇), 80 °C (□) and 100 °C (+) determined for CO₂ partial pressures p_{CO_2} corresponding to CO₂ mole fractions y_{CO_2} in the range of (a) 100–400 ppm and of (b) 1–20 %, at a total pressure of 10⁵ Pa. Evolution of the isotherms predicted by *Toth* model, fitted to the experimental results from *BTC* and *TGA* experiments of this work (model 6, Table 3.1), is visualized by solid lines (-) for the corresponding temperatures. For validation purpose data from literature sources at kPa-level are shown in shades of gray in (b): Sonnleitner et al.¹⁶⁶ (○), Sutanto et al.¹⁶⁷ (●). Isotherm data given for 95 °C by Sonnleitner et al.¹⁶⁶ are visualized by gray triangles (▼). Moreover, isotherm data at a CO₂ partial pressure of 40 Pa and temperatures of 25 °C (▲) and 35 °C (▼) published by Veneman et al.¹³⁷ are depicted in (a). Error bars for experimental data are derived from error propagation studies summarized in Appendix A.3.7.1 and A.4.7. A comparison between the experimentally determined and predicted CO₂ loadings, $q_{\text{eq},\text{CO}_2,\text{exp}}$ and $q_{\text{eq},\text{CO}_2,\text{sim}}$, respectively, is given in (c).

Data fitting to theoretically derived adsorption isotherm models is performed. *Toth* isotherm model^{176,177}

$$q_{\text{eq},\text{CO}_2} = \frac{q_{\text{max},\text{Tot}} \cdot b_{\text{Tot}} \cdot p_{\text{CO}_2}}{\left(1 + (b_{\text{Tot}} \cdot p_{\text{CO}_2})^{t_{\text{Tot}}}\right)^{\frac{1}{t_{\text{Tot}}}}} \quad (3.2a)$$

$$q_{\text{max},\text{Tot}} = q_{\text{max},0,\text{Tot}} \cdot \exp\left(\chi_{\text{Tot}} \cdot \left(1 - \frac{T}{T_{0,\text{Tot}}}\right)\right) \quad (3.2b)$$

Table 3.1: *Toth* isotherm parameter sets given in the literature and determined via model fitting to the experimental data recorded. Besides the parameter sets determined based on *TGA* and *BTC* data from this work, results of additional parameter fitting based on *BTC* data from this work and data provided by Sutanto et al.¹⁶⁷ for CO₂ shares larger than 1 kPa are presented. Coefficients of determination R^2 indicate good accuracy of the data fit.

Research group	TU Wien	University of Twente		TU Dortmund University			
	Sonnleitner et al. ¹⁶⁶	Veneman et al. ^{137,157}	Sutanto et al. ¹⁶⁷	This work			This work Literature ¹⁶⁷
Model no.	1	2	3	4	5	6	7
p -level	kPa	kPa	kPa	Pa	kPa	Pa–kPa	Pa–kPa
T -level	/°C	40–102	30–100	30–130	30–100	30–100	30–130
Method	<i>BTC/TGA</i>	<i>TGA</i>	<i>TGA</i>	<i>BTC</i>	<i>TGA</i>	<i>BTC/TGA</i>	<i>BTC/TGA</i>
$T_{0,Tot}$	/K	343.00	353.00	353.00	353.00	353.00	353.00
$q_{max,0,Tot}$	/mol kg ⁻¹	3.13	3.40	3.70	3.22	3.20	2.92
χ_{Tot}	/-	0.00	0.00	0.00	0.00	0.00	0.00
$b_{0,Tot}$	/10 ⁻⁵ Pa ⁻¹	282.00	408.84	188.60	19.60	21.79	27.41
$\Delta h_{0,Tot}$	/kJ mol ⁻¹	106.00	86.70	111.00	107.76	102.38	107.88
$t_{0,Tot}$	/-	0.34	0.30	0.30	0.50	0.46	0.46
$\alpha_{0,Tot}$	/-	0.42	0.14	0.5	0.73	0.73	0.62
R^2	/-	–	–	–	0.9996	0.9965	0.9968
							0.9946

$$b_{Tot} = b_{0,Tot} \cdot \exp \left(\frac{\Delta h_{0,Tot}}{R_{id} \cdot T_{0,Tot}} \cdot \left(\frac{T_{0,Tot}}{T} - 1 \right) \right) \quad (3.2c)$$

$$t_{Tot} = t_{0,Tot} + \alpha_{0,Tot} \cdot \left(1 - \frac{T_{0,Tot}}{T} \right) \quad (3.2d)$$

is commonly used for the description of CO₂ adsorption on *Lewatit*.^{137,157,166,167} Being an empirical modification of the well-known *Langmuir* isotherm model,¹⁷⁶ this model allows to describe inhomogeneities of the adsorption side by introduction of an additional parameter t_{Tot} . For $t_{Tot} = 1$ this model equals the *Langmuir* formulation. Including the maximum loading $q_{max,Tot}$ and adsorption affinity b_{Tot} , in total three physical motivated parameters are used in the *Toth* model, which can be expressed as functions of temperature, using common exponential (3.2b)–(3.2c) or linear (3.2d) approaches related to the reference state $T_{0,Tot}$. Overall, this results in a set of 6 fitting parameters, from which in particular the adsorption enthalpy at zero loading $\Delta h_{0,Tot}$ is of interest.^{176,177}

Parameter sets obtained via data fitting in *Matlab*^{®178} (Appendix A.5) are summarized in Table 3.1. Besides the parameter set that describes the whole range of experimental data, also fits for the Pa- and kPa-level subsets are presented. Coefficients of determination R^2 close to one indicate good match of experimental data and isotherm models. Reasoned in the high number of parameters to be fitted to different data sets, no exact match of the parameter sets shown is expected. Nevertheless, general thermophysical ten-

dencies, e.g., high values of b_{Tot} that indicate high affinity of *Lewatit* for CO_2 adsorption can be confirmed. Moreover, with exception of the data set given by Veneman et al.^{137,157}, $\Delta h_{0,\text{Tot}}$ takes values in the order of magnitude of 100 kJ mol^{-1} . These compare well with the heat of CO_2 adsorption found for primary amine-based solid sorbents.¹⁷⁹ Also the maximum CO_2 loading $q_{\text{max},0,\text{Tot}}$ seems to be in a physically sound region throughout the studies. It is in good accordance with maximum amine loadings experimentally determined. Alesi et al.¹⁶³ calculated amine loadings of 7.5 mol kg^{-1} based on *energy-dispersive X-ray spectroscopy (EDS)* experiments and concluded the maximum quantity of amine groups available for adsorption to be in the order of magnitude of 6.7 mol kg^{-1} , reasoned in the consideration that 8–10 wt % of the resin is cross-linked. Thus, based on the reaction mechanism for dry CO_2 adsorption (Section 3.1.2), maximum CO_2 loadings of about 3.4 mol kg^{-1} are to be expected.

As visualized in Figure 3.5 the *Toth* isotherm parameter set derived in this work is able to capture the characteristics of CO_2 adsorption with high accuracy. Even more accurate predictions in the ranges investigated might be reached by separate data fitting to the corresponding subsets (Figure A.8). However, it is intended to capture CO_2 under ambient conditions, i.e., at partial pressures in the order of magnitude of 40 Pa (Figure 1.1(a)), and reach CO_2 shares at %-level in the desorption step that operates at pressure levels close to 10^5 Pa . Thus, isotherm parameters that are derived from simultaneous data fit to both regions of interest are required in the subsequent process studies. In this respect, the comparatively low slope of the adsorption isotherm modeled in the high-temperature region, i.e., at 100°C , becomes of special interest for *DAC* operation. Here, minor variations in CO_2 loading are associated with more significant changes in the partial pressure of carbon dioxide achievable in the *DAC* product gas. As already mentioned, the equilibrium loadings experimentally determined by Brillman and coworkers^{137,157,167} in general take higher values compared to the other data sets available. An isotherm fit (Figure A.8) to a data set that incorporates *TGA* data provided by this research group¹⁶⁷ for CO_2 partial pressures at kPa-level and *BTC* measurements obtained in this work results in the worst case isotherm model 7 (Table 3.1) to be used in process analysis.

3.2.2.2 Heat of CO_2 adsorption

With the isotherm data at hand, the isosteric heat of adsorption can be calculated using *Clausius-Clapeyron* equation

$$\Delta h_{\text{ads},i_{\text{spe}}} (q_{\text{eq},i_{\text{spe}}}, T) = R_{\text{id}} \cdot \left. \frac{\partial \ln p_{i_{\text{spe}}}}{\partial \frac{1}{T}} \right|_{q_{\text{eq},i_{\text{spe}}}} \quad (3.3)$$

under the assumption of ideal gas behavior and negligible adsorbed phase volume.^{167,180} The results of this evaluation are visualized in Figure 3.6. Decline of $-\Delta h_{\text{ads},\text{CO}_2} (q_{\text{eq},\text{CO}_2}, T)$ with decreasing temperature or increasing CO_2 loading is observed. This is in line with the findings of Sutanto et al.¹⁶⁷. Comparison of the models evaluated indicates small differences in the heat of adsorption predicted that reflect minor variations in the slope of the adsorption isotherms and motivate a more detailed experimental analysis of the heat of adsorption. With absolute values ranging

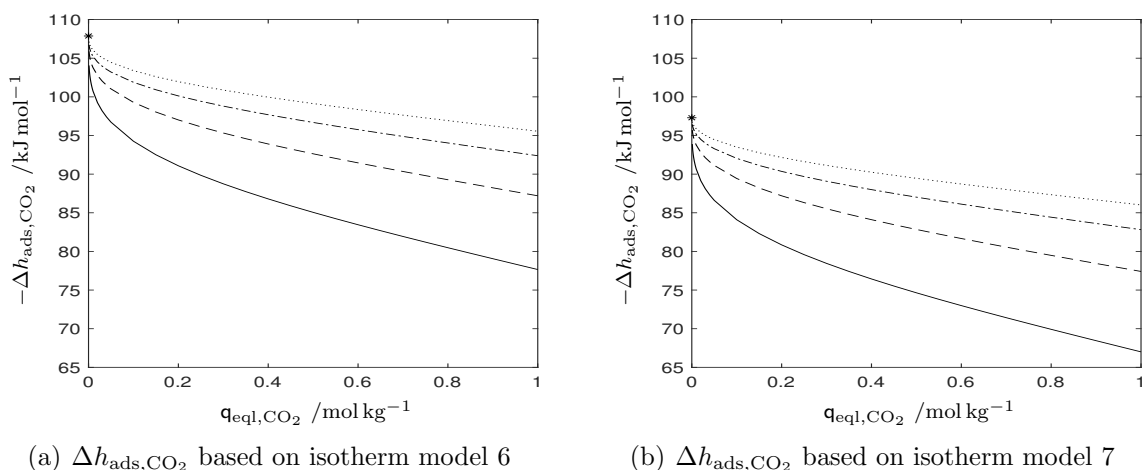


Figure 3.6: Dependency of the isosteric heat of adsorption $\Delta h_{\text{ads,CO}_2}$ on the CO_2 loading $q_{\text{eql,CO}_2}$ for temperatures of 25 (-), 50 (- -), 75 (- ·) and 100 °C (· ·) based on the evaluation of adsorption isotherms by means of *Clausius-Clapeyron* equation (3.3). Isotherm models derived from (a) *BTC* and *TGA* data of this work as well as from (b) *BTC* data of this work and *TGA* data of Sutanto et al.¹⁶⁷ are investigated. The heat of adsorption at zero loading $\Delta h_{0,\text{Tot}}$ is denoted by a star (*).

65–110 kJ mol^{-1} , the isosteric heats of adsorption are in the typical range of heats of CO_2 adsorption on amine groups.^{137,156,157} Their order of magnitude clearly indicates chemisorption to be the dominating mechanism.^{166,179}

3.2.2.3 Adsorption kinetics

Kinetic information of the adsorption process are determined via model-based parameter fitting in *Matlab*^{®178}. Within these models (*BTC* (Appendix A.3.6), *TGA* (Appendix A.4.6)), kinetics of the adsorption process are described based on the approach

$$\frac{dq_{\text{CO}_2}}{dt} = k_{\text{df,ads,CO}_2} \cdot (q_{\text{eql,CO}_2} - q_{\text{CO}_2})^{n_{\text{ord}}}, \quad (3.4)$$

which depends on the two parameters $k_{\text{df,ads,CO}_2}$ and n_{ord} . As indicated by the examples provided in Figure 3.7, a good match between the experimentally obtained data and simulation is reached. Hereafter only a brief summary of the kinetic analysis will be given. For a detailed insight the reader is referred to Appendix A.3.6.4 and A.4.6.2.

Results received in the analysis of *BTC* experiments (Appendix A.3.6.4) reveal good applicability of the linear driving force model, i.e., $n_{\text{ord}} = 1$. In accordance with the study of Bos et al.¹⁶⁴, kinetic coefficients determined (Table A.6) well match predictions based on the assumption of mass transfer limitation by *molecular* and *Knudsen diffusion* (Tables A.8 and A.9). The contribution of the latter mechanism is found to lie in the order of magnitude of 86%. *Arrhenius*-type evaluation of $k_{\text{df,ads,CO}_2}$ (Figure A.5(a), Table A.7) indicates strong dependency of $k_{\text{df,ads,CO}_2}$ on operation temperature. Activation energies of about 65 kJ mol^{-1} suggest strong influence of the adsorption isotherm slope on $k_{\text{df,ads,CO}_2}$, which is in line with theoretical expectations (Appendix A.3.6.2).

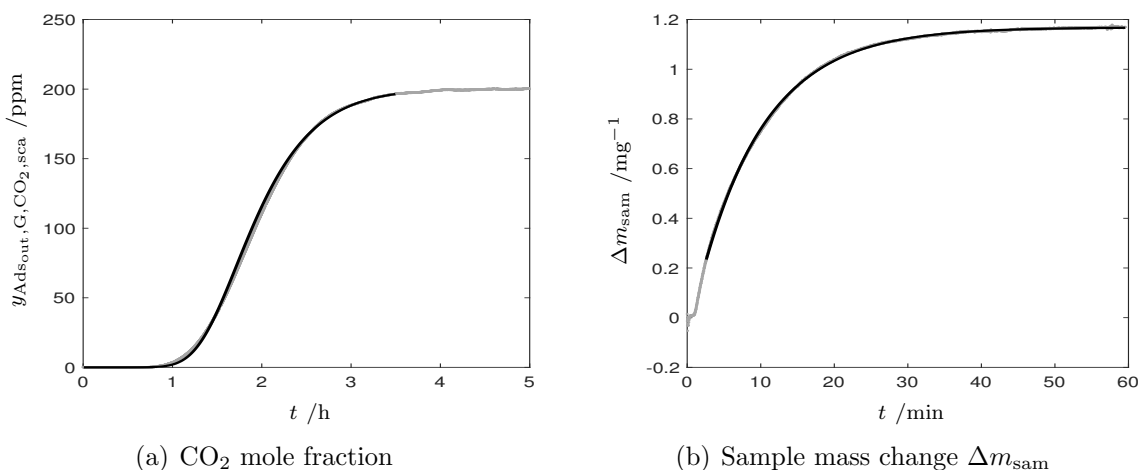


Figure 3.7: Kinetic fit to *BTC* and *TGA* data. Experimentally determined (\bullet) and simulated ($-$) state variable profiles, i.e., (a) CO_2 mole fraction $y_{\text{Ads,out,G,CO}_2,\text{sca}}$ at adsorber outlet in *BTC* experiments and (b) sample mass change Δm_{sam} with reference to the end of segment S3. Measurements at (a) $T_{\text{exp,asp}} = 40^\circ\text{C} / p_{\text{CO}_2,\text{exp,asp}} = 20\text{ Pa}$ and (b) $T_{\text{exp,asp}} = 60^\circ\text{C} / p_{\text{CO}_2,\text{exp,asp}} = 1\text{ kPa}$ are evaluated exemplarily. The time interval from the start of the experiment (a), or the start of the CO_2 supply (b), to the equilibrium time is shown.

Increase of n_{ord} with CO_2 partial pressure from levels of 1 up to 2.4 is noticed in the evaluation of *TGA* experiments (Figures A.6 and A.7, Table A.16). Presence of higher orders of the driving force term^{164,181} suggests increasing influence of chemisorption on the overall adsorption kinetics.¹⁸² In line with this observation, activation energies of about 35 kJ mol^{-1} derived from *Arrhenius*-type evaluation (Figure A.7, Table A.18) are in the typical range ($15\text{--}38\text{ kJ mol}^{-1}$)^{164,183,184} expected for amine– CO_2 reactions.

3.2.3 Adsorption properties under humid conditions

As air capture concepts are bound to operate under near ambient conditions (Section 2.2), the sorbent selected needs to be stable against moisture. Amine-based sorbents can meet this requirement. For various sorbents even a promoting effect of moisture on CO_2 adsorption, reasoned in different reaction mechanisms available (Section 3.1.2), is found.^{67,157,160} As the presence of water significantly increases the degrees of freedom of the adsorption system, this phenomenon is intensively researched.^{67,137,185–188} However, the interactions between CO_2 , H_2O and the amine are complex, e.g., amine surface coverage is observed to influence possible interactions.¹⁸⁵ Consequently, the effect of water on CO_2 capacity is found to be very diverse.¹⁸⁶ Increase of the amine efficiency ranges from less than 20%^{186,189} to levels close to 100%¹⁹⁰, but also declines of this variable under humid conditions have been documented.^{186,189}

An estimation of the humidity influence on the adsorption process based on theoretical concepts or on extrapolation of data available for similar sorbents seems hardly possible due to the complex interactions of water in the reaction system. Similarly, determination of a detailed, theoretically profound mechanistic insight into the co-adsorption process is beyond the scope of this work and not target-oriented with respect to its objectives.

However, besides its possible influence on the adsorption process, water co-adsorption can have a severe influence on the process energy balance and design (Chapters 5 and 6). Consequently, a basic investigation of this phenomenon that includes the analysis of single component water adsorption (Section 3.2.3.1) and CO₂ adsorption under humid conditions (Section 3.2.3.2) is required. Moreover, a discussion on the determination of kinetic parameters is given in Appendix A.3.6.5.

3.2.3.1 Single component adsorption of H₂O

In this section, the adsorption properties of water on *Lewatit* including the equilibrium loading, isosteric heat and kinetics of the adsorption process are summarized.

Equilibrium loading In line with the findings of Veneman et al.¹³⁷ experimental data visualized in Figure 3.8(a) indicate that the influence of temperature and partial pressure on H₂O adsorption on *Lewatit* can in good accordance be described as a function of the lumped variable relative humidity ϕ_{rh} . Basic *BET* (Brunauer, Emmett, Teller) model¹⁹¹

$$\frac{q_{\text{eq},\text{H}_2\text{O}}}{q_{\text{eq},\text{H}_2\text{O},\text{mon}}} = \frac{c_{\text{BET}} \cdot \phi_{rh}}{(1 - \phi_{rh}) \cdot (1 + (c_{\text{BET}} - 1) \cdot \phi_{rh})} \quad (3.5)$$

is investigated. Among others, this model is based on the assumption that multilayer adsorption is possible in an infinite number of layers, with the adsorption enthalpy from the second layer onwards being equal to the heat of condensation. Good accuracy of the data fit (Appendix A.5) is reached (Table 3.2). However, the intrinsic limitation of convergence of $q_{\text{eq},\text{H}_2\text{O}}$ to infinity with increasing relative humidity motivates investigation of extended versions of this model. Introduction of a finite number of adsorption layers

$$\frac{q_{\text{eq},\text{H}_2\text{O}}}{q_{\text{eq},\text{H}_2\text{O},\text{mon}}} = \frac{c_{\text{BET}} \cdot \phi_{rh}}{1 - \phi_{rh}} \cdot \frac{1 - (n_{\text{BET}} + 1) \cdot \phi_{rh}^{n_{\text{BET}}} + n_{\text{BET}} \cdot \phi_{rh}^{n_{\text{BET}}+1}}{1 + (c_{\text{BET}} - 1) \cdot \phi_{rh} - c_{\text{BET}} \cdot \phi_{rh}^{n_{\text{BET}}+1}} \quad (3.6)$$

results in a 3-parameter isotherm model (*n-BET* model).^{177,191} Besides the maximum number of layers n_{BET} , also the parameter c_{BET} , which resembles the affinity between sorbent and sorptive, and the monolayer loading $q_{\text{eq},\text{H}_2\text{O},\text{mon}}$ are physically motivated. On the other hand, extension of *BET* isotherm approach by an additional parameter K_{GAB} that accounts for differences in the energy state of molecules bound in the multilayer compared to the free bulk liquid is taken into account.^{192,193} The resulting equation

$$\frac{q_{\text{eq},\text{H}_2\text{O}}}{q_{\text{eq},\text{H}_2\text{O},\text{mon}}} = \frac{c_{\text{BET}} \cdot K_{\text{GAB}} \cdot \phi_{rh}}{(1 - K_{\text{GAB}} \cdot \phi_{rh}) \cdot (1 + (c_{\text{BET}} - 1) \cdot K_{\text{GAB}} \cdot \phi_{rh})} \quad (3.7)$$

is commonly known as the *GAB* (Guggenheim, Anderson, de Boer) isotherm model.¹⁹³

Coefficients of determination summarized in Table 3.2 indicate good agreement between the experimental and simulated results, which is underlined by parity plot visualization (Figures 3.8(b) and A.9). Even if the isotherm models are only fitted to the experimental results obtained in this work, a comparison with the experimental data published by Veneman et al.¹⁵⁷ indicates that the *n-BET* and *GAB* model determined might allow for

extrapolation to high humidity levels not captured by the experimental investigations in this work. This motivates thermophysical interpretation of the isotherm parameters summarized in Table 3.2.

Monolayer loadings determined vary between the isotherm models, which can be attributed to the not very pronounced plateau formation in the loading profile experimentally determined. This is in line with the order of magnitude of c_{BET} . Values higher, but close to one indicate that the state of molecules in the monolayer differs only slightly from that of the molecules adsorbed in the multilayer.¹⁹³ On the other hand, values of K_{GAB} smaller than one indicate the multilayer to be more structured than the bulk liquid. Here, the magnitude of K_{GAB} found suggests minor differences between molecules present in multilayer or bulk liquid.¹⁹³

Table 3.2: Isotherm data for H₂O adsorption on *Lewatit* determined based on model fit (Appendix A.5) of the experimental data obtained in this work (Table A.5).

Model	$q_{\text{eq},\text{H}_2\text{O},\text{mon}}$ /mol kg ⁻¹	c_{BET} /-	n_{BET} /-	K_{GAB} /-	R^2 /-
<i>BET</i>	2.45	3.97	–	–	0.975
<i>n-BET</i>	2.81	2.75	8.53	–	0.983
<i>GAB</i>	4.01	2.12	–	0.82	0.982

Overall, the investigation performed indicates that the water adsorbed behaves in good accordance like bulk liquid. In analogy to the carbon dioxide loading, the experimental data presented are lower than the measurements taken by Veneman et al.¹³⁷. However, the differences between the data sets are minor, especially with respect to the main conclusion drawn from a comparison of the H₂O with the CO₂ loadings. This is, under ambient conditions $q_{\text{eq},\text{H}_2\text{O}}$ will even at moderate relative humidity by far exceed $q_{\text{eq},\text{CO}_2}$.

Isosteric heat of adsorption In line with findings published in the literature¹³⁷, the isosteric heat of H₂O adsorption on *Lewatit* calculated by *Clausius-Clapeyron* equation (3.3) compares well with the heat of H₂O evaporation and shows independence of sorbent loading. This does not come by surprise, as in the modeling approach used the sorbent loading is described as a function of relative humidity that incorporates phase change information of H₂O.

3.2.3.2 Influence of moisture on CO₂ adsorption

In line with the expectations based on the general mechanism of CO₂ adsorption (Section 3.1.2), the results summarized in Figure 3.9 indicate that presence of moisture can have a significant promoting influence on the CO₂ capacity of *Lewatit*. Despite the aspect that moisture is well known to influence CO₂ adsorption on amine-based solid sorbents (Section 3.1), a lack of profound co-adsorption models seems to exist in the current literature.¹⁹⁴ Consequently, basic empirical approaches that, e.g., correlate the CO₂ capacity under humid conditions to the one obtained in the absence of moisture

$$q_{\text{eq},\text{CO}_2,\text{wet}}(p_{\text{CO}_2}, T, \phi_{\text{rh}}) = \phi_{q_{\text{eq},\text{CO}_2,\text{wet},\text{dry}}}(p_{\text{CO}_2}, \phi_{\text{rh}}) \cdot q_{\text{eq},\text{CO}_2,\text{dry}}(p_{\text{CO}_2}, T) \quad (3.8)$$

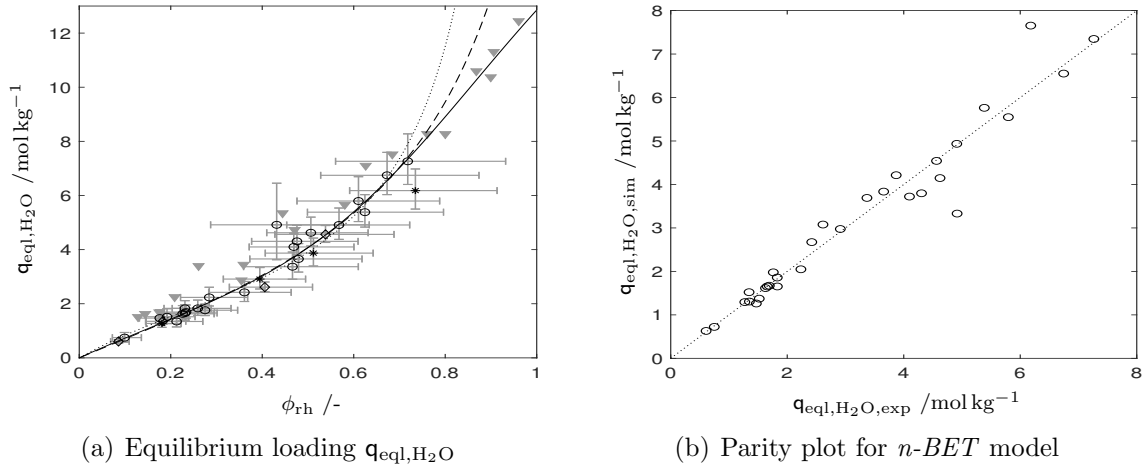


Figure 3.8: (a) Isotherm data for H_2O adsorption on *Lewatit*. To reduce the parameter set the influence of temperature and H_2O partial pressure on the sorbent loading $q_{\text{eq},\text{H}_2\text{O}}$ is described in dependence of the single, lumped variable relative humidity ϕ_{rh} . Sorbent loadings for different levels of relative humidity are measured at temperatures of ca. 25 (*), 30 (o) and 45 °C (◊). For validation purpose, data determined by Veneman et al.¹³⁷ (▼) are shown. Experimental data are summarized in Table A.5. Error bars for experimental data are derived from error propagation studies outlined in Appendix A.3.7.2. Isotherm evolution predicted based on BET ($\cdot\cdot$), n - BET (-) and GAB model (- -) is visualized in (a). (b) Parity plot visualization of data prediction with n - BET isotherm model.

are investigated.¹⁹⁴ Motivated by these approaches, extension of the isotherm model by a factor $\phi_{q_{\text{eq},\text{CO}_2,\text{wet,dry}}}$ that in general form reads

$$\phi_{q_{\text{eq},\text{CO}_2,\text{wet,dry}}} = 1 + \phi_{\text{rh}} \cdot (c_{\text{wet},\phi_{\text{rh}}} \cdot \phi_{\text{rh}}^{n_{\text{ord,wet},\phi_{\text{rh}}}-1} + c_{\text{wet},p_{\text{CO}_2}} \cdot p_{\text{CO}_2}^{n_{\text{ord,wet},p_{\text{CO}_2}}}) \quad (3.9)$$

is proposed in this contribution.

Results of the data fit (Appendix A.5) are summarized in Table 3.3. Coefficients of determination as well as parity plot visualization (Figure 3.9(b)) indicate high accuracy of the data fit. Promoting influence of moisture on CO_2 capacity is confirmed for all measurements taken. Decline in sensitivity toward relative humidity with increasing CO_2 loading is noticed. Increase in CO_2 partial pressure seems to reduce the promoting effect of water co-adsorption, which has also been observed by other authors for amine-based sorbents.¹⁹⁴ Overall, this leads to the observation that only at comparatively low partial pressures and high levels of relative humidity factor $\phi_{q_{\text{eq},\text{CO}_2,\text{wet,dry}}}$ approaches the theoretical limit of two (Section 3.1.2).

Table 3.3: Results of the data fit (Appendix A.5) for CO_2 adsorption on *Lewatit* under humid conditions based on (3.8) and (3.9). Experimental data are summarized in Table A.4.

$c_{\text{wet},\phi_{\text{rh}}}$	$n_{\text{ord,wet},\phi_{\text{rh}}}$	$c_{\text{wet},p_{\text{CO}_2}}$	$n_{\text{ord,wet},p_{\text{CO}_2}}$	R^2
/-	/-	/Pa ^{-$n_{\text{ord,wet},p_{\text{CO}_2}}$}	/-	/-
0.87	0.55	38.98	-1.66	0.998

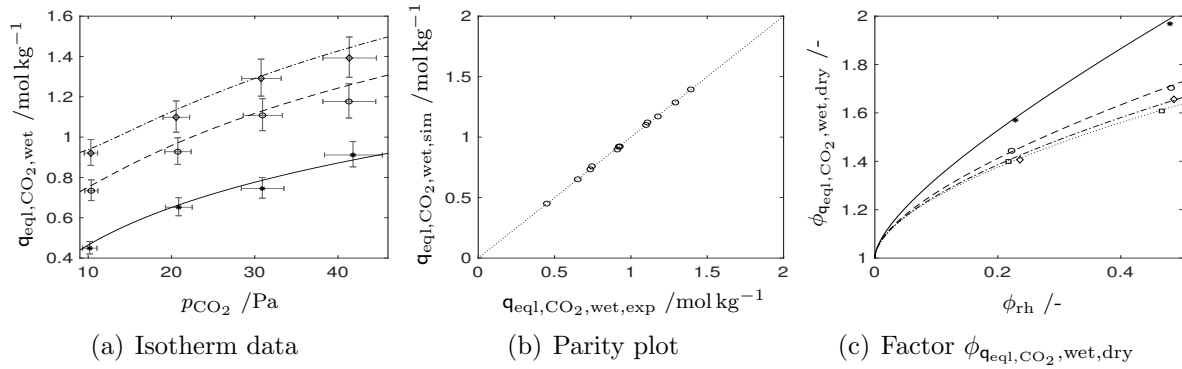


Figure 3.9: CO₂ adsorption on *Lewatit* under humid conditions at a temperature of ca. 30 °C. (a) Evolution of sorbent loading $q_{\text{eq},\text{CO}_2,\text{wet}}$ with CO₂ partial pressure p_{CO_2} . Besides sorbent loadings under dry conditions (*), experimental data obtained at ca. 25 (o) and 50% (◇) relative humidity are shown. Additionally, the simulated evolution of the CO₂ loading is depicted for 0 (-), 25 (- -) and 50% (- ·) relative humidity. (b) Comparison of experimentally determined and simulated CO₂ loadings, $q_{\text{eq},\text{CO}_2,\text{wet},\text{exp}}$ and $q_{\text{eq},\text{CO}_2,\text{wet},\text{sim}}$, respectively. (c) Experimentally determined and simulated evolution of factor $\phi_{q_{\text{eq},\text{CO}_2,\text{wet},\text{dry}}}$ with relative humidity ϕ_{rh} for CO₂ partial pressures of ca. 10 (*/-), 20 (o/--), 30 (◇/-·) and 40 Pa (□/··). Simulation results are based on dry CO₂ isotherm model 4 (Table 3.1) extended by (3.8) and (3.9). Here, the parameter set summarized in Table 3.3 is used. Derivation of error bars for experimental data is outlined in Appendix A.3.7.3.

The order of magnitude of the exponents $n_{\text{ord,wet},\phi_{\text{rh}}}$ and $n_{\text{ord,wet},p_{\text{CO}_2}}$ obtained in the data fitting seems not to lie in a physically unsound region with regard to an underlying intrinsic reaction mechanism. This motivates continuation of the work presented with emphasis on mechanistic studies in subsequent contributions. However, with regard to the focus of this work, i.e., the basic *DAC* process design, the key conclusion drawn from the co-adsorption studies lies in the observation that presence of moisture promotes CO₂ adsorption on *Lewatit*, while the strength of this effect seems to diminish with increasing levels of CO₂ partial pressure.

3.3 Additional properties of the sorbent

Mechanical, thermophysical and chemical properties of *Lewatit* are summarized in Section 3.3.1 and its thermal stability is analyzed in Section 3.3.2.

3.3.1 Mechanical, thermophysical and chemical properties

Basic properties of *Lewatit* obtained from experimental investigations (Appendix A.3.6.4 and A.6) and from literature review are summarized in Table 3.4. The appearance of the sorbent can be described as opaque, spherical beads. The experimentally determined bulk density ρ_{B} of 450 kg m⁻³ is in good accordance with data provided by Alesi and Kitchin¹⁶³, and the bed void fraction ψ_{B} of 38% observed lies in the typical range of 26–48% expected for sphere packings¹¹⁵ (Appendix A.6.1). Tortuosity factors (Appendix A.3.6.4) and the particle porosity (Appendix A.6.1) determined are in good accordance with the data published by Bos et al.¹⁶⁴. High mechanical stability found¹⁶⁶ and excellent

Table 3.4: Mechanical, thermophysical and chemical properties of *Lewatit*. Values for which no literature reference is given have been determined within this work (Appendix A.3.6.4 and A.6). In addition to the mean parameters obtained, 95 % confidence bounds (t-distribution) are given. ^a molar basis, ^b maximum available considering cross-linked structure

Mechanical, thermophysical and chemical properties							
Unif. coeff.	α_{unf}	/-	1.8 [162]	BET surface	a_{BET}	$/10^3 \text{ m}^2 \text{ kg}^{-1}$	50 [162]
Particle size	D_{P}	$/10^{-3} \text{ m}$	0.3–1.25 [162]	Pore volume	v_{Por}	$/10^{-6} \text{ m}^3 \text{ kg}^{-1}$	270 [162]
Effective size	$D_{\text{P},10}$	$/10^{-3} \text{ m}$	0.52 [162]	Pore diameter	D_{Por}	$/10^{-9} \text{ m}$	25 [162]
Fines	ϕ_{fie}	/%	3 [162]	Porosity	ϵ_{P}	/%	19.5 ± 0.3
Bed void fraction	ψ_{B}	/%	37.9 ± 0.9	Tortuosity	$\tau_{\text{Por,mol}}$	/-	1.2
Carr index	CI	/%	2.7 ± 1.7	Tortuosity	$\tau_{\text{Por,Knu}}$	/-	1.4
Angle of repose	α_{rep}	/°	24.1 ± 2.6	Amine loading	q_{Ami}	$/\text{mol kg}^{-1}$	$7.5^{\text{a}}, 6.7^{\text{b}}$ [163]
Bulk density	ρ_{B}	$/\text{kg m}^{-3}$	450 ± 5	Heat capacity	$c_{p,\text{P}}$	$/10^3 \text{ J kg}^{-1} \text{ K}^{-1}$	1.50 [163]
Particle density	ρ_{P}	$/\text{kg m}^{-3}$	724 ± 10	Th. conductivity	λ_{P}	$/10^{-3} \text{ W K}^{-1} \text{ m}^{-1}$	27 [157]

flowability, indicated by a *Carr index* (CI) smaller 15 % and an angle of repose α_{rep} of less than 30° (Appendix A.6.2),¹⁹⁵ seem favorable for fixed and moving bed applications.

With regard to the realization of a thermally driven regeneration process via *TSA*, thermal properties of *Lewatit* are of special interest. A low heat capacity of about $1.5 \text{ kJ kg}^{-1} \text{ K}^{-1}$ is named by various authors^{157,163,166}. This is in good agreement with data available for polystyrene (PS), ranging $1.1 - 1.7 \text{ kJ kg}^{-1} \text{ K}^{-1}$ in the temperature range $0 - 100^\circ\text{C}$.¹¹⁶ However, a large deviation between the thermal conductivity of *Lewatit* ($27 \text{ mW K}^{-1} \text{ m}^{-1}$), used by Veneman et al.¹⁵⁷, and PS ($160 \text{ mW K}^{-1} \text{ m}^{-1}$)¹¹⁶ is found, with the former being in the order of the thermal conductivity of air¹¹⁶. Influence of the thermal conductivity on the *DAC* concepts is discussed in more detail in Sections 4.3.2.2 and 4.4.1.3.

3.3.2 Thermal stability

Thermal stability of the sorbent becomes elementary in the *TSA*-based regeneration concepts proposed. The vendor names temperature ranges of $1 - 100^\circ\text{C}$ as a stable operating window.¹⁶² In single *TGA* experiments of Sonnleitner et al.¹⁶⁶ no degradation in pure nitrogen below 100°C was found after 35 h, whereas a reduction of the sorbent mass in the order of magnitude of 1 % was detected when increasing the temperature to 200°C . Moreover, enhancing effects of oxygen on sorbent degradation at temperatures above 80°C were revealed. Yu et al.¹⁶⁸ even observed stability in nitrogen for 50 h below temperatures of 150°C . Besides, high influence of oxygen on the degradation process is confirmed at temperatures above 70°C . Moreover, degradation effects resulting from urea formation at high temperatures and CO_2 concentrations are revealed, whereas in line with other authors¹⁹⁶ enhanced oxidative stability in the presence of H_2O and CO_2 was found. Studies by other research groups^{163,165} confirm the general thermal stability of *Lewatit* and its high dependence on the gas phase composition present.

3.4 Summary and conclusion

The selection of sorbents for use in air capture applications is bound to various constraints (Chapter 2). Different classes of sorbents are investigated. Especially use of supported amine sorbents (*SAS*) appears to be favorable for air capture. The commercially available polymeric ion exchange resin with primary amine moiety *Lewatit VP OC 1065*, assigned to this class, is selected as reference sorbent and analyzed in more detail.

Section 3.1 State of the art

summarizes the current state of research with regard to *DAC* sorbents. Solid, amine-based sorbents are identified as the most promising alternative (Section 3.1.1). Investigations of the reaction mechanism of CO_2 with this class of sorbents (Section 3.1.2) indicate possible interactions with water vapor present in ambient air. Humid conditions allow for CO_2 adsorption in the form of carbonate or bicarbonate instead of carbamate. This can result in doubling of the amine efficiency. Moreover, the current state of knowledge with regard to the reference sorbent selected is summarized (Section 3.1.3). Lack of data with respect to its adsorption characteristics under ambient conditions and to its thermophysical / mechanical properties relevant for large-scale applications is revealed.

Section 3.2 Adsorption properties of the sorbent

confirms good adsorption properties of *Lewatit* over a broad range of temperature (30–100 °C) and CO_2 partial pressure ($10 - 2 \cdot 10^4$ Pa). *Toth* isotherm model is found to best fit the experimental data obtained by thermogravimetric analysis and by breakthrough curve experiments (Sections 3.2.1 and 3.2.2). An analysis of the heat of adsorption and kinetic investigations allow for more detailed insights into the characteristics of the adsorption process. Focusing on humid conditions (Section 3.2.3), high water adsorption capacity of *Lewatit* is confirmed. *BET*-type and *GAB* isotherm models are found to well fit the experimental data. Complex influence of humidity on CO_2 capacity is revealed.

Section 3.3 Additional properties of the sorbent

is dedicated to the analysis of additional sorbent properties. Its low heat capacity, high mechanical stability and good flowability (Section 3.3.1) favor an application in innovative *moving bed adsorber* concepts. High thermal stability at temperatures below 100 °C allows for efficient *TGA* operation, whereas degradation observed at moderate temperatures in the presence of oxygen indicates the necessity of purge steps and of careful temperature control to avoid sorbent capacity loss (Section 3.3.2).

Based on the analysis given *Lewatit* is used as reference sorbent. It allows for a moderate CO_2 capacity under ambient conditions and offers superior mechanical and thermophysical properties, beneficial for use in the heat integrated *DAC* processes proposed (Chapter 4). Typical characteristics of *SAS* with respect to water co-adsorption are observed that motivate the analysis of measures to reduce high water co-desorption within the process (Chapter 5).

4 Approaches to intensified heat integrated DAC units

Scientific contributions

Parts of this chapter have been published in the following scientific contributions:

Peer-reviewed journal articles

- Drechsler, C.; Agar, D. W. Comparison of Highly Heat-Integrated Adsorber Concepts for Use in Direct Air Capture Processes. *Chem. Ing. Tech.* **2020**, *92*, 282–287.
- Drechsler, C.; Agar, D. W. Simulation and optimization of a novel moving belt adsorber concept for the direct air capture of carbon dioxide. *Comp. Chem. Eng.* **2019**, *126*, 520–534.

Conference talks

- Drechsler, C.; Agar, D. W. Hoch-Energieintegrierte Adsorberkonzepte für eine Anwendung in Direct Air Capture Verfahren. Presented at Jahrestreffen der ProcessNet-Fachgruppen Adsorption und Hochdruckverfahrenstechnik, Freiberg, Germany, February 18-20, 2019.
- Asmanoglo, C.; Agar, D. W. Entwicklung wärmeintegrierter Adsorber/Desorber-Konzepte für eine Anwendung in Direct Air Capture (DAC) Technologien. Presented at Doktorandenseminar der 1. Statuskonferenz zur BMBF Fördermaßnahme CO₂Plus, Berlin, Germany, April 17-18, 2018.

Conference poster presentations

- Drechsler, C.; Agar, D. W. Highly heat-integrated temperature-vacuum-swing adsorption process for the direct air capture of carbon dioxide. Presented at Gordon Research Conference on Carbon Capture, Utilization and Storage, Les Diablerets, Switzerland, May 05-10, 2019.
- Drechsler, C.; Agar, D. W. Highly heat-integrated temperature-vacuum-swing adsorption process for the direct air capture of carbon dioxide. Presented at Gordon Research Seminar on Carbon Capture, Utilization and Storage, Les Diablerets, Switzerland, May 04-05, 2019.
- Asmanoglo, C.; Agar, D. W. Entwicklung wärmeintegrierter Adsorber/Desorber-Konzepte für eine Anwendung in Direct Air Capture (DAC) Technologien. Presented at 1. Statuskonferenz zur BMBF Fördermaßnahme CO₂Plus, Berlin, Germany, April 17-18, 2018.

Abstract

Motivated by the high CO₂-specific energy demand of air capture, technological approaches to intensified heat integrated *DAC* concepts are investigated. Novel *moving belt (MBtA)* and *moving bed adsorber (MBdA)* concepts are proposed as representatives for direct and indirect heat integration strategies. Feasibility studies reveal low energy requirements and availability of efficient sealing strategies for the sorbent conveying technologies applied. Use of transfer media with directional dependent heat transfer characteristics is found to be beneficial. High potential for optimized heat transfer by use of fin-like structures on the transfer medium is revealed. Numeric simulations of *MBtA* and *MBdA* allow for detailed insights into the characteristics of operation in spatial cyclic state. Especially high mass transfer resistances in the gas phase are found to take severe influence on process performance. An experimental investigation of transport phenomena underlines this aspect. Results of detailed cost estimation stress the importance of transfer limitations, which are reflected in high investment costs dominated by the sorbent. Potential for severe cost reduction is outlined. Studies performed indicate trade-off considerations between the investment costs and energy spent to arise. Based on the current carbon footprint of energy supply, the latter is found to take a severe influence on the potential for realization of net negative emissions.

This chapter is structured as follows:

Section 4.1 State of the art

summarizes the state of knowledge with respect to the technological realization of *DAC*.

Section 4.2 Conceptual design

presents the *moving belt (MBtA)* and *moving bed adsorber (MBdA)* concepts designed.

Section 4.3 Feasibility study and constraints

evaluates limitations and constraints of the concepts proposed.

Section 4.4 In-depth simulation

allows for a detailed insight into the cyclic steady state operation of *MBtA* and *MBdA*.

Section 4.5 Experimental investigation of transport phenomena

discusses the results of the experimental analysis of transport phenomena.

Section 4.6 Cost estimation and net negative emission

evaluates the cost structure and ecologic impact of *MBtA* and *MBdA*.

Section 4.7 Summary and conclusion

extracts the key findings of this chapter that motivate the detailed analysis of water co-adsorption in Chapter 5.

4.1 State of the art

Motivated by the high capacity of *NETs* required in the second half of this century (Chapter 1), technological approaches to *DAC* are intensively researched. Various companies provide *DAC* technology on a commercial level.^{92,105,107,197–199} The continuously growing number of publications with respect to *DAC* sorbents (Chapter 3) and broad range of process configurations proposed (Chapter 2) reveal high potential for optimization. This is also reflected by the estimates of *DAC* energy demands and economics, summarized in Table B.1. Carbon dioxide-specific energy demands determined vary by more than one order of magnitude ($\sim 50–500 \text{ kJ mol}^{-1}$) and cost estimates even range from $30 \text{ \$ t}^{-1}$ to $1000 \text{ \$ t}^{-1}$.^{67,85} A comparison with cost estimates for flue gas capture that span $30 \text{ \$ t}^{-1}–100 \text{ \$ t}^{-1}$ suggests that no impeding limitation from an economic point of view exists.⁶⁷

Water co-adsorption, pressure losses in air–sorbent contacting and high carbon dioxide-specific energy demand can currently be identified as key challenges faced by *DAC* (Chapter 2).⁴¹ With respect to energy efficient contacting, trade-off considerations between pressure loss and mass transfer arise.⁹⁹ To overcome these limitations, various *DAC* designs at different levels of technological maturity have been proposed. At this stage only a brief overview is provided. For more detailed information, the reader is referred to Table B.1 and to the reviews^{40,41,67,85,110,200} available.

In the bench-scale scenario by the *American Physical Society (APS)*, counter-current flow between air and an alkaline solution that wets a packing in a fixed bed adsorber is realized.¹⁷ Optimization studies with respect to the packing used confirm high influence of operation parameters and of contactor design on overall process performance.¹¹¹ Inspired by *APS* report, a cooling tower design with an open contactor of slab geometry that allows for cross flow operation was proposed.²⁰¹ Motivated by the severely optimized economics of this patented design,²⁰² field tests²⁰³ were realized by *Carbon Engineering*. The detailed plant design for pilot-scale operation published⁹³ reveals CO_2 -specific energy demands to be in an order of magnitude of 390 kJ mol^{-1} . Further optimization studies based on *APS* system have been performed.⁹¹ These identify high influence of capital costs to *DAC* economics and underline the potential for severe cost reduction⁶⁷. In this respect, studies^{204,205} based on an aqueous reference process indicate that compression of air, to increase sorbent capacity, can become beneficial, even from an energy point of view.

Use of solid sorbents seems more promising compared to liquid systems with respect to process energy demand.⁹⁹ A variety of basic adsorber concepts for this class of sorbents were proposed by Lackner⁹⁹. Among those one may name heat exchanger-like designs or honeycomb-like structures. Moreover, filter mats composed of fine, loose fibers are proposed. Prototypes based on anionic-exchange resins were tested in humidity swing operation. Energy demands in the order of magnitude of 50 kJ mol^{-1} have been estimated. Moreover, this moisture swing approach to *DAC* was investigated with respect to a possible coupling with carbon sequestration and production of synthetic fuels.^{118,206}

Aminosilica sorbent-based cordierite monolith contactors were investigated by Kulkarni and Sholl⁹⁸. A *TSA* concept based on diurnal operation was found to be inferior compared to additional use of steam as heating medium and purge gas. Moreover, their analysis indicates that sensible heat demand can contribute to more than 60 % to the overall energy

requirement. Reduction of this contribution was identified as key research priority. Sinha et al.¹⁰⁰ also used low-temperature *TSA* operation for regeneration of their amino-modified *MOF* and reported CO₂-specific energy demands in an order of 160 kJ mol⁻¹.

Overall, intensive research results in commercially realized solid sorbent-based *DAC* technologies by various companies. *Infinitree*¹⁹⁸ applies the *humidity swing* approach^{99,101,102} to produce CO₂ streams at levels suitable for use in greenhouses. A similar approach to *DAC* is followed by *Skytree*¹⁹⁹. However, no detailed information on the technologies used by these two companies is available. Focusing on common *TSA* application, one may name *Hydrocell*¹⁹⁷. This company provides a *DAC* technology that fits into standard shipping containers and is fully portable.²⁰⁰ *Global Thermostat*¹⁰⁷ uses monolith contactor designs based on porous amine sorbents that have been documented in various patents.^{207–210} Low temperature steam (85–100 °C), e.g., produced from residual process heat, is used for sorbent regeneration. A CO₂ product gas at a purity of 98 % can be obtained.¹⁰⁷ Heat recovery in the order of 50 % is realized within this concept.^{200,211} Also *Climeworks*¹⁰⁵ applies amine-based sorbents. These are used in a filter composed of special cellulose fibers that can be regenerated by temperature swing to 80–100 °C. Various patents^{212–214} were granted, which besides others focus on adsorber designs that ensure low pressure losses.

4.2 Conceptual design

This section is dedicated to the conceptual design of heat integrated adsorber units. First an estimate of the operation range is given (Section 4.2.1). *Moving belt adsorber (MBtA)*, Section 4.2.2) and *moving bed adsorber (MBdA)*, Section 4.2.3) concepts are introduced.

4.2.1 General considerations

The general method of heat integration developed (Section 2.3.2) is independent of the specific technology used for realization of sorbent movement. General feasibility and characteristics of the concepts are discussed based on well selected representatives. The direct heat integration is represented by *MBtA* concept (Section 4.2.2), whereas applicability of the indirect heat integration concept by *MBdA* design is evaluated (Section 4.2.3). Moreover, it seems beneficial to investigate the sensible heat recovery strategies independent of the phenomenon of water co-adsorption revealed in Section 3.2.3. This allows for a more general analysis in which the results obtained are not subject to the constraints imposed by water co-adsorption discussed in Chapter 5.

Figure 4.1 evaluates the possible operation range for a cyclic adsorption process. Solely changing the temperature from adsorption to desorption cycle seems sufficient to reach CO₂ equilibrium mole fractions higher than 20 % in the desorption cycle. This implies that use of hydrogen as strip gas might allow for generation of a *DAC* product gas with a composition according to the stoichiometry of *Sabatier* reaction (2.I) in a single step (*temperature-composition-swing-adsorption, TCSA*). Strong dependency of equilibrium loading $q_{\text{eq},\text{CO}_2}$ on the CO₂ partial pressure in the adsorption cycle $p_{\text{CO}_2,\text{ads}}$ (Figure 4.1(a)) and of $p_{\text{CO}_2,\text{des}}$ on $q_{\text{eq},\text{CO}_2}$ during desorption (Figure 4.1(b)) is noticed. Decrease of CO₂

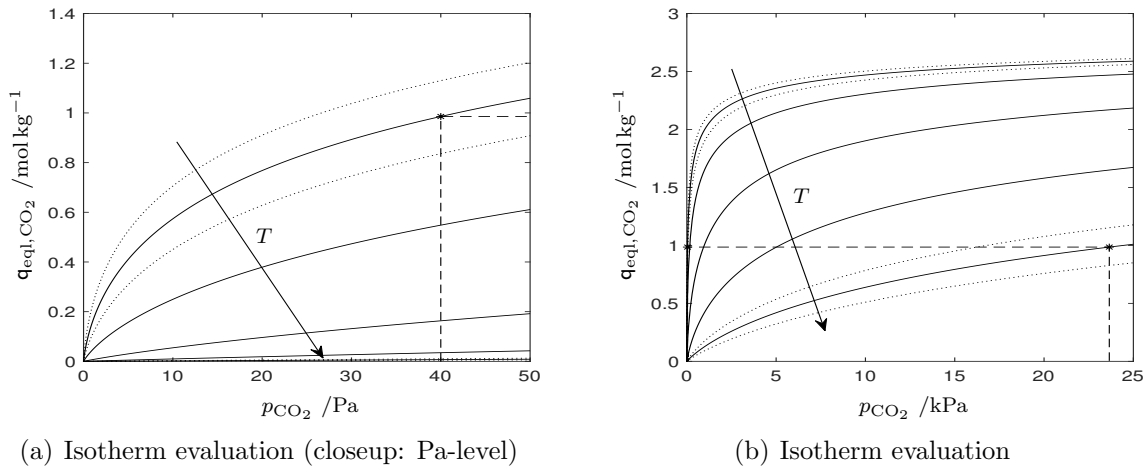


Figure 4.1: Possible operation range of *TVCSA* based on the isotherms for CO_2 adsorption under dry conditions. A closeup view on the CO_2 partial pressure (p_{CO_2}) range relevant for adsorption is given in (a), whereas (b) shows the whole range of CO_2 partial pressures and loadings ($q_{\text{eq},\text{CO}_2}$) investigated. Adsorption isotherms for temperatures T of 25, 40, 60, 80 and 100 °C are shown (-). Influence of temperature variation of ± 5 K is depicted for the isotherms at 25 and 100 °C by dotted lines ($\cdot\cdot$). Additionally, the course of operation from adsorption ($p_{\text{CO}_2,\text{ads}} = 40$ Pa, $T_{\text{ads}} = 25$ °C) to desorption cycle ($p_{\text{CO}_2,\text{des}} = 24$ kPa, $T_{\text{des}} = 100$ °C) is visualized by a dashed line (- -).

partial pressure in the adsorption cycle can lead to substoichiometric CO_2 shares in the *DAC* product gas with respect to *Sabatier* reaction. Moreover, strong dependency of $q_{\text{eq},\text{CO}_2}$ on temperature T is revealed. These observations result in various design considerations in view of single step *DAC* operation without use of strip gas other than H_2 or additional gas purification steps:

1. Counter-current operation of strip gas and sorbent seems beneficial to allow for high CO_2 shares. Realization of this operation mode is eased by sorbent movement
2. The desorption temperature level can become an efficient variable for process control, but it is limited by sorbent stability (Section 3.3.2). Selection of the *DAC* site with regard to ambient temperature is of great importance
3. Desorption pressure level can become an additional degree of freedom (*temperature-vacuum-composition-swing-adsorption*, *TVCSA*). Low pressure at the strip gas outlet can be used as the driving force for gas flow through the sorbent bed

The *MBtA* approach is analyzed as representative for *TCSA* operation. Application of the *TVCSA* concept is exemplified based on the *MBdA* design. Water co-adsorption implies presence of an additional gas phase species to be separated, which relaxes the constraints of *DAC* product gas CO_2 shares and identifies water vapor as additional, potential strip gas choice. This extended problem is discussed in Chapters 5 and 6.

4.2.2 Moving belt adsorber: conceptual design

Figure 4.2 visualizes the realization of the direct heat integration concept by *MBtA*. Sorbent particles are physically immobilized within a supporting mesh structure. Alter-

natively, impregnation or chemical bond of the amine moiety on the support might be realized. Overall, this results in a conveyor belt-like structure. This allows for transport of the sorbent through different zones and transformation of the cyclic adsorption process from time to space domain. The orientation of the belt in space domain enables direct thermal coupling between different parts of the belt by means of a (solid) transfer medium.

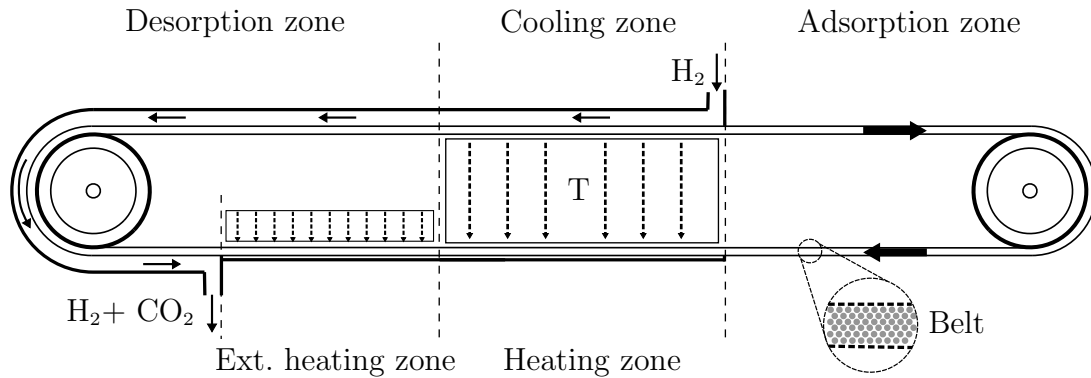


Figure 4.2: Moving belt adsorber (*MBtA*) design as representative of the direct heat integration concept. The different zones the belt is moving through are visualized. Direct heat transfer between different parts of the belt is realized by a (solid) heat transfer medium with uniaxial transfer characteristics (*T*). Heat flows are visualized by dashed arrows. Heat supply to the desorption zone and heat exchange with the ambient is not shown. Reproduced from Drechsler and Agar²¹⁵.

The path of the belt can be summarized as follows: in the adsorption zone air – sorbent contacting is realized. Overflow instead of flow through the sorbent bed allows for low pressure losses. Leaving this zone the sorbent bed is heated by means of direct heat exchange realized by a (solid) heat transfer medium with uniaxial transfer characteristics. The maximum temperature increase is limited by the minimum temperature difference required for an efficient heat transfer $\Delta T_{\text{ldf,DAC}}$. This results in the need of additional heat supply realized in the external heating zone, in which the sorbent temperature is raised to desorption level. The maximum bed temperature is aspired to be reached at the end of this zone. Regeneration of the sorbent is realized in the adjacent desorption zone. Additional heat supply in this zone is possible and counter-current strip gas flow allows for high CO_2 concentrations in the gas phase. In case of hydrogen strip gas use, maximization of the desorption time is enabled by already contacting the strip gas with the sorbent in the cooling zone, where the sorbent sensible heat is recovered.

4.2.3 Moving bed adsorber: conceptual design

The *MBdA* adsorber design sketched in Figure 4.3 is chosen as representative for the indirect heat integration concept. Sorbent movement through different zones is realized by gravitational forces. This allows for the additional degree of freedom to split the design into different units connected by sorbent transport.

Similar to the *MBtA* concept, sorbent particles enter a heating zone after CO_2 – sorbent contacting in the adsorption zone. The sorbent temperature is raised to desorption level by means of counter-current heat exchange with a (liquid) transfer medium. In the subsequent desorption zone the sorbent is regenerated by counter-current strip gas flow through

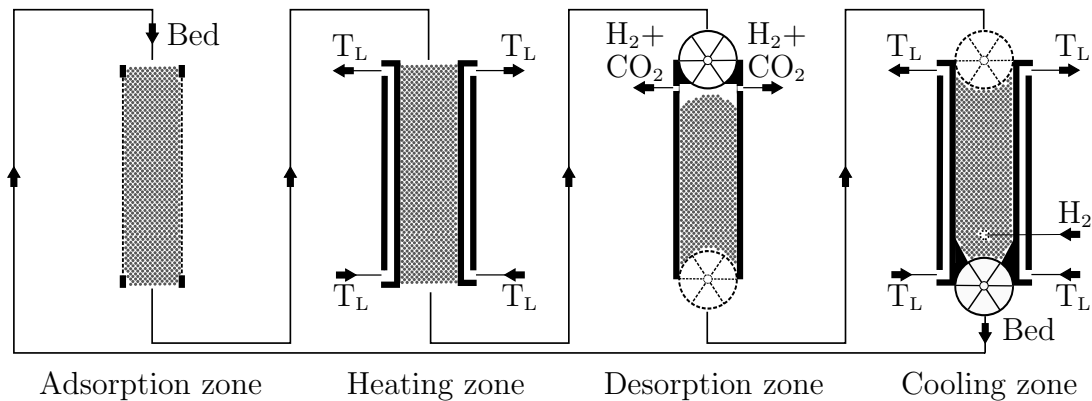


Figure 4.3: Sketch of the *moving bed adsorber (MBdA)* concept as representative of the indirect heat integration concept. Flow of the bed through different zones allows for transformation of the cyclic steady state operation profile from time to space domain. Heat integration is realized by counter-current heat exchange with a (liquid) transfer medium (T_L). Additional heat supply to the desorption zone is not shown in detail. Rotary valves that allow for vacuum operation are depicted.

the bed and by possible external heat supply. Desorption already starts in the cooling zone. Strip gas is introduced and sorbent sensible heat is recovered by counter-current exchange with the transfer medium that thereafter is externally heated and transferred to the heating zone. Rotary valves used for possible realization of vacuum operation are shown.

4.3 Feasibility study and constraints

The moving sorbent designs proposed (Section 4.2) diverge from adsorber concepts typically used. Exploitation of advantages arising from solid movement is not uncommon though. Moving belt devices for *Central Processing Unit (CPU)* cooling have been patented²¹⁶ and a true moving bed chromatography process was already commercially realized by *DOW Chemicals* and *Union Oil Co.* in 1947.²¹⁷ Table 4.1 provides a brief comparison of *MBtA* and *MBdA*. For a detailed insight, the reader is referred to the corresponding sections that discuss sorbent movement and gas sealing (Section 4.3.1), heat and mass transfer characteristics (Section 4.3.2) and large-scale realization (Section 4.3.3).

Table 4.1: Comparison of *MBtA* and *MBdA* concept with respect to the technical feasibility, strengths and drawbacks of the concepts. The rating of the concepts is performed according to the scale: good (+), intermediate (o), drawback(-).

	<i>MBtA</i>	<i>MBdA</i>	Section		<i>MBtA</i>	<i>MBdA</i>	Section
Thermal integration	+	o	4.3.2, 4.4	Scale and numbering up	o	+	4.3.3
Heat transfer	o	o	4.3.2, 4.4	Size	o/-	-	4.3.1, 4.3.3, 4.4
Mass transfer	o	o/+	4.3.2, 4.4	Flexibility	o	+	4.3.1, 4.3.3, 4.4
Working capacity	o	+	4.2.1, 4.4				

4.3.1 Sorbent movement and gas sealing

Efficient strategies for sorbent movement are required, in which the sorbent velocity becomes of particular importance. Cycle times for *DAC* applications given in the literature vary from 0.5 to 6 h.^{98,99,200,211} This implies the need for low sorbent velocities in the order of magnitude of 1 mm s^{-1} to limit *DAC* unit size to reasonable dimensions.

For *MBtA* similarities to common conveyor belt operation can be drawn, whereas in *MBdA* sorbent particles can be lifted, e.g., by vertical bucket elevators, and gravitational forces are used for bed movement. Power requirement for sorbent movement is estimated via *DIN 22101*²¹⁸ and *VDI 2324*²¹⁹ (Appendix B.2.1). Figure 4.4(a) compares key contributions identified for both designs. In *MBdA* energy demand for lifting the sorbent $\dot{E}_{\text{lif,Sor}}$ becomes dominating. Additional contributions, e.g., dead load or frictional power, scale with the mass of sorbent to be lifted, with effective friction coefficients $f_{\text{frc,eff}}$ typically ranging $3.5 \cdot 10^{-3} - 10 \cdot 10^{-3}$.²¹⁹ Thus, $\dot{E}_{\text{lif,Sor}}$ gives a good estimate for energy requirement of sorbent movement in *MBdA* concepts. For reasons of symmetry, the sorbent lift force is not accounted for in *MBtA* concepts. Contributions arising from mass change reasoned in adsorption can even contribute to drive sorbent movement, e.g., in realization of a vertical belt orientation with the adsorption zone at the top of the structure. As shown in Figure 4.4(a), these contributions remain comparatively small, even for high levels of water desorption, unfavorable with regard to the overall target of energy efficiency. Additional friction forces scale again with the sorbent mass to be moved ($f_{\text{frc,eff}} \approx 1 \cdot 10^{-2} - 4 \cdot 10^{-2}$).²¹⁸

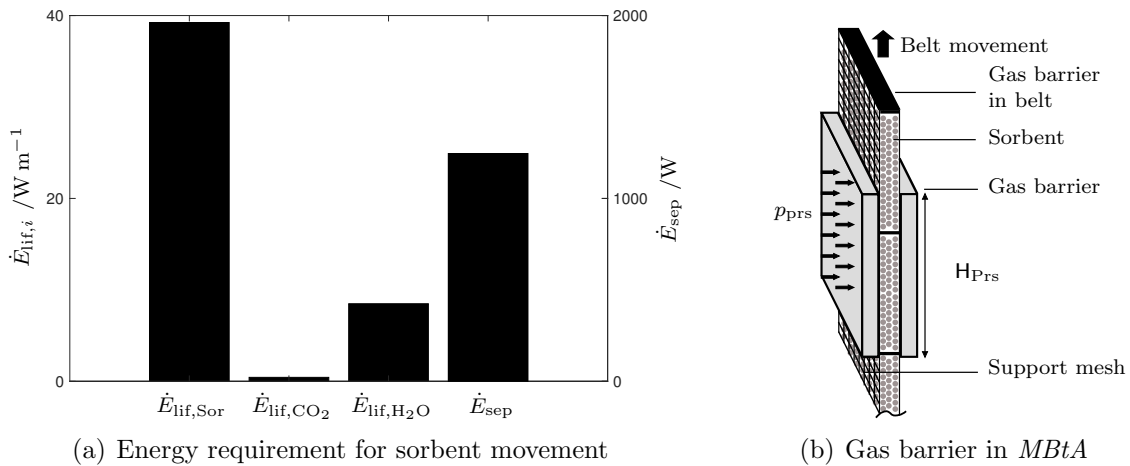


Figure 4.4: (a) Contributions to energy demand of sorbent movement for a reference CO_2 product flow of 1 mol s^{-1} and working capacities of $\Delta q_{\text{wor,CO}_2} = 0.25 \text{ mol kg}^{-1}$ and $\Delta q_{\text{wor,H}_2\text{O}} = 12 \text{ mol kg}^{-1}$. The energy requirement to lift the sorbent $\dot{E}_{\text{lif,Sor}}$ and the energy flows attributed to change of mass by adsorption $\dot{E}_{\text{lif},i,\text{spe}}$ per meter of lifting high are shown. The energy requirement per sealing device of the belt \dot{E}_{sep} realized is shown for a sorbent bed width of 0.5 cm. Calculations are based on *DIN 22101*²¹⁸ and *VDI 2324*²¹⁹ (Appendix B.2.1). (b) Sketch of gas barriers to be realized in *MBtA* concept. The sealing device is pressed with a contact pressure p_{Prs} onto the belt. Combined with separation of the belt in different chambers, this can reduce gas phase slip streams to a minimum.

Overall, a minor contribution of pure sorbent movement to the overall energy balance is estimated. However, sealing of the different zones within the concepts is required to

avoid losses to the ambient and to allow for vacuum operation. For *MBtA* operation gas barriers sketched in Figure 4.4(b) might be realized. The belt is pressed between sealing plates that limit the gas flow between the different sections of the belt that are separated by thin, gas impermeable walls. A pessimistic estimate based on the analogy to wiper strips²¹⁸ indicates severe increase in energy demand per gas barrier implemented in *MBtA* (\dot{E}_{sep} , Figure 4.4(a)). The *MBdA* concept allows for a significant reduction of this contribution through realization of the gas sealing by common rotary valves or by implementation of alternative sealing strategies, e.g., parallel slide valves.²²⁰

Additional constraints for gravitation force-based sorbent flow in *MBdA* arise. Sorbent termination velocities in the order of 2 m s^{-1} are estimated.²²¹ These are well above the phase velocities aspired such that flow control by means of sorbent discharge control seems possible. Excellent flowability and mechanical stability of *Lewatit* (Section 3.3.1, Table 3.4) underline its good applicability in moving bed concepts. Wall effects in moving beds typically arise up to a distance of 5–10 particle diameters from the supporting structure.^{222–225} Consequently, it seems reasonable to limit the minimum distance between the supporting walls to at least 10–20 D_{Lew} ,²²² e.g., to 0.5–1 cm based on $D_{\text{P},10}$.

4.3.2 Heat and mass transfer

High heat and mass transfer orthogonal to solid movement as well as the limitation of slip streams normal to the sorbent's direction of motion is aspired. Section 4.3.2.1 investigates the relation between the stability of the support structure and the sorbent bed dimensions. Section 4.3.2.2 is dedicated to thermal integration studies.

4.3.2.1 Width of sorbent bed and of support structures

In *MBtA* the sorbent is immobilized in a wire mesh-like structure (Figures 4.2 and 4.4(b)). Low belt widths and high open areas of the mesh $a_{\text{ope,Mes}}$ are favored with respect to efficient mass transfer. With additional focus on low wire mass, mesh configurations that allow for $a_{\text{ope,Mes}} = 37\%$ are selected based on *DIN ISO 4783-2*²²⁶ (Appendix B.2.2.1).

Analysis based on the mesh selected (Appendix B.2.2.1) indicates mechanical stability of the belt even at high bed length $L_{\text{B,x}}$ of 30 m and width $H_{\text{B,z}}$ of 5 cm (Figure B.1(a)). Results obtained also confirm basic mechanical stability of *MBdA* design. Besides stability, the mass of support structure relative to sorbent mass becomes of importance, especially in *MBtA*. Small belt widths are favorable for heat and mass transfer (Section 4.4). But severe increase in mesh contribution to belt weight is observed below sorbent bed widths of 1 cm. Use of smaller wire diameters D_{Wir} counteracts this tendency. However, only small reduction of mesh mass can be reached, with this being accompanied by a decrease of $a_{\text{ope,Mes}}$.²²⁶

4.3.2.2 Thermal integration and transfer media

Realization of a high degree of thermal integration is aspired. The analysis based on $\Delta T_{\text{ldf,DAC}}$ (Figure 2.7) suggests that *MBtA* offers higher potential for maximum thermal integration compared to *MBdA*. Efficiency of heat integration will depend on the transfer medium chosen, which motivates more detailed investigation of its characteristics.

In *MBdA Dowtherm J* (Table B.7) is selected as thermal oil¹¹⁶ to be used as liquid transfer medium. Transfer medium flows in the order of 3 kg s^{-1} are required to match the heat capacity flow of the sorbent (productivity $\dot{n}_{\text{Pro,DAC,CO}_2} = 1 \text{ mol s}^{-1}$, working capacity $\Delta q_{\text{wor,CO}_2} = 0.25 \text{ mol kg}^{-1}$). A worst case analysis (Appendix B.2.2.2) shows that the CO_2 -specific energy demand per bed height in the transfer medium phase, e.g., attributed to friction ($< 0.5 \text{ J m}^{-1} \text{ mol}^{-1}$) or static pressure to be overcome ($\sim 29.8 \text{ J m}^{-1} \text{ mol}^{-1}$), becomes negligible small compared to process energy demand (Section 6.4.4). Thus, no stringent constraints with regard to transfer medium flow arise from an energy perspective.

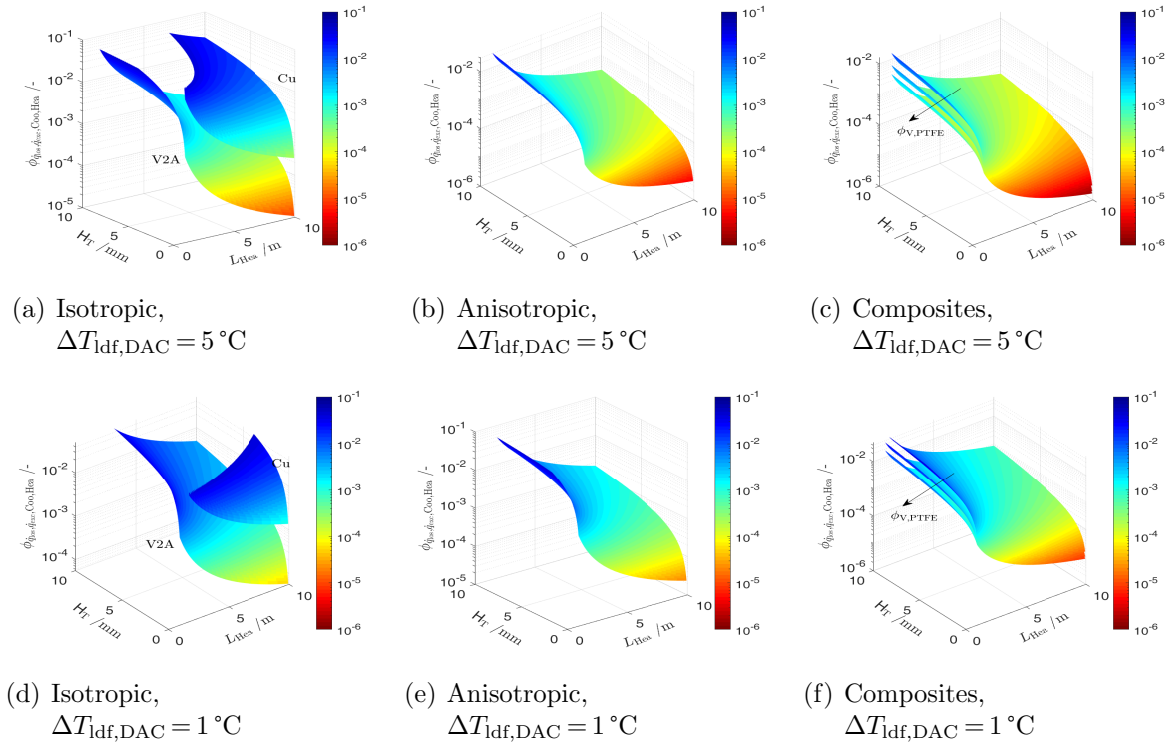


Figure 4.5: Influence of the solid transfer medium on the ratio of conductive heat losses to heat transferred between heating and cooling zone $\phi_{\dot{q}_{\text{los}},\dot{q}_{\text{exc,Coo,Hea}}}$ in dependence of heating zone length L_{Hea} and transfer medium width H_T for various materials: (a) and (d) isotropic: steel (V2A) and copper (Cu), (b) and (e) anisotropic: expanded natural graphite (EG), (c) and (f) composites: parallel layers of copper (Cu) and polytetrafluorethylen (PTFE) with PTFE volume fraction $\phi_{V,\text{PTFE}}$ of 0.10, 0.25 and 0.5. Temperature differences between heating and cooling zone $\Delta T_{\text{1df,DAC}}$ of $5 \text{ }^\circ\text{C}$ and $1 \text{ }^\circ\text{C}$, (a)–(c) and (d)–(f), respectively, are investigated at temperature difference between the ad- and desorption zone $\Delta T_{\text{ads,des}}$ of $75 \text{ }^\circ\text{C}$. Only parameter combinations that allow for $\phi_{\dot{q}_{\text{los}},\dot{q}_{\text{exc,Coo,Hea}}} \leq 5\%$ are shown. Properties of materials used are summarized in Table B.2. Influence of a gas duct $H_{\text{Mes,T}}$ of 1 mm is included in the calculations (Appendix B.2.2.2). Pure air is used as reference gas phase in the heating zone and hydrogen in the cooling zone.

The *MBtA* approach uses a solid transfer medium (Figure 4.2). High thermal conductivity is aspired to limit the length of the transfer zone. Basic comparison between conductive heat losses in the transfer zone and heat exchanged in this zone is given by the ratio $\phi_{\dot{q}_{\text{los}},\dot{q}_{\text{exc,Coo,Hea}}}$. Figure 4.5 exemplifies its dependency on heating zone length L_{Hea} and transfer medium width H_T for materials with different transfer characteristics. Within

the class of isotropic transfer media (Figures 4.5(a) and 4.5(d)) *V2A* steel performs better than Cu, despite Cu providing the higher thermal conductivity. When switching to the material with higher thermal conductivity, raise in thermal losses outruns increase in heat recovery due to additional gas phase transfer resistance orthogonal to belt movement. This motivates investigation of transfer media with anisotropic heat transfer characteristics.

Heat transfer media with directional thermal conductivity are intensively researched.^{227,228} Expanded natural graphite (EG) sheets,²²⁹ e.g., used in heat exchangers, are selected as representatives. Significant reduction of $\phi_{\dot{q}_{\text{los}},\dot{q}_{\text{exc}},\text{Coo,Hea}}$ is reached compared to the isotropic materials (Figures 4.5(b) and 4.5(e)). This might also be achieved by composite materials of conductive and insulating parts, e.g., parallel layers of Cu and PTFE (Figures 4.5(c) and 4.5(f)), with a defined degree of anisotropic thermal conductivity. Variation of PTFE volume fraction $\phi_{V,\text{PTFE}}$ suggests that already low degrees of anisotropy can result in severe reduction of thermal losses.

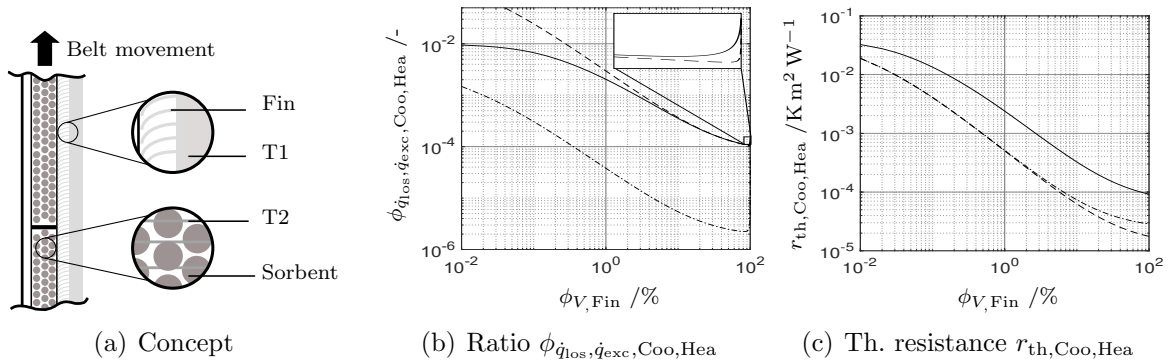


Figure 4.6: Investigation of concepts to reduce gas phase heat transfer resistances. (a) Visualization of the concept. Implementation of high-conductive, solid fins in the duct between belt and transfer medium (T1), and use of high-conductive fibers in the belt (T2) is proposed. Influence of fiber volume fraction in duct $\phi_{V,\text{Fin}}$ on (b) relative conductive heat loss $\phi_{\dot{q}_{\text{los}},\dot{q}_{\text{exc}},\text{Coo,Hea}}$ and (c) thermal resistance between cooling and heating zone $r_{\text{th,Coo,Hea}}$. *V2A/V2A* (-), Cu/Cu (- -) and EG/Cu (- ·) are investigated as transfer medium/fiber material combinations for geometric dimensions of $L_{\text{Hea}} = 5 \text{ m}$, $H_{\text{T}} = 5 \text{ mm}$, $H_{\text{Mes,T1}} = 1 \text{ mm}$ and operation parameters of $\Delta T_{\text{df,DAC}} = 1 \text{ }^\circ\text{C}$, $\Delta T_{\text{ads,des}} = 75 \text{ }^\circ\text{C}$. Properties of materials used are summarized in Table B.2. Pure air is used as reference gas phase in the heating zone and hydrogen in the cooling zone (Appendix B.2.2.2).

The results presented hint at high heat transfer resistances orthogonal to the belt movement. The low thermal conductivity of the gas present in the duct between transfer medium and belt is found to dominate the belt–belt heat exchange. Use of high thermal conductive, fin-like structures on the transfer medium (Figure 4.6(a)) is investigated. These might enable an intense thermal coupling between belt and transfer medium without the need of direct transfer medium–belt contact. Figure 4.6(b) compares the influence of solid fin use on $\phi_{\dot{q}_{\text{los}},\dot{q}_{\text{exc}},\text{Coo,Hea}}$ for different combinations of transfer medium and fiber material. Fiber volume fractions in duct space $\phi_{V,\text{Fin}}$ of less than 1% already lead to a severe decrease of $\phi_{\dot{q}_{\text{los}},\dot{q}_{\text{exc}},\text{Coo,Hea}}$. Convergence of $\phi_{\dot{q}_{\text{los}},\dot{q}_{\text{exc}},\text{Coo,Hea}}$ for *V2A* steel and Cu at high levels $\phi_{V,\text{Fin}}$ underlines the strong influence of the heat transfer system on gas phase resistances. Remarkable increase of $\phi_{\dot{q}_{\text{los}},\dot{q}_{\text{exc}},\text{Coo,Hea}}$ in the vicinity of complete fiber coverage reflects superiority of anisotropic heat transfer.

Use of fins moreover reduces the overall thermal resistance of heat transfer between the heating and cooling zone $r_{\text{th,Coo,Hea}}$. This will reflect in smaller heat transfer areas required, lower levels of $\Delta T_{\text{ldf,DAC}}$ and, thus, lower convective heat losses. As indicated by Figure 4.6(c), only small fin coverage $\phi_{V,\text{Fin}}$ suffices to decrease $r_{\text{th,Coo,Hea}}$ by several orders of magnitude. This again underlines the severe importance of the gas phase transfer resistance in the overall energy integration approach and motivates an additional analysis with respect to the use of high conductive transfer medium fibers (T2, Figure 4.6(a)) in the belt or moving bed, to be performed in Section 4.4.

Overall, use of anisotropic transfer media seems favorable if operation at very low $\Delta T_{\text{ldf,DAC}}$ and short zone length L_{Hea} is aspired. But in dependence of the degree of thermal recovery aspired, use of isotropic transfer media with low thermal conductivity and small width H_{T} can become a reasonable alternative. With regard to belt–belt heat exchange, the thermal conductivity of the transfer medium is noticed to be of less importance, due to the dominating influence of the gas phase heat transfer resistance. High potential for reducing this limitation by use of transfer medium fibers is revealed.

4.3.3 Large-scale realization

Large-scale operation of both concepts can be realized by increase of bed length or by numbering up. Economy of scale and use of synergies speak in favor for high capacity *DAC* plants (Appendix B.2.3). Limitations can arise from convective CO_2 transport in air. Figure 4.7 gives an impression of the *DAC* dimensions required for realization of a CO_2 product flow of 1 mols^{-1} . Via Figure 4.7(a) the total horizontal dimension of the adsorption zone $L_{z,\text{DAC}_{\text{Ads},\Sigma}}$ in dependence of the total height of the adsorption zone $L_{x,\text{DAC}_{\text{Ads}}}$ and level of CO_2 recovery $\phi_{\dot{n}_{\text{cap,DAC,CO}_2},\dot{n}_{\text{DAC}_{\text{Ads},\text{in}},\text{CO}_2}}$ can be estimated. With these parameters selected, Figure 4.7(b) allows to determine the depth of the adsorption zone $L_{y,\text{DAC}_{\text{Ads}}}$ in dependence of the width of one functional unit $H_{z,\text{Fun}}$ composed of bed, support structure and gas duct. Finally, the number of functional units to be parallelized I_{Fun} can be estimated from the graphs shown in Figure 4.7(c). To give a basic impression of the dimensions, at a recovery of 50 %, one obtains for $L_{x,\text{DAC}_{\text{Ads}}} = 12 \text{ m}$ and $H_{z,\text{Fun}} = 3 \text{ cm}$: $L_{z,\text{DAC}_{\text{Ads},\Sigma}} = 5.2 \text{ m}$, $L_{y,\text{DAC}_{\text{Ads}}} = 10.3 \text{ m}$, $I_{\text{Fun}} = 172$. Overall, elevated degrees of recovery are reached at comparatively high values of $L_{y,\text{DAC}_{\text{Ads}}}$, which indicate minor influence of convective transport limitations in the ambient.

4.4 In-depth simulation

Detailed thermophysical models of *MBtA* (Appendix B.3.2) and *MBdA* (Appendix B.4.2) are proposed that describe the evolution of the strongly coupled state variables by a system of partial differential algebraic equations (*PDAE*). Operation profiles in spatial cyclic steady state are determined numerically by use of *method of lines* (*MOL*) (Appendix B.3.3 and B.4.3). *MBtA* simulation results (Section 4.4.1) allow for deep insights into the limitations of the concept. These motivate investigation of hybrid *TVCSA* approaches, use of which is exemplified in evaluation of *MBdA* design (Section 4.4.2). Focus is placed

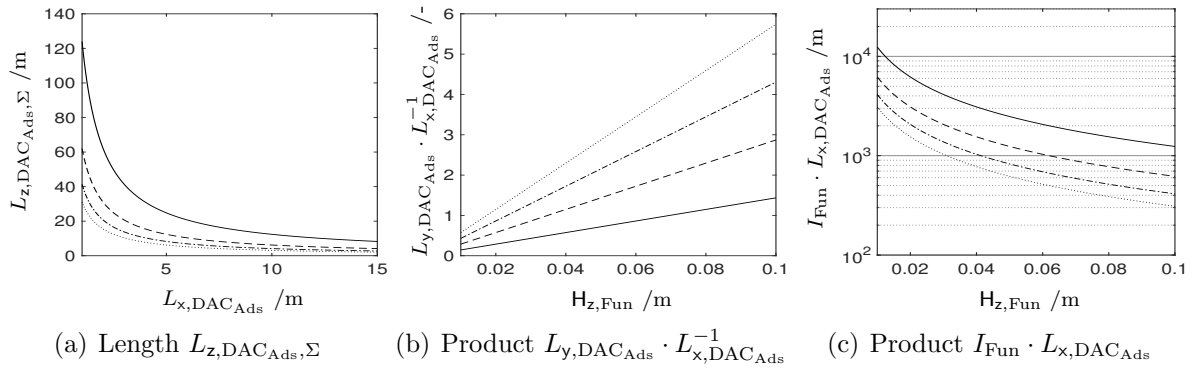


Figure 4.7: Large-scale realization of the DAC unit adsorption zone. Results are shown for the reference scenario: product mole flow $\dot{n}_{Pro,DAC,CO_2} = 1 \text{ mol s}^{-1}$, working capacity $\Delta q_{wor,CO_2} = 0.25 \text{ mol kg}^{-1}$, sorbent velocity $u_B = 1 \text{ mm s}^{-1}$, sorbent bed width $H_{B,z} = 0.5 \text{ cm}$ and air velocity $u_{Amb,Air} = 2 \text{ m s}^{-1}$ (Section 2.2.2). (a) Total horizontal dimension of the adsorption zone $L_{z,DAC_{Ads},\Sigma}$ in dependence of the total height of the adsorption zone $L_{x,DAC_{Ads}}$. (b) Depth of adsorption zone parallel to air stream $L_{y,DAC_{Ads}}$ scaled by $L_{x,DAC_{Ads}}$. (c) Product of the number of functional units to be parallelized I_{Fun} and $L_{x,DAC_{Ads}}$. The variable $H_{z,Fun}$ defines the width of one functional unit orthogonal to the flow of air. The evaluation is performed for CO_2 recoveries $\phi_{\dot{n}_{cap,DAC,CO_2},\dot{n}_{DAC_{Ads},in,CO_2}}$ of 0.25 (-), 0.5 (- -), 0.75 (- ·) and for $\phi_{\dot{n}_{cap,DAC,CO_2},\dot{n}_{DAC_{Ads},in,CO_2}} \rightarrow 1$ (· ·). Dimensions for the limiting case, i.e., with no kinetic limitations being considered, are shown.

on a detailed analysis of the more promising counter-current operation mode. For a more detailed insight the reader is also referred to the corresponding publication²³⁰.

4.4.1 Simulation results TCSA – MBtA

Figure 4.8 visualizes the two-dimensional modeling approach used to evaluate the characteristics of *MBtA* operation. Operation with defined wall temperature in the external heating and desorption zone is investigated based on the parameter set summarized in Table B.6. Heat exchange and CO_2 removal is realized from one side of the belt (Figure 4.8). Based on this model, the characteristic state variable profiles (Section 4.4.1.1), the influence of operation and design parameters (Section 4.4.1.2), and the concept to overcome transfer limitations (Section 4.4.1.3) are evaluated.

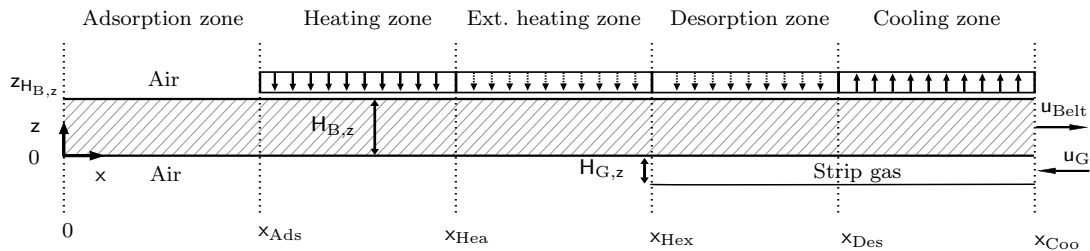


Figure 4.8: Sketch of *MBtA* model. DAC unit internal heat flows are visualized by solid arrows (-). External heat supply is represented by dotted arrows (- -). Characteristic spatial coordinates x_i and $z_{HB,z}$ that represent transition between zones and the upper boundary of the belt, respectively, are depicted. The width of the sorbent bed $H_{B,z}$ and of the duct for strip gas $H_{G,z}$, as well as the velocity of the phases u_i , are depicted. Figure reproduced from Drechsler and Agar²³⁰.

4.4.1.1 Characteristic state variable profiles

Figure 4.9 provides a basic insight into the characteristic state variable profiles of *MBtA* operation. The bed temperature profile T_B shows the hysteresis-like profile aspired (Figure 4.9(a)). But even at a long cooling zone length of 3 m the mean temperature difference between the solid phase outlet and ambient reaches 4.9°C . This motivates the investigation of measures to reduce heat transfer limitations (Sections 4.3.2.2 and 4.4.1.2). Moreover, a possibility of increasing the potential for heat recovery via the external heating zone is revealed. This is, if the sorbent temperature is increased by more than the temperature difference required for heat transfer, it acts as a thermal reservoir, the heat stored in which can be recovered by the heat of desorption. This comprises the advantage of less heat transfer required between heating and cooling zone as well as higher temperature gradients between these zones at the start of the cooling zone.

The analysis of the CO_2 loading profile (Figure 4.9(b)) reveals strong interactions between heat and mass transfer. Superimposed effects of temperature and concentration profiles result in a complex evolution of the loading profile q_{CO_2} . Re-adsorption of CO_2 is observable in the desorption and cooling zone. Intense coupling between the CO_2 content in the bed void space and its loading at the sorbent is noticed, which is attributed to the low slopes of the adsorption isotherms at high temperatures. This dependency allows for a strong influence of minor temperature gradients in the bed on the maximum carbon dioxide mole share present. Moreover, severe gradients of q_{CO_2} along z -coordinate are noticed in the adsorption zone that reveal strong limitations by diffusion. Even at a high adsorption zone length the mean levels of q_{CO_2} are found to be significantly lower than the equilibrium loading under ambient conditions. Due to the strong dependency of y_{B,CO_2} on q_{CO_2} , this can become a significant drawback with regard to the maximum CO_2 product concentration attainable.

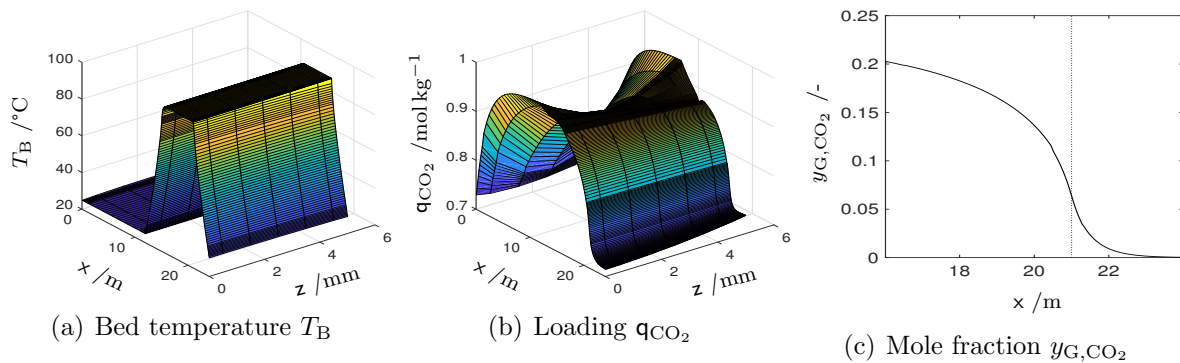


Figure 4.9: Characteristic state variable profiles obtained in *MBtA*, based on the operation parameters summarized in Table B.6. (a) Bed temperature T_B , (b) loading q_{CO_2} and (c) CO_2 mole fraction in strip gas phase y_{G,CO_2} are shown as a function of the spatial coordinates x and z . The boundary between the desorption and cooling zone is visualized in Figure (c) by a dotted line (\cdots).

The last mentioned aspect is underlined by Figure 4.9(c) that visualizes the evolution of the CO_2 mole fraction in the strip gas phase. Strong dependency of adsorption equilibrium on temperature results in a negligible contribution of the major part of the cooling zone on

the increase of y_{G,CO_2} . This is also confirmed by the formation of an inflection point that suggests a severe influence of equilibrium loading, and thus temperature, on the kinetics of CO_2 desorption. Noticeable decline of the increase in CO_2 mole fraction after the inflection point is revealed, which already suggests a strong decrease of the contribution of the desorption zone length to the CO_2 mole fraction increase at high desorption zone length.

4.4.1.2 Influence of operation and design parameters

The analysis given in Section 4.4.1.1 indicates strong interactions between the different state variables that are besides others attributed to the cyclic operation in spatial domain. A more detailed investigation reveals strong couplings between the state variable profiles in the different zones and phases that result in various operation regimes. For example, at long adsorption zone length limitations arising from desorption effects become more dominating and vice versa. An analysis of basic tendencies via a parameter study (Figure 4.10) is performed based on the characteristic indicators: heat ratio between *Sabatier* reaction heat release and external heat supply $\phi_{\dot{Q}_{Sab}, \dot{Q}_{ext}}$, CO_2 mole fraction in product gas y_{Pro, CO_2} and bed length-specific CO_2 product flow $\dot{m}_{Pro, CO_2, spe_{L_x}}$.

Strong influence of all zone lengths L_{x, DAC_i} , besides of the external heating zone, is revealed (Figures 4.10(a) - 4.10(d)). Maxima formations in length-specific productivity $\dot{m}_{Pro, CO_2, spe_{L_x}}$ underline the strong coupled nature of the process, which can be subject to various limitations, e.g., mass transfer in adsorption or desorption zone. Relations between the evolution of $\dot{m}_{Pro, CO_2, spe_{L_x}}$ and y_{Pro, CO_2} become of special interest. These indicate that allowance for CO_2 mole shares lower than the level of 20% aspired can result in a severe increase of the length-specific productivity and decrease of adsorber dimensions. However, the reduction of adsorber dimensions is limited by the lower bound set for $\phi_{\dot{Q}_{Sab}, \dot{Q}_{ext}}$ that, besides others, depends on the level of heat recovery and productivity of the *DAC* unit. Only for an increase in the external heating zone length decrease of $\phi_{\dot{Q}_{Sab}, \dot{Q}_{ext}}$ with zone length is observed, which suggests that the advantage of additional heat supply on CO_2 desorption is outrun by the lower level of heat integration achieved.

Severe decrease of all indicators at high bed width $H_{B,z}$ (Figure 4.10(e)) suggests strong influence of transfer limitations. As a result of limited heat recovery and transfer in the bed, temperatures in the desorption zone close to the gas phase outlet only reach levels significantly below the desorption temperature aspired. These result in high equilibrium loading and re-adsorption in the desorption zone close to the gas phase outlet.

Influence of gas phase inlet velocity $u_{G,in}$ shows the tendencies expected. Higher volume flows result in dilution of the gas phase, i.e., in a decrease in y_{Pro, CO_2} , while the increase in productivity leads to higher values of $\phi_{\dot{Q}_{Sab}, \dot{Q}_{ext}}$. In contrast to these observations, all performance indicators shown decrease with increase in belt velocity u_{Belt} . High heat losses and temperature gradients in the sorbent bed that result in temperatures significantly below the level aspired in the desorption zone are found to cause this behavior. Formation of complex loading profiles with re-adsorption normal and orthogonal to belt movement is noticed.

Especially with respect to long-term operation, the sensitivity of the performance indicators toward changes of the CO_2 content in the adsorption zone (Figure 4.10(h)) becomes of special interest. Strong decrease of all indicators shown with y_{wor, CO_2} is revealed. Single-

4 Approaches to intensified heat integrated DAC units

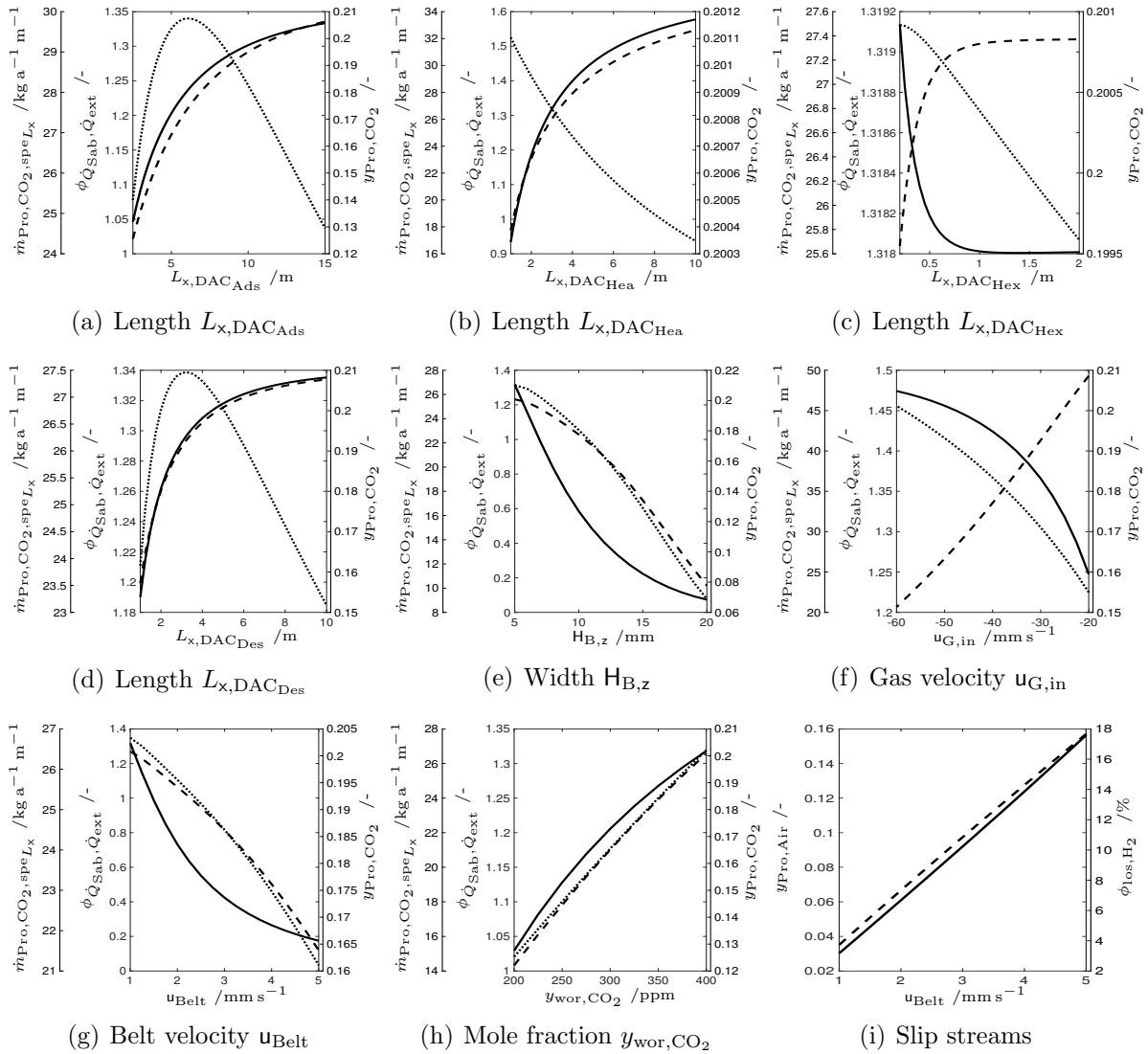


Figure 4.10: Characteristic performance indicators of *MBtA*. Influence of: (a)-(d) *MBtA* zone lengths L_{x,DAC_i} , (e) bed width $H_{B,z}$, (f)-(g) phase velocities u_i and (h) CO_2 share in gas phase y_{wor,CO_2} on heat ratio between *Sabatier* reaction heat release and external heat supply $\phi_{\dot{Q}_{Sab}, \dot{Q}_{ext}}$ (-), CO_2 mole fraction in product gas y_{Pro,CO_2} (-) and bed length-specific CO_2 product flow $\dot{m}_{Pro,CO_2,speL_x}$ (\cdot) is shown. Influence of belt velocity u_{Belt} on content of air in the product gas $y_{Pro,Air}$ (-) and on relative hydrogen loss ϕ_{los,H_2} (-) is depicted in Figure (i). Single parameter variation is investigated, with other parameters kept at reference configuration (Table B.6). Results are shown for a reference belt depth $L_{y,Belt}$ of 1 m.

stage *TCSA* operation with solely use of hydrogen as strip gas to reach CO_2 shares of 20 % in the product gas becomes unreachable at low levels of y_{wor,CO_2} (Figure 4.1). Nevertheless, results suggest that even at low levels of y_{wor,CO_2} autothermal *DAC-PtG* operation can remain feasible. Moreover, in the framework of the integrated process, slip streams in the *DAC* unit, e.g., as a result of gas transport in the sorbent bed void space between adsorption and heating or cooling zone, become of relevance (Figure 4.10(i)). Shares of air in the product gas $y_{Pro,Air}$ and hydrogen losses relative to its stream at the gas phase

Table 4.2: Influence of an increase in the overall thermal conductivity normal to belt movement equivalent to the presence of a volume fraction $\phi_{V_z, T, Belt}$ of the transfer medium for various bed widths $H_{B, z}$. Operation parameters not explicitly named take values summarized in Table B.6. Heat ratios between *Sabatier* reaction heat release and external heat supply $\phi_{\dot{Q}_{Sab}, \dot{Q}_{ext}}$, CO₂ mole fractions in product gas y_{Pro, CO_2} and bed length-specific CO₂ product flows $\dot{m}_{Pro, CO_2, spe_{L_x}}$ are evaluated. Results are shown for a reference belt depth $L_{y, Belt}$ of 1 m.

$H_{B, z}$ / 10^{-3} m	$\phi_{V_z, T, Belt}$ /%	$\phi_{\dot{Q}_{Sab}, \dot{Q}_{ext}}$ /-	y_{Pro, CO_2} /-	$\dot{m}_{Pro, CO_2, spe_{L_x}}$ /kg a ⁻¹ m ⁻¹
5	0	1.32	0.201	26.78
5	1	1.57	0.201	26.81
10	0	0.58	0.178	23.06
10	1	0.95	0.182	23.81
20	0	0.07	0.078	9.10
20	1	0.24	0.144	18.10

inlet ϕ_{los, H_2} significantly increase with belt velocity u_{Belt} . This underlines the importance of this operation parameter and suggests operation at high working capacities to be beneficial. A more detailed discussion in the framework of the integrated *DAC-PtG* process, which also includes use of additional gas separation steps, is provided in Section 6.4.3.

In summary, cyclic steady state operation with intense heat integration and strong coupling of state variables, e.g., via the adsorption isotherms, results in complex state variable profiles and interactions between the operation parameters. Especially the superimposed influence of heat as well as mass transfer limitations is found to offer potential for improved operation by extensions of the basic concept to be discussed in Sections 4.4.1.3 and 4.4.2.

4.4.1.3 Overcome of heat transfer limitations

In a first step, an increase of the heat transfer coefficients orthogonal to belt movement (Figure 4.6) is investigated as a measure to decrease heat transfer limitations, without changes of the basic design proposed. Table 4.2 summarizes the influence of an increase in thermal conductivity orthogonal to the sorbent movement, equivalent to the presence of a volume fraction $\phi_{V_z, T, Belt}$ of the transfer medium in the sorbent bed and gas duct between the belt and the wall, which is used for external supply and recovery of heat, on the key performance indicators. At low and intermediate bed width $H_{B, z}$ increase of $\phi_{V_z, T, Belt}$ only takes a minor influence on y_{Pro, CO_2} and $\dot{m}_{Pro, CO_2, spe_{L_x}}$. This picture changes at large bed dimensions that, as a result of the one-sided heating concept, reflect in significant heat transfer limitations. Here, increase of thermal conductivity orthogonal to sorbent movement results in a remarkable increase of all performance indicators. However, especially $\phi_{\dot{Q}_{Sab}, \dot{Q}_{ext}}$ still remains significantly below a value of one required for autothermal operation, which motivates additional extensions of the concept to be discussed in Section 4.4.2.

4.4.2 Simulation results TVCSA – MBdA

The *MBdA* design presented (Figure 4.3) exemplifies further modifications to the basic concept to overcome limitations arising from:

- Heat transfer: heating from both sides of the bed, avoidance of additional gas ducts
- Mass transfer: flow through sorbent bed in desorption zone
- Adsorption equilibrium: *TVCSA* operation to increase CO₂ mole shares $y_{\text{Pro,CO}_2}$

Figures 4.11(a) and 4.11(b) present key state variable profiles of *MBdA* obtained based on a parameter set (Table B.8, set 1) similar to the *MBtA* reference configuration (Table B.6). Temperature profiles formed allow for a slip of 2.7 K at the particle phase outlet that results in a degree of autothermality $\phi_{\dot{Q}_{\text{Sab}}, \dot{Q}_{\text{ext}}}$ of 1.50. This parameter significantly exceeds its level obtained for a similar parameter set in *MBtA* (Table 4.2) with the product gas CO₂ mole fraction $y_{\text{Pro,CO}_2}$ of 20.2% and productivity $\dot{m}_{\text{Pro,CO}_2, \text{spe}_{L_x}}$ of 26.96 kg a⁻¹ m⁻¹ taking values similar to the *MBtA* performance indicators obtained. This underlines the positive impact of the conceptual modifications. However, the comparatively low working capacity of the sorbent observed (Figure 4.11(b)) indicates additional potential for increase in productivity.

Figure 4.11(c) compares the influence of an increase in strip gas mole flow by a factor $\phi_{\dot{n}_{\text{H}_2, \text{in}}, \dot{n}_{\text{H}_2, \text{in,ref}}}$ relative to the reference configuration (Table B.8, set 1) on the specific productivity $\dot{m}_{\text{Pro,CO}_2, \text{spe}_{L_x}}$ and product gas CO₂ content $y_{\text{Pro,CO}_2}$. Low-pressure operation is found to allow for a significant increase of both performance indicators. But this is paid for by high additional compression energy demand (Figure 4.11(d)), e.g., at gas phase outlet pressures of $0.5 \cdot 10^5$ Pa the ratio between the energy required for compression and the heat released in *Sabatier* reaction $\phi_{\dot{E}_{\text{com}}, \dot{Q}_{\text{Sab}}}$ takes values in the order of magnitude of 10%. Even if a decrease in operation pressure simultaneously leads to less external heat demand relative to *Sabatier* reaction heat release ($\phi_{\dot{Q}_{\text{ext}}, \dot{Q}_{\text{Sab}}}$), with view on exergy considerations this relativizes the benefits arising from low pressure operation.

The responses of the system to changes in the operation pressure also provide more detailed insights into its operation characteristics. Comparison of the CO₂ loading profile q_{CO_2} (Figures 4.11(b) and 4.11(e)) exemplifies one of the various self-inhibitory couplings of state variables in the system. Higher desorption of CO₂ results in lower q_{CO_2} at the solid phase inlet to the adsorption zone, which allows for an increased uptake of CO₂. But this increase does not suffice to counteract the higher CO₂ desorption. This leads to a shift in the cyclic steady state loading profile to lower levels, which favors CO₂ adsorption and simultaneously counteracts the increase in CO₂ desorption. Besides, analysis of the sorbent loading distance to its equilibrium state with the gas phase (Figure 4.11(f)) underlines the impact of CO₂ mass transfer limitations in the adsorption zone on CO₂ uptake. At small temperature differences to the ambient, trade-off between adsorption kinetics and mass transfer to the particles is reached by mean CO₂ concentrations in the bed significantly below ambient state. Moreover, presence of a distinct maximum in the $q_{\text{eq,CO}_2} - q_{\text{CO}_2}$ profile in the desorption zone indicates a low contribution of the center of this zone to the overall desorption process, which can become even more severe in realization of higher working capacities, e.g., by increase of the desorption zone length.

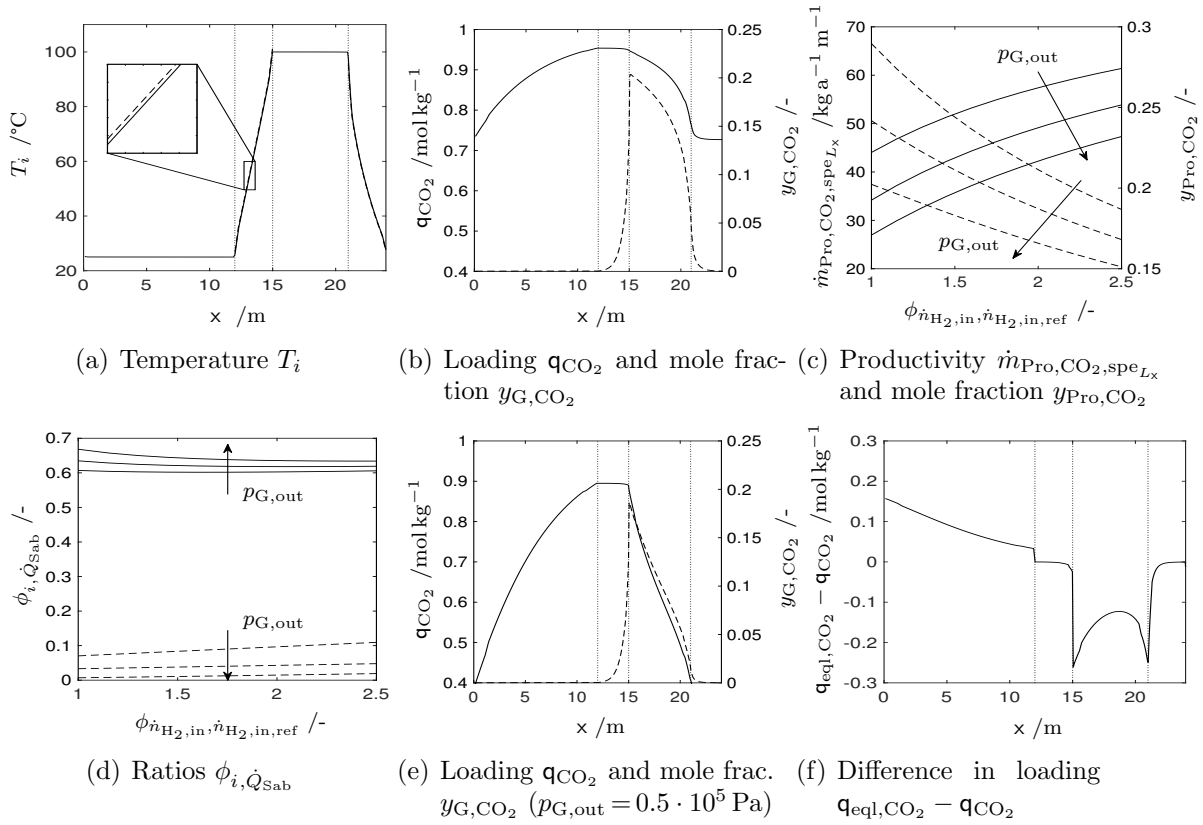


Figure 4.11: Simulation results of *MBdA*. (a) Temperature profile of the particle phase T_P (-) and transfer medium phase T_{TL} (- -) as well as (b) sorbent loading profile q_{CO_2} (-) and CO_2 gas phase mole fraction profile $y_{\text{G,CO}_2}$ (- -) are shown in dependence of the spatial coordinate x . Results shown are based on the reference configuration (set 1) summarized in Table B.8. The influence of changing the strip gas mole flow by a factor $\phi_{\dot{n}_{\text{H}_2,\text{in}}, \dot{n}_{\text{H}_2,\text{in,ref}}}$ on (c) bed length specific productivity $\dot{m}_{\text{Pro,CO}_2,\text{spe}_{L_x}}$ (-) and product gas CO_2 mole fraction $y_{\text{Pro,CO}_2}$ (- -) as well as on (d) the ratios between the external heat demand $\phi_{\dot{Q}_{\text{ext}}, \dot{Q}_{\text{Sab}}}$ (-), or compression energy requirement $\phi_{\dot{E}_{\text{com}}, \dot{Q}_{\text{Sab}}}$ (- -), and *Sabatier* reaction heat release are visualized. Operation at gas phase outlet pressures $p_{\text{G,out}}$ of $0.5 \cdot 10^5$, $0.75 \cdot 10^5$ and $1 \cdot 10^5 \text{ Pa}$ is shown. Profiles of (e) q_{CO_2} (-) and $y_{\text{G,CO}_2}$ (- -) as well as of (f) the difference between the CO_2 loading q_{CO_2} and the equilibrium loading with the gas phase $q_{\text{eql,CO}_2}$ are depicted for the operation at $p_{\text{G,out}} = 0.5 \cdot 10^5 \text{ Pa}$ and $\phi_{\dot{n}_{\text{H}_2,\text{in}}, \dot{n}_{\text{H}_2,\text{in,ref}}} = 2.5$ (Table B.8, set 2). Dotted lines ($\cdot \cdot$) in (a), (b), (e) and (f) indicate transitions between the different zones, with the zero point of the spatial coordinate x being at the solid phase inlet of the adsorption zone.

In conclusion, *TVCSA* operation can allow for a significant increase in CO_2 working capacity, but can be accompanied by the need of intense compression energy requirement. The further modifications of the basic concept proposed result in a less severe influence of both, mass and heat transfer limitations. With view on larger bed widths $H_{B,z}$ additional increase of heat transfer characteristics might be realized by use of a solid transfer medium inside the bed similar to the concept exemplified in *MBtA* analysis (Section 4.4.1.3). The detailed insight provided allows for physically sound interpretation of the operation characteristics of the concepts, which are characterized by intense couplings of the state variables and suggest basic feasibility of realizing *MBtA* and *MBdA* approaches.

4.5 Experimental investigation of transport phenomena

The results presented in Section 4.4 indicate that diffusive mass transfer in the adsorption zone might become a crucial drawback. The experimental setup shown in Figure 4.12(a) is built to investigate transfer limitations based on evaluation of *BTCs* (Section 3.2.1.1). These are recorded online via infrared devices. By use of a modular adsorber design (Figure B.2), realized via 3D printing, different adsorber configurations can be evaluated. The sorbent bed is mechanically immobilized at the adsorber wall by use of different inlays that allow for variations of the gas channel and sorbent bed dimensions. Data recording and plant control is realized via *Labview*.¹⁶⁹ The reader is referred to Appendix B.5 for more detailed information on the experimental setup and procedure.

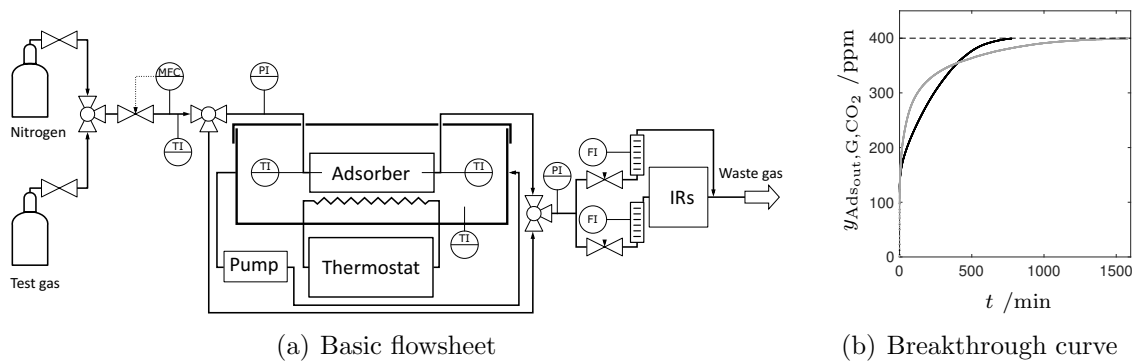


Figure 4.12: *BTC* experiments to determine the influence of bed width on overall kinetics. The experimental setting realized (a) and breakthrough curves measured at the adsorber outlet (b) are shown. Measurements are based on the parameter setting defined in Table B.10. Cooling water flow to the thermostat as well as the filter before IR devices is not shown in detail. *BTCs* measured at bed widths $H_{B,z}$ of 2.5 mm (●) and 7.5 mm (★), with other operation and design parameters being kept constant (Appendix B.5), are visualized. A CO_2 mole fraction level of 400 ppm, which is close to the mole fractions expected in steady state, is depicted by a dashed line (-) in (b).

Figure 4.12(b) exemplarily shows the dependency of *BTCs* on the sorbent bed width $H_{B,z}$ observed based on the parameter setting summarized in Table B.10. Same mass of *Lewatit* and same operation and design parameters, despite of the bed width and of the mass of glass beads (Appendix B.5.2), are used to allow for a direct comparison between the breakthrough curves. Reaching the same capacity in saturation state is aspired. It is expected that higher transport resistances are reflected in an initially faster increase in the CO_2 mole fraction recorded, due to less efficient CO_2 removal from the gas phase, followed by a longer period needed to saturate the sorbent. Experimental results obtained for bed widths of 2.5 mm and 7.5 mm show these tendencies and suggest strong increase of mass transfer limitations with increasing bed width. This motivates research of bed designs that simultaneously account for small mass transfer limitations and low pressure losses.

4.6 Cost estimation and net negative emission

Class 4 cost estimate based on *factorial method*²¹⁷ is performed. *MBtA* operation is evaluated at a working capacity $\Delta q_{\text{wor,CO}_2}$ of 0.25 mol kg^{-1} and thermal slip in the solid phase $\Delta T_{\text{los,DAC}}$ of 5 K. These parameters read for *MBdA* operation: $\Delta q_{\text{wor,CO}_2} = 0.5 \text{ mol kg}^{-1}$, $\Delta T_{\text{los,DAC}} = 2.5 \text{ K}$ (Section 4.4). The basics of the cost estimation are only briefly outlined in this section, whereas the reader is referred to Appendix B.6 for a detailed insight.

Figure 4.13 evaluates the economy and the ecologic footprint of the *MBtA* concept operated in *TCSA* mode. With increasing bed width $H_{B,z}$ sorbent costs dominate the zone length related CO_2 -specific capture costs (Figure 4.13(a)). Costs to drive the belt are found to be of minor importance (Figure 4.13(b)). Decrease of these with increasing $H_{B,z}$ can be attributed to lower frictional resistances at the belt sealings. CO_2 -specific costs attributed to H_2 strip gas use ($\sim 1900 \text{ \$ t}^{-1}$) (Appendix B.6.4) are not included in the analysis, as these are related to the characteristics of the global process structure rather than to the capture process itself.

Low contribution of electric to overall energy demand is found (Figure 4.13(c)). The heat of adsorption significantly contributes to the thermal energy requirement. High ratios between the integrated and external heat, required to change sorbent temperature, underline the benefit of thermal integration with regard to *MBtA* overall energy demand. CO_2 -specific costs are summarized in Figure 4.13(d). Major contribution arises from depreciation of capital investment. Electric and thermal energy demand take a minor influence on cost structure. Severe reduction in energy costs through heat integration is revealed.

Similar tendencies are observed in *MBdA* evaluation (Figure 4.14). *TVCSA* operation with pressure decrease to $0.5 \cdot 10^5 \text{ Pa}$ is analyzed. Avoidance of the supporting mesh structure leads to reduced costs of the heating, desorption and cooling zone. Also in *MBdA* costs for additional key investments are of minor importance (Figure 4.14(b)). Only compressor costs reach a noticeable level compared to the overall *MBdA* cost structure.

Similarities to *MBtA* are also observed with respect to energy demand (Figure 4.14(c)). Thermal energy requirement is found to be the dominating contribution. High electric energy demand attributed to vacuum operation is observed, whereas transfer medium pump and bucket elevator operation take insignificant shares of the overall demand. The severe influence of compressor operation is also reflected in the cost structure presented in Figure 4.14(d). Shares of electric and thermal energy are in a similar order of magnitude. However, these costs are still small compared to the depreciation of investment costs.

The concepts proposed are characterized by high CO_2 -specific capital investment and low energy demand. Data of other approaches to *DAC* published are summarized in Table B.1. CO_2 -specific costs attributed to depreciation (Figures 4.13(d) and 4.14(d)) are found to be a factor of more than two higher compared to capture costs of, e.g., $600 \text{ \$ t}^{-1}$ currently named by *Climeworks*.⁸⁵ However, this comparison seems to lack of fairness, as an intensified cost optimized process is compared to concepts that primarily focus on minimum energy requirements and are evaluated based on worst case assumptions.

Potential for severe decrease in investment through reduction of sorbent mass demand is noticed. Working capacity, cycle time and sorbent-specific costs become of high importance. For example, the maximum CO_2 capacity of *Lewatit* at ambient CO_2 pressures

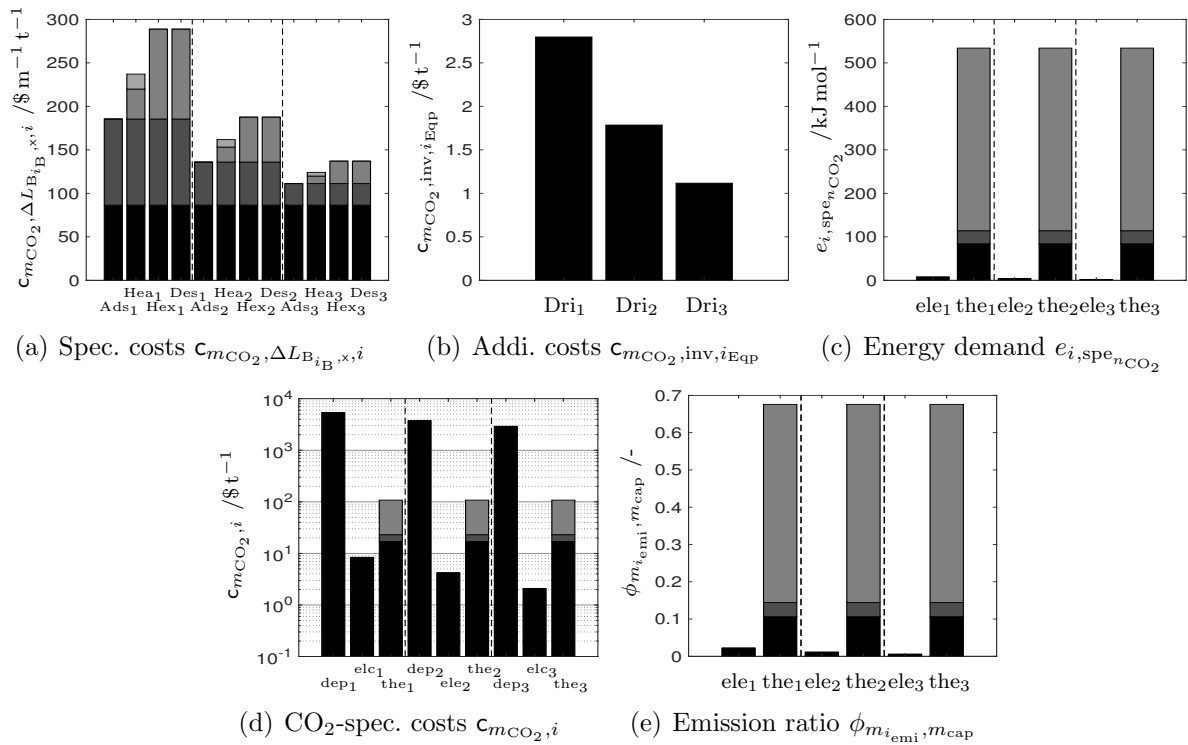


Figure 4.13: Economy and ecology of *MBTA* (Appendix B.6). Three scenarios that differ in the sorbent bed width $H_{B,z}$ (1: 5 mm, 2: 10 mm, 3: 20 mm) are investigated. (a) CO₂-specific capture costs per meter of belt length realized in adsorption (Ads), heating (Hea), ext. heating (Hex) and desorption (Des) zone $c_{mCO_2, \Delta L_{B_{iB,x,i}}}$. Contributions from (dark to bright): *Lewatit*, supporting mesh, additional support, e.g., realization of gas duct, and solid transfer medium in heat recovery zone are shown. The costs of the cooling zone equal the ones determined for the heating zone. (b) Additional CO₂-specific capture costs attributed to the drive of the belt. (c) CO₂-specific energy demand $e_{i, spe_{nCO_2}}$, split into electric (ele) and thermal (the) contributions. (d) Overall CO₂-specific costs $c_{mCO_2, i}$ arising from: equipment and sorbent (dep), electric energy (ele) and thermal energy (the) use. (e) Ratio $\phi_{m_{i, emi}, m_{cap}}$ between CO₂ emissions attributed to electric (ele) energy demand, or thermal (the) demand, and mass of CO₂ captured. Contributions to thermal energy requirement in Figures (c)-(e) are indicated by different color tones (dark to bright): heat of desorption, sorbent sensible heat requirement and energy recovered by heat integration.

takes a value of about 1 mol kg^{-1} , whereas sorbents optimized for *DAC* can offer capacities larger than 2 mol kg^{-1} (Section 3.1.1). Influence of moisture might even lead to an additional increase in capacity. Overall this can result in a significant increase of the maximum capacity. Use of tailor-made *DAC* sorbents and realization of convective CO₂ transport to the sorbent can additionally enable lower sorbent-specific costs by reduction of cycle times and decrease in unit costs through larger mass ratios between the sorbent bed and its peripheries. This suggests that CO₂-specific capture costs can be decreased below $1000 \$ t^{-1}$.

With regard to a cost-based optimization, reduction of the level of energy integration or use of air compression to accelerate convective CO₂ transport results in trade-off considerations between the costs avoided and energy spent. Even if the capture costs can be reduced, the increase in energy demand can take severe influence on the level of net negative emissions achieved. Figures 4.13(e) and 4.14(e) underline this aspect by visualization

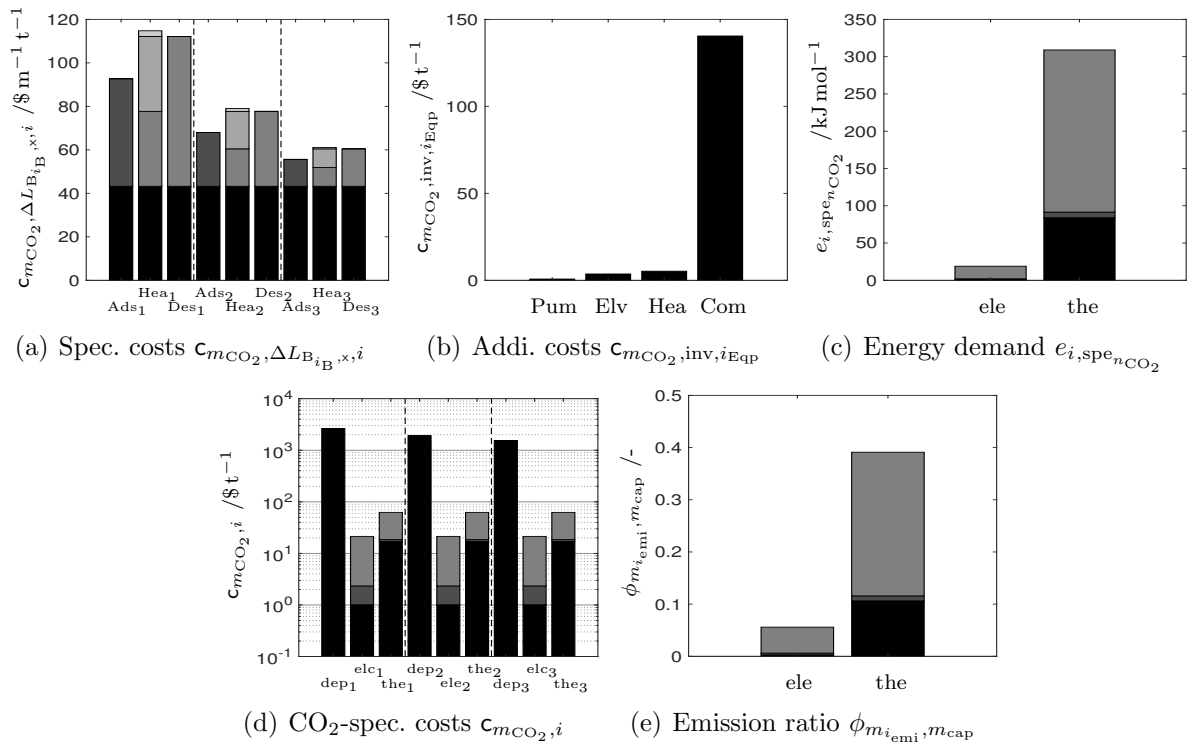


Figure 4.14: Economy and ecology of the *MBdA* concept operated in *TVCSA* mode (Appendix B.6). Three scenarios that differ in the sorbent bed width $H_{B,z}$ (1: 5 mm, 2: 10 mm, 3: 20 mm) are investigated. (a) CO₂-specific capture cost per meter of bed length realized in adsorption (Ads), heating (Hea) and desorption (Des) zone $c_{mCO_2, \Delta LB_{iB}, x, i}$. Contributions from (dark to bright): *Lewatit*, supporting mesh, additional support, e.g., realization of gas duct, solid transfer medium in heating zone and liquid transfer medium are shown. Costs of the cooling zone equal the ones for the heating zone. (b) Additional CO₂-specific capture cost $c_{mCO_2, inv, iEqp}$ attributed to transfer medium pump (Pum), bucket elevator (Elv), external heat exchange for transfer medium (Hea) and vacuum operation (Com). (c) CO₂-specific energy demand $e_{i, spe_{nCO_2}}$, split into electric (ele) and thermal (the) contribution. (d) Overall CO₂-specific costs $c_{mCO_2, i}$ arising from: equipment, sorbent and transfer medium (dep), electric energy (ele) and thermal energy (the) use. (e) Ratio $\phi_{m_{i_{emi}}, m_{cap}}$ between CO₂ emissions attributed to electric (ele) energy demand, or thermal (the) demand, and mass of CO₂ captured. Contributions to thermal energy requirement in Figures (c)-(e) are indicated by different color tones (dark to bright): heat of desorption, sorbent sensible heat requirement, energy recovered by heat integration. Shares of liquid pump, sorbent elevation and gas compression in electric energy demand are visualized (from dark to bright) in Figures (c)-(e).

of the emissions resulting from energy demands relative to the amount of CO₂ captured. Severe influence of heat integration and electric energy use on net negative emissions is revealed. This already suggests that use of air compression in *DAC* concepts might contradict the aim of generating net negative emission. Compression of air by 1 kPa requires a CO₂-specific energy input in the order of magnitude of 62 kJ mol⁻¹ (Figure 2.2(a)), which equals CO₂ specific emissions of 0.18 kg kg⁻¹ (Appendix B.6.3) and underlines the questionability of intense energy use to reduce *DAC* costs. In view of an efficient use of *DAC*, these results stress the urgency of a fast transition to a renewables-based energy supply and the importance of realizing *DAC* concepts that focus on low energy demands.

4.7 Summary and conclusion

Realization of heat integration concepts proposed in Section 2.3 is investigated in detail.

Section 4.1 State of the art

gives an overview of approaches to *DAC*. Cost and energy estimates differ by three orders of magnitude. *T(V)SA* driven solid sorbent-based concepts dominate current research.

Section 4.2 Conceptual design

is dedicated to the technological approaches proposed. Isotherm evaluation indicates maximum CO₂ shares in the product gas of 24 % for *TCSA* concepts. This motivates additional investigation of *TVCSA* operation (Section 4.2.1). Designs of novel *moving belt adsorber* (*MBtA*, Section 4.2.2) and *moving bed adsorber* (*MBdA*, Section 4.2.3) are discussed.

Section 4.3 Feasibility study and constraints

investigates technological limitations of the concepts proposed. Characteristic features of sorbent movement within the concepts are analyzed that reveal high influence of the gas sealing on energy requirements (Section 4.3.1). Constraints with respect to heat and mass transfer are discussed in Section 4.3.2. Directional-dependent transfer characteristics of solid transfer media are found to be beneficial and concepts to overcome heat transfer limitations, e.g., use of fin-like structures, are proposed. With respect to large-scale realization, restrictions arising from transport of CO₂ in ambient air are analyzed (Section 4.3.3).

Section 4.4 In-depth simulation

provides detailed insights into *MBtA* (Section 4.4.1) and *MBdA* (Section 4.4.2) operation characteristics, which are characterized by intense couplings of the state variable profiles. Limitations that result from mass and heat transfer are revealed. *TVCSA* operation allows for significant increase in sorbent working capacity, but is accompanied by high compression energy requirement.

Section 4.5 Experimental investigation of transport phenomena

confirms presence of mass transfer limitations in the sorbent bed based on breakthrough curve analysis. Use of 3D printing allows for investigation of different adsorber configurations that resemble characteristics of *MBtA* and *MBdA* operation during CO₂ adsorption.

Section 4.6 Cost estimation and net negative emission

evaluates economic and ecologic aspects of *MBtA* and *MBdA*. CO₂-specific capture costs that exceed 1000 \$ t⁻¹ are found, with high potential for cost reduction below this level being revealed. Investment costs, especially of the sorbent, are noticed to dominate the cost structure. Energy costs seem to be of minor importance. Severe influence of energy use on the potential for realization of net negative emissions is noticed.

Overall, high potential of intensified heat integrated approaches to *DAC* is revealed. Limitations, especially with respect to mass transfer, motivate more detailed investigation of low-pressure loss contacting concepts, from both, economic and ecologic perspective. High dependency of potential for realization of net negative emissions on energy demand underlines the importance of a fast transition to a renewables-based energy supply and motivates a detailed analysis of energy penalties attributed to water co-adsorption in Chapter 5.

5 Handling water co-adsorption

Scientific contributions

Parts of this chapter have been published in the following scientific contributions:

Peer-reviewed journal article

- Drechsler, C.; Agar, D. W. Investigation of water co-adsorption on the energy balance of solid sorbent based direct air capture processes. *Energy* **2020**, *192*, 116587.

Conference poster presentation

- Drechsler, C.; Agar, D. W. Analyse der Wasser-Co-Adsorption auf die Energiebilanz von Direct Air Capture Verfahren mit festen Sorbentien. Presented at Abschlusskonferenz zur BMBF Fördermaßnahme CO₂Plus, Berlin, Germany, September 24-25, 2019.

Abstract

Handling of water co-adsorption is a key challenge in the design and operation of *DAC* concepts. Extension of the criterion of autothermal operation by water co-adsorption and its application reveals that the maximum permissible amount of water desorption is smaller than the amount of water adsorbed under ambient conditions by a factor of more than 4.7. An analysis based on equilibrium adsorber models indicates the potential for significant reduction of $\text{H}_2\text{O}:\text{CO}_2$ desorption ratios by counter-current operation at high desorption temperatures. But levels of water desorption still remain prohibitively high.

Ad-, de- and post-desorption approaches to limit water co-adsorption influence on the process mass and energy balance are investigated. Analysis of chemical modification of the sorbent and of the use of kinetic effects reveals perspectives for future research priorities. Post-desorption approaches including control of water desorption by use of water vapor strip gas and by recovery of the energy stored in water vapor via multi-stage mechanical vapor recompression (*MVR*) are found to be promising measures, realizable by use of common technologically mature engineering concepts. Model-based analysis and optimization of integrated *DAC* – *MVR* operation allows for detailed insights into the complex interactions between operation parameters and potential for heat recovery. Promising results achieved in the analysis performed underline the benefit of extending *DAC* approaches by post-desorption heat recovery concepts and strip gas-based water desorption control. In this respect, superiority of cyclic adsorber operation in the spacial domain is emphasized.

This chapter is structured as follows:

Section 5.1 State of the art

summarizes the current state of knowledge with regard to the influence of water co-adsorption on point source capture and *DAC* processes.

Section 5.2 Quantifying the influence of water co-adsorption

provides a quantitative analysis of water co-adsorption on a mass and energy level. Favorable *DAC* operation parameters are determined based on equilibrium adsorber models.

Section 5.3 Counteracting the influence of water co-adsorption

investigates measures to counteract the influence of water co-adsorption. Ad-, de- and post-desorption approaches are analyzed. Special focus is placed on chemical modification of the sorbent, kinetic effects and post-desorption heat recovery strategies.

Section 5.4 Summary and conclusion

gives a brief summary of the results obtained and relates those to the context of the overall process design analyzed in Chapter 6.

5.1 State of the art

The analysis performed in Chapter 4 indicates that sufficient recovery of the sorbent sensible heat can allow for autothermal operation of a *DAC*–*PtG* process in an ideal setting, i.e., in a setting without consideration of H₂O co-adsorption. However, as shown in Chapter 3 significant H₂O co-adsorption has to be expected.

Water co-adsorption is a well-known problem in common CO₂ adsorption processes as well as in *DAC* applications.^{103,137} Water desorption in the sorbent regeneration step can lead to dilution of the CO₂ product gas that can result in the need of additional gas purification in the downstream. Even worse, it can be accompanied by severe energy demand.^{102,137} Especially in *DAC* applications, in which energy demand is scaled with the amount of CO₂ captured (Chapter 2), heat demands attributed to the desorption of one mole H₂O, which can reach levels of about half of the energy required to release one mole CO₂,¹³⁷ can become an impeding limitation. In this regard, studies by Wurzbacher et al.¹⁰⁴ indicate heat demands for sorbent regeneration to be in the order of magnitude of 640 kJ mol⁻¹. Those were found to significantly depend on the amount of H₂O desorbed. Consequently, energy penalties attributed to H₂O desorption can take severe influence on process energy balance.¹³⁷

Common measures proposed to avoid H₂O co-adsorption within point source capture are pre-conditioning of the feed gas to reduce its water content, increase of adsorption temperature in view of shifting the CO₂:H₂O adsorption ratio or use of kinetic effects that favor CO₂ adsorption.¹³⁷ Moreover, use of water vapor as strip gas to suppress water desorption is discussed for point source capture and *DAC* applications.^{137,231}

The choice of sorbent or its modification (Chapter 3.1), e.g., in terms of hydrophobic properties can also be considered. In this respect, even new sorbent regeneration strategies are developed, e.g., *moisture-swing-adsorption*.^{101,102,232} Here, the sorbent adsorbs CO₂ in dry state and releases it under humid conditions. Thus, water desorption and attributed energy penalties are reduced. However, these concepts require comparatively dry ambient conditions, which limits the free choice of location for the *DAC* unit.

Even if the severe influence of H₂O co-adsorption is well-known and significant research is conducted to understand its mechanistic characteristics (Section 3.1.2), only a limited amount of studies consider this phenomenon from an unit operation or process point of view.^{103,104,137} However, with regard to the scope of realizing a highly energy efficient process, handling water co-adsorption can become crucial. Thus, this chapter is dedicated to a more detailed quantification of this non-ideality and to the development of tailor-made measures to reduce its influence on the *DAC* process energy balance.

5.2 Quantifying the influence of water co-adsorption

Chapter 3 provides information on H₂O co-adsorption based on single component adsorption isotherms. Significant higher equilibrium capacity of H₂O (9 mol kg⁻¹) compared to CO₂ (1 mol kg⁻¹) achieved under ambient conditions hints at a severe influence of H₂O co-adsorption. A quantitative analysis with respect to the process energy balance (Sec-

tion 5.2.1) and mass balance on an unit operation level (Section 5.2.2) is required to allow for more profound statements with regard to its influence on a process level.

5.2.1 Energy penalty of water co-adsorption

Modification of the criterion for autothermal operation (2.4) by the heat requirement of H₂O co-adsorption

$$-\Delta h_{\text{rea,Sab}}^{\circ} \geq -\Delta h_{\text{ads,CO}_2} - \Delta h_{\text{ads,H}_2\text{O}} \cdot \phi_{\Delta q_{\text{wor,H}_2\text{O}}, \Delta q_{\text{wor,CO}_2}} + \frac{c_{p,\text{Sor}} \cdot \Delta T_{\text{los,DAC}}}{\Delta q_{\text{wor,CO}_2}} = q_{\text{dem,DAC,spenCO}_2} \quad (5.1)$$

allows estimating its influence on the process energy balance. The variable $\phi_{\Delta q_{\text{wor,H}_2\text{O}}, \Delta q_{\text{wor,CO}_2}}$ is the ratio between the H₂O and CO₂ working capacities achieved, and $\Delta T_{\text{los,DAC}} = (1 - \eta_{\text{int,the}}) \cdot \Delta T_{\text{ads,des}}$ combines the efficiency of sorbent sensible heat recovery and cycle temperature difference of the *DAC* process. For the sake of clarity, (5.1) explicitly neglects contributions arising from the sorbate sensible heat that will, besides others, depend on the ambient conditions present, e.g., on the maximum loading reached during adsorption. Thus, $q_{\text{dem,DAC,spenCO}_2}$ gives the minimum CO₂-specific heat required in the case of H₂O co-desorption as a function of $\phi_{\Delta q_{\text{wor,H}_2\text{O}}, \Delta q_{\text{wor,CO}_2}}$.

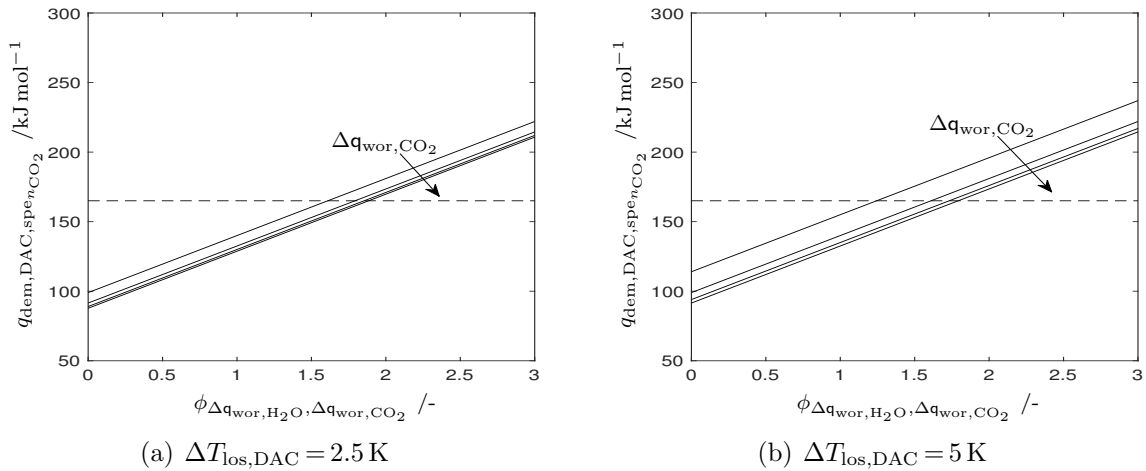


Figure 5.1: Influence of working capacity ratio $\phi_{\Delta q_{\text{wor,H}_2\text{O}}, \Delta q_{\text{wor,CO}_2}}$ on CO₂-specific energy demand of the *DAC* unit $q_{\text{dem,DAC,spenCO}_2}$ for sensible heat losses of the sorbent proportional to a thermal slip $\Delta T_{\text{los,DAC}}$ of (a) 2.5 K and (b) 5 K. Working capacities $\Delta q_{\text{wor,CO}_2}$ of 0.25, 0.5, 0.75 and 1 mol kg⁻¹ are investigated (-). Heat release by *Sabatier* reaction $-\Delta h_{\text{rea,Sab}}^{\circ}$ (2.1) is denoted by a dashed line (- -). Desorption of species at $T_{\text{DAC,Des}} = 100 \text{ }^{\circ}\text{C}$ is assumed. Thermophysical properties used in the evaluation are summarized in Appendix C.1.

Figure 5.1 evaluates (5.1) for selected values of $\Delta T_{\text{los,DAC}}$. In the best case, maximum ratios of $\phi_{\Delta q_{\text{wor,H}_2\text{O}}, \Delta q_{\text{wor,CO}_2}}$ in the order of magnitude of 1.9 are allowed if autothermal operation is aspired. Strong influence of CO₂ working capacity on $q_{\text{dem,DAC}}$ underlines the important contribution of the sorbent sensible heat, which increases with higher values of $\Delta T_{\text{los,DAC}}$. High values of $\Delta T_{\text{los,DAC}}$ and low CO₂ working capacities can result in a

significant decrease of the maximum allowed amount of H₂O co-desorbed per mole CO₂ captured to levels below 1.5. This is significantly less than the ratio between the H₂O and CO₂ equilibrium loading on *Lewatit* reached under ambient conditions, which was found to be in the order of 9 (Chapter 3). Consequently, the evaluation on an isotherm level indicates that autothermal operation is not possible without consideration of strategies to reduce H₂O co-adsorption-induced energy penalties.

5.2.2 Water desorption on unit operation level

The analysis at the single particle level only allows for a limited insight into the impact of H₂O co-adsorption, as various degrees of freedom that arise at an unit operation level are not considered. But in-depth analysis at an unit operation level would require detailed information on the 2-component isotherm and kinetics of the ad- and desorption process that are neither available for *Lewatit* (Chapter 3) nor for other *SAS*¹⁰⁴. In this respect, application of equilibrium adsorber models can provide a reasonable estimate with regard to the worst-case scenario.

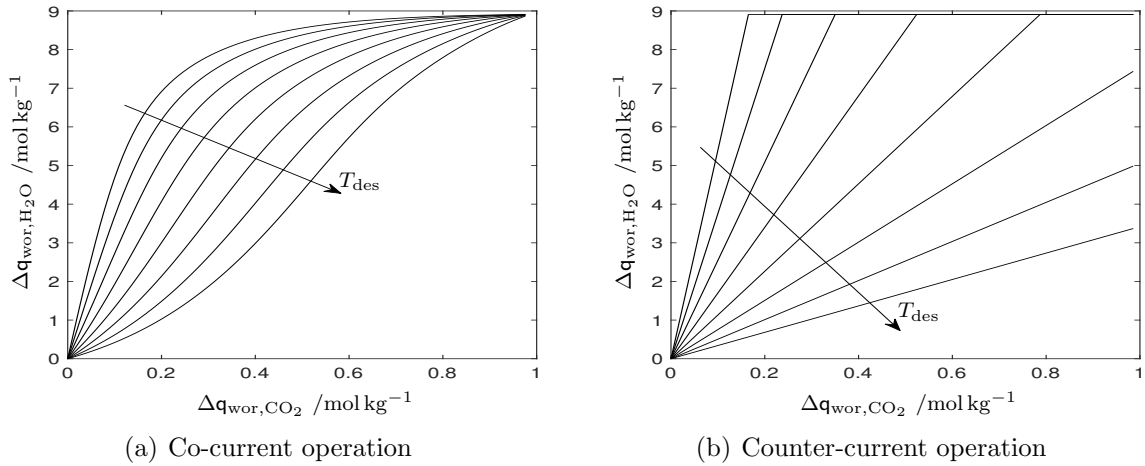


Figure 5.2: Working capacity of H₂O $\Delta q_{\text{wor,H}_2\text{O}}$ as a function of CO₂ working capacity $\Delta q_{\text{wor,CO}_2}$ based on application of an equilibrium adsorber model (Appendix C.2). (a) Co-current and (b) counter-current operation are investigated for desorption temperatures T_{des} ranging 30–100 °C, equally distributed in intervals of 10 °C.

Figure 5.2 visualizes the evolution of H₂O working capacity $\Delta q_{\text{wor,H}_2\text{O}}$ as a function of CO₂ working capacity $\Delta q_{\text{wor,CO}_2}$, determined based on application of an equilibrium adsorber model (Appendix C.2). Independent of the operation mode significant influence of desorption temperature T_{des} is revealed. High temperatures favor CO₂ over H₂O desorption, especially in counter-current operation. Thus, one may conclude that operation at the highest temperature that is allowed by the stability of the sorbents (~ 100 °C, Section 3.3.2) is beneficial with respect to H₂O co-adsorption.

Besides this similarity, significant differences in the evolution of $\Delta q_{\text{wor,H}_2\text{O}}$ between the operation modes are revealed. In co-current operation (Figure 5.2(a)) lines of constant desorption temperature are of a sigmoidal shape, whereas these take the form of straight lines in the counter-current mode (Figure 5.2(b)). This leads to the observation that

at low desorption temperatures, co-current operation can become favorable with respect to the CO_2 -specific amount of H_2O desorption, whereas counter-current operation seems superior for desorption at elevated temperature levels. For the intended operation at high desorption temperatures and high working capacities, $\text{H}_2\text{O}:\text{CO}_2$ minimum working capacity ratios in the order of magnitude of 3.4 are obtained. These are significantly lower compared to the ratio of the species equilibrium loadings of about 9 obtained from isotherm analysis for ambient conditions (Chapter 3). But even these values still exceed the maximum level of H_2O co-adsorption allowed (Figure 5.1) by a factor of more than 1.8. Consequently, this analysis confirms that measures to counteract energy penalties attributed to H_2O co-adsorption will become crucial from an energy point of view.

Analysis of the equilibrium adsorber model also allows for statements with respect to the *DAC* unit product gas composition. Figure 5.3 summarizes this information for co- and counter-current operation. Severe influence of desorption temperature T_{des} and relative CO_2 working capacity

$$\Delta q_{\text{wor},\text{CO}_2,\text{rel}} = \frac{\Delta q_{\text{wor},\text{CO}_2}}{q_{\text{eq},\text{CO}_2,\text{Amb}}} \quad (5.2)$$

is revealed. High-temperature operation allows for elevated CO_2 partial pressures in the gas phase, reasoned in the endothermic characteristic of the desorption process. Focusing on co-current operation (Figure 5.3(a)), significant decrease in CO_2 partial pressure with increasing relative working capacity is observed. Consequently, realization of high relative working capacities in this operation mode requires intensive use of additional strip gas or operation below atmospheric pressure. Both alternatives involve high costs and the question of additional gas purification steps, in dependence of the strip gases used, has to be answered.

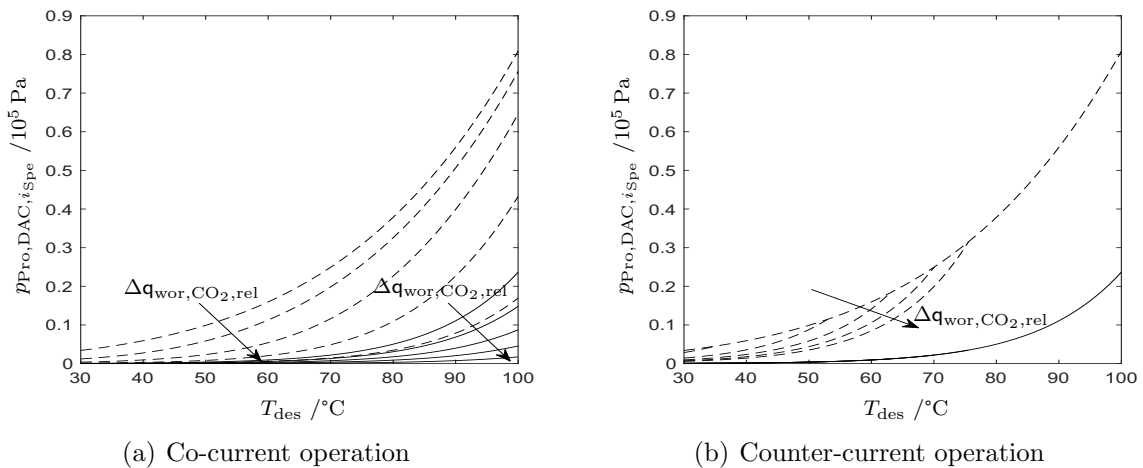


Figure 5.3: Partial pressure $p_{\text{Pro},\text{DAC},i\text{Spe}}$ of CO_2 (-) and H_2O (--) in *DAC* product gas, in dependence on desorption temperature T_{des} , evaluated based on an equilibrium adsorber model (Appendix C.2). (a) Co-current and (b) counter-current operation of the *DAC* unit is investigated for relative working capacities $\Delta q_{\text{wor},\text{CO}_2,\text{rel}}$ ranging 0.2–0.8 and 0.2–1, respectively, equally spaced in intervals of $\Delta q_{\text{wor},\text{CO}_2,\text{rel}} = 0.2$. Moreover, the limiting case $\Delta q_{\text{wor},\text{CO}_2,\text{rel}} \rightarrow 0$ is shown.

On the contrary, the counter-current operation (Figure 5.3(b)) can benefit from high working capacities. Increase of $\text{CO}_2 : \text{H}_2\text{O}$ partial pressure ratio in the gas phase with rising relative working capacity is observed and severe influence of desorption temperature is confirmed. Only at temperature levels below 75°C H_2O partial pressure is observed to be a function of $\Delta q_{\text{wor},\text{CO}_2,\text{rel}}$. This is attributed to the possibility of complete desorption of this specie at low-temperature operation in the desorption step. Overall, superiority of the counter-current operation mode is confirmed, especially in the more economically relevant region of elevated relative working capacities.

Concluding, the analysis given reveals high influence of H_2O co-adsorption. In the best case scenario $\text{H}_2\text{O} : \text{CO}_2$ desorption ratios of about 3.4 can be reached. Consequently, efficient strategies to avoid H_2O co-adsorption or to limit its influence on the process mass and energy balance are required. In the counter-current operation mode, the analysis of the components' partial pressures reveals necessity of additional strip gas use or of low-pressure operation if the desorption step is performed below a temperature of about 99°C . Even if these tendencies are not as pronounced as in the co-current operation mode, they still need to be taken into account in the analysis to follow.

5.3 Counteracting the influence of water co-adsorption

Severe impact of H_2O co-adsorption on a mass and energy level is revealed (Section 5.2) that motivates measures to limit its influence. After evaluation of approaches available (Section 5.3.1), in-depth analysis of a promising post-desorption concept is performed (Section 5.3.2) and the overall concept to be used is discussed (Section 5.3.3).

5.3.1 General considerations

As shown in Figure 5.4, the different concepts investigated might be assigned to the categories: adsorption – avoiding H_2O adsorption, desorption – avoiding H_2O desorption and post-desorption – gas separation and heat recovery.

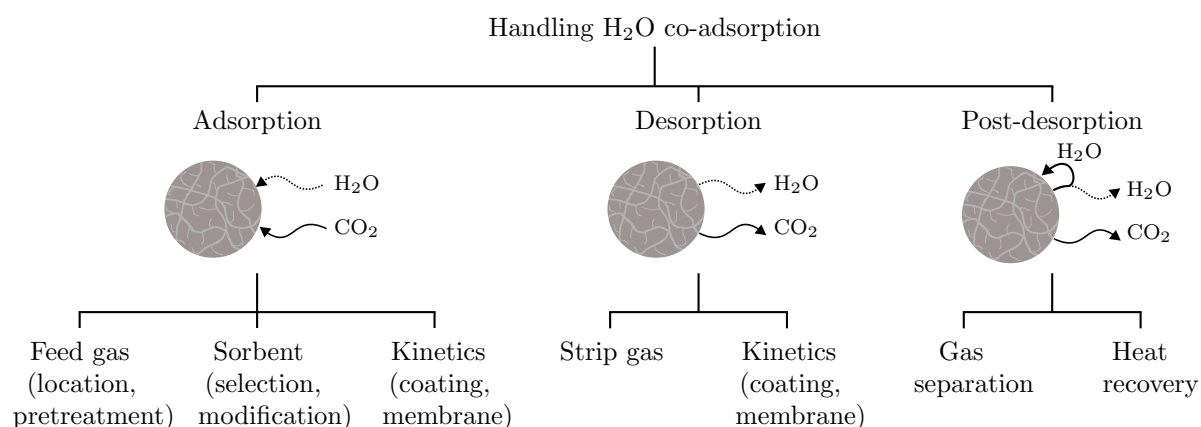


Figure 5.4: Measures to counteract the influence of water co-adsorption. Strategies are categorized into adsorption, desorption and post-desorption concepts. Solid arrows (-) indicate large streams, whereas dashed arrows (--) resemble streams of small magnitude.

Avoiding H₂O adsorption might be achieved by modification of the *DAC* feed gas, selection of sorbent properties or use of kinetic effects. An approach that is commonly applied in point source capture is feed gas pretreatment, e.g., predrying to avoid H₂O co-adsorption in subsequent process steps.¹³⁷ But in *DAC* applications the feed gas is ambient air and the CO₂-specific energy required to change its thermophysical state can not be afforded by *DAC* systems (Section 2.2).³⁶ Nevertheless, feed gas properties might be adjusted by selection of the location where the *DAC* unit is built. Realization of *DAC* in areas with low relative humidity can reduce H₂O co-adsorption. But even in hot deserts the mean annual relative humidity is typically in the range of 40–50%.²³³ Even if these humidity levels are significantly below the global mean, latitude-averaged values that range 70–85%,²³⁴ these still result in considerable H₂O co-adsorption of more than 3 mol kg⁻¹ (Figure 3.8(a)). Moreover, high temperatures present would significantly reduce the CO₂ capacity of the sorbent (Figure 3.5). Consequently, selection of the operation site can reduce the problem of H₂O co-adsorption, but does not solve it to a satisfactory degree.

Also sorbent selection and modification with respect to hydrophobic properties might be considered. From an operation point of view, use of hydrophobic sorbents that only allow for limited amount of H₂O adsorption would be favorable. The fact that the problem of H₂O co-adsorption is well-known from point source capture since a long period of time might give cause for pessimism with respect to the fast development of hydrophobic sorbents. But dealing with moisture becomes a key challenge in *DAC* applications.⁴¹ In this respect, the intensified research for *DAC* sorbents currently conducted (Section 3.1) might reveal new strategies with regard to hydrophobic sorbent designs.

In contrast to the aforementioned strategies that focus on a modification of the H₂O equilibrium loading, measures that favor the overall CO₂ adsorption kinetics compared to the H₂O adsorption kinetics might be taken into account. Use of hydrophobic membranes or coatings can help to decrease the kinetics of H₂O ad- and desorption. In this respect, high ratios $\phi_{p_{\text{H}_2\text{O}}, p_{\text{CO}_2}}$ between the partial pressure of H₂O and CO₂ during adsorption and desorption, e.g., $\phi_{p_{\text{Amb}, \text{H}_2\text{O}}, p_{\text{Amb}, \text{CO}_2}} = 63.6$ at a relative humidity $\phi_{\text{rh}, \text{Amb}}$ of 80% and $\phi_{p_{\text{Pro}, \text{DAC}, \text{H}_2\text{O}}, p_{\text{Pro}, \text{DAC}, \text{CO}_2}} = 3.4$ estimated based on counter-current operation with $T_{\text{des}} = 100^\circ\text{C}$, respectively, suggest the need for realization of high separation factors. Experimental investigations by Scholes et al.^{235,236} indicate design of membranes that favor CO₂ over H₂O transport to be possible, e.g., by use of perfluorinated polymeric membranes. However, H₂O:CO₂ selectivities $S_{\text{H}_2\text{O}, \text{CO}_2}$ presented in these studies^{235,236} are still in the order of magnitude of one, e.g., $S_{\text{H}_2\text{O}, \text{CO}_2} = 0.8$ is obtained for *Teflon AF1600* membranes.²³⁶ Based on the analysis given, this is significantly below the levels of water retention required. Also with regard to an efficient sorbent–CO₂ contacting, use of membranes or coatings seems unfavorable, such that application of this strategy currently does not seem beneficial.

With focus on H₂O desorption-based strategies, an additional measure to drive back H₂O desorption can be the use of water vapor strip gas. As the adsorption enthalpy can considerably exceed the heat of evaporation, typically $1.2 \cdot \Delta h_{\text{lv}} \lesssim \Delta h_{\text{ads}} \lesssim 3.0 \cdot \Delta h_{\text{lv}}$,¹²⁷ this approach can significantly reduce the process heat requirement. But the influence of this measure on the process energy balance is limited as H₂O adsorption on *Lewatit* is found to be dominated by physisorption (Section 3.2.3.1). Generation of water vapor comes with

additional energy costs, such that, without an efficient heat or vapor recovery strategy, the heat requirement is simply shifted from the *DAC* unit to the vapor generation. This indicates that post-desorption recovery strategies, which combine gas separation and heat recovery steps, might become promising measures.

Overall, the analysis given reveals various research priorities to limit the influence of H₂O co-adsorption. From an engineering point of view post-desorption recovery strategies that are discussed in more detail in Section 5.3.2 seem most promising.

5.3.2 Post-desorption recovery

Post-desorption recovery focuses on the energy rather than mass balance. Two options for its efficient realization might be considered. These are:

1. Vapor recovery: reuse as strip gas and avoidance of vapor generation
2. Recovery of heat stored in H₂O vapor

Membrane- (Figure 5.5(a)) or sorbent-based concepts (Figure 5.5(b)) might be applied to realize the first approach. Low CO₂ selectivities (Section 5.3.1) and large streams of H₂O to be separated compared to the CO₂ product gas flow argue against membrane use. Moreover, a comparatively high level of water vapor recovery is required. This results, e.g., in the need for high transmembrane pressure differences. On the other hand, removal of water by adsorbents, e.g., zeolites²³⁷, at high temperatures is possible, if the temperature cycle of the adsorber works between the temperature level of *Sabatier* reaction and *DAC* unit. This would shift the temperature level of the heat source available from the *Sabatier* reaction to the adsorption temperature of the adsorbent. However, energy supply by *Sabatier* reaction is a limiting factor that restricts the applicability of this concept to H₂O : CO₂ ratios below the order of magnitude of 2. In addition, a considerable amount of water would have to be adsorbed compared to the CO₂ product flow, which is associated with a high sorbent mass needed and high heat flows. Consequently, use of membrane- or sorbent-based strategies does not appear to be advantageous.

As an alternative to the aforementioned strategies, direct recovery of the heat stored in water vapor by means of high-temperature condensation is considered. This can be realized through *mechanical vapor recompression (MVR)*, well known from particle drying processes²³⁸ or from heat integrated distillation columns²³⁹. Compared to the alternatives evaluated, this concept is characterized by low energy flows and equipment costs, while being based on a simple, technologically mature approach. Figure 5.6 visualizes the promising multi-stage *MVR* concept proposed within the framework of this contribution. A more detailed analysis of the water recovery (Section 5.3.2.1) and of the heat integration potential compared to the compression energy requirement (Sections 5.3.2.2-5.3.2.3) is given in the subsequent sections. Detailed information with respect to the modeling performed is summarized in Appendix C.3.

5.3.2.1 MVR: water recovery and product gas mole fractions

Figure 5.7(a) analyzes the H₂O fraction recovered at high temperatures in *MVR* $\phi_{\text{rec,H}_2\text{O}}$ for *DAC* educt gas compositions achieved at desorption temperatures of 80, 90 and

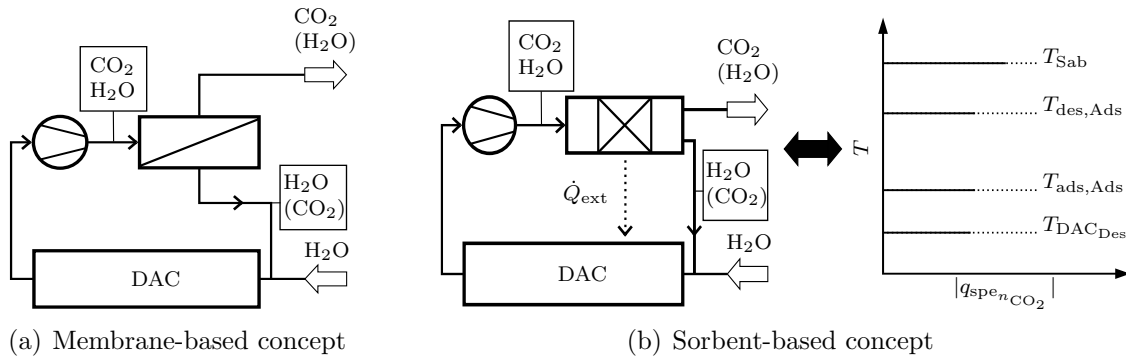


Figure 5.5: Simplified visualization of (a) membrane- and (b) sorbent-based strategies to limit H₂O co-adsorption influence on the process. Only the desorption zone of the *DAC* process is shown. For sorbent-based strategies, a lumped visualization of the water adsorber cyclic operation is used. The order of magnitude of heat sources and sinks per mole of CO₂ captured $q_{i_U, spe_{n_{CO_2}}}$ (-) at their characteristic temperature levels T_{i_U} (· · ·), required for heat integration, are shown. Possible heat integration between the water adsorber and *DAC* unit \dot{Q}_{ext} is visualized.

100 °C in counter-current operation mode. A minimum temperature difference between the two units $\Delta T_{df, MVR_{Con}, DAC_{Des}}$ of 10 K is assumed. Compression pressure levels p_{fin} ranging $1 \cdot 10^5 - 10 \cdot 10^5$ Pa are investigated. In dependence of the H₂O content present critical pressure levels need to be overcome before condensation can take place. Above these thresholds severe increase in ϕ_{rec, H_2O} is observed. Sensitivity of ϕ_{rec, H_2O} on pressure significantly decreases in the high-pressure regime. Moreover, comparison of the scenarios with additional inert strip gas use with the corresponding cases in which only H₂O and CO₂ are achieved as *DAC* product gases, e.g., high-temperature or low-pressure operation in *DAC* unit desorption zone, indicates a severe influence of inert gases on the efficiency of the *MVR* unit.

Diverse influence of *DAC* desorption temperature level $T_{DAC_{Des}}$ is observed. Lower temperature allows for lower partial pressure of H₂O in the product gas, but also results in higher H₂O : CO₂ desorption ratios (Figure 5.2) and possible higher (inert) strip gas content. Without additional strip gas use, increase of temperature has a negative effect on ϕ_{rec, H_2O} , whereas with additional strip gas use, a positive influence is observed. Figure 5.7(b) confirms this observation by quantifying the molar amount of water not recovered per mole CO₂ captured. Limited influence of operation temperature $T_{DAC_{Des}}$ at intermediate and high pressure levels p_{fin} achieved after *MVR* is observed in the absence of inert strip gas. However, with additional strip gas use severe influence of operation temperature is noticed, especially in low-pressure operation of the *MVR* unit.

5.3.2.2 MVR: operation at constant compression ratio

Based on a reference *DAC* product gas composition of $y_{Pro, DAC, CO_2} \approx 0.23$, $y_{Pro, DAC, H_2O} \approx 0.77$ and $y_{Pro, DAC, Ine} = 0$, obtained for counter-current *DAC* operation at $T_{DAC_{Des}} = 100$ °C, more detailed insight into the influence of final operation pressure p_{fin} and of the number of compression stages $I_{Com} = I_{Con}$ on the *DAC* – *MVR* energy balance is given by Figure 5.8. Multi-stage compression with constant compression ratios is as-

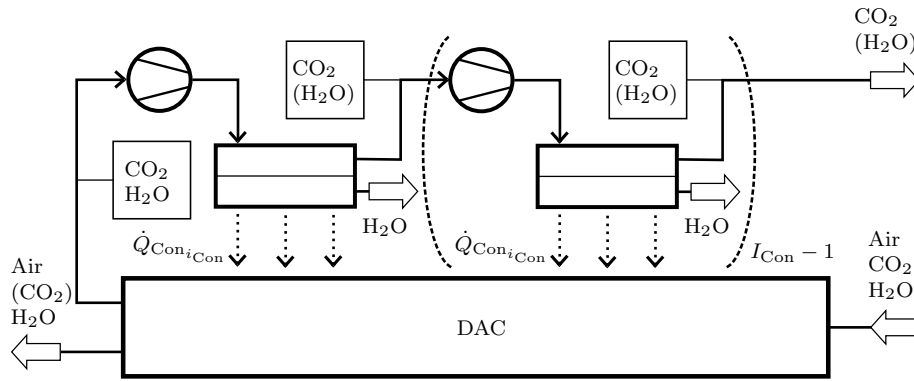


Figure 5.6: Sketch of I_{Con} -stage mechanical vapor recompression for the recovery of water vapor heat of evaporation. For reasons of clarity DAC unit cyclic operation, heat recovery within this unit as well as strip gas use and water recycle is not shown in detail. Heat flows between the units are visualized by dotted arrows ($\cdot\cdot$). $\dot{Q}_{\text{Con}_i\text{Con}}$ denotes the overall heat source characteristic of condenser i_{Con} . In this figure the lumped specie Air does not include the components H_2O and CO_2 . Figure reproduced from Drechsler and Agar²⁴⁰.

sumed. Intermediate condensation takes places at 110°C . More detailed insight into the models used is provided in Appendix C.3.

Figures 5.8(a) - 5.8(c) investigate the CO_2 -specific contributions to the $DAC - MVR$ energy balance, which reads

$$\begin{aligned} e_{\text{MVR-DAC},\Sigma,\text{spe}_{n\text{CO}_2}} &= q_{\text{des},\text{CO}_2,\text{spe}_{n\text{CO}_2}} + q_{\text{des},\text{H}_2\text{O},\text{spe}_{n\text{CO}_2}} + q\Delta T_{\text{df},\text{MVR}_{\text{Con}},\text{DAC}_{\text{Des}},\text{spe}_{n\text{CO}_2}} \\ &= e_{\text{adi},\text{spe}_{n\text{CO}_2}} + e_{\text{Com},\text{spe}_{n\text{CO}_2}} + q_{\text{con},\text{spe}_{n\text{CO}_2}}^0. \end{aligned} \quad (5.3)$$

Contributions from the desorption of CO_2 $q_{\text{des},\text{CO}_2,\text{spe}_{n\text{CO}_2}}$ and of H_2O $q_{\text{des},\text{H}_2\text{O},\text{spe}_{n\text{CO}_2}}$ as well as from the temperature change of the gas phase from DAC to MVR outlet $q\Delta T_{\text{df},\text{MVR}_{\text{Con}},\text{DAC}_{\text{Des}},\text{spe}_{n\text{CO}_2}}$ need to be compensated by additional energy supply to the system $e_{\text{adi},\text{spe}_{n\text{CO}_2}}$, energy input by compression $e_{\text{Com},\text{spe}_{n\text{CO}_2}}$ and heat release by the condensation of water $q_{\text{con},\text{spe}_{n\text{CO}_2}}^0$.

In the low-pressure region ($p_{\text{fin}} \lesssim 1.84 \cdot 10^5 \text{ Pa}$), only an exchange between the energy of compression and additional energy requirement of the system is found. This is attributed to the aspect that no condensation takes place in this region. Potential for significant exchange of additional energy requirement by heat of water condensation is revealed at pressure levels that only slightly exceed the pressure level of first condensation. But the heat recoverable by condensation is limited by the amount of water present. Consequently, already at intermediate pressure levels ($\sim 4 \cdot 10^5 \text{ Pa}$) the sensitivity of heat recovery on p_{fin} significantly decreases. This leads to the observation that at high pressure levels changes in the energy balance are dominated by an exchange between additional energy supply to the system and energy input by compression. In this respect, an increase in the number of compression stages can reduce the sensitivity of compression energy requirement on p_{fin} . Whereas a severe change between 1- and 2-state compression is observed, realization of a third compression stage only results in a comparatively small variation in the graphs

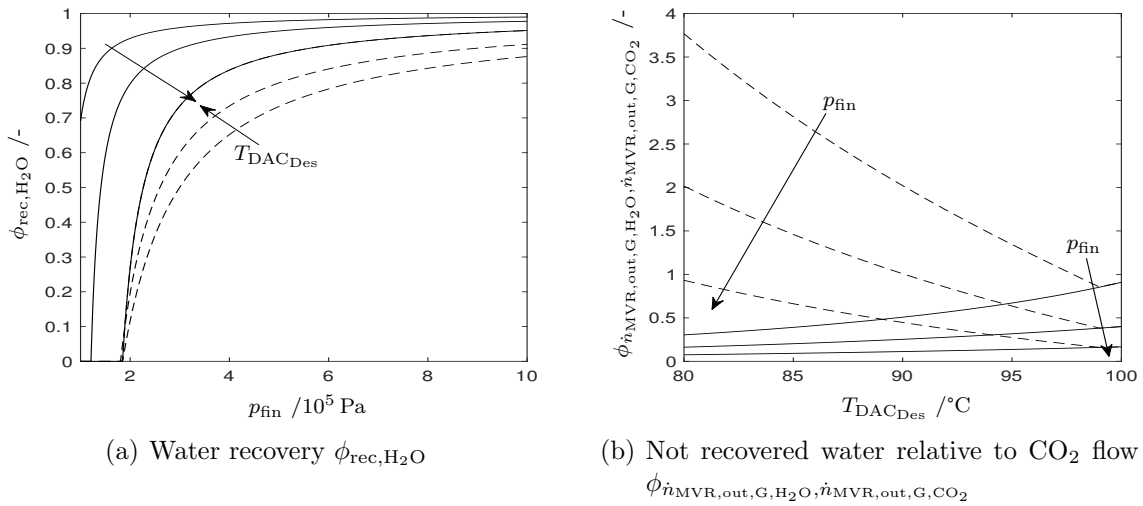


Figure 5.7: Influence of MVR pressure level p_{fin} and DAC unit desorption temperature T_{DACDes} on (a) the water recovery $\phi_{\text{rec,H}_2\text{O}}$ and (b) the ratio between the water not recovered and the CO_2 captured $\phi \dot{n}_{\text{MVR,out,G,H}_2\text{O}} / \dot{n}_{\text{MVR,out,G,CO}_2} \cdot \phi_{\text{rec,H}_2\text{O}}$ is investigated for desorption temperatures T_{DACDes} of 80, 90 and 100°C . In the analysis of $\phi \dot{n}_{\text{MVR,out,G,H}_2\text{O}} / \dot{n}_{\text{MVR,out,G,CO}_2}$ isolines for pressure levels of $3 \cdot 10^5$, $5 \cdot 10^5$ and $10 \cdot 10^5 \text{ Pa}$ are depicted. Scenarios that include operation with (--) and without (-) additional use of inert strip gas are considered. The condenser is operated 10 K above T_{DACDes} .

shown. Consequently, for the pressure range considered, limitation of the compression stage number to a maximum of three stages seems reasonable. Operation in the vicinity of the pressure level of first condensation seems beneficial if solely considering the *DAC* – *MVR* system. Pressurization to elevated levels in view of the integrated *DAC* – *PtG* process can be realized without significant increase in the compression power required.

A comparison with the heat release by *Sabatier* reaction shown as a reference in Figures 5.8(a) - 5.8(c) suggests that application of *MVR* can ensure autothermal operation of an integrated *DAC* – *PtG* approach in the limiting case analysis, i.e., the energy supply by *Sabatier* reaction is larger than the additional heat requirement $e_{\text{adi,spen}_{\text{CO}_2}}$. The results shown indicate the availability of excess heat in the order of magnitude of 100 kJ per mole CO_2 captured. This seems to be sufficient to satisfy the sensible heat demands of the heat integrated *DAC* approaches proposed (Figures 4.13(c) and 4.14(c)). However, high recovery of the heat stored in water vapor is paid for with additional compression energy requirement $e_{\text{Com,spen}_{\text{CO}_2}}$. Figures 5.8(d) - 5.8(f) investigate this aspect by comparing the influence of the pressure level p_{fin} at the multi-stage compressor outlet on the ratio

$$\phi_{q_{\text{Con},e_{\text{Com}}}} = \frac{q_{\text{Con,spen}_{\text{CO}_2}}}{e_{\text{Com,spen}_{\text{CO}_2}}} \quad (5.4)$$

between the overall CO_2 -specific heat release in the condensers $q_{\text{Con,spen}_{\text{CO}_2}}$ and the compressor energy requirement $e_{\text{Com,spen}_{\text{CO}_2}}$. The combination of low energy input by the compressor and no heat release by condensation results in negative values of $\phi_{q_{\text{Con},e_{\text{Com}}}}$ at low pressure levels, as the condensers act like heaters in this operation range. Convergence of $\phi_{q_{\text{Con},e_{\text{Com}}}}$ to one before the minimum condensation pressure level is reached underlines

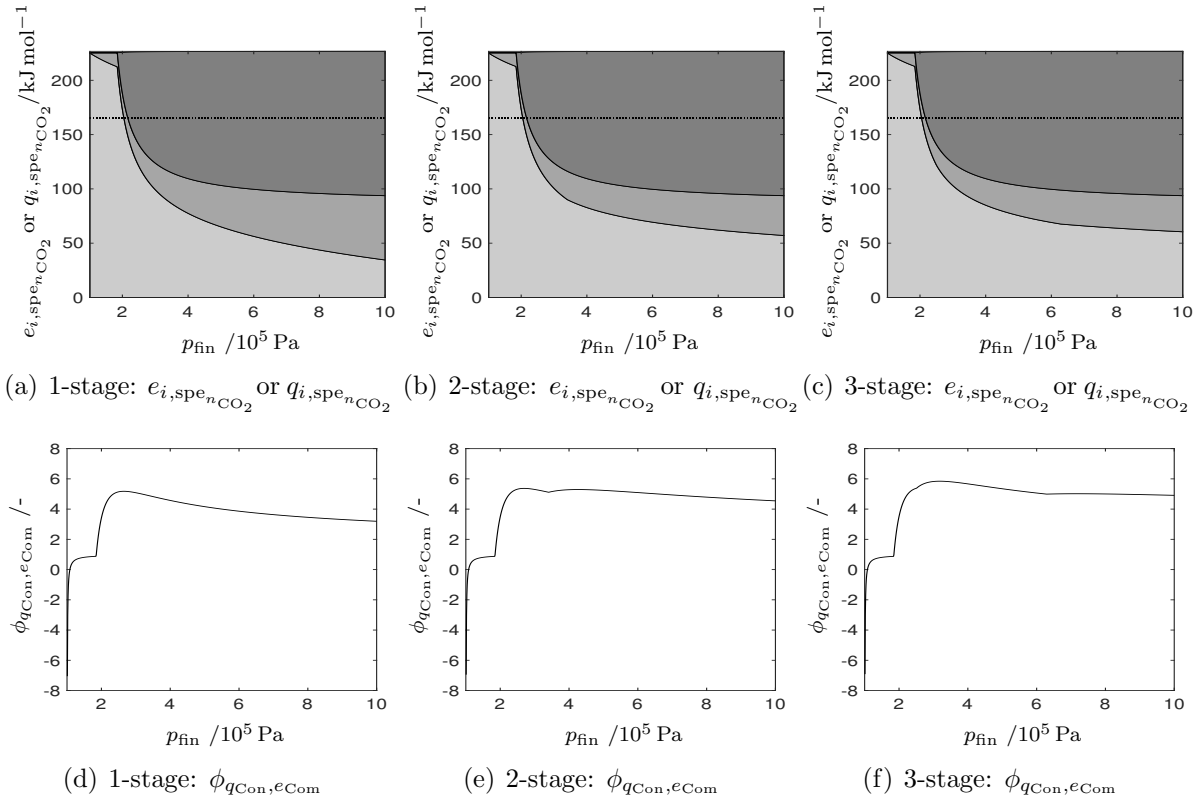


Figure 5.8: (a)-(c) Contributions to the MVR – DAC energy balance, visualized in color tones from bright to dark: additional heating power $e_{\text{adi}, \text{spe}_{n\text{CO}_2}}$, compression energy requirement $e_{\text{Com}, \text{spe}_{n\text{CO}_2}}$ and heat release by condensation of water $q_{\text{con}, \text{spe}_{n\text{CO}_2}}^0$. The dashed line (--) represents the heat release for a 100% conversion of the captured CO_2 in *Sabatier* reaction. The evolution of the energy ratio $\phi_{q_{\text{Con}}, e_{\text{Com}}}$ is visualized in (d)-(f). Influence of final operation pressure to be achieved in MVR p_{fin} and of number of compression stages with intermediate cooling to 110 °C is investigated.

the exchange of additional heat supply with compression energy input in the low-pressure regime. Further raise of p_{fin} leads to a significant increase of $\phi_{q_{\text{Con}}, e_{\text{Com}}}$. Levels reached by this indicator larger than five indicate application of vapor recompression to be promising from a heat integration point of view. In this respect, minor decrease of $\phi_{q_{\text{Con}}, e_{\text{Com}}}$ with pressure in case of multi-stage compression underlines the superiority of this process configuration if high-pressure operation is aspired.

Formation of multiple maxima and of unsmooth trajectories of $\phi_{q_{\text{Con}}, e_{\text{Com}}}$ as a function of p_{fin} is noticed for compression stage numbers greater than one. Detailed analysis reveals that these observations result from the interactions between condensation, i.e., reduction of gas phase volume flow, and compression energy requirement. Figure 5.9 exemplifies the results of this investigation by evaluating the influence of the intermediate compression pressure level $p_{\text{Com}_i, \text{out}}$ on the overall compression power demand $e_{\text{Com}, \text{spe}_{n\text{CO}_2}}$. Formation of multiple minima is confirmed. Overall, the analysis given motivates a more detailed optimization of MVR operation in Section 5.3.2.3, which aims at determination of the optimal operation point and at analysis of the possible benefits that arise from operation at non-equal pressurization stages.

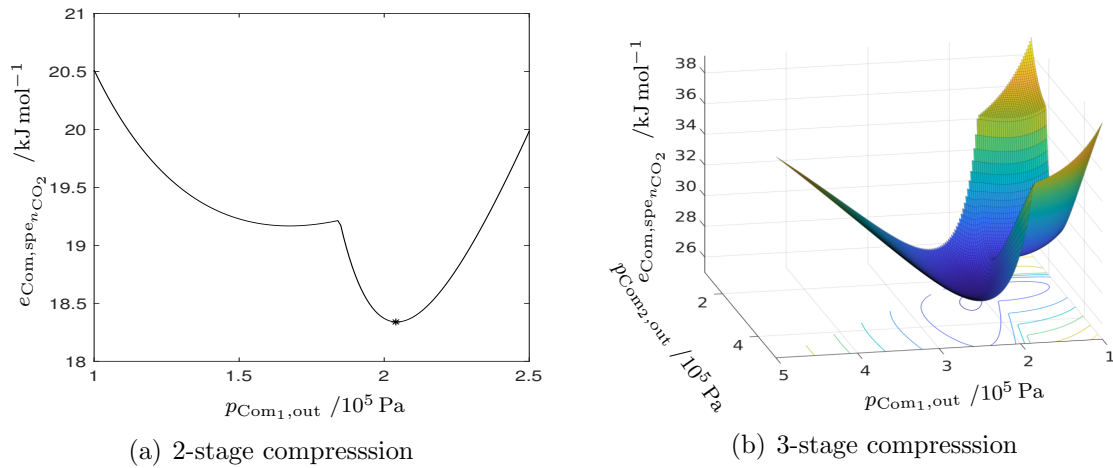


Figure 5.9: *MVR* compression energy requirement in dependence of the intermediate compression pressure. (a) Influence of the pressure level of the first compression stage $p_{Com1,out}$ on the overall compression energy demand $e_{Com,sp_{e_{nCO_2}}}$ of a 2-stage compression. The position of the minimum compression energy requirement is denoted by a star (*). (b) Dependency of $e_{Com,sp_{e_{nCO_2}}}$ on the pressure levels of the first ($p_{Com1,out}$) and of the second compression stage ($p_{Com2,out}$) for *MVR* with three compression stages. Pressures p_{fin} of (a) $2.5 \cdot 10^5$ Pa and (b) of $5 \cdot 10^5$ Pa are investigated.

5.3.2.3 MVR: optimization of the compression ratio

The global optimization problem

$$\min_{\vec{p}_{Com}} e_{Com,sp_{e_{nCO_2}}} = \sum_{i_{Com}} e_{Com_{i_{Com}},sp_{e_{nCO_2}}} \quad (5.5a)$$

$$\text{s.t.} \quad p_{DAC_{Des},out} \leq p_{Com_{i_{Com}}} \leq p_{fin} \quad (5.5b)$$

$$p_{Com_{i_{Com}}} \leq p_{Com_{i_{Com}+1}} \quad (5.5c)$$

is solved to investigate *MVR* operation at optimal compression ratios. *Matlab*^{®178} *fmincon* routine is used in combination with multiple starting points and definition of specific search regions to determine the global minimum energy requirement for compression from the *DAC* unit outlet pressure $p_{DAC_{Des},out}$ to a defined final operation pressure p_{fin} . The region boundary for the 2-stage compression is defined at $p_{Com1} = p_{sat,H_2O}(T_{Con}, y_{Pro,DAC,H_2O})$ resulting in two different search regions, whereas for the 3-stage compression three different regions are separated by the boundaries: $p_{Com1} = p_{sat,H_2O}(T_{Con}, y_{Pro,DAC,H_2O})$ and $p_{Com2} = p_{sat,H_2O}(T_{Con}, y_{Pro,DAC,H_2O})$.

Figures 5.10(a) and 5.10(d) compare the energy ratios $\phi_{q_{Con},e_{Com}}$ obtained for operation with equal and optimized compression ratios. No unsmooth evolution or formation of local maxima is observed at elevated pressure levels in the optimized scenarios. This confirms the observation that these characteristics result from water condensation, the appearance of which subdivides the compression power maps (Figure 5.9) in regions connected by unsmooth transitions. Only comparatively small differences between the optimized and non-optimized scenarios are noticed, especially at elevated operation pressures. Thus, in dependence of the operation pressure aspired, the benefit of reduced compression energy

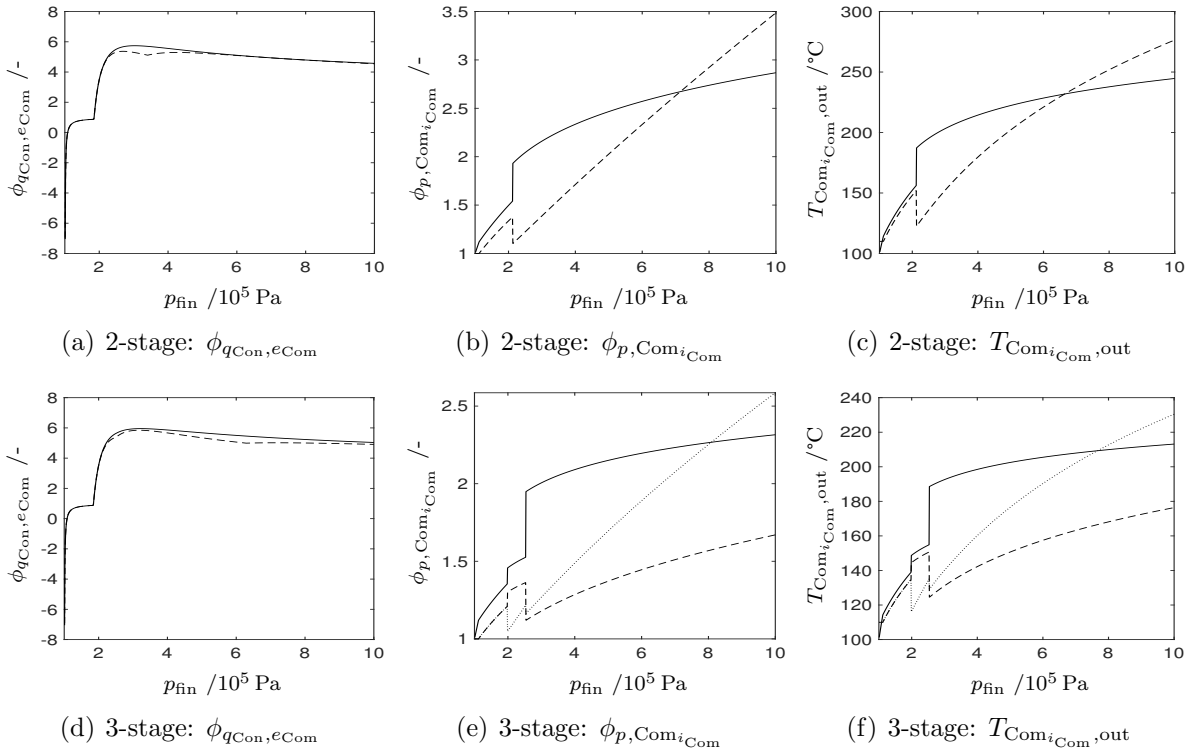


Figure 5.10: Influence of the final operation pressure p_{fin} on energy ratio $\phi_{q_{Con},e_{Com}}$, compression ratio $\phi_{p,Com_{i_{Com}}}$ and compressor outlet temperature $T_{Com_{i_{Com}},out}$ for 2- and 3-stage *MVR* operation with optimized intermediate pressure levels. Energy ratios obtained in the optimized (-) and non-optimized (--) scenarios are shown in (a) and (d). Moreover, a comparison of the different compression stages: $i_{Com} = 1$ (-), $i_{Com} = 2$ (--) and $i_{Com} = 3$ (··) is given in (b)–(c) and (e)–(f).

obtained in the optimized scenarios might be outrun by the economic advantage arising from a simple operation with equal compression ratios.

Even if comparatively small differences in $\phi_{q_{Con},e_{Com}}$ between the optimized and non-optimized scenarios are observed, this does not reflect in the optimized compression ratios $\phi_{p,Com_{i_{Com}}}$ shown in Figures 5.10(b) and 5.10(e). Even in the absence of condensation, $\phi_{p,Com_{i_{Com}}}$ does not take the same values per compression stage, reasoned in the difference between the compressor inlet temperatures of the first and subsequent stages. This leads to the effect that at very low final operation pressure no compression in the second and third stage is observed.

Focusing on 2-stage *MVR* operation (Figure 5.10(b)), a significant change of the compression ratios slightly above the minimum pressure of first condensation is visible. Reduction of gas phase volume by condensation after the first compression stage is favorable from an energy point of view. Thus, the compression ratio of the first stage increases, whereas the level of gas phase compression within the second stage is reduced. However, the amount of water condensable is limited and the sensitivity of water recovery on pressure decreases with increasing pressure (Figure 5.7(a)). This leads to the effect that the benefit of further reduction of the gas phase volume flow by an increase of the 1-stage compression ratio is run out by the advantage of less energy intensive compression of a smaller gas phase volume in the second stage. Hence, a greater increase in the compression ratio

of the second compared to the first compression stage is observed with further increase of p_{fin} , such that compression within the second stage is favored at high levels of p_{fin} .

An even more complex influence of p_{fin} on $\phi_{p,\text{Com}_{i_{\text{Com}}}}$ for 3-stage *MVR* operation is visualized by Figure 5.10(e). In accordance with the division of the compression power map into three regions indicated by Figure 5.9(b), an additional unsteady transition of the optimized compression ratios $\phi_{p,\text{Com}_{i_{\text{Com}}}}$ as a function of p_{fin} is observed. Moreover, the order of the compression stages slopes as a function of p_{fin} is noticed to increase with i_{Com} in the high-pressure region. This again underlines the importance of a more energy efficient compression of smaller gas phase volumes at elevated pressure levels.

The aim of maximum high-temperature heat recovery for *DAC* forces the *MVR* unit to be operated at comparatively high levels of water recovery and of compressor inlet temperatures. As shown by Figures 5.10(c) and 5.10(f), this can result in high compressor outlet temperatures $T_{\text{Com}_{i_{\text{Com}}},\text{out}}$. For 2-stage operation, maximum temperatures of up to 276 °C are reached that might exceed the mechanical stability limit of the compressors (~ 260 °C)²⁴¹. 3-stage *MVR* allows for lower maximum discharge temperatures that stay below the mechanical stability limit. This suggests that operation with three or more compression stages is beneficial from a mechanical point of view. On the other hand, use of equal compression stages can reduce the maximum discharge temperature (2-stage: $T_{\text{Com,max}} = 261$ °C, 3-stage: $T_{\text{Com,max}} = 212$ °C at $p_{\text{fin}} = 10 \cdot 10^5$ Pa). Thus, given the comparatively small difference in energy ratio between the optimized and non-optimized pressure ratios achieved at elevated levels of p_{fin} , one might consider sacrificing the advantage of lower energy requirements in favor of lower maximum discharge temperatures.

5.3.3 Concept to counteract the influence of water co-adsorption

Sections 5.3.1 and 5.3.2 evaluate strategies to overcome the energy penalty arising from H₂O co-adsorption. Especially post-desorption concepts seem promising. These engineering approaches can efficiently limit the impact of H₂O co-adsorption on the process energy balance, and their applicability is nearly independent of the sorbent selected. Moreover, these strategies are based on mature technologies, ready to be applied on a large scale, whereas, even if being intensively researched,⁶⁷ tailor-made *DAC* sorbents are still in a more early stage of development.

Based on these considerations a post-desorption approach that comprises:

- Stripping with water vapor to avoid excessive H₂O desorption
- Use of multi-stage *MVR* for high-temperature recovery of water and of its heat of condensation

is pursued. In this respect, a crucial advantage of the intensified heat integrated *DAC* concepts proposed (Section 4.2) is revealed: these concepts transform the cyclic operation from the time to the spatial domain, which results in steady state operation in time. This significantly simplifies the control of humidity levels during the desorption process compared to common approaches in which the state variables are a function of time and of space. Use of water vapor as strip gas would require a change of the *DAC* unit strip gas inlet to regions of higher temperature and the control of temperature profiles in the

desorption zone. These measures are needed to limited water desorption and to avoid significant adsorption of water vapor. On the basis of the designs proposed in this work (Chapter 4), realization of this requirements with common engineering tools seems possible. However, the lack of data with regard to the 2-component adsorption isotherms and kinetics (Chapter 3) currently hinders the detailed modeling of this concept. Nevertheless, simplified representations of the *moving bed* and *belt* concepts by equilibrium-based models (Appendix D.2.2) can allow for basic insights into the *DAC* operation characteristics in an intensified energy and mass integrated *DAC-PtG* process (Chapter 6).

5.4 Summary and conclusion

The findings presented in Chapter 4 reveal a high potential for the realization of an intensified heat integrated *DAC* process in an ideal setting, in which solely CO_2 adsorption is taken into account. But H_2O co-adsorption (Chapter 3) can lead to severe energy penalties that challenge the feasibility of autothermal operation.

Section 5.1 State of the art

summarizes the current state of knowledge with regard to the limitations resulting from H_2O co-adsorption. Strategies to overcome this burden are discussed.

Section 5.2 Quantifying the influence of water co-adsorption

extends the criterion for autothermal operation by the influence of H_2O co-adsorption (Section 5.2.1). Maximum levels of H_2O desorption allowed are found to be a factor of more than 4.7 smaller than the sorbent H_2O loading obtained under ambient conditions. Investigations on an unit operation level (Section 5.2.2) underline the potential to lower H_2O co-desorption compared to considerations drawn from isotherm analysis. Counter-current operation at high desorption temperatures is found to favor high $\text{CO}_2:\text{H}_2\text{O}$ desorption ratios. Levels of H_2O desorption of 3.4 moles per mole CO_2 desorbed still seem prohibitively high.

Section 5.3 Counteracting the influence of water co-adsorption

evaluates strategies to counteract H_2O co-adsorption (Section 5.3.1). Adsorption-, desorption- and post-desorption-based strategies are discussed. Realization of multi-stage *mechanical vapor recompression (MVR)* is found to be promising (Section 5.3.2). In-depth modeling and optimization reveal a strong influence of H_2O condensation on the compression energy demand and on the optimized compression stage levels. Based on these results the overall concept to limit the influence of H_2O co-adsorption pursued in this contribution (Section 5.3.3) is presented. It focuses on a post-desorption approach that comprises *MVR* and H_2O vapor strip gas use to limit the amount of water desorption and to control the process mass and energy balance by efficient high-temperature water recovery.

The analysis performed allows to quantify the influence of H_2O co-adsorption on a mass and energy level. The concept derived to limit its influence is based on mature technologies. This enables a straightforward integration of this approach into the overall *DAC-PtG* process investigated in Chapter 6.

6 Intensified mass and energy integrated DAC - PtG process

Scientific contributions

Parts of this chapter have been published in the following scientific contributions:

Peer-reviewed journal articles

- Drechsler, C.; Agar, D. W. Characteristics of DAC operation within integrated PtG concepts. *Int. J. Greenhouse Gas Control* **2021**, *105*, 103230.
- Drechsler, C.; Agar, D. W. Intensified integrated direct air capture - power-to-gas process based on H₂O and CO₂ from ambient air. *Appl. Energy* **2020**, *273*, 115076.

Conference talk

- Drechsler, C.; Agar, D. W. Development of an intensified integrated DAC-PtG process for sustainable production of CH₄ from CO₂ and H₂O. Presented at Wissenschaft trifft Wirtschaft: Forschung für eine klimaneutrale und wettbewerbsfähige Grundstoffindustrie, online, Germany, December 4, 2020.

Abstract

Integration of *DAC* technologies in *PtG* approaches incorporates the exceptional potential of closing the carbon cycle by production of methane based solely on renewable energy supply and on ambient air as raw material source. The intensified use of renewable energy sources is promoted by the process proposed through realization of efficient electric energy storage via chemical reaction and through implementation of water electrolysis as a measure to balance the electric grid. Detailed process simulation and pinch analysis reveal strong couplings between the different process sections that can result in beneficial synergies within an intensified mass and energy integrated *DAC*–*PtG* process. High potential for resource efficient, autothermal production of methane based on carbon dioxide and water captured from ambient air is underlined. Especially *DAC* and electrolysis operation points are identified to become crucial with respect to process performance.

This chapter is structured as follows:

Section 6.1 State of the art

gives a brief overview of the current state of research with respect to carbon source–*power-to-X* (*PtX*) technologies. Special focus is placed on the integration of *DAC* technologies in *PtG* concepts.

Section 6.2 Methanation of CO₂

investigates the reaction mechanisms of CO₂ methanation in detail. Beneficial operation parameters and reactions to be considered are identified.

Section 6.3 Process design and key process units

summarizes the synergies arising within the intensified integrated process design and provides a detailed analysis of the electrolysis and reactor unit.

Section 6.4 Process performance

evaluates the process performance with special focus on resource efficiency and on potential for autothermal operation. In addition to the analysis of the process water balance and of the *DAC* unit operation point, a detailed investigation of energy flows within the process is performed.

Section 6.5 Summary and conclusion

gives a brief summary of the results and implications drawn from the process analysis.

6.1 State of the art

Chapters 2-5 provide an intensified integrated concept for the direct capture of CO₂ from air. However, strategies for long-term storage or for use of CO₂ are required to enable an efficient use of *DAC* as a measure against global warming. Among the various scenarios discussed in Section 1.2, integrated operation of *DAC* and *PtG* seems very promising. Detailed *life cycle assessment (LCA)* indicates that activation of CO₂ by H₂, produced on a renewable basis, to form CH₄ can be environmentally beneficial.^{69,70,242,243} Versatile strategies for use of the methane produced can be pursued. Usage as *SNG* comes with the advantage of existing well-developed infrastructures and conversion processes, incorporating the potential of closing the carbon cycle on a global scale.^{73,75} Additionally, methane pyrolysis^{77,244} becomes an option that allows for use or for safe long-term storage of the solid carbon produced, while valuable hydrogen can be recovered.

Energy demands and selection of energy sources, e.g., renewable electricity supply for electrolysis-based hydrogen production, are crucial for the ecologic benefit of CO₂-based methane production.^{70,242,243} An increasing share of renewables in the energy supply is expected. For the *EU-27*, contributions of about 50 % of these energy sources by 2050 are estimated.²⁴⁵ However, unsteady energy supply by wind or solar power calls for measures to balance fluctuations in the electric grid.²⁴⁶ In this respect, the multiple benefits that can arise from realization of integrated *DAC – PtG* concepts are revealed. These technologies enable carbon neutrality of sectors difficult to be decarbonized in the short period of time available (Section 1.1.3), e.g., of aircraft. Moreover, several studies^{247–249} indicate *PtG* concepts to be an efficient measure to balance the electric grid. This can pave the way for a reliable energy supply based on renewable sources.

PtG concepts have intensively been researched.^{246,250,251} More than 40 pilot-plants have been realized.²⁵² From an engineering point of view, research focuses on electrolysis design and integration,^{246,253} e.g., *alkaline (AE)*, *polymer electrolyte membrane (PEM)* or *solid oxide (SOEC)*, and on the methanation process itself. Biological and chemically catalyzed processes, operating at temperature and pressure levels of 20–70 °C and 1 · 10⁵–10 · 10⁵ Pa, 200–550 °C and 1 · 10⁵–100 · 10⁵ Pa, respectively, are proposed.²⁴⁶ With regard to the chemical approaches, profound information on reactor design,²⁴⁶ e.g., fixed bed²⁵⁴, fluidized bed²⁵⁵, three-phase methanation²⁵⁶ or structured reactors²⁵⁷, and on catalyst selection^{246,258,259} is provided in the literature. Moreover, a variety of studies with respect to dynamic operation^{260,261} and to process design^{262,263}, including heat integration scenarios^{264,265}, were published. Especially electrolysis optimization and integration of the carbon source are found to be key directions for future research.²⁴⁶

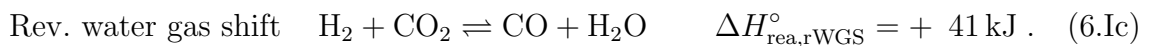
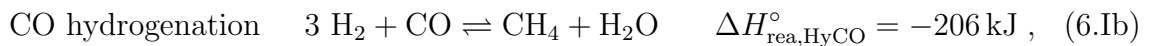
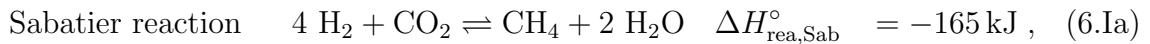
Carbon sources typically named for *PtG* applications are biogas plants, biomass gasification, industrial processes or power plants.²⁴⁶ Also strategies to integrate the carbon source in the *PtG* concept are evaluated.^{262,264} However, even if the technological maturity of *PtG* on its own has reached a high level, it is still not common practice to consider *DAC* as the carbon source. Nevertheless, reasoned in the severe progress in the development of *DAC* applications, interest in air as carbon source increases. *PtG* pilot plants are realized in Switzerland, Italy and Germany within the *EU* project *STORE&GO*.²⁶⁶ CO₂ supply by *Climeworks* air capture technology is investigated at the Italian site.²⁶⁷ An analysis of

new reactor designs²⁶⁸, as well as process modeling²⁶⁹ and cost estimation for optimized *PtG* operation with intermediate hydrogen storage²⁷⁰, was realized within this project. Also Swiss *HSR* project²⁷¹ makes use of *Climeworks DAC* units¹⁰⁵ in a pilot-scale *PtG* process. But even if formulated as a project target, the *DAC* unit was not integrated in the process heat management system. Focusing on more general *DAC – power-to-X (PtX)* concepts,⁸⁵ one may name the *SOLETAIR* project.²⁷² It aims for 100% renewables-based production of hydrocarbons. Besides realization of solar photovoltaic for electric energy generation, air is used as a carbon source, with *Hydrocell* air capture technology¹⁹⁷ being applied. Moreover, the CO₂ educt gas for *Sunfire power-to-liquid (PtL)* technology is provided by *Climeworks DAC* units¹⁰⁵ within the Norwegian *Heroya* project¹⁰⁶ that aims for the production of the CO₂-neutral, synthetic crude oil substitute *Blue Crude*.

Findings within the projects named are in line with several studies^{73,75,273} that underline the high potential of sustainable hydrocarbon production based on air capture approaches. However, *DAC* is generally treated as a black box carbon source or established approaches available on the market are used, while focus is placed on the *PtX* concept. This neglects the valuable synergies arising within process development that simultaneously focuses on the *PtG* as well as *DAC* component and on their interaction on a mass and energy level.

6.2 Methanation of CO₂

The concept proposed aims for use of CO₂ methanation heat release to compensate for the *DAC* unit heat demand. Use of chemically catalyzed methanation reaction typically operated between 200–550 °C seems superior compared to biological-based processes with operation temperatures commonly ranging 20–70 °C that contradict the aim of *DAC* operation at elevated temperatures (~100 °C, Chapters 4-5).²⁴⁶ To describe CO₂ methanation, one may consider a set of reactions²⁵⁸ comprising



Reactions (6.1a) and (6.1c) provide a set of stoichiometrically independent equations on the basis of which the influence of operation conditions on the equilibrium composition of the methanation process is evaluated (Figure 6.1). Strong influence of the equilibrium composition on methanation temperature T_{Met} is noticed (Figure 6.1(a)), whereas the influence of operation pressure p_{Met} is found to significantly decrease at elevated pressure levels (Figure 6.1(b)). Mole fractions of carbon monoxide well below 0.1% indicate that the formation of this species might be neglected under the reaction conditions aspired. This allows for a more simple evaluation of the methanation process solely based on (6.1a). Strong influence of the H₂O mole shares in the educt gas $y_{\text{Met,in,H}_2\text{O}}$ on CO₂ conversion $X_{\text{eq, Met, CO}_2}$ (Figure 6.1(c)) underlines the need of water removal from process gas if high levels of conversion are to be reached. In this respect, operation at elevated pressure levels seems beneficial to ease the removal of water and to shift the reaction equilibrium to high levels of CO₂ conversion.

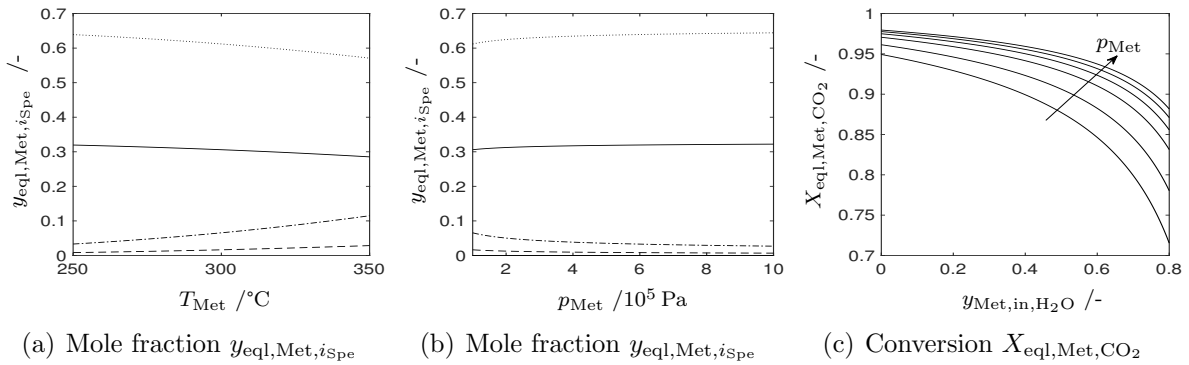


Figure 6.1: Evaluation of the reaction equilibrium of the methanation reaction based on reactions (6.1a) and (6.1c). Equilibrium gas phase mole fractions $y_{\text{eq}, \text{Met}, i_{\text{Spe}}}$ of the species CH₄ (-), CO₂ (- -), H₂ (- ·) and H₂O (· ·) are evaluated in dependence of (a) operation temperature T_{Met} and (b) operation pressure p_{Met} for an operation pressure p_{Met} of $1 \cdot 10^5 \text{ Pa}$ and temperature of T_{Met} 300°C , respectively. The molar composition of the educt gas reads $y_{\text{Met}, \text{in}, \text{CO}_2} = 0.2$ and $y_{\text{Met}, \text{in}, \text{H}_2} = 0.8$. Mole shares of CO are not explicitly shown as these stay significantly below 0.1%. The influence of an increase in the H₂O mole fraction $y_{\text{Met}, \text{in}, \text{H}_2\text{O}}$ in an educt gas with a constant ratio of H₂ : CO₂ of four on CO₂ conversion $X_{\text{eq}, \text{Met}, \text{CO}_2}$ is investigated in (c). Operation conditions are set to a methanation temperature T_{Met} of 300°C and pressure levels p_{Met} of $1 \cdot 10^5$, $2 \cdot 10^5$, $4 \cdot 10^5$, $6 \cdot 10^5$, $8 \cdot 10^5$ and $10 \cdot 10^5 \text{ Pa}$.

6.3 Process design and key process units

An intensified mass and energy integrated *DAC* – *PtG* process is proposed. Special attention is given to the analysis of synergies arising within the process structure (Section 6.3.1) and to a detailed investigation of key process units (Sections 6.3.2 and 6.3.3).

6.3.1 Basic considerations

The aim of the concept proposed is the realization of autothermal, resource efficient production of CH₄ based on CO₂ and H₂O captured from ambient air. For this purpose the different process sections are intensively coupled by a water and heat management system, the basic concept of which is sketched in Figure 6.2. By means of this system, the specific drawbacks that arise from an independent realization of the four main process sections: *DAC* – heat recovery (Section 6.3.1.1), hydrogen generation (Section 6.3.1.2), reaction part (Section 6.3.1.3) and downstream (Section 6.3.1.4) can be reduced. Table 6.1 summarizes the key synergies that arise from an intensive coupling of these sub-processes within the overall process structure outlined in Figure 6.3. These are discussed in Sections 6.3.1.1–6.3.1.5, with special attention being given to the process water balance (Section 6.3.1.5).

6.3.1.1 Process section: *DAC* – heat recovery

The operation of the *DAC* process incorporates the challenge of high heat demands. Equilibrium adsorber models (Appendix D.2.2) of the *DAC* unit are used that represent operation of the *MBtA* and *MBdA* concepts developed (Chapter 4) on a detailed level. The application of these concepts allows for a severe reduction of the unit sensible heat

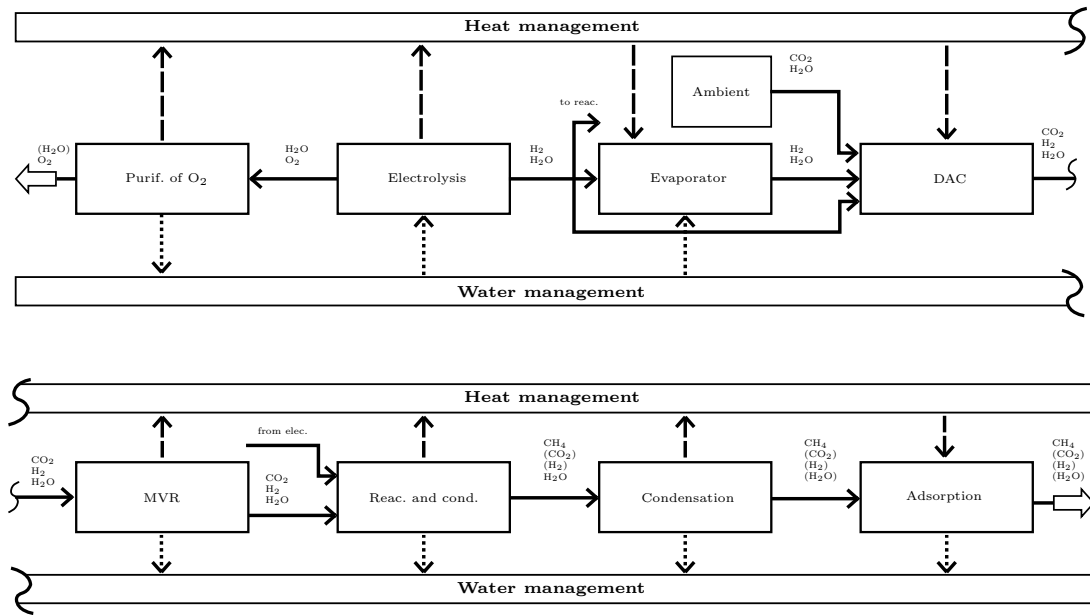


Figure 6.2: Water and heat management system of the intensified integrated *DAC - PtG* process. Heat flows are symbolized by dashed arrows (---). Streams of water are represented by dotted arrows (· ·). A scenario in which the electrolysis acts as heat source is shown. Heat and water flows within the water management system as well as interactions between the heat and water management system are not depicted. Figure reproduced from Drechsler and Agar²⁷⁴.

demand, but the heat consumption attributed to the desorption of CO_2 and H_2O still has to be invested. In this respect, use of water vapor strip gas and of *MVR* (Section 5.3.2) can minimize the energy penalty arising from water co-adsorption.

The byproduct of *MVR* operation at moderate temperatures and elevated pressures is high purity liquid water with no special use. Consequently, the imperfection of H_2O co-adsorption only adds costs for CO_2 drying if no use of the humid product stream in water tolerable processes, e.g., algal biorefineries²⁷⁶, is intended. Integrated *DAC - PtG* operation relativizes this drawback. Pressurization of the product gas comes with the benefit of faster kinetics and higher equilibrium conversion in the reaction section. Moreover, the water recovered in *MVR* can be used as feed for the electrolysis unit and excess heat release by *Sabatier* reaction can become an additional heat source for *DAC*.

6.3.1.2 Process section: hydrogen generation

The stoichiometry of *Sabatier* reaction (6.Ia) indicates high pressurization energy requirements that result from compression of five moles educt gas per mole CH_4 produced. High purity water vapor at elevated pressures is formed as unused byproduct of this reaction. This implies hydrogen losses of 50 % by oxidation of this specie to water. The integration of a pressurized liquid phase water electrolysis allows to overcome both drawbacks. Use of electrochemical compression²⁷⁷ can avoid energy intense hydrogen gas phase compression and in case of water recycle (6.Ia) reduces to



Table 6.1: Synergies arising within the *DAC – PtG* concept according to Drechsler and Agar²⁷⁵. Interactions with respect to the water balance, heat demand and operation pressure are investigated.

	<i>DAC</i> - heat recovery	Hydrogen production	Reaction	Downstream
Water balance	Byproduct (high purity)	Educt (high purity)	Byproduct (high purity)	Byproduct (high purity)
Thermal energy	Demand at low temperature	Release or demand at low temperature	Release at high temperature	Demand at low temperature
Operation pressure	Gas purification (high pressure)	Electrochemical compression	Kinetic, eq. conversion (high pressure)	Gas purification (high pressure)

However, electrolysis water demand can still put a strain to fresh water resources and additional water purification steps might be needed to provide water at the high purities required.^{278,279} In this respect, recycle of water produced in *Sabatier* reaction and compensation of additional electrolysis water demand by controlled water desorption in the *DAC* unit opens up the potential of methane and oxygen production



solely based on renewable energy and on educts captured from ambient air. However, heats of adsorption $\Delta h_{\text{ads},i_{\text{SPE}}}$ typically range 1.2–3.0 times the heat of evaporation $\Delta h_{\text{lv},i_{\text{SPE}}}$.¹²⁷ In this perspective, even fresh water production via reverse osmosis desalination can be significantly more energy efficient compared to adsorption-based processes.¹⁰⁴ Consequently, in dependence of the constraints imposed by the location selected, trade-off considerations with regard to the water source selected on an economic and ecologic level have to be taken into account.

Note that this work focuses on technological mature *AE* and *PEM* electrolysis.^{246,253,277,280} Cell temperatures can reach 90–100 °C,²⁷⁷ where operation below 80 °C is commonly aspired.^{277,280} Detailed analysis of electrolysis operation, based on the unit operation model described in Appendix D.2.3, is provided in Section 6.3.2.

6.3.1.3 Process section: reaction

Streams from the hydrogen generation and *DAC*–heat recovery section are mixed to meet the stoichiometric ratio given by (6.Ia). After preheating to reaction temperature (Appendix D.3.2), conversion to methane is achieved in two catalytic reactors (Appendix D.2.9) that are modeled as isothermally operated, plug flow-type units.

Intermediate cooling allows for a shift of the reaction equilibrium to the product side by removal of water. Minimum temperatures in the intermediate condenser of

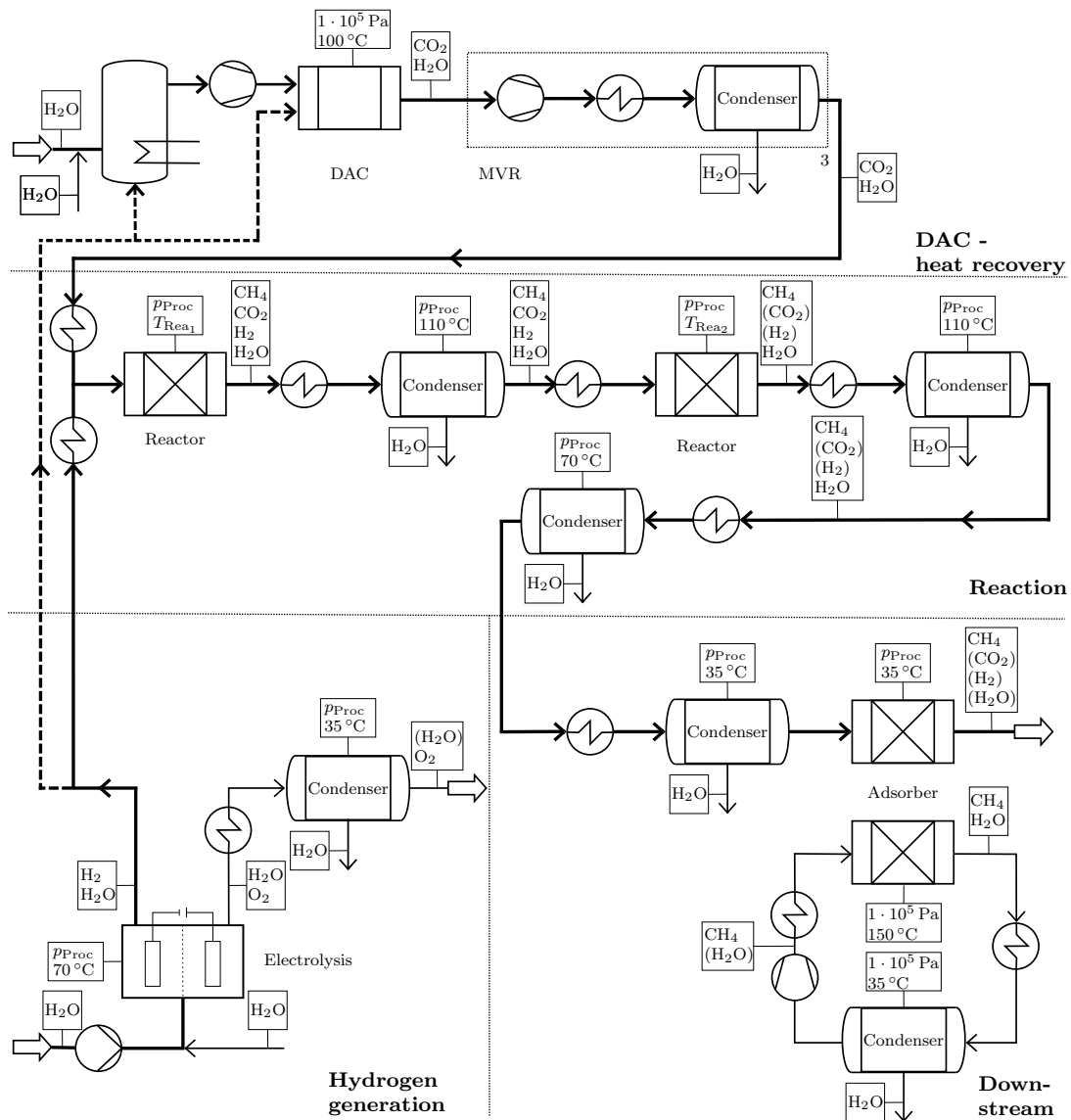


Figure 6.3: Flow sheet of the intensified integrated *DAC - PtG* process proposed that comprises the process sections: *DAC*–heat recovery, hydrogen generation, reaction and downstream. Reactor temperatures ($T_{\text{Rea},\text{Rea}}$) between 250 and 350°C , and operation pressures p_{Proc} of up to $10 \cdot 10^5$ Pa are investigated. The idealized case of no air slip streams in the *DAC* unit is shown. Streams from the electrolysis to the evaporator and *DAC* unit can vary in dependence of the *DAC* unit operation point. For reasons of clarity, neither water recycle and treatment nor streams entering or leaving the *DAC* unit during the adsorption stage are depicted. A detailed summary of the models used and of the process operation characteristics is provided in Appendix D.2 and D.3, respectively. Figure reproduced from Drechsler and Agar²⁷⁴.

$T_{\text{Con}} = T_{\text{DACDes}} + \Delta T_{\text{pin}}$ are reached, with a pinch point temperature difference ΔT_{pin} of 10K being selected. Definition of T_{Con} in this way allows for maximum heat recovery of the latent heat stored in water vapor, but comes with the disadvantage of slower kinetics and lower maximum conversion in the reaction section (Section 6.4.3.2). This already indicates that the reaction section will be strongly coupled to the other process sections.

6.3.1.4 Process section: downstream

A high CO_2 conversion ($X_{\text{CO}_2} > 98.9\%$) and an additional processing of the reaction section product gas in the downstream is required to reach specifications, typical for natural gas grids, e.g., $y_{\text{Pro,H}_2\text{O}} \leq 85 - 150 \text{ ppm}$, $y_{\text{Pro,CO}_2} \leq 2 - 4\%$ and $y_{\text{Pro,ine}} \leq 4 - 5\%$.²⁸¹ Water removal by condensation and by *temperature-pressure-composition-swing-adsorption* (*TPCSA*, adsorption: 35°C , p_{PrC} , desorption: 150°C , $1 \cdot 10^5 \text{ Pa}$) on *zeolite 3A* (Appendix D.2.11 and D.3.3) is realized to ensure product gas water mole fractions lower than 50 ppm for the operation conditions investigated. Selection of methane as strip gas in the desorption cycle avoids product gas contamination and methane losses without the need for additional purge steps in *TPCSA* operation. The heat of water adsorption and the sensible heat release of sorbent cooling are assumed to be available at 35°C , as the intensified integration of these heat sources seems unreasonable due to their negligibly small contributions to the overall energy balance (Section 6.4.1). Nevertheless, the regeneration of the water adsorber requires thermal energy that might be provided by *Sabatier* reaction. Additionally, the high pressure of the reaction section product gas allows for efficient water condensation and *TPCSA* operation without additional gas phase compression.

6.3.1.5 Water balance

Process water management becomes of great importance in the realization of a resource efficient operation of the *DAC-PtG* process proposed. Key considerations comprise maximized recovery of the heat stored in water vapor and minimization of process external water demand and of water recycles (Appendix D.3.4 and D.3.5).

Water management distinguishes between external water source, i.e., water supply to the steam generation unit (Appendix D.2.4) and to the electrolysis, as well as H_2O desorption in the *DAC* unit, and internal sources, i.e., the *Sabatier* reaction. Maximized use of process internal sources via intense recycle of water is aspired to approach the limit defined by (6.III). This allows satisfying the electrolysis water demand exclusively by water recycle. Moreover, if methane production solely based on educts from ambient air is aspired, the external water supply to the steam generation unit becomes zero. This leaves H_2O co-desorption in the *DAC* unit as the only external water source. Besides, efficient water management is also motivated from an heat integration point of view. High-temperature condensation enables efficient integration of the heat stored in water vapor. Moreover, each mole of water not recycled results in higher external water supply. This implies higher heat flows and demands within the *DAC* unit, if the process water demand is solely satisfied by co-desorption. Reducing the amount of water co-desorbed to a minimum appears to be favorable with regard to overall energy considerations.

Recycle of large streams of water can result in significant increases of process streams and costs. Trade-off considerations between the amount of water co-desorbed and size of recycle streams, or water supply to the evaporator, need to be taken into account. In this respect, the operating point of the *DAC* unit becomes of great importance in the process water balance. Here, the amount of water strip gas can be used as a variable to control the quantities of water co-desorbed, while the gas phase composition at the *DAC* outlet and, thus, the size of recycles, is determined by equilibrium constraints (Section 5.2).

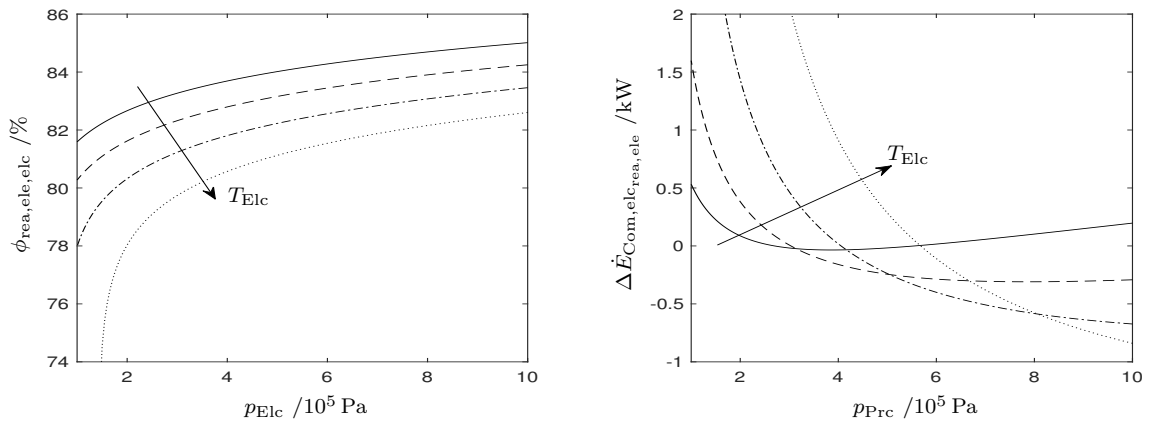
6.3.2 Detailed investigation of electrolysis operation

Electrolysis operation takes considerable influence on the process energy and water balance. High-pressure operation is expected to be beneficial, as a high water content in the electrolysis product gas is suppressed. This reduces recycles and allows for more efficient high-temperature operation, e.g., cooling of recycled water streams is reduced. Besides, additional operation of gas phase compressors can be avoided by use of electrochemical compression. The analysis to follow quantitatively investigates these considerations, where for the sake of generality, non-idealities, other than water evaporation, e.g., overpotentials, are neglected. The results presented are subject to the worst case approximation of a water saturated electrolysis gas phase. For more detailed information on the model used, the reader is referred to Appendix D.2.3.

Figure 6.4(a) visualizes the influence of operation pressure p_{Elc} and temperature T_{Elc} on

$$\phi_{\text{rea,ele,elc}} = \frac{\Delta g_{\text{rea,elc}}}{\Delta h_{\text{rea,elc}}}, \quad (6.1)$$

which represents the ratio between the electric energy demand $\Delta g_{\text{rea,elc}}$ and the total energy requirement of water splitting $\Delta h_{\text{rea,elc}}$. Dilution effects of water are explicitly included in the investigation. Raising system pressure leads to an increase in the relative electric energy demand of water splitting. Comparatively small sensitivity of this parameter toward operation pressure is observed, which increases with temperature.



(a) Relative electric energy demand $\phi_{\text{rea,ele,elc}}$ (b) Difference in energy demand $\Delta \dot{E}_{\text{Com,elc,rea,ele}}$

Figure 6.4: Influence of electrolysis pressure $p_{\text{Elc}} = p_{\text{Prc}}$ on (a) electrolysis relative electric energy demand $\phi_{\text{rea,ele,elc}}$ (6.1) and on (b) the difference between the energy demand of a multi-stage gas phase and electrochemical compression $\Delta \dot{E}_{\text{Com,elc,rea,ele}}$ (6.2), based on a hydrogen mole flow of 1 mol s^{-1} . Operation temperatures T_{Elc} of 50 (-), 70 (- -), 90 (- ·) and 110 °C (· ·) are investigated.

However, absolute changes of the electrolysis electric energy demand with pressure can be large (Figure 6.4(b)). For exemplifying purpose, the energy requirement of a 3-stage gas phase compression with constant compression ratio and intermediate cooling to 35 °C

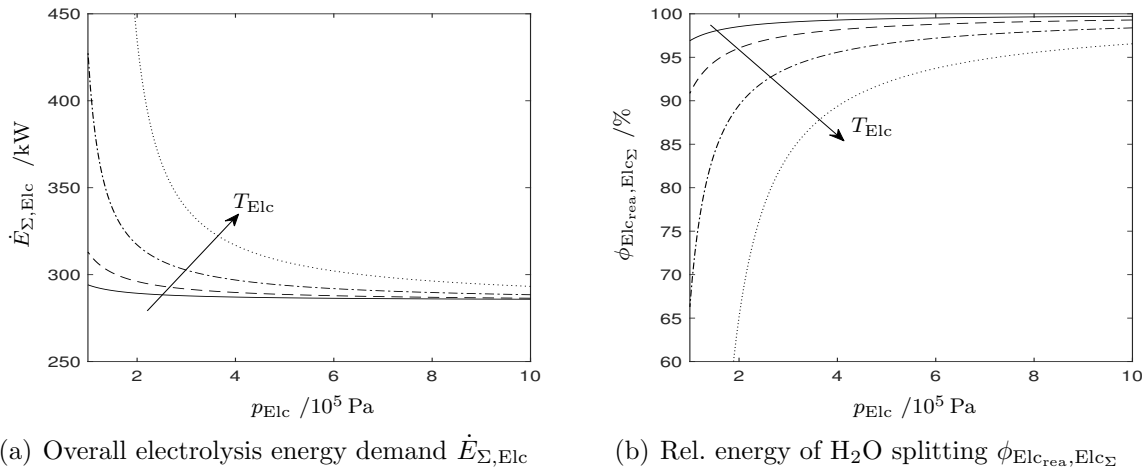
$$\Delta \dot{E}_{\text{Com,elc,rea,ele}} = \dot{E}_{\text{Com}}(p_{\text{Prc}}, \dot{n}_{\text{H}_2}) - \dot{n}_{\text{H}_2} \cdot (\Delta g_{\text{rea,elc},p=p_{\text{Prc}}} - \Delta g_{\text{rea,elc},p=10^5 \text{ Pa,ide}}) \quad (6.2)$$

is selected as a reference. Electrochemical compression is not always superior compared to common multistage compression. Severe influence of water dilution effects on electrochemical compression is revealed by the graphs' ordinate intersects that visualize the difference between the electrolysis electric energy demand with and without water dilution effects, $\Delta g_{\text{rea,elc},p=10^5 \text{ Pa}}$, and $\Delta g_{\text{rea,elc},p=10^5 \text{ Pa,ide}}$, respectively. Complex dependency of $\Delta \dot{E}_{\text{Com,elc,rea,ele}}$ on p_{PrC} is observed, with significant variations compared to the overall energy demand, e.g., of 9.4 kJ mol^{-1} for multi-stage compression to $10 \cdot 10^5 \text{ Pa}$, being noticed. A more detailed analysis reveals this behavior to be attributed to 1. water dilution effects, 2. intermediate cooling in multi-stage compression and 3. simultaneous electrochemical compression of oxygen and hydrogen. For detailed insights, the reader is referred to the corresponding publication²⁷⁵.

Figure 6.4 reveals a diverse influence of operation temperature. When raised, it lowers the relative electric energy demand. But it also leads to a strong negative influence of pressure in the comparison of gas phase with electrochemical compression (Figure 6.4(b)). This observation is also reflected in the analysis of the electrolysis overall energy demand (Figure 6.5(a)). Ideal energy demand of water splitting decreases with temperature, e.g., from 285 kJ mol^{-1} (50°C) to 283 kJ mol^{-1} (110°C). However, attributed to evaporation of water, the reverse tendency is observed for the overall electrolysis energy demand

$$\dot{E}_{\Sigma,\text{Elc}} = \dot{E}_{\text{rea,Elc}} + \dot{E}_{\text{lv,Elc}} \quad (6.3)$$

especially at low pressure levels. Note that the heat demand for evaporation of water in the electrolysis $\dot{E}_{\text{lv,Elc}}$ can significantly exceed the energy release per mole hydrogen converted in *Sabatier* reaction ($\sim 41 \text{ kJ mol}^{-1}$).



(a) Overall electrolysis energy demand $\dot{E}_{\Sigma,\text{Elc}}$

(b) Rel. energy of H_2O splitting $\phi_{\text{Elc,rea,Elc}\Sigma}$

Figure 6.5: Influence of operation pressure p_{Elc} on (a) overall energy demand of the electrolysis $\dot{E}_{\Sigma,\text{Elc}}$ (6.3) and on (b) relative energy demand of water splitting $\phi_{\text{Elc,rea,Elc}\Sigma}$ (6.4). Results based on a hydrogen product flow of 1 mol s^{-1} are shown for operation temperatures of T_{Elc} of 50°C (-), 70°C (- -), 90°C (- ·) and 110°C (· ·). Figure reproduced from Drechsler and Agar²⁷⁵.

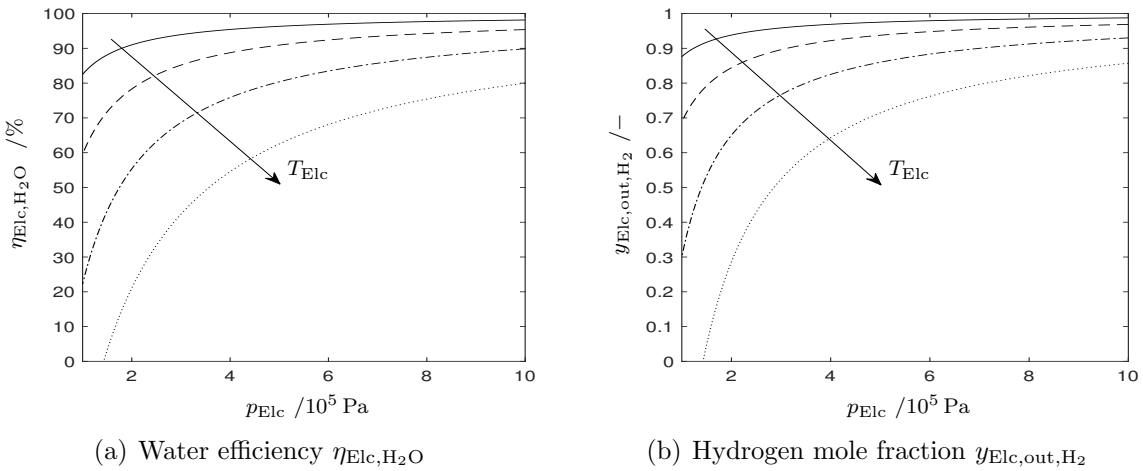


Figure 6.6: (a) Electrolysis water efficiency $\eta_{\text{Elc,H}_2\text{O}}$ and (b) hydrogen mole fraction in electrolysis product gas $y_{\text{Elc,out,H}_2}$, as a function of operation pressure p_{Elc} for electrolysis temperatures T_{Elc} of 50 (-), 70 (--), 90 (-·) and 110 °C (··). Figure reproduced from Drechsler and Agar²⁷⁵.

Figure 6.5(b) confirms that water evaporation can become of great importance with respect to the electrolysis overall energy demand. The contribution of water splitting to the overall electrolysis energy demand

$$\phi_{\text{Elc,rea,Elc}\Sigma} = \frac{\dot{E}_{\text{rea,Elc}}}{\dot{E}_{\Sigma,\text{Elc}}} \quad (6.4)$$

only takes high values for low-temperature or high-pressure operation, whereas at elevated operation temperatures $\phi_{\text{Elc,rea,Elc}\Sigma}$ drops below 80 % if low-pressure operation is aspired.

The electrolysis operation point can also take a severe influence on the process mass balance. Analysis of water efficiency $\eta_{\text{Elc,H}_2\text{O}}$ (Figure 6.6(a)), i.e., of the ratio between the water converted to hydrogen and its flow entering the electrolysis, indicates that significant quantities of water are not processed to hydrogen. Figure 6.6(b) reveals another drawback that arises with regard to the reaction section product gas specification. Low water mole fractions are favorable with respect to the kinetics and equilibrium conversion of *Sabatier* reaction (6.1a). But in dependence of the electrolysis operation point, high water content in the reactor educt gas prevails. Even when neglecting its influence on *Sabatier* reaction, water shares of, e.g., 20 % in electrolysis product flow imply that per mole of CO_2 methanized one mole of water is evaporated in the electrolyzer. If the heat of evaporation is not recovered, this increases the process energy demand by about 41 kJ per mole CO_2 converted, which is about 25 % of the energy released in *Sabatier* reaction and 50 % of the heat of CO_2 adsorption on *Lewatit*. In the best case, high temperature condensation of water is possible, which allows to avoid excessive water losses and to recover the heat of condensation. However, this is paid for by large recycle streams.

If the focus is solely on electrolysis and reaction, avoidance of water evaporation, e.g., by low-temperature or high-pressure operation seems favorable. Again, this interpretation is changed by inclusion of the *DAC* unit in the analysis. In dependence of the *DAC* unit operation point, use of feed gas mixtures that are composed of water and an inert

(Figure 5.3), instead of negative pressure operation, might be taken into account. Use of hydrogen as inert in *DAC* operation avoids additional gas separation steps and does not influence the maximum level of water recovery within the process. Overall, this approach relativizes the drawback of water evaporation in the electrolysis unit, while it underlies the importance of integrating considerations with respect to the carbon source in the conceptual design of *PtG* approaches.

6.3.3 Detailed investigation of reactor operation

The reactors are the major high-temperature heat sources. Their operation points become key aspects of process design. With respect to the operation conditions diverse behavior is expected, as high temperatures favor kinetics but reduce the equilibrium conversion attainable, whereas high pressures favor both, the reaction equilibrium and kinetics. Moreover, optimal reactor operation becomes a function of the feed gas composition that itself depends on the upstream units and on the level of intermediate condensation.

Sabatier reaction is typically operated at temperatures well above the maximum temperature of the main heat sinks within the process. Thus, with respect to energy integration there seem to exist no mandatory constraints for the operation temperature. However, high operation temperature results in higher reactor costs, e.g., due to the use of carbon molybdenum steel above temperature levels of 350 °C,²⁸² and favors formation of carbon monoxide (Section 6.2). Similarly, operation at pressure levels below $10 \cdot 10^5$ Pa are commonly aspired from a cost point of view.²⁸² Consequently, reactor operation is investigated for temperature and pressure levels ranging 250–350 °C and $1 \cdot 10^5$ – $10 \cdot 10^5$ Pa, respectively, which is in line with investigations of other research groups^{283,284}.

To allow for a deeper insight into the optimal reactor operation and its interactions with other process sections, the constraint, multi-variable optimization problem

$$\min_{\vec{\Phi}_{\text{dec}}} \quad m_{\text{Rea}_{\Sigma}, \text{Cat}} = m_{\text{Rea}_1, \text{Cat}} + m_{\text{Rea}_2, \text{Cat}} \quad (6.5a)$$

$$\text{s.t.} \quad \begin{pmatrix} 250 \text{ °C} \\ 250 \text{ °C} \\ 0 \\ 0 \end{pmatrix} \leq \vec{\Phi}_{\text{dec}} = \begin{pmatrix} T_{\text{Rea}_1} \\ T_{\text{Rea}_2} \\ \phi_{\text{eq}, X_{\text{Rea}_1}, \text{CO}_2} \\ \phi_{\text{eq}, X_{\text{Rea}_2}, \text{CO}_2} \end{pmatrix} \leq \begin{pmatrix} 350 \text{ °C} \\ 350 \text{ °C} \\ 1 \\ 1 \end{pmatrix} \quad (6.5b)$$

$$y_{\text{Pro}, \text{CO}_2} \leq 0.02 \quad (6.5c)$$

$$0.95 \leq y_{\text{Pro}, \text{CH}_4} \quad (6.5d)$$

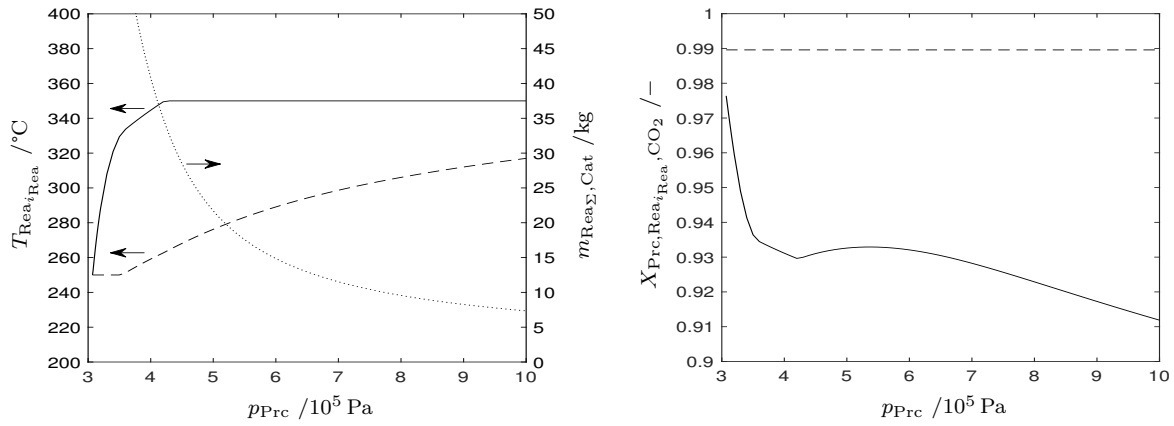
is solved, which takes the catalyst mass $m_{\text{Rea}_{i\text{Rea}}, \text{Cat}}$ required as reference for the reactor costs. Besides reactor temperatures $T_{\text{Rea}_{i\text{Rea}}}$, levels of conversion, described as ratios with reference to the equilibrium conversion attainable

$$\phi_{\text{eq}, X_{\text{Rea}_{i\text{Rea}}, \text{CO}_2}} = \frac{X_{\text{Rea}_{i\text{Rea}}, \text{out}, \text{CO}_2}}{X_{\text{eq}, \text{Rea}_{i\text{Rea}}, \text{CO}_2}}, \quad (6.6)$$

are selected as decision variables in (6.5b). Product specifications are ensured by constraints (6.5c) and (6.5d). Product gas water mole fractions well below 85 ppm are realized

by the operation point of downstream units (Appendix D.2.11 and D.3.3) For the sake of generality, the optimization is performed based on a basic, isothermal plug flow-type reactor model (Appendix D.2.9).

Figure 6.7 exemplifies the results obtained by solving the optimization problem (6.5). Findings for process pressure levels above $3.07 \cdot 10^5$ Pa are shown, as below this threshold product specifications are not satisfied. Raising pressure allows for higher operation temperatures $T_{\text{Rea}_i\text{Rea}}$. Temperature T_{Rea_1} takes higher values in favor of kinetics, compared to T_{Rea_2} for which a lower operation temperature is found to be beneficial, reasoned in the temperature dependency of the reaction equilibrium (Section 6.2). This strong interaction between kinetics and equilibrium is also reflected in Figure 6.7(b) that evaluates the overall CO_2 conversion $X_{\text{Prc,Rea}_i\text{Rea},\text{CO}_2}$ reached at the reactor outlet. Formation of a local minimum and maximum is observed for $X_{\text{Prc,Rea}_1,\text{CO}_2}$. A comparison to the reactor temperature levels $T_{\text{Rea}_i\text{Rea}}$ reveals that changes in the appearance of $X_{\text{Prc,Rea}_1,\text{CO}_2}$ correspond to the evolution of $T_{\text{Rea}_i\text{Rea}}$ with pressure p_{Prc} .



(a) Temperature $T_{\text{Rea}_i\text{Rea}}$ and catalyst mass $m_{\text{Rea}\Sigma,\text{Cat}}$ (b) Overall conversion $X_{\text{Prc,Rea}_i\text{Rea},\text{CO}_2}$

Figure 6.7: (a) Reactor operation temperatures T_{Rea_1} (-), T_{Rea_2} (- -) and catalyst mass required $m_{\text{Rea}\Sigma,\text{Cat}}$ ($\cdot\cdot$) as well as (b) overall CO_2 conversion $X_{\text{Prc,Rea}_1,\text{CO}_2}$ (-) and $X_{\text{Prc,Rea}_2,\text{CO}_2}$ (- -) reached in the reactors in dependence of process pressure p_{Prc} . Results after optimization are shown for a CO_2 mole flow of 1 mol s^{-1} , reacting with a stoichiometric equivalent amount of H_2 according (6.1a). *MVR* condensers and the intermediate condensation stage are operated at 110°C . The electrolysis and the *DAC* unit desorption zone are operated at 70°C and 100°C , respectively. Additional operation parameters of the process are summarized in Appendix D.4.2. Figure reproduced from Drechsler and Agar²⁷⁵.

Overall, a noteworthy reduction of the catalyst mass required with operation pressure is revealed. The sensitivity of the catalyst mass toward operation pressure significantly decreases in the high-pressure region, indicating that raise of system pressure significantly above $10 \cdot 10^5$ Pa might not be reasonable from a cost point of view. Moreover, T_{Rea_2} does not touch the upper boundary set, even at the highest pressure investigated, which indicates presence of limitations attributed to the reaction equilibrium. A measure to reduce this drawback, discussed in Section 6.4.3.2, might be the reduction of the temperature of intermediate condensation between the reactors to increase the quantity of water removed from the gas phase.

6.4 Process performance

Investigations of process performance with special focus on autothermal operation and on process water balance are performed. An analysis of the potential for autothermal operation (Section 6.4.1) and of the process water balance (Section 6.4.2) builds the basis for a detailed investigation of the *DAC* unit operation point within the integrated process structure (Section 6.4.3) and of the energy flow analysis for different process configurations (Section 6.4.4). Finally, considerations with regard to the economics and ecological impact of the concepts are outlined (Section 6.4.5).

6.4.1 Potential for autothermal operation

Potential for autothermal operation is estimated by analysis of process composite curves (Figure 6.8), based on the process configuration summarized in Appendix D.4.3. Contributions of the main equipment that result in characteristic similarities of the composite curves are denoted. Investigation of temperature dependent (partial) condensation of water results in a concave curvature of the composite curves rather than in an energy release at constant temperature level. In this respect, discontinuous transitions of the hot composite curve can indicate the onset of condensation at the temperature level evaluated.

Figures 6.8(a)-6.8(c) visualize the limiting scenario with thermodynamic minimum electric energy input to the electrolysis, i.e., operation at equilibrium cell voltage. None of the scenarios shown allows for autothermal operation, but characteristic responses of the system to a change of operation pressure can be identified. Increase of pressure results in a shift of *Sabatier* reaction temperature to higher temperature levels and allows for condensation of water at elevated temperatures. This does not significantly change the positions of the process pinch points. But it increases the potential of the process to release heat at more elevated temperatures, interesting with respect to exergy considerations, temperature differences in heat transfer systems and possible use of heat in other processes.

Decrease of process external heat demand with operation pressure p_{PrC} is observed. On the one hand, this can be attributed to a higher degree of heat integration. Increase of water condensation results in a decrease of external cooling power requirement (waste heat) of $\Delta\dot{Q}_{\text{cool,ext},3.07 \cdot 10^5 - 10 \cdot 10^5 \text{ Pa}} = 13 \text{ kW}$. On the other hand, operation at higher pressure levels results in the need of higher electric energy input to the compressors and to the electrolysis (Figure 6.4(a)). Overall, results shown indicate that even in the limiting case of no dissipative heat release in the electrolysis, autothermal operation is nearly possible.

Overpotentials and other non-idealities, e.g., ohmic resistances, require technically realized water electrolysis to operate at cell voltages above equilibrium level ($\Delta U_{\text{eq,Elc}}^{\circ} = 1.23 \text{ V}$) that typically range $1.75 - 2.05 \text{ V}$.²⁸⁵ This operation mode is analyzed by investigation of electrolysis operation at $1.5 \cdot \Delta U_{\text{eq,Elc}}$ in Figures 6.8(d)-6.8(f). In these scenarios, autothermal operation of the process seems possible. Significant generation of excess heat in the low- and high-temperature region is observed. However, this does not necessarily imply that the process has become more energy efficient. Rather, heat demand at low temperature is compensated by electric heating that results from energy dissipation in the electrolysis. In line with other contributions^{70,242,243} this underlines the severe

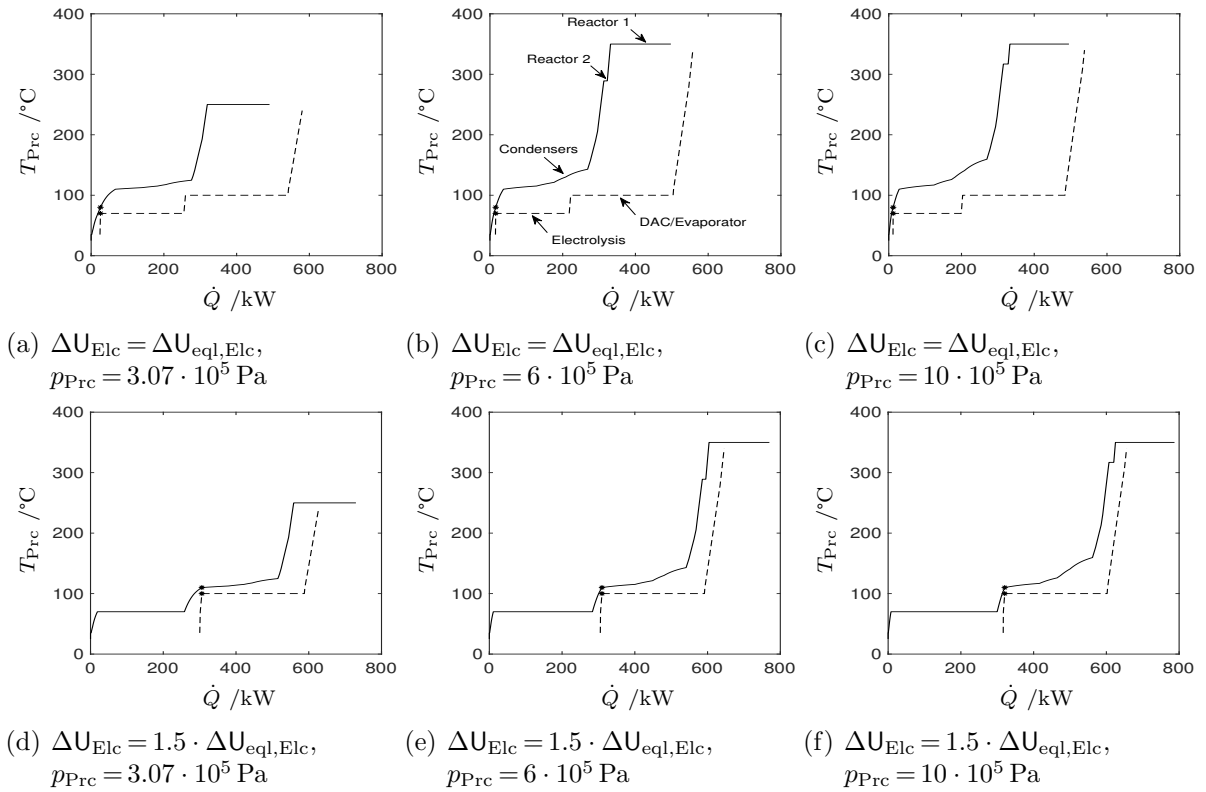


Figure 6.8: Hot (-) and cold (--) composite curves for six illustrative scenarios. Process pressure levels p_{Prc} of $3.07 \cdot 10^5$, $6 \cdot 10^5$ and $10 \cdot 10^5$ Pa are investigated for electrolysis operation at (a)–(c) equilibrium cell voltage $\Delta U_{\text{Elc}} = \Delta U_{\text{eql,Elc}}$ and (d)–(f) $\Delta U_{\text{Elc}} = 1.5 \cdot \Delta U_{\text{eql,Elc}}$. The *DAC* unit desorption zone is operated at 100°C and the electrolysis temperature is set to 70°C . Additional operation parameters are summarized in Appendix D.4.3. Pinch points are indicated by stars (*).

importance of efficient hydrogen production in *PtG* concepts. In this respect, the strong heat released in the electrolysis suggests use of this unit as heat source for *DAC* operation. However, for an efficient assessment of this scenario (Section 6.4.4), previous, more detailed investigation of the process water balance (Section 6.4.2) and of the influence of the *DAC* unit operation point on the process mass and energy balance (Section 6.4.3) seems reasonable.

6.4.2 Process water balance

The process water balance is strongly coupled to its energy balance, e.g., to the heat of desorption in the *DAC* unit. It takes severe influence on the size of recycle streams and, thus, on the heat flows in the condensers. Figure 6.9 visualizes the dependency of the water balance on process pressure for three reference scenarios (Appendix D.4.4).

The electrolysis becomes the major water sink, whereas convective water losses within the methane product steam are negligibly small. The only noticeable water losses result from water not recovered from the electrolysis oxygen product flow and from water losses in the *DAC* sorbent bed void space. However, even these losses are comparatively small, which underlines the water-efficient operation of the process. This seems beneficial with

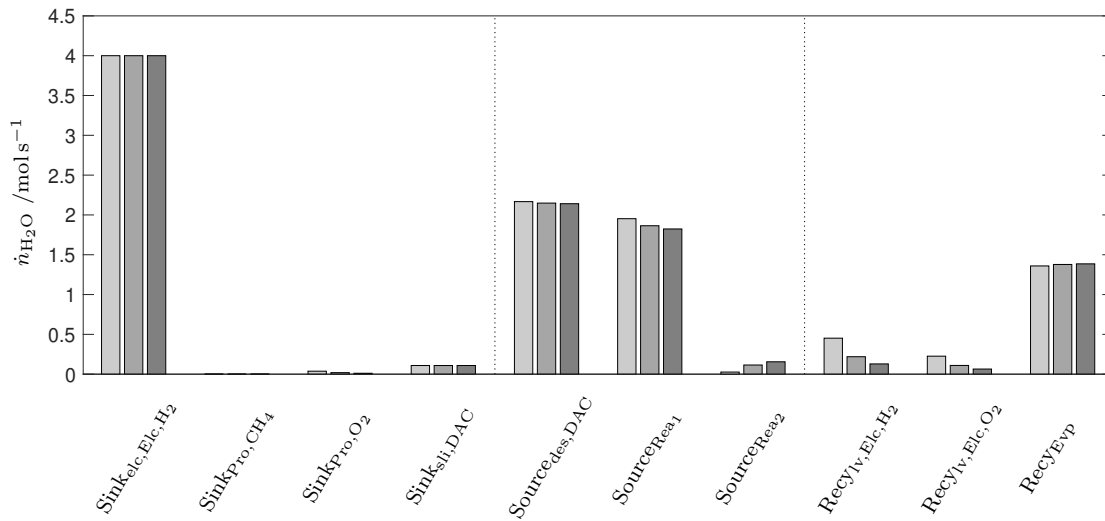


Figure 6.9: Influence of operation pressure p_{PrC} on the water balance of the intensified integrated $DAC-PtG$ process. Results for pressure levels of $3.07 \cdot 10^5$ (bright), $6 \cdot 10^5$ (intermediate) and $10 \cdot 10^5$ Pa (dark) are depicted. Four sinks for water are identified, these are: water split in the electrolysis ($Sink_{elc,Elc,H_2}$), losses in the CH_4 product gas ($Sink_{P_{ro},CH_4}$), losses in the O_2 product gas ($Sink_{P_{ro},O_2}$) and losses attributed to slip streams in the DAC sorbent bed void space ($Sink_{sli,DAC}$). Process water sources: desorption of water in DAC unit ($Source_{des,DAC}$) and water formation in *Sabatier* reaction ($Source_{Rea1,Rea2}$) are shown. Water streams evaporated in the electrolysis ($Recy_{lv,Elc,i_{spe}}$) and recycled to the evaporator ($Recy_{Evvp}$) are visualized.

regard to the use of air as water source, as energy requirements that result from additional water demand are reduced to a minimum.

By adjusting the DAC operation point, i.e., the $H_2O : CO_2$ desorption ratio, the process water balance can be controlled. When subtracting the water sinks, which result from losses in the product gases and from slip streams in the DAC unit, from the amount of CO_2 desorbed in the DAC unit, a residual water mole flow larger two is obtained. This implies presence of additional water losses, as based on the stoichiometry of the reaction aspired (6.III) only two moles of external water supply are required. A more detailed analysis reveals that these indirect losses result from incomplete conversion of hydrogen. Even if levels of conversion in the order of magnitude of 99% are attained, losses attributed to incomplete conversion can exceed the water losses in the product gas by more than 80%. This underlines the high resource efficiency of the process designed and additionally stresses the importance of water losses in the DAC sorbent bed void space. These might efficiently be reduced by operation at higher working capacities.

With regard to the process water balance, high-pressure operation seems beneficial. Increase of the overall efficiency of water recovery with pressure is noticed, e.g., indicated by a noticeable reduction of the water losses in the product gases and by a significant decrease of the water recycles required to compensate for the water evaporated in the electrolysis. Acknowledging that the size of the water recycles can take a high order of magnitude compared to the overall process streams, potential for significant decrease of equipment size and heat transfer area is revealed for high-pressure operation.

6.4.3 Influence of DAC operation point on process performance

This section is dedicated to a detailed investigation of *DAC* unit operation point influence on *PtG* process performance. Focus is placed on the analysis of air slip streams (Section 6.4.3.1) and on the selection of *DAC* operation temperatures (Section 6.4.3.2). Results presented are based on the process configuration summarized in Appendix D.4.5.

6.4.3.1 Slip stream of air into DAC unit product gas

The analysis given in Sections 6.4.1 and 6.4.2 considers an ideal separation process, i.e., no slip stream of air into *DAC* unit product gas is taken into account. This implies use of additional energy, e.g., for drawing vacuum, or of purge gas to prevent this additional gas stream in the order of magnitude of 14% of the CO₂ product stream to enter the *DAC* unit desorption zone. Consequently, the influence of air slip streams on process performance is investigated to assess to what extent reduction of this stream is necessary.

Figure 6.10(a) visualizes the evolution of the catalyst mass required in dependence of operation pressure p_{PrC} and of the slip ratio of air into the *DAC* desorption zone $\phi_{\text{DAC,sl}_{\text{Ads,Des}}}$. The latter defines the fraction of the gas phase present in the sorbent bed void space that is allowed to enter the desorption zone. Strong influence of $\phi_{\text{DAC,sl}_{\text{Ads,Des}}}$ on catalyst mass with increasing sensitivity at high levels of $\phi_{\text{DAC,sl}_{\text{Ads,Des}}}$ or at low operation pressure is observed. This reflects the strong influence of the reaction system equilibrium conversion on the kinetics and, thus, on the catalyst mass required.

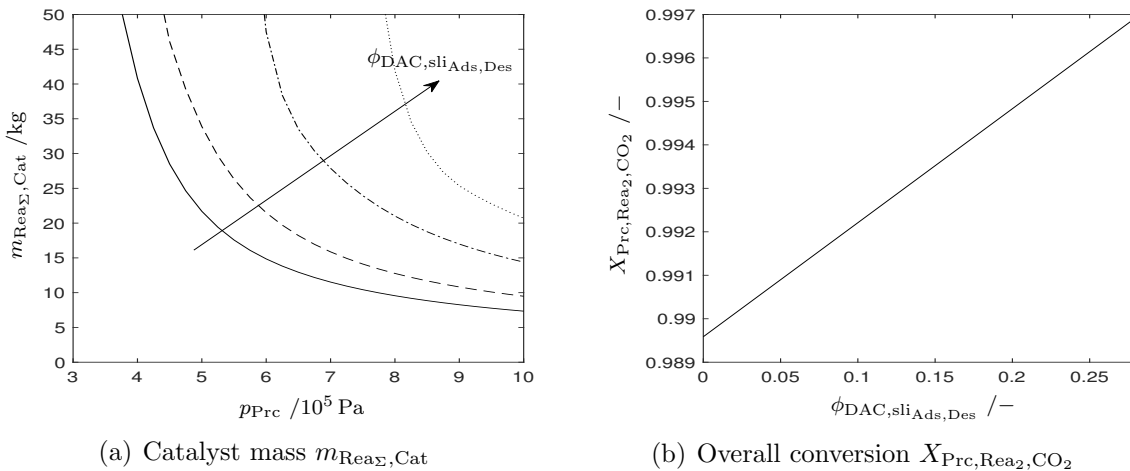


Figure 6.10: (a) Overall catalyst mass demand $m_{\text{Rea}\Sigma,\text{Cat}}$ in dependence of process operation pressure p_{PrC} for *DAC* slip ratios between ad- and desorption zone $\phi_{\text{DAC,sl}_{\text{Ads,Des}}}$ of 0 (-), 0.10 (--), 0.20 (-·), 0.25 (··). (b) Overall conversion $X_{\text{PrC,Rea2,CO}_2}$ required to reach the product gas specifications as a function of $\phi_{\text{DAC,sl}_{\text{Ads,Des}}}$. Operation at a pressure level p_{PrC} of $10 \cdot 10^5 \text{ Pa}$ is investigated.

Figure 6.10(b) confirms this interpretation. The dependency of the CO₂ conversion, required to reach product gas specifications, on $\phi_{\text{DAC,sl}_{\text{Ads,Des}}}$ is exemplified for an operation pressure of $10 \cdot 10^5 \text{ Pa}$. Only minor variations are noticed for operation at lower pressure levels, reasoned in the lower efficiency of water removal by the zeolite adsorber. Variation of the conversion required by less than 1% results in an increase of the catalyst mass

demand by a factor of more than 2.8. This underlines the strong dependency of the kinetics on the level of conversion to be achieved and, thus, on the equilibrium state of the system.

Figure 6.11(a) underlines this interpretation by visualization of the evolution of optimized reactor temperatures $T_{\text{Rea}_i\text{Rea}}$ in dependence of $\phi_{\text{DAC},\text{sl}_{\text{Ads,Des}}}$. Operation at high levels of $\phi_{\text{DAC},\text{sl}_{\text{Ads,Des}}}$ results in lower operation temperatures to shift the reaction equilibrium to the product side and, thus, to avoid operation in the close vicinity of the equilibrium state. Consequently, as high purity of the product gas ($y_{\text{Pro,CH}_4} \geq 95\%$) is aspired, even a minor increase of the impurity level takes a severe influence on process performance. Besides, for the scenario investigated, mole fractions of oxygen in product gas can reach levels greater than 0.7% (Figure 6.11(b)). Reaction of O_2 with H_2 , which will, most likely, take place under methanation conditions, can allow for relaxation of conversion requirements, as separation of the water additionally formed is easily realizable. However, besides the loss of hydrogen by water formation, various considerations indicate oxygen avoidance to be reasonable. Pipeline specifications typically allow for maximum O_2 product gas shares of less than 0.01% and uncontrolled oxyhydrogen gas reaction can become a threat with regard to process safety. Moreover, in presence of oxygen severe decrease of sorbent long-term stability is observed, especially if operation at elevated desorption temperatures is aspired (Section 3.3.2). If these concerns can be overcome, controlled oxyhydrogen gas reaction might be considered as an additional measure to reduce the oxygen content in the product gas. However, the additional effort to remove the air present in the *DAC* sorbent bed void space seems comparatively small. Thus, removal by vacuum operation or by purge gas use seems beneficial with respect to process considerations.

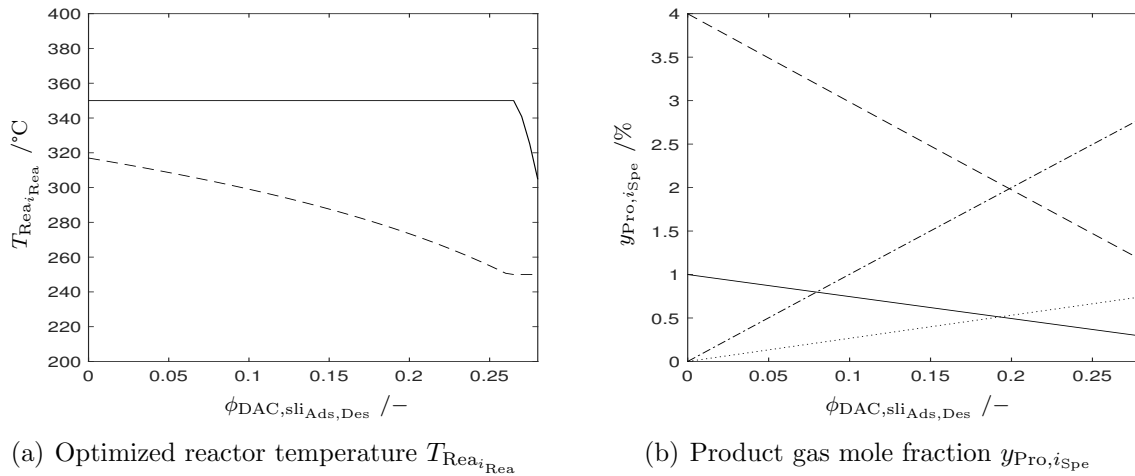


Figure 6.11: (a) Optimized reactor temperatures T_{Rea_1} (-) and T_{Rea_2} (--), as well as, (b) gas phase mole fraction $y_{\text{Pro},i\text{Spe}}$ of species CO_2 (-), H_2 (--), N_2 ($\cdot\cdot$) and O_2 ($\cdot\cdot$), as functions of *DAC* slip ratio between ad- and desorption zone $\phi_{\text{DAC},\text{sl}_{\text{Ads,Des}}}$. Process operation at $10 \cdot 10^5$ Pa is investigated.

6.4.3.2 Varying *DAC* unit operation temperature

With respect to a thermal integration of the electrolysis as heat source for the *DAC* desorption zone (Section 6.4.4), *DAC* operation at low temperature levels becomes of interest. Higher levels of water co-desorption in the *DAC* unit are expected, whereas

potential of water condensation at lower temperatures might allow for more efficient heat recovery. Besides, necessity of low-pressure operation or of additional strip gas use is indicated by the equilibrium pressure levels of components present in the *DAC* gas phase. Here, use of $\text{H}_2\text{O}-\text{H}_2$ strip gas mixtures is elaborated in more detail.

Water content and recovery Figure 6.12(a) depicts the evolution of *DAC* product gas composition with desorption temperature. Decrease of water content at lower desorption temperature is confirmed. However, the CO_2 share also decreases with temperature. This results in an overall increase of the $\text{H}_2\text{O}:\text{CO}_2$ ratio. Moreover, strip gas requirement significantly increases in case of low-temperature operation. This indicates necessity of using $\text{H}_2:\text{CO}_2$ ratios larger than the stoichiometric ratio given by (6.1a), other strip gas use, or additional vacuum operation. More complex gas separation or higher energy demands and design constraints for *DAC* make these options appear less promising.

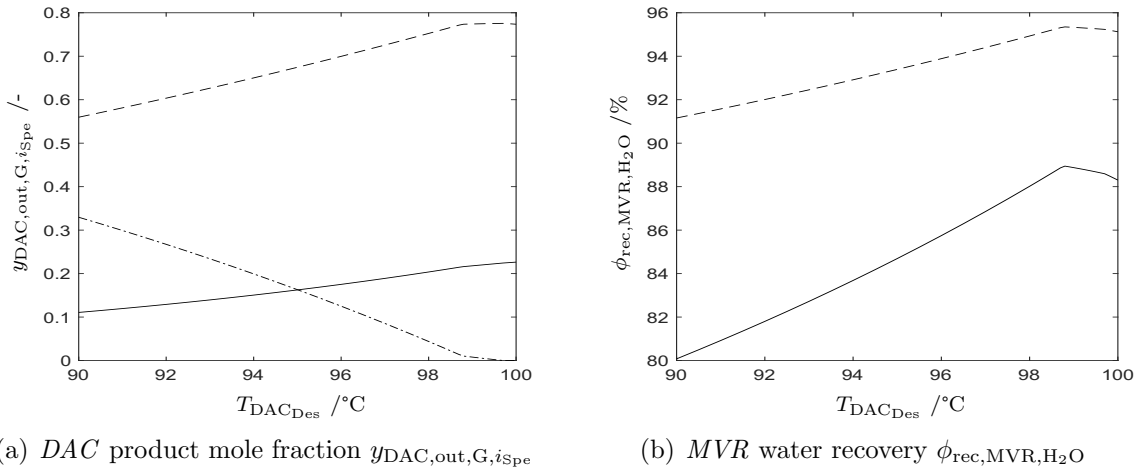


Figure 6.12: Influence of *DAC* unit desorption temperature T_{DACDes} on (a) shares of species: CO_2 (-), H_2O (--) and H_2 (-·) in *DAC* product gas and on (b) level of water recovery reached in *MVR* $\phi_{\text{rec,MVR,H}_2\text{O}}$ at operation pressures p_{PrC} of $5 \cdot 10^5$ Pa (-) and $10 \cdot 10^5$ Pa (--).

Even if T_{DACDes} is limited to levels at which solely use of $\text{H}_2\text{O}-\text{H}_2$ strip gas mixtures is sufficient to drive the desorption process, the energy requirement for gas phase compression can more than double in dependence of T_{DACDes} (Figure 6.16). On the other hand, one intuitively expects T_{DACDes} to take strong influence on the efficiency of water recovery, e.g., in *MVR* on $\phi_{\text{rec,MVR,H}_2\text{O}}$, if operation with the minimum temperature differences between the condensers and *DAC* desorption unit is aspired. Strong decline of $\phi_{\text{rec,MVR,H}_2\text{O}}$ with decreasing desorption temperatures, and, thus, decrease of minimum condensation temperature, is observed in the low-temperature region (Figure 6.12(b)). Dilution effects of hydrogen, which reduce the water partial pressure, can be identified to cause this behavior. In conclusion, operation at elevated desorption temperatures and at high process pressures is found to be beneficial with regard to the *DAC*-heat recovery section, with a crucial influence of *DAC* desorption temperature being revealed.

Equilibrium driven kinetics As noted in Section 6.3.3, the equilibrium of the reaction system can take severe influence on the methanation process. This suggests a high depen-

density of the reaction section on its educt gas composition. In this respect, the evolution of the water content in the reaction section educt gas as function of $T_{\text{DAC}_{\text{Des}}}$ (Figure 6.13(a)) indicates favorable operation points to be at high *DAC* desorption zone temperatures.

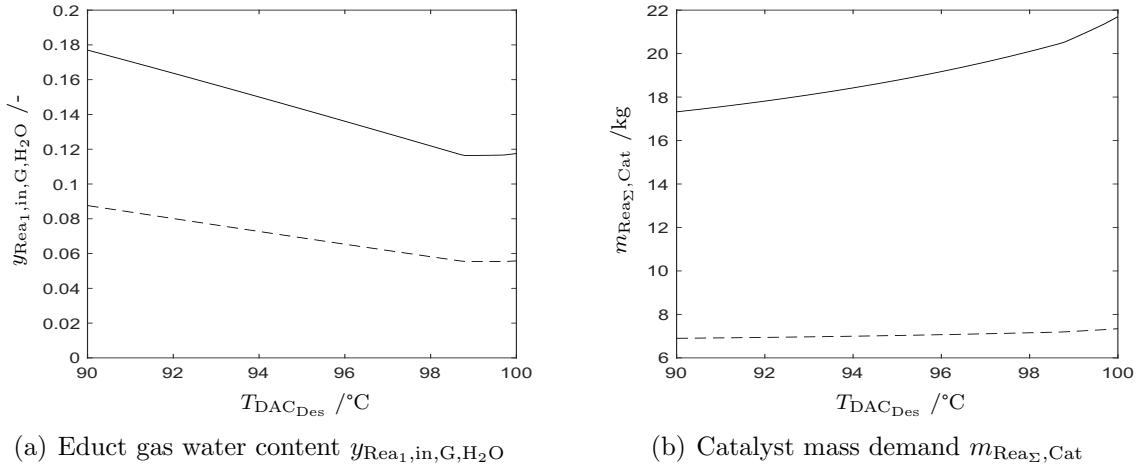


Figure 6.13: (a) Water content in reaction section educt gas $y_{\text{Rea}_{1,\text{in,G,H}_2\text{O}}}$ and (b) overall catalyst demand $m_{\text{Rea}_{\Sigma,\text{Cat}}}$ as functions of *DAC* desorption zone temperature $T_{\text{DAC}_{\text{Des}}}$. Process pressures of $5 \cdot 10^5$ Pa (-) and $10 \cdot 10^5$ Pa (- -) are investigated.

Figure 6.13(b) shows that the optimized amount of catalyst mass $m_{\text{Rea}_{\Sigma,\text{Cat}}}$ increases with *DAC* unit desorption temperature. On a first view, this might seem counterintuitive, especially with regard to the evolution of the educt gas water content with temperature (Figure 6.13(a)). However, $T_{\text{DAC}_{\text{Des}}}$ also takes influence on the educt gas composition of the second reactor via the level of intermediate condensation. This is, condensers work at the minimum temperature possible that is dictated by the aim of using the heat recovered by water condensation to compensate for the heat demand of the *DAC* and evaporator unit. Thus, results shown indicate the influence of intermediate condensation to be more dominant compared to the reaction section educt gas composition, which underlines the influence of reaction equilibrium on process performance. This is especially revealed at lower operation pressures, at which absolute variations in the gas phase water content with condensation temperature are more pronounced.

Energy penalty attributed to hydrogen loss Even if no variation in electrolysis operation temperature is considered, the *DAC* desorption temperature affects the electrolysis energy demand via variation in hydrogen losses attributed to the temperature-dependent shares of this specie in the *DAC* unit strip gas. Figure 6.14(a) evaluates the evolution of the hydrogen losses relative to its amount produced in the electrolysis $\phi_{\text{los,DAC,H}_2}$ in dependence of $T_{\text{DAC}_{\text{Des}}}$. Small relative losses of less than 1.4% indicate *DAC* unit slip streams to take a minor influence on the process hydrogen balance. However, these losses scale with a factor of four relative to the CO_2 product flow and splitting of water is an energy intensive process step. Consequently, even these small losses are associated with considerable energy penalties (Figure 6.14(b)) that can reach levels in the order of magnitude of 10% of *Sabatier* reaction heat release.

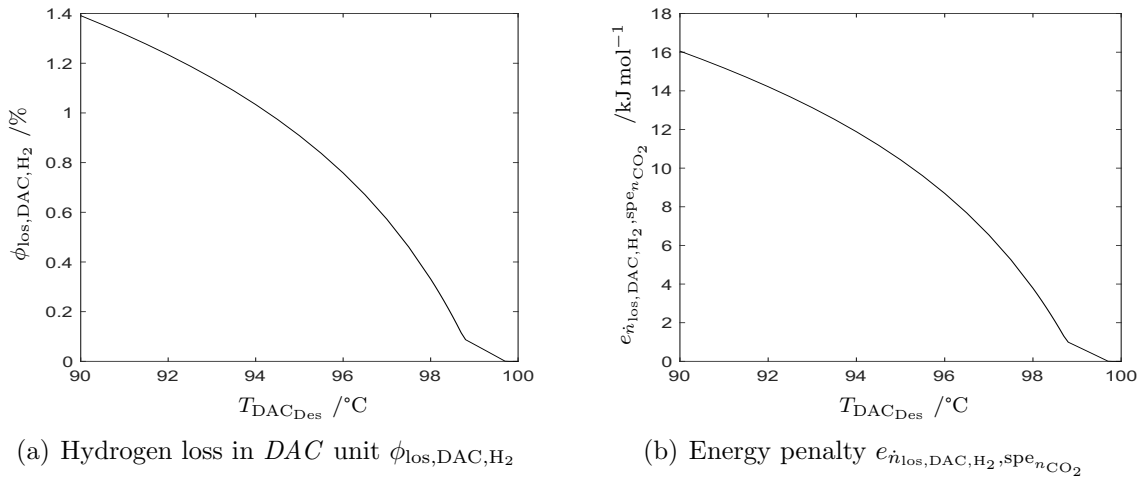


Figure 6.14: Influence of *DAC* unit operation temperature T_{DACDes} on (a) relative hydrogen loss in *DAC* unit $\phi_{\text{los,DAC,H}_2}$ and (b) attributed energy penalties arising from hydrogen loss $e_{\dot{n}_{\text{los,DAC,H}_2,\text{spe}_{\text{CO}_2}}}$ per mole of CO_2 in the *DAC* product gas. For reasons of clarity, the energy penalty $e_{\dot{n}_{\text{los,DAC,H}_2,\text{spe}_{\text{CO}_2}}}$ is calculated based on the thermoneutral energy requirement for water splitting. Additional contributions to electrolysis energy demand, e.g., dissipative losses or evaporation of water, are not included, as these might be recovered within the process.

A comparison of the findings achieved by the analysis of Figures 6.11-6.14 reveals a diverse influence of the *DAC* operation point on the performance of the process sections. High-temperature operation reduces possible hydrogen losses in *DAC* and shifts the ratios of $\text{CO}_2:\text{H}_2\text{O}$ as well as of $\text{CO}_2:\text{H}_2$ in the *DAC* product gas to higher levels. On the contrary, low-temperature operation allows for an overall more efficient level of water recovery and for less catalyst demand. Thus, trade-off considerations on an energy, economic and ecologic level need to be taken into account to determine the optimal operation temperature of the *DAC* unit. With respect to the scope of this work, the analysis on an energy level is extended to the entire process structure in Section 6.4.4.

6.4.4 Energy flow analysis

Currently, technically realized water electrolysis operates significantly above thermoneutral level.²⁷⁷ This motivates use of electrolysis as additional heat source for *DAC*. Besides variation of *DAC* desorption temperature, operation of electrolysis at elevated temperature levels is imaginable to realize this integration. However, operation of the electrolysis at temperatures above the limit of 80 °C typically named^{277,280} can result in accelerated corrosion in case of *AE* concepts or in increased mechanical and thermal degradation in *PEM* electrolysis.²⁸⁶ Besides, high-temperature operation can significantly increase the water content in the electrolysis product gas (Figure 6.6).

Based on the aforementioned considerations, electrolysis operation at the lowest temperature that allows for heat integration with the *DAC* unit seems reasonable. As the *DAC* unit itself is already intensified heat integrated, the predominant share of heat demand arises at desorption temperature level. Choosing $T_{\text{DACDes}} = 90$ °C, which is close to the limit at which low-pressure operation or additional strip gas use becomes necessary

(Figure 6.12(a)), results in an electrolysis operation temperature T_{Elc} of 100°C . Note that *Nafion* membranes typically applied in *PEM* concepts exhibit glass transition temperatures of 120°C , which are close to the operation temperature T_{Elc} defined. Even if this suggests stability problems in high-temperature applications, current trends in membrane development indicate that membrane stability above 100°C can be guaranteed, e.g., stable operation of modified *Nafion* membranes²⁸⁷ at 120°C or of *Solvay Aquivion*[®]²⁸⁸ at 140°C .

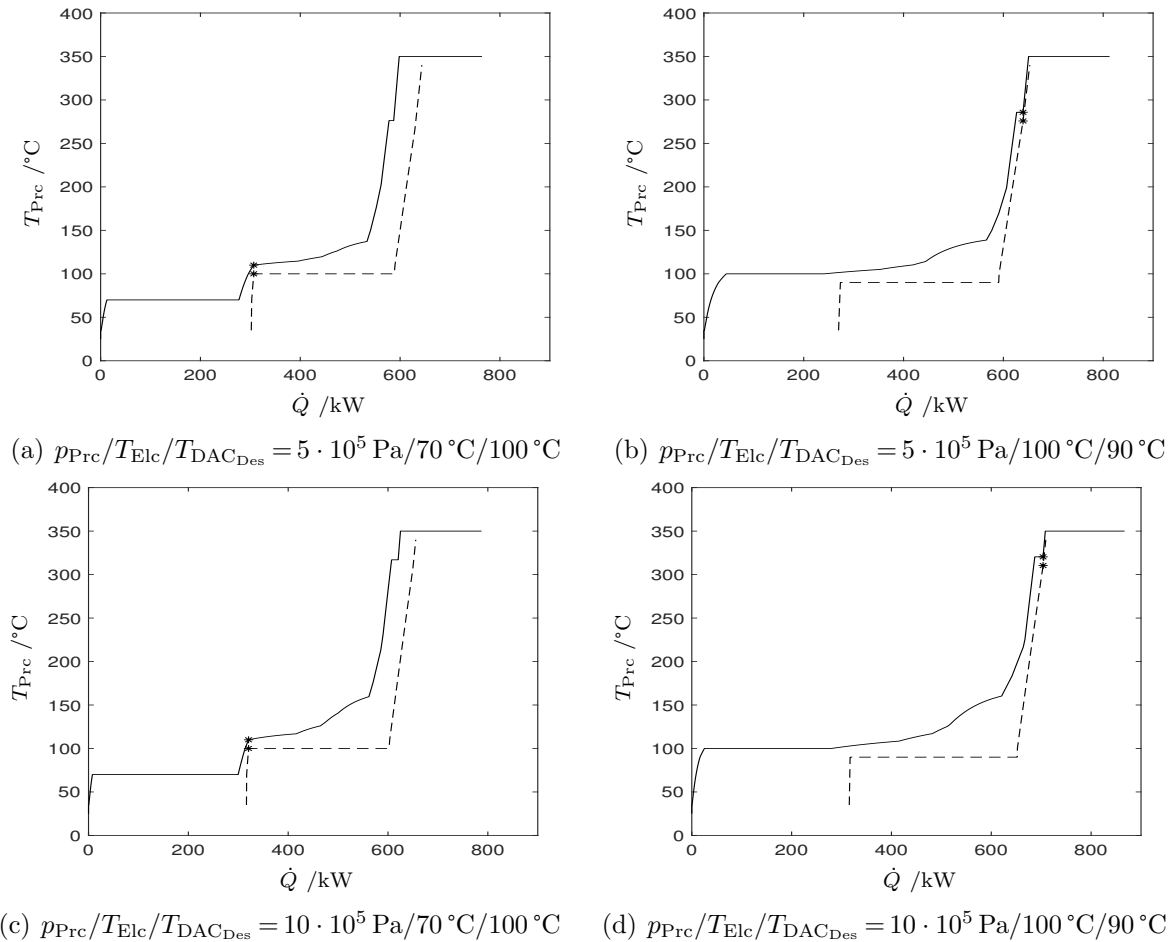


Figure 6.15: Influence of operation pressure p_{Prc} (a)–(b): $5 \cdot 10^5 \text{ Pa}$, (c)–(d): $10 \cdot 10^5 \text{ Pa}$ on process hot (-) and cold (--) composite curves. Operation at different temperature levels in the *DAC* and electrolysis unit is investigated: $T_{\text{Elc}} = 70^\circ\text{C}/T_{\text{DACDes}} = 100^\circ\text{C}$ in (a) and (c), $T_{\text{Elc}} = 100^\circ\text{C}/T_{\text{DACDes}} = 90^\circ\text{C}$ in (b) and (d). The electrolysis is operated at $\Delta U_{\text{Elc}} = 1.5 \cdot \Delta U_{\text{eq,Elc}}$. Positions of pinch points are indicated by stars (*). Operation parameters are summarized in Appendix D.4.6.

A joint analysis of process composite curves (Figure 6.15) and of characteristic energy flows within the process (Figure 6.16) allows for detailed insights into the influence of process pressure, electrolysis operation and *DAC* desorption temperature on the process energy balance. For all scenarios shown, autothermal operation is reached, with significant excess heat being available. Characteristic differences in the shapes of the process composite curves are revealed between the scenarios. As expected, electrolysis heat release significantly contributes to low-temperature excess heat release. Use of electrolysis as *DAC* heat

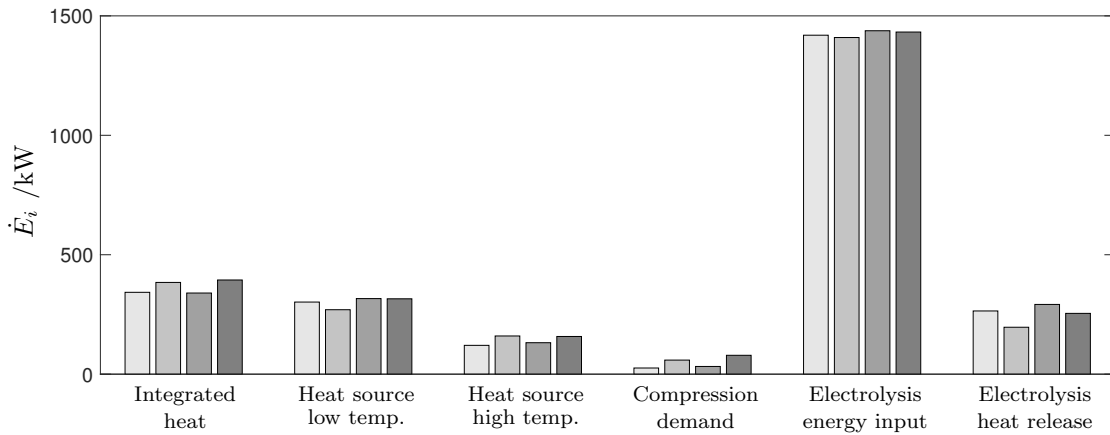


Figure 6.16: Characteristic energy flows of the process \dot{E}_i in dependence of pressure p_{PrC} , electrolysis temperature T_{Elc} and *DAC* desorption temperature $T_{\text{DAC,Des}}$. Influence of the parameter set $p_{\text{PrC}}/T_{\text{Elc}}/T_{\text{DAC,Des}}$ is investigated for four scenarios (from bright to dark): (a) $5 \cdot 10^5$ Pa/70°C/100°C, (b) $5 \cdot 10^5$ Pa/100°C/90°C, (c) $10 \cdot 10^5$ Pa/70°C/100°C, (d) $10 \cdot 10^5$ Pa/100°C/90°C. In addition to the heat flows, electric energy demand for gas and liquid phase compression as well as for electrolysis operation at $\Delta U_{\text{Elc}} = 1.5 \cdot \Delta U_{\text{eq,Elc}}$ is shown. Heat flows integrated within single devices are not shown. Operation parameters are given in Appendix D.4.6.

source (Figures 6.15(b) and 6.15(d)) comes with a severe increase of the amount of heat to be integrated, which besides others results from the process water balance, i.e., from larger water streams within the process. Moreover, heat release within electrolysis seems not sufficient to satisfy the heat demand arising from *DAC* and evaporator operation.

Focusing on operation pressure, the shift of the temperatures of the heat sources to higher levels with increasing pressure, observed in Section 6.4.1, is confirmed (Figure 6.15). However, only minor sensitivity of the amount of heat integrated on pressure is found (Figure 6.16). Besides, change of pressure results in an exchange between the heat source characteristic of the electrolysis and the additional heat release by condensation of the water evaporated in this unit. This is, water evaporated in the electrolysis reduces the unit's heat release, but its condensation allows to recover this energy at high temperatures.

Besides influence on a thermal energy level, the choice of operation parameters can lead to noticeable variations in the process electric energy demand. The operation temperatures of the electrolysis and *DAC* unit are found to have a greater influence on compression energy demand than the operation pressure (Figure 6.16). This is reasoned in the increasing ratio between non-condensable components, or H_2O , and CO_2 in the *DAC* product stream (Figure 6.12). Moreover, the small influence of p_{PrC} on compression energy requirement can be attributed to water condensation in the first *MVR* stage that only leaves a small stream to be compressed to final operation pressure in the subsequent *MVR* stages. Concluding, with respect to the compression energy demand, the shares of non-condensable components in the *DAC* product gas should be kept at a minimum.

Focusing on the electrolysis unit, high-temperature operation is found to decrease the electrolysis potential for heat release even if the thermoneutral voltage, and thus, energy demand per mole H_2 split declines with temperature. This is attributed to three effects: 1) Total electric energy input to electrolysis for operation at $\Delta U_{\text{Elc}} = 1.5 \cdot \Delta U_{\text{eq,Elc}}$

decreases with temperature as a result of lower equilibrium cell voltage. 2) Total energy demand for the production of hydrogen increases, reasoned in necessity of more hydrogen production to compensate for higher hydrogen losses in *DAC*. 3) Increased thermal energy demand resulting from water evaporation within electrolysis. On the contrary, increase of operation pressure favors the electrolysis heat source characteristics. Besides the increase of the electric energy input required to operate at $\Delta U_{\text{Elc}} = 1.5 \cdot \Delta U_{\text{eq,Elc}}$, the reduction of water evaporation in the electrolysis is identified as the major contribution to this effect.

Overall, use of heat release in electrolysis as heat source for *DAC* seems possible but not beneficial. Besides limitations imposed by material properties that suggest increase in equipment costs, larger water recycles and higher hydrogen losses argue against this option. Even if a part of the heat generated is used to produce water vapor, this scenario still resembles evaporation by electric heating that does not seem reasonable from an exergetic point of view, especially as sufficient high-temperature heat is available. Consequently, with focus on energy considerations, reducing electrolysis energy demand becomes crucial. However, currently realized electrolysis cells are typically operated significantly above thermoneutral voltage. If this is not avoidable from an economic point of view, deliberated, limited evaporation of water can allow for efficient cooling, while the $\text{H}_2\text{-H}_2\text{O}$ stream produced can be used as strip gas for the *DAC* unit.

6.4.5 Economics and ecological impact

Various studies that discuss the framework conditions of *DAC*^{85,200,289–292}, *PtG*^{69,246} and of the CO_2 -based production of fuels or of basic chemicals^{70,289,293} on a detailed level have been published. In line with these contributions, the key findings of this investigation read:

- The climate impact of the *DAC* concept and of the integrated *DAC-PtG* approach proposed severely depends on the energy source selected. Intense heat integration allows for autothermal operation, but a significant influence of hydrogen production by water electrolysis on the process energy balance is revealed. For example, if one considers the current CO_2 footprint of electric energy supply in Germany²⁹⁴ of 468 g kWh^{-1} , energy demands for electrolysis-based hydrogen production in the order of magnitude of 1400 kJ per mole CO_2 captured (Figure 6.16) would result in emissions of about 4 moles CO_2 per mole CO_2 captured
- Without additional constraints,²⁴⁶ e.g., CO_2 -certificate prices, the costs of methane produced via *Sabatier* reaction reach levels significantly above the current natural gas price²⁴⁶ of $0.02\text{--}0.03 \text{ \$ kWh}^{-1}$. For example, CO_2 costs of $1 \text{ \$ kg}^{-1}$ would result in *SNG* costs from *PtG*²⁴⁶ of $0.20 \text{ \$ kWh}^{-1}$ and current costs for H_2 production via water electrolysis²⁸⁰ of about $10 \text{ \$ kg}^{-1}$ would add costs of $0.38 \text{ \$ kWh}^{-1}$

Overall, importance of H_2 and CO_2 supply in the context of a sustainable realization of *PtG* approaches is underlined. At current state, use of *PtG* concepts does not appear to be beneficial from neither an economic nor an environmental perspective. However, these approaches can become key technologies in realization of a fast transition to a sustainable energy system based on renewable sources, with applications reaching from balancing of fluctuations in the electric grid to defossilization of the transport sector (Section 6.1).²⁴⁶

6.5 Summary and conclusion

Based on the findings presented in Chapter 5, which indicate that efficient measures to counteract the energy penalty arising from H₂O co-adsorption can be realized on a process level, detailed investigation of an intensified integrated *DAC – PtG* process is conducted.

Section 6.1 State of the art

indicates that there seems to exist a lack of research with respect to the integration of *DAC* technologies in *PtX* concepts. Even if some projects explicitly consider *DAC* as carbon source, integration is in general limited to application of approaches established on the market rather than simultaneous, integrated process development of *DAC* along *PtX*.

Section 6.2 Methanation of CO₂

reveals pressures of $1 \cdot 10^5 - 10 \cdot 10^5$ Pa and temperatures ranging 250–350 °C to be a promising operation window for the methanation process intended. Formation of carbon monoxide is noticed to become negligibly small, which allows for sufficiently accurate description of the methanation process by *Sabatier* reaction.

Section 6.3 Process design and key process units

identifies various synergies arising within the intensified integrated *DAC – PtG* process proposed (Section 6.3.1). The process water balance is found to become of great importance. The influence of the electrolysis operation point on process energy demand and water recycle is analyzed. Superiority of electrochemical compared to gas phase compression is not always confirmed (Section 6.3.2). Detailed analysis of the reaction section indicates definition of the reactor operation temperature and conversion via formulation of an optimization problem to be beneficial (Section 6.3.3).

Section 6.4 Process performance

is dedicated to the detailed analysis of process performance. High potential for autothermal operation is revealed (Section 6.4.1) and importance of process water balance (Section 6.4.2) for process energy and resource efficiency is underlined. Detailed investigation of the *DAC* unit (Section 6.4.3) confirms the high impact of its operation point on process water balance, energy demand and hydrogen losses. With this information at hand, the detailed investigation of process energy flows presented in Section 6.4.4 allows for profound insight into the dependency of the process behavior on its operation parameters. Autothermal production of CH₄ based on CO₂ and H₂O from ambient air is found to be feasible, with electrolysis energy demand being identified as key research priority. Moreover, simulation results indicate that use of electrolysis as heat source for *DAC* seems not beneficial. Basic evaluation of the economics and ecological impact of the concept proposed (Section 6.4.5) underlines the importance of the H₂ and CO₂ supply in the context of a sustainable realization of the intensified integrated *DAC-PtG* concept proposed.

In conclusion, the modeling and simulation conducted in this chapter combines the experimental results as well as concepts and approaches developed throughout this work to an intensified integrated process design that incorporates the exceptional potential of closing the carbon cycle by resource efficient, autothermal production of methane based on carbon dioxide and water captured from ambient air.

7 Conclusions and implications for future research

Abstract

Theoretical and experimental studies were performed to investigate an autothermally operated process design for the production of methane. For this purpose, intensified integrated air capture facilities that operate in spatial cyclic steady state were developed, which allow for significant reduction of the CO₂-specific energy demand of the capture process. Experimental investigations indicate the ion exchange resin *Lewatit VP OC 1065* to be a promising *DAC* sorbent. However, severe water co-adsorption on this sorbent is experimentally revealed. Heat recovery by vapor recompression along with water vapor strip gas use proves to be most promising among a variety of strategies investigated to counteract co-adsorption-based energy penalties. Integration of the concepts developed into a *PtG* approach results in various synergies that reduce the drawbacks arising in separate operation of the process steps. In-depth modeling and pinch analysis not only show feasibility of resource efficient, autothermal operation of the intensified integrated *DAC* – *PtG* process proposed, but moreover reveal potential for methane production solely based on educts captured from ambient air. Overall, results summarized indicate that future research priorities need to focus on more detailed experimental investigation of H₂O co-adsorption phenomena, on experimental validation of the *DAC* approaches proposed and on cost-optimized process designs.

This chapter is structured as follows:

Section 7.1 Conclusions

summarizes the interconnections between the different parts of this contribution and recapitulates the key findings.

Section 7.2 Implications for future research

evaluates the findings of this work with respect to future research implications.

7.1 Conclusions

Motivated by the conclusions summarized in the *Parisian Agreement*²⁷ and implications formulated in the *IPCC Special Report*³⁵ that large-scale use of *NET* seems mandatory to ensure the 1.5 °C target, this contribution is dedicated to the design of an intensified integrated approach to *DAC* and its integration into a *PtG* concept to realize autothermal, resource efficient production of methane. This can contribute to a closure of the global carbon cycle or even to a realization of net negative emissions (Chapter 1).

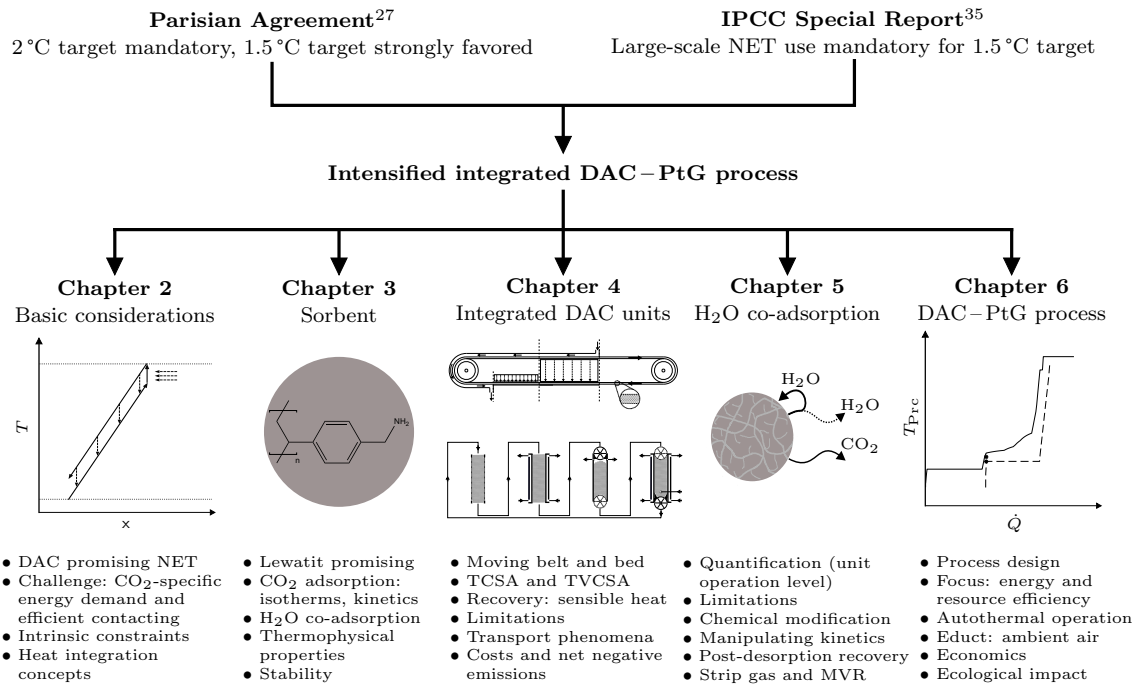


Figure 7.1: Graphical abstract of main findings obtained within the framework of this contribution.

Figure 7.1 outlines the overall structure of this work, which indicates that investigations in diverse research areas contribute to the realization of the process design proposed. Even if *DAC* is a promising approach to *NET*, the analysis given in Chapter 2 underlines that intrinsic constraints have to be overcome to realize its efficient large-scale use. Especially the high CO₂-specific energy demand of the separation process and the need of low pressure losses during air – sorbent contacting motivate the research of novel intensified integrated *DAC* designs. Transformation of the cyclic steady state of the adsorption process from time to space domain is proposed to allow for superior recovery of the sorbent sensible heat in commonly applied *TSA* processes.

With this concept and defined constraints at hand (Chapter 2), the amine grafted ion exchange resin *Lewatit VP OC 1065* is identified as suitable reference sorbent (Chapter 3). CO₂ isotherms represented by *Toth* model, determined by means of *BTC* and *TGA* experiments over a broad temperature and CO₂ pressure range of 30 – 100 °C and 40 – 2 · 10⁴ Pa, respectively, are found to be in good accordance with experimental data published by other research groups. Experimentally determined mechanical and thermophysical properties of this commercially available sorbent indicate its good applicability with respect to the heat

integration concepts intended. Moreover, water co-adsorption, well predictable by *BET*-type isotherm models, is confirmed for this sorbent. Even if the experiments conducted reveal increase of CO₂ capacity of up to 100 % under humid conditions, impedingly high H₂O : CO₂ capacity ratios of about 9 under ambient conditions motivate investigation of measures to counteract the influence of water co-adsorption on *DAC* performance.

Two research priorities arise from the results summarized in Chapters 2 and 3. These are the conceptual adsorber designs to realize the heat integration concepts proposed (Chapter 4) and the extension of these approaches by measures to reduce limitations attributed to water co-adsorption (Chapter 5). Detailed modeling and simulation indicate superior heat integration properties of novel *moving belt* and *moving bed adsorber* concepts developed. *TCSA* as well as *TVCSA* operation is investigated. Levels of sorbent sensible heat recovery greater than 95 % can be achieved. Moreover, the concepts are designed in accordance with the requirement of low gas phase pressure losses in the adsorption zone, such that CO₂–sorbent contacting driven by the kinetic energy of ambient air, i.e., by wind, seems feasible. A simulation-based analysis allows for insights into the operation characteristics of the systems and reveals mass transport limitations that result from CO₂ diffusion in the sorbent bed. Basic experimental investigations confirm this observation. A final ecologic evaluation underlines the severe influence of intensified heat integration on realization of net negative emissions, with an increase of the net negative CO₂ emissions of more than 0.5 kg kg⁻¹ relative to the CO₂ captured being noticed. Estimated capture costs above 1000 \$ t⁻¹ are at the upper limit of cost estimates for *DAC*. High potential for optimization of the economics of the concepts proposed is noticed.

Even if the sorbent sensible heat can efficiently be recovered by the concepts developed, the results presented in Chapter 5 reveal that water co-adsorption can result in high energy penalties that may impede the autothermal operation of an integrated *DAC-PtG* process. Without additional measures, maximum allowable H₂O : CO₂ desorption ratios are in the order of 1.9 mol mol⁻¹. These are significantly above the level of water co-adsorption determined by isotherm analysis of about 9 mol mol⁻¹. Evaluation on an unit operation level shows that decrease of water co-desorption to a level of 3.4 mol mol⁻¹ can be realized by careful selection of the *DAC* operation point. Motivated by the aim of further reducing energy penalties induced by water desorption, measures that take into account the adsorption and desorption process as well as post-desorption recovery strategies are evaluated. In-depth modeling and optimization reveals multi-stage *MVR* to be a promising measure that, based on use of mature technologies, can allow for a significant reduction of the water energy penalty. Overall, combined use of water vapor strip gas and of *MVR* is found to be one of the most promising strategies currently available to reduce the burden of water co-adsorption.

With an energy-efficient *DAC*–heat recovery concept at hand, focus is placed on an intensified integrated *DAC*–*PtG* process design in Chapter 6. Various synergies are identified, which reduce drawbacks that arise in independent operation of the subprocesses. Detailed analysis of the electrolysis used for hydrogen production reveals a significant influence of this unit on the process energy and water balance. Moreover, strong dependency between operation pressure, reaction temperature and CO₂ conversion attained within the multi-stage methanation process is shown using multi-variable optimization.

Process simulation, pinch analysis and cost estimation allow for profound insights into process performance. Strong influence of *DAC* operation on all process sections is noticed. Implementation of the electrolysis as heat source for the *DAC* unit is found to be not beneficial. Overall, high potential for realization of a resource efficient, autothermal production of methane based on carbon dioxide and water captured from ambient air is revealed.

7.2 Implications for future research

Even if great care was taken to ensure reliability of the experimental data obtained and of the theoretical models developed, implemented and evaluated, the results summarized are still subject to intrinsic constraints and uncertainties. These indicate need of future research priorities to focus on a more detailed experimental investigation and on cost-based optimizations. Reliable models for single component adsorption isotherms were determined and the influence of H₂O co-adsorption on CO₂ capacity is quantitatively confirmed. However, a more detailed experimental analysis is required to develop a physically sound 2-component isotherm model. This also holds true for a more detailed investigation of the sorption kinetics, especially with respect to the co-desorption of water.

Consequently, the models developed are subject to this lack of detailed data and correlations. Worst case approximations taken and evaluation of characteristic constraints limit the influence of these inaccuracies on the overall conclusions drawn. But a more detailed numerical simulation of the *DAC* unit on the basis of an extended set of experimental data is recommended for validation purpose. In this respect, realization of sorbent movement within the experimental setting is of great interest. However, it seems reasonable to limit the experimental effort to basic investigations, as detailed full-scale realization of the *moving belt* or *bed* concept proposed seems hard to achieve in lab-scale.

Use of *MVR* in combination with water vapor strip gas is found to be an efficient measure to counteract the influence of water co-adsorption. Additional concepts to support this approach might be realized through use of kinetic effects or through design of sorbents with hydrophobic properties. With focus on the former, need for a targeted development of hydrophobic membranes or coatings that offer high separation factors is revealed. Moreover, with respect to the realization of hydrophobic sorbent properties, extension of research to targeted sorbent synthesis seems beneficial.

Also in the field of process design deepening the research conducted becomes of interest. The intensive research of *PtX* currently conducted motivates extensions of the process simulation performed by more detailed unit operation models and by novel concepts, e.g., with respect to reactor design or to electrolysis operation. Multi-variable, mixed-integer optimization in combination with detailed *life cycle assessment (LCA)* might be utilized to determine optimal process configurations under economic as well as ecologic constraints.

In conclusion, the findings summarized in this contribution underline the great potential of air capture technologies to become an additional, powerful measure that contributes to the effort of realizing the 1.5 °C target of climate change. However, future research priorities formulated indicate that there are still various challenges to be addressed while time is pressing.

A Appendix: Characterization of the sorbent

Parts of this appendix have been published in a peer-reviewed journal article and in the corresponding supplementary information.²⁴⁰

A.1 State of the art: liquid sorbents

Strong interactions between sorbent and adsorbate provided by chemisorbents are required for an efficient realization of air capture technologies. Thus, use of solutions containing inorganic compounds is preferred to application of organic solutions that physically bind CO₂.^{41,85} In particular, research of liquid sorbents focuses on alkali and alkali-earth hydroxides. Besides others, calcium hydroxide Ca(OH)₂ belongs to this class of sorbents. Its ability to form calcium carbonate (CaCO₃) in a reaction with CO₂ built the basis for one of the first air capture concepts proposed.⁸⁴ High binding energy between CO₂ and the hydroxide allows for selective capture of CO₂. However, it comes along with a considerable energy requirement of the regeneration process⁹⁹ that includes high-temperature calcination (> 700 °C) of the carbonate to calcium oxide (CaO) associated with a heat requirement of 179 kJ mol⁻¹.⁶⁷ Besides this drawback, Ca(OH)₂ only shows a comparatively low solubility in water, which limits the specific capacity of the liquid sorbent.⁶⁷ Consequently, alternative sorbents have become subject to a more detailed investigation.

Change of the hydroxide to a sodium based system would allow to use regeneration concepts known from the paper industry (*Kraft process*). Moreover, these systems offer the advantage of a high water solubility of the carbonate formed.^{67,295} However, also for sodium hydroxide (NaOH) the binding energy of CO₂ is significantly higher than required.⁹⁹ This results in a minimum energy demand of the separation process of 109 kJ mol⁻¹, with the *Kraft process* also including a high temperature calcination step with a high energy requirement of 179 kJ mol⁻¹. Consequently, also the application of sodium based aqueous sorbents will come along with considerable energy demands.^{67,296} Besides the aforementioned hydroxides, potassium carbonate (KOH) might be applied as sorbent.²⁹⁷ However, reasoned in its higher costs compared to NaOH solutions, it is less intensively researched.⁶⁷

A.2 Applicability of BTC and TGA: ranges of validity

Pre-tests have been performed to investigate the range of validity of the measuring devices used. Generally, both experimental methods allow investigations in the Pa and kPa-range

of CO₂ partial pressure. However, considering *BTC* experiments, presence of CO₂ at a partial pressure in the kPa-range could lead to non-isothermal behavior, not observed at Pa-level (Appendix A.3.4). To avoid this difficulty, one might consider to lower the gas volume flow. But only limited changes are possible reasoned in the operation range of the *IR* gas analyzers ($20\text{ h}^{-1} \leq \dot{V}_{\text{IR,G}} \leq 100\text{ h}^{-1}$).¹⁷¹ Decrease of sample mass would be an alternative. But this would result in a faster breakthrough that leads to a reduced accuracy of the measurements. In dry residence time experiments the time scale of initial breakthrough is found to be in the order of 13 s, while an additional time span of typically less than 8 s is required to reach 50% of the final mole fraction. Thus, only a minor influence of this effect is noticed at Pa-level, at which adsorption times can exceed several hours. However, at high kPa-level the time scale of adsorption experiments typically lies in the order of 100 s, even at low adsorption temperatures. This indicates severe influence of residence time effects. Consequently, the range of validity of *BTC* experiments in the setting build up at high mole shares of the species to be adsorbed, especially in combination with high temperature levels, is limited.

TGA experiments were investigated for their applicability to measure the sorbent equilibrium loading at the CO₂ concentrations of interest. Long adsorption times required at Pa-level that can exceed several hours can result in comparatively high errors attributed to drifts of the mass measured in the *TGA* and minor fluctuations in the mass measured can limit the range of accuracy, especially at low sorbent loadings of significantly less than 1 mol kg⁻¹ expected (Appendix A.4.7). This indicates that the range of validity of *TGA* measurements at Pa-level is limited.

As a result of this basic analysis, *TGA* experiments are performed for investigations in the CO₂ mole fraction range larger than 1% and *BTC* experiments are realized to investigate the sorbent loading and adsorption kinetics in the ppm mole fraction range (reference pressure ca. 10⁵ Pa). As no humidification setup could be build up for *TGA* experiments, the analysis of humidity influence on CO₂ adsorption is limited to Pa-level experiments.

A.3 BTC experiments

This section provides more detailed information about the *BTC* experiments performed. Appendix A.3.1 gives a detailed insight into the materials and experimental design used. Based on this information, Appendix A.3.2- A.3.4 discuss the evaluation of the sorbent loading, temperature profile and of the pressure levels. Moreover, insight into the processing of humidity data is given (Appendix A.3.5). Finally, the analysis of kinetic information (Appendix A.3.6) and the derivation of error bounds (Appendix A.3.7) is presented in detail.

A.3.1 Material and experimental design

In this section the experimental setting and material used (Appendix A.3.1.1) is outlined. Moreover, a detailed insight into the adsorber design (Appendix A.3.1.2) is given.

A.3.1.1 Experimental setting and material

The detailed flow sheet of the *BTC* laboratory plant is outlined in Figure A.1, while a summary of the key equipment and of the material used is given in Table A.1. Automated plant control is realized by a *Labview*¹⁶⁹ interface, which is connected to the measurement devices and to the controllers via *Apax modules* from *Advantech*,²⁹⁸ provided by the electronic workshop of *TU Dortmund University*.

Three thermal mass flow controllers from *Bronkhorst (EL-Flow)*¹⁷⁰ allow for realization of defined gas flows of N_2 , CO_2 and test gas, i.e., synthetic air with a defined fraction of CO_2 . All gases are provided by *Messer*.²⁹⁹ Their purities are summarized in Table A.1. Temperature and pressure is recorded at various positions in the plant. Multiple temperature measurements are realized inside the adsorber by means of a 5-point thermocouple provided by *SE Sensor Electric*.³⁰⁰ Moreover, pressure, temperature and relative humidity measurements are recorded at the adsorber inlet and at its outlet. Besides, CO_2 share in the gas phase can be evaluated by two infrared devices, *URAS26 EL3020* from *ABB*.¹⁷¹ These allow for in situ determination of the CO_2 gas phase content in the range 0–500 pmm (IR-1) and 0–40 % (IR-2).

After leaving the mass flow controllers the gas can either be send to the IR devices, to the adsorber or to the humidifier. The design of the latter unit is visualized in Figure A.2. It is made up of a vessel with cooling jacket for temperature control. In its inner volume humidification of the gas phase is realized by dispersion of the gas flow inside the liquid phase. H_2O saturation pressure is adjusted by temperature control of the liquid phase via heat exchange with a cooling brine that flows inside the cooling jacket. The temperature of the brine is controlled via a cryostat with circulation pump (*F-25 ME*) from *Julabo*.³⁰¹

To avoid unwanted condensation of water, pipes and valves between the humidifier and adsorber are heated, by means of four electric heating belts from *HORST*,³⁰² and isolated. Temperature control is also required in the adsorber, the design of which is discussed in detail in Appendix A.3.1.2. It is realized by flow of a heating medium (silicon oil M50) through the double jacketed of the adsorber. The heating medium temperature is controlled by two thermostats with circulation pumps. To reduce heating and cooling times, thermostat 1 (*MV-4, Julabo*)³⁰³ provides a heating medium flow at adsorption temperature, while thermostat 2 (*SE-6, Julabo*)³⁰⁴ keeps the heating medium temperature at desorption temperature. By adjusting the various three way valves between the thermostats and adsorber, simultaneous operation of both thermostats is possible. Moreover, to allow for a better adjustment of the adsorption temperature, additional cooling of thermostat 1 is realized by means of a cooling spiral flown through with cooling water with a temperature of ca. 7 °C. Besides, additional cooling of the adsorber can be enabled by means of VE water flow through the cooling spiral inside of the adsorber heating jacket.

Leaving the adsorber, the gas phase can be cooled down in a cooler, which is realized as an inclined cylindrical vessel ($D_{Con,in} \approx 3$ cm, $L_{Con} \approx 24$ cm) with cooling jacket and internal cooling spiral. Temperature control is realized by cooling water flow with a temperature of ca. 7 °C. If a gas stream with relative humidity level close to or above its saturation point enters the gas cooler, reduction of the humidity level can be reached within this unit. Possible water condensed is removed in the separator, which is realized as a T-connector in the pipe, with the water being stored in the lower part of the hori-

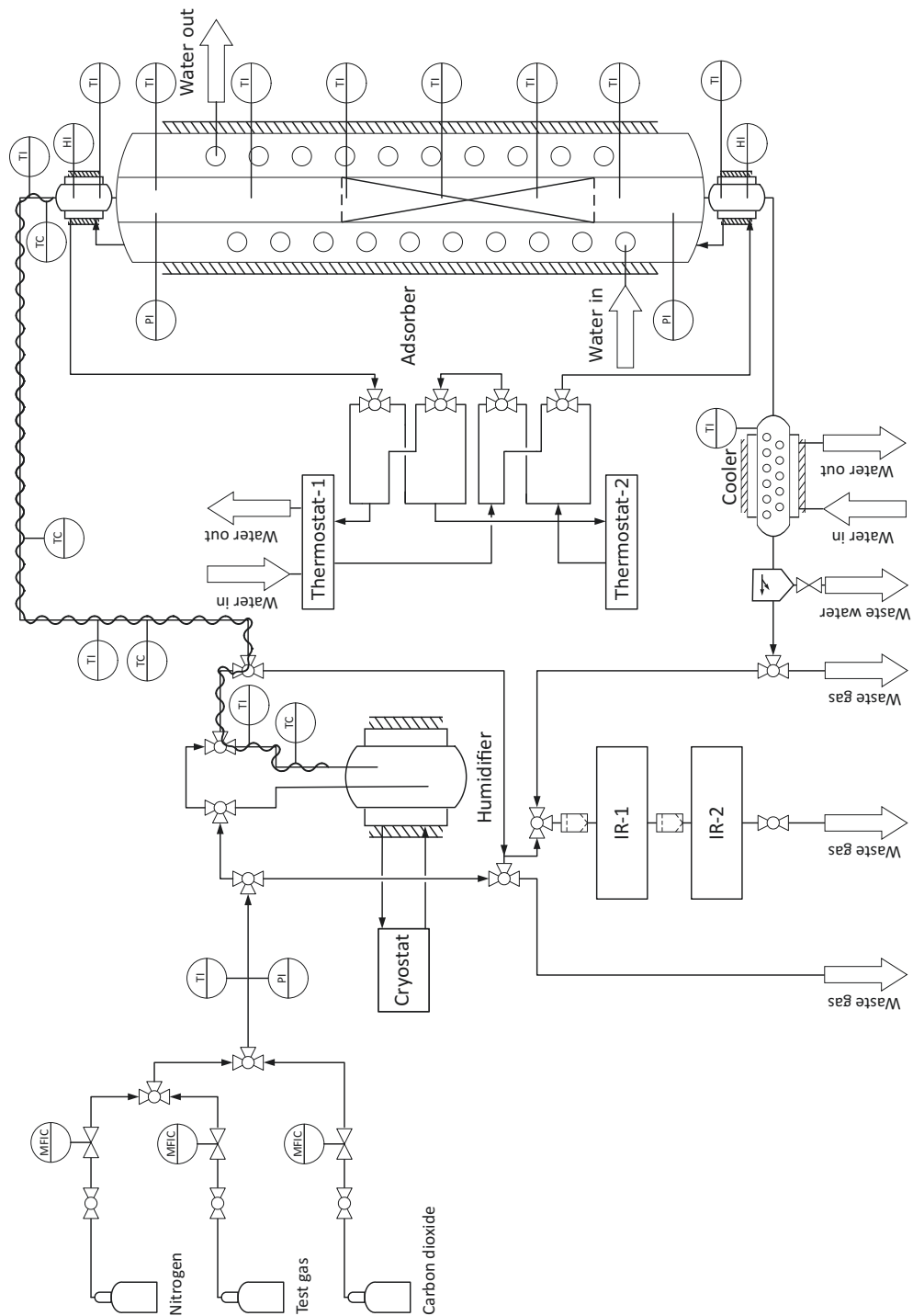


Figure A.1: Detailed flow sheet of the experimental setting used for *BTC* experiments. For reasons of clarity cooling water flow and adsorber design are not depicted in detail. For a detailed insight into the adsorber design, the reader is referred to Appendix A.3.1.2.

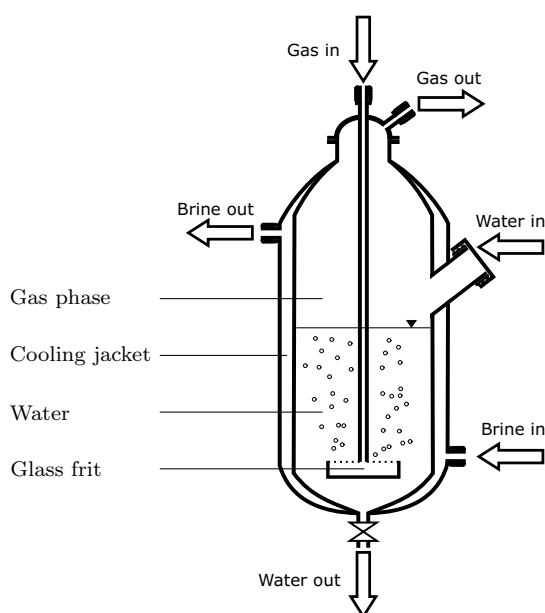


Figure A.2: Basis design of the humidifier used in *BTC* experiments. In contrast to the gas and cooling brine flow, the flow of water is not continuous. For reasons of clarity the isolation of the device is not shown.

zontal tube of ca. 6 mm diameter. The tube used as water reservoir is closed during the experiments. Its length measured from the T-connector to the closed end is ca. 4 cm. As an additional safety measure to prevent entrainment of water into the IR devices, removal of this component is realized by means of a filter (*Disposable filter 50K, ABB*).

A.3.1.2 Adsorber design

The basic design of the adsorber, including the humidity measurement, is visualized in Figure A.3. Key dimensions and properties are summarized in Table A.2.

As shown in Figure A.3 the design of the adsorber and of the measurement devices associated can be subdivided in three main parts. These are the humidity measurements, the central part of the adsorber, i.e., the element between the heating spirals, and the upper / lower connectors with associated measurement devices. The central part of the adsorber has been taken from the inventory of the *Laboratory of Chemical Reaction Engineering (CVT)*, whereas all other parts shown have been designed and built within the course of this contribution.

At the adsorber inlet and at its outlet the relative humidity in the gas phase is measured. To avoid water condensation and strong temperature differences relative to the sorbent bed, the probes for humidity measurement are inserted via common PTFE screw connectors (*GL25, Schott*)³¹⁰ into a gas phase that is surrounded by a heating jacket. This is flown through by the same thermal oil used for temperature control of the adsorber. The piping between the humidity measurement devices and upper / lower glass elements of the adsorber is kept at a minimum, i.e., at less than 1 cm.

Table A.1: Equipment and material used to perform *BTC* experiments. *Workshop of *TU Dortmund University*

	Provided by	Additional information	Source
Equipment			
Adsorber	Glass workshop*	Detailed description in Appendix A.3.1.2	
Apax Box	Electronic workshop* <i>Advantech</i>		[298]
Cooler	Glass workshop* (<i>CVT</i> inventory)	Pipe with cooling jacket and cooling spiral $D_{\text{Co}_2, \text{in}} \approx 3 \text{ cm}$, $L_{\text{Co}_2} \approx 24 \text{ cm}$	
Cryostat	<i>Julabo</i>	Model: <i>F-25 ME</i> , cryostat with circulation pump	[301]
Filter	<i>ABB</i>	Model: <i>Disposable filter 50K</i>	
Heating belt	<i>HORST</i> Electronic workshop*	Model: <i>020302</i> , electric heating belt Module for power supply realized by electronic workshop	[302]
Humidifier	Glass workshop* (<i>CVT</i> inventory)	Vessel with cooling jacket and gas dispersing device Visualization in Figure A.2 $V_{\text{Hum,G}} \approx 97 \text{ ml}$, $V_{\text{Hum,L}} \approx 74 \text{ ml}$	
Humidity indicator	<i>GHM Messtechnik</i> <i>VWR international</i>	Model: <i>TFS 0100 E</i> , Capacitive polymer humidity sensors Model: <i>Qhygro-temp 60</i> (adsorber inlet), data processing Model: <i>GMH3350-CO</i> (adsorber outlet), data processing	[172, 305]
Infrared device	<i>ABB</i>	Model: <i>URAS26 EL3020</i> , IR-1: 0–500 pmm, IR-2: 0–40 %	[171]
Mass flow control	<i>Bronkhorst</i>	Model: <i>EL-Flow</i> , thermal mass flow controllers	[170]
Scale	<i>Kern & Sohn</i>	Model: <i>ALS 220-4</i>	[306]
Thermocouple (1-point)	<i>CVT</i> inventory	Type K (NiCr-Ni)	
Thermocouple (5-point)	<i>SE Sensor Electric</i>	Type K (NiCr-Ni), $D_{\text{The}} \approx 5 \text{ mm}$	[300]
Thermostat	<i>Julabo</i>	Model: <i>MV-4</i> (thermostat-1), <i>SE-6</i> (thermostat-2) Thermostat with circulation pump	[303, 304]
Pressure sensor	<i>Gems</i> <i>WIKA</i>	$0 \text{ Pa} \leq p_{\text{mea}} \leq 2.5 \cdot 10^5 \text{ Pa}$ Model: <i>3300B025A05G000</i> (<i>Gems</i> , adsorber inlet and outlet) Model: <i>S-10-A-SBF-GB-ZGA4ZAZ-ZZZ</i> (<i>WIKA</i> , periphery)	[307, 308]
Gas			
Nitrogen	<i>Messer</i>	Quality: technical	[299]
Test gas (ppm fraction)	<i>Messer</i>	CO_2 in syn. air, quality CO_2 : 4.5, quality syn. air: 5.0 Relative error in CO_2 content $\pm 2\%$	[299]
Test gas (% fraction)	<i>Messer</i>	CO_2 in N_2 , quality CO_2 : 4.5, quality N_2 : 5.0 Relative error in CO_2 content $\pm 2\%$	[299]
Additional material			
Cooling brine	<i>TU Dortmund Uni.</i>	Mixture of VE water (<i>TU Dortmund University</i>) and isopropanol Volume ration ca. 7 : 3	
Cooling water	<i>TU Dortmund Uni.</i>	Provided by <i>TU Dortmund University</i> , temperature ca. 7 °C	
Glass beads	<i>Netzsch</i>	<i>GlasBeads 0.5</i> , $D_{\text{Gla}} \approx 0.4\text{--}0.6 \text{ mm}$, $\rho_{\text{Gla}} = 2.5 \cdot 10^3 \text{ kg m}^{-3}$	[173]
<i>Lewatit</i>	<i>Lanxess</i>	Information summarized in Table 3.4	[162]
Silicon oil	<i>CVT</i> inventory	Silicon oil M50	
VE water	<i>TU Dortmund Uni.</i>		

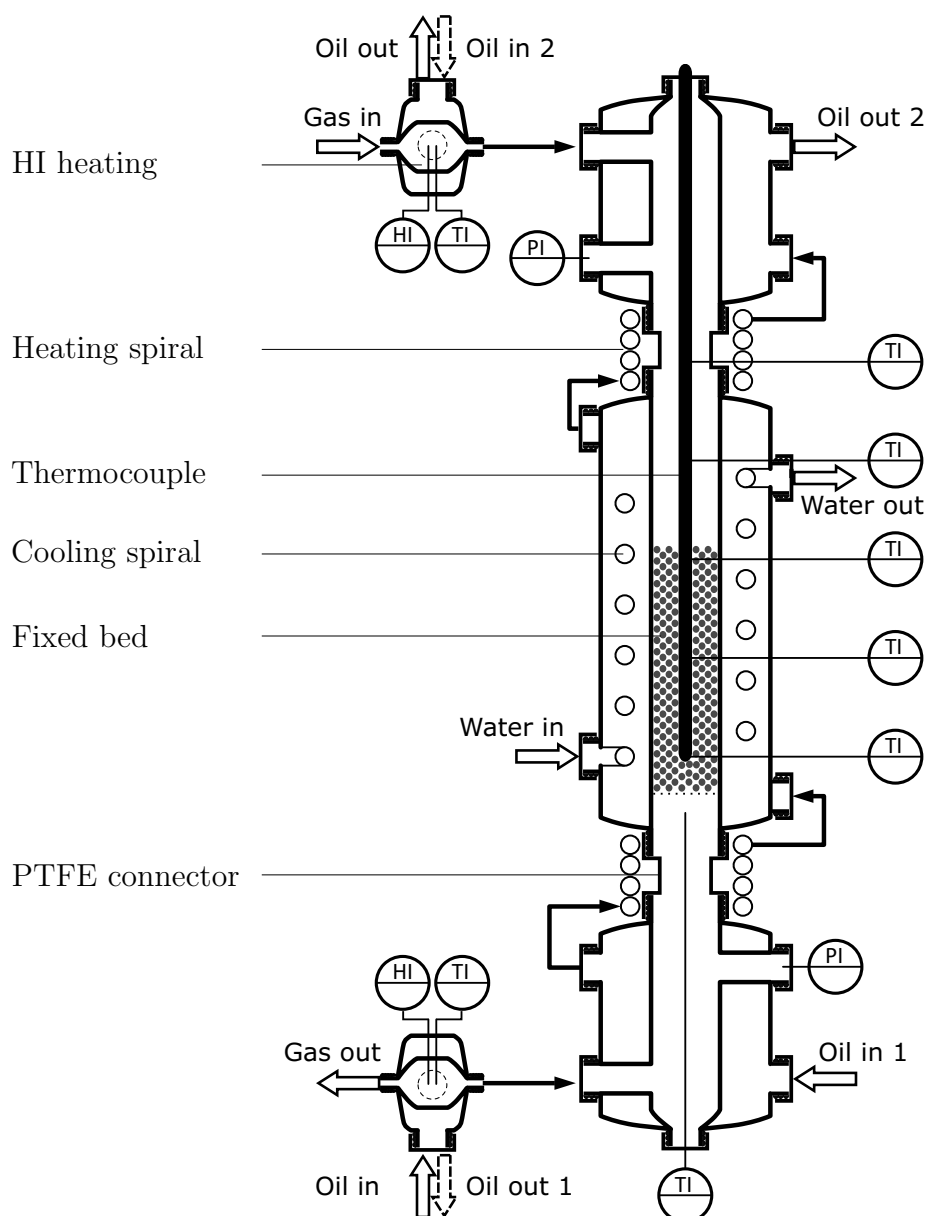


Figure A.3: Closeup of the adsorber column and of the humidity indicators. All devices shown are isolated with glass wool. For reasons of clarity the isolation is not depicted in detail. Characteristic dimensions and properties of the adsorber are summarized in Table A.2.

Glass elements below and above the adsorber central element provide PTFE screw connectors for pressure (*GL18, Schott*)³¹⁰ and temperature probes (*GL14, Schott*).³¹⁰ Temperature control is realized by a heating jacket. The thermal oil used also flows through the adsorber heating jacket and through the heating spirals that surround the PTFE screw elements (*GL32, Schott*)³¹⁰ used to connect the adsorber central part to the upper and lower glass elements.

The central element of the adsorber is made up of a glass tube with a diameter of 2 cm that is surrounded by a heating jacket. In addition to thermal oil flow for heating purpose,

Table A.2: Characteristics of the adsorber.

Characteristics			Source
Bed			
Bed height	L_B	Adsorber bed height, $L_B = 17.4$ cm	
Bed diameter	D_B	Adsorber bed diameter, $D_B = 2$ cm	
Void fraction	ψ_B	Bed void fraction for calculations, $\psi_B = 0.34$	
Fill			
Sorbent	m_{Sor}	<i>Lewatit VP OC 1065</i> Sorbent mass (air dried) $m_{\text{Sor,loa}} \approx 5.01$ g, sorbent mass $m_{\text{Sor}} \approx 4.27$ g (Appendix A.4.2)	[162]
Glass beads	m_{Gla}	<i>GlasBeads 0.5</i> Mass (adsorption experiments) $m_{\text{Gla}} \approx 75.12$ g Mass (breakthrough curve experiments) $m_{\text{Gla}} \approx 86.98$ g	[309]
Thermoelement (5-point)			
Height	$L_{B,\text{The}}$	Height of thermoelement in bed, $L_{B,\text{The}} \approx 11.3$ cm	
Diameter	D_{The}	Diameter of thermoelement, $D_{\text{The}} \approx 0.5$ cm	[300]
Gas phase			
Height (in)	$L_{G,\text{in}}$	Height of gas phase above bed (up to adsorber inlet), $L_{G,\text{in}} \approx 23.6$ cm	
Height (out)	$L_{G,\text{out}}$	Height of gas phase below bed (up to adsorber outlet), $L_{G,\text{out}} \approx 17$ cm	
Diameter	D_G	Diameter of gas phase, $D_G \approx 2$ cm	

flow of VE water through a cooling spiral inside the double jacket is possible. Connectors for cooling water flow and all connectors for thermal oil are of common PTFE screw type (*GL18, Schott*).³¹⁰ The fixed bed is made up of the sorbent and of glass particles (Table A.2). It is supported by a glass frit that allows for gas flow while preventing sorbent and glass particles from leaving the adsorber. Information about the temperature profile inside the bed is obtained using a 5-point thermocouple,³⁰⁰ which records the temperature at 5 cm intervals, starting at the lower end of the device. Moreover, a single point temperature measurement is realized directly below the glass frit.

A.3.2 Sorbent loading

The loading of CO₂ in dry (Appendix A.3.2.1) and humid atmosphere (Appendix A.3.2.2), as well as of H₂O (Appendix A.3.2.3) on *Lewatit* is determined via breakthrough curve experiments, the results of which are exemplified in Figure A.4.

A.3.2.1 CO₂ loading in dry atmosphere

Figure A.4(a) depicts the results obtained from CO₂ *BTC* experiments in dry atmosphere. The typical sigmoidal evolution of the CO₂ mole fraction $y_{\text{Adsout,G,CO}_2,\text{exp}}$ measured at the adsorber outlet with time t is observed. Minor fluctuations in the profiles recorded are only noticed at CO₂ shares close to the mole fractions expected to be reached in equilibrium

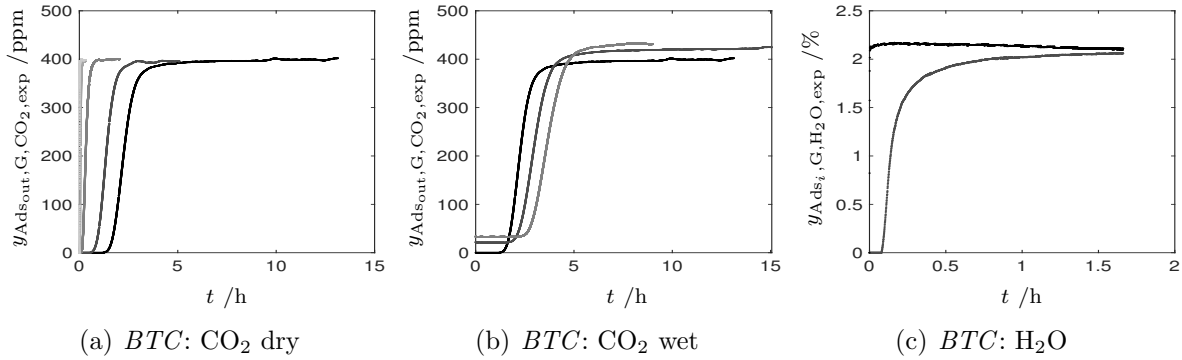


Figure A.4: Examples of experimentally obtained breakthrough curves. (a) CO₂ breakthrough curves for a mole fraction set of 400 ppm at a system pressure $p_{\text{exp,asp}}$ of $1 \cdot 10^5$ Pa. Different temperature level $T_{\text{exp,asp}}$ investigated are shown in shades of gray (from dark to bright): 30, 40, 60, 80 and 100 °C. (b) CO₂ breakthrough curves for a mole fraction set of 400 ppm and temperature level $T_{\text{exp,asp}}$ of 30 °C, for levels of relative humidity aspired $\phi_{\text{rh,exp,asp}}$ shown in shades of gray (from dark to bright): 0, 25 and 50 %. (c) Breakthrough curves of water measured at the adsorber inlet (●) and at its outlet (◐) recorded at $\phi_{\text{rh,exp}} = 50\%$ and $T_{\text{exp,asp}} = 30\text{ °C}$.

with the solid phase. As expected, increase in operation temperature $T_{\text{exp,asp}}$ shifts the start of the breakthrough to lower times.

Sorbent loadings are calculated by means of (3.1). The start of the adsorption time is determined based on the response of the mass flow controller and of the operation pressure recorded to the change in the flow controller set point, to account for delays in its response. The experiment is stopped when the influence of fluctuations observed exceeds the general trend of increase in measurements. This way, relative differences between the maximum mole fraction recorded and equilibrium mole fraction expected based on the certified mole fraction of the test gases used of less than 1.2 % are reached. However, the maximum mole fractions recorded are noticed to exceed the levels expected based on the certificate of the test gases used. This is mainly attributed to the sensitivity of the *IR* device used towards temperature as well as to the confidence range of the test gas mole fractions of $\pm 2\%$ given by the vendor.²⁹⁹ However, the realization of multiple *IR* re-calibration cycles in dependence of the experimental parameters seems not beneficial with respect to the error arising from re-calibration and to the comparability of the experiments. Nevertheless, to account for the inaccuracies named, mole fractions measured are scaled ($y_{\text{Ads}_{\text{out}}, \text{G}, \text{CO}_2, \text{sca}}$) such that the maximum mole fraction recorded equals the mole fraction defined by the test gas certificate. Moreover, the final time in evaluation of the integral in (3.1) is defined by the point in time at which the maximum mole fraction is recorded.

Great care is taken to ensure that the volumes of the adsorber and of its periphery are kept as small as possible. A detailed analysis reveals residence time effects to take small influence on low temperature measurements, e.g., the sorbent loadings calculated are affected by less than 0.5 % for measurements taken at 30 °C. However, a significant influence on high temperature measurements is noticed, e.g., an increase of the loading calculated in the order of 40 % for measurements taken at 100 °C is noticed. Consequently, to account for this effect in the calculation of the sorbent loadings, q_{CO_2} obtained based on (3.1) is reduced by the fictitious loading $\Delta q_{\text{res}, \text{CO}_2}$ derived via application of (3.1) on

breakthrough curves obtained from residence time experiments. CO₂ loadings determined by application of the procedure described are summarized in Table A.3.

Table A.3: CO₂ loading $q_{\text{eq1,CO}_2,\text{exp}}$ obtained from *BTC* experiments in dependence of the CO₂ partial pressure $p_{\text{CO}_2,\text{exp,asp}}$ and temperature level $T_{\text{exp,asp}}$ aspired to be realized in the experiments. The loading is given in the dimension mol kg⁻¹.

$T_{\text{exp,asp}}$ /°C	$p_{\text{CO}_2,\text{exp,asp}}$ /Pa			
	10	20	30	40
30	0.449	0.652	0.745	0.911
40	0.245	0.367	0.443	0.516
60	0.042	0.073	0.110	0.127
80	0.006	0.011	0.016	0.022
100	0.001	0.002	0.003	0.004

A.3.2.2 CO₂ loading in humid atmosphere

Figure A.4(b) visualizes the dependency of the CO₂ breakthrough curves measured on the level of relative humidity present. Similar to the experiments performed in dry atmosphere (Appendix A.3.2.1), sigmoidal mole fraction profiles are recorded. Formation of an offset in the mole fraction data recorded by the *IR* device is noticed to be caused by the water content in the gas phase. As indicated in Figure A.4(b), the observed offset appears to take on a constant value. This motivates its correction by reducing the measured CO₂ fractions by a constant offset. To account for minor, fast fluctuations within the measurements taken, this correction is determined based on the mean mole fraction recorded over the first 180 s after the start of the experiment for co-adsorption measurements, first 6 s for residence time measurements, respectively. After this correction is applied, the determination of sorbent loading q_{CO_2} is performed in analogy to the evaluation of the dry sorbent loading (Appendix A.3.2.1). Here, additionally the diluting effect of water vapor on CO₂ mole fraction is considered. Moreover, separate experimental investigation and correction of residence time effects is performed. CO₂ loadings obtained are summarize in Table A.4.

A.3.2.3 H₂O loading

The evolution of the water breakthrough curves in time is exemplified in Figure A.4(c). In contrast to CO₂ *BTC* experiments the H₂O mole fraction in the gas phase is determined before and after the adsorber unit. Mole fraction data are derived from relative humidity $\phi_{\text{rh,exp}}$ measurements under the assumption of ideal gas phase behavior. The water saturation pressure $p_{\text{sat,H}_2\text{O}}$ required for the calculation is evaluated by means of basic *Antoine* equation with a parameter set given by Poling et al.¹²⁶ Time resolved information on gas phase temperature and pressure required are provided by the humidity indicators and pressure sensors, respectively, before and after the adsorber.

Table A.4: CO₂ loading $q_{\text{eq},\text{CO}_2,\text{exp}}$ obtained from *BTC* experiments in dependence of the CO₂ partial pressure $p_{\text{CO}_2,\text{exp,asp}}$ and relative humidity level $\phi_{\text{rh,exp,asp}}$ aspired to be realized in the experiment. Operation at a temperature $T_{\text{exp,asp}}$ of 30 °C is targeted. The loading is given in the dimension mol kg⁻¹.

$\phi_{\text{rh,exp,asp}}$ /%	$p_{\text{CO}_2,\text{exp,asp}}$ /Pa			
	10	20	30	40
0	0.449	0.652	0.745	0.911
25	0.734	0.928	1.108	1.177
50	0.921	1.098	1.291	1.392

A fast increase in H₂O mole shares with time is recorded before the adsorber, whereas a sigmoidal evolution of this state variable in time domain is observed at the adsorber outlet. Great care is taken to achieve step function-like profiles measured before the adsorber. However, overshoots could not always be avoided. These are attributed to the strong dependency of the profiles obtained on the experimental setting, especially on the water bath temperature and on the pipe heating.

The sorbent H₂O loading is determined by means of equation (3.1). Similar to the calculation of the CO₂ loading (Appendix A.3.2.1 and A.3.2.2), the starting point of the integration is defined based on the response of the mass flow controller and of the operation pressure to a change in the flow controller set point. The experiment is stopped when the formation of a plateau in the humidity data recorded is observed. This is, the slope of the water mole fraction profile recorded over the last 180 s of the experiment (resolution of 2 s) takes values below 0.5 % min⁻¹ relative to the mean mole share measured. However, even if the humidity indicators have been calibrated with great care, minor variations between the mole fractions obtained at the adsorber inlet and at its outlet are observed. A detailed analysis suggests that these effects result from measurement inaccuracies of the humidity indicators rather than adsorption effects. To minimize these inaccuracies, all mole fraction profiles, including H₂O residence time measurements, are scaled such that the mean H₂O mole share calculated from the data taken over the last 180 s of the measurement at a single humidity indicator ($y_{\text{G,H}_2\text{O},\text{sca}}$) equals the mean H₂O fraction calculated based on the $y_{\text{G,H}_2\text{O},\text{exp}}$ profiles of both humidity indicators in this time frame.

Residence time effects are found to affect the sorbent loadings calculated by less than 8 %. Similar to the determination of the CO₂ loadings, these inaccuracies are minimized by consideration of the fictitious loading $\Delta q_{\text{res,H}_2\text{O}}$ derived via application of (3.1) on breakthrough curves obtained from residence time experiments. An overview of the sorbent loadings $q_{\text{eq},\text{H}_2\text{O},\text{exp}}$ in dependence of the mean relative humidity $\phi_{\text{rh,exp,ads,end,men}}$ (Appendix A.3.5), pressure $p_{\text{exp,ads,end,men}}$ (Appendix A.3.3) and temperature $T_{\text{exp,ads,end,men}}$ (Appendix A.3.4) in the sorbent bed is given in Table A.5.

Table A.5: Sorbent loadings $q_{\text{eq},\text{H}_2\text{O},\text{exp}}$ in dependence of the mean temperature $T_{\text{exp,ads,end,men}}$ and of the mean relative humidity $\phi_{\text{rh,exp,ads,end,men}}$ for different temperature levels aspired to be reached in the experiment $T_{\text{exp,asp}}$.

$T_{\text{exp,asp}}$ / $^{\circ}\text{C}$	$T_{\text{exp,ads,end,men}}$ / $^{\circ}\text{C}$	$\phi_{\text{rh,exp,ads,end,men}}$ /-	$q_{\text{eq},\text{H}_2\text{O},\text{exp}}$ / mol kg^{-1}
25.0	26.1	0.18	1.27
25.0	25.9	0.39	2.91
25.0	25.8	0.51	3.87
25.0	25.8	0.73	6.18
30.0	30.2	0.10	0.75
30.0	31.3	0.18	1.47
30.0	30.0	0.19	1.52
30.0	31.7	0.21	1.34
30.0	30.3	0.23	1.63
30.0	30.4	0.23	1.83
30.0	30.0	0.23	1.66
30.0	31.0	0.23	1.69
30.0	30.9	0.26	1.83
30.0	30.7	0.27	1.76
30.0	29.9	0.28	2.23
30.0	30.7	0.36	2.42
30.0	30.1	0.43	4.92
30.0	30.6	0.47	3.37
30.0	30.2	0.47	4.10
30.0	30.3	0.48	4.31
30.0	30.3	0.48	3.66
30.0	30.0	0.51	4.62
30.0	31.1	0.57	4.91
30.0	31.2	0.61	5.80
30.0	31.2	0.62	5.38
30.0	31.4	0.67	6.75
30.0	30.7	0.72	7.26
40.0	40.1	0.09	0.61
40.0	40.1	0.18	1.35
40.0	40.2	0.41	2.61
40.0	40.0	0.54	4.56

A.3.3 Pressure levels

The operation pressures in the adsorber bed relevant for the evaluation of the adsorption isotherms and for the kinetics are measured by the pressure indicators before and after the adsorber unit. A low pressure loss over the adsorber bed is recorded that typically takes values in the order of $2 \cdot 10^3$ Pa. This motivates definition of the bed pressure as the mean value recorded by the indicators. This operation parameter typically lies in

the order of $1.04 \cdot 10^5$ Pa. For the isotherm analysis, the mean over the measurements taken in the last 180 s of the evaluation time defines the bed pressure ($p_{\text{exp,ads,end,men}}$). For kinetic evaluation this parameter is determined by the mean pressure over the time frame during which the kinetic analysis is performed ($p_{\text{exp,kin,men}}$). The CO₂ partial pressure for isotherm evaluation is defined via the product of $p_{\text{exp,ads,end,men}}$ with the CO₂ gas phase mole fraction given by the test gas certificate. For humidity measurements the CO₂ mole share is corrected by the dilution effect of water vapor. Similarly, the reference CO₂ partial pressure for kinetic evaluation $p_{\text{CO}_2,\text{exp,kin,men}}$ is calculated via the product of $p_{\text{exp,kin,men}}$ and the test gas CO₂ mole fraction.

A.3.4 Temperature levels

Temperature is recorded at three positions in the sorbent bed. The bed temperature is defined based on the mean of these measurements. In analogy to the pressure level (Appendix A.3.3), temperature levels for isotherm evaluation $T_{\text{exp,ads,end,men}}$ and for kinetic evaluation $T_{\text{exp,kin,men}}$ are defined. During the adsorption experiments a maximum variation of temperature with time at the single measuring points of less than 1.5 °C for CO₂ measurements, 6.7 °C for H₂O measurements, respectively, is observed. High temperature variations in H₂O adsorption experiments are attributed to the heat release by adsorption. Consequently, hot spot formations in the early phase of the adsorption experiments are noticed. However, maximum deviations between the mean bed temperature during adsorption and the temperature level aspired $T_{\text{exp,asp}}$ of less than 1.5 °C for CO₂ adsorption experiments and of 1.9 °C for H₂O adsorption measurements underline that the adsorber in general operates close to the temperature level aspired.

A.3.5 Relative humidity levels

The level of relative humidity is determined by the humidity indicators before and after the adsorber. As discussed in Appendix A.3.2.3, time resolved data obtained are converted to scaled H₂O mole fraction profiles $y_{\text{G,H}_2\text{O,sca}}$. The mean mole fraction $y_{\text{G,H}_2\text{O,exp,ads,end,men}}$ is defined in analogy to $p_{\text{exp,ads,end,men}}$ (Appendix A.3.4). Finally, the mean relative humidity in the sorbent bed $\phi_{\text{rh,exp,ads,end,men}}$ is obtained based on the state variables $y_{\text{G,H}_2\text{O,exp,ads,end,men}}$, $p_{\text{exp,ads,end,men}}$ and $T_{\text{exp,ads,end,men}}$. Here, ideal gas behavior is assumed and the water saturation pressure $p_{\text{sat,H}_2\text{O}}$ is calculated by means of basic *Antoine* equation¹²⁶.

A.3.6 Kinetic parameters

In this section the thermophysical model used for evaluation of the adsorption kinetics based on the *BTC* experiments conducted is outlined (Appendix A.3.6.1). The thermophysical interpretation of the driving force coefficient is discussed (Appendix A.3.6.2) and the results obtained from data fit (Appendix A.3.6.3) based on these models are analyzed (Appendix A.3.6.4). Moreover, the evaluation of the kinetics for humid gas phase conditions is discussed in Appendix A.3.6.5.

A.3.6.1 Thermophysical model

In analogy to the evaluation of the equilibrium loading (Appendix A.3.2), the analysis of CO₂ adsorption kinetics is based on single point measurements ($y_{\text{Adsout,G,CO}_2}$) at the adsorber outlet. The time resolved information taken at this point are influenced by the state variable profiles formed in the adsorber. Consequently, the thermophysical model proposed needs to take into account the evolution of state variables along the adsorber axis. No significant influence of wall effects is expected, as the limiting diameter of gas flow within the column even in the worst case scenario is in the dimension of 15 particle diameters.³¹¹ Thus, a one-dimensional modeling approach is proposed that assumes ideal gas behavior in an adsorber with axial dispersed plug flow. As the cross-section area of the thermocouple housing inside the adsorber only reduces the adsorber cross-section by 6.25 %, influence of this device is not accounted for in the modeling. For more detailed information on the adsorber design and on the sorbent bed configuration, the reader is referred to Appendix A.3.1

The evolution of the CO₂ concentration in the gas phase $c_{\text{G,CO}_2}$ is defined by

$$\begin{aligned} \frac{\partial c_{\text{G,CO}_2}}{\partial t} = & - \frac{\partial}{\partial x} (\mathbf{u}_{\text{G}} \cdot c_{\text{G,CO}_2}) + \frac{\partial}{\partial x} \left(D_{\text{dis,x}} \cdot \frac{\partial c_{\text{G,CO}_2}}{\partial x} \right) \\ & - \frac{k_{\text{df,ads,CO}_2} \cdot \rho_{\text{B,Sor}}}{\psi_{\text{B}}} \cdot (\mathbf{q}_{\text{eq,CO}_2} - \mathbf{q}_{\text{CO}_2})^{n_{\text{ord}}} . \end{aligned} \quad (\text{A.1})$$

Here, $D_{\text{dis,x}}$ describes the axial dispersion coefficient

$$D_{\text{dis,x}} = \frac{D_{\text{dif,CO}_2,\text{Air,mol}}}{\sqrt{2}} + \frac{\mathbf{u}_{\text{G}} \cdot D_{\text{men,P}}}{2} \quad (\text{A.2})$$

calculated in dependence of the diffusion coefficient $D_{\text{dif,CO}_2,\text{Air,mol}}$, the derivation of which is summarized in Table B.3, and of the mean particle diameter $D_{\text{men,P}}$.³¹¹ In good accordance to the effective particle diameter of *Lewatit*¹⁶² and to the mean diameter of the glass beads³⁰⁹ used, $D_{\text{men,P}}$ takes a value of 0.5 mm. Moreover, axial dispersion is influenced by the gas phase velocity \mathbf{u}_{G} , the profile of which is evaluated by

$$0 = -c_{\text{G}} \cdot \frac{\partial \mathbf{u}_{\text{G}}}{\partial x} - \frac{k_{\text{df,ads,CO}_2} \cdot \rho_{\text{B,Sor}}}{\psi_{\text{B}}} \cdot (\mathbf{q}_{\text{eq,CO}_2} - \mathbf{q}_{\text{CO}_2})^{n_{\text{ord}}} . \quad (\text{A.3})$$

This equation is derived based on the assumption of operation at constant pressure $p_{\text{exp,kin,men}}$ and temperature $T_{\text{exp,kin,men}}$. Determination of these state variables is outlined in Appendix A.3.3 and A.3.4. Equation (3.4) that describes the evolution of sorbent loading \mathbf{q}_{CO_2} , completes the set of equations used. This is solved by means of time integration via *Matlab*^{®178} after discretization of the spatial domain via a finite volume schema (*method of lines, MOL*)³¹².

Boundary conditions applied represent an ideal step function of the concentration profile in time domain at the adsorber inlet. The conditions in spatial domain read

$$c_{\text{G,CO}_2}|_{x=0,t} = c_{\text{Adsin,G,CO}_2} + \frac{D_{\text{dis,x}}}{\mathbf{u}_{\text{Adsin,G}}} \cdot \frac{\partial c_{\text{G,CO}_2}}{\partial x} \quad (\text{A.4})$$

$$\left. \frac{\partial c_{G,CO_2}}{\partial x} \right|_{x=L_{Ads,B},t} = 0 \quad (A.5)$$

$$u_G|_{x=0,t} = u_{Ads_{in},G} , \quad (A.6)$$

whereas the initial conditions can be summarized as follows

$$c_{G,CO_2}|_{x,t=0} = 0 \quad (A.7)$$

$$q_{CO_2}|_{x,t=0} = 0 . \quad (A.8)$$

The gas phase concentration at the adsorber inlet c_{Ads_{in},G,CO_2} is calculated based on the gas phase properties in the adsorber and on the CO_2 mole share in the test gas. Moreover, the gas phase velocity at the adsorber inlet $u_{Ads_{in},G}$ is assumed to stay constant in time and to take the average value calculated from the data recorded by the corresponding mass flow controller during the time frame of kinetic investigation $u_{Ads_{in},G,exp,kin,men}$.

Note that the model proposed focuses on the influence of the adsorber on the shape of the mole fraction profile recorded by the *IR* device. Consequently, it does not include influences of residence time distribution by the adsorber peripheries. A slow increase in CO_2 mole fraction that can exceed several hours in low temperature adsorption measurements is noticed, whereas less than 8 s are required to reach 50 % of the final mole fraction starting from the first increase in mole fraction detected in the residence time experiments. This suggests that the influence of the residence time distribution that arises from the adsorber peripheries is small for low-temperature experiments and, thus, motivates to place the focus of the kinetic analysis on experiments conducted at $T_{exp,asp} \leq 60$ °C. In line with the determination of the sorbent loading (Appendix A.3.2), the influence of dead times, which is not captured by the model itself, is taken into account to further increase the accuracy of the kinetic evaluation. This is realized by shifting the start time of the kinetic evaluation compared to the start of the adsorption experiment by

$$\Delta t_{dea,kin} = \frac{\Delta q_{res,CO_2} \cdot m_{Sor}}{c_{Ads_{in},G,CO_2} \cdot \dot{V}_{Ads_{in},G,exp,kin,men}} - \frac{V_{Ads,B,Voi}}{\dot{V}_{Ads_{in},G,exp,kin,men}} . \quad (A.9)$$

$V_{Ads,B,Voi}$ is defined as the sorbent bed void space and $\dot{V}_{Ads_{in},G,exp,kin,men}$ describes the mean gas phase volume flow that enters the adsorber during evaluation of the adsorption kinetics.

Besides residence time considerations, the choice of an appropriate isotherm model becomes crucial in the evaluation of the adsorption kinetics. To increase the accuracy of the kinetic fit, the evaluation of the equilibrium loading is performed based on isotherm model 4 (Table 3.1).

A.3.6.2 Driving force coefficient

Determination of the driving force coefficient k_{df,ads,CO_2} becomes a central element of the kinetic investigation. As a lumped parameter it combines the adsorption kinetics as well as mass transfer resistances in the sorbent particle and in the fluid film that surrounds the particles.

Contribution of film transfer resistances to the overall mass transfer resistances can be estimated by evaluation of the *Biot* number^{116,313–315}

$$Bi_{CO_2} = \frac{k_{df,GP,CO_2} \cdot D_P}{6 \cdot D_{dif,P,CO_2}} \quad (A.10)$$

that depends on the mass transfer coefficient between the gas and particle phase k_{df,GP,CO_2} , on the particle diameter D_P , which is estimated to be the center of the particle size range for *Lewatit* given by the vendor¹⁶² of 0.775 mm (Table 3.4), and on the effective diffusion coefficient of the specie in the particle D_{dif,P,CO_2} . The transfer coefficient k_{df,GP,CO_2} can be calculated based on the system *Sherwood* number

$$Sh_{CO_2} = \frac{k_{df,GP,CO_2} \cdot D_{men,P}}{D_{dif,CO_2,mol}}, \quad (A.11)$$

which can be determined based on common correlations for fixed bed systems, e.g., by Gnielinski, provided in the literature.^{116,315}

If mass transport limitations in the particle are the rate limiting step in the adsorption process, the linear driving force coefficient

$$k_{df,ads,CO_2} = \frac{60}{D_P^2} \cdot D_{dif,CO_2,eff}^* \quad (A.12)$$

can be correlated to the pseudo, lumped diffusion coefficient $D_{dif,CO_2,eff}^*$ of the species in the particle.¹²⁷

Different transport mechanisms, e.g., *molecular diffusion*, *Knudsen diffusion*, *viscous flow* and *surface diffusion* can contribute to the mass transfer in the particle.¹²⁷ Commonly, diffusion limitations in the macro pores are identified as the rate limiting step of the adsorption process,¹²⁷ which is in accordance with the kinetic study of CO_2 adsorption on *Lewatit* by Bos et al..¹⁶⁴ If this is the case,

$$k_{df,ads,CO_2} = \frac{60}{D_P^2} \cdot \frac{D_{dif,Por,CO_2,eff}}{\tau_{Por,eff} \left(1 + \frac{\rho_P}{\epsilon_P} \cdot \frac{\partial q_{CO_2}}{\partial c_{CO_2}} \right)} \quad (A.13)$$

might allow for a first estimate of the linear driving force coefficient.^{127,313,314} Here,

$$\frac{D_{dif,Por,CO_2,eff}}{\tau_{P,eff}} = \left(\frac{\tau_{Por,mol}}{D_{dif,CO_2,mol}} + \frac{\tau_{Por,Knu}}{D_{dif,CO_2,Knu}} \right)^{-1} \quad (A.14)$$

combines the *molecular diffusion* in the pore (Table B.3) and *Knudsen diffusion*, estimated via

$$D_{dif,CO_2,Knu} = \frac{4}{3} \cdot D_{Por} \cdot \left(\frac{R_{id} \cdot T}{2 \cdot \pi \cdot M_{CO_2}} \right)^{0.5} \cdot^{127} \quad (A.15)$$

Corrections by tortuosities $\tau_{\text{Por},i}$ are applied to account for non-linearity of the pores. One may use empirical correlations to relate $\tau_{\text{Por},\text{mol}}$ and $\tau_{\text{Por},\text{Knu}}$, e.g.,

$$\tau_{\text{Por},\text{Knu}} = \tau_{\text{Por},\text{mol}}^{1.7} \cdot^{127} \quad (\text{A.16})$$

The reader is referred to the contribution of Birkmann³¹⁴ for a detailed discussion on the different contributions to $k_{\text{df,ads,CO}_2}$. However, already the simplified approach defined in (A.13) allows for an important insight into the characteristics of the linear driving force concept. This is, $k_{\text{df,ads,CO}_2}$ combines information on the kinetics of the adsorption process as well as on its thermodynamics, i.e., on slope of the adsorption isotherm.

A.3.6.3 Data fit

A data fit to minimize the least square error between the simulated and the scaled, experimentally obtained mole fraction data ($y_{\text{Ads}_{\text{out,G,CO}_2,\text{sca}}}$, Appendix A.3.2) at the adsorber outlet is performed, using *Matlab*^{®178} non-linear data fitting routine. A simultaneous determination of the kinetic parameters $k_{\text{df,ads,CO}_2}$ and n_{ord} is realized. The comparatively long tailing of the breakthrough curves in the close vicinity of the gas phase equilibrium composition is observed to take strong influence on the kinetic fit. Consequently, to minimize errors attributed to this effect, the kinetic evaluation is focused on data $y_{\text{Ads}_{\text{out,G,CO}_2,\text{sca}}}$ below 98% of the gas phase equilibrium composition.

A.3.6.4 Results

A detailed investigation of the simulation results indicates that a 2-parameter fit allows for good approximation of the experimental results. However, the results obtained additionally indicate that model reduction to a linear driving force approach might be possible. Indeed, detailed simulation studies reveal that by use of $n_{\text{ord}} = 1$ good agreement between the experimentally obtained and simulated breakthrough curves can be reached. Figure 3.7(a) provides an example of the curves fitted.

To investigate the influence of operation temperature on the kinetics of the adsorption process, kinetic coefficients $k_{\text{df,ads,CO}_2}$ obtained (Table A.6) are visualized by *Arrhenius* plot (Figure A.5(a)). Moreover, dependency of $k_{\text{df,ads,CO}_2}$ on CO_2 partial pressure is depicted in Figure A.5(b). Minor dependency of $k_{\text{df,ads,CO}_2}$ on CO_2 partial pressure is noticed, whereas strong increase of the kinetic constant with temperature is observed. High coefficients of determination (Table A.7) indicate that the temperature dependency can in good accordance be described by *Arrhenius* approach. Activation energies in the order of 65 kJ mol^{-1} are obtained, which show a decrease with CO_2 partial pressure in the gas phase.

Even if a detailed evaluation of the contributions to $k_{\text{df,ads,CO}_2}$ is out of the scope of this contribution, basic investigations with reference to (A.13) are performed to investigate the thermophysical consistency of the $k_{\text{df,ads,CO}_2}$ data obtained. In line with the work of Birkmann³¹⁴ the evaluation is based on the mean slope of the adsorption isotherm. Based on this approach estimates for $\tau_{\text{Por,eff}}^{-1} \cdot D_{\text{dif,Por,CO}_2,\text{eff}}$ can be gained from $k_{\text{df,ads,CO}_2}$ data via (A.13). These are summarized in Table A.8 and allow for analysis of the system *Biot*

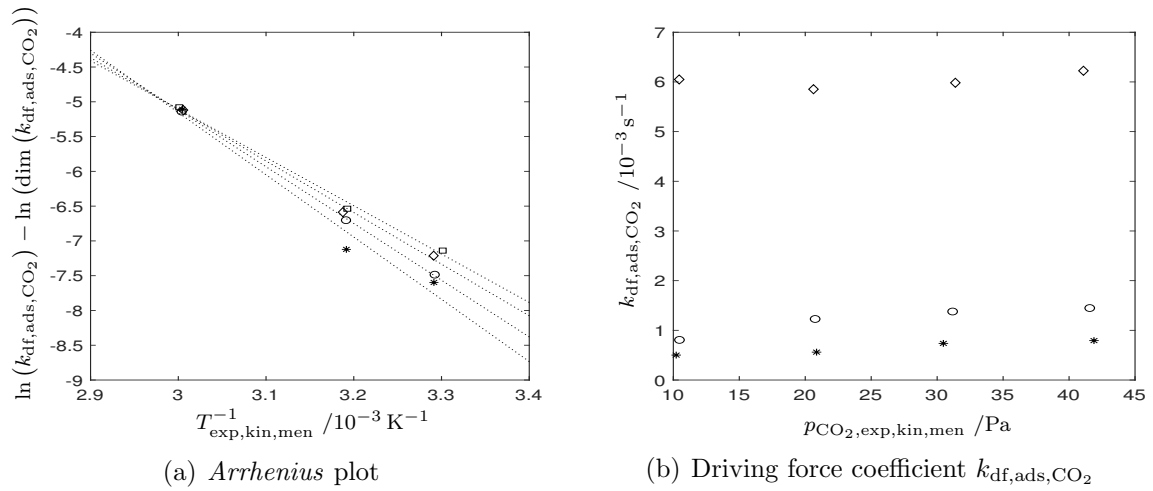


Figure A.5: Visualization of results obtained from 1-parameter fit. (a) Dependency of k_{df,ads,CO_2} on the mean temperature measured during kinetic evaluation $T_{exp,kin,men}$ visualized by *Arrhenius* plot for CO_2 partial pressure levels aspired $p_{CO_2,exp,asp}$ of 10 (*), 20 (o), 30 (◇) and 40 Pa (□). (b) Influence of mean CO_2 partial pressure levels $p_{CO_2,exp,kin,men}$ reached in the experiments on the linear driving force coefficient k_{df,ads,CO_2} shown for temperature levels $T_{exp,asp}$ of 30 (*), 40 (o) and 60 °C (◇).

Table A.6: Kinetic constant k_{df,ads,CO_2} in $10^{-3} s^{-1} mol^{1-n_{ord}} kg^{n_{ord}-1}$ as a function of the CO_2 partial pressure $p_{CO_2,exp,asp}$ and of the temperature level $T_{exp,asp}$ aspired to be realized in the experiments. Driving force coefficient data k_{df,ads,CO_2} are obtained from 1-parameter kinetic fit with $n_{ord} = 1$.

$T_{exp,asp}$ /°C	$p_{CO_2,exp,asp}$ /Pa			
	10	20	30	40
30	0.50	0.56	0.74	0.79
40	0.81	1.23	1.38	1.45
60	6.05	5.85	5.98	6.22

Table A.7: *Arrhenius* parameters and associated coefficient of determination of the linear fit calculated based on k_{df,ads,CO_2} data obtained from 1-parameter kinetic fit of the *BTC* data.

		$p_{CO_2,exp,asp}$ /Pa			
		10	20	30	40
R^2	/-	0.9717	0.9997	0.9950	0.9940
$\ln(k_{df,ads,\infty,CO_2})$	in $\ln(s^{-1})$	21.7	19.4	17.1	15.7
E_A	/kJ mol ⁻¹	74.4	67.8	61.7	57.7

number defined in (A.10) by use of $D_{dif,P,CO_2} = \epsilon_P \cdot \tau_{Por,eff}^{-1} \cdot D_{dif,Por,CO_2,eff}$. Even in the limiting case of negligible convective contribution to the gas phase mass transfer, Bi_{CO_2} takes values in the order of 46. This suggests that the mass transfer in the fluid film

outside of the particle only takes a minor influence on the overall mass transfer resistance such that the neglect of this contribution in the first case analysis performed seems to be justified.

Table A.8: Effective diffusion coefficient of CO₂ in the sorbent $\tau_{\text{Por,eff}}^{-1} \cdot D_{\text{dif,Por,CO}_2,\text{eff}}$ in $10^{-6} \text{ m}^2 \text{ s}^{-1}$, estimated from $k_{\text{df,ads,CO}_2}$ data based on (A.13), in dependence of the CO₂ partial pressure $p_{\text{CO}_2,\text{exp,asp}}$ and of the temperature level $T_{\text{exp,asp}}$ aspired to be realized in the experiments.

$T_{\text{exp,asp}}$ /°C	$p_{\text{CO}_2,\text{exp,asp}}$ /Pa			
	10	20	30	40
30	2.08	1.63	1.72	1.59
40	1.79	2.09	1.93	1.82
60	2.59	2.23	2.13	2.00

Evaluation of temperature influence on the mean adsorption isotherm slope indicates that the possible influence of the slope of the adsorption isotherm on the activation energy of $k_{\text{df,ads,CO}_2}$ decreases from 67 to 52 kJ mol⁻¹ with $p_{\text{CO}_2,\text{exp,asp}}$. This suggests that the activation energies of $k_{\text{df,ads,CO}_2}$ found (Table A.7) are influenced by the slope of the adsorption isotherms. Similarly the dependency of $k_{\text{df,ads,CO}_2}$ on CO₂ partial pressure might be attributed to the non-linearity of the adsorption isotherms.

Table A.9: Effective diffusion coefficient of CO₂ in the sorbent $\tau_{\text{Por,eff}}^{-1} \cdot D_{\text{dif,Por,CO}_2,\text{eff}}$ in $10^{-6} \text{ m}^2 \text{ s}^{-1}$, predicted based on (A.14), in dependence of the CO₂ partial pressure $p_{\text{CO}_2,\text{exp,asp}}$ and of the temperature level $T_{\text{exp,asp}}$ aspired to be realized in the experiments. The calculation is based on $p_{\text{exp,kin,men}}$ and $T_{\text{exp,kin,men}}$.

$T_{\text{exp,asp}}$ /°C	$p_{\text{CO}_2,\text{exp,asp}}$ /Pa			
	10	20	30	40
30	1.92	1.91	1.92	1.91
40	1.96	1.96	1.96	1.95
60	2.04	2.04	2.04	2.04

Based on A.13- A.16 the order of magnitude of contributions to the mass transfer in the particle pores is investigated. Here, $\tau_{\text{Por,mol}}$ is used as a fit parameter. Best match in a least-square sense between $\tau_{\text{Por,eff}}^{-1} \cdot D_{\text{dif,Por,CO}_2,\text{eff}}$ data estimated from the experiment (Table A.8) and predicted based on (A.14) (Table A.9) is reached for $\tau_{\text{Por,mol}} = 1.2$ ($\tau_{\text{Por,Knu}} = 1.4$). Good agreement between the data is noticed. Moreover, the order of magnitude of the tortuosity factors determined seems to be low compared to the range of tortuosities expected from theoretical considerations³¹⁵ of 3–6 and to its value used for *Knudsen diffusion* in *Lewatit* ($\tau_{\text{Por,Knu}} = 2.3$) by other studies¹⁶⁴. With a value of $\tau_{\text{Por,mol}}$ at hand, the contribution of *molecular* and *Knudsen diffusion* to the mass transfer in the sorbent pores can be estimated by means of (A.14). With shares in the order of 86 % *Knudsen diffusion* is found to dominate $\tau_{\text{Por,eff}}^{-1} \cdot D_{\text{dif,Por,CO}_2,\text{eff}}$.

Overall, the basic analysis performed suggests that the $k_{\text{df,ads,CO}_2}$ data determined are physically sound and that these can allow for basic insights into the adsorption kinetics of CO_2 on *Lewatit* at CO_2 partial pressures relevant for *DAC* applications. This motivates more detailed research in the kinetics of this system to be performed in subsequent studies.

A.3.6.5 Kinetics under humid conditions

Even though the thermophysical model outlined in Appendix A.3.6.1 might be used in the analysis of the kinetics of H_2O and of $\text{CO}_2\text{--H}_2\text{O}$ co-adsorption, no detailed discussion is given in this work. This is reasoned in the specific features of the adsorption process. With regard to co-adsorption, profound 2-component isotherm data would be required to allow for a reliable kinetic analysis. In this respect, the results summarized in Section 3.2.3.2 indicate presence of complex interactions for CO_2 adsorption in humid environment, which is in line with expectations based on theoretical investigations (Section 3.1.2). This motivates a more detailed analysis of mechanistic models based on which physically interpretable kinetic parameters might be derived. Even if this raises an interesting research question, further evaluation of this direction is out of scope with regard to the research priorities of this contribution.

Similarly, a detailed investigation of water adsorption does not seem to be target-oriented. Overshoots in mole fraction profiles and comparatively small adsorption times, which indicate presence of high residence time influence, increase the complexity of the kinetic evaluation and limit the range of validity of the results obtained. On the other hand, simulation results (Section 4.4) indicate that limitation by diffusion is to be expected for CO_2 adsorption in the concepts proposed. Thus, based on the significant excess of H_2O compared to CO_2 in ambient air, a positive influence of the overall adsorption kinetics on the *DAC* process, i.e., favored CO_2 adsorption, seems unlikely. This is in line with the findings of Wurzbacher et al.¹⁹⁴ that, besides other, denote significantly faster kinetics of H_2O desorption compared to CO_2 release.

A.3.7 Error estimation

Even if great care was taken to minimize experimental errors, the results obtained are still subject to experimental inaccuracies attributed to the characteristics of the measurement devices used. Basic error propagation studies³¹⁶ are performed to investigate the influence of these inaccuracies on the experimental data obtained. The procedure of error estimation is outlined for CO_2 adsorption from dry (Appendix A.3.7.1) and from humid (Appendix A.3.7.3) gas phase. Moreover, errors arising in H_2O adsorption experiments are investigated (Appendix A.3.7.2). The influence of errors on the sorbent loading is analyzed based on the evaluation of the state variable profiles over time, whereas inaccuracies in the state variables used for isotherm evaluation are investigated based on their mean values at the end of integration time, which is in line with the basic evaluation principle of *BTC* data outlined in Appendix A.3.2- A.3.5.

Table A.10: Overview of errors arising in *BTC* operation for CO₂ adsorption from dry gas phase. The order of magnitude of a single error is solely determined via reference experiments if no source is given. Lower and upper limits of the single errors are presented.

Error source	Variable		Lower bound	Upper bound	Source
Sorbent loading q_{CO_2}					
Sample mass	$\delta_{\text{err},Sca,m_{\text{sam}}}$	/mg	-0.2	+0.2	[306]
Sorbent mass	$\delta_{\text{err},\phi_{m_{\text{los,Sor}}}}$	/-	-0.0045	+0.0093	
Gas composition	$\delta_{\text{err},y_{\text{sam},\text{CO}_2}}$	/-	$-0.02 \cdot y_{\text{sam},\text{CO}_2}$	$+0.02 \cdot y_{\text{sam},\text{CO}_2}$	[299]
MFC mole flow	$\delta_{\text{err},\dot{n}_{\text{MFC}}}$	/mols ⁻¹	$-0.04 \cdot \dot{n}_{\text{MFC}}$	$+0.04 \cdot \dot{n}_{\text{MFC}}$	
Residence time	$\delta_{\text{err},n_{\text{res}}}$	/mol	$-f(\Phi_{\text{res},i})$	$+f(\Phi_{\text{res},i})$	
Aging	$\delta_{\text{err},age}$	/mol kg ⁻¹	± 0	$(\phi_{n_{\text{ads}},n_{\text{ads},age}} - 1) \cdot q_{\text{CO}_2}$	
Pressure p_{CO_2}					
Pressure level	$\delta_{\text{err},p,p_{\text{CO}_2}}$	/10 ⁵ Pa	$-f(p_{\text{B}_i})$	$+f(p_{\text{B}_i})$	[307, 308]
Gas composition	$\delta_{\text{err},y_{\text{sam},\text{CO}_2}}$	/-	$-0.02 \cdot y_{\text{sam},\text{CO}_2}$	$+0.02 \cdot y_{\text{sam},\text{CO}_2}$	[299]
Temperature T_{B}					
Temperature level	$\delta_{\text{err},T_{\text{B}_i},T_{\text{B}}}$	/K	$-f(T_{\text{B}_i})$	$+f(T_{\text{B}_i})$	[300]

A.3.7.1 CO₂ adsorption from dry gas phase

Table A.10 gives an overview of the single sources of errors considered for *BTC* experiments in dry atmosphere. Worst case combinations of the error bounds given are used to derive a pessimistic estimate of the overall error present.

The accuracy of the laboratory scale $\delta_{\text{err},Sca,m_{\text{sam}}}$ used to measure the weight of sample filled in the adsorber and errors from the estimation of the dry sorbent mass $\delta_{\text{err},\phi_{m_{\text{los,Sor}}}}$ (Appendix A.4.7) are taken into account. CO₂ loadings calculated depend on the sample gas composition. Here, the vendor²⁹⁹ names a level of accuracy of $\pm 2\%$. Additionally, reference measurements indicate the accuracy of mass flow controller calibration $\delta_{\text{err},\dot{n}_{\text{MFC}}}$ to be in the order of $\pm 4\%$.

Also inaccuracies in determination of residence time corrections $\delta_{\text{err},n_{\text{res}}}$ are taken into account. A pessimistic estimate is given by use of the lowest or highest value for the fictitious loading $\Delta q_{\text{res},\text{CO}_2}$ obtained from residence time experiments. Here, the influence of errors in the state variables on the evaluation of this correction term are taken into account to ensure the thermophysically consistency of the error bounds determined. Finally, in line with the observations of other research groups, aging effects $\delta_{\text{err},age}$ at high temperatures are observed (Section 3.3.2). Reference experiments indicate capacity losses of up to 9% for operation above 80 °C, whereas high reproducibility of the experiment is underlined by deviations of less than 0.5% between the reference experiments. Errors introduced by the *IR* device are not explicitly taken into account, as these are minimized by scaling of the measurements obtained during data processing (Appendix A.3.2).

Besides inaccuracies in sorbent loading q_{CO_2} , also errors with regard to CO₂ partial pressure p_{CO_2} need to be taken into account. The inaccuracies of the pressure indicators

used are estimated to be in the order of $5 \cdot 10^3$ Pa.^{307,308} Moreover, pressure losses in the sorbent bed, determined from the pressure indicators at its inlet and outlet (p_{B_i}) are recorded to be in the order of $2 \cdot 10^3$ Pa. Both influences on the total bed pressure determined are taken into account in the worst case estimate. Moreover, as the partial pressure of CO₂ is of interest in the evaluation of the isotherms, also the errors in the test gas composition are considered.

The error estimate of the bed temperature considers the accuracy of the thermocouples and of the mean temperature level at the end of the integration time recorded by each thermocouple in the sorbent bed. The temperatures in the sorbent bed (T_{B_i}) are measured by type K thermoelements with an accuracy of ± 1.5 °C.³⁰⁰ With regard to isothermal operation during CO₂ adsorption, maximum temperature variations with time in the order of 1.5 °C are observed at a single measuring point. Overall, the mean bed temperature varies typically less than 1.5 °C from $T_{\text{exp,asp}}$.

A.3.7.2 H₂O adsorption

The error estimate for H₂O adsorption is performed similarly to the evaluation of CO₂ adsorption experiments (Appendix A.3.7.1). H₂O mole shares in the gas phase are indirectly determined based on the relative humidity and on the pressure level measured before and after the adsorber. Absolute variations between the steady state values of the H₂O mole shares determined before and after the adsorber are typically in the order of magnitude of 0.09 %.

Worst case estimates for minimum or maximum sorbent loading are realized by selection of either the H₂O mole share calculated before or after the adsorber as reference for the scaling of the breakthrough curves (Appendix A.3.2.3), with the possible error of the corresponding pressure indicator ($\pm 5 \cdot 10^3$ Pa) being additionally taken into account. To include inaccuracies in the determination of the residence time corrections, these are also evaluate based on performing the scaling to the higher or lower H₂O mole fraction profile determined. The maximum or minimum loading, respectively, derived from the residence time experiments is selected for correction purpose.

The mean relative humidity within the sorbent bed $\phi_{\text{rh,B}}$ depends on the mole share of H₂O, on the mean bed pressure and on the mean bed temperature. The calculation of errors in the mole share is discussed in the previous paragraph. A worst case estimate of the bed pressure with regard to the error bounds is reached by either setting the bed pressure to the pressure level reached before or after the adsorber, which typically diverge by $2 \cdot 10^3$ Pa. Additionally, the correction of the pressure level by the error of the pressure indicator ($\pm 5 \cdot 10^3$ Pa) is taken into account. Physically unsound estimates, e.g., simultaneous correction of a pressure indicator to a higher level in the estimate for $y_{\text{B,H}_2\text{O}}$ and lower level in the estimate for the bed pressure, are excluded from the analysis. With these estimates at hand, only the evaluation of the bed temperature T_{B} is missing in the derivation of the error bars for $\phi_{\text{rh,B}}$. The maximum deviation of the temperature recorded in the last 180 s of the experiments between the sensors is found to be less than 1.8 °C and the average of these temperatures diverges by less than 1.9 °C from $T_{\text{exp,asp}}$ in all water adsorption experiments performed. Selection of the minimum or maximum temperature level in steady state, recorded by the three temperature sensors in the sorbent

Table A.11: Overview of errors arising in *BTC* operation for H₂O adsorption. The order of magnitude of the single error is solely determined via reference experiments if no source is given. Lower and upper limits of the single errors are presented.

Error source	Variable		Lower bound	Upper bound	Source
Sorbent loading $q_{\text{H}_2\text{O}}$					
Sample mass	$\delta_{\text{err},\text{Sca},m_{\text{sam}}}$	/mg	- 0.2	+ 0.2	[306]
Sorbent mass	$\delta_{\text{err},\phi_{m_{\text{los}},\text{Sor}}}$	/-	- 0.0045	+ 0.0093	
MFC mole flow	$\delta_{\text{err},\dot{n}_{\text{MFC}}}$	/mols ⁻¹	- 0.04 · \dot{n}_{MFC}	+ 0.04 · \dot{n}_{MFC}	
Residence time	$\delta_{\text{err},n_{\text{res}}}$	/mol	- $f(\Phi_{\text{res},i})$	+ $f(\Phi_{\text{res},i})$	
Relative humidity	$\delta_{\text{err},\phi_{\text{rh}},q_{\text{H}_2\text{O}}}$	/-	- $f(\phi_{\text{rh},i})$	+ $f(\phi_{\text{rh},i})$	
Pressure level	$\delta_{\text{err},p,q_{\text{H}_2\text{O}}}$	/10 ⁵ Pa	- $f(p_{\text{B}_i})$	+ $f(p_{\text{B}_i})$	[307, 308]
Rel. humidity $\phi_{\text{rh},\text{B}}$					
Pressure level	$\delta_{\text{err},p,\phi_{\text{rh},\text{B}}}$	/10 ⁵ Pa	- $f(p_{\text{B}_i})$	+ $f(p_{\text{B}_i})$	[307, 308]
Relative humidity	$\delta_{\text{err},\phi_{\text{rh},i},\phi_{\text{rh},\text{B}}}$	/-	- $f(\phi_{\text{rh},i})$	+ $f(\phi_{\text{rh},i})$	
Temperature level	$\delta_{\text{err},T_{\text{B}_i},\phi_{\text{rh},\text{B}}}$	/K	- $f(T_{\text{B}_i})$	+ $f(T_{\text{B}_i})$	[300]
Temperature T_{B}					
Temperature level	$\delta_{\text{err},T_{\text{B}_i},T_{\text{B}}}$	/K	- $f(T_{\text{B}_i})$	+ $f(T_{\text{B}_i})$	[300]

bed and an additional consideration of the error in temperature measurement with type K thermocouples ($\pm 1.5^\circ\text{C}$) allows for derivation of a worst case estimate with respect to the error bars of $\phi_{\text{rh},\text{B}}$.

A.3.7.3 CO₂ adsorption from humid gas phase

Minor variations in the error estimate are required for CO₂ adsorption from humid gas phase compared to the experiments without presence of moisture (Appendix A.3.7.1). The single sources of errors investigated are summarized in Table A.12. No aging effects are considered, as the operation temperatures aspired are 30 °C. On the other hand, in co-adsorption experiments dilution effects of water vapor influence the CO₂ mole fraction calculated at the adsorber outlet. To account for this effect, the inaccuracies of the humidity indicators $\delta_{\text{err},\phi_{\text{rh}},q_{\text{CO}_2}}$ and of the pressure sensors $\delta_{\text{err},p,q_{\text{CO}_2}}$ are integrated in the error estimate of the CO₂ loading. To be more specific, the influence of these quantities on the water gas phase mole share calculated and, thus, on the CO₂ mole flow is investigated. For error estimation H₂O mole fractions can be calculated either on the basis of the process data available before or after the adsorber. Here, absolute variations between H₂O mole fraction data throughout the experiments are typically in the order of 0.07 %. Additionally, inaccuracies of the pressure indicators in the order of $\pm 5 \cdot 10^3 \text{ Pa}$ ^{307,308} are taken into account. The selection of the water mole share for the further calculation is performed with regard to the realization of the highest error bound. Moreover, the presence of different water mole fractions in the gas phase is also accounted for in the

evaluation of the residence time experiments to realize worst case estimates with regard to the overall error bounds.

In addition to the influences investigated in the CO₂ adsorption from dry gas phase (Appendix A.3.7.1), dilution effects of water need to be considered in the determination of the CO₂ partial pressure. A worst case estimate of the H₂O mole share based on the mole fraction data calculated before and after the adsorber is used. In determination of the H₂O mole fraction, the influence of inaccuracies in the pressure levels determined is taken into account. Great care is taken to prevent physically unsound combinations of pressure levels with regard to the additional variations in the bed pressure considered.

Also error bars for the additional state variables in the sorbent bed are derived. Estimates for inaccuracies of the mean relative humidity in the sorbent bed are calculated in analogy to the evaluation of the water adsorption experiments (Appendix A.3.7.2). The error in the temperature level is investigated in analogy to the CO₂ adsorption from dry gas phase (Appendix A.3.7.1). Variations over time of less than 1.5 °C are noticed for the temperature sensors in the sorbent bed and the mean bed temperature is found to vary less than 1.4 °C from the temperature level aspired to be realized in the experiment.

Table A.12: Overview of errors arising in *BTC* operation for CO₂ adsorption from humid gas phase. The order of magnitude of the single error is solely determined via reference experiments if no source is given. Lower and upper limits of the single errors are presented.

Error source	Variable		Lower bound	Upper bound	Source
Sorbent loading q_{CO_2}					
Sample mass	$\delta_{\text{err,Sca},m_{\text{sam}}}$	/mg	- 0.2	+ 0.2	[306]
Sorbent mass	$\delta_{\text{err},\phi_{m_{\text{los}},\text{Sor}}}$	/-	- 0.0045	+ 0.0093	
Gas composition	$\delta_{\text{err},y_{\text{sam},\text{CO}_2}}$	/-	- 0.02 · $y_{\text{sam},\text{CO}_2}$	+ 0.02 · $y_{\text{sam},\text{CO}_2}$	[299]
MFC mole flow	$\delta_{\text{err},\dot{n}_{\text{MFC}}}$	/mol s ⁻¹	- 0.04 · \dot{n}_{MFC}	+ 0.04 · \dot{n}_{MFC}	
Residence time	$\delta_{\text{err},n_{\text{res}}}$	/mol	- $f(\Phi_{\text{res},i})$	+ $f(\Phi_{\text{res},i})$	
Relative humidity	$\delta_{\text{err},\phi_{\text{rh}},q_{\text{CO}_2}}$	/-	- $f(\phi_{\text{rh},i})$	+ $f(\phi_{\text{rh},i})$	
Pressure level	$\delta_{\text{err},p,q_{\text{CO}_2}}$	/10 ⁵ Pa	- $f(p_{\text{B}_i})$	+ $f(p_{\text{B}_i})$	[307, 308]
Pressure p_{CO_2}					
Pressure level	$\delta_{\text{err},p,p_{\text{CO}_2}}$	/10 ⁵ Pa	- $f(p_{\text{B}_i})$	+ $f(p_{\text{B}_i})$	[307, 308]
Gas composition	$\delta_{\text{err},y_{\text{sam},\text{CO}_2}}$	/-	- 0.02 · $y_{\text{sam},\text{CO}_2}$	+ 0.02 · $y_{\text{sam},\text{CO}_2}$	[299]
Relative humidity	$\delta_{\text{err},\phi_{\text{rh}},p_{\text{CO}_2}}$	/-	- $f(\phi_{\text{rh},i})$	+ $f(\phi_{\text{rh},i})$	
Rel. humidity $\phi_{\text{rh},\text{B}}$					
Pressure level	$\delta_{\text{err},p,\phi_{\text{rh},\text{B}}}$	/10 ⁵ Pa	- $f(p_{\text{B}_i})$	+ $f(p_{\text{B}_i})$	[307, 308]
Relative humidity	$\delta_{\text{err},\phi_{\text{rh},i},\phi_{\text{rh},\text{B}}}$	/-	- $f(\phi_{\text{rh},i})$	+ $f(\phi_{\text{rh},i})$	
Temperature level	$\delta_{\text{err},T_{\text{B}_i},\phi_{\text{rh},\text{B}}}$	/K	- $f(T_{\text{B}_i})$	+ $f(T_{\text{B}_i})$	[300]
Temperature T_{B}					
Temperature level	$\delta_{\text{err},T_{\text{B}_i},T_{\text{B}}}$	/K	- $f(T_{\text{B}_i})$	+ $f(T_{\text{B}_i})$	[300]

A.4 TGA experiments

In this section information on the experimental setting (Appendix A.4.1) is given. The procedure to determine the mass of unloaded sorbent (Appendix A.4.2) and the sorbent loading (Appendix A.4.3) is outlined. Moreover, information on the pressure (Appendix A.4.4) and temperature levels (Appendix A.4.5) realized in the experiments are given. Finally, the analysis of kinetic parameters (Appendix A.4.6) and the procedure of error estimation (Appendix A.4.7) is discussed.

A.4.1 Material and methods

The key equipment and material used to perform *TGA* experiments is summarized in Table A.13. The initial sample mass is determined by use of the high precision scale *METTLER TOLEDO MT5*³¹⁷. Changes in sample mass and in temperature during the course of the experiment are measured and recorded by the *TGA* device *TG 409 C/3/E* from *Netzsch*¹⁷⁴. Samples are placed in a sample carrier of crucible type. Instead of placing the sample at the bottom of the carrier, three tubes made from wire mesh, with an inner diameter in the order of magnitude of the *Lewatit* particle diameter, are used to hold the sample inside the carrier. This is done to reduce possible gas phase diffusion through the sorbent bed suggested by preliminary studies with a gas phase that contains CO₂ shares at ppm-level.

Table A.13: Equipment and material used to perform *TGA* experiments.

	Provided by	Additional information	Source
Equipment			
Flow control	<i>ABB</i>	Float type flow meter with needle valve Model: <i>10AG142DA3B1X0</i>	[175]
Sample carrier	<i>Netzsch</i>	Sample carrier of crucible type (<i>459.478</i> , modified) for <i>Netzsch TGA (TG 409 C/3/E)</i> Inner diameter: $D_{\text{Car}} \approx 6$ mm, height: $L_{\text{Car}} \approx 10$ mm	[174]
Scale	<i>Mettler-Toledo</i>	Model: <i>METTLER TOLEDO MT5</i>	[317]
<i>TGA</i>	<i>Netzsch</i>	Model: <i>TG 409 C/3/E</i>	[174]
Gas			
Nitrogen	<i>Messer</i>	Quality: 5.0	[299]
Test gas (ppm fraction)	<i>Messer</i>	CO ₂ in syn. air, quality CO ₂ : 4.5, quality syn. air: 5.0 Relative error in CO ₂ content $\pm 2\%$	[299]
Test gas (% fraction)	<i>Messer</i>	CO ₂ in N ₂ , quality CO ₂ : 4.5, quality N ₂ : 5.0 Relative error in CO ₂ content $\pm 2\%$	[299]
Additional material			
<i>Lewatit</i>	<i>Lanxess</i>	Information summarized in Table 3.4 Sample mass ca. 40 mg (air dried)	[162]

A.4.2 Sorbent mass

Besides adsorption of CO₂, *Lewatit* is able to adsorb water in large quantities. This results in the difficulty that the sample mass m_{sam} could differ from the sorbent mass m_{Sor} . Thus, to allow for a well defined reference state, all sorbent mass-dependent data are referred to the sorbent in desorbed, empty state, i.e., after desorption of species attached. The sorbent mass m_{Sor} is related to the mass of the loaded sorbent $m_{\text{Sor,loa}}$ by

$$m_{\text{Sor}} = (1 - \phi_{m_{\text{los,Sor}}}) \cdot m_{\text{Sor,loa}}. \quad (\text{A.17})$$

The scaling factor $\phi_{m_{\text{los,Sor}}}$ is determined separately in each experiment by

$$\phi_{m_{\text{los,Sor}}} = \frac{\Delta m_{\text{sam,exp,men}}(t_{\text{S2end}})}{m_{\text{sam,in}}}. \quad (\text{A.18})$$

The variable $m_{\text{sam,in}}$ is the initial weight of the sample and $\Delta m_{\text{sam,exp,men}}$ gives the sample mass change from the start of the experiment till the end of the desorption phase. To account for fluctuations in the measurement, $\Delta m_{\text{sam,exp,men}}$ is determined based on the mean over the sample mass data taken in the last 240s of segment S2 (Figure 3.4). Note that this procedure neglects possible effects arising from lift forces, e.g., associated with the temperature-dependent gas phase density. In this respect, reference experiments indicate errors arising from TGA temperature change between ambient and desorption temperature to be in the order of less than 3% of $\phi_{m_{\text{los,Sor}}}$. The parameter $\phi_{m_{\text{los,Sor}}}$ typically takes values in the order of 15%. This implies that errors from temperature changes are in the order of less than 1% related to the sorbent mass, which seems acceptable small.

A.4.3 Sorbent loading

The equilibrium CO₂ loading of the sorbent is determined based on the sample mass change recorded in segment S4 (Figure 3.4). It is assumed that the sample mass change solely results from CO₂ adsorption. The change of the gas phase from pure nitrogen to test gas mixtures is observed to be associated with intense, random fluctuations of the sample mass measured in the close vicinity of the switching point. Thus, it seems reasonable to use the sample mass measured at the end of segment S3, i.e., just before the start of gas phase change, as the reference mass for the start of CO₂ adsorption. This way, the influence of errors attributed to gas switching and to drifts in the sample mass before the start of the adsorption (Appendix A.4.7) is kept at a minimum. To account for minor, fast fluctuations in the sample mass, the sample reference mass at the end of segment S3 is determined by averaging the sample mass data over the last 240s of this segment.

If the change in sample mass Δm_{sam} is dominated by the variation in sorbent loading q_{CO_2} , these two variables can be correlated according

$$\Delta m_{\text{sam}} = m_{\text{sam}}(t) - m_{\text{sam,ref}}(t_{\text{ref}}) = m_{\text{Sor}} \cdot M_{\text{CO}_2} \cdot (q_{\text{CO}_2}(t) - q_{\text{CO}_2,\text{ref}}(t_{\text{ref}})). \quad (\text{A.19})$$

Thus, by selecting the reference time t_{ref} to be at the end of segment S3 and assuming that at this time no CO_2 is bound to the sorbent, i.e., $q_{\text{CO}_2,\text{ref}}(t_{\text{ref}}) = 0$, the CO_2 loading of the sorbent can directly be calculated from the change in sample mass measured. The evolution of the sorbent loading predicted is carefully investigated to determine the equilibrium loading that is indicated by a plateau formation in the loading profile. An automated search based on the maximum loading predicted is used. However, some measurements required manual adjustment of the equilibrium time found, e.g., reasoned in *TGA* drifts noticed. To determine the sorbent equilibrium loading, the loadings predicted based on the measurements taken in the last 240s prior to the equilibrium time are averaged to account for minor fluctuations within the *TGA* data. The sorbent loadings determined are summarized in Table A.14.

Table A.14: CO_2 loading $q_{\text{eq},\text{CO}_2,\text{exp}}$ in the dimension mol kg^{-1} , obtained from *TGA* experiments in dependence of the CO_2 partial pressure level $p_{\text{CO}_2,\text{exp,asp}}$ and temperature level $T_{\text{exp,asp}}$ aspired.

$T_{\text{exp,asp}}$ / $^{\circ}\text{C}$	$p_{\text{CO}_2,\text{exp,asp}}$ /kPa				
	1	5	10	15	20
30	1.61	2.14	2.55	2.57	2.41
40	1.49	1.88	2.30	2.43	2.33
60	0.75	1.37	1.61	1.75	1.86
80	0.31	0.77	1.13	1.30	1.31
100	0.05	0.21	0.39	0.48	0.57

A.4.4 Pressure levels

In the *TGA* device¹⁷⁴ from *Netzsch* used, a small quantity of sample (~ 40 mg) is exposed to the gas phase inside a measurement chamber that provides large open cross section areas for the low gas phase volume flows of ca. 93 Nml min^{-1} and is connected to the ambient. Thus, the gas phase within the measurement chamber is assumed to be at ambient pressure, e.g., pressure losses in the gas pipes of 6 mm diameter in the order of 1 Pa m^{-1} , estimated from basic laminar pressure loss correlations,³¹⁸ are not considered. Moreover, to determine the CO_2 partial pressure levels, information on the CO_2 mole shares in the gas phase is required. Differences between the CO_2 shares of the sample gas $y_{\text{sam},\text{CO}_2}$ named by the vendor and CO_2 mole fractions aspired to be realized in the experiment $y_{\text{G},\text{CO}_2,\text{exp,asp}}$ of 1, 5, 10, 15 and 20 % are in absolute less than 0.01 %. Errors in the CO_2 partial pressure levels set in the experiment are evaluated in Appendix A.4.7.

A.4.5 Temperature levels

Isothermal conditions are favored for the determination of the sorbent loading and of the kinetic parameters in *TGA* experiments. The temperature profiles are measured by a single temperature sensor positioned below the sample. The temperature levels for adsorption isotherm evaluation $T_{\text{exp,ads,end,men}}$ are obtained as the mean of the temperature

profile recorded over the last 240 s before the equilibrium time determined. The temperatures used in the evaluation of the kinetics $T_{\text{exp,kin,men}}$ are defined as the mean of the temperature signal over the time frame of kinetic evaluation. A discussion on the errors arising in the temperature control is given in Appendix A.4.7.

A.4.6 Kinetic parameters

In this section the thermophysical model and the approach to data fitting (Appendix A.4.6.1) are outlined. Moreover, the results obtained from a 2-parameter kinetic fit (Appendix A.4.6.2) are summarized.

A.4.6.1 Thermophysical model and kinetic fit

The zero-dimensional model proposed takes into account the evolution of the mean sorbent loading (3.4) to predict the change of sample mass Δm_{sam} based on CO₂ adsorption. As denoted by (A.19), a change in the sorbent loading can be correlated to a change in the sample mass and vice versa. Here, the reference point t_{ref} might be freely chosen.

For kinetic data fitting a reliable, well interpretable set of data is required. Reasoned in random fluctuations during the initialization of the gas phase change and in gas phase residence time induced delays in the increase of the sample mass observed, a reliable prediction of the state variables in the close vicinity of the initialization of the gas phase change is hard to realize. Additionally, errors in measurements arising in this phase limit the range of validity of the kinetic data determined. To overcome these hurdles, the quality of the data is increased by the reduction of the amount of data points used in the kinetic fits. This is, the kinetic data fitting is performed for sorbent loadings predicted above a certain threshold, e.g., relative to the equilibrium loading determined. Selection of this threshold value has been performed with great care. On the one hand, the exclusion of data needs to be kept at a minimum to increase the accuracy of the data fit. On the other hand, the avoidance of possible errors arising from effects attributed to the gas phase change needs to be taken into account. A threshold value of 20 % of the equilibrium loading determined is found to be a good compromise.

Following the approach described, the first measurement value with a corresponding CO₂ loading, derived from sorbent mass change (Appendix A.4.3), that exceeds 20 % of the equilibrium loading, estimated from the data set used, defines the initial conditions of (3.4). If the equilibrium loading was known, (3.4) could be used to predict the evolution of sorbent loading and, thus, of the sample mass change based on the kinetic parameters to be determined. Here, one might intuitively use the isotherm model at hand to predict the equilibrium loading. Indeed, this is a valid option. However, this way errors arising in the fit of the adsorption isotherm are included in the kinetic evaluations. Consequently, to minimize this effect, a different approach is proposed. Here, the single data equilibrium loading determined from the data set at hand is used to define the equilibrium loading in (3.4). As only the difference to the equilibrium loading and not its exact value is required in the evaluation of (3.4), this strategy allows for a reliable determination of the kinetic parameters, while effects arising from measurement errors with respect to the exact isotherm data are minimized. The kinetic fit is performed by application of *Matlab*^{®178}

routine *lsqcurvefit*. Here, the least square error between the experimentally recorded and simulated evolution of the sample mass in time domain is minimized by variation of the kinetic parameters.

A.4.6.2 Results

In analogy to the evaluation of the *BTC* curves, a simultaneous variation of $k_{\text{df,ads,CO}_2}$ and n_{ord} is investigated. As exemplarily shown in Figure 3.7(b), a good accordance between the predicted and measured evolution of the sample mass is reached by this 2-parameter fit. This motivates a more detailed investigation of the kinetic parameters, the values of which are summarized in Tables A.15 and A.16. The *Arrhenius*-type visualization of $k_{\text{df,ads,CO}_2}$ (Figure A.6(a)) shows a strong decrease of this parameter with temperature. The tendency of an increase in the exponent of the driving force n_{ord} with CO_2 partial pressure is noticed (Figure A.6(b)), whereas no distinct influence of operation temperature on n_{ord} is detected. The mean values of n_{ord} over the temperature levels investigated increase in dependence of $p_{\text{CO}_2,\text{exp,asp}}$ from 1.0 to 2.4. This might suggest an increasing influence of the chemical reaction on the overall kinetics, as, e.g., pseudo-second order kinetic approaches are commonly interpreted to be in line with chemisorption being the rate limiting step¹⁸².

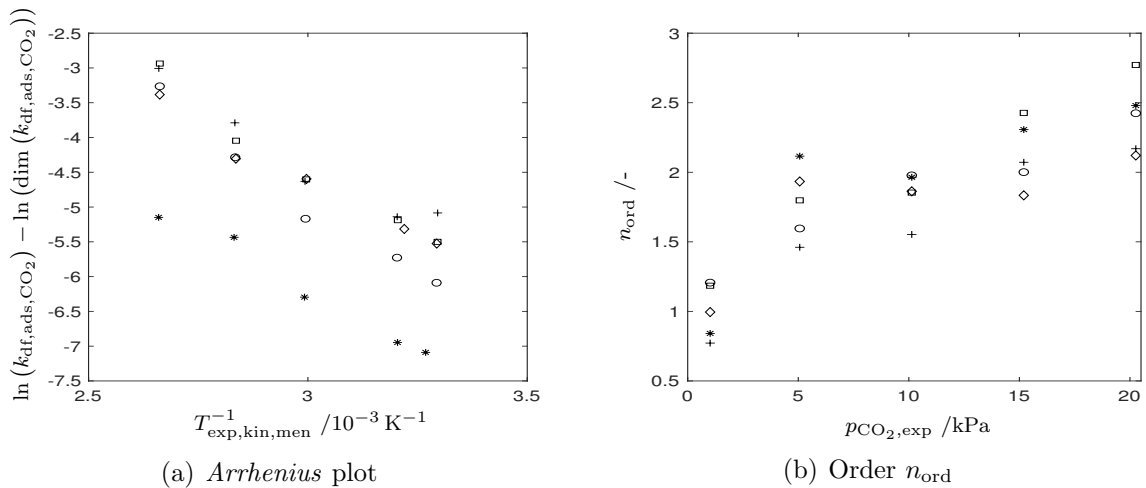


Figure A.6: Visualization of results obtained from 2-parameter fit. (a) Dependency of $k_{\text{df,ads,CO}_2}$ on the mean temperature measured during kinetic evaluation $T_{\text{exp,kin,men}}$ visualized by *Arrhenius* plot for CO_2 partial pressures $p_{\text{CO}_2,\text{exp}}$ of ca. 1 (*), 5 (○), 10 (◇), 15 (□) and 20 kPa (+). (b) Influence of CO_2 partial pressure $p_{\text{CO}_2,\text{exp}}$ on the exponent n_{ord} of the driving force term shown for temperature levels $T_{\text{exp,asp}}$ of 30 (*), 40 (○), 60 (◇), 80 (□) and 100 °C (+).

The tendencies observed with regard to n_{ord} motivate a 1-parameter optimization of $k_{\text{df,ads,CO}_2}$ based on the mean values of n_{ord} summarized in Table A.16. Results of this investigation are outlined in Table A.17 and visualized in Figure A.7. Again, a good agreement between the simulated and experimental data is found. The linear trends for the data at constant $p_{\text{CO}_2,\text{exp,asp}}$ levels, observable in the *Arrhenius* plot visualization (Figure A.7), motivate the analysis of *Arrhenius* parameters. Coefficients of determination

Table A.15: Kinetic constant $k_{\text{df,ads,CO}_2}$ in the dimension $10^{-3} \text{ s}^{-1} \text{ mol}^{1-n_{\text{ord}}} \text{ kg}^{n_{\text{ord}}-1}$ as a function of the CO_2 partial pressure level $p_{\text{CO}_2,\text{exp,asp}}$ and of the temperature level $T_{\text{exp,asp}}$. Data are derived by means of a 2-parameter fit.

$T_{\text{exp,asp}}$ /°C	$p_{\text{CO}_2,\text{exp,asp}}$ /kPa				
	1	5	10	15	20
30	0.83	2.27	3.99	4.09	6.19
40	0.96	3.26	4.92	5.58	5.86
60	1.84	5.69	10.10	10.03	9.75
80	4.36	13.78	13.50	17.49	22.62
100	5.81	38.24	33.93	53.02	49.45

Table A.16: Exponent of the driving force term n_{ord} as a function of the CO_2 partial pressure level $p_{\text{CO}_2,\text{exp,asp}}$ and of the temperature level $T_{\text{exp,asp}}$. Data are derived by means of a 2-parameter fit.

$T_{\text{exp,asp}}$ /°C	$p_{\text{CO}_2,\text{exp,asp}}$ /kPa				
	1	5	10	15	20
30	0.84	2.12	1.96	2.31	2.48
40	1.21	1.60	1.98	2.00	2.42
60	1.00	1.93	1.86	1.83	2.12
80	1.18	1.80	1.85	2.43	2.77
100	0.77	1.46	1.55	2.07	2.17
Mean	1.00	1.78	1.84	2.12	2.39

in the order of 0.9 (Table A.18) indicate a good applicability of *Arrhenius* equation for describing the temperature dependency of $k_{\text{df,ads,CO}_2}$. The activation energies are found to be in the order of 33 kJ mol^{-1} (Table A.18). Only for the experiments performed at $p_{\text{CO}_2,\text{exp,asp}} = 5 \text{ kPa}$ a higher value of 46 kJ mol^{-1} is found that might be attributed to the high level of $k_{\text{df,ads,CO}_2}$ determined in the 100°C experiment.

The activation energies found are in good accordance with activation energies for CO_2 -amine reactions published in the literature. In dependence of the isotherm parameter set selected and of the kinetic mechanism used, Bos et al.¹⁶⁴ report activation energies for CO_2 adsorption on *Lewatit* in the absence of mass transfer limitations that range $15\text{--}38 \text{ kJ mol}^{-1}$. Moreover, the E_A data summarized in Table A.18 compare well with activation energies in the order of 38 kJ mol^{-1} for CO_2 adsorption on quaternary ammonium moieties in solid resins¹⁸⁴ and with the levels of E_A of 38 kJ mol^{-1} for aqueous CO_2 adsorption¹⁸³.

In summary, the kinetic evaluation of *TGA* experiments performed allows for a first insight into the adsorption kinetics at CO_2 partial pressures at kPa level. A comparison with results published in the literature and with theoretical expectations suggests that a basic physical interpretation of the results obtained with respect to the underlying mechanism is possible. This motivates more detailed research, e.g., evaluation of a broader

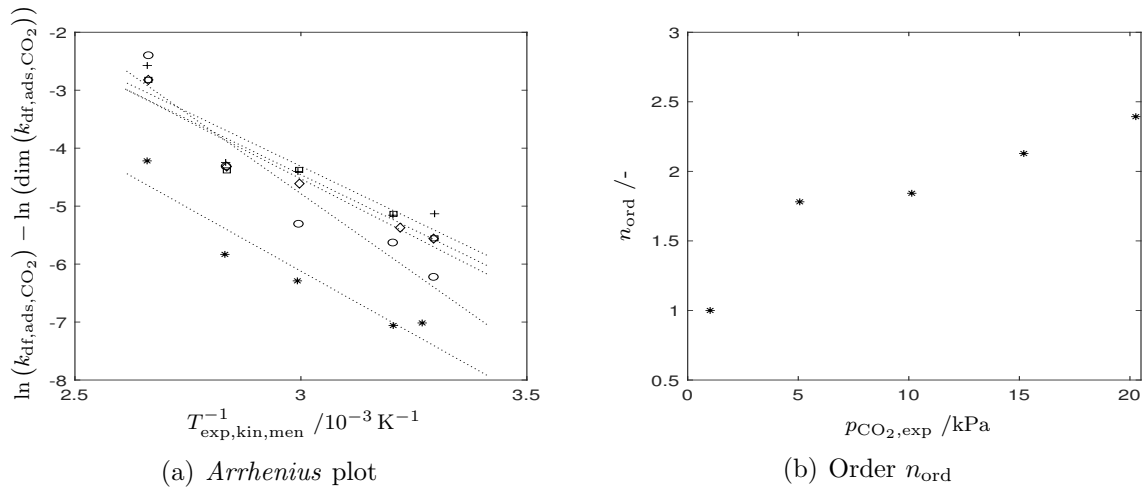


Figure A.7: Visualization of results obtained from 1-parameter fit. (a) Dependency of k_{df,ads,CO_2} on the mean temperature measured during kinetic evaluation $T_{exp,kin,men}$ visualized by *Arrhenius* plot for CO₂ partial pressures $p_{CO_2,exp}$ of ca. 1 (*), 5 (o), 10 (◇), 15 (□) and 20 kPa (+). (b) Influence of CO₂ partial pressure $p_{CO_2,exp}$ on the mean exponent n_{ord} of the driving force term (Table A.16).

variety of kinetic models proposed in the literature^{164,181,182} and in depth analysis of rate influencing steps, to be performed in subsequent studies.

Table A.17: Kinetic constant k_{df,ads,CO_2} in the dimension $10^{-3} s^{-1} mol^{1-n_{ord}} kg^{n_{ord}-1}$ as a function of the CO₂ partial pressure level $p_{CO_2,exp,asp}$ and temperature level $T_{exp,asp}$ aspired. Data are derived by means of 1-parameter fit with constant mean values of n_{ord} (Table A.16) being used.

$T_{exp,asp}$ /°C	$p_{CO_2,exp,asp}$ /kPa				
	1	5	10	15	20
30	0.90	1.99	3.85	3.87	5.91
40	0.86	3.60	4.65	5.89	5.76
60	1.86	4.97	9.94	12.59	12.25
80	2.93	13.43	13.33	12.48	14.33
100	14.71	91.02	59.47	59.53	76.25

A.4.7 Error estimation

In analogy to the *BTC* error estimate (Appendix A.3.7), the influence of inaccuracies in the measurements are evaluated by an error propagation analysis. Table A.19 gives an overview of the single sources of errors, worst case combinations of which are used to derive the overall error bounds. The estimates for single errors resulting within *TGA* operation are derived from empty crucible experiment.

The influence of measurement noises, i.e., of fast fluctuations, is minimized by taking averaged quantities into account. Additionally, $\delta_{err,noi,m_{sam}}$ is considered in the estimate of

Table A.18: Arrhenius parameters and associated coefficient of determination R^2 of the linear fit. Parameter estimates are based on $k_{\text{df,ads,CO}_2}$ data obtained from 1-parameter optimization (Table A.17). Pre-exponential factors $k_{\text{df,ads},\infty,\text{CO}_2}$, activation energies E_A and coefficients of determination R^2 are evaluated in dependence of the CO_2 partial pressure level $p_{\text{CO}_2,\text{exp,asp}}$.

		$p_{\text{CO}_2,\text{exp,asp}}$ /kPa				
		1	5	10	15	20
R^2	/-	0.91	0.90	0.92	0.90	0.86
$\ln(k_{\text{df,ads},\infty,\text{CO}_2})$	$\ln(\text{s}^{-1} \text{mol}^{1-n_{\text{ord}}} \text{kg}^{n_{\text{ord}}-1})$	7.0	11.7	7.4	7.0	6.9
E_A	/kJ mol $^{-1}$	36.3	45.6	33.2	31.6	31.0

the error bounds, which gives a worst case approximation. Also the weight of the initial sample mass measured includes uncertainties that result from the precision $\delta_{\text{err,sta},m_{\text{sam}}}$ of the laboratory scale (*METTLER TOLEDO MT5*³¹⁷) used.

Besides the influences named, inaccuracies attributed to heating effects during the temperature increase to desorption level $\delta_{\text{err,S1},m_{\text{sam}}}$ and to drifts $\delta_{\text{err,dri}_i,m_{\text{sam}}}$ are noticed in empty crucible experiments. Errors arising from drifts take into account the time scale of the corresponding segment Δt_i , e.g., $\delta_{\text{err,driS}_{\text{end,S4eq1}},m_{\text{sam}}}$ considers the time required to reach the adsorption equilibrium starting from the end of the equilibration step (S3). Moreover, fluctuations of the measured sample mass that are observed during the gas phase change in empty crucible experiments $\delta_{\text{err,G}_{\text{S4}},m_{\text{sam}}}$ are taken into account.

Also error bounds for the CO_2 partial pressures p_{CO_2} , at which the experiments are conducted, are derived. Uncertainties in the sample gas composition $\delta_{\text{err,y}_{\text{sam,CO}_2}}$ given by the vendor²⁹⁹ need to be taken into account. Moreover, the experiments are conducted at ambient pressure. For the error estimate a change in atmospheric pressure of $\pm 5\%$ is assumed. This can be regarded as a pessimistic scenario, considering that atmospheric pressure in Central Europe typically fluctuates between $0.99 \cdot 10^5$ and $1.05 \cdot 10^5$ Pa.³¹⁹

The accuracy of the operation temperature becomes of interest for the evaluation of the adsorption isotherms ($T_{\text{exp,ads,end,men}}$) as well as for the kinetic analysis ($T_{\text{exp,kin,men}}$). Temperature fluctuations during the adsorption phase of typically less than 2°C are recorded. Moreover, the TGA temperature control ensures differences between the temperature level aspired $T_{\text{exp,asp}}$ and temperature levels reached to take values of less than 3 K, with significantly lower differences being obtained for the majority of experiments. Additionally, one may take into account the accuracy of the S-type thermocouple used. Here, the calibration documents indicate that the error in the temperature measurement of the device used is in the order of -0.4 K.³²⁰

A.5 Isotherm data fitting

The isotherm parameters are fitted to the experimental data using *Matlab*^{®178} *Curve Fitting Toolbox*. *Trust-Region Algorithm* is selected to minimize the mean squared differences between the loading predicted and experimentally determined in dependence of the isotherm parameters. Convergence from different starting points to the same optimized

Table A.19: Overview of errors arising in *TGA* operation. The duration of the measurement intervals Δt_i is defined in the unit hours. If no source is given, the order of magnitude of the error source is solely determined via reference experiments. The mean atmospheric pressure p_{Ambexp} for the evaluation of the experiment is assumed to be $1.01325 \cdot 10^5$ Pa.

Error source	Variable		Lower bound	Upper bound	Source
Sample mass m_{sam}					
Measurement noise	$\delta_{\text{err,noi},m_{\text{sam}}}$	/mg	- 0.01	+ 0.01	
Sample mass (start)	$\delta_{\text{err,sta},m_{\text{sam}}}$	/mg	- 0.01	+ 0.01	[317]
Heating effects (S1)	$\delta_{\text{err,S1},m_{\text{sam}}}$	/mg	- 0.2	± 0	
Drift (S1, S2)	$\delta_{\text{err,driS1,S2},m_{\text{sam}}}$	/mg	$- 0.03 \cdot \Delta t_{\text{S1,S2}}$	$+ 0.03 \cdot \Delta t_{\text{S1,S2}}$	
Gas phase change	$\delta_{\text{err,Gs4},m_{\text{sam}}}$	/mg	- 0.05	± 0	
Drift (S3, S4)	$\delta_{\text{err,driS3_{end},S4_{\text{eq}}},m_{\text{sam}}}$	/mg	$- 0.03 \cdot \Delta t_{\text{S3}_{\text{end}},\text{S4}_{\text{eq}}}$	$+ 0.03 \cdot \Delta t_{\text{S3}_{\text{end}},\text{S4}_{\text{eq}}}$	
Pressure p_{CO_2}					
Pressure level	$\delta_{\text{err,p}}$	/10 ⁵ Pa	$-0.05 \cdot p_{\text{Ambexp}}$	$+0.05 \cdot p_{\text{Ambexp}}$	[319]
Gas composition	$\delta_{\text{err},y_{\text{sam,CO}_2}}$	/-	$- 0.02 \cdot y_{\text{sam,CO}_2}$	$+ 0.02 \cdot y_{\text{sam,CO}_2}$	[299]
Temperature $T_{\text{exp},i}$					
Temperature level	$\delta_{\text{err},T_{\text{exp}},T_{\text{exp},i}}$	/K	$-f(T_{\text{exp}}(t))$	$+f(T_{\text{exp}}(t))$	[320]

parameter set indicates a minor influence of local optima on the parameter fit. Moreover, to account for the aspect that the experimentally determined CO₂ loading can span several orders of magnitude, the contributions of the measurement points are adjusted by weights

$$f_{\text{wei},q_{\text{eq},\text{CO}_2}} = \frac{1}{q_{\text{eq},\text{CO}_2,\text{exp}}}, \quad (\text{A.20})$$

which are formulated as a function of the experimental loading $q_{\text{eq},\text{CO}_2,\text{exp}}$ measured. In accordance with the isotherm data published by other research groups^{137,157,166,167}, χ_{Tot} is set to zero and not varied in the optimization routine. Figure A.8 visualizes the results of the data fit to either the *BTC* data or the *TGA* data obtained in this work, as well as the results obtained from a simultaneous fit of the *BTC* data from this work and the *TGA* data provided by Sutanto et al.¹⁶⁷ for CO₂ partial pressures at kPa-level.

In the data fitting of the water adsorption measurements, data at 43 % and 73 % relative humidity (Table A.5) have been excluded from the data fit, as these significantly diverge from the trend shown by the other data points in the set. Moreover, as no distinct influence of operation temperature except from its influence on relative humidity is noticed in the experimentally obtained data and in the measurements published by Veneman et al.¹³⁷, no temperature influence on the *BET*, *n-BET* or *GAB* isotherm parameters is taken into account in this contribution.

To increase the accuracy of the data fit, the extension of the isotherm model by the influence of humidity is performed based on isotherm model 4 (Table 3.1). The determination of the parameters used in the evaluation of $\phi_{q_{\text{eq},\text{CO}_2,\text{wet,dry}}}$ (Table 3.3) is performed

similar to the isotherm data fitting by application of *Matlab*^{®178} *Curve Fitting Toolbox*. No weights are used in the fit as the experimentally obtained CO₂ loadings are found to be in the same order of magnitude.

A.6 Additional properties of the sorbent

In Section A.6.1 the determination of the characteristic densities and void fractions is outlined. Moreover, the experiments to investigate the flowability of the sorbent are summarized in Section A.6.2.

A.6.1 Density and void fraction

The determination of the characteristic densities ρ_i is based on a sorbent sample from which a fraction is analyzed via *TGA* experiments to determine the mass fraction of the species adsorbed on the sample. Thus, densities and masses given are related to the pure sorbent. 11 measurements are performed.

The bulk density

$$\rho_B = \frac{m_{B,Sor}}{V_B} \quad (A.21)$$

is calculated based on measurements of the bulk mass $m_{B,Sor}$ for samples with a volume V_B of typical 30 ml. To obtain information on the particle density ρ_P and on the bed void fraction ψ_B , the gas volume present in the sorbent bed is exchanged by water¹²⁸, the added mass of which is recorded. It is assumed that due to the hydrophilic nature of *Lewatit* water is able to enter its pores. The pore volume is estimated based on the mass-specific pore volume v_{Por} given by the vendor¹⁶² (Table 3.4), which is in good accordance with v_{Por} data provided by other authors^{163,165}. Based on this information, the particle density is calculated by

$$\rho_P = \frac{m_{B,Sor}}{V_B - V_{H_2O} + m_{B,Sor} \cdot v_{Por}} \quad (A.22)$$

Moreover, the porosity of the sorbent particle is estimated via

$$\epsilon_P = 1 - \frac{V_B - V_{H_2O}}{V_B - V_{H_2O} + m_{B,Sor} \cdot v_{Por}} \quad (A.23)$$

and the bed void fraction is given by

$$\psi_B = 1 - \frac{\rho_B}{\rho_P} \quad (A.24)$$

Note that this definition of ψ_B does not include the void space in the particles, i.e., the pore volume.

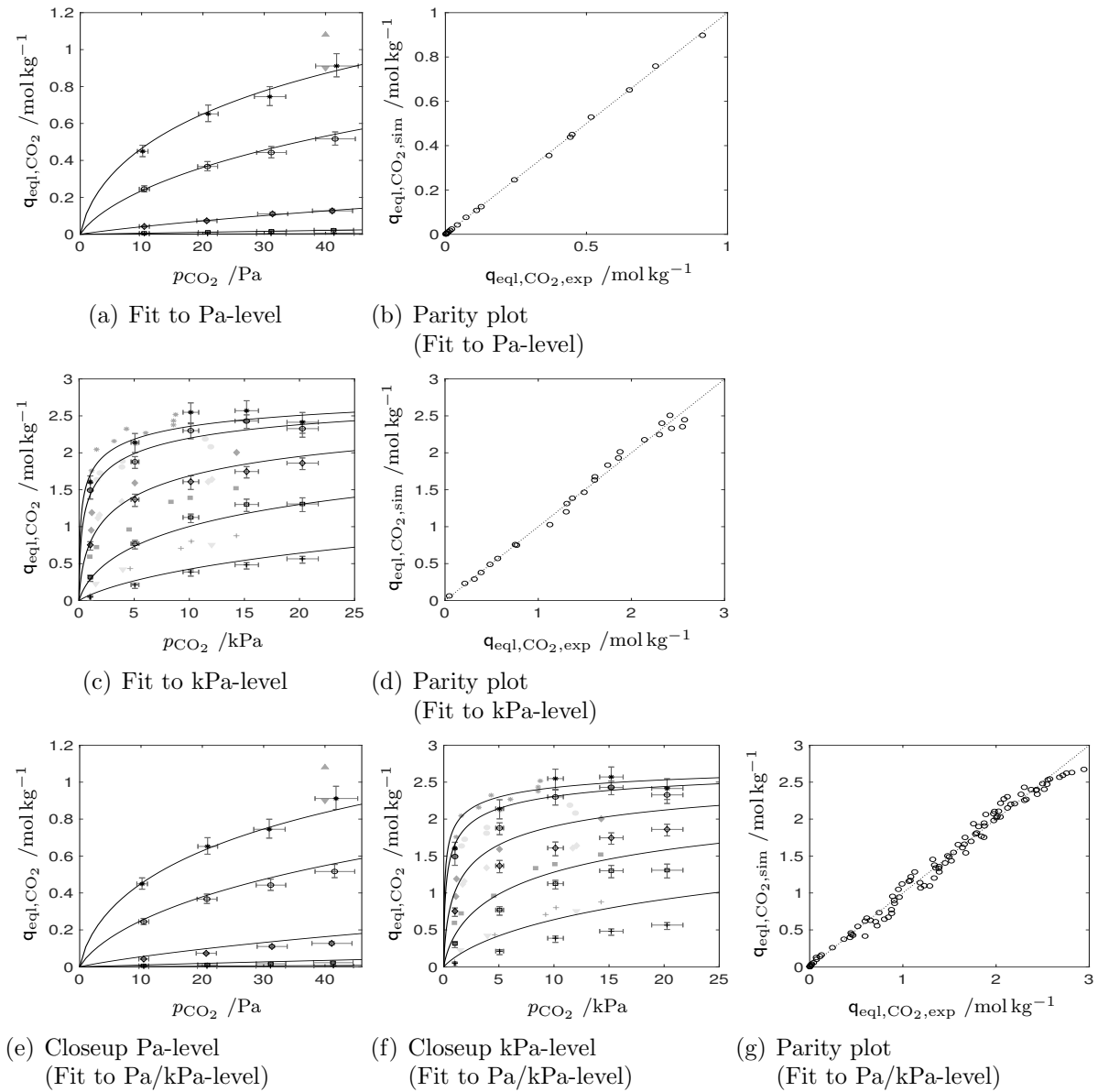


Figure A.8: CO₂ equilibrium loading $q_{\text{eq},\text{CO}_2}$ on *Lewatit* for temperatures of 30 °C (*), 40 °C (o), 60 °C (◇), 80 °C (□) and 100 °C (+) determined for CO₂ partial pressures p_{CO_2} that correspond to CO₂ mole fractions at ppm- and %-level at a total pressure of $1 \cdot 10^5$ Pa. Predictions by a *Toth* isotherm model fitted to: (a)–(b) *BTC* data (this work, isotherm model 4), (c)–(d) *TGA* data (this work, isotherm model 5) and (e)–(g) simultaneous fit to *BTC* data (this work) and to *TGA* data (Sutanto et al.¹⁶⁷) (isotherm model 7) are investigated. The simulated loadings are visualized by solid lines (-). Data from literature sources at %-level are shown in shades of gray: Sonnleitner et al.¹⁶⁶ (+), Sutanto et al.¹⁶⁷ (o). The isotherm data given for 95 °C by Sonnleitner et al.¹⁶⁶ are visualized by gray triangles (▽). Moreover, isotherm data at a CO₂ partial pressure of 40 Pa and at temperatures of 25 °C (▲) and 35 °C (▼) published by Veneman et al.¹³⁷ are depicted in (a) and (e). Error bars for experimental data are derived from error propagation studies summarized in Appendix A.3.7.1 and A.4.7. A comparison between the experimentally determined and predicted CO₂ loadings, $q_{\text{eq},\text{CO}_2,\text{exp}}$ and $q_{\text{eq},\text{CO}_2,\text{sim}}$, respectively, is given in Figures (b), (d) and (g).

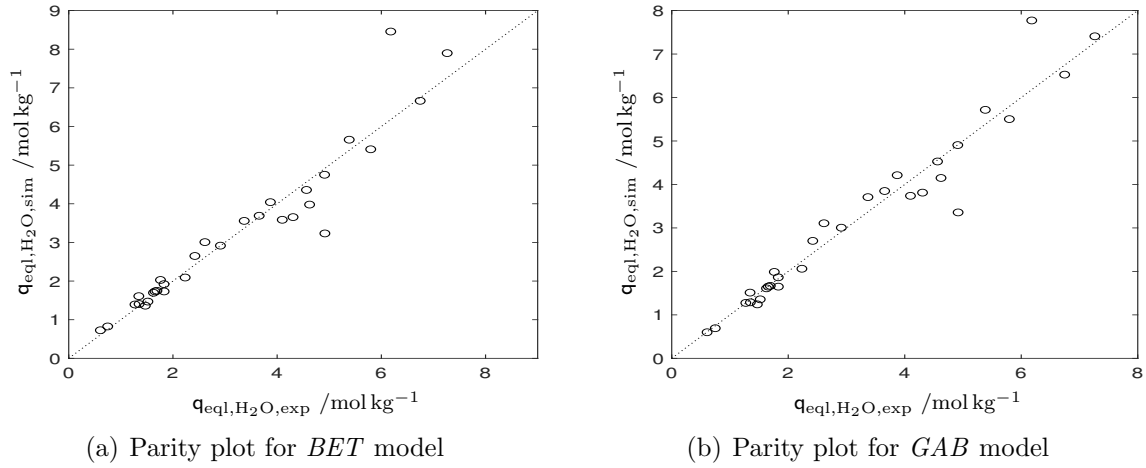


Figure A.9: Parity plot visualization of data prediction with (a) *BET* and (b) *GAB* isotherm model for H₂O adsorption on *Lewatit*. Experimental data are summarized in Table A.5.

A.6.2 Flowability of the sorbent

The sorbent samples used are exposed to a defined gas atmosphere of 20 °C and 80 % relative humidity for two days to ensure defined conditions for flowability tests. Three measurements are taken for each parameter to be evaluated.

The *Carr index*

$$CI = \frac{\rho_{B,tap} - \rho_B}{\rho_{B,tap}} \quad (\text{A.25})$$

is defined via the sorbent bulk density in poured ρ_B and tapped $\rho_{B,tap}$ state. The densities are measured in a cylindrical measuring vessel of 100 ml readable to 1 ml, filled with a sample mass typically in the order of 35 g. To obtain the tapped density, *Tapped Density Tester TD1*³²¹ of *Sotax GmbH* is used.

The determination of the angle of repose α_{rep} is performed based on measurements of sorbent bed height H_B . The sorbent bed is generated by pouring the particles from a hopper onto an underlying circular surface with a defined diameter D_B of 98 mm. Based on these data, the angle of repose is calculated via the basic geometric correlation

$$\alpha_{rep} = \arctan\left(\frac{2 \cdot H_B}{D_B}\right). \quad (\text{A.26})$$

B Appendix: Approaches to intensified heat integrated DAC units

Parts of this appendix have been published in peer-reviewed journal articles and in the corresponding supplementary information.^{215,230}

B.1 Energy demand and economics of DAC

Table B.1 provides an overview of the current state of research with regard to DAC costs and energy demands.

B.2 Feasibility study

In this section the fundamentals of the feasibility study performed are outlined, which include: an investigation of sorbent movement and gas sealing (Appendix B.2.1), an analysis of heat and mass transfer (Appendix B.2.2) and a discussion of large-scale realization (Appendix B.2.3).

B.2.1 Sorbent movement and gas sealing

The power requirement for sorbent movement is estimated via *DIN 22101*²¹⁸ and *VDI 2324*²¹⁹. The sorbent properties summarized in Table 3.4 are used. Calculations are performed for a reference CO₂ product flow of 1 mol s⁻¹, achieved at a CO₂ working capacity of 0.25 mol kg⁻¹. H₂O working capacities of 12 mol kg⁻¹ are used as a worst case approximation. The estimate of the energy requirement per sealing device is calculated for the reference parameter set: sorbet bed width $H_{B,z} = 0.5$ cm, contact width of the sealing $H_{Prs} = 5$ cm and contact pressure $p_{Prs} = 0.1 \cdot 10^5$ Pa. The friction coefficient between the belt and the gas barrier is pessimistically estimated to be 0.7.^{218,328}

B.2.2 Heat and mass transfer

The analysis of the width of the sorbent bed and of the support structure (Appendix B.2.2.1) as well as of the thermal integration and of the transfer media used (Appendix B.2.2.2) form the basis for the investigations of heat and mass transfer characteristics.

Table B.1: Literature review of *DAC* technology with focus on cost estimation and on energy demand. Investigations are classified with regard to the data basis used in the categories: basic *DAC* models (Basic) and commercial applications (Com.).

Author	Year	Costs /\$t ⁻¹	Energy		Class	Remarks	Source
			electric /kJ mol ⁻¹	thermal /kJ mol ⁻¹			
<i>APS</i>	2011	430–550	78	268	Basic	Alkaline (NaOH) solution as sorbent. Regeneration via CaO [17] loop. High-temperature heat input required ($T > 800$ °C)	[17]
Eisaman et al.	2009	–	< 400	–	Basic	Electrochemical approach to <i>DAC</i> , besides other modified fuel cell-based. CO ₂ transport via electrochemical pumping. Desorption at 25 °C	[322]
Goldberg et al. (Lackner)	2013	–	< 100	–	Basic	Hybrid <i>TSA</i> and <i>MSA</i> operation, desorption temperature 45 °C. Assumption: thermal recovery of 80%. Use of heat pumps to provide thermal energy (without use of heat pump: 344 kJ mol ⁻¹)	[118]
House et al.	2009	1000	–	> 400	Basic	Unspecified process, calculations based on thermodynamic minimum energy demand	[323]
Kulkarni and Sholl	2012	40–400	34	262	Basic	Solid sorbent (monolith, TRI-PE-MCM-41) regenerated via <i>TSA</i> operation. Different process configurations including steam as purge gas. Additional analysis of regeneration via diurnal temperature change	[98]

Author	Year	Costs /\$ t ⁻¹	Energy electric /kJ mol ⁻¹	Energy thermal /kJ mol ⁻¹	Class	Remarks	Source
Lackner	2009	30 – 200		50	Basic	Basic estimations based on an amine sorbent. Regeneration at 45 °C using water vapor (<i>MSA</i>). Optimistic estimation of cost decrease	[99]
Li et al.	2015	–	442	–	Basic	Liquid sorbent-based system (NaOH, Ca(OH) ₂ loops). Focus on wind power use for regeneration	[324]
Mazzotti et al.	2013	376 – 430	63 – 117	266	Basic	In-depth analysis of <i>APS</i> system (liquid alkaline sorbent). Detailed discussion of avoided costs and of potential for optimization	De- [111]
PARC	2011	–	100 – 200	–	Basic	Caustic sorbents, regenerated via bipolar membrane electrolysis. Basic experiments	[86]
ZSW (CORAL)	2019	–	79 – 158	317 – 396	Basic	General investigation of various sorbents. Basic laboratory experiments with liquid polyethyleneimine (PEI) in <i>TSA</i> operation (regeneration temperature 110 °C)	[85, 325]

Author	Year	Costs	Energy electric	Energy thermal	Class	Remarks	Source
		/\$t ⁻¹	/kJ mol ⁻¹	/kJ mol ⁻¹			
<i>Carbon Engineering</i>	2018- 2020	94–232	0–58	231–388	Com.	Liquid sorbent based process. Optimized version of <i>APS</i> concept. Regeneration via calcination (> 850 °C)	[85, 92, 93]
<i>Climeworks</i>	2019- 2020	600 (2019) 100 (2030)	79	238–396	Com.	Optimized solid sorbent based <i>TVSA</i> process. Desorption at 100 °C. Customized sorbents, e.g., amine moiety on cellulose fibers	[85, 105, 200]
<i>CO2MAY</i>	2017	< 20	–	–	Com.	Use of alkaline solution. Use of waste heat at 95 °C	[326]
<i>Global Thermostat</i>	2018- 2020	12–42	24–41	185–223	Com.	<i>TVSA</i> process (regeneration temperature 85–95 °C), based on solid amino-polymer. Use of water vapor as strip gas. 50 % of heat spent in regeneration process is recovered	[107, 200, 211]
<i>Hydrocell</i>	2018- 2020	–	–	–	Com.	Solid sorbent based <i>TVSA</i> process. Regeneration temperature 70–80 °C	[197, 200, 327]
<i>Infinitee (Carbon Sink)</i>	2019- 2020	–	–	–	Com.	Use of solid sorbents (ion exchange materials) in <i>MSA</i> mode	[198, 200]
<i>Skytree</i>	–	–	–	–	Com.	Use of solid sorbents. Electrostatic adsorption and regeneration via <i>MSA</i> at temperature levels ranging 80–90 °C. Spin-off of the <i>European Space Agency</i>	[199, 200]

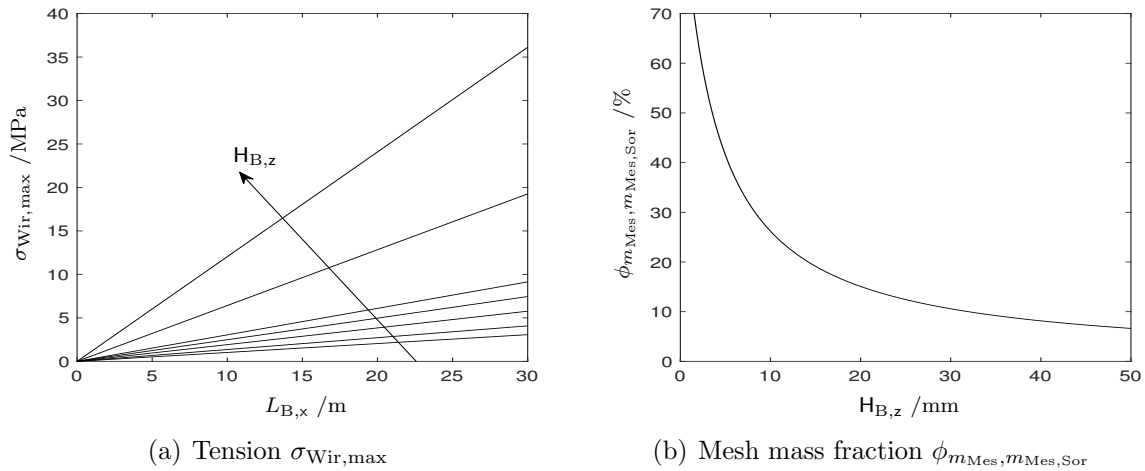


Figure B.1: (a) Maximum tension in the wire cross section normal to solid movement $\sigma_{Wir,max}$ induced by gravitational forces that results from the mass of the sorbent m_{Sor} and of the mesh m_{Mes} . Dependency on the length of the moving belt $L_{B,x}$ for bed width $H_{B,z}$ ranging 1.0, 2.5, 5.0, 7.5, 10.0, 25.0 and 50.0 mm is investigated. (b) Contribution $\phi_{m_{Mes}, m_{Mes,Sor}}$ of the supporting mesh mass to the overall mass of the moving belt, which comprises the mass of the sorbent particles and of the mesh, in dependence of bed width $H_{B,z}$. Mesh specifications of $H_{Mes} = 0.25$ mm and $D_{Wir} = 0.16$ mm according *DIN ISO 4783-2*²²⁶ are used in the calculations.

B.2.2.1 Width of sorbent bed and support structures

With view on efficient mass transfer, large open surface areas $a_{ope,Mes}$ of the support structure are aspired. The mesh size H_{Mes} is limited by the minimum sorbent particle diameter $D_{Lew,min} = 0.30$ mm.¹⁶² Use of a low wire diameter D_{Wir} is favored to reduce the material demand and the weight of the structure. Based on *DIN ISO 4783-2*²²⁶ mesh specifications in line with these requirements are selected which read: $H_{Mes} = 0.25$ mm and $D_{Wir} = 0.16$ mm. These allow for $a_{ope,Mes} = 37\%$.

Based on these data the maximum tension expected in the wire cross section normal to the solid movement is investigated. Gravitational forces that results from sorbent and wire mass are taken into account. Wires are assumed to be made up of stainless steel with a density of 7900 kg m^{-3} .²²⁶ A vertical installation of the belt is analyzed.

Results of the investigation are summarized in Figure B.1(a). Maximum tensions in the order of magnitude of 36 MPa from gravitational forces are noticed. If the additional tension from 5 sealing positions is considered (~ 36 MPa), even in the limiting case of high belt length and of high bed width only tensions lower than the maximum allowable stresses for carbon (~ 89 MPa) or stainless steel (V2A, 119 MPa) at 100°C are obtained.²¹⁷ Thus, in the framework of the preliminary feasibility study aspired, the results obtained suggest basic mechanic stability of the belt. In *MBdA* the pressure at the bottom of the structure that results from the sorbent mass equals in the worst case twice the sorbent induced pressure in the *MBtA* concept of same bed length. Thus, the results depicted in Figure B.1(a) also suggest stability, e.g., for use of tube like support structures in *MBdA*. Compared to parallel wall support structures, these allow for higher surface to volume ratios and for operational independence with regard to the wind direction. However, simpler design and operation favors parallel wall type structures.

Table B.2: Thermal conductivities of solid transfer media and of the gas phases used for evaluation of thermal resistances. Thermal conductivities calculated at 25 °C are used in the evaluation.

Specie		Cu	V2A	EG	PTFE	Air	H ₂	
Th. cond.	λ /W K ⁻¹ m ⁻¹	401	15	5	217	$260 \cdot 10^{-3}$	$26 \cdot 10^{-3}$	$172 \cdot 10^{-3}$
Source		[329]	[116]	[229]	[116]		Appendix B.3.1	

B.2.2.2 Thermal integration and transfer media

MBdA energy demands attributed to overcome friction and static pressure losses in the transfer medium phase of the *MBdA* are estimated based on worst case assumptions. Flow of the medium in channels of 1 mm width on either side of a solid sorbent bed spanning $H_{B,z} = 50$ mm is assumed. The transfer medium properties are evaluated based on the properties of the thermal oil *Dowtherm J*¹¹⁶ (Table B.7). The operation point of the *DAC* unit reads: productivity $\dot{n}_{Pro,CO_2} = 1$ mol s⁻¹, working capacity $\Delta q_{wor,CO_2} = 0.25$ mol kg⁻¹ and sorbent velocity $u_B = 1$ mm s⁻¹. Pressure losses are estimated based on correlations for laminar flow in a duct with infinite depth.¹¹⁶ In the calculation of the laminar drag coefficient a correction factor of 1.5 is taken into account.¹¹⁶

MBtA heat losses in the adsorption zone relative to the heat transferred in this zone are estimated based on parallel and series connections of thermal resistances.¹¹⁶ A temperature difference between the adsorption and desorption zone $\Delta T_{ads,des}$ of 75 °C is assumed. The thermal resistance of a gas duct $H_{Mes,T}$ of 1 mm between the belt and transfer medium is accounted for in the calculations. For reasons of clarity, air is used as a reference gas phase in the heating zone, whereas the properties of pure hydrogen are used to describe the gas phase in the cooling zone. The thermal conductivities used in the calculations are summarized in Table B.2.

B.2.3 Large scale realization

Both concepts proposed can benefit from numbering up, as energy losses and specific efforts for gas supply can be reduced. In *MBtA* motors can be used to drive multiple belts, the material demand for realization of gas ducts can be decreased and an alternating parallelization of the heating and cooling zone might allow for potential to increase the efficiency of heat exchange. The *MBdA* design offers more degrees of freedom relevant for large-scale applications, e.g., external heating of the transfer medium, independent length of the heating and cooling zone or possible design of different zones as spatially independent units. Besides others, the use of bucket elevators, of transfer medium pumps or of vacuum pumps by multiple beds might be named as an advantage. Moreover, the gas sealing, e.g., by rotary valves, can be combined for parallel beds.

B.3 MBtA

This section provides a brief overview of the thermophysical properties (Appendix B.3.1), modeling approach (Appendix B.3.2) and numeric implementation (Appendix B.3.3) used to determine the state variable profiles of the *MBtA* concept. Moreover, basic operation and design parameters used in the evaluation of the concept are summarized in Appendix B.3.4.

B.3.1 MBtA: thermophysical and adsorption properties

Various thermophysical parameters and correlations are used within the model proposed. Correlations used to evaluate the properties of the gas phase (Appendix B.3.1.1) and of the solid particles (Appendix B.3.1.2) are presented. Moreover, the adsorption equilibrium, kinetics and thermodynamics are discussed in Appendix B.3.1.3.

B.3.1.1 Thermophysical properties: gas phase

Table B.3 summarizes information with regard to the gas phase thermophysical properties. In the model the pseudo-species Air is used that on a molar basis is composed of 79 % nitrogen and 21 % oxygen.³³⁰ Besides information on the single species, Table B.3 also defines how the thermophysical quantities of the mixed gas phase Φ_G are estimated. Based on the single component properties $\Phi_{i_{\text{Spe}}}$, a simple mole fraction-based mixing rule

$$\Phi_G = \sum_{i_{\text{Spe}}} y_{i_{\text{Spe}}} \cdot \Phi_{i_{\text{Spe}}} \quad (\text{B.1})$$

as well as more complex correlations are used. The effective *Fickian* diffusion coefficient

$$D_{\text{dif},j_{\text{Spe}},\text{mol}} = \frac{1 - y_{j_{\text{Spe}}}}{\sum_{i_{\text{Spe}} \neq j_{\text{Spe}}} \frac{y_{i_{\text{Spe}}}}{D_{\text{dif},i_{\text{Spe}},j_{\text{Spe}},\text{mol}}}} \quad (\text{B.2})$$

of a specie j_{Spe} in the multi-component mixture is estimate based on the binary diffusion coefficients $D_{\text{dif},i_{\text{Spe}},j_{\text{Spe}},\text{mol}}$.³³¹

B.3.1.2 Thermophysical properties: sorbent particle

The thermophysical properties of *Lewatit* define the properties of the solid particles. These are discussed in Section 3.3 and summarized in Table 3.4. Here, the thermal conductivity of *Lewatit* particles is assumed to take a value of $0.16 \text{ W K}^{-1} \text{ m}^{-1}$, which equals that of polystyrene.¹¹⁶

B.3.1.3 Adsorption equilibrium, kinetics and thermodynamics

Based on the kinetic evaluation performed in Section 3.2.2.3, as a first estimate, a linear driving force approach, i.e., (3.4) with $n_{\text{ord}} = 1$, based on the sorbent loading $q_{i_{\text{Spe}}}$ is used

Table B.3: Thermophysical properties of the gas phase used in the *MBA* concept. * Calculated based on pure components data, $\omega_{N_2} = 0.037$ and $\omega_{O_2} = 0.022$,³³⁰ weighted with their mole fraction³³²

Property	Symbol	Unit	CO ₂	H ₂	Air	Mix (G)
Molar mass	M	/g mol ⁻¹	44.00950 [128]	2.01588 [128]	28.850 [333]	(B.1)
Crit. pressure	p_{crit}	/10 ⁵ Pa	73.74 [126]	12.93 [126]	38.24 [333]	–
Crit. temperature	T_{crit}	/K	304.12 [126]	32.98 [126]	132.45 [333]	–
Crit. volume	V_{crit}	/10 ⁻⁶ m ³ mol ⁻¹	94.07 [126]	64.20 [126]	92.17 [333]	–
Acentric factor	ω	/-	0.225 [126]	-0.217 [126]	0.034* [330, 332]	–
Collision diameter	σ_{cool}	/10 ⁻¹⁰ m	3.941 [126]	2.827 [126]	3.711 [126]	–
Min. of pair-potential energy/ <i>Boltzmann</i> con.	$\frac{\epsilon_{pair}}{k_{B,ol}}$	/K	195.2 [126]	59.7 [126]	78.6 [126]	–
Heat capacity	c_p	/JK ⁻¹ mol ⁻¹	<i>Shomate</i> equation ¹²⁸ for single components Add. mixing rule (B.1) for pseudo-species			(B.1)
Enthalpy	h	/J mol ⁻¹	<i>Shomate</i> equation ¹²⁸ for single components Add. mixing rule (B.1) for pseudo-species			(B.1)
Viscosity	μ	/Pas	Derived from <i>Chapman-Enskog</i> theory ¹²⁶ Collision integral Ω_{tr} estimated via correlation from Neufeld et al. ^{126,335} based on $\frac{\epsilon_{pair}}{k_{B,ol}}$ data			Method of Wilke ^{126,334}
Th. conductivity	λ	/WK ⁻¹ m ⁻¹	Correlation from Chung et al. ^{126,336,337}			<i>Wassiljewa</i> equation ^{126,338} with modification from Mason and Saxena ^{126,339} (parameter ϵ set to 1 in accordance with Poling et al. ¹²⁶)

Property	Symbol	Unit	CO ₂	H ₂	Air	Mix (G)
Mol. diffusion coefficient	$D_{\text{dif,mol}}$	$\text{m}^2 \text{s}^{-1}$	Binary diffusion coefficients derived from <i>Chapman-Enskog</i> theory. ¹²⁶ In accordance with Poling et al. correction factor $f_{D_{\text{dif}}}$ is set to 1 and the assumption of ideal gas behavior is applied. ¹²⁶			Mixing rule (B.2) based on binary diffusion coefficients ³³¹
			Characteristic <i>Lennard-Jones</i> energy and length of the binary system is estimated via mixing rule based on pure component properties: σ_{co1} and ϵ_{pai} . ¹²⁶			
			Collision integral for diffusion $\Omega_{D_{\text{dif}}}$ is estimated via a correlation of Neufeld et al. ^{126,335}			

to describe the kinetics of the adsorption and desorption process. Neither adsorption of H_2 nor of Air is considered. For CO_2 adsorption, the equilibrium loading q_{eq,CO_2} is calculated based on *Toth* isotherm model (3.2), with the parameter set 7 summarized in Table 3.1 being used. Moreover, the driving force coefficient $k_{\text{df,ads},CO_2}$ is assumed to take a constant value of $5 \cdot 10^{-4} \text{ s}^{-1}$, which can be interpreted as a worst case assumption with respect to the results presented in Section 3.2.2.3 and published in the literature¹⁵⁷. The heat of CO_2 adsorption $\Delta h_{\text{ads},CO_2}$ is assumed to take a constant value of -84 kJ mol^{-1} , which is estimated based on the analysis of the isosteric heat of adsorption in a temperature range of $25-100 \text{ }^\circ\text{C}$ for CO_2 loadings that span $0-1 \text{ mol kg}^{-1}$ (Figure 3.6(b)).

B.3.2 MBtA: model

Figure 4.8 presents the structure of the modeling approach that is selected to describe the evolution of the *MBtA* state variables. Two submodels are used to represent the different phases. These are linked via boundary conditions of mass and energy transfer. A one-dimensional, time-dependent model is applied to investigate the thermophysical behavior of the strip gas phase (Appendix B.3.2.1), whereas a two-dimensional model for the belt phase allows for detailed investigations of transfer phenomena orthogonal to the belt movement (Appendix B.3.2.2).

B.3.2.1 Governing equations: gas phase

The state of the strip gas phase is defined by its temperature T_G , velocity u_G and by the concentration of the gas phase species $c_{G,i_{\text{Spe}}}$. The species i_{Spe} : CO_2 , H_2 and pseudo-component Air are considered. Assuming ideal gas behavior and plug flow, the law of mass conservation reads

$$\frac{\partial c_{G,i_{\text{Spe}}}}{\partial t} = -\frac{\partial (u_G \cdot c_{G,i_{\text{Spe}}})}{\partial x} - \frac{1}{H_{G,z}} \cdot k_{\text{df,BG},i_{\text{Spe}}} \cdot (c_{G,i_{\text{Spe}}} - c_{B,i_{\text{Spe}}}|_{z=0}) . \quad (\text{B.3})$$

Here, $c_{B,i_{\text{Spe}}}|_{z=0}$ describes the concentration of species i_{Spe} at the sorbent bed surface and $H_{G,z}$ defines the height of the duct in which the gas is flowing. To describe the mass transfer between the sorbent bed and gas phase, a linear driving force approach is used. The mass transfer coefficient $k_{\text{df,BG},i_{\text{Spe}}}$ is calculated by use of a correlation for *Sherwood* number Sh_G provided by Mercer¹¹⁶ that is based on *Reynolds* and *Schmidt* number, Re_G and Sc_G , respectively, of the gas phase. Moreover,

$$c_{G,i_{\text{Spe}}}|_{x=x_{\text{Coo}}} = c_{G,i_{\text{Spe},\text{in}}} \quad (\text{B.4})$$

is used as a boundary condition, which defines the gas phase concentration at its inlet.

In analogy to (B.3), the governing equation of energy conservation reads

$$\frac{\partial T_G}{\partial t} = -u_G \cdot \frac{\partial T_G}{\partial x} - \frac{1}{H_{G,z} \cdot \sum_{i_{\text{Spe}}} (c_{G,i_{\text{Spe}}} \cdot c_{p,G,i_{\text{Spe}}})} \cdot h_{\text{df,BG}} \cdot (T_G - T_B|_{z=0}) . \quad (\text{B.5})$$

The heat transfer coefficient $h_{\text{df,BG}}$ between gas and bed is calculated in analogy to the mass transfer coefficient. Here, Sh_G and Sc_G are substituted by *Nusselt* number Nu_G and *Prandtl* number Pr_G , respectively.¹¹⁶ Again, the definition of the state variable at the gas phase inlet

$$T_G|_{x=x_{\text{Coo}}} = T_{G,\text{in}} \quad (\text{B.6})$$

gives the spatial boundary condition required. Moreover, variation of the gas phase velocity \mathbf{u}_G along the spatial coordinate \mathbf{x} is considered. In this respect, the assumption of ideal gas behavior allows for formulation of an additional constraint with regard to the overall gas phase concentration

$$\sum_{i_{\text{Spe}}} c_{G,i_{\text{Spe}}} = c_G = \frac{p}{R_{\text{id}} \cdot T_G}. \quad (\text{B.7})$$

Substitution of the sum over all gas phase concentrations on the left hand side of (B.7) by (B.3) leads to

$$0 = \frac{p}{R_{\text{id}} \cdot T_G^2} \cdot \frac{\partial T_G}{\partial t} - \frac{p}{R_{\text{id}}} \cdot \frac{\partial}{\partial \mathbf{x}} \left(\frac{\mathbf{u}_G}{T_G} \right) - \frac{1}{H_{G,z}} \cdot \sum_{i_{\text{Spe}}} (k_{\text{df,BG},i_{\text{Spe}}} \cdot (c_{G,i_{\text{Spe}}} - c_{B,i_{\text{Spe}}}|_{z=0})) \quad (\text{B.8})$$

that implicitly defines \mathbf{u}_G in dependency of the other gas phase state variables. Note that no pressure change in the gas phase is considered, i.e., operation pressure p stays constant. In analogy to the other state variables of this phase, the definition of the state variable at the gas phase inlet is used as the spatial boundary condition required

$$\mathbf{u}_G|_{x=x_{\text{Coo}}} = \mathbf{u}_{G,\text{in}}. \quad (\text{B.9})$$

B.3.2.2 Governing equations: belt phase

A two-dimensional modeling approach is used for the belt phase that is composed of the moving sorbent particles and of the gas in the void space between those. Convective mass and heat transfer by belt movement with constant velocity \mathbf{u}_{Belt} is taken into account in \mathbf{x} direction, whereas mass and heat transport orthogonal to the belt movement is assumed to be dominated by diffusion and by conductive heat transfer, respectively, which gives a worst case assumption. Cyclic state and continuity between the zones, through which the belt is moving, are enforced via the boundary conditions in \mathbf{x} -domain, i.e., via the continuity of flows at the interfaces between the zones. The boundary conditions in \mathbf{z} -coordinate are summarized in Tables B.4 and B.5.

The law of mass conservation in the bed void space

$$\begin{aligned} \frac{\partial c_{B,i_{\text{Spe}}}}{\partial t} = & - \mathbf{u}_{\text{Belt}} \cdot \frac{\partial c_{B,i_{\text{Spe}}}}{\partial \mathbf{x}} + \frac{\partial}{\partial \mathbf{z}} \left(D_{\text{dif},i_{\text{Spe}},\text{mol}} \cdot \frac{\partial c_{B,i_{\text{Spe}}}}{\partial \mathbf{z}} \right) \\ & - \frac{1 - \psi_B}{\psi_B} \cdot \rho_P \cdot k_{\text{df,ads},i_{\text{Spe}}} \cdot (\mathbf{q}_{\text{eql},i_{\text{Spe}}} - \mathbf{q}_{i_{\text{Spe}}}) \end{aligned} \quad (\text{B.10})$$

Table B.4: Spatial boundary conditions (z-domain) of temperature profile T_B in the sorbent bed.

Zone	Spatial coordinate		Boundary conditions
	x	z	
Adsorption]0, x _{Ads} [0	$T_B = T_{Amb}$
		z _{H_{B,z}}	$T_B = T_{Amb}$
Heating]x _{Ads} , x _{Hea} [0	$\frac{\partial T_B}{\partial z} = 0$
		z _{H_{B,z}}	$-\lambda_B \cdot \frac{\partial T_B}{\partial z} = h_{df,BB} \cdot (T_B(x, z) - T_B(x_{Coo} - (x - x_{Ads}), z))$
Ext. heating]x _{Hea} , x _{Hex} [0	$\frac{\partial T_B}{\partial z} = 0$
		z _{H_{B,z}}	$\lambda_B \cdot \frac{\partial T_B}{\partial z} = \dot{q}_{ext,Hex}$
Desorption]x _{Hex} , x _{Des} [0	$\lambda_B \cdot \frac{\partial T_B}{\partial z} = h_{df,BG} \cdot (T_B - T_G)$
		z _{H_{B,z}}	$\lambda_B \cdot \frac{\partial T_B}{\partial z} = \dot{q}_{ext,Des}$
Cooling]x _{Des} , x _{Coo} [0	$\lambda_B \cdot \frac{\partial T_B}{\partial z} = h_{df,BG} \cdot (T_B - T_G)$
		z _{H_{B,z}}	$-\lambda_B \cdot \frac{\partial T_B}{\partial z} = h_{df,BB} \cdot (T_B(x, z) - T_B(x_{Ads} + (x_{Coo} - x), z))$

is formulated in terms of the component concentrations $c_{G,i_{Spe}}$. $D_{dif,i_{Spe},mol}$ is the molecular diffusion coefficient and ψ_B denotes the void fraction of the bed that is composed of sorbent particles of density ρ_P .

In analogy to (B.10) the law of energy conservation reads

$$\begin{aligned} \frac{\partial T_B}{\partial t} = & -u_{Belt} \cdot \frac{\partial T_B}{\partial x} + \frac{1}{(1 - \psi_B) \cdot \rho_P \cdot c_{p,P}} \cdot \frac{\partial}{\partial z} \left(\lambda_B \cdot \frac{\partial T_B}{\partial z} \right) \\ & + \frac{1}{c_{p,P}} \cdot \sum_{i_{Spe}} \left(-\Delta h_{ads,i_{Spe}} \cdot k_{df,ads,i_{Spe}} \cdot (q_{eq,i_{Spe}} - q_{i_{Spe}}) \right), \end{aligned} \quad (B.11)$$

which includes the assumptions of a negligible contribution of the void gas phase heat capacity, compared to that of the solid phase, and of thermal equilibrium between the void gas phase and the sorbent particles. Note that

$$\lambda_B = \psi_B \cdot \lambda_{B,G} + (1 - \psi_B) \cdot \lambda_P \quad (B.12)$$

defines the effective thermal conductivity of the sorbent bed.

Focusing on the boundary conditions of the sorbent bed temperature profile (Table B.4), one notices that linear driving force approaches are also used to describe the heat exchange between the sorbent beds as well as the external heat transfer to the bed. The coefficient

$$h_{df,BB} = \left(\frac{H_{BT,Hea}}{\lambda_{BT,Hea}} + \frac{H_T}{\lambda_T} + \frac{H_{BT,Coo}}{\lambda_{BT,Coo}} \right)^{-1}, \quad (B.13)$$

is introduced to model the thermal coupling between the heating and cooling zone. It combines heat transfer resistances arising from the transfer medium itself and from the gas ducts between the bed and the transfer medium in the heating and cooling zone.

Table B.5: Spatial boundary conditions (z-domain) of concentration profile $c_{i_{\text{Spe}}}$ in the sorbent bed.

Zone	Spatial coordinate		Boundary conditions
	x	z	
Adsorption]0, x _{Ads} [0	$c_{B,i_{\text{Spe}}} = c_{\text{Amb},i_{\text{Spe}}}$
		z _{H_{B,z}}	$c_{B,i_{\text{Spe}}} = c_{\text{Amb},i_{\text{Spe}}}$
Heating]x _{Ads} , x _{Hea} [0	$\frac{\partial c_{B,i_{\text{Spe}}}}{\partial z} = 0$
		z _{H_{B,z}}	$\frac{\partial c_{B,i_{\text{Spe}}}}{\partial z} = 0$
Ext. heating]x _{Hea} , x _{Hex} [0	$\frac{\partial c_{B,i_{\text{Spe}}}}{\partial z} = 0$
		z _{H_{B,z}}	$\frac{\partial c_{B,i_{\text{Spe}}}}{\partial z} = 0$
Desorption]x _{Hex} , x _{Des} [0	$\psi_B \cdot D_{\text{dif},i_{\text{Spe}},\text{mol}} \cdot \frac{\partial c_{B,i_{\text{Spe}}}}{\partial z} = k_{\text{df,BG},i_{\text{Spe}}} \cdot (c_{B,i_{\text{Spe}}} - c_{G,i_{\text{Spe}}})$
		z _{H_{B,z}}	$\frac{\partial c_{B,i_{\text{Spe}}}}{\partial z} = 0$
Cooling]x _{Des} , x _{Coo} [0	$\psi_B \cdot D_{\text{dif},i_{\text{Spe}},\text{mol}} \cdot \frac{\partial c_{B,i_{\text{Spe}}}}{\partial z} = k_{\text{df,BG},i_{\text{Spe}}} \cdot (c_{B,i_{\text{Spe}}} - c_{G,i_{\text{Spe}}})$
		z _{H_{B,z}}	$\frac{\partial c_{B,i_{\text{Spe}}}}{\partial z} = 0$

Heat transfer characteristics of the solid medium are assumed to be uniaxial, i.e., the heat transfer is solely modeled in z coordinate. A transfer medium height H_T of 2 mm is used in the calculations and its thermal conductivity is assumed to be in the order of $15 \text{ W K}^{-1} \text{ m}^{-1}$, which equals the thermal conductivity of *V2A* steel (Table B.2).

Additional need of heat transfer coefficients can arise in the definition of the external heat supply in the external heating and desorption zone (Table B.4). Use of defined heat flows $\dot{q}_{\text{ext,Hex}}$ and $\dot{q}_{\text{ext,Des}}$, respectively, is investigated, as well as, a prescription of the adsorber wall temperature profiles. In the latter case, heat flows are defined by

$$\dot{q}_{\text{ext},i} = h_{\text{df,BW},i} \cdot (T_{W,i} - T_B) . \quad (\text{B.14})$$

Here,

$$h_{\text{df,BW},i} = \frac{\lambda_{\text{BW,G}}}{H_{\text{BW},i}} \quad (\text{B.15})$$

gives a worst case approximation of the heat transfer coefficient between the adsorber wall and the sorbent bed based on the assumption of a pure thermal conductivity-driven transport process. The heights of the gas ducts $H_{\text{BT,Hea}}$, $H_{\text{BT,Coo}}$ and $H_{\text{BW},i}$ are estimated to be 1 mm. Note that these gas phases are not explicitly represented by differential equations as only minor contributions on the bed or strip gas phase state variable profiles are to be expected in steady state. Moreover, the influence of the support structure, e.g., of the mesh, is not considered in the model.

Table B.6: Reference parameter set used in the evaluation of *MBtA*.

$L_{x,DAC_{Ads}}$ /m	$L_{x,DAC_{Hea}}$ /m	$L_{x,DAC_{Hex}}$ /m	$L_{x,DAC_{Des}}$ /m	$L_{x,DAC_{Coo}}$ /m	$H_{B,z}$ / 10^{-3} m	u_{Belt} / 10^{-3} m s $^{-1}$
12	3	1	5	3	5	1
$u_{G,in}$ / 10^{-3} m s $^{-1}$	$T_{G,in}$ / $^{\circ}$ C	p_{opr} / 10^5 Pa	$H_{G,z}$ / 10^{-3} m	T_W / $^{\circ}$ C	$\phi_{V_z,T,Belt}$ /-	y_{Amb,CO_2} / 10^{-6}
-25	25	1	2	100	0	400

An additional equation for the sorbent loading $q_{i_{Spe}}$ is required, which reads

$$\frac{\partial q_{i_{Spe}}}{\partial t} = -u_{Belt} \cdot \frac{\partial q_{i_{Spe}}}{\partial x} + k_{df,ads,i_{Spe}} \cdot (q_{eq,i_{Spe}} - q_{i_{Spe}}) . \quad (B.16)$$

In accordance with (B.10) and (B.11) a linear driving force approach is used to describe the adsorption process of the component CO_2 .

B.3.3 MBtA: numeric

The modeling approach presented results in a coupled *PDAE* system. The spatial coordinate is discretized by means of a *finite volume scheme (FVS)*.³⁴⁰ Here, a first-order *upwind scheme (UWS)* is used to describe the convective flows in the solid and strip gas phase, i.e., in direction of belt movement or strip gas flow, respectively.^{312,340} Moreover, the cyclic behavior in the spatial domain is enforced by the boundary conditions used in direction of the belt movement along x -coordinate (Appendix B.3.2). Steady state operation profiles are obtained via integration in time domain using *Matlab*[®] *ode15s* function.¹⁷⁸ A convergence analysis under consideration of numerical tolerances reveals relative changes of the state variables to be in the order of magnitude of $10^{-7} \% s^{-1}$ or lower for the steady state profiles obtained.

To speed up the calculations and to limit the amount of computational resources used, the *sparsity pattern* of the *Jacobian* is provided. Moreover, a mesh refinement strategy in x -direction is used, to account for steep gradients that especially arise at the boundaries of the different zones.

B.3.4 MBtA: parameter set

Table B.6 summarizes the parameter set used as reference case in the analysis of *MBtA* operation. The gas duct between the belt and adsorber wall is assumed to be 1 mm. Stainless steel (*V2A*) is selected as the solid heat transfer medium. A transfer medium height H_T of 2 mm is selected, with a worst case estimate for its thermal conductivity of $15 \text{ W K}^{-1} \text{ m}^{-1}$ being used.¹¹⁶

Table B.7: Thermophysical properties of the thermal oil. Values are given for *Dowtherm J* at a temperature of 65 °C that equals the mean of the operation temperature range expected that spans 25–105 °C.

Density	ρ_{T_L}	/kg m ⁻³	829	[116]
Dyn. viscosity	μ_{T_L}	/10 ⁻⁶ Pa s	538	[116]
Heat capacity	c_{p,T_L}	/J kg ⁻¹ K ⁻¹	1973	[116]
Th. conductivity	λ_{T_L}	/10 ⁻³ W K ⁻¹ m ⁻¹	119	[116]

B.4 MBdA

This section summarizes the characteristics of the *MBdA* evaluation that comprise: a definition of thermophysical properties (Appendix B.4.1), a description of the mathematical model (Appendix B.4.2), a presentation of the numeric approach used to obtain the operation profiles in steady state (Appendix B.4.3) and a summary of the design and operation parameters of the configurations analyzed (Appendix B.4.4).

B.4.1 MBdA: thermophysical and adsorption properties

The thermophysical and adsorption properties are evaluated in analogy to *MBtA* (Appendix B.3.1, Table B.3). *Dowtherm J* is selected as a representative of a typical thermal oil,¹¹⁶ the properties of which are given in Table B.7.

B.4.2 MBdA: model

Figure 4.3 allows for a basic insight into the *MBdA* design. A one-dimensional model is proposed. The x-coordinate is orientated in direction of the sorbent flow, starting at the sorbent inlet in the adsorption zone. Governing equations for three different submodels that describe the gas G (Appendix B.4.2.1), particle P (Appendix B.4.2.2), and liquid transfer medium phase T_L (Appendix B.4.2.3) are used. Concentration and temperature profiles in the sorbent bed are estimated via the assumption of parabolic profiles, to derive the corresponding gradients at the bed outer interface, relevant for mass and energy transfer. Here, it is assumed that the integral mean of the parabolic profile equals the corresponding state variable in the differential equations discussed below. Moreover, a brief discussion on the compression energy requirement is given in Appendix B.4.2.4.

B.4.2.1 Governing equations: gas phase

The law of mass conservation in the void space between the sorbent particles reads

$$\frac{\partial c_{G,i_{\text{Spe}}}}{\partial t} = -\frac{\partial (\mathbf{u}_G \cdot c_{G,i_{\text{Spe}}})}{\partial \mathbf{x}} - \frac{1 - \psi_B}{\psi_B} \cdot \rho_P \cdot k_{\text{df,ads},i_{\text{Spe}}} \cdot (\mathbf{q}_{\text{eql},i_{\text{Spe}}} - \mathbf{q}_{i_{\text{Spe}}}) - a_{z,B} \cdot \dot{N}_{\text{GAmb},i_{\text{Spe}}} \cdot \quad (\text{B.17})$$

The parameter $a_{z,B}$ defines the specific area of the bed in z-coordinate, which reads

$$a_{z,B} = \frac{2}{H_{B,z}} \quad (\text{B.18})$$

and

$$\dot{N}_{GAmb,i_{Spe}} = 6 \cdot D_{\text{dif},i_{Spe},\text{mol}} \cdot \frac{c_{G,i_{Spe}} - c_{Amb,i_{Spe}}}{H_{B,z}} \quad (\text{B.19})$$

gives the area-specific mass transfer between the bed and the ambient. $\dot{N}_{GAmb,i_{Spe}}$ equals zero for all zones except from the adsorption unit.

The profile of the gas phase temperature along the axial coordinate x is defined by

$$\begin{aligned} \frac{\partial T_G}{\partial t} = & \frac{1}{\sum_{i_{Spe}} c_{G,i_{Spe}} \cdot c_{p,G,i_{Spe}}} \cdot \frac{\partial p_G}{\partial t} - u_G \cdot \frac{\partial T_G}{\partial x} \\ & - \frac{1}{\sum_{i_{Spe}} c_{G,i_{Spe}} \cdot c_{p,G,i_{Spe}}} \cdot a_{z,B} \cdot \dot{q}_{GEx} \\ & - \frac{a_P}{\sum_{i_{Spe}} c_{G,i_{Spe}} \cdot c_{p,G,i_{Spe}}} \cdot \frac{1 - \psi_B}{\psi_B} \cdot h_{\text{df},GP} \cdot (T_G - T_P) . \end{aligned} \quad (\text{B.20})$$

Here, the volume-specific outer surface area of the sorbent

$$a_P = \frac{6}{D_P} \quad (\text{B.21})$$

is calculated based on the assumption of ideal sphere-like particles with a diameter of $D_P = D_{P,10}$ (Table 3.4). The linear driving force coefficient $h_{\text{df},GP}$ between the gas and particle phase is estimated based on a common *Nusselt* correlation proposed by *Gnielinski*¹¹⁶ and the area-specific heat flux between the gas phase and adsorber bed periphery in the different zones reads:

$$\text{Adsorption zone} \quad \dot{q}_{GEx} = 6 \cdot \lambda_G \cdot \frac{T_G - T_{Amb}}{H_{B,z}} \quad (\text{B.22a})$$

$$\text{Heating / cooling zone} \quad \dot{q}_{GEx} = h_{\text{df},T_\Sigma} \cdot (T_{GT_L} - T_{T_L}) \quad (\text{B.22b})$$

$$\text{Desorption zone} \quad \dot{q}_{GEx} = 6 \cdot \lambda_G \cdot \frac{T_G - T_W}{H_{B,z}} \quad (\text{B.22c})$$

In (B.22b) T_{GT_L} is the temperature at the bed-transfer medium interphase defined via the parabolic profile and

$$h_{\text{df},T_\Sigma} = \left(\frac{1}{h_{\text{df},T_L}} + \frac{H_{T_{Sol}}}{\lambda_{T_{Sol}}} \right)^{-1} \quad (\text{B.23})$$

gives the overall heat transfer coefficient from the transfer medium to the outer surface of the solid bed. In analogy to *MBtA* (Appendix B.3.4), the solid transfer medium is

assumed to be a sheet of *V2A* steel with a width $H_{T_{Sol}}$ of 2 mm. The heat transfer coefficient from the bulk phase of the liquid transfer medium to the wall of the bordering duct is calculated based on common *Nusselt* correlations proposed by Mercer for laminar flows.¹¹⁶

Whereas the gas phase velocity equals the bed velocity in the adsorption and heating zone, additional equations are required to describe the coupled evolution of gas phase pressure and velocity in the desorption and cooling zone. Summation of (B.17) and use of the assumption of ideal gas phase behavior results in

$$\begin{aligned} \sum_{i_{S_{pe}}} \frac{\partial c_{G,i_{S_{pe}}}}{\partial t} &= \frac{1}{R_{id}} \cdot \frac{\partial}{\partial t} \left(\frac{p_G}{T_G} \right) \\ &= -\frac{1}{R_{id}} \cdot \frac{\partial}{\partial x} \left(\frac{\mathbf{u}_G \cdot p_G}{T_G} \right) - \sum_{i_{S_{pe}}} \frac{1 - \psi_B}{\psi_B} \cdot \rho_P \cdot k_{df,ads,i_{S_{pe}}} \cdot (\mathbf{q}_{eq,i_{S_{pe}}} - \mathbf{q}_{i_{S_{pe}}}) . \end{aligned} \quad (B.24)$$

Ergun equation¹¹⁶

$$\frac{\partial p_G}{\partial x} = 150 \cdot \frac{(1 - \psi_B)^2}{\psi_B^3} \cdot \frac{\mu_G}{D_P^2} \cdot (\mathbf{u}_B - \mathbf{u}_G) \cdot \psi_B + 1.75 \cdot \frac{1 - \psi_B}{\psi_B^3} \cdot \frac{\rho_G}{D_P} \cdot ((\mathbf{u}_B - \mathbf{u}_G) \cdot \psi_B)^2 \quad (B.25)$$

provides additional information about the evolution of the gas phase pressure along the spatial coordinate x . Besides the equations given, spatial boundary conditions to be fulfilled need to be defined. Continuity of the fluxes at the boundaries between the different zones in x -coordinate results in cyclic behavior in the spatial domain. Additionally, the finite volume elements at the gas phase inlet and outlet are treated like mixing cells that incorporate the convective transport of gas with gas velocity \mathbf{u}_G in stream direction and contributions from the convective transport of the gas phase in direction of the solid phase movement with solid phase velocity \mathbf{u}_B . Gas phase temperature $T_{G,in}$, pressure $p_{G,in}$, velocity $\mathbf{u}_{G,in}$ and concentrations $c_{G,i_{S_{pe},in}}$ define the boundary conditions at the gas phase inlet that is located at the transition between the cooling and adsorption zone.

B.4.2.2 Governing equations: particle phase

Sorbent movement through the different zones results in cyclic operation of the particle phase in the spatial domain. The governing equation for sorbent loading reads

$$\frac{\partial \mathbf{q}_{i_{S_{pe}}}}{\partial t} = -\mathbf{u}_B \cdot \frac{\partial \mathbf{q}_{i_{S_{pe}}}}{\partial x} + k_{df,ads,i_{S_{pe}}} \cdot (\mathbf{q}_{eq,i_{S_{pe}}} - \mathbf{q}_{i_{S_{pe}}}) . \quad (B.26)$$

Convective transport by sorbent movement with velocity \mathbf{u}_B is assumed. The driving force approach that is used to model the adsorption of CO_2 is discussed in Appendix B.3.1.3.

The sorbent particle temperature is defined by

$$\begin{aligned} \frac{\partial T_P}{\partial t} = & -\mathbf{u}_B \cdot \frac{\partial T_P}{\partial \mathbf{x}} - \frac{a_{z,B}}{\rho_P \cdot c_{p,P}} \cdot \dot{q}_{PEX} + \frac{a_P}{\rho_P \cdot c_{p,P}} \cdot h_{df,GP} \cdot (T_G - T_P) \\ & + \sum_{i_{S_{pe}}} \frac{k_{df,ads,i_{S_{pe}}}}{c_{p,P}} \cdot (\mathbf{q}_{eq,i_{S_{pe}}} - \mathbf{q}_{i_{S_{pe}}}) \cdot (-\Delta h_{ads,i_{S_{pe}}}) . \end{aligned} \quad (B.27)$$

The heat exchange with the bed peripheries \dot{q}_{PEX} is defined in analogy to (B.22a) - (B.22c) and the calculation of the heat flows between the particle and gas phase is discussed in Section B.4.2.1.

B.4.2.3 Governing equations: transfer medium phase

Flow of the transfer medium counter-current to the solid sorbent is realized in the heating and cooling zone on both sides of the sorbent bed. The transfer medium phase temperature profile T_{TL} in a single channel is defined by

$$\begin{aligned} \frac{\partial T_{TL}}{\partial t} = & -\mathbf{u}_{TL} \cdot \frac{\partial T_{TL}}{\partial \mathbf{x}} + a_{z,TL} \cdot (1 - \psi_B) \cdot \frac{h_{df,T\Sigma}}{\rho_{TL} \cdot c_{p,TL}} \cdot (T_{PTL} - T_{TL}) \\ & + a_{z,TL} \cdot \psi_B \cdot \frac{h_{df,T\Sigma}}{\rho_{TL} \cdot c_{p,TL}} \cdot (T_{GTL} - T_{TL}) . \end{aligned} \quad (B.28)$$

The definition of the heat transfer coefficient $h_{df,T\Sigma}$ is discussed in Section B.4.2.1 and the specific surface area of one transfer medium channel is calculated by

$$a_{z,TL} = \frac{1}{H_{TL,z}} . \quad (B.29)$$

Properties of the transfer medium (Table B.7) as well as its velocity \mathbf{u}_{TL} and the width of the transfer medium duct $H_{TL,z}$ take constant values. Cyclic operation is realized by continuity of fluxes between the stream that leaves the heating and enters the cooling zone. The transfer medium flow that leaves the cooling zone is assumed to be externally heated to heating zone inlet temperature $T_{Hea_{in},TL}$. Thus, prescription of $T_{Hea_{in},TL}$ is used as spatial boundary condition of (B.28) in the heating zone.

B.4.2.4 Compression energy requirement

Compression energy requirement \dot{E}_{com} is calculated based on the compressor model outlined in Appendix C.3.3.1. Contributions from low-pressure operation, i.e., pressure change from gas phase outlet pressures $p_{G,out}$ to ambient pressure and from ambient pressure to gas phase inlet pressure $p_{G,in}$ are taken into account. In the calculation of the former contribution, the properties of the gas phase at the compressor inlet equal the one at the gas phase outlet of the *DAC* unit, whereas for the estimation of the latter contribution a compressor inlet temperature of 25 °C is assumed. For the sake of clarity, neither recovery of the additional thermal energy stored in the gas phase after compression nor use of turbines, to recover the energy stored in the gas phase pressure during pressure

change to low pressure levels, is taken into account, as realization of these concepts will depend on the specific characteristics of strip gas supply and of *DAC* product gas use. This way, a worst case analysis with regard to the additional energy demand that arises from gas phase compression is obtained.

B.4.3 MBdA: numeric

In analogy to *MBtA*, a coupled *PDAE* system needs to be solved in view of obtaining the state variable profiles of *MBdA* in steady state. The spatial coordinate is discretized by means of a *finite volume scheme (FVS)*.³⁴⁰ Here, a first-order *upwind scheme (UWS)*^{312,340} is used to describe the convective flows in the particle and gas phase, in direction of bed movement and strip gas flow, respectively. Cyclic behavior in spatial domain is enforced by the boundary conditions used in direction of the bed movement. Integration in time domain via use of *Matlab*[®] *ode15s* function¹⁷⁸ allows to obtain the steady state solution. A convergence analysis under consideration of numerical tolerances reveals relative changes of state variables to be in the order of magnitude of $10^{-15} \% \text{s}^{-1}$ or lower for the steady state profiles obtained. To realize the gas phase outlet pressure and strip gas mole flow at the gas phase inlet aspired, the gas phase inlet pressure and velocity are adjusted by the *Matlab*[®] function *fsolve*¹⁷⁸.

In view of computing time the *Sparsity pattern* of the *Jacobian* is provided to *Matlab*[®] *ode15s* function.¹⁷⁸ A mesh refinement strategy in x-direction is used, to account for steep gradients that especially arise at the boundaries of the different zones.

B.4.4 MBdA: parameter set

Table B.8 summarizes the key operation parameters of *MBdA*. In analogy to *MBtA* (Appendix B.3.4) stainless steel (*V2A*) is used as solid transfer medium with a width H_T of 2 mm. *Dowtherm J* is selected as liquid transfer medium. Its thermophysical properties are summarized in Table B.7. The transfer medium velocity is adjusted such that its heat capacity flow equals the one of the sorbent. The transfer medium inlet temperature $T_{\text{Hea,in},T_L}$ is defined, such that the temperature of the particles that enter the desorption zone equals desorption temperature level $T_{\text{des}} = T_W$. Use of an additional solid heat transfer medium to increase the heat transfer in the sorbent bed is not considered in the parameter sets used. With view on low-pressure operation, gas phase inlet velocity $u_{G,\text{in},\text{sup}}$ and pressure $p_{G,\text{in}}$ are adjusted, such that the pressure at the gas phase outlet $p_{G,\text{out}}$ takes a defined value and the ratio between the mole flow of strip gas used and the quantity of this stream in the *MBtA* reference case ($H_{G,z,\text{ref}} = 2 \cdot 10^{-3} \text{ m}$, $u_{G,\text{in},\text{sup},\text{ref}} = 25 \cdot 10^{-3} \text{ m s}^{-1}$, $p_{G,\text{in},\text{ref}} = 1 \cdot 10^5 \text{ Pa}$ and $T_{G,\text{in},\text{ref}} = 25 \text{ °C}$) equals the factor $\phi_{\dot{n}_{\text{H}_2,\text{in}},\dot{n}_{\text{H}_2,\text{in},\text{ref}}}$.

B.5 Experimental investigation of transport phenomena

A brief overview of the experimental setting (Appendix B.5.1), of the adsorber design (Appendix B.5.2) as well as of the experimental procedure and of the data evaluation (Appendix B.5.3) is given.

Table B.8: Parameter set used in the evaluation of *MBdA*.

Set	$L_{x,DACAds}$ /m	$L_{x,DACHea}$ /m	$L_{x,DACDes}$ /m	$L_{x,DACCo}$ /m	$H_{B,z}$ / 10^{-3} m	u_B / 10^{-3} m s $^{-1}$	$\phi \dot{n}_{H_2,in}, \dot{n}_{H_2,in,ref}$ /-	$u_{G,in,sup}$ / 10^{-3} m s $^{-1}$
1	12	3	6	3	5	1	1	-9.4
2	12	3	6	3	5	1	2.5	-33.5
Set	$p_{G,in}$ / 10^5 Pa	$T_{G,in}$ / $^{\circ}C$	$p_{G,out}$ / 10^5 Pa	$H_{TL,z}$ / 10^{-3} m	$T_{Hea,in}, T_L$ / $^{\circ}C$	T_W / $^{\circ}C$	y_{Amb,CO_2} / 10^{-6}	
1	1.07	25	1.0	2	102	100	400	
2	0.75	25	0.5	2	102	100	400	

B.5.1 Experimental setting

The basic flow sheet of the experimental setup is visualized in Figure 4.12(a). A summary of the devices and materials used is provided in Table B.9. Flows of nitrogen and test gas are controlled by a *Bronkhorst* mass flow controller.¹⁷⁰ This gas stream is sent to the analysis section after either flowing through the adsorber unit or bypass. Flow splitting allows to meet the specific volume flow requirements of the *URAS26 EL3020* infrared devices (IR-1: 0–500 pmm, IR-2: 0–40 %) from *ABB*¹⁷¹ used for online measurement of the CO₂ gas phase mole content.

A modular adsorber design based on structures build by 3D printing is realized to allow for flexibility. Two gas tightened support elements that form a channel, the walls of which can be modified by inlays of different designs, e.g., to vary the width of the channel or of the sorbent bed (Figure B.2), build the core of the adsorber unit. The sorbent bed consists of a mixture of glass beads³⁰⁹ and *Lewatit*¹⁶², which is immobilized by a wire mesh. For the sake of temperature control the support elements are surrounded by a gas-tight housing that is dropped into a water bath. The temperature of the bath is adjusted by a thermostat (*SE-6*, Julabo)³⁰⁴ with additional cooling device. Fast homogenization of temperature inside the water bath is realized by convective circulation of the liquid through a pump provided by *Ismatec*³⁴¹. Data recording and plant control is realized via *Labview*¹⁶⁹.

B.5.2 Adsorber design

Figure B.2(a) gives a basic overview of the modular adsorber design used for the analysis of mass transport phenomena. Elements are made up of acrylonitrile butadiene styrene (ABS) and formed via 3D printing using *Ultimaker2*[®] from *Ultimaker*³⁴². A wire mesh, the properties²²⁶ of which are approximately: $H_{Mes} = 106 \mu\text{m}$, $D_{Wir} = 63 \mu\text{m}$ and $a_{ope,Mes} = 39 \%$, is used to immobilize the sorbent bed in the support structure printed. The bed is formed by *Lewatit*¹⁶² particles and glass beads¹⁷³. Table B.10 gives an overview of the geometric dimensions and operation parameters of the experimental

Table B.9: Equipment and material used to perform *BTC* experiments in the studies of mass transport phenomena. *Workshop of *TU Dortmund University*

	Provided by	Additional information	Source
Equipment			
3D printer	<i>Ultimaker</i>	Model: <i>Ultimaker2</i> [®]	[342]
Adsorber	Mechanic workshop* 3D print	Outer support provided by mechanic workshop Detailed description of inner design in Appendix B.5.2	
Apax Box	Electronic workshop* <i>Advantech</i>		[298]
Filter	<i>ABB</i>	Model: <i>Disposable filter 50K</i>	
Infrared device	<i>ABB</i>	Model: <i>URAS26 EL3020</i> , IR-1: 0–500 pmm, IR-2: 0–40 %	[171]
Mass flow control	<i>Bronkhorst</i>	Model: <i>EL-Flow</i> , thermal mass flow controllers	[170]
Mass flow control	<i>KOBOLD</i>	Model: <i>KFR-4240NO</i> (flow to IR) <i>KFR-4243NO</i> (flow to bypass) Manual mass flow controllers with needle valve used for flow splitting before IRs	[343]
Pump	<i>Ismatec</i>	Model: <i>Reglo-z</i>	[341]
Scale	<i>Kern & Sohn</i>	Model: <i>ALS 220-4</i>	[306]
Scale	<i>Sartorius</i>	Model: <i>QUINTIX3102-1S</i>	[344]
Thermocouple (1-point)	<i>CVT</i> inventory	Typ K (NiCr-Ni)	
Thermostat	<i>Julabo</i>	Model: <i>SE-6</i> Thermostat with circulation pump	[304]
Pressure sensor	<i>JUMO</i>	$0 \text{ Pa} \leq p_{\text{mea}} \leq 2.5 \cdot 10^5 \text{ Pa}$ Model: <i>MIDAS C08</i>	[345]
Gas			
Nitrogen	<i>Messer</i>	Quality: technical	[299]
Test gas (ppm fraction)	<i>Messer</i>	CO ₂ in syn. air, quality CO ₂ : 4.5, quality syn. air: 5.0 Relative error in CO ₂ content $\pm 2\%$	[299]
Additional material			
Cooling water	<i>TU Dortmund Uni.</i>	Provided by <i>TU Dortmund University</i> , temperature ca. 7 °C	
Glass beads	<i>Netzsch</i>	<i>GlasBeads 0.5</i> , $D_{\text{Gla}} \approx 0.4\text{--}0.6 \text{ mm}$, $\rho_{\text{Gla}} = 2.5 \cdot 10^3 \text{ kg m}^{-3}$	[173]
<i>Lewatit</i>	<i>Lanxess</i>	Information summarized in Table 3.4	[162]
Silicon oil	<i>CVT</i> inventory	Silicon oil M50	
VE water	<i>TU Dortmund Uni.</i>		

setup.

B.5.3 Experimental procedure and data evaluation

The experimental procedure reads as follows:

- **Desorption** is performed under nitrogen flow of 0.75 Nl min^{-1} at 60 °C . Regeneration time in general takes several hours and varies in dependence of the bed

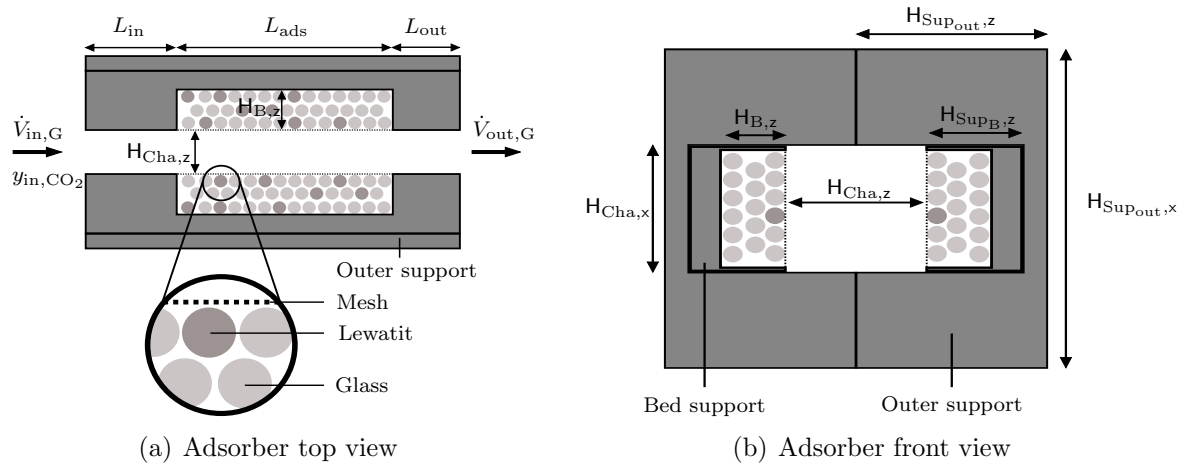


Figure B.2: Sketch of the adsorber used for the experimental analysis of mass transport phenomena. The housing is not shown. (a) Top view of the adsorber cross section and (b) front view of the adsorber cross section are depicted. Dimensions of the bed (B), gas channel (Cha), bed support structure (Sup_B) and outer support structure (Sup_{out}) are shown. The channel height equals the height of the bed support structure: $H_{\text{Cha},x} = H_{\text{Sup}_B,x}$. The walls of the bed support structure between the sorbent bed and the outer support in x direction are of a depth of 1.25 mm.

Table B.10: Main operation and design parameters used in the experimental analysis of mass transport phenomena. Variables resemble the ones defined in Figure B.2. The mass of *Lewatit* and glass beads is given for the whole fill, i.e., for the sum over all wall elements. The parameter $y_{\text{sam},\text{CO}_2}$ is the CO_2 mole fraction defined by the test gas certificate.

$\dot{V}_{\text{in},\text{G}}$ /Nl min ⁻¹	$H_{\text{B},z}$ /mm	$H_{\text{Cha},x}$ /mm	$H_{\text{Cha},z}$ /mm	$H_{\text{Sup}_B,z}$ /mm	$H_{\text{Sup}_B,x}$ /mm	$H_{\text{Sup}_{\text{out}},x}$ /mm	$H_{\text{Sup}_{\text{out}},z}$ /mm	L_{in} /mm	L_{ads} /mm	L_{out} /mm	m_{Sor} /g	m_{Gla} /g	$y_{\text{sam},\text{CO}_2}$ /ppm
1.5	2.5	12.5	10	12.5	1.25	50	25	150	440.5	2	3.9	26.5	402
1.5	7.5	12.5	10	12.5	1.25	50	25	150	440.5	2	3.9	98.4	400

configuration. The desorption is stopped if the CO_2 content measured is lower than 2 ppm

- **Cooling** to adsorption temperature of ca. 30 °C is performed under nitrogen flow. Exchange of the water in the water bath with cool, fresh water allows to reduce the time span required for cooling to less than 1 h. At the end of the cooling time, isothermal conditions are reached with no trend in the temperature profile being observable and temperature fluctuations of less than 0.5 °C over more than 5 min being noticed
- **Adsorption** phase is started by changing the flow from nitrogen to a defined flow of test gas. In dependence of the configuration used, the adsorption time can exceed more than 24 h

Data evaluation:

- Data evaluation is performed in *Matlab*^{®178}
- The curves shown are not corrected with regard to the influence of the plant residence time distribution. This is reasoned in the aspect that residence time experiments indicate a negligible influence of this contribution on the results of the discussion performed, e.g., the initial breakthrough times observed in the residence time experiments are less than 1 min

B.6 Cost estimation

CO₂-specific capture costs

$$c_{mCO_2} = \sum_{i_{Eqp}} c_{mCO_2,inv,i_{Eqp}} + c_{mCO_2,Sor} + c_{mCO_2,\dot{E}} + c_{mCO_2,\dot{n}_{adi}} \quad (B.30)$$

comprise contributions from equipment costs $c_{mCO_2,inv,i_{Eqp}}$ (Appendix B.6.1), sorbent cost $c_{mCO_2,Sor}$ (Appendix B.6.2), energy demand ($c_{mCO_2,\dot{E}}$) (Appendix B.6.3) and additional component requirement $c_{mCO_2,\dot{n}_{adi}}$ (Appendix B.6.4). Moreover, the definition of zone length-specific costs used in the calculations is given in Appendix B.6.5. An exchange rate from Euro to USD of 1.12 \$€⁻¹ is assumed that equals the mean value reached in 2019.³⁴⁶

Cost are evaluated based on the reference scenario: CO₂ product flow $\dot{n}_{Pro,CO_2} = 5 \text{ mol s}^{-1}$ and solid velocity $u_B = 1 \text{ mm s}^{-1}$. A working capacity $\Delta q_{wor,CO_2}$ of 0.25 mol kg⁻¹ and thermal slip in the solid phase $\Delta T_{los,DAC}$ of 5 K in *MBtA* is assumed, whereas these parameters take values of $\Delta q_{wor,CO_2} = 0.5 \text{ mol kg}^{-1}$ and $\Delta T_{los,DAC} = 2.5 \text{ K}$ for *MBdA* operation (Section 4.4). In *MBdA* a decrease of the desorption pressure to $p_{G,out} = 0.5 \cdot 10^5 \text{ Pa}$ is taken into account. No increase of heat transfer by solid fins or by solid transfer medium use in the sorbent bed is considered.

B.6.1 Equipment-related costs

The cost estimation is performed based on the *factorial method*, which results in a *Class 4* cost estimate. It is in general based on limited cost data and design information.²¹⁷

In the *factorial method*²¹⁷ project capital investment is calculated based on the key equipment costs. Factors $\phi_{ISBL,i_{Eqp}}$ are used to correlate carbon steal-based equipment costs $C_{i_{Eqp}}$ to battery limits investment

$$C_{ISBL,i_{Eqp}} = \phi_{ISBL,i_{Eqp}} \cdot C_{i_{Eqp}} \quad (B.31)$$

that comprises cost components from: equipment erection, piping, instrumentation and control, electrical work, civil engineering work, structures and buildings as well as lagging, insulation and paint. For fluids-solids-based processes build in carbon steal $\phi_{ISBL,i_{Eqp}}$ takes a value of 3.2, whereas in case of stainless steal use $\phi_{ISBL,i_{Eqp}}$ increases to 3.7 if equipment costs are given on a carbon steel basis.²¹⁷ If costs for equipment purchased in stainless

steel are used, $\phi_{\text{ISBL},i_{\text{Eqp}}}$ takes a value of 2.8, if the process is to be build in stainless steel.²¹⁷ Construction in stainless steel is aspired.

Contributions to total capital investment

$$C_{\text{inv},i_{\text{Eqp}}} = C_{\text{ISBL},i_{\text{Eqp}}} \cdot (1 + \phi_{\text{OSBL}}) \cdot (1 + \phi_{\text{D\&E}} + \phi_{\text{Cot}}) \quad (\text{B.32})$$

are calculated based on $C_{\text{ISBL},i_{\text{Eqp}}}$ by additionally taking into account contributions from outside battery limits costs (ϕ_{OSBL}), which account for modifications of the site infrastructure required. For chemical projects ϕ_{OSBL} typically takes values between 0.2 and 0.5.²¹⁷ In line with Towler and Sinnott²¹⁷ $\phi_{\text{OSBL}} = 0.4$ is assumed for fluids-solids systems. Moreover, costs for design and engineering ($\phi_{\text{D\&E}}$) are accounted for. For fluids-solids processes a value of 0.25 is suggested,²¹⁷ which is at the upper limit of values typically used for $\phi_{\text{D\&E}}$ (0.1–0.3).²¹⁷ A safety margin ϕ_{Cot} of 50% is used that gives a worst case estimate with regard to safety margins of 10–50% typically taken into account.²¹⁷

The capital investment $C_{\text{inv},i_{\text{Eqp}}}$ is transformed to CO₂-specific capture costs by equating

$$c_{m_{\text{CO}_2},\text{inv},i_{\text{Eqp}}} = \frac{C_{\text{inv},i_{\text{Eqp}}}}{\dot{n}_{\text{Pro,CO}_2} \cdot M_{\text{CO}_2} \cdot \Delta t_{\text{dep}} \cdot \phi_{t_{\text{opr}},t_{\text{yea}}}} \quad (\text{B.33})$$

Linear depreciation over 10 years (Δt_{dep}), which is in line with the typical usable life for chemical manufacture processes of 9.5 years,²¹⁷ and a plant availability³⁴⁷ $\phi_{t_{\text{opr}},t_{\text{yea}}}$ of 8000 h a⁻¹ is assumed.

A discussion on the investment costs that arise from additional key equipment and from the basic structure of the *moving belt* or *bed adsorber* is given in Appendix B.6.1.1 and B.6.1.2, respectively.

B.6.1.1 Costs for additional key equipment

Cost for additional capital investment are derived from cost curves of basic equipment provided in the literature.^{217,282} Costs derived based on correlations ($C_{i_{\text{Eqp}},\text{ref}}$) are corrected via *Chemical Engineering Plant Cost Index (CEPCI)*

$$C_{i_{\text{Eqp}}} = \frac{CEPCI(t)}{CEPCI_{\text{ref}}} \cdot C_{i_{\text{Eqp}},\text{ref}} \quad (\text{B.34})$$

to account for influence of inflation. For the studies $CEPCI = 607.5$ is used, which equals the mean $CEPCI$ in 2019.³⁴⁸ Table B.11 summarizes the correlations used for additional costs considered in *MBtA* and *MBdA*. Belt movement in *MBtA* is assumed to be realized by an explosion proof motor. Its power consumption is estimated based on the friction forces at the sealings (Appendix B.2.1). A worst case assumption for the motor efficiency of 84% is used.²⁸²

In *MBdA* compression power requirement for low-pressure operation is estimated based on the assumption of adiabatic compression (Appendix B.4.2.4). The efficiency of the compression is pessimistically estimated to be 70%.²⁸² For the external temperature change of the transfer medium, a shell and tube heat exchanger is used. Based on the operation

Table B.11: Overview of correlations used for calculation of costs $C_{i_{\text{Eqp,ref}}}$ that result from additional equipment use in the *MBdA* and *MBtA* approaches.

Equipment	Description	Source
<i>MBtA</i>		
Drive	Explosion proof motor	[217]
<i>MBdA</i>		
Compressor	Centrifugal compressor	[217]
Heat exchanger	U-tube shell and tube heat exchanger	[217]
Liquid pump	Centrifugal pump (AVS, with motor, 1–23 kW) Pressure factor of one is selected Costs recalculated to carbon steal by factor of 1.46 ^{217,282}	[282]
Elevator	Bucket elevator for solids excluding motor Centrifugal discharge of chain-bucket Malleable iron buckets (no material conversion factor given) Explosion proof motor to drive the elevator	[282] [217]

conditions aspired, this is in line with the suggestions given by Woods²⁸². To estimate the heat transfer area, an overall transfer coefficient of 0.5 kW m^{-2} , typically used for fluid systems as water,²⁸² and a linear driving force of 5 K for heat transfer is assumed. To realize the convective flow of the transfer medium, use of a centrifugal pump is analyzed. A worst case estimate for its power requirement is given by the assumption that the pump needs to overcome a static pressure of the transfer medium equivalent to the height of all zones the bed is moving through. A pump efficiency of 40 % is assumed.²⁸² Lift of solid particles to allow for bed movement by gravitational forces can be realized by bucket elevators. Their energy consumption is estimated based on the sorbent flow and on the maximum lift height with an overall efficiency for electric energy conversion of 40 % being assumed based on the typical range of energy consumption for bucket elevator operation that spans $13\text{--}23 \text{ J kg}^{-1} \text{ m}^{-1}$.²⁸² Based on the power requirement calculated, the cost for the bucket elevator drive is estimated via correlations for an explosion proof motor²¹⁷. Use of a single elevator module is assumed. Split in different modules, e.g., if the *MBdA* zones are not placed above each other, is possible. Due to the economy of scale, this would result in larger costs for the elevator modules. However, as in the preliminary analysis only a basic insight into the overall cost structure is aspired and as the cost of the elevator module is small compared to the overall concept costs, a more detailed analysis does not seem beneficial at this stage. Moreover, costs and energy demands for the sealings are not explicitly analyzed. These will depend on the specific sealing design and, based on Figures 4.13(a) and 4.13(b), can be estimated to take minor influence on the energy demand as well as on the cost structure.

If not stated differently, all equipment prices are carbon steal-based. Only for the bucket elevator no conversion factors to a carbon steal basis could be obtained. Moreover, costs are not corrected by location factors, as these, if given, only take a minor influence

on the cost estimate, e.g., the difference between US gulf cost and Germany is about 11%.²¹⁷

B.6.1.2 Zone length-related equipment costs

Costs for the basic setup of *MBdA* and *MBtA*

$$c_{i_{\text{Eqp}}} = \phi_{\text{cos}} \cdot \sum_{i_{\text{B}}} c_{\Delta L_{\text{B},i_{\text{B}},x},\text{Mat}} \cdot \Delta L_{\text{B},i_{\text{B}},x} \quad (\text{B.35})$$

are calculated based on the zone length $\Delta L_{\text{B},i_{\text{B}},x}$, defined in direction of the solid phase movement (x), and on the zone length-specific cost $c_{\Delta L_{\text{B},i_{\text{B}},x},\text{Mat}}$ of the key material. These are multiplied by the factor ϕ_{cos} that accounts for costs associated to the construction of the equipment. An analysis of the cost structure of steel constructions by Bollinger et al.³⁴⁹ and Janisch³⁵⁰ indicates costs for construction to be similar to raw material costs. Thus, ϕ_{cos} is estimated to take a value of two. Zone length-specific costs

$$c_{\Delta L_{\text{B},i_{\text{B}},x},\text{Mat}} = \Delta L_{\text{B},y} \cdot \sum_{i_{\text{Mat}}} \phi_{\text{Mat},i_{\text{B}},i_{\text{Mat}}} \cdot c_{\text{Mat},i_{\text{Mat}}} \quad (\text{B.36})$$

are derived based on the ratio of m^2 material required per m^2 bed (in x - y plane) $\phi_{\text{Mat},i_{\text{B}},i_{\text{Mat}}}$ and on the costs per m^2 of material $c_{\text{Mat},i_{\text{Mat}}}$. The depth of the sorbent bed in y -coordinate

$$\Delta L_{\text{B},y} = \frac{\dot{n}_{\text{Pro},\text{CO}_2}}{\Delta q_{\text{wor},\text{CO}_2}} \cdot \frac{1}{(1 - \psi_{\text{B}}) \cdot \rho_{\text{P}} \cdot u_{\text{B}} \cdot H_{\text{B},z}} \quad (\text{B.37})$$

is calculated in dependence of the sorbent bed properties (Table 3.4), bed width $H_{\text{B},z}$, solid phase velocity $u_{\text{B}} = u_{\text{Belt}}$ and product mole flow $\dot{n}_{\text{Pro},\text{CO}_2}$.

Table B.12 provides an overview of the material costs and associated factors for the materials i_{Mat} used in the different zones i_{B} of the concepts. Prices of thin steel sheets (2 mm, *V2A*) are used, raw material costs of which are estimated based on a price for *V2A* steel of ca. $1.12 \text{ \$ kg}^{-1}$ in 2019.³⁵¹ These metal plates are used as heat transfer media for heat exchange from bed to bed $c_{\text{Mat},\text{BB}}$ and from the bed to a fluid phase, i.e., to the transfer medium in the heating and cooling zone $c_{\text{Mat},\text{BF},\text{rec}}$ or to the external heating medium in the external heating and desorption zone $c_{\text{Mat},\text{BF},\text{ext}}$. Moreover, material for housing is required ($c_{\text{Mat},\text{Hou}}$). Use of *V2A* steel is intended to avoid corrosion and embrittlement by hydrogen. Similarly, the wire mesh used ($c_{\text{Mat},\text{Mes}}$) is made up of *V2A* steel.

At this point, it is explicitly stated that the presented cost estimate does not claim to provide exact capture costs and is rather to be understood as an order of magnitude estimate through which the various contributions to the cost structure are analyzed. For example, additional costs for support elements in *MBtA* or for pressure valves and for sorbent distributors in *MBdA* are not considered. On the other hand, possible discounts on material costs attributed to purchase of large quantities of material are not taken into account. In this respect, also recalculation of the zone length-related costs by *CEPCI* does not seem advantageous with regard to the overall accuracy of the cost estimate.

Table B.12: Costs $c_{\text{Mat},i_{\text{Mat}}}$ per m^2 of material and associated factors $\phi_{\text{Mat},i_{\text{B}},i_{\text{Mat}}}$ that correlate the area of material i_{Mat} required to the area of the sorbent bed (in x-y plane) for the specific zones i_{B} the sorbent bed is moving through: adsorption (Ads), heating (Hea), external heating (Hex), desorption (Des) and cooling (Coo). The cost for the steel mesh is given for mesh properties: $H_{\text{Mes}} = 0.25 \text{ mm}$ and $D_{\text{Wir}} = 0.16 \text{ mm}$. Raw material costs for a steel sheet of 2 mm width are estimated based on the cost of V2A steel of $1.12 \text{ \$ kg}^{-1}$ in 2019.³⁵¹

	$c_{\text{Mat,Mes}}$	$c_{\text{Mat,BB}}$	$c_{\text{Mat,BF,rec}}$	$c_{\text{Mat,BF,ext}}$	$c_{\text{Mat,Hou}}$
	$/\text{\$ m}^{-2}$	$/\text{\$ m}^{-2}$	$/\text{\$ m}^{-2}$	$/\text{\$ m}^{-2}$	$/\text{\$ m}^{-2}$
V2A mesh or sheet	25	18	18	18	18
	[352]	[351]	[351]	[351]	[351]
<i>MBtA</i>					
$\phi_{\text{Mat,Ads},i_{\text{Mat}}}$	/-	2	0	0	0
$\phi_{\text{Mat,Hea},i_{\text{Mat}}}$	/-	2	0.5	0	1
$\phi_{\text{Mat,Hex},i_{\text{Mat}}}$	/-	2	0	0	1
$\phi_{\text{Mat,Des},i_{\text{Mat}}}$	/-	2	0	0	1
$\phi_{\text{Mat,Coo},i_{\text{Mat}}}$	/-	2	0.5	0	1
<i>MBdA</i>					
$\phi_{\text{Mat,Ads},i_{\text{Mat}}}$	/-	2	0	0	0
$\phi_{\text{Mat,Hea},i_{\text{Mat}}}$	/-	0	0	2	2
$\phi_{\text{Mat,Des},i_{\text{Mat}}}$	/-	0	0	0	2
$\phi_{\text{Mat,Coo},i_{\text{Mat}}}$	/-	0	0	2	2

B.6.2 Sorbent-related costs

Sorbent-related contributions to CO_2 -specific capture costs

$$c_{m_{\text{CO}_2,\text{Sor}}} = \frac{\sum i_{\text{B}} c_{\Delta L_{\text{B},i_{\text{B}},x,\text{Sor}}} \cdot \Delta L_{\text{B},i_{\text{B}},x}}{\dot{n}_{\text{Pro,CO}_2} \cdot M_{\text{CO}_2} \cdot \Delta t_{\text{dep,Sor}} \cdot \phi_{t_{\text{opr}},t_{\text{yea}}}} \quad (\text{B.38})$$

are calculated similar to zone length-related equipment costs (Appendix B.6.1.2). The maximum stability of the sorbent given by the vendor¹⁶² is two years. Based on this information, it is assumed that the frequency of sorbent exchange $\Delta t_{\text{dep,Sor}}$ equals two years. Bed length-specific costs

$$c_{\Delta L_{\text{B},i_{\text{B}},x,\text{Sor}}} = c_{m_{\text{Sor}}} \cdot (1 - \psi_{\text{B}}) \cdot \rho_{\text{P}} \cdot H_{\text{B},z} \cdot \Delta L_{\text{B},y} \quad (\text{B.39})$$

are obtained as a function of sorbent bed properties (Table 3.4), bed dimensions ($H_{\text{B},z}$, $L_{\text{B},y}$) and the sorbent mass-specific cost³⁵³ $c_{m_{\text{Sor}}}$ of $55 \text{ \$ kg}^{-1}$.

B.6.3 Energy-related costs and carbon footprint

Prices for thermal ($0.032 \text{ \$ kWh}^{-1}$) and electric energy ($0.179 \text{ \$ kWh}^{-1}$) supply to industry for Germany in 2019 are used in the calculations.³⁵⁴ Specific CO_2 emissions of electric en-

ergy²⁹⁴ supply of 468 g kWh⁻¹ and of thermal energy supply by natural gas combustion³⁵⁵ of 200 g kWh⁻¹ are taken into account.

B.6.4 Additional component-related costs

In *MBdA* additional component-related costs take into account the costs attributed to liquid transfer medium use. *Dowtherm J* is selected as reference medium (Table B.7). Costs of 11 \$ kg⁻¹ are given by the vendor.³⁵⁶ The contribution to the CO₂-specific capture costs

$$c_{m_{\text{CO}_2}, \text{T}_L} = \frac{\sum_{i_B} c_{\Delta L_{B_{i_B}, x}, \text{T}_L} \cdot \Delta L_{B_{i_B}, x}}{\dot{n}_{\text{Pro}, \text{CO}_2} \cdot M_{\text{CO}_2} \cdot \Delta t_{\text{dep}, \text{T}_L} \cdot \phi_{t_{\text{opr}}, t_{\text{yea}}}} \quad (\text{B.40})$$

is calculated in analogy to the sorbent-related costs (Appendix B.6.2) in dependency of the bed length-specific costs

$$c_{\Delta L_{B_{i_B}, x}, \text{T}_L} = c_{m_{\text{T}_L}} \cdot \phi_{\text{T}_L, i_B} \cdot \rho_{\text{T}_L} \cdot H_{\text{T}_L, z} \cdot \Delta L_{B, y} \quad (\text{B.41})$$

The width of the transfer medium duct $H_{\text{T}_L, z}$ is selected to be 2 mm. Similar to the zone length-related equipment costs, ϕ_{T_L, i_B} defines the ratio of transfer medium ducts per moving sorbent bed in the corresponding zone i_B . ϕ_{T_L, i_B} takes a value of two for the heating and cooling zone, whereas in the other zones considered no flow of this cooling medium is taken into account. In analogy to the equipment depreciation time, the exchange frequency of the liquid transfer medium $\Delta t_{\text{dep}, \text{T}_L}$ is estimated to be 10 years.

Costs for additional heat transfer medium use, e.g., in the desorption zone are not considered in this basic estimate, as these depend on the concept of heat supply, e.g., by steam or by transfer medium, and basic costs of these contributions are already reflected within the energy costs analyzed.

Also costs for hydrogen strip gas might be included in the analysis. Costs range between 1.5 \$ kg⁻¹ and 10.3 \$ kg⁻¹ in dependence of the production process, with electrolysis processes being at the upper limit of this cost range.²⁸⁰ Hydrogen production by electrolysis in a stoichiometric ratio of 4:1 related to the CO₂ product gas stream of the *DAC* unit would result in additional CO₂-specific capture costs of 1900 \$ t⁻¹. However, as the use of hydrogen strip gas results from the target of CO₂ activation in *Sabatier* reaction and is in general no intrinsic constraint of the capture process itself, it seems reasonable to not include these costs in the calculation of the CO₂-specific capture costs.

B.6.5 Zone length-specific contributions to CO₂-specific capture costs

Zone length-specific contributions to CO₂-specific capture costs $c_{m_{\text{CO}_2}, \Delta L_{B_{i_B}, x}, i}$ are derived in analogy to the CO₂-specific capture costs by neglect of multiplication with the zone length $\Delta L_{B_{i_B}, x}$ and by solely evaluation of a single zone i_B in (B.35), (B.38) or (B.40).

C Appendix: Handling water co-adsorption

Parts of this appendix have been published in a peer-reviewed journal article and in the corresponding supplementary information.²⁴⁰

C.1 Thermophysical properties

Thermophysical properties of liquid water and water vapor are derived based on correlations provided in *IAPWS International Steam Tables*³⁵⁷. Influence of pressure in these correlations is not considered. The enthalpy of the water adsorbed on the sorbent is assumed to equal its enthalpy in liquid state (Section 3.2.3.1). *n-BET* isotherm model (3.6), the parameters of which are summarized in Table 3.2, is used to evaluate H₂O equilibrium loading on *Lewatit*. Water saturation pressure in the gas phase is calculated by *Antoine* equation with a parameter set given by Poling et al.¹²⁶.

Thermophysical properties of CO₂ are calculated based on the correlations outlined in Table B.3. The heat of CO₂ desorption $-\Delta h_{\text{ads,CO}_2}$ is assumed to take a constant value of 84 kJ mol⁻¹, which is estimated based on the analysis of the isosteric heat of adsorption in a temperature range of 25–100 °C for CO₂ loadings that span 0–1 mol kg⁻¹ (Figure 3.6(b)). *Toth* isotherm model (3.2) with parameter set 7 summarized in Table 3.1 is used to evaluate CO₂ equilibrium loading on *Lewatit*.

Thermophysical properties of *Lewatit* are outlined in Table 3.4.

C.2 Equilibrium adsorber model

Basic equilibrium adsorber models are designed to evaluate the influence of H₂O co-adsorption on an unit operation level. Slip streams in the sorbent bed void space are not considered. Sorbent particles are assumed to enter the isothermally operated regeneration unit with CO₂ and H₂O loadings, $q_{\text{eq,CO}_2,\text{Amb}}$ and $q_{\text{eq,H}_2\text{O,Amb}}$, respectively, that equal their loadings in equilibrium with ambient conditions. Note that this incorporates the assumption of a negligible change in loading during sorbent heating, which is justified by the small ratio of the sorbent bed void space to the sorbent volume-specific loading.

The governing equations derived for co-current operation at desorption temperature T_{des} read

$$\mathbf{q}_{\text{wor,CO}_2} = \mathbf{q}_{\text{eq1,CO}_2,\text{Amb}} - \Delta \mathbf{q}_{\text{wor,CO}_2} = \mathbf{q}_{\text{eq1,CO}_2,\text{Amb}} \cdot (1 - \Delta \mathbf{q}_{\text{wor,CO}_2,\text{rel}}) \quad (\text{C.1a})$$

$$p_{\text{wor,CO}_2} = p_{\text{eq1,CO}_2}(\mathbf{q}_{\text{wor,CO}_2}, p_{\text{wor,H}_2\text{O}}, T_{\text{des}}) \quad (\text{C.1b})$$

$$\mathbf{q}_{\text{wor,H}_2\text{O}} = \mathbf{q}_{\text{eq1,H}_2\text{O},\text{Amb}} - \Delta \mathbf{q}_{\text{wor,H}_2\text{O}} = \mathbf{q}_{\text{eq1,H}_2\text{O},\text{Amb}} \cdot (1 - \Delta \mathbf{q}_{\text{wor,H}_2\text{O},\text{rel}}) \quad (\text{C.1c})$$

$$p_{\text{wor,H}_2\text{O}} = p_{\text{eq1,H}_2\text{O}}(\mathbf{q}_{\text{wor,H}_2\text{O}}, T_{\text{des}}) \quad (\text{C.1d})$$

$$\frac{p_{\text{wor,CO}_2}}{\Delta \mathbf{q}_{\text{wor,CO}_2}} = \frac{p_{\text{wor,CO}_2}}{\mathbf{q}_{\text{eq1,CO}_2,\text{Amb}} - \mathbf{q}_{\text{wor,CO}_2}} = \frac{p_{\text{wor,H}_2\text{O}}}{\mathbf{q}_{\text{eq1,H}_2\text{O},\text{Amb}} - \mathbf{q}_{\text{wor,H}_2\text{O}}} = \frac{p_{\text{wor,H}_2\text{O}}}{\Delta \mathbf{q}_{\text{wor,H}_2\text{O}}} \quad (\text{C.1e})$$

This operation mode always allows for solutions that are in line with the equilibrium constraints. However, this does not always hold true for counter-current operation, for which the set of governing equations can be summarized as follows

$$\mathbf{q}_{\text{wor,CO}_2} = \mathbf{q}_{\text{eq1,CO}_2,\text{Amb}} - \Delta \mathbf{q}_{\text{wor,CO}_2} = \mathbf{q}_{\text{eq1,CO}_2,\text{Amb}} \cdot (1 - \Delta \mathbf{q}_{\text{wor,CO}_2,\text{rel}}) \quad (\text{C.2a})$$

$$p_{\text{wor,CO}_2} = p_{\text{eq1,CO}_2}(\mathbf{q}_{\text{eq1,CO}_2,\text{Amb}}, p_{\text{wor,H}_2\text{O}}, T_{\text{des}}) \quad (\text{C.2b})$$

$$\mathbf{q}_{\text{wor,H}_2\text{O}} = \mathbf{q}_{\text{eq1,H}_2\text{O},\text{Amb}} - \Delta \mathbf{q}_{\text{wor,H}_2\text{O}} = \mathbf{q}_{\text{eq1,H}_2\text{O},\text{Amb}} \cdot (1 - \Delta \mathbf{q}_{\text{wor,H}_2\text{O},\text{rel}}) \quad (\text{C.2c})$$

$$p_{\text{wor,H}_2\text{O}} = p_{\text{eq1,H}_2\text{O}}(\mathbf{q}_{\text{eq1,H}_2\text{O},\text{Amb}}, T_{\text{des}}) \quad (\text{C.2d})$$

$$\frac{p_{\text{wor,CO}_2}}{\Delta \mathbf{q}_{\text{wor,CO}_2}} = \frac{p_{\text{wor,CO}_2}}{\mathbf{q}_{\text{eq1,CO}_2,\text{Amb}} - \mathbf{q}_{\text{wor,CO}_2}} = \frac{p_{\text{wor,H}_2\text{O}}}{\mathbf{q}_{\text{eq1,H}_2\text{O},\text{Amb}} - \mathbf{q}_{\text{wor,H}_2\text{O}}} = \frac{p_{\text{wor,H}_2\text{O}}}{\Delta \mathbf{q}_{\text{wor,H}_2\text{O}}} \quad (\text{C.2e})$$

Relative working capacities $\Delta \mathbf{q}_{\text{wor,H}_2\text{O},\text{rel}}$ larger than one can be required to simultaneously satisfy (C.2a) - (C.2e). In other words, the water loading at the gas phase outlet can be required to take negative values. Physically, this case can be interpreted as a scenario in which the amount of H_2O desorption is limited by the convective transport of H_2O , which is bound to the sorbent, into the desorption zone. This allows to define a physically sound set of equations for these cases by replacing (C.2c) - (C.2d) with

$$\mathbf{q}_{\text{wor,H}_2\text{O}} = 0 \quad (\text{C.3a})$$

$$\Delta \mathbf{q}_{\text{wor,H}_2\text{O}} = \mathbf{q}_{\text{eq1,H}_2\text{O},\text{Amb}} = \Delta \mathbf{q}_{\text{wor,H}_2\text{O},\text{rel}} \cdot \mathbf{q}_{\text{eq1,H}_2\text{O},\text{Amb}} \quad (\text{C.3b})$$

Additional variables used in the governing equations are $\mathbf{q}_{\text{wor},i_{\text{Spe}}}$ that describes the sorbent loading at the solid phase outlet and $p_{\text{wor},i_{\text{Spe}}}$ that gives the gas phase pressure of specie i_{Spe} in the gas phase outlet, i.e., the gas phase pressure of component i_{Spe} in *DAC* product gas $p_{\text{Pro,DAC},i_{\text{Spe}}}$. Gas phase pressures in equilibrium with the solid phase $p_{\text{eq1},i_{\text{Spe}}}$ are calculated based on the isotherms summarized in Appendix C.1. Note that the implementation of these sets of equations in *Matlab*^{®178} also takes into account the influence of humidity on CO_2 capacity, such that basic estimates of the influence of this coupling based on (C.1a) - (C.1e) and (C.2a) - (C.2e) are possible. However, a profound data basis with regard to the 2-component isotherms is lacking and estimation of water influence on $p_{\text{wor,CO}_2}$ (C.2b) in case of non-equilibrium conditions at the gas phase outlet calls for more detailed modeling including, besides others, kinetic data currently not available. Thus, the discussion of these scenarios is not explicitly presented in this contribution.

C.3 Integrated DAC–MVR operation

The evaluation of integrated *DAC–MVR* operation comprises assumptions and modeling with regard to *DAC* unit operation (Appendix C.3.1), *DAC–MVR* heat transfer (Appendix C.3.2) and *MVR* operation (Appendix C.3.3). Moreover, an overview of the characteristic energy and heat flows evaluated in the analysis is provided in Appendix C.3.4.

C.3.1 DAC unit operation

For the sake of generality, the analysis performed solely focuses on the desorption zone of the *DAC* unit. No slip streams of gas in the bed void space are considered. An extended model that takes into account the characteristic features of *MBtA* and *MBdA* operation is discussed in the analysis of the integrated *DAC–PtG* process in Chapter 6.

The desorption temperature T_{des} is assumed to equal the constant temperature $T_{\text{DAC}_{\text{Des}}}$ adjusted in the desorption zone of the *DAC* unit. Species thermophysical properties relevant for *DAC* operation are summarized in Appendix C.1. *DAC* product gas composition is evaluated based on the equilibrium adsorber models outlined in Appendix C.2. Presence of an inert strip gas or low-pressure operation is assumed if the sum of H_2O and CO_2 partial pressures stays below the *DAC* reference operation pressure of $1 \cdot 10^5$ Pa. If the sum of the partial pressures of these two species exceeds the reference operation pressure of the *DAC* unit, the mole fractions of these species in the *DAC* product gas are assumed to equal the ratio of their equilibrium pressures, with a total *DAC* product gas pressure and temperature being $1 \cdot 10^5$ Pa and $T_{\text{DAC}_{\text{Des}}}$, respectively.

C.3.2 Heat transfer between DAC and MVR

The heat transfer characteristics from the *MVR* condensers to the *DAC* desorption zone are characterized by the minimum temperature difference for heat transfer $\Delta T_{\text{df,MVR}_{\text{Con}},\text{DAC}_{\text{Des}}}$. As a first proxy, this value is pessimistically estimated to be 10 K. In subsequent studies that take into account trade-off considerations between the investment costs and the potential for heat recovery this parameter might vary in dependence on the characteristic operation points of the process units. However, use of a fixed value of $\Delta T_{\text{df,MVR}_{\text{Con}},\text{DAC}_{\text{Des}}}$ seems sufficient with respect to the basic investigation aspired in this contribution.

C.3.3 Mechanical vapor recompression MVR

The *DAC* product gas is sent to the multi-stage compression-condensation unit sketched in Figure 5.6. After each compression stage (Appendix C.3.3.1) the gas phase is cooled down in a condenser (Appendix C.3.3.2) that operates at $T_{\text{Con}_i\text{Con}} = T_{\text{DAC}_{\text{Des}}} + \Delta T_{\text{df,MVR}_{\text{Con}},\text{DAC}_{\text{Des}}}$. If water condenses, it is separated from the gas stream before the gas is sent to the next compression stage. For reasons of clarity heat losses to the environment and preheating before a compression stage, e.g., to avoid formation of droplets in the compressors, are not considered.

C.3.3.1 Model: compressor

Gas phase compression is modeled assuming:

- Ideal gas behavior
- Adiabatic compression
- Compressor efficiency²⁸²: $\eta_{\text{Com}_{i_{\text{Com}}}} = 0.7$

Ideal compressor outlet temperature is implicitly calculated by solving

$$\int_{T_{\text{Com}_{i_{\text{Com}}},\text{in}}}^{T_{\text{Com}_{i_{\text{Com}}},\text{out,ide}}} \frac{\sum_{i_{\text{Spe}}} y_{\text{Com}_{i_{\text{Com}}},\text{in},i_{\text{Spe}}} \cdot c_{p,i_{\text{Spe}}}(T)}{T} dT = R_{\text{id}} \cdot \ln \left(\frac{p_{\text{Com}_{i_{\text{Com}}},\text{out}}}{p_{\text{Com}_{i_{\text{Com}}},\text{in}}} \right). \quad (\text{C.4})$$

Based on the ideal compressor outlet temperature $T_{\text{Com}_{i_{\text{Com}}},\text{out,ide}}$, the compression energy requirement is estimated by equating

$$\dot{E}_{\text{Com}_{i_{\text{Com}}}} = \frac{\sum_{i_{\text{Spe}}} \dot{n}_{\text{Com}_{i_{\text{Com}}},\text{in},i_{\text{Spe}}} \cdot \left(h_{\text{G},i_{\text{Spe}}}(T_{\text{Com}_{i_{\text{Com}}},\text{out,ide}}) - h_{\text{G},i_{\text{Spe}}}(T_{\text{Com}_{i_{\text{Com}}},\text{in}}) \right)}{\eta_{\text{Com}_{i_{\text{Com}}}}} \quad (\text{C.5})$$

and the real compressor outlet temperature is implicitly obtained from

$$\dot{E}_{\text{Com}_{i_{\text{Com}}}} = \sum_{i_{\text{Spe}}} \dot{n}_{\text{Com}_{i_{\text{Com}}},\text{in},i_{\text{Spe}}} \cdot \left(h_{\text{G},i_{\text{Spe}}}(T_{\text{Com}_{i_{\text{Com}}},\text{out}}) - h_{\text{G},i_{\text{Spe}}}(T_{\text{Com}_{i_{\text{Com}}},\text{in}}) \right). \quad (\text{C.6})$$

The overall energy input to the compressors

$$\dot{E}_{\text{Com}} = \sum_{i_{\text{Com}}} \dot{E}_{\text{Com}_{i_{\text{Com}}}} \quad (\text{C.7})$$

is calculated based on the energy requirements of the single compression stages.

C.3.3.2 Model: condenser

The phase change enthalpy of water vapor is recovered by means of water condensation. The condenser model is based on the assumptions:

- Ideal gas phase behavior
- Isobaric operation
- Temperatures of the streams at the condenser outlet equal $T_{\text{Con}_{i_{\text{Con}}}}$
- If condensation appears, equilibrium between the phases is reached at the condenser outlet
- Water saturation pressure $p_{\text{sat},\text{H}_2\text{O}}$ is calculated by means of basic *Antoine* equation with a parameter set given by Poling et al.¹²⁶

- Ideal separation of the liquid and gas phase, i.e., no entrainment of liquid water in the gas phase or solubility of the gas phase in water is considered

With these assumptions at hand, the mass balance of component i_{Spe} in condenser i_{Con} reads

$$\dot{n}_{\text{Con}_{i_{\text{Con}}},\text{in,G},i_{\text{Spe}}} = \dot{n}_{\text{Con}_{i_{\text{Con}}},\text{out,G},i_{\text{Spe}}} + \dot{n}_{\text{Con}_{i_{\text{Con}}},\text{out,L},i_{\text{Spe}}} \quad (\text{C.8})$$

with $\dot{n}_{\text{Con}_{i_{\text{Con}}},\text{out,G},i_{\text{Spe}}}$ denoting the mole flow in the gas phase and $\dot{n}_{\text{Con}_{i_{\text{Con}}},\text{out,L},i_{\text{Spe}}}$ being the mole flow of a specie in the condensed phase. Condensation is assumed to appear if the partial pressure of H_2O exceeds its saturation pressure. The assumption of phase equilibrium at the condenser outlet

$$p_{\text{Con}_{i_{\text{Con}}},\text{out,G},\text{H}_2\text{O}} = p_{\text{Con}_{i_{\text{Con}}}} \cdot y_{\text{Con}_{i_{\text{Con}}},\text{out,G},\text{H}_2\text{O}} = p_{\text{sat},\text{H}_2\text{O}} \left(T_{\text{Con}_{i_{\text{Con}}}} \right) \quad (\text{C.9})$$

allows for calculation of the H_2O mole fraction $y_{\text{Con}_{i_{\text{Con}}},\text{out,G},\text{H}_2\text{O}}$ in the gas phase at the condenser outlet. Based on this information the amount of water condensed

$$\dot{n}_{\text{Con}_{i_{\text{Con}}},\text{out,L},\text{H}_2\text{O}} = \frac{\dot{n}_{\text{Con}_{i_{\text{Con}}},\text{in,G},\text{H}_2\text{O}} - \dot{n}_{\text{Con}_{i_{\text{Con}}},\text{in,G}} \cdot y_{\text{Con}_{i_{\text{Con}}},\text{out,G},\text{H}_2\text{O}}}{1 - y_{\text{Con}_{i_{\text{Con}}},\text{out,G},\text{H}_2\text{O}}} \quad (\text{C.10})$$

and the heat release of condenser i_{Con}

$$\begin{aligned} \dot{Q}_{\text{Con}_{i_{\text{Con}}}} &= \sum_{i_{\text{Spe}}} \dot{n}_{\text{Com}_{i_{\text{Com}}},\text{out},i_{\text{Spe}}} \cdot h_{\text{G},i_{\text{Spe}}} \left(T_{\text{Com}_{i_{\text{Com}}},\text{out}} \right) \\ &\quad - \sum_{i_{\text{Spe}}} \dot{n}_{\text{Con}_{i_{\text{Con}}},\text{out,G},i_{\text{Spe}}} \cdot h_{\text{G},i_{\text{Spe}}} \left(T_{\text{Con}_{i_{\text{Con}}},\text{out}} \right) \\ &\quad - \sum_{i_{\text{Spe}}} \dot{n}_{\text{Con}_{i_{\text{Con}}},\text{out,L},i_{\text{Spe}}} \cdot h_{\text{L},i_{\text{Spe}}} \left(T_{\text{Con}_{i_{\text{Con}}},\text{out}} \right) \end{aligned} \quad (\text{C.11})$$

can be calculated. Here, compressor and condenser numbers take the same value $i_{\text{Con}} = i_{\text{Com}}$, which equals the number of the corresponding *MVR* stage. Finally, the overall heat release of the condensers

$$\dot{Q}_{\text{Con}} = \sum_{i_{\text{Con}}} \dot{Q}_{\text{Con}_{i_{\text{Con}}}} \quad (\text{C.12})$$

can be calculated from the contributions $\dot{Q}_{\text{Con}_{i_{\text{Con}}}}$ of the single condensation stages i_{Con} in *MVR*.

C.3.4 Characteristic energy flows

Various energy flows

$$\dot{E}_{\text{MVR-DAC},\Sigma} = \dot{Q}_{\text{des},\text{CO}_2} + \dot{Q}_{\text{des},\text{H}_2\text{O}} + \dot{Q}_{\Delta T_{\text{df},\text{MVR}_{\text{Con}},\text{DAC}_{\text{Des}}}} = \dot{E}_{\text{adi}} + \dot{E}_{\text{Com}} + \dot{Q}_{\text{con}}^0 \quad (\text{C.13})$$

are investigated in the overall analysis of the coupled *DAC-MVR* process. Heat demands result from desorption of CO_2

$$\dot{Q}_{\text{des,CO}_2} = \dot{n}_{\text{Pro,DAC,CO}_2} \cdot (-\Delta h_{\text{ads,CO}_2}(T_{\text{DACDes}})) \quad (\text{C.14})$$

and of H_2O

$$\dot{Q}_{\text{des,H}_2\text{O}} = \dot{n}_{\text{Pro,DAC,H}_2\text{O}} \cdot (-\Delta h_{\text{ads,H}_2\text{O}}(T_{\text{DACDes}})) \quad (\text{C.15})$$

in the *DAC* unit. An additional contribution to the energy balance arises from the sensible heat

$$\begin{aligned} \dot{Q}_{\Delta T_{\text{df,Con,DAC}}} = & \sum_{i_{\text{Spe}}} \dot{n}_{\text{Con}_{i_{\text{Con}},\text{out,G},i_{\text{Spe}}}} \cdot \left(h_{\text{G},i_{\text{Spe}}}(T_{\text{Con}_{i_{\text{Con}},\text{out}}}) - h_{\text{G},i_{\text{Spe}}}(T_{\text{DACDes}}) \right) \\ & + \sum_{i_{\text{Con}}} \dot{n}_{\text{Con}_{i_{\text{Con}},\text{out,L,H}_2\text{O}}} \cdot \left(h_{\text{L,H}_2\text{O}}(T_{\text{Con}_{i_{\text{Con}},\text{out}}}) - h_{\text{L,H}_2\text{O}}(T_{\text{DACDes}}) \right) \end{aligned} \quad (\text{C.16})$$

that is required to change the temperature of the species from *DAC* desorption temperature to condenser outlet temperature.

The heat sources of the coupled *DAC-MVR* process are summarized on the right hand side of (C.13). The energy input via the compressors \dot{E}_{Com} is discussed in Appendix C.3.3.1. Additionally, the heat release

$$\dot{Q}_{\text{con}}^0 = \sum_{i_{\text{Con}}} \dot{n}_{\text{Con}_{i_{\text{Con}},\text{out,L,H}_2\text{O}}} \cdot (h_{\text{G,H}_2\text{O}}(T_{\text{DACDes}}) - h_{\text{L,H}_2\text{O}}(T_{\text{DACDes}})) \quad (\text{C.17})$$

that results from the phase change of water and the additional energy input

$$\dot{E}_{\text{adi}} = \dot{E}_{\text{MVR-DAC},\Sigma} - \dot{E}_{\text{Com}} - \dot{Q}_{\text{con}}^0, \quad (\text{C.18})$$

required to close the energy balance, are taken into account. CO_2 -specific energy and heat demands

$$e_{i,\text{spe}_{n_{\text{CO}_2}}} = \frac{\dot{E}_i}{\dot{n}_{\text{Pro,DAC,CO}_2}} \quad (\text{C.19})$$

and

$$q_{i,\text{spe}_{n_{\text{CO}_2}}} = \frac{\dot{Q}_i}{\dot{n}_{\text{Pro,DAC,CO}_2}}, \quad (\text{C.20})$$

respectively, are scaled with the *DAC* unit product gas flow $\dot{n}_{\text{Pro,DAC,CO}_2}$ of this specie.

D Appendix: Intensified heat and mass integrated DAC - PtG process

Parts of this appendix have been published in peer-reviewed journal articles and in the corresponding supplementary information.^{240,274,275}

D.1 Thermophysical properties

In this chapter information on the thermophysical properties of the the liquid and gas / vapor phase are provided (Appendix D.1.1). Characteristics with regard to the adsorbents and to the adsorption of species on *zeolite 3A* (Appendix D.1.2) and on *Lewatit* (Appendix D.1.3) are discussed.

D.1.1 Species in the liquid and gas/vapor phase

Enthalpies, entropies and heat capacities of the gas phase species are calculated based on *Shomate* equation¹²⁸. For water in liquid and vapor state correlations provided in *IAPWS International Steam Tables*³⁵⁷ are used. Influence of pressure in these correlations is not considered. Ideal gas phase behavior is assumed. Properties of the mixed gas/vapor phase are calculated based on (B.1). Water saturation pressure in the gas/vapor phase is calculated by *Antoine* equation with a parameter set given by Poling et al.¹²⁶.

D.1.2 Zeolite 3A and water adsorption on zeolite 3A

Thermophysical properties of *zeolite 3A* provided by *Grace*³⁵⁸ are used. According to this data a heat capacity of the sorbent of $960 \text{ J kg}^{-1} \text{ K}^{-1}$ is assumed. Water equilibrium loading $q_{\text{eq},\text{Z3A},\text{H}_2\text{O}}$ is calculated by a generalized statistical thermodynamic adsorption model proposed by LLano-Restrepo et al.²³⁷ for *Grace* adsorbents. This isotherm model was derived based on adsorption data that span a temperature and H_2O partial pressure range of $-20 - 100 \text{ }^\circ\text{C}$ and $10^{-2} - 10^5 \text{ Pa}$, respectively. Investigations performed by Gabruś et al.³⁵⁹ suggest that the isotherms derived can be used to evaluate H_2O equilibrium loadings on the sorbent up to temperature levels of $250 \text{ }^\circ\text{C}$. A constant heat of adsorption $\Delta h_{\text{ads},\text{Z3A},\text{H}_2\text{O}} = -64.7 \text{ kJ mol}^{-1}$ is assumed, which equals the limiting value for

zero H₂O loading presented in the studies of LLano-Restrepo et al.²³⁷. The enthalpy of the water adsorbed on *zeolite 3A*

$$h_{Z3A,H_2O} = h_{G,H_2O} + \Delta h_{ads,Z3A,H_2O} \quad (D.1)$$

is estimated based on the heat of adsorption $\Delta h_{ads,Z3A,H_2O}$ and on the enthalpy of water vapor in the gas phase h_{G,H_2O} .

D.1.3 Lewatit and adsorption of species on Lewatit

Thermophysical properties of *Lewatit* that define the bed and solid phase characteristics are summarized in Table 3.4 and discussed in Section 3.3. Equilibrium loadings for CO₂ and H₂O are modeled based on *Toth* isotherm model (3.2) (model no. 7, Table 3.1) and on *n-BET* model (3.6) (Table 3.2), respectively.

The enthalpy of CO₂ in the sorbate phase

$$h_{Soa,CO_2} = h_{G,CO_2} + \Delta h_{ads,CO_2} \quad (D.2)$$

is calculated based on the enthalpy of gaseous CO₂ with a constant heat of adsorption $\Delta h_{ads,CO_2}$ of -84 kJ mol⁻¹ being assumed. This value is estimated based on the analysis of the isosteric heat of adsorption in a temperature range of 25–100 °C for CO₂ loadings that span 0–1 mol kg⁻¹ (Figure 3.6(b)). Based on the analysis outlined in Section 3.2.3.1, the enthalpy of water in the sorbate phase is assumed to equal its corresponding value in liquid state

$$h_{Soa,H_2O} = h_{L,H_2O} \quad (D.3)$$

D.2 Models of the main equipment

Models that describe the operation characteristics of the basic process units and devices: condenser (Appendix D.2.1), *DAC* unit (Appendix D.2.2), electrolysis (Appendix D.2.3), evaporator (Appendix D.2.4), heater / cooler (Appendix D.2.5), mixing of streams (Appendix D.2.6), *MVR* unit (Appendix D.2.7), pump (Appendix D.2.8), reactor (Appendix D.2.9), throttling valve (Appendix D.2.10) and water adsorber unit (Appendix D.2.11) are implemented in *Matlab*^{®178}. If not stated differently, no pressure losses in the units are considered. For reasons of clarity, unit counting indices are omitted in the equations derived for the single units in Appendix D.2.1 - D.2.11, e.g., $\dot{Q}_{Hea} = \dot{Q}_{Hea_iHea}$.

D.2.1 Model: condenser

Condensers are used to recover the heat of water condensation. The model of this unit is described in detail in Appendix C.3.3.2.

D.2.2 Model: direct air capture unit

In the *DAC* unit CO_2 and H_2O are adsorbed under ambient conditions and released at desorption temperature level and at elevated concentrations. Species thermophysical properties of special relevance for *DAC* applications are summarized in Appendix D.1.3. Assumptions made in modeling of the *DAC* unit (Appendix D.2.2.1) and the corresponding governing equations (Appendix D.2.2.2) are discussed in this section.

D.2.2.1 Assumptions

Various assumptions are made in modeling of the *DAC* unit, which can be summarized as follows:

- Counter-current operation between the gas / vapor phase and sorbent is assumed
- *Lewatit VP OC 1065* is used as adsorbent
- Thermophysical properties of relevance and adsorption isotherms are discussed in Appendix D.1
- No interactions between H_2O and CO_2 adsorbed are taken into account
- Equilibrium with the ambient is reached at the end of the adsorption zone
- Ambient conditions read: temperature $T_{\text{Amb}} = 298.15 \text{ K}$, pressure $p_{\text{Amb}} = 10^5 \text{ Pa}$, CO_2 content $y_{\text{Amb,G,CO}_2} = 400 \cdot 10^{-6}$, relative humidity $\phi_{\text{rh,Amb}} = 0.8$, composition of dry, CO_2 -free air $y_{\text{Air,N}_2} = 0.79$ and $y_{\text{Air,O}_2} = 0.21$
- Operation of the *DAC* unit is discussed in Appendix D.3.6
- A working capacity of CO_2 $\Delta q_{\text{wor,DAC,CO}_2}$ of 0.25 mol kg^{-1} is assumed
- The temperature at which a possible purge gas stream leaves the heating zone $T_{\text{purge,DAC}}$ is assumed to equal ambient temperature T_{Amb}
- The heat losses in the sorbent phase are characterized by the thermal slip $\Delta T_{\text{los,DAC}} = 5 \text{ K}$
- The heat of adsorption as well as the sensible heat release of the gas / vapor phase (in the bed void space), sorbent and sorbate in the adsorption zone are assumed to be transferred to the ambient. These heat flows are not shown in the pinch analysis

D.2.2.2 Governing equations

The basic model outlined allows for estimates of the operation characteristics of *MBdA* and *MBtA* by definition of the variables: relative working capacity $\Delta q_{\text{wor,DAC,CO}_2}$, desorption temperature T_{DACDes} , pressure level at *DAC* outlet $p_{\text{DACDes,out}}$, thermal slip in the sorbent phase $\Delta T_{\text{los,DAC}}$.

Mass balance Based on the relative working capacity

$$\Delta \mathbf{q}_{\text{wor,DAC,CO}_2,\text{rel}} = \frac{\Delta \mathbf{q}_{\text{wor,DAC,CO}_2}}{\mathbf{q}_{\text{eq1,CO}_2,\text{Amb}}} \quad (\text{D.4})$$

and on the CO_2 product stream $\dot{n}_{\text{Pro,DAC,CO}_2}$ to be obtained, the amount of CO_2 to be desorbed

$$\dot{n}_{\text{des,DAC}_{\text{Des,CO}_2}} = \frac{\dot{n}_{\text{Pro,DAC,CO}_2} - \dot{n}_{\text{DAC,in,coc,G,CO}_2} - \dot{n}_{\text{DAC,in,cuc,G,CO}_2}}{1 + y_{\text{DAC,sli}_{\text{Ads,Hea,G,CO}_2}} \cdot \phi_{\text{DAC,sli}_{\text{Ads,Hea,des}}}} \cdot \frac{1}{-y_{\text{DAC,in,cuc,G,CO}_2} \cdot \phi_{\text{DAC,sli}_{\text{Des,Coo,des}}}} \quad (\text{D.5})$$

can be calculated. Here, $\dot{n}_{\text{DAC,in,cuc,G,CO}_2}$ describes the stream of CO_2 that enters the *DAC* unit in the strip gas flowing in counter-current operation mode relative to the sorbent movement. For the scenarios analyzed no additional use of strip gas $\dot{n}_{\text{DAC,in,coc}}$ in co-current operation mode relative to the sorbent movement is considered.

Contributions of additional slip streams are taken into account by the denominator of (D.5). The parameter

$$\phi_{\text{DAC,sli}_{\text{Ads,Hea,des}}} = \frac{p_{\text{Amb}}}{R_{\text{id}} \cdot T_{\text{Amb}}} \cdot \frac{\psi_{\text{B}}}{(1 - \psi_{\text{B}}) \cdot \Delta \mathbf{q}_{\text{wor,DAC,CO}_2} \cdot \rho_{\text{P}}} \cdot \phi_{\text{DAC,sli}_{\text{Ads,Des}}} \quad (\text{D.6})$$

gives the ratio between the mole flow of CO_2 that is transferred from the adsorption to the desorption zone via the void space of the sorbent bed and the amount of CO_2 desorbed into the product gas. In (D.6) $\phi_{\text{DAC,sli}_{\text{Ads,Des}}}$ gives the fraction of the slip stream that is not removed by additional purge gas use or by vacuum operation. Analogously,

$$\phi_{\text{DAC,sli}_{\text{Des,Coo,des}}} = \frac{p_{\text{DAC,in,cuc}}}{R_{\text{id}} \cdot T_{\text{DAC,in,cuc}}} \cdot \frac{\psi_{\text{B}}}{(1 - \psi_{\text{B}}) \cdot \Delta \mathbf{q}_{\text{wor,DAC,CO}_2} \cdot \rho_{\text{P}}} \quad (\text{D.7})$$

defines the slip stream in the sorbent bed void space between the desorption and cooling zone. Based on these definitions, the flow of specie i_{Spe} that is transferred in the bed void space from the adsorption to the desorption zone becomes

$$\dot{n}_{\text{DAC,sli}_{\text{Ads,Des,G},i_{\text{Spe}}}} = y_{\text{DAC,sli}_{\text{Ads,Hea,G},i_{\text{Spe}}}} \cdot \phi_{\text{DAC,sli}_{\text{Ads,Hea,des}}} \cdot \dot{n}_{\text{des,DAC}_{\text{Des,CO}_2}} \quad (\text{D.8})$$

the definition of the stream that is purged between these zones reads

$$\dot{n}_{\text{DAC,purge}_{\text{Ads,Des,G},i_{\text{Spe}}}} = y_{\text{DAC,sli}_{\text{Ads,Hea,G},i_{\text{Spe}}}} \cdot \frac{p_{\text{Amb}}}{R_{\text{id}} \cdot T_{\text{Amb}}} \cdot \frac{\psi_{\text{B}}}{(1 - \psi_{\text{B}}) \cdot \Delta \mathbf{q}_{\text{wor,DAC,CO}_2} \cdot \rho_{\text{P}}} \cdot (1 - \phi_{\text{DAC,sli}_{\text{Ads,Des}}}) \cdot \dot{n}_{\text{des,DAC}_{\text{Des,CO}_2}} \quad (\text{D.9})$$

and the mole flow of species in the bed void space at the boundary between the desorption and cooling zone becomes

$$\dot{n}_{\text{DAC,sli}_{\text{Des,Coo,G},i_{\text{Spe}}}} = y_{\text{DAC,in,cuc,G},i_{\text{Spe}}} \cdot \phi_{\text{DAC,sli}_{\text{Des,Coo,des}}} \cdot \dot{n}_{\text{des,DAC}_{\text{Des,CO}_2}} \quad (\text{D.10})$$

Moreover, the overall flow of specie i_{Spe} that enters the desorption zone in co-current flow with the sorbent can be calculated as follows

$$\dot{n}_{\text{DAC}_{\text{Des}},\text{in},\text{coc}_{\Sigma},\text{G},i_{\text{Spe}}} = \dot{n}_{\text{DAC},\text{in},\text{coc},\text{G},i_{\text{Spe}}} + \dot{n}_{\text{DAC},\text{sli}_{\text{Ads,Des}},\text{G},i_{\text{Spe}}} \cdot \quad (\text{D.11})$$

Based on the mole flow of CO_2 required to be desorbed $\dot{n}_{\text{des},\text{DAC}_{\text{Des}},\text{CO}_2}$, the sorbent mass flow

$$\dot{m}_{\text{P,DAC}} = \frac{\dot{n}_{\text{des},\text{DAC}_{\text{Des}},\text{CO}_2}}{\Delta q_{\text{wor,DAC},\text{CO}_2}} \quad (\text{D.12})$$

can be calculated. This parameter is used in the determination of the stream of H_2O desorbed

$$\dot{n}_{\text{des},\text{DAC}_{\text{Des}},\text{H}_2\text{O}} = \Delta q_{\text{wor,H}_2\text{O,rel}} \cdot q_{\text{eq1,H}_2\text{O,Amb}} \cdot \dot{m}_{\text{P,DAC}} \quad (\text{D.13})$$

that also depends on the relative working capacity of H_2O

$$\Delta q_{\text{wor,DAC,H}_2\text{O,rel}} = \frac{\Delta q_{\text{ads,H}_2\text{O}}}{q_{\text{eq1,H}_2\text{O,Amb}}} \cdot \quad (\text{D.14})$$

In line with the description of the *DAC* operation characteristics given in Section D.3.6, $\Delta q_{\text{wor,DAC,H}_2\text{O,rel}}$ is controlled by adjusting the flow of water vapor strip gas. Summarizing the different contributions to the H_2O balance of the *DAC* unit, it reads

$$\begin{aligned} \dot{n}_{\text{Pro,DAC,H}_2\text{O}} = & \dot{n}_{\text{DAC},\text{in},\text{cuc},\text{G},\text{H}_2\text{O}} + \dot{n}_{\text{DAC}_{\text{Des}},\text{in},\text{coc}_{\Sigma},\text{G},\text{H}_2\text{O}} \\ & + \dot{n}_{\text{des},\text{DAC}_{\text{Des}},\text{H}_2\text{O}} - \dot{n}_{\text{DAC},\text{sli}_{\text{Des,Coo}},\text{G},\text{H}_2\text{O}} \cdot \end{aligned} \quad (\text{D.15})$$

The mole balances of species other than CO_2 and H_2O

$$\begin{aligned} \dot{n}_{\text{Pro,DAC},i_{\text{Spe}}} = & \dot{n}_{\text{DAC},\text{in},\text{cuc},\text{G},i_{\text{Spe}}} + \dot{n}_{\text{DAC}_{\text{Des}},\text{in},\text{coc}_{\Sigma},\text{G},i_{\text{Spe}}} \\ & - \dot{n}_{\text{DAC},\text{sli}_{\text{Des,Coo}},\text{G},i_{\text{Spe}}} \end{aligned} \quad (\text{D.16})$$

do not take into account contributions from adsorption, as these species are considered to be inerts. Additional adsorption effects between adsorption and desorption zone or desorption and adsorption zone might be taken into account. However, due to the high ratio between the moles of species present in the sorbate phase related to the gas phase in the bed void space, no significant contributions on a mass balance level are to be expected. This allows for neglect of the influence of desorption during sorbent heating on the sorbent loading and on the gas phase composition at the gas phase outlet of the *DAC* unit, if the stream introduced in co-current operation, e.g., to avoid slip streams in the heating and external heating zone, becomes negligible small. If this is not the case, the gas phase composition at the *DAC* unit outlet is defined by this co-currently operated part of the *DAC* unit, if no complete desorption of water takes place. However, as this operation mode results in a decrease of the maximum CO_2 share in the gas phase available at the *DAC* unit outlet, selecting this operation region for the *DAC* unit does not seem reasonable. Adsorption and desorption effects can also take place between the

inlet of the strip gas that is operated in counter-current flow relative to the sorbent flow and the sorbent's outlet to the ambient. Here, it is assumed that equilibrium between the gas phase species present in the bed void space and their corresponding loadings at the sorbent is reached at the solid phase outlet to the adsorption zone. With regard to the mass balance, again, these contributions become negligible small. However, re-adsorption, e.g., of water vapor from the bed void space can result in an additional heat source to be exploited in the cooling zone.

Energy balance The heat demand of the *DAC* unit

$$\dot{Q}_{\text{ext},\text{DAC},\Sigma} = \dot{Q}_{\text{hea},\text{DAC},\Sigma} + \dot{Q}_{\text{coo},\text{DAC},\Sigma} + \sum_{i_{\text{Spe}}} \dot{Q}_{\text{adi},\text{DAC},\text{in},\text{cuc},\text{G},i_{\text{Spe}}} + \sum_{i_{\text{Spe}}} \dot{Q}_{\text{des},\text{DAC}_{\text{Des}},i_{\text{Spe}}} \quad (\text{D.17})$$

comprises various contributions, which are discussed below.

Heat sinks in the *DAC* unit attributed to sensible heat demands

$$\dot{Q}_{\text{hea},\text{DAC},\Sigma} = \dot{Q}_{\text{hea},\text{DAC},\text{P}} + \sum_{i_{\text{Spe}}} \dot{Q}_{\text{hea},\text{DAC},\text{Soa},i_{\text{Spe}}} + \sum_{i_{\text{Spe}}} \dot{Q}_{\text{hea},\text{DAC}_{\text{Des}},\text{in},\text{coc}\Sigma,\text{G},i_{\text{Spe}}} \quad (\text{D.18})$$

arise from the sorbent heat demand

$$\dot{Q}_{\text{hea},\text{DAC},\text{P}} = \dot{m}_{\text{P},\text{DAC}} \cdot (h_{\text{P},\text{DAC}}(T_{\text{DAC}_{\text{Des}}}) - h_{\text{P},\text{DAC}}(T_{\text{Amb}})) \quad , \quad (\text{D.19})$$

from the adsorbent heat demand

$$\dot{Q}_{\text{hea},\text{DAC},\text{Soa},i_{\text{Spe}}} = \dot{m}_{\text{P},\text{DAC}} \cdot \mathbf{q}_{\text{eql},i_{\text{Spe}},\text{Amb}} \cdot (h_{\text{Soa},i_{\text{Spe}}}(T_{\text{DAC}_{\text{Des}}}) - h_{\text{Soa},i_{\text{Spe}}}(T_{\text{Amb}})) \quad (\text{D.20})$$

and from the temperature change of species in the bed void space

$$\begin{aligned} \dot{Q}_{\text{hea},\text{DAC}_{\text{Des}},\text{in},\text{coc}\Sigma,\text{G},i_{\text{Spe}}} &= \dot{n}_{\text{DAC},\text{in},\text{coc},\text{G},i_{\text{Spe}}} \cdot (h_{\text{G},i_{\text{Spe}}}(T_{\text{DAC}_{\text{Des}}}) - h_{\text{G},i_{\text{Spe}}}(T_{\text{G},\text{coc},\text{in}})) \\ &+ \dot{n}_{\text{DAC},\text{purge}_{\text{Ads},\text{Des}},\text{G},i_{\text{Spe}}} \cdot (h_{\text{G},i_{\text{Spe}}}(T_{\text{purge},\text{DAC}}) - h_{\text{G},i_{\text{Spe}}}(T_{\text{Amb}})) \\ &+ \dot{n}_{\text{DAC},\text{sli}_{\text{Ads},\text{Des}},\text{G},i_{\text{Spe}}} \cdot (h_{\text{G},i_{\text{Spe}}}(T_{\text{DAC}_{\text{Des}}}) - h_{\text{G},i_{\text{Spe}}}(T_{\text{Amb}})) \quad . \end{aligned} \quad (\text{D.21})$$

Analogously, in the calculation of the heat release between the desorption and adsorption zone

$$\dot{Q}_{\text{coo},\text{DAC},\Sigma} = \dot{Q}_{\text{coo},\text{DAC},\text{P}} + \sum_{i_{\text{Spe}}} \dot{Q}_{\text{coo},\text{DAC},\text{Soa},i_{\text{Spe}}} + \sum_{i_{\text{Spe}}} \dot{Q}_{\text{coo},\text{DAC},\text{sli}_{\text{Coo},\text{Ads}},\text{G},i_{\text{Spe}}} \quad (\text{D.22})$$

contributions from the sorbent

$$\dot{Q}_{\text{coo},\text{DAC},\text{P}} = \dot{m}_{\text{P},\text{DAC}} \cdot (h_{\text{P},\text{DAC}}(T_{\text{Amb}} + \Delta T_{\text{los},\text{DAC}}) - h_{\text{P},\text{DAC}}(T_{\text{DAC}_{\text{Des}}})) \quad , \quad (\text{D.23})$$

from the species bound to the sorbent

$$\begin{aligned} \dot{Q}_{\text{coo,DAC,Soa},i_{\text{Spe}}} = & \dot{m}_{\text{P,DAC}} \cdot \mathbf{q}_{\text{Coo,Ads},i_{\text{Spe}}} \cdot h_{\text{Soa},i_{\text{Spe}}} (T_{\text{Amb}} + \Delta T_{\text{los,DAC}}) \\ & - (\dot{m}_{\text{P,DAC}} \cdot \mathbf{q}_{\text{eql},i_{\text{Spe},\text{Amb}}} - \dot{n}_{\text{des,DACDes},i_{\text{Spe}}}) \cdot h_{\text{Soa},i_{\text{Spe}}} (T_{\text{DACDes}}) \end{aligned} \quad (\text{D.24})$$

and from species transported in the bed void space

$$\begin{aligned} \dot{Q}_{\text{coo,DAC,sliCoo,Ads,G},i_{\text{Spe}}} = & \dot{n}_{\text{DAC,sliCoo,Ads,G},i_{\text{Spe}}} \cdot h_{\text{G},i_{\text{Spe}}} (T_{\text{Amb}} + \Delta T_{\text{los,DAC}}) \\ & - \dot{n}_{\text{DAC,sliDes,Coo,G},i_{\text{Spe}}} \cdot h_{\text{G},i_{\text{Spe}}} (T_{\text{DAC,in,cuc}}) \end{aligned} \quad (\text{D.25})$$

are taken into account. Note that in $\dot{Q}_{\text{coo,DAC},\Sigma}$ contributions of re-adsorption phenomena are included via the definition of $\dot{Q}_{\text{coo,DAC,Soa},i_{\text{Spe}}}$ and $\dot{Q}_{\text{coo,DAC,sliCoo,Ads,G},i_{\text{Spe}}}$.

An additional contribution from the species in the counter-current strip gas stream to the energy balance

$$\begin{aligned} \dot{Q}_{\text{adi,DAC,in,cuc,G},i_{\text{Spe}}} = & (\dot{n}_{\text{DAC,in,cuc,G},i_{\text{Spe}}} - \dot{n}_{\text{DAC,sliDes,Coo,G},i_{\text{Spe}}}) \\ & \cdot (h_{\text{G},i_{\text{Spe}}} (T_{\text{DACDes}}) - h_{\text{G},i_{\text{Spe}}} (T_{\text{DAC,in,cuc}})) \end{aligned} \quad (\text{D.26})$$

needs to be taken into account, if the strip gas stream is introduced at temperatures different from T_{DACDes} . Note that application of (D.26) implies that either $T_{\text{DACDes}} = T_{\text{DAC,in,cuc}}$ hold, i.e., the strip gas stream temperature at its inlet to the desorption zone equals the sorbent bed temperature at this position, or the counter-current strip gas stream is larger than the strip stream.

The last contribution to (D.17) arises from the desorption of species. It reads for a single specie

$$\dot{Q}_{\text{des,DACDes},i_{\text{Spe}}} = \dot{n}_{\text{des,DACDes},i_{\text{Spe}}} \cdot (h_{\text{G},i_{\text{Spe}}} (T_{\text{DACDes}}) - h_{\text{Soa},i_{\text{Spe}}} (T_{\text{DACDes}})) . \quad (\text{D.27})$$

$\dot{Q}_{\text{ext,DAC},\Sigma}$ derived via (D.17) gives the overall external heat demand of the *DAC* unit. For *MBtA* operation this heat is assumed to be required at T_{DACDes} , which gives a worst case estimate with regard to the temperature level of heat supply. For *MBdA* operation, the external heat supply $\dot{Q}_{\text{ext,DAC},\Sigma}$ might be subdivided in a contribution from heating of the transfer medium at temperatures higher than T_{DACDes} and from heat transfer to the *DAC* unit desorption zone required at T_{DACDes} . However, the temperature difference between these two heat sinks scales with the heat losses in the solid phase $\Delta T_{\text{los,DAC}}$, which by purpose are kept very small. Consequently, it does not seem reasonable to differentiate between the temperature levels of heat supply between these two sinks in the basic analysis intended.

Compression energy requirement that results from vacuum operation is not considered in the *DAC* unit model, as the energy required for this operation mode is assumed to be provided to the *MVR* unit. This is, the *DAC* unit desorption pressure set defines the gas phase inlet pressure to the *MVR* unit.

D.2.3 Model: electrolysis

In this section the assumptions made (Appendix D.2.3.1) and governing equations derived (Appendix D.2.3.2) to describe the electrolysis unit are outlined.

D.2.3.1 Assumptions

The electrolysis model is based on the assumptions summarized below:

- Ideal gas behavior
- Isothermal operation
- Isobaric operation
- No crossover between the product gas streams at the oxygen and hydrogen outlet
- Product gas streams are saturated with water vapor
- Water saturation pressure in the gas phase is calculated based on *Antoine* equation (Appendix D.1.1)

D.2.3.2 Governing equations

Mass balance The total mole flow of the components leaving the electrolysis is determined based on the assumption of a water saturated gas phase, which allows to calculate the H₂O mole share in the gas phase

$$y_{\text{Elc,out,G,H}_2\text{O}} = \frac{p_{\text{sat,H}_2\text{O}}(T_{\text{Elc}})}{p_{\text{PrC}}} \quad (\text{D.28})$$

based on the water saturation pressure $p_{\text{sat,H}_2\text{O}}$. For a defined amount of hydrogen to be produced ($\dot{n}_{\text{Elc,outH}_2,\text{G,H}_2} = 2 \cdot \dot{n}_{\text{Elc,outO}_2,\text{G,O}_2}$), the water mole flow at the hydrogen outlet reads

$$\dot{n}_{\text{Elc,outH}_2,\text{G,H}_2\text{O}} = \frac{\dot{n}_{\text{Elc,outH}_2,\text{G,H}_2} \cdot y_{\text{Elc,out,G,H}_2\text{O}}}{1 - y_{\text{Elc,out,G,H}_2\text{O}}} \quad (\text{D.29})$$

and its mole flow at the oxygen outlet becomes

$$\dot{n}_{\text{Elc,outO}_2,\text{G,H}_2\text{O}} = \frac{\dot{n}_{\text{Elc,outO}_2,\text{G,O}_2} \cdot y_{\text{Elc,out,G,H}_2\text{O}}}{1 - y_{\text{Elc,out,G,H}_2\text{O}}} \quad (\text{D.30})$$

These losses and the amount of water split define the overall electrolysis water demand

$$\dot{n}_{\text{Elc,in,L,H}_2\text{O}} = \dot{n}_{\text{Elc,outH}_2,\text{G,H}_2} + \sum_{i_{\text{Str}}} \dot{n}_{\text{Elc,out}_{i_{\text{Str}}},\text{G,H}_2\text{O}} \quad (\text{D.31})$$

Energy balance The total H₂-specific energy demand for water splitting

$$\Delta h_{\text{rea,elc}} = h_{\text{G,H}_2} + 0.5 \cdot h_{\text{G,O}_2} - h_{\text{L,H}_2\text{O}} = \frac{\dot{E}_{\text{rea}\Sigma,\text{elc}}}{\dot{n}_{\text{Elc,outH}_2,\text{G,H}_2}} = e_{\text{rea}\Sigma,\text{elc,spenH}_2} \quad (\text{D.32})$$

is defined by the enthalpy flows that enter and leave the unit. The H₂-specific electric energy requirement

$$\Delta g_{\text{rea,elc}} = \Delta h_{\text{rea,elc}} - T_{\text{Elc}} \cdot \Delta s_{\text{rea,elc}} = \frac{\dot{E}_{\text{reaele,elc}}}{\dot{n}_{\text{Elc,out}\Sigma,\text{G,H}_2}} = e_{\text{reaele,elc,spenH}_2} \quad (\text{D.33})$$

is given by the change in *Gibbs* free energy, calculation of which requires information about the entropic contribution

$$\begin{aligned} \Delta s_{\text{rea,elc}}(T_{\text{Elc}}, p_{\text{Elc}}) &= s_{\text{G,H}_2}(T_{\text{Elc}}, p^\circ) - R_{\text{id}} \cdot \ln\left(\frac{p_{\text{Elc,outH}_2,\text{G,H}_2}}{p^\circ}\right) \\ &\quad + 0.5 \cdot \left(s_{\text{G,O}_2}(T_{\text{Elc}}, p^\circ) - R_{\text{id}} \cdot \ln\left(\frac{p_{\text{Elc,outO}_2,\text{G,O}_2}}{p^\circ}\right) \right) \\ &\quad - s_{\text{L,H}_2\text{O}}(T_{\text{Elc}}, p_{\text{Elc}}) \\ &= \frac{\dot{E}_{\text{reathe,elc}}}{\dot{n}_{\text{Elc,out}\Sigma,\text{G,H}_2} \cdot T_{\text{Elc}}} = \frac{e_{\text{reathe,elc,spenH}_2}}{T_{\text{Elc}}} . \end{aligned} \quad (\text{D.34})$$

Moreover, heat input is required to compensate for the additional heat demand

$$\dot{Q}_{\text{lv,Elc}} = \dot{n}_{\text{Elc,out}\Sigma,\text{G,H}_2\text{O}} \cdot \Delta h_{\text{lv,H}_2\text{O}} \quad (\text{D.35})$$

that results from the evaporation of water.

The cell voltage in thermodynamic equilibrium

$$\Delta U_{\text{Elc,eql}} = \frac{\Delta g_{\text{rea,elc}}}{2 \cdot k_{\text{Far}}} \quad (\text{D.36})$$

and the thermoneutral voltage

$$\Delta U_{\text{Elc,thn}} = \frac{\Delta h_{\text{rea,elc}}}{2 \cdot k_{\text{Far}}} \quad (\text{D.37})$$

can be derived from the energy contributions determined.²⁸⁰ These definitions allow for calculation of the overall electric energy supply to the electrolysis

$$\begin{aligned} \dot{E}_{\text{ele,Elc}} &= 2 \cdot k_{\text{Far}} \cdot \Delta U_{\text{Elc}} \cdot \dot{n}_{\text{Elc,out}\Sigma,\text{G,H}_2} \\ &= 2 \cdot k_{\text{Far}} \cdot \Delta U_{\text{Elc,eql}} \cdot \phi \Delta U_{\text{Elc}} \cdot \dot{n}_{\text{Elc,out}\Sigma,\text{G,H}_2} \end{aligned} \quad (\text{D.38})$$

in dependence of the factor

$$\phi \Delta U_{\text{Elc}} = \frac{\Delta U_{\text{Elc}}}{\Delta U_{\text{Elc,eql}}} \quad (\text{D.39})$$

that defines the operation voltage of the electrolysis relative to the equilibrium cell voltage. Based on the different energy flows defined, the overall electrolysis energy balance reads

$$\dot{Q}_{\text{adi,Elc}} = \dot{E}_{\text{rea}\Sigma,\text{elc}} + \dot{Q}_{\text{lv,Elc}} - \dot{E}_{\text{ele,Elc}} , \quad (\text{D.40})$$

with $\dot{Q}_{\text{adi,Elc}}$ defining the additional heat release or demand of the electrolysis unit.

D.2.4 Model: evaporator

The demand of water vapor used in the *DAC* unit can be provided by the evaporator unit. This unit is operated at the same temperature and pressure levels that are adjusted in the *DAC* unit desorption zone. If the water saturation pressure in this unit stays below its operation pressure, a stream of hydrogen from the electrolysis is used to support water evaporation. In this case, a water-saturated stream of hydrogen is assumed to leave the evaporator unit.

As water adsorption on *Lewatit* is found to be a function of relative humidity, water adsorption in the *DAC* unit can arise if water vapor with a partial pressure close to its saturation pressure is contacted with the sorbent. However, the significant heat release by water adsorption and the strong temperature dependency of relative humidity can be assumed to counteract high levels of water adsorption at the strip gas inlet. This suggests that realization of minor temperature differences between the *DAC* unit and evaporator, allowance for temperature gradients in the *DAC* unit desorption zone or use of overheated steam can be beneficial in a technical setting. However, for the sake of clarity, none of these additional measures will be considered in the basic analysis performed. Assumptions applied and governing equations derived are discussed in Appendix D.2.4.1 and in Appendix D.2.4.2, respectively.

D.2.4.1 Assumptions

Modeling of the evaporator unit comprises the assumptions of:

- Ideal gas behavior
- Isothermal operation at $T_{\text{DAC}_{\text{Des}}}$
- Isobaric operation at $p_{\text{DAC}_{\text{Des}}}$

D.2.4.2 Governing equations

The law of mass conservation in the evaporator unit reads

$$\dot{n}_{\text{Evp,out,G},i_{\text{Spe}}} = \sum_{i_{\text{Str}}} \dot{n}_{\text{Evp,in},i_{\text{Str}},\text{L},i_{\text{Spe}}} + \sum_{i_{\text{Str}}} \dot{n}_{\text{Evp,in},i_{\text{Str}},\text{G},i_{\text{Spe}}} \quad (\text{D.41})$$

and the heat duty of this unit is defined by

$$\begin{aligned} \dot{Q}_{\text{Evp}} = & \sum_{i_{\text{Spe}}} \dot{n}_{\text{Evp,out,G},i_{\text{Spe}}} \cdot h_{\text{G},i_{\text{Spe}}} (T_{\text{Evp,out,G}}) \\ & - \sum_{i_{\text{Str}}} \sum_{i_{\text{Spe}}} \dot{n}_{\text{Evp,in},i_{\text{Str}},\text{G},i_{\text{Spe}}} \cdot h_{\text{G},i_{\text{Spe}}} (T_{\text{Evp,in},i_{\text{Str}},\text{G}}) \\ & - \sum_{i_{\text{Str}}} \sum_{i_{\text{Spe}}} \dot{n}_{\text{Evp,in},i_{\text{Str}},\text{L},i_{\text{Spe}}} \cdot h_{\text{L},i_{\text{Spe}}} (T_{\text{Evp,in},i_{\text{Str}},\text{L}}) . \end{aligned} \quad (\text{D.42})$$

D.2.5 Model: heater and cooler

No heat losses to the ambient or phase changes are considered in the modeling of heaters and coolers. The heat duty of these units is calculated by

$$\dot{Q}_{\text{Hea}} = \sum_{i_{\text{Spe}}} \dot{n}_{\text{Hea,in},i_{\text{Spe}}} \cdot (h_{i_{\text{Spe}}} (T_{\text{Hea,out}}) - h_{i_{\text{Spe}}} (T_{\text{Hea,in}})) . \quad (\text{D.43})$$

D.2.6 Model: mixing of streams

Mixing of streams is assumed to happen in an ideal, adiabatic mixing chamber. The law of mass conservation reads

$$\sum_{i_{\text{Str}}} \dot{n}_{\text{Mix,in},i_{\text{Str}},i_{\text{Spe}}} = \sum_{i_{\text{Str}}} \dot{n}_{\text{Mix,out},i_{\text{Str}},i_{\text{Spe}}} \quad (\text{D.44})$$

and conservation of energy is ensured by

$$\sum_{i_{\text{Str}}} \sum_{i_{\text{Spe}}} \dot{n}_{\text{Mix,in},i_{\text{Str}},i_{\text{Spe}}} \cdot h_{i_{\text{Spe}}} (T_{\text{Mix,in},i_{\text{Str}}}) = \sum_{i_{\text{Str}}} \sum_{i_{\text{Spe}}} \dot{n}_{\text{Mix,out},i_{\text{Str}},i_{\text{Spe}}} \cdot h_{i_{\text{Spe}}} (T_{\text{Mix,out},i_{\text{Str}}}) . \quad (\text{D.45})$$

D.2.7 Model: multi-stage vapor recompression unit

The model of the multi-stage vapor recompression unit is outlined in Appendix C.3.3. Condensers are operated at $T_{\text{DAC}_{\text{Des}}} + \Delta T_{\text{pin}}$ and the compressor energy requirement is minimized by solving (5.5).

D.2.8 Model: pump

Pressurization of the liquid phase, e.g., of the water recycled or additionally supplied to the process, is realized by pumps. Assumptions with regard to the modeling (Appendix D.2.8.1) and governing equations (Appendix D.2.8.2) are outlined.

D.2.8.1 Assumptions

Pumps are modeled under the assumptions of

- Constant concentration of the liquid phase c_L^0 (reference temperature 25 °C)
- Pump efficiency²⁸² $\eta_{\text{Pum}} = 0.4$
- Neglect of fluid temperature change in the pump

D.2.8.2 Governing equations

No mass losses or phase changes in the pumps are considered. The ideal compression energy requirement is estimated by

$$\dot{E}_{\text{Pum,ide}} = \dot{n}_{\text{Pum,L,in}} \cdot \frac{1}{c_L^0} \cdot (p_{\text{Pum,L,out}} - p_{\text{Pum,L,in}}) \quad (\text{D.46})$$

and the real energy input required is given by

$$\dot{E}_{\text{Pum}} = \frac{\dot{E}_{\text{Pum,ide}}}{\eta_{\text{Pum}}} . \quad (\text{D.47})$$

As the energy input of the pump to the liquid is very small, its temperature is assumed to stay unchanged in the compression process.

D.2.9 Model: reactor

In this section the assumptions made in modeling of the reactor are discussed (Appendix D.2.9.1). Reaction kinetics and catalyst mass requirements are investigated in Appendix D.2.9.2. The governing equations of the reactor model are summarized in Appendix D.2.9.3.

D.2.9.1 Assumptions

Modeling of the reactor comprises the assumptions:

- Ideal plug flow reactor
- Ideal gas phase
- Isobaric operation at p_{Prc}
- Isothermal operation at T_{Rea}
- Heat supply and recovery at T_{Rea}
- No thermal losses

D.2.9.2 Kinetics and catalyst mass

The gas phase composition in equilibrium state is calculated by solving

$$0 = K_{\text{eq},p,\text{Sab}} \cdot \left(\frac{p_{\text{PrC}}}{p^\circ} \right)^2 - \frac{y_{\text{H}_2\text{O}}^2 \cdot y_{\text{CH}_4}}{y_{\text{CO}_2} \cdot y_{\text{H}_2}^4}, \quad (\text{D.48})$$

with the equilibrium constant

$$K_{\text{eq},p,\text{Sab}} = e^{-\frac{\Delta g_{\text{Sab}}^\circ(T_{\text{Rea}})}{R_{\text{id}} \cdot T_{\text{Rea}}}} \quad (\text{D.49})$$

being derived from the change of *Gibbs* free energy in the reaction $\Delta g_{\text{Sab}}^\circ$. In the calculation of this parameter, properties of water vapor are estimated based on *Shomate* equation¹²⁸.

The catalyst mass required

$$m_{\text{Rea,Cat}} = \dot{n}_{\text{Rea,in,CO}_2} \cdot \int_0^{X_{\text{Rea,out,CO}_2}} \frac{1}{r_{\text{rea,Sab,CO}_2}} dX_{\text{Rea,CO}_2} \quad (\text{D.50})$$

is obtained from the rate of reaction $r_{\text{rea,Sab,CO}_2}$ that is evaluated based on *Langmuir-Hinshelwood-Hougen-Watson* (*LHHW*) rate equation proposed by Koschany et al.³⁶⁰.

D.2.9.3 Governing equations

The mole flows of the species at the reactor outlet

$$\dot{n}_{\text{Rea,out},i_{\text{Spe}}} = \dot{n}_{\text{Rea,in},i_{\text{Spe}}} - \frac{\nu_{\text{Sab},i_{\text{Spe}}}}{\nu_{\text{Sab,CO}_2}} \cdot \dot{n}_{\text{Rea,in,CO}_2} \cdot X_{\text{Rea,out,CO}_2} \quad (\text{D.51})$$

are calculated in dependence of the carbon dioxide conversion set $X_{\text{Rea,out,CO}_2}$ in accordance to the stoichiometry of *Sabatier* reaction (2.I). Based on this information the reactor heat duty

$$\dot{Q}_{\text{Rea}} = \sum_{i_{\text{Spe}}} \dot{n}_{\text{Rea,out},i_{\text{Spe}}} \cdot h_{i_{\text{Spe}}}(T_{\text{Rea}}) - \dot{n}_{\text{Rea,in},i_{\text{Spe}}} \cdot h_{i_{\text{Spe}}}(T_{\text{Rea,in}}) \quad (\text{D.52})$$

can be calculated.

D.2.10 Model: throttling valve

Throttling of the gas and liquid phase is used to decrease the pressure of the fluids. Change of the fluid temperature during throttling is not taken into account.

D.2.11 Model: water adsorber

Specifications with respect to the product gas water content are reached by water removal via adsorption on *zeolite 3A* in the final stage of the downstream process. Assumptions

applied (Appendix D.2.11.1) and governing equations derived (Appendix D.2.11.2) are summarized in this section.

D.2.11.1 Assumptions

The cyclic adsorption process of the water adsorption unit is modeled assuming:

- Ideal gas behavior
- Use of a pseudo steady state model of the cyclic ad- and desorption process
- Neglect of pressure losses in the unit
- Adsorption pressure equals process gas pressure p_{PrC}
- Desorption pressure equals 10^5 Pa
- Sorbent regeneration via hot-gas desorption
- Strip gas inlet temperature $T_{Ads_{des},in,G}$ during desorption phase equals the desorption temperature level aspired $T_{des,Ads_{des}}$. Its outlet temperature $T_{Ads_{des},out,G} = T_{ads,Ads_{ads}} + \Delta T_{sli,Ads}$ is calculated based on the adsorption temperature level $T_{ads,Ads_{ads}}$ aspired, assuming a thermal slip of $\Delta T_{sli,Ads}$ of 10 K
- Due to the high selectivity of H₂O adsorption on *zeolite 3A*,³⁶¹ adsorption of species other than water is neglected
- Exchange of gas phase species in the bed void space is neglected
- Thermophysical properties of *zeolite 3A* and of H₂O adsorption on *zeolite 3A*, which are summarized in Appendix D.1.2, are used in the evaluation

D.2.11.2 Governing equations

Modeling of the adsorber unit is performed similar to the procedure proposed by BATHEN and BREITBACH¹²⁷.

Mass balance The mass balance of the water adsorber unit is evaluated for pseudo steady state operation. Equilibrium between the process product gas phase and regenerated sorbent

$$p_{Ads_{ads},out,G,H_2O} = p_{eq,Z3A,H_2O} (q_{eq,Z3A,H_2O} (T_{des,Ads_{des}}, p_{Ads_{des},in,G,H_2O}), T_{ads,Ads_{ads}}) \quad (D.53)$$

is assumed to be reached at the water adsorber outlet during the adsorption cycle.

Based on the water partial pressure at the adsorber outlet during the adsorption step p_{Ads_{ads},out,G,H_2O} the stream of water adsorbed

$$\dot{n}_{ads,Ads_{ads},H_2O} = \frac{y_{Ads_{ads},out,G,H_2O} \cdot \dot{n}_{Ads_{ads},in,G} - \dot{n}_{Ads_{ads},in,G,H_2O}}{y_{Ads_{ads},out,G,H_2O} - 1} \quad (D.54)$$

can be determined. Mole flows of species other than water in the gas stream flowing through the water adsorber during the adsorption cycle stay constant. With this information and the definition of the sorbent working capacity

$$\begin{aligned} \Delta \mathbf{q}_{\text{wor,Ads,H}_2\text{O}} = & \mathbf{q}_{\text{eq1,Z3A,H}_2\text{O}}(T_{\text{ads,Ads}_{\text{ads}}}, p_{\text{Ads}_{\text{ads,in,G,H}_2\text{O}}}) \\ & - \mathbf{q}_{\text{eq1,Z3A,H}_2\text{O}}(T_{\text{des,Ads}_{\text{des}}}, p_{\text{Ads}_{\text{des,in,G,H}_2\text{O}}}) \end{aligned} \quad (\text{D.55})$$

at hand, the mean amount of sorbent required per unit time

$$\dot{m}_{\text{Ads,Z3A}} = \frac{\dot{n}_{\text{ads,Ads}_{\text{ads,H}_2\text{O}}}}{\Delta \mathbf{q}_{\text{wor,Ads,Z3A,H}_2\text{O}}} \quad (\text{D.56})$$

can be calculated.

The assumption of hot-gas desorption allows to estimate the overall flow of strip gas

$$\begin{aligned} \dot{n}_{\text{Ads}_{\text{des,in,G}}} = & \frac{1}{\sum_{i_{\text{Spe}}} y_{\text{Ads}_{\text{des,in,G},i_{\text{Spe}}}} \cdot (h_{\text{G},i_{\text{Spe}}}(T_{\text{Ads}_{\text{des,in,G}}}) - h_{\text{G},i_{\text{Spe}}}(T_{\text{ads,Ads}_{\text{ads}}} + \Delta T_{\text{sli,Ads}}))} \\ & \cdot (\dot{m}_{\text{Ads,Z3A}} \cdot c_{p,\text{Z3A}} \cdot (T_{\text{des,Ads}_{\text{des}}} - T_{\text{ads,Ads}_{\text{ads}}}) \\ & + \dot{m}_{\text{Ads,Z3A}} \cdot \mathbf{q}_{\text{eq1,Z3A,H}_2\text{O}}(T_{\text{des,Ads}_{\text{des}}}, p_{\text{Ads}_{\text{des,in,G,H}_2\text{O}}}) \\ & \cdot (h_{\text{Z3A,H}_2\text{O}}(T_{\text{des,Ads}_{\text{des}}}) - h_{\text{Z3A,H}_2\text{O}}(T_{\text{ads,Ads}_{\text{ads}}})) \\ & + \dot{m}_{\text{Ads,Z3A}} \cdot \Delta \mathbf{q}_{\text{wor,Ads,H}_2\text{O}} \\ & \cdot (h_{\text{G,H}_2\text{O}}(T_{\text{ads,Ads}_{\text{ads}}} + \Delta T_{\text{sli,Ads}}) - h_{\text{Z3A,H}_2\text{O}}(T_{\text{ads,Ads}_{\text{ads}}})) \end{aligned} \quad (\text{D.57})$$

required to match the heat demand of the unit. The mole flows of species other than water do not change in the water adsorber. The stream of water at the water adsorber outlet in the desorption cycle reads

$$\dot{n}_{\text{Ads}_{\text{des,out,G,H}_2\text{O}}} = \dot{n}_{\text{Ads}_{\text{des,in,G,H}_2\text{O}}} + \dot{m}_{\text{Ads,Z3A}} \cdot \Delta \mathbf{q}_{\text{wor,Ads,H}_2\text{O}} \cdot \quad (\text{D.58})$$

Energy balance The heat demand of the water adsorber unit

$$\dot{Q}_{\text{Ads}_{\text{des}}} = \sum_{i_{\text{Spe}}} \dot{n}_{\text{Ads}_{\text{des,in,G},i_{\text{Spe}}}} \cdot (h_{\text{G},i_{\text{Spe}}}(T_{\text{Ads}_{\text{des,in,G}}}) - h_{\text{G},i_{\text{Spe}}}(T_{\text{ads,Ads}_{\text{ads}}} + \Delta T_{\text{sli,Ads}})) \quad (\text{D.59})$$

is provided by the thermal energy of the strip gas used, the flow of which is defined based on the energy balance outlined in (D.57).

Heat released by the water adsorber unit is assumed to be available at adsorption temperature level $T_{\text{ads,Ads}_{\text{ads}}}$. Contributions from temperature change of the sorbent

$$\dot{Q}_{\text{senZ3A,Ads}_{\text{ads}}} = \dot{m}_{\text{Ads,Z3A}} \cdot c_{p,\text{Z3A}} \cdot (T_{\text{ads,Ads}_{\text{ads}}} - T_{\text{des,Ads}_{\text{des}}}) \quad (\text{D.60})$$

and of the adsorbent

$$\begin{aligned} \dot{Q}_{\text{senZ3A,H}_2\text{O,Ads}_{\text{ads}}} = & \dot{m}_{\text{Ads,Z3A}} \cdot \mathbf{q}_{\text{eql,Z3A,H}_2\text{O}}(T_{\text{des,Ads}_{\text{des}}}, p_{\text{Ads}_{\text{des,in,G,H}_2\text{O}}}) \\ & \cdot (h_{\text{Z3A,H}_2\text{O}}(T_{\text{ads,Ads}_{\text{ads}}}) - h_{\text{Z3A,H}_2\text{O}}(T_{\text{des,Ads}_{\text{des}}})) \end{aligned} \quad (\text{D.61})$$

between desorption and adsorption phase as well as from the heat of water adsorption

$$\dot{Q}_{\text{adsZ3A,H}_2\text{O,Ads}_{\text{ads}}} = \dot{n}_{\text{ads,Ads}_{\text{ads,H}_2\text{O}}} \cdot (h_{\text{Z3A,H}_2\text{O}}(T_{\text{ads,Ads}_{\text{ads}}}) - h_{\text{G,H}_2\text{O}}(T_{\text{ads,Ads}_{\text{ads}}})) \quad (\text{D.62})$$

are considered. No contribution of the gas flowing through the adsorber during the adsorption phase is taken into account, as this enters the water adsorber at adsorption temperature level. The assumption of low-temperature heat release by the water adsorber unit gives a worst case estimate with regard to the process heat integration potential. A more detailed analysis of the process composite curves reveals that the amount of heat recoverable in this unit becomes negligible small compared to the other flows of heat integrated, such that use of this heat source does not seem beneficial from neither an economic nor from an engineering point of view.

D.3 Process operation

In this section the characteristics of process operation are outlined that comprise: operation of condensers (Appendix D.3.1), characteristics of heaters before the *Sabatier* reactors (Appendix D.3.2), a discussion of the water adsorber regeneration cycle (Appendix D.3.3), strategies for water recycle (Appendix D.3.4), a discussion with regard to additional water supply to the process (Appendix D.3.5), outline of strategies for strip gas supply to the *DAC* unit (Appendix D.3.6) and a basic insight into the numeric approach used for the evaluation of the recycle streams (Appendix D.3.7).

D.3.1 Condensers

Condensers are treated as coolers / heaters if no condensation in these units takes place.

D.3.2 Heating of streams before the Sabatier reactors

If streams that will be fed to the *Sabatier* reactors are of a higher temperature than the cooling temperature T_{Rea} of the corresponding reactor, these are cooled down to T_{Rea} before entering this unit. If the temperature of a feed stream to a *Sabatier* reactor is between T_{Rea} and $T_{\text{Rea}} - \Delta T_{\text{pin}}$, its temperature is not changed. If the feed stream temperature is below $T_{\text{Rea}} - \Delta T_{\text{pin}}$, the stream is heated up to $T_{\text{Rea}} - \Delta T_{\text{pin}}$.

D.3.3 Water adsorber regeneration cycle

The submodel of the regeneration cycle of the water adsorber unit comprises

- The desorption cycle of the water adsorber unit

- Removal of the water desorbed by a condenser
- Temperature increase of the strip gas by a heater to the desorption temperature level of the water adsorber unit

Methane is used as strip gas in the regeneration cycle. This allows for minimization of product gas contamination that results from slip streams in the sorbent bed between adsorption and desorption cycle. The modeling of this part of the process is based on the assumptions and operation parameters outlined below:

- Ideal gas behavior
- Condenser operation at $T_{\text{Con}} = T_{\text{Amb}} + \Delta T_{\text{pin}}$
- Single stage condensation with temperature change from $T_{\text{des,Ads,des}}$ to $T_{\text{Con}} = T_{\text{Amb}} + \Delta T_{\text{pin}}$
- Neglect of pressure losses
- Operation at ambient pressure
- Neglect of methane losses or of its recycle via the condensed phase, justified by the small amount of H₂O removed from the process stream, by the water adsorber, and by the low solubility of CH₄ in H₂O, e.g., Henry constant¹²⁸ $k_{\text{Hen,CH}_4,\text{H}_2\text{O}}(T_{\text{Amb}}) \leq 0.0015 \cdot 10^{-5} \text{ mol kg}^{-1} \text{ Pa}^{-1}$
- Strip gas is heated to water adsorber desorption temperature $T_{\text{des,Ads,des}}$

D.3.4 Water recycle

Recycle of water to the evaporator and electrolysis unit is considered. The two scenarios

1. $T_{\text{DAC}_{\text{Des}}} \geq T_{\text{Elc}}$ (Appendix D.3.4.1)
2. $T_{\text{DAC}_{\text{Des}}} < T_{\text{Elc}}$ (Appendix D.3.4.2)

are differentiated with respect to the water recycle strategy, which require use of additional equipment in the water management system (Appendix D.3.4.3). Streams are either recycled to the evaporator or to the electrolysis unit, with additional supply of liquid water to both units being possible. Satisfying electrolysis water demand with recycle streams is ranged with a higher priority compared to water recycling to the evaporator unit. If the water recycle from a stream exceeds the water demand of the corresponding unit, this stream is split to exactly match the water requirement of the unit. Only operation points with no excess production of water are analyzed.

D.3.4.1 Scenario 1: $T_{\text{DAC}_{\text{Des}}} \geq T_{\text{Elc}}$

As satisfying the electrolysis water demand by recycle streams is assumed to be of a higher priority compared to the *DAC* unit water requirement, first recycle of the cold streams seems reasonable from an energy integration point of view. Thus, the order of recycle streams reads

1. Oxygen product stream (condensation at $T_{\text{Amb}} + \Delta T_{\text{pin}}$ and p_{PrC})
2. 3. condenser before water adsorber ($T_{\text{Amb}} + \Delta T_{\text{pin}}$ and p_{PrC})
3. 2. condenser before water adsorber (T_{Elc} and p_{PrC})
4. Streams that condense at $T_{\text{DAC}_{\text{Des}}} + \Delta T_{\text{pin}}$ and p_{PrC} . Priority of this streams is defined based on their size
5. Streams from *MVR* condensed at $T_{\text{DAC}_{\text{Des}}} + \Delta T_{\text{pin}}$ and pressures lower than p_{PrC} . Recycle of the stream with the higher pressure is prioritized
6. Water recovered in the water adsorber regeneration cycle (condensation at $T_{\text{Amb}} + \Delta T_{\text{pin}}$ and p_{Amb})

Prioritization of recycle streams is done with focus on low heat flows and exchange in the process. This is represented by the aspect that streams at low temperature levels are recycled to the electrolysis, whereas streams with a higher temperature are sent to the evaporator unit. Only the stream of water recovered in the water adsorber does not follow this systematic. It is of a significantly lower pressure than the other streams recycled and does not contribute significantly to the overall energy flows in the process. Consequently, it seems more reasonable to recycle this stream to the evaporator, especially in view of a possible mixing of this stream with additional external water supply from the ambient to the evaporator unit.

In the multi-stage vapor recompression unit condensation can take place at $T_{\text{DAC}_{\text{Des}}} + \Delta T_{\text{pin}}$ and pressures lower than p_{PrC} . Prioritization of recycles of these streams is done according to their pressure levels, with a higher priority being assigned to the stream with higher pressure. Moreover, an additional condensation stage at T_{Elc} is realized between the second *Sabatier* reactor and the downstream process. This is done based on consideration of two scenarios:

1. Water demand of the electrolysis is not satisfied. The additional condensation stage at T_{Elc} allows for recycle of the stream condensed at T_{Elc} and p_{PrC} to the electrolysis without the need for a prior change of pressure or of temperature
2. Water demand of the electrolysis is already satisfied. The recycle stream recovered at $T_{\text{Amb}} + \Delta T_{\text{pin}}$ before the water adsorber is reduced and a stream at a higher temperature can be recycled to the evaporator. Definition of the temperature level of this additional recycle stage to be T_{Elc} incorporates the advantage of a better comparability between the concepts, which seems beneficial with regard to the basic

analysis intended. From a technical and economic point of view, however, selection of this condensation temperature level results into an additional optimization problem to be addressed in subsequent studies

The recycle streams recovered from the oxygen product gas and from the product stream that enters the water adsorber are of the same temperature and pressure. Recycle of the former is assigned a higher priority. This is reasoned by two aspects. First, in view of pressure losses within the process, the recycle stream of water recovered from the oxygen product stream can be expected to be of a higher pressure. Second, presence of oxygen can harm the sorbent used in the *DAC* unit (Section 3.3.2), such that limiting oxygen transport, e.g., arising from oxygen dissolved in the water recycle stream to the evaporator, seems reasonable.

D.3.4.2 Scenario 2: $T_{\text{DAC}_{\text{Des}}} < T_{\text{Elc}}$

Similarly to scenario 1 (Appendix D.3.4.1), satisfying the electrolysis water demand via water recycle is assumed to be of a higher priority than water recycle to the evaporator unit. Streams of water recovered at high temperatures are sent to the electrolysis, whereas recycles at low temperature levels are used as feed to the evaporator unit. Again, recycle of streams with higher pressure levels is assigned a higher priority. This leads to a systematic of water recycle that can be summarized as follows:

1. Streams at process pressure p_{PrC} . These are rated according to their temperature (first priority) and their size (second priority)
2. Stream from *MVR* with a pressure lower than p_{PrC} and temperature of $T_{\text{DAC}_{\text{Des}}} + \Delta T_{\text{pin}}$. The streams are prioritized according to their pressure levels, with high pressure being favored
3. Water recycle from the water adsorber unit regeneration cycle (condensation at $T_{\text{Amb}} + \Delta T_{\text{pin}}$ and p_{Amb})

D.3.4.3 Additional equipment for water recycle

Thermophysical properties of the streams recycled can be changed by pumps, heaters and throttling valves. Use of turbines to recover the the energy stored in high-pressure recycles is not considered in the base case analysis presented. In these units the state of the streams is adjusted to the operation temperature and pressure of the corresponding unit. With regard to the operation temperature this procedure gives a worst case estimate in the pinch analysis. For example, if a stream with a temperature higher than the evaporator unit operation temperature is recycled to this unit, only cooling down the stream to $T_{\text{Evp}} + \Delta T_{\text{pin}}$ could be considered to use the additional energy content of this stream without being restricted by the minimum temperature difference of heat transfer ΔT_{pin} . For the sake of clarity and generality, these additional degrees of freedom are not considered in the base case analysis performed.

D.3.5 Additional water supply

Additional, external water supply to the evaporator and to the electrolysis is required if the amount of water released in the *DAC* unit does not suffice to match the process water demand. In these cases, fresh water from the ambient is pressurized and heated to the operation pressure and temperature, respectively, of the corresponding unit.

D.3.6 Strip gas supply to the DAC unit

The choice of strip gas in the *DAC* unit depends on the CO_2 and H_2O partial pressures at the *DAC* outlet in equilibrium with the sorbent, as well as on the *DAC* unit operation pressure. The two scenarios

1. *DAC* strip gas supply via the evaporator and electrolysis (Appendix D.3.6.1)
2. *DAC* strip gas supply via the evaporator (Appendix D.3.6.2)

are considered.

D.3.6.1 Scenario 1: DAC strip gas supply via the evaporator and electrolysis

If the sum of CO_2 and H_2O partial pressures in equilibrium with the solid phase at the solid phase inlet to the desorption zone stays below the desorption pressure level aspired $p_{\text{DAC}_{\text{Des}}}$, presence of additional gas phase species, e.g., air from the bed void space or strip gas other than water vapor, is required.

Selection of the operation temperature of the evaporator T_{Evp} and of the electrolysis T_{Elc} prescribes the composition of the streams from these two units. This defines a process in which the three constraints

1. CO_2 mole fraction in *DAC* product gas:

$$y_{\text{Pro,DAC,CO}_2} \cdot p_{\text{DAC}_{\text{Des}}} = p_{\text{eq1,CO}_2} (q_{\text{DAC}_{\text{Des,in,CO}_2}}, T_{\text{DAC}_{\text{Des}}})$$
2. H_2O mole fraction in *DAC* product gas:

$$y_{\text{Pro,DAC,H}_2\text{O}} \cdot p_{\text{DAC}_{\text{Des}}} = p_{\text{eq1,H}_2\text{O}} (q_{\text{DAC}_{\text{Des,in,H}_2\text{O}}}, T_{\text{DAC}_{\text{Des}}})$$
3. The water source characteristic of the *DAC* unit suffices to satisfy the overall process water demand

are met by adjustment of the variables and operation parameters

1. Size of the stream from the electrolysis to the *DAC* unit
2. Size of the stream from the electrolysis to the evaporator
3. Relative working capacity of water $\Delta q_{\text{wor,DAC,H}_2\text{O,rel}}$

D.3.6.2 Scenario 2: DAC strip gas supply via the evaporator

If the constraints defined in scenario 1 (Appendix D.3.6.1) can only be satisfied at operation pressures above the current *DAC* desorption pressure level, applicability of the equilibrium adsorber model proposed becomes limited. However, if the sum of the partial pressures of the gas phase species only slightly exceeds the desorption pressure level aspired (Figure 5.3), extrapolation of the gas phase composition based on the ratio of the partial pressures in equilibrium with the solid phase might be used as a first estimate. This allows for a basic insight into the *DAC* operation characteristics without the need for detailed modeling and kinetic information.

In this scenario, pure water vapor or mixtures of water saturated hydrogen gas flow from the evaporator to the *DAC* unit, to be used as strip gas. The relative working capacity of H_2O and the flow of strip gas from the evaporator to the *DAC* unit are adjusted such that

1. The $\text{CO}_2 : \text{H}_2\text{O}$ mole fraction ratio in the *DAC* product gas $y_{\text{Pro,DAC,CO}_2} : y_{\text{Pro,DAC,H}_2\text{O}}$ equals the ratio of partial pressures of these species in equilibrium with the sorbent $p_{\text{eqI,CO}_2,q_{\text{DACDes,in,CO}_2}} : p_{\text{eqI,H}_2\text{O},q_{\text{DACDes,in,H}_2\text{O}}}$
2. The water source characteristic of the *DAC* unit suffices to satisfy the overall process water demand

D.3.7 Numeric for recycles

Wegstein method³⁶² is used to ensure a fast convergence of the process recycle streams in the iterative calculation performed. The maximum relative deviation of the state variables between two iterations

$$\Delta\Phi_{i_{\text{Te}},\text{rel,max}} = \max\left(\Delta\vec{\Phi}_{i_{\text{Te}},\text{rel}}\right) \quad (\text{D.63})$$

is used as the convergence criterion. As an upper boundary for the maximum relative error a value of $1 \cdot 10^{-4}$ is selected. Components of $\Delta\vec{\Phi}_{i_{\text{Te}},\text{rel}}$ are defined as

$$\Delta\Phi_{i_{\text{Te}},i_{\Phi},\text{rel}} = \frac{|\Phi_{i_{\text{Te}},i_{\Phi}} - \Phi_{i_{\text{Te}}-1,i_{\Phi}}|}{\Phi_{i_{\text{Te}},i_{\Phi}}} \quad (\text{D.64})$$

in dependence of the single state variables properties $\Phi_{i_{\Phi}}$ reached in the steps i_{Te} of the iteration. If $\Phi_{i_{\Phi}}$ becomes zero in iteration step i_{Te}

$$\Delta\Phi_{i_{\text{Te}},i_{\Phi},\text{rel}} = \frac{|\Phi_{i_{\text{Te}},i_{\Phi}} - \Phi_{i_{\text{Te}}-1,i_{\Phi}}|}{\Phi_{i_{\text{Te}}-1,i_{\Phi}}} \quad (\text{D.65})$$

is used instead of (D.64). In case that $\Phi_{i_{\Phi}}$ becomes zero in steps i_{Te} and $i_{\text{Te}} - 1$,

$$\Delta\Phi_{i_{\text{Te}},i_{\Phi},\text{rel}} = 0 \quad (\text{D.66})$$

is used.

D.4 Operation parameters used in the parameter studies

In this section the operation parameters used in the reference case are outlined (Appendix D.4.1). Variations with reference to this base case are summarized for the investigation of the reactor performance (Appendix D.4.2), the analysis of autothermal operation (Appendix D.4.3), the investigation of the process water balance (Appendix D.4.4), the determination of *DAC* unit operation characteristics (Appendix D.4.5) and the energy flow analysis (Appendix D.4.6).

D.4.1 Operation parameters: reference configuration

The reference configuration of the process is visualized in Figure 6.3 and comprises the operation parameters outlined below:

- Pinch temperature $\Delta T_{\text{pin}} = 10 \text{ K}$
- Process pressure $p_{\text{PrC}} = 10 \cdot 10^5 \text{ Pa}$
- Reference CO_2 mole flow of $\dot{n}_{\text{Pro,DAC,CO}_2} = 1 \text{ mol s}^{-1}$ at the *DAC* outlet
- *DAC* working capacity of CO_2 $\Delta q_{\text{wor,DAC,CO}_2}$ of 0.25 mol kg^{-1} and thermal slip of $\Delta T_{\text{los,DAC}} = 5 \text{ K}$
- *DAC* desorption temperature $T_{\text{DACDes}} = 100 \text{ }^\circ\text{C}$ and pressure $p_{\text{DACDes}} = 1 \cdot 10^5 \text{ Pa}$
- No slip streams of air enter the *DAC* unit desorption zone: $\phi_{\text{DAC,slis,Ads,Des}} = 0$
- Readsorption and strip gas losses in the sorbent bed void space of the *DAC* unit are considered
- Strip gas supply to the *DAC* unit according Appendix D.3.6
- The effective water source characteristic of the *DAC* unit is adjusted to match the process overall water demand
- Condensers in *MVR* and between the reactors operate at $T_{\text{DACDes}} + \Delta T_{\text{pin}}$
- The electrolysis is operated at $T_{\text{Elc}} = 70 \text{ }^\circ\text{C}$, $p_{\text{Elc}} = p_{\text{PrC}}$ and $\Delta U_{\text{Elc}} = 1.5 \cdot \Delta U_{\text{eq,Elc}}$
- Operation temperatures and levels of conversion reached in the reactors are defined via the optimization problem outlined in (6.5)
- The strip gas in the water adsorber desorption cycle is heated to $150 \text{ }^\circ\text{C}$

D.4.2 Operation parameters: reactor operation

Only the operation pressure p_{PrC} is varied in the analysis of the reactor operation compared to the reference scenario summarized in Appendix D.4.1.

D.4.3 Operation parameters: potential for autothermal operation

In contrast to the reference configuration (Appendix D.4.1), the process pressure p_{PrC} and the electrolysis cell voltage ΔU_{Elc} are changed.

D.4.4 Operation parameters: process water balance

Only the operation pressure p_{PrC} varies between this analysis and the reference scenario outlined in Appendix D.4.1.

D.4.5 Operation parameters: DAC unit operation point

Based on the reference scenario summarized in Appendix D.4.1, additional slip streams of air are considered in the analysis outlined in Section 6.4.3.1 by variation of $\phi_{\text{DAC,sl}_{\text{Ads,Des}}}$. Moreover, the influence of changes in the process pressure p_{PrC} , *DAC* desorption and electrolysis operation temperature, $T_{\text{DAC}_{\text{Des}}}$ and T_{Elc} , respectively, on process performance is investigated in Section 6.4.3.2, with other operation parameters being kept at reference configuration (Appendix D.4.1).

D.4.6 Operation parameters: energy flow analysis

Process pressure p_{PrC} , *DAC* desorption temperature $T_{\text{DAC}_{\text{Des}}}$ and electrolysis operation temperature T_{Elc} are adjusted as outlined, whereas all other parameters stay at reference configuration (Appendix D.4.1).

References

- [1] Popper, K. R. *Conjectures and Refutations: The Growth of Scientific Knowledge*, 2nd ed.; Routledge: London, UK and New York, NY, 2002.
- [2] IPCC. *Climate Change 2014: Synthesis Report. Contribution of Working Groups I, II and III to the Fifth Assessment Report of the Intergovernmental Panel on Climate Change*; Pachauri, R. K., Allen, M. R., Eds., Geneva, Switzerland, 2015.
- [3] Hansen, J.; Ruedy, R.; Sato, M.; Lo, K. GLOBAL SURFACE TEMPERATURE CHANGE. *Rev. Geophys.* **2010**, *48*, RG4004, DOI: 10.1029/2010rg000345.
- [4] Vose, R. S.; Arndt, D.; Banzon, V. F.; Easterling, D. R.; Gleason, B.; Huang, B.; Kearns, E.; Lawrimore, J. H.; Menne, M. J.; Peterson, T. C.; Reynolds, R. W.; Smith, T. M.; Williams, C. N.; Wuertz, D. B. NOAA's Merged Land–Ocean Surface Temperature Analysis. *Bull. Amer. Meteor. Soc.* **2012**, *93*, 1677–1685, DOI: 10.1175/bams-d-11-00241.1.
- [5] Morice, C. P.; Kennedy, J. J.; Rayner, N. A.; Jones, P. D. Quantifying uncertainties in global and regional temperature change using an ensemble of observational estimates: The HadCRUT4 data set. *J. Geophys. Res.: Atmos.* **2012**, *117* (D08), D08101, DOI: 10.1029/2011jd017187.
- [6] Ishii, M.; Shouji, A.; Sugimoto, S.; Matsumoto, T. Objective analyses of sea-surface temperature and marine meteorological variables for the 20th century using ICOADS and the Kobe Collection. *Int. J. Climatol.* **2005**, *25*, 865–879, DOI: 10.1002/joc.1169.
- [7] Kennedy, J. J.; Rayner, N. A.; Smith, R. O.; Parker, D. E.; Saunby, M. Reassessing biases and other uncertainties in sea surface temperature observations measured in situ since 1850: 2. Biases and homogenization. *J. Geophys. Res.: Atmos.* **2011**, *116* (D14), D14104, DOI: 10.1029/2010jd015220.
- [8] Rayner, N. A.; Parker, D. E.; Horton, E. B.; Folland, C. K.; Alexander, L. V.; Rowell, D. P.; Kent, E. C.; Kaplan, A. Global analyses of sea surface temperature, sea ice, and night marine air temperature since the late nineteenth century. *J. Geophys. Res.: Atmos.* **2003**, *108* (D14), ALC 2, DOI: 10.1029/2002jd002670.
- [9] Smith, T. M.; Reynolds, R. W.; Peterson, T. C.; Lawrimore, J. Improvements to NOAA's Historical Merged Land–Ocean Surface Temperature Analysis (1880–2006). *J. Climate* **2008**, *21*, 2283–2296, DOI: 10.1175/2007jcli2100.1.
- [10] Dlugokencky, E.; Tans, P. NOAA/ESRL. <https://www.esrl.noaa.gov/gmd/> (accessed Dec. 7, 2019).

- [11] Prather, M. J.; Holmes, C. D.; Hsu, J. Reactive greenhouse gas scenarios: Systematic exploration of uncertainties and the role of atmospheric chemistry. *Geophys. Res. Lett.* **2012**, *39*, L09803, DOI: 10.1029/2012gl1051440.
- [12] Etheridge, D. M.; Steele, L. P.; Langenfelds, R. L.; Francey, R. J.; Barnola, J.-M.; Morgan, V. I. Natural and anthropogenic changes in atmospheric CO₂ over the last 1000 years from air in Antarctic ice and firn. *J. Geophys. Res.: Atmos.* **1996**, *101*, 4115–4128, DOI: 10.1029/95jd03410.
- [13] Dlugokencky, E. J.; Myers, R. C.; Lang, P. M.; Masarie, K. A.; Crotwell, A. M.; Thoning, K. W.; Hall, B. D.; Elkins, J. W.; Steele, L. P. Conversion of NOAA atmospheric dry air CH₄ mole fractions to a gravimetrically prepared standard scale. *J. Geophys. Res.: Atmos.* **2005**, *110* (D18), D18306, DOI: 10.1029/2005jd006035.
- [14] Etheridge, D. M.; Steele, L. P.; Francey, R. J.; Langenfelds, R. L. Atmospheric methane between 1000 A.D. and present: Evidence of anthropogenic emissions and climatic variability. *J. Geophys. Res.: Atmos.* **1998**, *103*, 15979–15993, DOI: 10.1029/98jd00923.
- [15] IPCC. *Climate Change 2013: The Physical Science Basis. Contribution of Working Group I to the Fifth Assessment Report of the Intergovernmental Panel on Climate Change*; Stocker, T. F., Plattner, D. Q. G.-K., Tignor, M., Allen, S. K., Boschung, J., Nauels, A., Xia, Y., Bex, V., Midgley, P. M., Eds.; Cambridge University Press: Cambridge, UK and New York, NY, 2013.
- [16] Tans, P. An Accounting of the Observed Increase in Oceanic and Atmospheric CO₂ and the Outlook for the Future. *Oceanogr.* **2009**, *22*, 26–35, DOI: 10.5670/oceanog.2009.94.
- [17] Socolow, R.; Desmond, M.; Aines, R.; Blackstock, J.; Bolland, O.; Kaarsberg, T.; Lewis, N.; Mazzotti, M.; Pfeffer, A.; Sawyer, K.; Siirola, J.; Smit, B.; Wilcox, J. *Direct Air Capture of CO₂ with Chemicals*; tech. rep.; APS Panel on Public Affairs, 2011.
- [18] Roedel, W.; Wagner, T. *Physik unserer Umwelt: Die Atmosphäre*, 5th ed.; Springer Spektrum: Berlin, Germany and Heidelberg, Germany, 2017, DOI: 10.1007/978-3-662-54258-3.
- [19] Wild, M.; Folini, D.; Schär, C.; Loeb, N.; Dutton, E. G.; König-Langlo, G. The global energy balance from a surface perspective. *Clim. Dyn.* **2012**, *40*, 3107–3134, DOI: 10.1007/s00382-012-1569-8.
- [20] United Nations. Presented at United Nations Conference on Environment and Development, UNCED, Rio de Janeiro, Brazil, June 3-14, 1992.
- [21] United Nations. *Agenda 21*; Bundesministerium für Umwelt, Naturschutz und Reaktorsicherheit, Köllen Druck+Verlag GmbH: Bonn, Germany, 1992.
- [22] United Nations. Presented at United Nations Climate Change Conference, Berlin, Germany, March 28 - April 7, 1995.
- [23] United Nations. *United Nations Framework Convention on Climate Change*; UN Doc FCCC/CP/1995/7/Add.1; Geneva, Switzerland, 1995.

-
- [24] United Nations. *Kyoto Protocol to the United Nations Framework Convention on Climate Change*; UN Doc FCCC/CP/1997/7/Add.1; Geneva, Switzerland, 1997.
- [25] United Nations. Presented at United Nations Climate Change Conference, Kyoto, Japan, December 1-10, 1997.
- [26] United Nations. Presented at United Nations Climate Change Conference, Paris, France, November 30 - December 12, 2015.
- [27] United Nations. *Paris Agreement*; Geneva, Switzerland, 2016.
- [28] Intergovernmental Panel on Climate Change (IPCC). About the IPCC. <https://www.ipcc.ch/about/> (accessed July 10, 2020).
- [29] IPCC. *IPCC Special Report on the Ocean and Cryosphere in a Changing Climate*; Pörtner, H.-O., Roberts, D. C., Masson-Delmotte, V., Zhai, P., Tignor, M., Poloczanska, E., Mintenbeck, K., Alegría, A., Nicolai, M., Okem, A., Petzold, J., Rama, B., Weyer, N. M., Eds.; Geneva, Switzerland, 2019.
- [30] IPCC. *Climate Change and Land: an IPCC special report on climate change, desertification, land degradation, sustainable land management, food security, and greenhouse gas fluxes in terrestrial ecosystems*; Shukla, P. R., Skea, J., Calvo Buendia, E., Masson-Delmotte, V., Pörtner, H.-O., Roberts, D. C., Zhai, P., Slade, R., Connors, S., van Diemen, R., Ferrat, M., Haughey, E., Luz, S., Neogi, S., Pathak, M., Petzold, J., Portugal Pereira, J., Vyas, P., Huntley, E., Kissick, K., Belkacemi, M., Malley, M., Eds.; Geneva, Switzerland, 2019.
- [31] European Environmental Agency. Trends in atmospheric concentrations of CO₂. www.eea.europa.eu/data-and-maps (accessed Dec. 15, 2019).
- [32] European Commission. EDGAR — Emissions Database for Global Atmospheric Research. <https://edgar.jrc.ec.europa.eu/overview.php?v=booklet2020> (accessed Mar. 22, 2021).
- [33] IPCC. *Climate Change 2014: Mitigation of Climate Change. Contribution of Working Group III to the Fifth Assessment Report of the Intergovernmental Panel on Climate Change*; Edenhofer, O., Pichs-Madruga, R., Sokona, Y., Farahani, E., Kadner, S., Seyboth, K., Adler, A., Baum, I., Brunner, S., Eickemeier, P., Kriemann, B., Savolainen, J., Schlömer, S., von Stechow, C., Zwickel, T., Minx, J. C., Eds.; Cambridge University Press: Cambridge, UK and New York, NY, 2014.
- [34] Rogelj, J.; Luderer, G.; Pietzcker, R. C.; Kriegler, E.; Schaeffer, M.; Krey, V.; Riahi, K. Energy system transformations for limiting end-of-century warming to below 1.5 °C. *Nat. Clim. Change* **2015**, *5*, 519–527, DOI: 10.1038/nclimate2572.
- [35] IPCC. *Global Warming of 1.5°C. An IPCC Special Report on the impacts of global warming of 1.5°C above pre-industrial levels and related global greenhouse gas emission pathways, in the context of strengthening the global response to the threat of climate change, sustainable development, and efforts to eradicate poverty*; Masson-Delmotte, V., Zhai, P., Pörtner, H.-O., Roberts, D., Skea, J., Shukla, P. R., Pirani, A., Moufouma-Okia, W., Péan, C., Pidcock, R., Connors, S., Matthews, J. B. R.,

- Chen, Y., Zhou, X., Gomis, M. I., Lonnoy, E., Maycock, T., Tignor, M., Waterfield, T., Eds.; in press, 2018.
- [36] Lackner, K. S.; Brennan, S.; Matter, J. M.; Park, A.; Wright, A.; van der Zwaan, B. The urgency of the development of CO₂ capture from ambient air. *Proc. Natl. Acad. Sci.* **2012**, *109*, 13156–13162, DOI: 10.1073/pnas.1108765109.
- [37] Baciocchi, R.; Storti, G.; Mazzotti, M. Process design and energy requirements for the capture of carbon dioxide from air. *Chem. Eng. Process. Process Intensif.* **2006**, *45*, 1047–1058, DOI: 10.1016/j.cep.2006.03.015.
- [38] Barkakaty, B.; Sumpter, B. G.; Ivanov, I. N.; Potter, M. E.; Jones, C. W.; Lokitz, B. S. Emerging materials for lowering atmospheric carbon. *Environ. Technol. Innovation* **2017**, *7*, 30–43, DOI: 10.1016/j.eti.2016.12.001.
- [39] Fuss, S.; Jones, C. D.; Kraxner, F.; Peters, G. P.; Smith, P.; Tavoni, M.; van Vuuren, D. P.; Canadell, J. G.; Jackson, R. B.; Milne, J.; Moreira, J. R.; Nakicenovic, N.; Sharifi, A.; Yamagata, Y. Research priorities for negative emissions. *Environ. Res. Lett.* **2016**, *11*, 115007, DOI: 10.1088/1748-9326/11/11/115007.
- [40] EASAC Science Advisory Council. *Negative emission technologies: What role in meeting Paris Agreement targets?*; tech. rep.; German National Academy of Sciences: Halle (Saale), Germany, 2018.
- [41] Fuss, S.; Lamb, W. F.; Callaghan, M. W.; Hilaire, J.; Creutzig, F.; Amann, T.; Beringer, T.; de Oliveira Garcia, W.; Hartmann, J.; Khanna, T.; Luderer, G.; Nemet, G. F.; Rogelj, J.; Smith, P.; Vicente, J. L. V.; Wilcox, J.; del Mar Zamora Dominguez, M.; Minx, J. C. Negative emissions—Part 2: Costs, potentials and side effects. *Environ. Res. Lett.* **2018**, *13*, 063002, DOI: 10.1088/1748-9326/aabf9f.
- [42] McLaren, D. A comparative global assessment of potential negative emissions technologies. *Process Saf. Environ. Prot.* **2012**, *90*, 489–500, DOI: 10.1016/j.psep.2012.10.005.
- [43] Smith, P. et al. Biophysical and economic limits to negative CO₂ emissions. *Nat. Clim. Change* **2015**, *6*, 42–50, DOI: 10.1038/nclimate2870.
- [44] Smith, P. Soil carbon sequestration and biochar as negative emission technologies. *Global Change Biol.* **2016**, *22*, 1315–1324, DOI: 10.1111/gcb.13178.
- [45] Ellison, D.; Morris, C. E.; Locatelli, B.; Sheil, D.; Cohen, J.; Murdiyarso, D.; Gutierrez, V.; van Noordwijk, M.; Creed, I. F.; Pokorny, J.; Gaveau, D.; Spracklen, D. V.; Bargués Tobella, A.; Ilstedt, U.; Teuling, A. J.; Gebreyohannis Gebrehiwot, S.; Sands, D. C.; Muys, B.; Verbist, B.; Springgay, E.; Sugandi, Y.; Sullivan, C. A. Trees, forests and water: Cool insights for a hot world. *Global Environ. Change* **2017**, *43*, 51–61, DOI: 10.1016/j.gloenvcha.2017.01.002.
- [46] Dingain, L. REGUA. www.regua.org (accessed Dec. 28, 2019).
- [47] Eden Reforestation Project. www.edenprojects.org (accessed Dec. 28, 2019).
- [48] International Tree Foundation. www.internationaltreefoundation.org (accessed Dec. 28, 2019).

- [49] Plant Your Future. www.plantyourfuture.org.uk (accessed Dec. 28, 2019).
- [50] 4 per Mille Initiative. www.4p1000.org (accessed Dec. 28, 2019).
- [51] Minasny, B. et al. Soil carbon 4 per mille. *Geoderma* **2017**, *292*, 59–86, DOI: 10.1016/j.geoderma.2017.01.002.
- [52] Woolf, D.; Amonette, J. E.; Street-Perrott, F. A.; Lehmann, J.; Joseph, S. Sustainable biochar to mitigate global climate change. *Nat. Commun.* **2010**, *1*, 56, DOI: 10.1038/ncomms1053.
- [53] Boyd, P. W.; Jickells, T.; Law, C. S.; Blain, S.; Boyle, E. A.; Buesseler, K. O.; Coale, K. H.; Cullen, J. J.; de Baar, H. J. W.; Follows, M.; Harvey, M.; Lancelot, C.; Levasseur, M.; Owens, N. P. J.; Pollard, R.; Rivkin, R. B.; Sarmiento, J.; Schoemann, V.; Smetacek, V.; Takeda, S.; Tsuda, A.; Turner, S.; Watson, A. J. Mesoscale Iron Enrichment Experiments 1993-2005: Synthesis and Future Directions. *Sci.* **2007**, *315*, 612–617, DOI: 10.1126/science.1131669.
- [54] Emerson, D. Biogenic Iron Dust: A Novel Approach to Ocean Iron Fertilization as a Means of Large Scale Removal of Carbon Dioxide From the Atmosphere. *Front. Mar. Sci.* **2019**, *6*, 22, DOI: 10.3389/fmars.2019.00022.
- [55] Buesseler, K. O.; Boyd, P. W. Will Ocean Fertilization Work? *Sci.* **2003**, *300*, 67–68, DOI: 10.1126/science.1082959.
- [56] Robinson, J.; Popova, E. E.; Yool, A.; Srokosz, M.; Lampitt, R. S.; Blundell, J. R. How deep is deep enough? Ocean iron fertilization and carbon sequestration in the Southern Ocean. *Geophys. Res. Lett.* **2014**, *41*, 2489–2495, DOI: 10.1002/2013gl1058799.
- [57] Andrews, M. G.; Taylor, L. L. Combating Climate Change Through Enhanced Weathering of Agricultural Soils. *Elements* **2019**, *15*, 253–258, DOI: 10.2138/gselements.15.4.253.
- [58] Schuiling, R. D.; Krijgsman, P. Enhanced Weathering: An Effective and Cheap Tool to Sequester CO₂. *Clim. Change* **2006**, *74*, 349–354, DOI: 10.1007/s10584-005-3485-y.
- [59] Taylor, L. L.; Quirk, J.; Thorley, R. M. S.; Kharecha, P. A.; Hansen, J.; Ridgwell, A.; Lomas, M. R.; Banwart, S. A.; Beerling, D. J. Enhanced weathering strategies for stabilizing climate and averting ocean acidification. *Nat. Clim. Change* **2016**, *6*, 402–406, DOI: 10.1038/nclimate2882.
- [60] Moosdorf, N.; Renforth, P.; Hartmann, J. Carbon Dioxide Efficiency of Terrestrial Enhanced Weathering. *Environ. Sci. Technol.* **2014**, *48*, 4809–4816, DOI: 10.1021/es4052022.
- [61] Harrison, D. P. A method for estimating the cost to sequester carbon dioxide by delivering iron to the ocean. *Int. J. Global Warming* **2013**, *5*, 231–254, DOI: 10.1504/ijgw.2013.055360.
- [62] Massachusetts Institute of Technology. Sleipner project. <https://sequestration.mit.edu/tools/projects/sleipner.html> (accessed Dec. 29, 2019).

- [63] Massachusetts Institute of Technology. Weyburn-Midale project. <https://sequestration.mit.edu/tools/projects/weyburn.html> (accessed Dec. 29, 2019).
- [64] Pagnier, H. RECOPOL project. <http://www.cgseurope.net/Sections.aspx?section=491.492.511> (accessed Dec. 29, 2019).
- [65] Kühn, M.; Clauser, C. Mineralische Bindung von CO₂ bei der Speicherung im Untergrund in geothermischen Reservoiren. *Chem. Ing. Tech.* **2006**, *78*, 425–434, DOI: 10.1002/cite.200600019.
- [66] Reykjavik Energy; CNRS; AMPHOS21; University of Iceland; Climeworks. Carb-Fix project. <https://www.carbfix.com/> (accessed Dec. 29, 2019).
- [67] Sanz-Pérez, E. S.; Murdock, C. R.; Didas, S. A.; Jones, C. W. Direct Capture of CO₂ from Ambient Air. *Chem. Rev.* **2016**, *116*, 11840–11876, DOI: 10.1021/acs.chemrev.6b00173.
- [68] Romanov, V.; Soong, Y.; Carney, C.; Rush, G. E.; Nielsen, B.; O'Connor, W. Mineralization of Carbon Dioxide: A Literature Review. *ChemBioEng Reviews* **2015**, *2*, 231–256, DOI: 10.1002/cben.201500002.
- [69] Sternberg, A.; Bardow, A. Life Cycle Assessment of Power-to-Gas: Syngas vs Methane. *ACS Sustainable Chem. Eng.* **2016**, *4*, 4156–4165, DOI: 10.1021/acssuschemeng.6b00644.
- [70] Sternberg, A.; Jens, C. M.; Bardow, A. Life cycle assessment of CO₂-based C1-chemicals. *Green Chem.* **2017**, *19*, 2244–2259, DOI: 10.1039/c6gc02852g.
- [71] Courtemanche, M.-A.; Légaré, M.-A.; Maron, L.; Fontaine, F.-G. A Highly Active Phosphine–Borane Organocatalyst for the Reduction of CO₂ to Methanol Using Hydroboranes. *J. Am. Chem. Soc.* **2013**, *135*, 9326–9329, DOI: 10.1021/ja404585p.
- [72] Huff, C. A.; Sanford, M. S. Cascade Catalysis for the Homogeneous Hydrogenation of CO₂ to Methanol. *J. Am. Chem. Soc.* **2011**, *133*, 18122–18125, DOI: 10.1021/ja208760j.
- [73] Graves, C.; Ebbesen, S. D.; Mogensen, M.; Lackner, K. S. Sustainable hydrocarbon fuels by recycling CO₂ and H₂O with renewable or nuclear energy. *Renewable Sustainable Energy Rev.* **2011**, *15*, 1–23, DOI: 10.1016/j.rser.2010.07.014.
- [74] Kaiser, P.; Unde, R. B.; Kern, C.; Jess, A. Production of Liquid Hydrocarbons with CO₂ as Carbon Source based on Reverse Water-Gas Shift and Fischer-Tropsch Synthesis. *Chem. Ing. Tech.* **2013**, *85*, 489–499, DOI: 10.1002/cite.201200179.
- [75] Zeman, F. S.; Keith, D. W. Carbon neutral hydrocarbons. *Philos. Trans. R. Soc., A* **2008**, *366*, 3901–3918, DOI: 10.1098/rsta.2008.0143.
- [76] Veselovskaya, J. V.; Parunin, P. D.; Netskina, O. V.; Okunev, A. G. A Novel Process for Renewable Methane Production: Combining Direct Air Capture by K₂CO₃/Alumina Sorbent with CO₂ Methanation over Ru/Alumina Catalyst. *Top. Catal.* **2018**, *61*, 1528–1536, DOI: 10.1007/s11244-018-0997-z.

- [77] Munera Parra, A. A.; Agar, D. W. Molten metal capillary reactor for the high-temperature pyrolysis of methane. *Int. J. Hydrogen Energy* **2017**, *42*, 13641–13648, DOI: 10.1016/j.ijhydene.2016.12.044.
- [78] Rahimi, N.; Kang, D.; Gelinas, J.; Menon, A.; Gordon, M. J.; Metiu, H.; McFarland, E. W. Solid carbon production and recovery from high temperature methane pyrolysis in bubble columns containing molten metals and molten salts. *Carbon* **2019**, *151*, 181–191, DOI: 10.1016/j.carbon.2019.05.041.
- [79] Herzog, H. *Assessing the Feasibility of Capturing CO₂ from the Air*; tech. rep.; Massachusetts Institute of Technology: Cambridge, MA, 2013.
- [80] Spiegler, K. S.; Routsis, K. Process and System for Removal of Acidic Gases from Influent Gas to Fuel Cell. U.S. Patent 555,724, 1966.
- [81] Sreenivasulu, B.; Gayatri, D. V.; Sreedhar, I.; Raghavan, K. V. A journey into the process and engineering aspects of carbon capture technologies. *Renewable Sustainable Energy Rev.* **2015**, *41*, 1324–1350, DOI: 10.1016/j.rser.2014.09.029.
- [82] Castle, W. F. Fifty-Years' Development of Cryogenic Liquefaction Processes. In *Cryogenic Engineering*; Timmerhaus, K. D., Reed, R. P., Rizzuto, C., Eds.; Springer: New York, NY, 2007; pp 146–160, DOI: 10.1007/0-387-46896-X.
- [83] Spector, N. A.; Dodge, B. F. Removal of carbon dioxide from atmospheric air. *Trans. Am. Inst. Chem. Eng.* **1946**, *42*, 827–848.
- [84] Lackner, K. S.; Grimes, P.; Ziock, H. J. Carbon dioxide extraction from air: Is it an option? In *The proceedings of the 24th international technical conference on coal utilization and fuel systems*, Proceedings of the 24th international technical conference on coal utilization and fuel systems, Clearwater, FL, March 3-11, 1999; Sakkestad, B. A., Eds.; Coal & Slurry Technology Association: Washington, DC, 1999; 885–896.
- [85] Viebahn, P.; Scholz, A.; Zelt, O. The Potential Role of Direct Air Capture in the German Energy Research Program—Results of a Multi-Dimensional Analysis. *Energies* **2019**, *12*, 3443, DOI: 10.3390/en12183443.
- [86] Eisaman, M. D.; Alvarado, L.; Larner, D.; Wang, P.; Garg, B.; Littau, K. A. CO₂ separation using bipolar membrane electrodialysis. *Energy Environ. Sci.* **2011**, *4*, 1319–1328, DOI: 10.1039/c0ee00303d.
- [87] Specht, M.; Bandi, A.; Elser, M.; Staiss, F. Comparison of CO₂ sources for the synthesis of renewable methanol. In *Studies in Surface Science and Catalysis*, Proceedings of the Fourth International Conference on Carbon Dioxide Utilization, Kyoto, Japan, September 7-11, 1997; Inui, T., Anpo, M., Izui, K., Yanagida, S., Yamaguchi, T., Eds.; Elsevier: Amsterdam, The Netherlands, 1998; 363–366, DOI: [https://doi.org/10.1016/S0167-2991\(98\)80771-4](https://doi.org/10.1016/S0167-2991(98)80771-4).

- [88] IPCC. *Special Report on Carbon Dioxide Capture and Storage. Prepared by Working Group III of the Intergovernmental Panel on Climate Change*; Metz, B., Davidson, O., de Coninck, H. C., Loos, M., Meyer, L. A., Eds.; Cambridge University Press: Cambridge, UK and New York, NY, 2015.
- [89] Keith, D. W.; Ha-Duong, M.; Stolaroff, J. K. Climate Strategy with CO₂ Capture from the Air. *Clim. Change* **2006**, *74*, 17–45, DOI: 10.1007/s10584-005-9026-x.
- [90] Nikulshina, V.; Hirsch, D.; Mazzotti, M.; Steinflod, A. CO₂ capture from air and co-production of H₂ via the Ca(OH)₂–CaCO₃ cycle using concentrated solar power—Thermodynamic analysis. *Energy* **2006**, *31*, 1715–1725, DOI: 10.1016/j.energy.2005.09.014.
- [91] Zeman, F. Reducing the Cost of Ca-Based Direct Air Capture of CO₂. *Environ. Sci. Technol.* **2014**, *48*, 11730–11735, DOI: 10.1021/es502887y.
- [92] Carbon Engineering. Direct Air Capture. <https://carbonengineering.com/> (accessed Jan. 4, 2020).
- [93] Keith, D. W.; Holmes, G.; St. Angelo, D.; Heidel, K. A Process for Capturing CO₂ from the Atmosphere. *Joule* **2018**, *2*, 1573–1594, DOI: 10.1016/j.joule.2018.05.006.
- [94] Stolaroff, J. K.; Keith, D. W.; Lowry, G. V. Carbon Dioxide Capture from Atmospheric Air Using Sodium Hydroxide Spray. *Environ. Sci. Technol.* **2008**, *42*, 2728–2735, DOI: 10.1021/es702607w.
- [95] Mahmoudkhani, M.; Keith, D. W. Low-energy sodium hydroxide recovery for CO₂ capture from atmospheric air—Thermodynamic analysis. *Int. J. Greenhouse Gas Control* **2009**, *3*, 376–384, DOI: 10.1016/j.ijggc.2009.02.003.
- [96] Choi, S.; Drese, J. H.; Eisenberger, P. M.; Jones, C. W. Application of Amine-Tethered Solid Sorbents for Direct CO₂ Capture from the Ambient Air. *Environ. Sci. Technol.* **2011**, *45*, 2420–2427, DOI: 10.1021/es102797w.
- [97] Chichilnisky, G.; Eisenberger, P.; Cohen, R. W.; Eisenberger, N. M.; Chance, R. R.; Jones, C. W. Global Warming and Carbon-Negative Technology: Prospects for a Lower-Cost Route to a Lower-Risk Atmosphere. *Energy Environ.* **2009**, 973–984, DOI: 10.2139/ssrn.1522281.
- [98] Kulkarni, A. R.; Sholl, D. S. Analysis of Equilibrium-Based TSA Processes for Direct Capture of CO₂ from Air. *Ind. Eng. Chem. Res.* **2012**, *51*, 8631–8645, DOI: 10.1021/ie300691c.
- [99] Lackner, K. S. Capture of carbon dioxide from ambient air. *Eur. Phys. J.: Spec. Top.* **2009**, *176*, 93–106, DOI: 10.1140/epjst/e2009-01150-3.
- [100] Sinha, A.; Darunte, L. A.; Jones, C. W.; Realff, M. J.; Kawajiri, Y. Systems Design and Economic Analysis of Direct Air Capture of CO₂ through Temperature Vacuum Swing Adsorption Using MIL-101(Cr)-PEI-800 and mmen-Mg₂(dobpdc) MOF Adsorbents. *Ind. Eng. Chem. Res.* **2017**, *56*, 750–764, DOI: 10.1021/acs.iecr.6b03887.

- [101] Wang, T.; Lackner, K. S.; Wright, A. Moisture Swing Sorbent for Carbon Dioxide Capture from Ambient Air. *Environ. Sci. Technol.* **2011**, *45*, 6670–6675, DOI: 10.1021/es201180v.
- [102] Wang, T.; Lackner, K. S.; Wright, A. B. Moisture-swing sorption for carbon dioxide capture from ambient air: a thermodynamic analysis. *Phys. Chem. Chem. Phys.* **2013**, *15* (2), 504–514, DOI: 10.1039/c2cp43124f.
- [103] Wurzbacher, J. A.; Gebald, C.; Steinfeld, A. Separation of CO₂ from air by temperature-vacuum swing adsorption using diamine-functionalized silica gel. *Energy Environ. Sci.* **2011**, *4*, 3584–3592, DOI: 10.1039/c1ee01681d.
- [104] Wurzbacher, J. A.; Gebald, C.; Piatkowski, N.; Steinfeld, A. Concurrent Separation of CO₂ and H₂O from Air by a Temperature-Vacuum Swing Adsorption/Desorption Cycle. *Environ. Sci. Technol.* **2012**, *46*, 9191–9198, DOI: 10.1021/es301953k.
- [105] Climeworks. Capturing CO₂ from air. <https://www.climeworks.com> (accessed Jan. 6, 2020).
- [106] Sunfire. First commercial plant for the production of Blue Crude in Norway. <https://www.sunfire.de/en/company/news/detail/first-commercial-plant-for-the-production-of-blue-crude-planned-in-norway> (accessed Apr. 29, 2020).
- [107] Global Thermostat. A Unique Capture Process. <https://globalthermostat.com/a-unique-capture-process/> (accessed Jan. 7, 2020).
- [108] Chichilnisky, G. The Role of Carbon Removals. <https://de.slideshare.net/GracielaChichilnisky/the-role-of-carbon-removalsbrussels> (accessed Jan. 10, 2020).
- [109] Chichilnisky, G. Frameworks in Energy Transformation. Presented at 18th Energy in Western Australia Conference, Perth, Australia, August 21-23, 2018.
- [110] Jones, C. W. CO₂ Capture from Dilute Gases as a Component of Modern Global Carbon Management. *Annu. Rev. Chem. Biomol. Eng.* **2011**, *2*, 31–52, DOI: 10.1146/annurev-chembioeng-061010-114252.
- [111] Mazzotti, M.; Baciocchi, R.; Desmond, M. J.; Socolow, R. H. Direct air capture of CO₂ with chemicals: optimization of a two-loop hydroxide carbonate system using a countercurrent air-liquid contactor. *Climatic Change* **2013**, *118*, 119–135, DOI: 10.1007/s10584-012-0679-y.
- [112] Lackner, K. S. The thermodynamics of direct air capture of carbon dioxide. *Energy* **2013**, *50*, 38–46, DOI: 10.1016/j.energy.2012.09.012.
- [113] International Energy Agency. *World Energy Outlook 2019*; OECD Publishing: Paris, France, 2019, DOI: 10.1787/caf32f3b-en.
- [114] Williams, J. L. Monolith structures, materials, properties and uses. *Catal. Today* **2001**, *69*, 3–9, DOI: 10.1016/s0920-5861(01)00348-0.

- [115] Zhang, W.; Thompson, K. E.; Reed, A. H.; Beenken, L. Relationship between packing structure and porosity in fixed beds of equilateral cylindrical particles. *Chem. Eng. Sci.* **2006**, *61*, 8060–8074, DOI: 10.1016/j.ces.2006.09.036.
- [116] VDI e.V. *VDI-Wärmeatlas*, 11th ed.; Springer Vieweg: Wiesbaden, Germany, 2013, DOI: 10.1007/978-3-642-19981-3.
- [117] Cybulski, A.; Moulijn, J. A. Monoliths in Heterogeneous Catalysis. *Catal. Rev.: Sci. Eng.* **1994**, *36*, 179–270, DOI: 10.1080/01614949408013925.
- [118] Goldberg, D. S.; Lackner, K. S.; Han, P.; Slagle, A. L.; Wang, T. Co-Location of Air Capture, Subseafloor CO₂ Sequestration, and Energy Production on the Kerguelen Plateau. *Environ. Sci. Technol.* **2013**, *47*, 7521–7529, DOI: 10.1021/es401531y.
- [119] Oertel, H. Jr. *Prandtl - Führer durch die Strömungslehre*, 13th ed.; Springer Vieweg: Wiesbaden, Germany, 2013, DOI: 10.1007/978-3-8348-2315-1.
- [120] Schmidt, P. *Lastannahmen - Einwirkungen auf Tragwerke*; Springer Vieweg: Wiesbaden, Germany, 2019, DOI: 10.1007/978-3-8348-9855-5.
- [121] Quaschnig, V. *Regenerative Energiesysteme*, 8th ed.; Carl Hanser Verlag GmbH & Co. KG: Munich, Germany, 2013, DOI: 10.3139/9783446435711.
- [122] Belmabkhout, Y.; Serna-Guerrero, R.; Sayari, A. Amine-bearing mesoporous silica for CO₂ removal from dry and humid air. *Chem. Eng. Sci.* **2010**, *65*, 3695–3698, DOI: 10.1016/j.ces.2010.02.044.
- [123] Gray, M. L.; Champagne, K. J.; Fauth, D.; Baltrus, J. P.; Pennline, H. Performance of immobilized tertiary amine solid sorbents for the capture of carbon dioxide. *Int. J. Greenhouse Gas Control* **2008**, *2*, 3–8, DOI: 10.1016/s1750-5836(07)00088-6.
- [124] Bollini, P.; Brunelli, N. A.; Didas, S. A.; Jones, C. W. Dynamics of CO₂ Adsorption on Amine Adsorbents. 1. Impact of Heat Effects. *Ind. Eng. Chem. Res.* **2012**, *51*, 15145–15152, DOI: 10.1021/ie301790a.
- [125] Smal, I. M.; Yu, Q.; Veneman, R.; Fränzel-Luiten, B.; Brilman, D. W. F. TG-FTIR Measurement of CO₂-H₂O co-adsorption for CO₂ air capture sorbent screening. *Energy Procedia* **2014**, *63*, 6834–6841, DOI: 10.1016/j.egypro.2014.11.717.
- [126] Poling, B. E.; Prausnitz, J. M.; O'Connell, J. P. *The Properties of Gases and Liquids*, 5th ed.; McGRAW-HILL Companies, Inc.: New York, NY, 2001, DOI: 10.1036/0070116822.
- [127] Bathen, D.; Breitbach, M. *Adsorptionstechnik*; Springer-Verlag GmbH: Berlin, Germany and Heidelberg, Germany, 2001, DOI: 10.1007/978-3-642-18235-8.
- [128] National Institute of Standards and Technology. *NIST Chemistry WebBook, NIST Standard Reference Database 69*; Linstrom, P. J., Mallard, W. G., Eds.; Gaithersburg, MD, 2020, DOI: 10.18434/T4D303.
- [129] Konrad, G.; Eigenberger, G. Rotoradsorber zur Abluftreinigung und Lösungsmittel-Rückgewinnung. *Chem. Ing. Tech.* **1994**, *66*, 321–331, DOI: 10.1002/cite.330660305.

- [130] Duarte, G. S.; Schürer, B.; Voss, C.; Bathen, D. Modeling and Simulation of a Tube Bundle Adsorber for the Capture of CO₂ from Flue Gases. *Chem. Ing. Tech.* **2016**, *88*, 336–345, DOI: 10.1002/cite.201500031.
- [131] Shi, X.; Xiao, H.; Azarabadi, H.; Song, J.; Wu, X.; Chen, X.; Lackner, K. S. Sorbents for the Direct Capture of CO₂ from Ambient Air. *Angew. Chem., Int. Ed.* **2020**, *59*, 6984–7006, DOI: 10.1002/anie.201906756.
- [132] Brilman, D. W. F.; Veneman, R. Capturing Atmospheric CO₂ Using Supported Amine Sorbents. *Energy Procedia* **2013**, *37*, 6070–6078, DOI: 10.1016/j.egypro.2013.06.536.
- [133] Ntiamoah, A.; Ling, J.; Xiao, P.; Webley, P. A.; Zhai, Y. CO₂ Capture by Temperature Swing Adsorption: Use of Hot CO₂-Rich Gas for Regeneration. *Ind. Eng. Chem. Res.* **2016**, *55*, 703–713, DOI: 10.1021/acs.iecr.5b01384.
- [134] Yang, Q.; Vaesen, S.; Ragon, F.; Wiersum, A. D.; Wu, D.; Lago, A.; Devic, T.; Martineau, C.; Taulelle, F.; Llewellyn, P. L.; Jobic, H.; Zhong, C.; Serre, C.; De Weireld, G.; Maurin, G. A Water Stable Metal-Organic Framework with Optimal Features for CO₂ Capture. *Angew. Chem., Int. Ed.* **2013**, *52*, 10316–10320, DOI: 10.1002/anie.201302682.
- [135] Yu, C.-H.; Huang, C.-H.; Tan, C.-S. A Review of CO₂ Capture by Absorption and Adsorption. *Aerosol Air Qual. Res.* **2012**, *12*, 745–769, DOI: 10.4209/aaqr.2012.05.0132.
- [136] Pirngruber, G. D.; Guillou, F.; Gomez, A.; Clausse, M. A theoretical analysis of the energy consumption of post-combustion CO₂ capture processes by temperature swing adsorption using solid sorbents. *Int. J. Greenhouse Gas Control* **2013**, *14*, 74–83, DOI: 10.1016/j.ijggc.2013.01.010.
- [137] Veneman, R.; Frigka, N.; Zhao, W.; Li, Z.; Kersten, S.; Brilman, W. Adsorption of H₂O and CO₂ on supported amine sorbents. *Int. J. Greenhouse Gas Control* **2015**, *41*, 268–275, DOI: 10.1016/j.ijggc.2015.07.014.
- [138] Nikulshina, V.; Gálvez, M. E.; Steinfeld, A. Kinetic analysis of the carbonation reactions for the capture of CO₂ from air via the Ca(OH)₂–CaCO₂–CaO solar thermochemical cycle. *Chem. Eng. J.* **2007**, *129*, 75–83, DOI: 10.1016/j.cej.2006.11.003.
- [139] Nikulshina, V.; Ayesa, N.; Gálvez, M. E.; Steinfeld, A. Feasibility of Na-based thermochemical cycles for the capture of CO₂ from air—Thermodynamic and thermogravimetric analyses. *Chem. Eng. J.* **2008**, *140*, 62–70, DOI: 10.1016/j.cej.2007.09.007.
- [140] Nikulshina, V.; Steinfeld, A. CO₂ capture from air via CaO-carbonation using a solar-driven fluidized bed reactor—Effect of temperature and water vapor concentration. *Chem. Eng. J.* **2009**, *155*, 867–873, DOI: 10.1016/j.cej.2009.10.004.
- [141] Stucki, S.; Schuler, A.; Constantinescu, M. Coupled CO₂ recovery from the atmosphere and water electrolysis: Feasibility of a new process for hydrogen storage. *Int. J. Hydrogen Energy* **1995**, *20*, 653–663, DOI: 10.1016/0360-3199(95)00007-z.

- [142] Bali, S.; Sakwa-Novak, M. A.; Jones, C. W. Potassium incorporated alumina based CO₂ capture sorbents: Comparison with supported amine sorbents under ultra-dilute capture conditions. *Colloids Surf., A* **2015**, *486*, 78–85, DOI: 10.1016/j.colsurfa.2015.09.020.
- [143] Przepiórski, J.; Czyżewski, A.; Pietrzak, R.; Morawski, A. W. MgO/CaO-Loaded Activated Carbon for Carbon Dioxide Capture: Practical Aspects of Use. *Ind. Eng. Chem. Res.* **2013**, *52*, 6669–6677, DOI: 10.1021/ie302848r.
- [144] Zhao, C.; Guo, Y.; Li, C.; Lu, S. Removal of low concentration CO₂ at ambient temperature using several potassium-based sorbents. *Appl. Energy* **2014**, *124*, 241–247, DOI: 10.1016/j.apenergy.2014.02.054.
- [145] Derevschikov, V. S.; Veselovskaya, J. V.; Kardash, T. Y.; Trubitsyn, D. A.; Okunev, A. G. Direct CO₂ capture from ambient air using K₂CO₃/Y₂O₃ composite sorbent. *Fuel* **2014**, *127*, 212–218, DOI: 10.1016/j.fuel.2013.09.060.
- [146] Chaikittisilp, W.; Khunsupat, R.; Chen, T. T.; Jones, C. W. Poly(allylamine)–Mesoporous Silica Composite Materials for CO₂ Capture from Simulated Flue Gas or Ambient Air. *Ind. Eng. Chem. Res.* **2011**, *50*, 14203–14210, DOI: 10.1021/ie201584t.
- [147] Sakwa-Novak, M. A.; Jones, C. W. Steam Induced Structural Changes of a Poly(ethylenimine) Impregnated γ -Alumina Sorbent for CO₂ Extraction from Ambient Air. *ACS Appl. Mater. Interfaces* **2014**, *6*, 9245–9255, DOI: 10.1021/am501500q.
- [148] Goepfert, A.; Zhang, H.; Czaun, M.; May, R. B.; Prakash, G. K. S.; Olah, G. A.; Narayanan, S. R. Easily Regenerable Solid Adsorbents Based on Polyamines for Carbon Dioxide Capture from the Air. *ChemSusChem* **2014**, *7*, 1386–1397, DOI: 10.1002/cssc.201301114.
- [149] Didas, S. A.; Kulkarni, A. R.; Sholl, D. S.; Jones, C. W. Role of Amine Structure on Carbon Dioxide Adsorption from Ultradilute Gas Streams such as Ambient Air. *ChemSusChem* **2012**, *5*, 2058–2064, DOI: 10.1002/cssc.201200196.
- [150] Sayari, A.; Belmabkhout, Y. Stabilization of Amine-Containing CO₂ Adsorbents: Dramatic Effect of Water Vapor. *J. Am. Chem. Soc.* **2010**, *132*, 6312–6314, DOI: 10.1021/ja1013773.
- [151] Chaikittisilp, W.; Lunn, J. D.; Shantz, D. F.; Jones, C. W. Poly(L-lysine) Brush–Mesoporous Silica Hybrid Material as a Biomolecule-Based Adsorbent for CO₂ Capture from Simulated Flue Gas and Air. *Chem. - Eur. J.* **2011**, *17*, 10556–10561, DOI: 10.1002/chem.201101480.
- [152] Qi, G.; Fu, L.; Giannelis, E. P. Sponges with covalently tethered amines for high-efficiency carbon capture. *Nat. Commun.* **2014**, *5*, 5796, DOI: 10.1038/ncomms6796.
- [153] Choi, S.; Gray, M. L.; Jones, C. W. Amine-Tethered Solid Adsorbents Coupling High Adsorption Capacity and Regenerability for CO₂ Capture From Ambient Air. *ChemSusChem* **2011**, *4*, 628–635, DOI: 10.1002/cssc.201000355.

- [154] Wilfong, W. C.; Kail, B. W.; Jones, C. W.; Pacheco, C.; Gray, M. L. Spectroscopic Investigation of the Mechanisms Responsible for the Superior Stability of Hybrid Class 1/Class 2 CO₂ Sorbents: A New Class 4 Category. *ACS Appl. Mater. Interfaces* **2016**, *8*, 12780–12791, DOI: 10.1021/acsami.6b02062.
- [155] Yue, M. B.; Sun, L. B.; Cao, Y.; Wang, Y.; Wang, Z. J.; Zhu, J. H. Efficient CO₂ Capturer Derived from As-Synthesized MCM-41 Modified with Amine. *Chem. - Eur. J.* **2008**, *14*, 3442–3451, DOI: 10.1002/chem.200701467.
- [156] Gray, M. L.; Hoffman, J. S.; Hreha, D. C.; Fauth, D. J.; Hedges, S. W.; Champagne, K. J.; Pennline, H. W. Parametric Study of Solid Amine Sorbents for the Capture of Carbon Dioxide. *Energy Fuels* **2009**, *23*, 4840–4844, DOI: 10.1021/ef9001204.
- [157] Veneman, R. Adsorptive systems for post-combustion CO₂ capture : Design, experimental validation and evaluation of a supported amine based process, Ph.D. Thesis, University of Twente, The Netherlands, 2015.
- [158] Sjoström, S.; Krutka, H. Evaluation of solid sorbents as a retrofit technology for CO₂ capture. *Fuel* **2010**, *89*, 1298–1306, DOI: 10.1016/j.fuel.2009.11.019.
- [159] Caplow, M. Kinetics of carbamate formation and breakdown. *J. Am. Chem. Soc.* **1968**, *90*, 6795–6803, DOI: 10.1021/ja01026a041.
- [160] Choi, S.; Drese, J. H.; Jones, C. W. Adsorbent Materials for Carbon Dioxide Capture from Large Anthropogenic Point Sources. *ChemSusChem* **2009**, *2*, 796–854, DOI: 10.1002/cssc.200900036.
- [161] Danckwerts, P. V. The reaction of CO₂ with ethanolamines. *Chem. Eng. Sci.* **1979**, *34*, 443–446, DOI: 10.1016/0009-2509(79)85087-3.
- [162] *Product information Lewatit® VP OC 1065*; Lanxess: Cologne, Germany, 2017.
- [163] Alesi, W. R.; Kitchin, J. R. Evaluation of a Primary Amine-Functionalized Ion-Exchange Resin for CO₂ Capture. *Ind. Eng. Chem. Res.* **2012**, *51*, 6907–6915, DOI: 10.1021/ie300452c.
- [164] Bos, M. J.; Kreuger, T.; Kersten, S. R. A.; Brilman, D. W. F. Study on transport phenomena and intrinsic kinetics for CO₂ adsorption in solid amine sorbent. *Chem. Eng. J.* **2019**, *377*, 120374, DOI: 10.1016/j.cej.2018.11.072.
- [165] Hallenbeck, A. P.; Kitchin, J. R. Effects of O₂ and SO₂ on the Capture Capacity of a Primary-Amine Based Polymeric CO₂ Sorbent. *Ind. Eng. Chem. Res.* **2013**, *52*, 10788–10794, DOI: 10.1021/ie400582a.
- [166] Sonnleitner, E.; Schöny, G.; Hofbauer, H. Assessment of zeolite 13X and Lewatit® VP OC 1065 for application in a continuous temperature swing adsorption process for biogas upgrading. *Biomass Convers. Biorefin.* **2018**, *8*, 379–395, DOI: 10.1007/s13399-017-0293-3.
- [167] Sutanto, S.; Dijkstra, J. W.; Pieterse, J. A. Z.; Boon, J.; Hauwert, P.; Brilman, D. W. F. CO₂ removal from biogas with supported amine sorbents: First technical evaluation based on experimental data. *Sep. Purif. Technol.* **2017**, *184*, 12–25, DOI: 10.1016/j.seppur.2017.04.030.

- [168] Yu, Q.; de la P. Delgado, J.; Veneman, R.; Brillman, D. W. F. Stability of a Benzyl Amine Based CO₂ Capture Adsorbent in View of Regeneration Strategies. *Ind. Eng. Chem. Res.* **2017**, *56*, 3259–3269, DOI: 10.1021/acs.iecr.6b04645.
- [169] *Labview*, 18; AMS Software GmbH: Ellerau, Germany, 2018.
- [170] *EL-FLOW[®] Select series Thermal Mass Flow Meters and Controllers*; Bronkhorst: Ruurlo, The Netherlands, 2020.
- [171] *EasyLine Continuous gas analyzers Models EL3020, EL3040*; ABB Automation GmbH: Frankfurt on the Main, Germany, 2016.
- [172] *Temperature/humidity measuring probe for GMH 3330 and GMH 3350*; GHM Messtechnik GmbH: Greisinger, Germany, 2020.
- [173] *NETZSCH-BEADS[®]*; NETZSCH-Feinmahltechnik GmbH: Selb, Germany, 2019.
- [174] *Bedienungsanleitung Simultan-Thermo-Analyse STA 409 C*; NETZSCH-Gerätebau GmbH: Selb, Germany, 1992.
- [175] ABB. Flow Measurement. <https://new.abb.com/products/measurement-products/flow> (accessed Dec. 28, 2020).
- [176] Ayawei, N.; Ebelegi, A. N.; Wankasi, D. Modelling and Interpretation of Adsorption Isotherms. *J. Chem.* **2017**, *2017*, 3039817, DOI: 10.1155/2017/3039817.
- [177] Do, D. D. *Adsorption Analysis: Equilibria and Kinetics*; Imperial College Press Press: London, UK, 1998; Vol. 2, DOI: 10.1142/p111.
- [178] *Matlab*, R2018a; The Mathworks, Inc.: Natick, MA, 2020.
- [179] Watabe, T.; Yogo, K. Isotherms and isosteric heats of adsorption for CO₂ in amine-functionalized mesoporous silicas. *Sep. Purif. Technol.* **2013**, *120*, 20–23, DOI: 10.1016/j.seppur.2013.09.011.
- [180] Pan, H.; Ritter, J. A.; Balbuena, P. B. Examination of the Approximations Used in Determining the Isosteric Heat of Adsorption from the Clausius-Clapeyron Equation. *Langmuir* **1998**, *14*, 6323–6327, DOI: 10.1021/1a9803373.
- [181] Glueckauf, E. Theory of chromatography. Part 10.—Formulæ for diffusion into spheres and their application to chromatography. *Trans. Faraday Soc.* **1955**, *51*, 1540–1551, DOI: 10.1039/tf9555101540.
- [182] Sharain-Liew, Y. L.; Joseph, C. G.; How, S.-E. Biosorption of lead contaminated wastewater using cattails (*Typha angustifolia*) leaves: Kinetic studies. *J. Serb. Chem. Soc.* **2011**, *76*, 1037–1047, DOI: 10.2298/jsc1006280841.
- [183] Richner, G.; Puxty, G.; Carnal, A.; Conway, W.; Maeder, M.; Pearson, P. Thermokinetic properties and performance evaluation of benzylamine-based solvents for CO₂ capture. *Chem. Eng. J.* **2015**, *264*, 230–240, DOI: 10.1016/j.cej.2014.11.067.
- [184] Wang, T.; Liu, J.; Huang, H.; Fang, M.; Luo, Z. Preparation and kinetics of a heterogeneous sorbent for CO₂ capture from the atmosphere. *Chem. Eng. J.* **2016**, *284*, 679–686, DOI: 10.1016/j.cej.2015.09.009.

- [185] Didas, S. A.; Sakwa-Novak, M. A.; Foo, G. S.; Sievers, C.; Jones, C. W. Effect of Amine Surface Coverage on the Co-Adsorption of CO₂ and Water: Spectral Deconvolution of Adsorbed Species. *J. Phys. Chem. Lett.* **2014**, *5*, 4194–4200, DOI: 10.1021/jz502032c.
- [186] Harlick, P. J. E.; Sayari, A. Applications of Pore-Expanded Mesoporous Silica. 5. Triamine Grafted Material with Exceptional CO₂ Dynamic and Equilibrium Adsorption Performance. *Ind. Eng. Chem. Res.* **2007**, *46*, 446–458, DOI: 10.1021/ie060774+.
- [187] Gebald, C.; Wurzbacher, J. A.; Borgschulte, A.; Zimmermann, T.; Steinfeld, A. Single-Component and Binary CO₂ and H₂O Adsorption of Amine-Functionalized Cellulose. *Environ. Sci. Technol.* **2014**, *48*, 2497–2504, DOI: 10.1021/es404430g.
- [188] Yu, J.; Zhai, Y.; Chuang, S. S. C. Water Enhancement in CO₂ Capture by Amines: An Insight into CO₂–H₂O Interactions on Amine Films and Sorbents. *Ind. Eng. Chem. Res.* **2018**, *57*, 4052–4062, DOI: 10.1021/acs.iecr.7b05114.
- [189] Kim, H.-J.; Chaikittisilp, W.; Jang, K.-S.; Didas, S. A.; Johnson, J. R.; Koros, W. J.; Nair, S.; Jones, C. W. Aziridine-Functionalized Mesoporous Silica Membranes on Polymeric Hollow Fibers: Synthesis and Single-Component CO₂ and N₂ Permeation Properties. *Ind. Eng. Chem. Res.* **2014**, *54*, 4407–4413, DOI: 10.1021/ie503781u.
- [190] Neil Ruckart, K.; O’Brien, R. A.; Woodard, S. M.; West, K. N.; Grant Glover, T. Porous Solids Impregnated with Task-Specific Ionic Liquids as Composite Sorbents. *J. Phys. Chem. C* **2015**, *119*, 20681–20697, DOI: 10.1021/acs.jpcc.5b04646.
- [191] Brunauer, S.; Emmett, P. H.; Teller, E. Adsorption of Gases in Multimolecular Layers. *J. Am. Chem. Soc.* **1938**, *60*, 309–319, DOI: 10.1021/ja01269a023.
- [192] Anderson, R. B. Modifications of the Brunauer, Emmett and Teller Equation. *J. Am. Chem. Soc.* **1946**, *68*, 686–691, DOI: 10.1021/ja01208a049.
- [193] Quirijns, E. J.; van Boxtel, A. J. B.; van Loon, W. K. P.; van Straten, G. Sorption isotherms, GAB parameters and isosteric heat of sorption. *J. Sci. Food Agric.* **2005**, *85*, 1805–1814, DOI: 10.1002/jsfa.2140.
- [194] Wurzbacher, J. A.; Gebald, C.; Brunner, S.; Steinfeld, A. Heat and mass transfer of temperature-vacuum swing desorption for CO₂ capture from air. *Chem. Eng. J.* **2016**, *283*, 1329–1338, DOI: 10.1016/j.cej.2015.08.035.
- [195] *Production, Handling and Characterization of Particulate Materials*; Merkus, H. G., Meesters, G. M. H., Eds.; Springer International Publishing: Cham, Switzerland, 2016, DOI: 10.1007/978-3-319-20949-4.
- [196] Heydari-Gorji, A.; Sayari, A. Thermal, Oxidative, and CO₂-Induced Degradation of Supported Polyethylenimine Adsorbents. *Ind. Eng. Chem. Res.* **2012**, *51*, 6887–6894, DOI: 10.1021/ie3003446.
- [197] Hydrocell. Direct Air Capture (DAC) appliances. <https://hydrocell.fi/en/air-cleaners-carbon-dioxide-filters-and-dac-appliances/dac-appliances/> (accessed Apr. 29, 2020).

- [198] Infinitree. Carbon Capture Greenhouse Enrichment. <http://www.infinitreellc.com> (accessed May 29, 2020).
- [199] Skytree. Harvesting CO₂. <https://www.skytree.eu/technology/> (accessed May 29, 2020).
- [200] Fasihi, M.; Efimova, O.; Breyer, C. Techno-economic assessment of CO₂ direct air capture plants. *J. Cleaner Prod.* **2019**, *224*, 957–980, DOI: 10.1016/j.jclepro.2019.03.086.
- [201] Holmes, G.; Keith, D. W. An air–liquid contactor for large-scale capture of CO₂ from air. *Philos. Trans. R. Soc., A* **2012**, *370*, 4380–4403, DOI: 10.1098/rsta.2012.0137.
- [202] Carbon Engineering Ltd. Carbon Dioxide Capture Method and Facility. U.S. Patent 9095813B2, 2009.
- [203] Holmes, G.; Nold, K.; Walsh, T.; Heidel, K.; Henderson, M. A.; Ritchie, J.; Klavins, P.; Singh, A.; Keith, D. W. Outdoor Prototype Results for Direct Atmospheric Capture of Carbon Dioxide. *Energy Procedia* **2013**, *37*, 6079–6095, DOI: 10.1016/j.egypro.2013.06.537.
- [204] Chan, H. X. M.; Yap, E. H.; Ho, J. H. Axial Compression for Direct Capture of Carbon Dioxide (CO₂). *Appl. Mech. Mater.* **2013**, *284-287*, 35–40, DOI: 10.4028/www.scientific.net/amm.284-287.35.
- [205] Chan, H. X. M.; Yap, E. H.; Ho, J. H. Overview of Axial Compression Technology for Direct Capture of CO₂. *Adv. Mater. Res.* **2013**, *744*, 392–395, DOI: 10.4028/www.scientific.net/amr.744.392.
- [206] Goldberg, D.; Lackner, K. Creating negative emissions at remote CO₂ sequestration sites. *Greenhouse Gases: Sci. and Technol.* **2015**, *5*, 238–240, DOI: 10.1002/ghg.1489.
- [207] Choi, S.; Drese, J. H.; Chance, R. R.; Eisenberger, P. M.; Jones, C. W. Application of amine-tethered solid sorbents to CO₂ fixation from air. U.S. Patent 20110179948A1, 2019.
- [208] Eisenberger, P.; Chichilnisky, G. System and method for removing carbon dioxide from an atmosphere and global thermostat using the same. U.S. Patent 20080289319A1, 2007.
- [209] Eisenberger, P. Carbon dioxide capture/regeneration structures and techniques. U.S. Patent 20110041688A1, 2010.
- [210] Eisenberger, P. System and method for carbon dioxide capture and sequestration. U.S. Patent 8500855B2, 2011.
- [211] Ping, E.; Sakwa-Novak, M.; Eisenberger, P. Global Thermostat low cost direct air capture technology: pilot to commercial deployment. Presented at International Conference on Negative CO₂ Emissions, Gothenburg, Sweden, May 22-24, 2018.
- [212] Climeworks AG. Low-Pressure Drop Structure of Particle Adsorbent Bed for Adsorption Gas Separation Process. WO Patent 2014170184A1, 2014.

- [213] Climeworks AG. Direct air capture device. U.S. Patent 20170106330A1, 2017.
- [214] Wurzbacher, J. A.; Gebald, C. Distributed building-integrated carbon dioxide extraction system reducing fresh air requirements. WO Patent 2013075981A3, 2013.
- [215] Drechsler, C.; Agar, D. W. Comparison of Highly Heat-Integrated Adsorber Concepts for Use in Direct Air Capture Processes. *Chem. Ing. Tech.* **2020**, *92*, 282–287, DOI: 10.1002/cite.201900069.
- [216] King Fahd University of Petroleum and Minerals. Moving carbon nanotube heat sink. U.S. Patent 7900690B2, 2011.
- [217] Towler, G.; Sinnott, R. *Chemical Engineering Design: Principles, Practice and Economics of Plant and Process Design*, 2nd ed.; Butterworth-Heinemann: Oxford, UK, 2012, DOI: 10.1016/c2009-0-61216-2.
- [218] DEUTSCHE NORM. *DIN 22101: Continuous conveyors - Belt conveyors for loose bulk materials - Basis for calculation and dimensioning*; ICS 53.040.20; DIN Deutsches Institut für Normung e. V.: Berlin, Germany, 2011.
- [219] VDI-Handbuch Technische Logistik, Band 4: Schüttgut-Fördertechnik. *VDI 2324: Vertical bucket elevators*; ICS 53.040.10; VDI-Gesellschaft Produktion und Logistik (GPL): Düsseldorf, Germany, 2018.
- [220] Nesbitt, B. *Handbook of Valves and Actuators*; Butterworth-Heinemann: Oxford, UK, 2007, DOI: 10.1016/B978-1-85617-494-7.X5027-5.
- [221] Jiménez, J. A.; Madsen, O. S. A Simple Formula to Estimate Settling Velocity of Natural Sediments. *J. Waterw. Port Coastal Ocean Eng.* **2003**, *129*, 70–78, DOI: 10.1061/(asce)0733-950x(2003)129:2(70).
- [222] Artoni, R.; Santomaso, A.; Canu, P. Coupling between countercurrent gas and solid flows in a moving granular bed: The role of shear bands at the walls. *Int. J. Multiphase Flow* **2011**, *37*, 1209–1218, DOI: 10.1016/j.ijmultiphaseflow.2011.07.005.
- [223] Chen, J.; Akiyama, T.; Nogami, H.; Yagi, J.-I.; Takahashi, H. Modeling of Solid Flow in Moving Beds. *ISIJ Int.* **1993**, *33*, 664–671, DOI: 10.2355/isijinternational.33.664.
- [224] Nedderman, R. M.; Laohakul, C. The thickness of the shear zone of flowing granular materials. *Powder Technol.* **1980**, *25*, 91–100, DOI: 10.1016/0032-5910(80)87014-8.
- [225] Toyama, S. The flow of granular materials in moving beds. *Powder Technol.* **1971**, *4*, 214–220, DOI: 10.1016/0032-5910(71)80037-2.
- [226] DEUTSCHE NORM. *DIN ISO 4783-2: Industrial wire screens and woven wire cloth - Guide to the choice of aperture size and wire diameter combinations - Part 2: Preferred combinations for woven wire cloth*; ICS 19.120; DIN Deutsches Institut für Normung e. V.: Berlin, Germany, 1996.

- [227] Roh, J. W.; Hippalgaonkar, K.; Ham, J. H.; Chen, R.; Li, M. Z.; Ercius, P.; Majumdar, A.; Kim, W.; Lee, W. Observation of Anisotropy in Thermal Conductivity of Individual Single-Crystalline Bismuth Nanowires. *ACS Nano* **2011**, *5*, 3954–3960, DOI: 10.1021/nn200474d.
- [228] Song, N.; Jiao, D.; Ding, P.; Cui, S.; Tang, S.; Shi, L. Anisotropic thermally conductive flexible films based on nanofibrillated cellulose and aligned graphene nanosheets. *J. Mater. Chem. C* **2016**, *4*, 305–314, DOI: 10.1039/c5tc02194d.
- [229] *SIGRATHERM®: Flexible graphite foils and sheets for thermal management applications*; SGL Carbon SE: Wiesbaden, Germany, 2020.
- [230] Drechsler, C.; Agar, D. W. Simulation and optimization of a novel moving belt adsorber concept for the direct air capture of carbon dioxide. *Comput. Chem. Eng.* **2019**, *126*, 520–534, DOI: 10.1016/j.compchemeng.2019.04.023.
- [231] Li, W.; Choi, S.; Drese, J. H.; Hornbostel, M.; Krishnan, G.; Eisenberger, P. M.; Jones, C. W. Steam-Stripping for Regeneration of Supported Amine-Based CO₂ Adsorbents. *ChemSusChem* **2010**, *3*, 899–903, DOI: 10.1002/cssc.201000131.
- [232] Yang, H.; Singh, M.; Schaefer, J. Humidity-swing mechanism for CO₂ capture from ambient air. *Chem. Commun.* **2018**, *54*, 4915–4918, DOI: 10.1039/c8cc02109k.
- [233] Laity, J. J. *Deserts and Desert Environments*; Wiley-Blackwell: Chichester, UK, 2008.
- [234] Ahrens, C. D. *Meteorology Today: An Introduction to Weather, Climate, and the Environment*, 8th ed.; Thomson Brooks/Cole: Belmont, CA, 2007.
- [235] Scholes, C. A.; Kanehashi, S.; Stevens, G. W.; Kentish, S. E. Water permeability and competitive permeation with CO₂ and CH₄ in perfluorinated polymeric membranes. *Sep. Purif. Technol.* **2015**, *147*, 203–209, DOI: 10.1016/j.seppur.2015.04.023.
- [236] Scholes, C. A. Water Resistant Composite Membranes for Carbon Dioxide Separation from Methane. *Appl. Sci.* **2018**, *8*, 829, DOI: 10.3390/app8050829.
- [237] Llano-Restrepo, M.; Mosquera, M. A. Accurate correlation, thermochemistry, and structural interpretation of equilibrium adsorption isotherms of water vapor in zeolite 3A by means of a generalized statistical thermodynamic adsorption model. *Fluid Phase Equilib.* **2009**, *283*, 73–88, DOI: 10.1016/j.fluid.2009.06.003.
- [238] Fehla, M.; Specht, E. Optimization of Vapor Compression for Cost Savings in Drying Processes. *Chem. Eng. Technol.* **2000**, *23*, 901–908, DOI: 10.1002/1521-4125(200010)23:10<901::aid-ceat901>3.0.co;2-q.
- [239] Jana, A. K. Advances in heat pump assisted distillation column: A review. *Energy Convers. Manage.* **2014**, *77*, 287–297, DOI: 10.1016/j.enconman.2013.09.055.
- [240] Drechsler, C.; Agar, D. W. Investigation of water co-adsorption on the energy balance of solid sorbent based direct air capture processes. *Energy* **2020**, *192*, 116587, DOI: 10.1016/j.energy.2019.116587.

- [241] Branan, C. R. *Rules of thumbs for chemical engineers*, 3rd ed.; Gulf Professional Publishing: Houston, TX, 2002.
- [242] Reiter, G.; Lindorfer, J. Global warming potential of hydrogen and methane production from renewable electricity via power-to-gas technology. *Int. J. Life Cycle Assess.* **2015**, *20*, 477–489, DOI: 10.1007/s11367-015-0848-0.
- [243] Zhang, X.; Bauer, C.; Mutel, C. L.; Volkart, K. Life Cycle Assessment of Power-to-Gas: Approaches, system variations and their environmental implications. *Appl. Energy* **2017**, *190*, 326–338, DOI: 10.1016/j.apenergy.2016.12.098.
- [244] Bode, A.; Agar, D. W.; Büker, K.; Hensmann, M.; Hunfeld, J.; Janhsen, U.; Klingler, D.; Schunck, S. Methane Pyrolysis and CO₂ Activation - Technologies with Application Options for Hydrogen, Carbon and Synthesis Gas Production. *Chem. Ing. Tech.* **2016**, *88*, 1342–1342, DOI: 10.1002/cite.201650483.
- [245] Capros, P.; De Vita, A.; Tasios, N.; Papadopoulos, D.; Siskos, P.; Apostolaki, E.; Zampara, M.; Paroussos, L.; Fragiadakis, K.; Kouvaritakis, N.; Höglund-Isaksson, L.; Winiwarter, W.; Purohit, P.; Böttcher, H.; Frank, S.; Havlík, P.; Gusti, M. *EU energy, transport and GHG emissions: trends to 2050, reference scenarios 2013*; Publications Office of the European Union: Luxembourg, Luxembourg, 2013, DOI: 10.2833/17897.
- [246] Götz, M.; Lefebvre, J.; Mörs, F.; McDaniel Koch, A.; Graf, F.; Bajohr, S.; Reimert, R.; Kolb, T. Renewable Power-to-Gas: A technological and economic review. *Renewable Energy* **2016**, *85*, 1371–1390, DOI: 10.1016/j.renene.2015.07.066.
- [247] Sytze de Boer, H.; Grond, L.; Moll, H.; Benders, R. The application of power-to-gas, pumped hydro storage and compressed air energy storage in an electricity system at different wind power penetration levels. *Energy* **2014**, *72*, 360–370, DOI: 10.1016/j.energy.2014.05.047.
- [248] Jentsch, M.; Trost, T.; Sterner, M. Optimal Use of Power-to-Gas Energy Storage Systems in an 85% Renewable Energy Scenario. *Energy Procedia* **2014**, *46*, 254–261, DOI: 10.1016/j.egypro.2014.01.180.
- [249] Pleßmann, G.; Erdmann, M.; Hlusiak, M.; Breyer, C. Global Energy Storage Demand for a 100% Renewable Electricity Supply. *Energy Procedia* **2014**, *46*, 22–31, DOI: 10.1016/j.egypro.2014.01.154.
- [250] Bailera, M.; Lisbona, P.; Romeo, L. M.; Espatolero, S. Power to Gas projects review: Lab, pilot and demo plants for storing renewable energy and CO₂. *Renewable Sustainable Energy Rev.* **2017**, *69*, 292–312, DOI: 10.1016/j.rser.2016.11.130.
- [251] Blanco, H.; Faaij, A. A review at the role of storage in energy systems with a focus on Power to Gas and long-term storage. *Renewable Sustainable Energy Rev.* **2018**, *81*, 1049–1086, DOI: 10.1016/j.rser.2017.07.062.
- [252] Gahleitner, G. Hydrogen from renewable electricity: An international review of power-to-gas pilot plants for stationary applications. *Int. J. Hydrogen Energy* **2013**, *38*, 2039–2061, DOI: 10.1016/j.ijhydene.2012.12.010.

- [253] Buttler, A.; Spliethoff, H. Current status of water electrolysis for energy storage, grid balancing and sector coupling via power-to-gas and power-to-liquids: A review. *Renewable Sustainable Energy Rev.* **2018**, *82*, 2440–2454, DOI: 10.1016/j.rser.2017.09.003.
- [254] Schaaf, T.; Grünig, J.; Schuster, M. R.; Rothenfluh, T.; Orth, A. Methanation of CO₂ - storage of renewable energy in a gas distribution system. *Energy Sustainability Soc.* **2014**, *4*, 2, DOI: 10.1186/s13705-014-0029-1.
- [255] Kopyscinski, J.; Schildhauer, T. J.; Biollaz, S. M. A. Methanation in a fluidized bed reactor with high initial CO partial pressure: Part I—Experimental investigation of hydrodynamics, mass transfer effects, and carbon deposition. *Chem. Eng. Sci.* **2011**, *66*, 924–934, DOI: 10.1016/j.ces.2010.11.042.
- [256] Lefebvre, J.; Götz, M.; Bajohr, S.; Reimert, R.; Kolb, T. Improvement of three-phase methanation reactor performance for steady-state and transient operation. *Fuel Process. Technol.* **2015**, *132*, 83–90, DOI: 10.1016/j.fuproc.2014.10.040.
- [257] Janke, C.; Duyar, M. S.; Hoskins, M.; Farrauto, R. Catalytic and adsorption studies for the hydrogenation of CO₂ to methane. *Appl. Catal., B* **2014**, *152-153*, 184–191, DOI: 10.1016/j.apcatb.2014.01.016.
- [258] Stangeland, K.; Kalai, D.; Li, H.; Yu, Z. CO₂ Methanation: The Effect of Catalysts and Reaction Conditions. *Energy Procedia* **2017**, *105*, 2022–2027, DOI: 10.1016/j.egypro.2017.03.577.
- [259] Su, X.; Xu, J.; Liang, B.; Duan, H.; Hou, B.; Huang, Y. Catalytic carbon dioxide hydrogenation to methane: A review of recent studies. *J. Energy Chem.* **2016**, *25*, 553–565, DOI: 10.1016/j.jechem.2016.03.009.
- [260] Bremer, J.; Rätze, K. H. G.; Sundmacher, K. CO₂ methanation: Optimal start-up control of a fixed-bed reactor for power-to-gas applications. *AIChE J.* **2016**, *63*, 23–31, DOI: 10.1002/aic.15496.
- [261] Matthischke, S.; Krüger, R.; Rönsch, S.; Güttel, R. Unsteady-state methanation of carbon dioxide in a fixed-bed recycle reactor — Experimental results for transient flow rate ramps. *Fuel Process. Technol.* **2016**, *153*, 87–93, DOI: 10.1016/j.fuproc.2016.07.021.
- [262] Bassano, C.; Deiana, P.; Vilardi, G.; Verdone, N. Modeling and economic evaluation of carbon capture and storage technologies integrated into synthetic natural gas and power-to-gas plants. *Appl. Energy* **2020**, *263*, 114590, DOI: 10.1016/j.apenergy.2020.114590.
- [263] Schiebahn, S.; Grube, T.; Robinius, M.; Tietze, V.; Kumar, B.; Stolten, D. Power to gas: Technological overview, systems analysis and economic assessment for a case study in Germany. *Int. J. Hydrogen Energy* **2015**, *40*, 4285–4294, DOI: 10.1016/j.ijhydene.2015.01.123.
- [264] Chauvy, R.; Dubois, L.; Lybaert, P.; Thomas, D.; Weireld, G. D. Production of synthetic natural gas from industrial carbon dioxide. *Appl. Energy* **2020**, *260*, 114249, DOI: 10.1016/j.apenergy.2019.114249.

- [265] Giglio, E.; Deorsola, F. A.; Gruber, M.; Harth, S. R.; Morosanu, E. A.; Trimis, D.; Bensaid, S.; Pirone, R. Power-to-Gas through High Temperature Electrolysis and Carbon Dioxide Methanation: Reactor Design and Process Modeling. *Ind. Eng. Chem. Res.* **2018**, *57*, 4007–4018, DOI: 10.1021/acs.iecr.8b00477.
- [266] Schweizerische Eidgenossenschaft, State Secretariat for Education, Research and Innovation SERI. STORE&GO. <https://www.storeandgo.info/> (accessed Apr. 28, 2020).
- [267] Climeworks. STORE&GO. <https://www.climeworks.com/case-studies/store-and-go/> (accessed Apr. 28, 2020).
- [268] Schollenberger, D.; Bajohr, S.; Gruber, M.; Reimert, R.; Kolb, T. Scale-Up of Innovative Honeycomb Reactors for Power-to-Gas Applications – The Project Store&Go. *Chem. Ing. Tech.* **2018**, *90*, 696–702, DOI: 10.1002/cite.201700139.
- [269] Morosanu, E. A.; Saldivia, A.; Antonini, M.; Bensaid, S. Process Modeling of an Innovative Power to LNG Demonstration Plant. *Energy Fuels* **2018**, *32*, 8868–8879, DOI: 10.1021/acs.energyfuels.8b01078.
- [270] Gorre, J.; Ortloff, F.; van Leeuwen, C. Production costs for synthetic methane in 2030 and 2050 of an optimized Power-to-Gas plant with intermediate hydrogen storage. *Appl. Energy* **2019**, *253*, 113594, DOI: 10.1016/j.apenergy.2019.113594.
- [271] Friedl, M. *Pilot- und Demonstrationsanlage Power-to-Methane HSR*; tech. rep.; HSR Hochschule für Technik Rapperswil: Rapperswil, Switzerland, 2015.
- [272] Vázquez, F. V.; Koponen, J.; Ruuskanen, V.; Bajamundi, C.; Kosonen, A.; Simell, P.; Ahola, J.; Frilund, C.; Elfving, J.; Reinikainen, M.; Heikkinen, N.; Kauppinen, J.; Piermartini, P. Power-to-X technology using renewable electricity and carbon dioxide from ambient air: SOLETAIR proof-of-concept and improved process concept. *J. CO₂ Util.* **2018**, *28*, 235–246, DOI: 10.1016/j.jcou.2018.09.026.
- [273] Olah, G. A.; Prakash, G. K. S.; Goepfert, A. Anthropogenic Chemical Carbon Cycle for a Sustainable Future. *J. Am. Chem. Soc.* **2011**, *133*, 12881–12898, DOI: 10.1021/ja202642y.
- [274] Drechsler, C.; Agar, D. W. Characteristics of DAC operation within integrated PtG concepts. *Int. J. Greenhouse Gas Control* **2021**, *105*, 103230, DOI: 10.1016/j.ijggc.2020.103230.
- [275] Drechsler, C.; Agar, D. W. Intensified integrated direct air capture - power-to-gas process based on H₂O and CO₂ from ambient air. *Appl. Energy* **2020**, *273*, 115076, DOI: 10.1016/j.apenergy.2020.115076.
- [276] Arora, P.; Chance, R.; Hendrix, H.; Realff, M. J.; Thomas, V. M.; Yuan, Y. Life cycle greenhouse gas emissions of different CO₂ supply options for an algal biorefinery. *J. CO₂ Util.* **2020**, *40*, 101213, DOI: 10.1016/j.jcou.2020.101213.
- [277] Carmo, M.; Fritz, D. L.; Mergel, J.; Stolten, D. A comprehensive review on PEM water electrolysis. *Int. J. Hydrogen Energy* **2013**, *38*, 4901–4934, DOI: 10.1016/j.ijhydene.2013.01.151.

- [278] Kuang, Y.; Kenney, M. J.; Meng, Y.; Hung, W. H.; Liu, Y.; Huang, J. E.; Prasanna, R.; Li, P.; Li, Y.; Wang, L.; Lin, M. C.; McGehee, M. D.; Sun, X.; Dai, H. Solar-driven, highly sustained splitting of seawater into hydrogen and oxygen fuels. *Proc. Natl. Acad. Sci. U.S.A.* **2019**, *116*, 6624–6629, DOI: 10.1073/pnas.1900556116.
- [279] Kumari, S.; White, R. T.; Kumar, B.; Spurgeon, J. M. Solar hydrogen production from seawater vapor electrolysis. *Energy Environ. Sci.* **2016**, *9*, 1725–1733, DOI: 10.1039/c5ee03568f.
- [280] Kumar, S. S.; Himabindu, V. Hydrogen production by PEM water electrolysis – A review. *Mater. Sci. Energy Technol* **2019**, *2*, 442–454, DOI: 10.1016/j.mset.2019.03.002.
- [281] Poe, W. A.; Mokhatab, S. *Modeling, Control, and Optimization of Natural Gas Processing Plants*; Gulf Professional Publishing: Cambridge, MA and Oxford, UK, 2017, DOI: 10.1016/c2014-0-03765-3.
- [282] Woods, D. R. *Rules of Thumb in Engineering Practice*; Wiley-VCH Verlag GmbH & Co. KGaA: Weinheim, Germany, 2007, DOI: 10.1002/9783527611119.
- [283] De Saint Jean, M.; Baurens, P.; Bouallou, C. Parametric study of an efficient renewable power-to-substitute-natural-gas process including high-temperature steam electrolysis. *Int. J. Hydrogen Energy* **2014**, *39*, 17024–17039, DOI: 10.1016/j.ijhydene.2014.08.091.
- [284] Müller, B.; Müller, K.; Teichmann, D.; Arlt, W. Energiespeicherung mittels Methan und energietragenden Stoffen - ein thermodynamischer Vergleich. *Chem. Ing. Tech.* **2011**, *83*, 2002–2013, DOI: 10.1002/cite.201100113.
- [285] Veziroglu, T. N.; Sherif, S. A.; Babir, F. Hydrogen Energy Solutions. In *Environmental Solutions*; Agardy, F. J., Nemerow, N. L., Eds.; Elsevier Academic Press: Burlington, MA, San Diego, CA and London, UK, 2005; pp 143–180, DOI: 10.1016/b978-012088441-4/50008-3.
- [286] Kai, J.; Saito, R.; Terabaru, K.; Li, H.; Nakajima, H.; Ito, K. Effect of Temperature on the Performance of Polymer Electrolyte Membrane Water Electrolysis: Numerical Analysis of Electrolysis Voltage Considering Gas/Liquid Two-Phase Flow. *J. Electrochem. Soc.* **2019**, *166*, F246–F254, DOI: 10.1149/2.0521904jes.
- [287] Antonucci, V.; Di Blasi, A.; Baglio, V.; Ornelas, R.; Matteucci, F.; Ledesma-Garcia, J.; Arriaga, L. G.; Aricò, A. S. High temperature operation of a composite membrane-based solid polymer electrolyte water electrolyser. *Electrochim. Acta* **2008**, *53*, 7350–7356, DOI: 10.1016/j.electacta.2008.04.009.
- [288] Arico', A. S.; Baglio, V.; Di Blasi, A.; Antonucci, V.; Cirillo, L.; Ghielmi, A.; Arcella, V. Proton exchange membranes based on the short-side-chain perfluorinated ionomer for high temperature direct methanol fuel cells. *Desalination* **2006**, *199*, 271–273, DOI: 10.1016/j.desal.2006.03.065.

- [289] Daggash, H. A.; Patzschke, C. F.; Heuberger, C. F.; Zhu, L.; Hellgardt, K.; Fennell, P. S.; Bhave, A. N.; Bardow, A.; Mac Dowell, N. Closing the carbon cycle to maximise climate change mitigation: power-to-methanol vs. power-to-direct air capture. *Sustainable Energy Fuels* **2018**, *2*, 1153–1169, DOI: 10.1039/c8se00061a.
- [290] Deutz, S.; Bardow, A. Life-cycle assessment of an industrial direct air capture process based on temperature-vacuum swing adsorption. *Nature Energy* **2021**, *6*, 203–213, DOI: 10.1038/s41560-020-00771-9.
- [291] Terlouw, T.; Bauer, C.; Rosa, L.; Mazzotti, M. Life cycle assessment of carbon dioxide removal technologies: a critical review. *Energy Environ. Sci.* **2021**, DOI: 10.1039/d0ee03757e.
- [292] Wilcox, J.; Psarras, P. C.; Liguori, S. Assessment of reasonable opportunities for direct air capture. *Environ. Res. Lett.* **2017**, *12*, 065001, DOI: 10.1088/1748-9326/aa6de5.
- [293] Hoppe, W.; Thonemann, N.; Bringezu, S. Life Cycle Assessment of Carbon Dioxide-Based Production of Methane and Methanol and Derived Polymers. *J. Ind. Ecol.* **2017**, *22*, 327–340, DOI: 10.1111/jiec.12583.
- [294] Icha, P.; Kuhs, G. *Entwicklung der spezifischen Kohlendioxid-Emissionen des deutschen Strommix in den Jahren 1990 - 2019*; tech. rep.; Umwelt Bundesamt: Dessau, Germany, 2020.
- [295] Zeman, F. S.; Lackner, K. S. CAPTURING CARBON DIOXIDE DIRECTLY FROM THE ATMOSPHERE. *World Resour. Rev.* **2004**, *16*, 157–172.
- [296] Zeman, F. Energy and Material Balance of CO₂ Capture from Ambient Air. *Environ. Sci. Technol.* **2007**, *41*, 7558–7563, DOI: 10.1021/es070874m.
- [297] Bandi, A.; Specht, M.; Weimer, T.; Schaber, K. CO₂ recycling for hydrogen storage and transportation — Electrochemical CO₂ removal and fixation. *Energy Convers. Manage.* **1995**, *36*, 899–902, DOI: 10.1016/0196-8904(95)00148-7.
- [298] Advantech. <https://www.advantech.eu> (accessed Dec. 23, 2020).
- [299] Messer. Gases for Life. <https://www.messergroup.com/de/home> (accessed Mar. 5, 2020).
- [300] *Thermoelement Typ K, NiCr-Ni nach IEC 584-1.ITS 90 (DIN EN 60 584)*; SE Sensor Electric e.K.: Siegburg, Germany, 2020.
- [301] *Betriebsanleitung ME*; Julabo Labortechnik GmbH: Seelbach, Germany, 2012.
- [302] *HORST Heizbänder Heizschläuche Temperaturregler Heizmanschetten Spezialheizungen*; HORST GmbH: Lorsch, Germany, 2021.
- [303] *Circulators MV-4/MV-6/MV-12/MV-26 MW-Z*; Julabo Labortechnik GmbH: Seelbach, Germany, 2003.
- [304] *Betriebsanleitung Umwälzthermostate*; Julabo Labortechnik GmbH: Seelbach, Germany, 2018.

- [305] *Betriebsanleitung GMH 3350*; GHM Messtechnik GmbH: Greisinger, Germany, 2021.
- [306] *Operating instruction Analytical balance KERN ALJ_N/ALS_N*; KERN & Sohn GmbH: Balingen, Germany, 2007.
- [307] *3300 Series Compact Low Pressure OEM Pressure Transmitters*; Automatic Company Controls: Clemmons, NC, 2011.
- [308] *Hochwertiger Druckmessumformer Für allgemeine industrielle Anwendungen Typ S-10*; WIKA Alexander Wiegand SE & Co. KG: Klingenberg, Germany, 2018.
- [309] *NETZSCH-Beads®*; NETZSCH-Feinmahltechnik GmbH: Selb, Germany, 2019.
- [310] Schott. Produkte. <https://www.schott.com/tubing/german/products/index.html> (accessed Dec. 29, 2020).
- [311] Delgado, J. M. P. Q. A critical review of dispersion in packed beds. *Heat Mass Transfer* **2005**, *42*, 279–310, DOI: 10.1007/s00231-005-0019-0.
- [312] Schiesser, W. E.; Griffiths, G. W. *A Compendium of Partial Differential Equation Models: Method of Lines Analysis with Matlab*; Cambridge University Press: Cambridge, UK, 2009, DOI: 10.1017/CB09780511576270.
- [313] Berg, F. Experimentelle und theoretische Untersuchungen zur adsorptiven Aufreinigung von Erdgasen, Ph.D. Thesis, Duisburg-Essen University, Germany, 2019.
- [314] Birkmann, F. Experimentelle und theoretische Untersuchungen zur Adsorption kurzkettiger Kohlenwasserstoffe bei tiefen Temperaturen, Ph.D. Thesis, Duisburg-Essen University, Germany, 2018.
- [315] Mersmann, A.; Kind, M.; Stichlmair, J. *Thermische Verfahrenstechnik*, 2nd ed.; Springer-Verlag GmbH: Berlin, Germany and Heidelberg, Germany, 2005, DOI: 10.1007/3-540-28052-9.
- [316] Mühl, T. *Elektrische Messtechnik*, 5th ed.; Springer Vieweg: Wiesbaden, Germany, 2017, DOI: 10.1007/978-3-658-15720-3.
- [317] *Bedienungsanleitung METTLER TOLEDO MT/UMT-Waagen*; Mettler-Toledo GmbH: Greifensee, Switzerland, 1999.
- [318] Zierp, J.; Bühler, K. *Grundzüge der Strömungslehre*, 8th ed.; Vieweg+Teubner: Wiesbaden, Germany, 2010, DOI: 10.1007/978-3-8348-9756-5.
- [319] Malberg, H. *Meteorologie und Klimatologie*, 5th ed.; Springer-Verlag GmbH: Berlin, Germany and Heidelberg, Germany, 2007, DOI: 10.1007/978-3-540-37222-6.
- [320] NETZSCH-Gerätebau GmbH. Zertifikat über die Kalibrierung der STA 409, 2000.
- [321] *TD1 Tapped Density Tester*; SOTAX GmbH: Lörrach, Germany, 2020.
- [322] Eisaman, M. D.; E, S. D.; Amic, S.; Larner, D.; Zesch, J.; Torres, F.; Littau, K. Energy-efficient electrochemical CO₂ capture from the atmosphere. In *Technical Proceedings of the 2009 Clean Technology Conference and Trade*, Proceedings of the 2009 Clean Technology Conference and Trade, Houston, TX, May 3-7, 2009; TechConnect Briefs, 175–178.

- [323] House, K. Z.; Baclig, A. C.; Ranjan, M.; van Nierop, E. A.; Wilcox, J.; Herzog, H. J. Economic and energetic analysis of capturing CO₂ from ambient air. *Proc. Natl. Acad. Sci.* **2011**, *108*, 20428–20433, DOI: 10.1073/pnas.1012253108.
- [324] Li, C.; Shi, H.; Cao, Y.; Kuang, Y.; Zhang, Y.; Gao, D.; Sun, L. Modeling and optimal operation of carbon capture from the air driven by intermittent and volatile wind power. *Energy* **2015**, *87*, 201–211, DOI: 10.1016/j.energy.2015.04.098.
- [325] Bazzanella, A. *CO₂Plus – Stoffliche Nutzung von CO₂ zur Verbreiterung der Rohstoffbasis: Abschlussbericht*; tech. rep.; DECHEMA Gesellschaft für Chemische Technik und Biotechnologie e.V.: Frankfurt am Main, Germany, 2019.
- [326] Ishimoto, Y.; Sugiyama, M.; Kato, E.; Moriyama, R.; Tsuzuki, K.; Kurosawa, A. *Putting costs of direct air capture in context*; tech. rep.; American University, School of International Service: Washington, DC, 2017.
- [327] Bajamundi, C.; Elfving, J.; Kauppinen, J. Assessment of the performance of a bench scale direct air capture device operated at outdoor environment. Presented at International Conference on Negative CO₂ Emissions, Gothenburg, Sweden, May 22-24, 2018.
- [328] Brillings, B. H.; Bleil, D. F.; Cook, R. K.; Crosswhite, H. M.; Frederikse, H. P. R.; Lindsay, R. B.; Marion, J. B.; Zemansky, M. W. *American Institute of Physics Handbook*, 3rd ed.; Gray, D. E., Ed.; McGraw-Hill: New York, NY, 1972.
- [329] Ho, C. Y.; Powell, R. W.; Liley, P. E. Thermal Conductivity of the Elements. *J. Phys. Chem. Ref. Data* **1972**, *1*, 279–421, DOI: 10.1063/1.3253100.
- [330] Lemmon, E. W.; Jacobsen, R. T.; Penoncello, S. G.; Friend, D. G. Thermodynamic Properties of Air and Mixtures of Nitrogen, Argon, and Oxygen From 60 to 2000 K at Pressures to 2000 MPa. *J. Phys. Chem. Ref. Data* **2000**, *29*, 331–385, DOI: 10.1063/1.1285884.
- [331] Subramaniam, S. Minimum Error Fickian Diffusion Coefficients for Mass Diffusion in Multicomponent Gas Mixtures. *J. Non-Equilib. Thermodyn.* **1999**, *24*, 1–39, DOI: 10.1515/jnetdy.1999.001.
- [332] Annamalai, K.; Puri, I. K.; Jog, M. A. *Advanced Thermodynamics Engineering*, 2nd ed.; CRC Press: Boca Raton, FL, 2011, DOI: 10.1201/9781439805718.
- [333] Yaws, C. C. *Handbook of Transport Property Data*; Gulf Publishing Company: Houston, TX, 1995.
- [334] Wilke, C. R. A Viscosity Equation for Gas Mixtures. *J. Chem. Phys.* **1950**, *18*, 517–519, DOI: 10.1063/1.1747673.
- [335] Neufeld, P. D.; Janzen, A. R.; Aziz, R. A. Empirical Equations to Calculate 16 of the Transport Collision Integrals $\Omega^{(l,s)*}$ for the Lennard-Jones (12-6) Potential. *J. Chem. Phys.* **1972**, *57*, 1100–1101, DOI: 10.1063/1.1678363.
- [336] Chung, T. H.; Lee, L. L.; Starling, K. E. Applications of kinetic gas theories and multiparameter correlation for prediction of dilute gas viscosity and thermal conductivity. *Ind. Eng. Chem. Fundam.* **1984**, *23*, 8–13, DOI: 10.1021/i100013a002.

- [337] Chung, T. H.; Ajlan, M.; Lee, L. L.; Starling, K. E. Generalized multiparameter correlation for nonpolar and polar fluid transport properties. *Ind. Eng. Chem. Res.* **1988**, *27*, 671–679, DOI: 10.1021/ie00076a024.
- [338] Wassiljewa, A. Heat-Conduction in gaseous mixtures. *Phys. Z.* **1904**, *5*, 737–742.
- [339] Mason, E. A.; Saxena, S. C. Approximate Formula for the Thermal Conductivity of Gas Mixtures. *Phys. Fluids* **1958**, *1*, 361–369, DOI: 10.1063/1.1724352.
- [340] Bärwolff, G. *Numerik für Ingenieure, Physiker und Informatiker*, 2nd ed.; Springer Spektrum: Berlin, Germany and Heidelberg, Germany, 2016, DOI: 10.1007/978-3-662-48016-8.
- [341] *Operation manual Reglo-z*; Ismatec: Wertheim, Germany, 2015.
- [342] Ultimaker. Ultimaker. <https://ultimaker.com/de/> (accessed July 30, 2020).
- [343] *INSTALLATION & OPERATION INSTRUCTIONS FOR KOBOLD KFR-1000 THRU KFR-4000 SERIES FLOWMETERS*; KOBOLD Instruments Inc.: Pittsburgh, PA, 2009.
- [344] *Die neue Quintix®. Komfortabel Wägen*; Sartorius Lab Instruments GmbH & Co. KG: Göttingen, Germany, 2014.
- [345] *JUMO MIDAS C08*; JUMO GmbH & Co. KG: Fulda, Germany, 2020.
- [346] Staista. Jährliche Entwicklung des Wechselkurses des Euro gegenüber dem US-Dollar von 1999 bis 2020. <https://de.statista.com/statistik/daten/studie/200194/umfrage/wechselkurs-des-euro-gegenueber-dem-us-dollar-seit-2001/> (accessed Jan. 18, 2021).
- [347] Couper, J. R.; Roy Penney, W.; Fair, J. R.; Walas, S. M. *Chemical Process Equipment*, 2nd ed.; Gulf Professional Publishing: Burlington, MA and Oxford, UK, 2005, DOI: 10.1016/b978-0-7506-7510-9.x5000-1.
- [348] Jenkins, S. 2019 Chemical Engineering Plant Cost Index Annual Average. <https://www.chemengonline.com/2019-chemical-engineering-plant-cost-index-annual-average/> (accessed Jan. 14, 2021).
- [349] Bollinger, K.; Grohmann, M.; Feldmann, M.; Giebeler, G.; Pfanner, D.; Zeumer, D. *Atlas moderner Stahlbau*; Institut für internationale Architektur-Dokumentation GmbH&Co. KG: Munich, Germany, 2011, DOI: 10.11129/detail.9783955530044.
- [350] Janisch, A. Kostenfaktoren im Stahlbau - was kostet ein Kg Stahlbau 2020? <https://jactio.com/kostenfaktoren-im-stahlbau/> (accessed Jan. 20, 2021).
- [351] Büchner, H.-J. Rohstoffpreise: Aktuelle Tendenzen: Der Weg nach unten? <https://www.ikb-blog.de/rohstoffpreise-aktuelle-tendenzen-der-weg-nach-unten/>.
- [352] Ilic, M. Online-Handel mit Edelstahl-Erzeugnissen. <https://www.drahtgeflecht-shop.de/drahtgewebe-aus-edelstahl/> (accessed Jan. 18, 2021).

-
- [353] Lanxess, Cologne, Germany. Personal communication, 2018.
- [354] Referat 603. *Monitoringbericht 2019*; tech. rep.; Bundesnetzagentur für Elektrizität, Gas, Telekommunikation, Post und Eisenbahnen: Bonn, Germany, 2020.
- [355] Gniffke, P. *Carbon Dioxide Emissions for the German Atmospheric Emission Reporting*; tech. rep.; Umwelt Bundesamt: Dessau, Germany, 2020.
- [356] Chempoint, Maastricht, Netherlands. Personal communication, 2020.
- [357] Wagner, W.; Kretzschmar, H.-J. *International Steam Tables*, 2nd ed.; Springer-Verlag GmbH: Berlin, Germany and Heidelberg, Germany, 2008, DOI: 10.1007/978-3-540-74234-0.
- [358] *SYLOBEAD[®] Adsorbents for Process Applications*; Grace Davison: Columbia, MD, 2010.
- [359] Gabruś, E.; Witkiewicz, K.; Nastaj, J. Modeling of regeneration stage of 3A and 4A zeolite molecular sieves in TSA process used for dewatering of aliphatic alcohols. *Chem. Eng. J.* **2018**, *337*, 416–427, DOI: 10.1016/j.cej.2017.12.112.
- [360] Koschany, F.; Schlereth, D.; Hinrichsen, O. On the kinetics of the methanation of carbon dioxide on coprecipitated NiAl(O)_x. *Appl. Catal., B* **2016**, *181*, 504–516, DOI: 10.1016/j.apcatb.2015.07.026.
- [361] Reiss, G. DIE VERWENDUNG VON MOLEKULARSIEB-ZEOLITHE IN DER ADSORPTIONSTECHNIK. *Period. Polytech., Chem. Eng.* **1975**, *19*, 137–164.
- [362] Wegstein, J. H. Accelerating convergence of iterative processes. *Commun. ACM* **1958**, *1* (6), 9–13, DOI: 10.1145/368861.368871.

Student support

I would like to thank the students who have conducted their research internships or theses in the framework of this project or have participated in it as student assistants.

My thanks go to Ufuk Alkan^{E.BT2}, Frodewin Brumshagen^{E.BI2,E.BT4}, Adriana Cabrera Del Risco^{E.MT5}, Kai Grenningloh^{E.BT5} and Steffen Nitsche^{E.BT1} who helped conducting the experiments to record the experimental raw data sets of the adsorption processes used in this work and if needed realized minor modifications of the plants for *BTC* and *TGA* experiments. Special thanks go to my colleague Florian Keuchel^{E.MT4}, who, under my supervision during his master thesis, helped modifying the *BTC* plant to allow for realization of experiments under humid conditions and conducted experiments to record preliminary raw data sets under humid conditions, which helped setting the framework for future experiments.

With regard to the experiments performed, I would also like to name Steffen Nitsche^{E.BT1} and Michael Rix^{T.BT1}, who helped determining the additional thermophysical properties of *Lewatit*. Moreover, my thanks go to Sabrina Covello-Grimm^{E.MT2} and Tobias Kanka^{E.MT3}, who both conducted their master theses within the framework of the experimental investigation of transport phenomena. Thank you for your support while building the plant and for the time you invested to record the experimental raw data sets.

I would also like to thank Juan Alava Cedeno^{T.MT1}, Hui Li^{T.MT4}, Theresa Overbeck^{T.MT2}, Michel Rix^{T.BT1} and Ruchika Tawani^{T.MT3}, who performed basic simulation studies under my supervision. Even if the results of your great works are not explicitly included in this contribution, I really value our conversations over the different topics that supported the progress of this work. In this respect, I would like to mention the results of the simplified, basic studies of solid transfer medium selection, mechanical stability of the concepts and cost estimation performed by Michel Rix^{T.BT1} that helped to reduce the effort of realizing more detailed and complex implementations and evaluations by myself.

Finally my thanks go to Jelena Auch^{E.MI2}, Christian Chodun^{E.MI1}, Michael Hähnel^{E.BI3}, Maurice Hesselmann^{E.MT1} and Simone Stolz^{E.BI1,E.BT3} who helped performing basic experimental investigations with regard to CO₂-mineralization and to hydrophobization of *Lewatit*. Even if, as a result of the early stage of research, the results we obtained are not published within the framework of this contribution, I nevertheless want to underline the great work you have done.

Overall, I would like to say that I really enjoyed working with all of you and that I am very proud of and impressed by your great works and the team spirit we realized.

Supervised experimental work

- [E.BI1] Stolz, S. Untersuchungen der Einflüsse verschiedener Suspensionsmittel auf die Kohlendioxidadsorptionskapazität des aminfunktionalisierten Ionenaustauscherharzes Lewatit VP OC 1065. Bachelor research internship, TU Dortmund University, Germany, 2020.
- [E.BI2] Brumshagen, F. Einfluss von Schadgasen auf das CO₂-Adsorptionsverhalten von Lewatit VP OC 1065. Bachelor research internship, TU Dortmund University, Germany, 2019.
- [E.BI3] Hähnel, M. Experimente zur Untersuchung der Mineralisierung von Calciummetasilicat mit DMC. Bachelor research internship, TU Dortmund University, Germany, 2018.
- [E.BT1] Nitsche, S. Detaillierte experimentelle Untersuchung der CO₂- und H₂O-Adsorption auf Lewatit VP OC 1065. Bachelor thesis, TU Dortmund University, Germany, 2020.
- [E.BT2] Alkan, U. Charakterisierung der Wasser- bzw. CO₂-Adsorption auf Lewatit VP OC 1065 mit Schwerpunkt auf DAC-Anwendungen. Bachelor thesis, TU Dortmund University, Germany, 2020.
- [E.BT3] Stolz, S. Untersuchung verschiedener Reaktionswege zur Hydrophobisierung des aminfunktionalisierten Ionenaustauscherharzes Lewatit VP OC 1065. Bachelor thesis, TU Dortmund University, Germany, 2020.
- [E.BT4] Brumshagen, F. Charakterisation of adsorption behaviour of Lewatit VP OC 1065. Bachelor thesis, TU Dortmund University, Germany, 2019.
- [E.BT5] Grenningloh, K. Untersuchung individueller Einflüsse auf die Adsorptionskinetik von CO₂ auf Lewatit VP OC 1065. Bachelor thesis, TU Dortmund University, Germany, April 2019.
- [E.MI1] Chodrun, C. Modifikation von Lewatit VPOC 1065 mittels FRIEDEL-CRAFTS-Alkylierung mit Chloralkanen. Master research internship, TU Dortmund University, Germany, 2019.
- [E.MI2] Auch, J. Hydrophobisierung des Ionenaustauscherharzes Lewatit VP OC 1065. Master research internship, TU Dortmund University, Germany, 2019.
- [E.MT1] Hesselmann, M. Chemische Modifizierung des aminfunktionalisierten Ionenaustauscherharzes Lewatit VP OC 1065 mit speziellem Fokus auf hydrophobe Eigenschaften. Master thesis, TU Dortmund University, Germany, 2021.
- [E.MT2] Covello-Grimm, S. Optimale Auslegung der Kontaktorgeometrie für feste Adsorbentien bei DAC-Anwendungen. Master thesis, TU Dortmund University, Germany, 2019.
- [E.MT3] Kanka, T. Evaluation of Compact Structures on their usability as DAC-system elements. Master thesis, TU Dortmund University, Germany, 2018.
- [E.MT4] Keuchel, F. Determination of the influence of humidity on the isotherms and kinetics of CO₂ adsorption on Lewatit. Master thesis, TU Dortmund University, Germany, 2018.
- [E.MT5] Cabrera Del Risco, A. P. Determination of the isotherms and kinetics of the CO₂ adsorption on Lewatit. Master thesis, TU Dortmund University, Germany, 2018.

Supervised theoretical work

- [T.BT1] Rix, M. Detaillierte Kostenschätzung und Machbarkeitsstudie für hoch wärmeintegrierte Direct Air Capture Konzepte. Bachelor thesis, TU Dortmund University, Germany, 2020.
- [T.MT1] Alava Cedeno, J. M. Optimal cost-based design of a highly energy integrated DAC-PTG process. Master thesis, TU Dortmund University, Germany, 2019.
- [T.MT2] Overbeck, T. Modeling and simulation of a continuously operated Temperature-Vacuum-Swing-Adsorption-Process for direct air capture of CO₂. Master thesis, TU Dortmund University, Germany, 2018.
- [T.MT3] Tawani, R. Simulation and Optimisation of a Rotating Wheel Adsorber Concept for Direct Air Capture of Carbon Dioxide. Master thesis, TU Dortmund University, Germany, 2018.
- [T.MT4] Li, H. Modeling and simulation of a moving band adsorber for the direct air capture of carbon dioxide. Master thesis, TU Dortmund University, Germany, 2018.

Additional support

At this place, I would like to thank the people who have supported me in realizing this work by giving additional technical support, scientific advice or valuable feedback to the content and style of this contribution.

Special thanks go to Prof. David W. Agar, for his support and guidance, as well as to my former and current colleagues. In this respect, I would like to especially thank Linda Arsenjuk, Tobias Becker, David Hellmann, Christian Schwarz and Maximilian Wieseahn for the discussions we had about the scientific problems related to the subject of this work. This also holds true for Marius Gelhausen, Florian Keuchel and Niclas von Vietinghoff who additionally provided valuable feedback with regard to the content and style of the manuscript.

I would like to name the teams of the mechanical, technical and glass workshops of TU Dortmund University, who supported this work while realizing parts of the equipment used. Moreover, my thanks go to the technical staff of the chairs of the Department of Biochemical and Chemical Engineering, from which I would like to especially name Volker Brandt and Michael Schlüter.

I would also like to thank my brother Tobias Kaiser for our scientific discussions and for his feedback on the style and content of this contribution. Last but not least, my thanks go to my good friend Clay Greene, my sister-in-law Miriam Kaiser and my wife Jana Drechsler for their valuable feedback with regard to the style of this work.

Curriculum vitae

Personal data

Name	Carsten Drechsler, né Asmanoglo
Date of birth	September 23, 1990
Place of birth	Castrop-Rauxel, Germany
Nationality	German
ORCID	0000-0003-2642-3303

Professional occupation

since 03/2017	Graduate research assistant, Chair of Chemical Reaction Engineering, TU Dortmund University, Germany
08/2018 – 11/2018	Visiting researcher, Department of Chemical Engineering, Laval University, Québec, Canada
04/2014 – 01/2016	Student research assistant, Chair of Chemical Reaction Engineering, TU Dortmund University, Germany

University education

11/2016	Academic degree: Master of Science (M.Sc.) in Chemical Engineering
04/2015 – 11/2016	Chemical Engineering (master studies), TU Dortmund University, Germany
03/2015	Academic degree: Bachelor of Science (B.Sc.) in Chemical Engineering
10/2011 – 03/2015	Chemical Engineering (bachelor studies), TU Dortmund University, Germany

School education

06/2010	Abitur (University-entrance Diploma), Heinrich-Heine-Gymnasium, Dortmund, Germany
---------	---

